

¹

DarkSide-20k Technical Design Report

²

The Global Argon Dark Matter Collaboration

³

INFN-DS20k-TDR– v3.0 For Public pre-Release

⁴

November 30, 2021

DarkSide-20k List of Authors and Participating Institutions

- 6 P. Agnes,^{1,2} I. Ahmad,³ S. Albergo,^{4,5} I. F. M. Albuquerque,⁶ T. Alexander,⁷ A. Alici,^{8,9}
 7 A. K. Alton,¹⁰ P. Amaudruz,¹¹ E. Aprile,¹² S. Arcelli,^{8,9} P. Arpaia,^{13,14} M. Ave,⁶ I. C. Avetisov,¹⁵
 8 R. I. Avetisov,¹⁵ O. Azzolini,¹⁶ H. O. Back,⁷ Z. Balmforth,² A. Barrado Olmedo,¹⁷
 9 P. Barrillon,¹⁸ A. Basco,¹⁴ G. Batignani,^{19,20} V. Bocci,²¹ A. Bondar,^{22,23} W. M. Bonivento,²⁴
 10 E. Borisova,^{22,23} B. Bottino,^{25,26} M. G. Boulay,²⁷ G. Buccino,²⁸ S. Bussino,^{29,30} J. Busto,¹⁸
 11 A. Buzulutskov,^{22,23} M. Cadeddu,^{31,24} M. Cadoni,^{31,24} R. Calabrese,^{32,14} A. Caminata,²⁶
 12 N. Canci,²⁸ A. Capra,¹¹ M. Caravati,²⁴ M. Cárdenas-Montes,¹⁷ N. Cargioli,^{31,24} M. Carleo,¹⁴
 13 M. Carlini,²⁸ F. Carnesecchi,^{9,8} P. Castello,^{33,24} V. Cataudella,^{32,14} D. Cavallo,^{34,26}
 14 S. Cavuoti,^{35,14} S. Cebríán,³⁶ J.M. Cela Ruiz,¹⁷ B. Celano,¹⁴ S. Chashin,³⁷ A. Chepurnov,³⁷
 15 S. Choudhary,³ E. Chyhrynets,¹⁶ C. Ciccalò,²⁴ L. Cifarelli,^{8,9} D. Cintas,³⁶ V. Cocco,²⁴
 16 M. Colocci,^{8,9} E. Conde Vilda,¹⁷ L. Consiglio,²⁸ S. Copello,^{26,38} G. Covone,^{32,14} S. D'Auria,³⁹
 17 M. D. Da Rocha Rolo,⁴⁰ M. Daniel,¹⁷ M. D'Aniello,^{41,14} O. Dadoun,⁴² S. Davini,²⁶
 18 A. De Candia,^{32,14} S. De Cecco,^{21,43} A. De Falco,^{31,24} G. De Filippis,^{32,14} D. De Gruttola,^{44,45}
 19 G. De Guido,⁴⁶ G. De Rosa,^{32,14} S. De Pasquale,^{44,45} M. Della Valle,^{35,14} G. Dellacasa,⁴⁰
 20 A. V. Derbin,⁴⁷ A. Devoto,^{31,24} F. Di Capua,^{32,14} L. Di Noto,²⁶ P. Di Stefano,⁴⁸ C. Dionisi,^{21,43}
 21 G. Dolganov,⁴⁹ F. Dordei,²⁴ L. Doria,⁵⁰ T. Erjavec,⁵¹ M. Fernandez Diaz,¹⁷ G. Fiorillo,^{32,14}
 22 A. Franceschi,⁵² P. Franchini,⁵³ D. Franco,⁵⁴ E. Frolov,^{22,23} N. Funicello,^{45,44} F. Gabriele,²⁴
 23 C. Galbiati,^{25,55,28} G. Gallina,^{25,11} M. Garbini,^{56,9} P. Garcia Abia,¹⁷ A. Gendotti,⁵⁷ C. Ghiano,²⁸
 24 R. A. Giampaolo,^{40,58} C. Giganti,⁴² G. K. Giovanetti,⁵⁹ V. Goicoechea Casanueva,⁶⁰ A. Gola,^{61,62}
 25 R. Graciani Diaz,⁶³ L. Grandi,⁶⁴ G. Grauso,¹⁴ G. Y. Grigoriev,⁴⁹ A. Grobov,^{49,65} M. Gromov,^{37,66}
 26 M. Guan,⁶⁷ M. Guerzoni,⁹ M. Gulino,^{68,69} C. Guo,⁶⁷ B. R. Hackett,⁷ A. Hallin,⁷⁰ A. Hamer,^{71,2}
 27 M. Haranczyk,⁷² S. Hill,² S. Horikawa,^{55,28} F. Hubaut,¹⁸ T. Hugues,³ E. V. Hungerford,¹
 28 An. Ianni,^{25,28} V. Ippolito,²¹ C. C. James,⁷³ C. Jillings,^{74,75} P. Kachru,^{55,28} A. A. Kemp,⁴⁸
 29 C. L. Kendziora,⁷³ G. Keppel,¹⁶ A. V. Khomyakov,¹⁵ S. Kim,⁷⁶ M. Kimura,³ A. Kish,⁶⁰
 30 I. Kochanek,²⁸ K. Kondo,²⁸ G. Korga,² A. Kubankin,⁷⁷ R. Kugathasan,^{40,58} M. Kuss,¹⁹
 31 M. Kuźniak,³ M. La Commara,^{78,14} M. Lai,^{31,24} E. Leason,² E. Le Guiriec,¹⁸ X. Li,²⁵
 32 J. Lipp,⁷⁹ M. Lissia,²⁴ G. Longo,^{32,14} L. Luzzi,¹⁷ I. N. Machulin,^{49,65} L. Mapelli,²⁵
 33 A. Margotti,⁹ S. M. Mari,^{29,30} C. Mariani,⁸⁰ J. Maricic,⁶⁰ A. Marini,^{38,26} M. Martínez,^{36,81}
 34 A. D. Martinez Rojas,^{40,58} C. J. Martoff,⁷⁶ A. Masoni,²⁴ K. Mavrokordidis,⁸² A. Mazzi,^{61,62}
 35 A. B. McDonald,⁴⁸ J. McLaughlin,^{11,2} A. Messina,^{21,43} P. D. Meyers,²⁵ T. Miletic,⁶⁰
 36 R. Milincic,⁶⁰ A. Mitra,⁸³ A. Moggi,¹⁹ A. Moharana,^{55,28} S. Moioli,⁴⁶ J. Monroe,² S. Morisi,^{32,14}
 37 M. Morrocchi,^{19,20} E. N. Mozhevitsina,¹⁵ T. Mróz,⁷² V. N. Muratova,⁴⁷ P. Musico,²⁶ R. Nania,⁹
 38 T. Napolitano,⁵² M. Nessi,⁸⁴ K. Ni,⁸⁵ G. Nieradka,³ I. Nikulin,⁷⁷ J. Nowak,⁵³ T. O'Donnell,⁸⁰
 39 A. Oleinik,⁷⁷ V. Oleynikov,^{22,23} P. Organtini,^{25,28} A. Ortiz de Solórzano,³⁶ L. Pagani,⁵¹
 40 M. Pallavicini,^{38,26} L. Pandola,⁶⁹ E. Pantic,⁵¹ E. Paoloni,^{19,20} G. Paternoster,^{61,62} D. Peddis,^{34,26}
 41 P. A. Pegoraro,^{33,24} K. Pelczar,⁷² L. A. Pellegrini,⁴⁶ C. Pellegrino,⁹ F. Perotti,^{86,39} V. Pesudo,¹⁷
 42 E. Picciau,^{31,24} F. Pietropaolo,⁸⁴ C. Pira,¹⁶ G. Plante,¹² A. Pocar,⁸⁷ M. Poehlmann,⁵¹
 43 S. Pordes,⁷³ S. S. Poudel,¹ P. Pralavorio,¹⁸ D. Price,⁸⁸ F. Ragusa,^{89,39} Y. A. Ramachers,⁸³
 44 A. Ramirez,¹ M. Razeti,²⁴ A. Razeto,²⁸ A. L. Renshaw,¹ S. Rescina,⁹⁰ M. Rescigno,²¹ F. Resnati,⁸⁴
 45 F. Retiere,¹¹ L. P. Rignanese,^{9,8} C. Ripoli,^{45,44} A. Rivetti,⁴⁰ A. Roberts,⁸² J. Rode,^{42,54}
 46 L. Romero,¹⁷ M. Rossi,^{26,38} A. Rubbia,⁵⁷ E. Sánchez García,¹⁷ P. Salatino,^{91,14} O. Samoylov,⁶⁶
 47 S. Sadashivajois,² E. Sandford,⁸⁸ S. Sanfilippo,^{30,29} D. Santone,² R. Santorelli,¹⁷ C. Savarese,²⁵
 48 E. Scapparone,⁹ G. Schillaci,⁶⁹ B. Schlitzer,⁵¹ G. Scioli,^{8,9} D. A. Semenov,⁴⁷ B. Shaw,¹¹
 49 A. Shchagin,⁷⁷ A. Sheshukov,⁶⁶ M. Simeone,^{91,14} P. Skensved,⁴⁸ M. D. Skorokhvatov,^{49,65}
 50 O. Smirnov,⁶⁶ B. Smith,¹¹ A. Sokolov,^{22,23} F. L. Spadoni,⁷ M. Spangenberg,⁸³ R. Stefanizzi,^{31,24}
 51 A. Steri,²⁴ S. Stracka,¹⁹ V. Strickland,²⁷ M. Stringer,⁴⁸ M. Suchenek,³ S. Sulis,^{33,24} A. Sung,²⁵
 52 Y. Suvorov,^{32,14,49} J. Z. Szűcs-Balazs,⁹² A. M. Szeli,⁷¹ C. Türkoglu,³ R. Tartaglia,²⁸ A. Taylor,⁸²

- 53 J. Taylor,⁸² G. Testera,²⁶ T. N. Thorpe,⁹³ S. Tombinski,⁷² A. Tonazzo,⁵⁴ S. Torres-Lara,¹
 54 G. Tortone,¹⁴ A. Tricomi,^{4,5} E. V. Unzhakov,⁴⁷ G. Usai,^{31,24} T. Vallivilayil John,^{55,28} T. Viant,⁵⁷
 55 S. Vicini,^{34,26} S. Viel,²⁷ A. Vishneva,⁶⁶ R. B. Vogelaar,⁸⁰ J. Vossebeld,⁸² M. Wada,³ M. Walczak,³
 56 H. Wang,⁹³ Y. Wang,⁶⁷ S. Westerdale,²⁵ R. J. Wheadon,⁴⁰ L. Williams,⁹⁴ I. Wingerter-Seez,¹⁸
 57 R. Wojaczyński,³ Ma. M. Wojcik,⁷² Ma. Wojcik,⁹⁵ X. Xiao,⁹³ C. Yang,⁶⁷ A. Zabihi,³ P. Zakhary,³
 58 A. Zani,⁸⁴ Y. Zhang,⁶⁷ A. Zichichi,^{8,9} M. Ziembicki,³ A. Zullo,²¹ G. Zuzel,⁷² and M. P. Zyкова¹⁵
- 59 ¹Department of Physics, University of Houston, Houston, TX 77204, USA
 60 ²Department of Physics, Royal Holloway University of London, Egham TW20 0EX, UK
 61 ³AstroCeNT, Nicolaus Copernicus Astronomical Center, 00-614 Warsaw, Poland
 62 ⁴INFN Catania, Catania 95121, Italy
 63 ⁵Università di Catania, Catania 95124, Italy
 64 ⁶Instituto de Física, Universidade de São Paulo, São Paulo 05508-090, Brazil
 65 ⁷Pacific Northwest National Laboratory, Richland, WA 99352, USA
 66 ⁸Department of Physics and Astronomy, Università degli Studi di Bologna, Bologna 40126, Italy
 67 ⁹INFN Bologna, Bologna 40126, Italy
 68 ¹⁰Physics Department, Augustana University, Sioux Falls, SD 57197, USA
 69 ¹¹TRIUMF, 4004 Wesbrook Mall, Vancouver, BC V6T 2A3, Canada
 70 ¹²Physics Department, Columbia University, New York, NY 10027, USA
 71 ¹³Department of Electrical Engineering and Information Technology,
 72 Università degli Studi "Federico II" di Napoli, Napoli 80125, Italy
 73 ¹⁴INFN Napoli, Napoli 80126, Italy
 74 ¹⁵Mendeleev University of Chemical Technology, Moscow 125047, Russia
 75 ¹⁶INFN Laboratori Nazionali di Legnaro, Legnaro (Padova) 35020, Italy
 76 ¹⁷CIEMAT, Centro de Investigaciones Energéticas, Medioambientales y Tecnológicas, Madrid 28040, Spain
 77 ¹⁸Centre de Physique des Particules de Marseille, Aix
 78 Marseille Univ, CNRS/IN2P3, CPPM, Marseille, France
 79 ¹⁹INFN Pisa, Pisa 56127, Italy
 80 ²⁰Physics Department, Università degli Studi di Pisa, Pisa 56127, Italy
 81 ²¹INFN Sezione di Roma, Roma 00185, Italy
 82 ²²Budker Institute of Nuclear Physics, Novosibirsk 630090, Russia
 83 ²³Novosibirsk State University, Novosibirsk 630090, Russia
 84 ²⁴INFN Cagliari, Cagliari 09042, Italy
 85 ²⁵Physics Department, Princeton University, Princeton, NJ 08544, USA
 86 ²⁶INFN Genova, Genova 16146, Italy
 87 ²⁷Department of Physics, Carleton University, Ottawa, ON K1S 5B6, Canada
 88 ²⁸INFN Laboratori Nazionali del Gran Sasso, Assergi (AQ) 67100, Italy
 89 ²⁹INFN Roma Tre, Roma 00146, Italy
 90 ³⁰Mathematics and Physics Department, Università degli Studi Roma Tre, Roma 00146, Italy
 91 ³¹Physics Department, Università degli Studi di Cagliari, Cagliari 09042, Italy
 92 ³²Physics Department, Università degli Studi "Federico II" di Napoli, Napoli 80126, Italy
 93 ³³Department of Electrical and Electronic Engineering
 94 Engineering, Università degli Studi, Cagliari 09042, Italy
 95 ³⁴Chemistry Department, Università degli Studi di Genova, Genova 16146, Italy
 96 ³⁵INAF Osservatorio Astronomico di Capodimonte, 80131 Napoli, Italy
 97 ³⁶Centro de Astropartículas y Física de Altas Energías, Universidad de Zaragoza, Zaragoza 50009, Spain
 98 ³⁷Skobeltsyn Institute of Nuclear Physics, Lomonosov Moscow State University, Moscow 119234, Russia
 99 ³⁸Physics Department, Università degli Studi di Genova, Genova 16146, Italy
 100 ³⁹INFN Milano, Milano 20133, Italy
 101 ⁴⁰INFN Torino, Torino 10125, Italy
 102 ⁴¹Department of Strutture per l'Ingegneria e l'Architettura,
 103 Università degli Studi "Federico II" di Napoli, Napoli 80134, Italy
 104 ⁴²LPNHE, CNRS/IN2P3, Sorbonne Université, Université de Paris, Paris 75252, France
 105 ⁴³Physics Department, Sapienza Università di Roma, Roma 00185, Italy
 106 ⁴⁴Physics Department, Università degli Studi di Salerno, Salerno 84084, Italy
 107 ⁴⁵INFN Salerno, Salerno 84084, Italy
 108 ⁴⁶Chemistry, Materials and Chemical Engineering Department
 109 "G. Natta", Politecnico di Milano, Milano 20133, Italy
 110 ⁴⁷Saint Petersburg Nuclear Physics Institute, Gatchina 188350, Russia

- 111 ⁴⁸*Department of Physics, Engineering Physics and Astronomy,
112 Queen's University, Kingston, ON K7L 3N6, Canada*
- 113 ⁴⁹*National Research Centre Kurchatov Institute, Moscow 123182, Russia*
- 114 ⁵⁰*Institut für Physik, Johannes Gutenberg-Universität Mainz, Mainz 55099, Germany*
- 115 ⁵¹*Department of Physics, University of California, Davis, CA 95616, USA*
- 116 ⁵²*INFN Laboratori Nazionali di Frascati, Frascati 00044, Italy*
- 117 ⁵³*Physics Department, Lancaster University, Lancaster LA1 4YB, UK*
- 118 ⁵⁴*APC, Université de Paris, CNRS, Astroparticule et Cosmologie, Paris F-75013, France*
- 119 ⁵⁵*Gran Sasso Science Institute, L'Aquila 67100, Italy*
- 120 ⁵⁶*Museo della fisica e Centro studi e Ricerche Enrico Fermi, Roma 00184, Italy*
- 121 ⁵⁷*Institute for Particle Physics, ETH Zürich, Zürich 8093, Switzerland*
- 122 ⁵⁸*Department of Electronics and Communications, Politecnico di Torino, Torino 10129, Italy*
- 123 ⁵⁹*Williams College, Physics Department, Williamstown, MA 01267 USA*
- 124 ⁶⁰*Department of Physics and Astronomy, University of Hawai'i, Honolulu, HI 96822, USA*
- 125 ⁶¹*Fondazione Bruno Kessler, Povo 38123, Italy*
- 126 ⁶²*Trento Institute for Fundamental Physics and Applications, Povo 38123, Italy*
- 127 ⁶³*Universitat de Barcelona, Barcelona E-08028, Catalonia, Spain*
- 128 ⁶⁴*Department of Physics and Kavli Institute for Cosmological
129 Physics, University of Chicago, Chicago, IL 60637, USA*
- 130 ⁶⁵*National Research Nuclear University MEPhI, Moscow 115409, Russia*
- 131 ⁶⁶*Joint Institute for Nuclear Research, Dubna 141980, Russia*
- 132 ⁶⁷*Institute of High Energy Physics, Chinese Academy of Sciences, Beijing 100049, China*
- 133 ⁶⁸*Engineering and Architecture Faculty, Università di Enna Kore, Enna 94100, Italy*
- 134 ⁶⁹*INFN Laboratori Nazionali del Sud, Catania 95123, Italy*
- 135 ⁷⁰*Department of Physics, University of Alberta, Edmonton, AB T6G 2R3, Canada*
- 136 ⁷¹*School of Physics and Astronomy, University of Edinburgh,
137 Peter Guthrie Tait Road, Edinburgh, EH9 3FD, UK*
- 138 ⁷²*M. Smoluchowski Institute of Physics, Jagiellonian University, 30-348 Krakow, Poland*
- 139 ⁷³*Fermi National Accelerator Laboratory, Batavia, IL 60510, USA*
- 140 ⁷⁴*SNOLAB, Lively, ON P3Y 1N2, Canada*
- 141 ⁷⁵*Department of Physics and Astronomy, Laurentian University, Sudbury, ON P3E 2C6, Canada*
- 142 ⁷⁶*Physics Department, Temple University, Philadelphia, PA 19122, USA*
- 143 ⁷⁷*Radiation Physics Laboratory, Belgorod National Research University, Belgorod 308007, Russia*
- 144 ⁷⁸*Pharmacy Department, Università degli Studi "Federico II" di Napoli, Napoli 80131, Italy*
- 145 ⁷⁹*Rutherford Appleton Laboratory, STFC Interconnect, Research Complex at Harwell, Didcot OX11 0DE, UK*
- 146 ⁸⁰*Virginia Tech, Blacksburg, VA 24061, USA*
- 147 ⁸¹*Fundación ARAID, Universidad de Zaragoza, Zaragoza 50009, Spain*
- 148 ⁸²*Department of Physics, Oliver Lodge, University of Liverpool, Oxford St, Liverpool L69 7ZE, UK*
- 149 ⁸³*Department of Physics, University of Warwick, Coventry CV4 7AL, UK*
- 150 ⁸⁴*CERN, European Organization for Nuclear Research 1211 Geneve 23, Switzerland, CERN*
- 151 ⁸⁵*Department of Physics, University of California, San Diego, CA 92093, USA*
- 152 ⁸⁶*Civil and Environmental Engineering Department, Politecnico di Milano, Milano 20133, Italy*
- 153 ⁸⁷*Amherst Center for Fundamental Interactions and Physics
154 Department, University of Massachusetts, Amherst, MA 01003, USA*
- 155 ⁸⁸*Department of Physics and Astronomy, The University of Manchester, Manchester M13 9PL, UK*
- 156 ⁸⁹*Physics Department, Università degli Studi di Milano, Milano 20133, Italy*
- 157 ⁹⁰*Brookhaven National Laboratory, Upton, NY 11973, USA*
- 158 ⁹¹*Chemical, Materials, and Industrial Production Engineering Department,
159 Università degli Studi "Federico II" di Napoli, Napoli 80126, Italy*
- 160 ⁹²*National Institute for Research and Development of Isotope
161 and Molecular Technologies, Cluj-Napoca 400293, Romania*
- 162 ⁹³*Physics and Astronomy Department, University of California, Los Angeles, CA 90095, USA*
- 163 ⁹⁴*Department of Physics and Engineering, Fort Lewis College, Durango, CO 81301, USA*
- 164 ⁹⁵*Institute of Applied Radiation Chemistry, Lodz University of Technology, 93-590 Lodz, Poland*

INFN-DS20k-TDR Approval and Revision History

Version	Lead Editors	Reviewed by	Approved by	Date
v1.0	Name1, Name2, Name3	Reviewer1, Reviewer2, Reviewer3	DS-20k IB	XXX YY 2021

TABLE I. Approval History

Version	Date	Description	Editors
v0.0	XXX YY 2021	First Version	Name1, Name2, Name3

TABLE II. Version History

CONTENTS

166	List of Figures	ii
167	List of Tables	x
169	1. Executive Summary	1
170	2. Scientific Motivations	5
171	3. R&D toward the DS-20k detector design	8
172	3.1. Material Assays	8
173	3.1.1. Goals of the R&D	8
174	3.1.2. Organization of the activity	8
175	3.1.3. Radio-purity database	9
176	3.1.4. Radioactivity budget	10
177	3.1.5. Surface contamination, material storage and cleaning	11
178	3.1.6. R&D results and conclusions	12
179	3.2. SiPMs	12
180	3.2.1. Goals of the R&D	12
181	3.2.2. Development of cryogenics SiPMs	12
182	3.2.3. Technology transfer	14
183	3.2.4. Backside metallization development	14
184	3.2.5. Through Silicon Vias (TSV) development	17
185	3.2.6. Validation procedures development	17
186	3.2.7. Photon Detection Efficiency (PDE)	21
187	3.2.8. R&D results and conclusions	22
188	3.3. Tiles and Front End Amplifiers	23
189	3.3.1. Goals of the R&D	23
190	3.3.2. Tiles and transimpedance amplifiers	23
191	3.3.3. CMOS Integrated Electronics for SiPM Readout	26
192	3.3.4. Front end board amplifier for the inner Veto readout	27
193	3.3.5. R&D results and conclusions	29
194	3.4. Photo Detection Unit (PDU)	30
195	3.4.1. Goals of the R&D	30
196	3.4.2. Signal Transmission	30
197	3.4.3. PDUSlim: Design, Performances and Test Results	31
198	3.4.4. PDU+: Design, Performances and Test Results	38
199	3.4.5. R&D results and conclusions	41
200	3.5. Cables and connectors	42
201	3.5.1. Goals of the R&D	42
202	3.5.2. Cables	42
203	3.5.3. Connectors	43
204	3.5.4. R&D results and conclusions	43
205	3.6. TPC design	43
206	3.6.1. Goals of the R&D	43
207	3.6.2. Electric field in the acrylic TPC	44
208	3.6.3. Cathode high HV cable	44
209	3.6.4. Field cage and Clevios tests	45
210	3.6.5. R&D results and conclusions	45
211	3.7. Reflectors and wavelength shifters	46
212	3.7.1. Goals of the R&D	46
213	3.7.2. Description of the activity	46

214	3.7.3. R&D results and conclusions	49
215	3.8. Gd-loaded acrylic	49
216	3.8.1. Goals of the R&D	49
217	3.8.2. Development of the material	50
218	3.8.3. Gadolinium oxide nano-grains dispersion	50
219	3.8.4. Gadolinium β -diketonate solution	52
220	3.8.5. Gd-loaded acrylic towards the final production	53
221	3.8.6. R&D results and conclusions	54
222	3.9. Calibration system mock-up	55
223	3.9.1. Goals of the R&D	55
224	3.9.2. Mock-up construction	55
225	3.9.3. R&D results and conclusions	56
226	3.10. UAr cryogenic system component testing at CERN	56
227	3.10.1. Goals of the R&D	56
228	3.10.2. Construction of the UAr system at CERN	56
229	3.10.3. R&D results and conclusions	57
230	4. Predecessor experiments relevant for the DS-20k design	60
231	4.1. The DarkSide-50 experiment	60
232	4.2. The DEAP-3600 experiment	62
233	4.3. The ReD experiment	62
234	5. Detector Design and Specifications	65
235	5.1. TPC and inner Veto	66
236	5.2. Light detection	68
237	5.3. Reflectors and wavelength shifters	69
238	5.4. Outer Cosmic Veto	69
239	5.5. Cryogenics	70
240	5.6. Calibrations	70
241	5.7. DAQ and Data Management	71
242	5.8. Materials and Radiopurity	73
243	5.8.1. Expected signals	73
244	5.8.2. Sources of background	73
245	5.8.3. Evaluation of the expected background rates	74
246	5.8.4. Nuclear Recoil-background rates	74
247	5.8.5. Backgrounds from uncorrelated and correlated coincidences	83
248	5.8.6. Electron Recoil-background rates	85
249	6. The Product Breakdown structure	88
250	7. Technical Description: DS-20k detector	89
251	7.1. Membrane Cryostat and AAr cryogenics	89
252	7.1.1. Warm Structure	90
253	7.1.2. Cold structure	91
254	7.1.3. Top caps	92
255	7.1.4. AAr cryogenics	93
256	7.1.5. Total cryogenics power consumption	95
257	7.2. TPC and inner Veto	97
258	7.2.1. PMMA windows	100
259	7.2.2. Wire grid	101
260	7.2.3. S2 system	103
261	7.2.4. HHV system for TPC	103
262	7.2.5. Field cage hardware	103

263	7.2.6. ESR & TPB	106
264	7.2.7. Titanium optical plane structure	108
265	7.2.8. Gd-loaded PMMA barrel	113
266	7.2.9. Gd-loaded PMMA endcaps	113
267	7.2.10. Cable trays	113
268	7.2.11. ESR & PEN	116
269	7.2.12. Chimneys	117
270	7.2.13. The titanium vessel	118
271	Vessel body	120
272	Top dome	121
273	7.2.14. Detector Support System	121
274	7.3. Outer Cosmic Veto Detector	124
275	7.4. The Calibration System	125
276	7.4.1. Calibration pipes system	126
277	7.4.2. Calibration control system	126
278	7.4.3. Gas Sources	126
279	7.4.4. Gamma-ray Sources	127
280	7.4.5. Neutron Sources	127
281	7.4.6. DD Neutron Generator	128
282	7.5. UAr Cryogenics	129
283	7.6. Readout and Data Acquisition System	133
284	7.6.1. Digitizer Boards.	135
285	Custom Firmware Specification	135
286	7.6.2. Trigger and Clock Module	136
287	7.6.3. Front-End Processors	137
288	7.6.4. Time Slice Processors	138
289	Trigger Algorithms	139
290	7.6.5. Flow Control and Data Transport	140
291	7.6.6. Data Logger	140
292	7.6.7. Online Monitoring	141
293	7.6.8. Infrastructure	141
294	7.7. Data	142
295	8. Technical Description: Light Detectors	145
296	8.0.1. PDU+	145
297	8.0.2. Cabling	149
298	8.0.3. Power Supply	150
299	9. Technical Description: Support Facilities	152
300	9.1. PDU production facility	152
301	9.2. PDU Test Facility	157
302	9.3. vPDU Production Facilities	160
303	9.4. Inner detector construction facilities not in Hall C	161
304	9.4.1. TPC assembly clean room	161
305	9.4.2. Coating facility	162
306	9.5. Hall C interfaces	163
307	9.5.1. Installation system inside the cryostat	163
308	9.5.2. Cryogenics support structure	164
309	9.5.3. Detector electrical power, grounding and shielding	164
310	9.5.4. Control room	164
311	9.6. Prototypes	165
312	9.6.1. DS-Proto0	165
313	9.6.2. Prototype for validation of the TPC mechanical design	166

314	10. Technical Description: Urания and Ария	171
315	10.1. Procurement of the low-radioactivity Argon	171
316	10.1.1. Urания	171
317	10.1.2. УAr transportation vessels	173
318	10.1.3. Ария	174
319	10.1.4. Purification plant	174
320	10.1.5. DArTInArDM	176
321	11. Procurement, Construction, Installation	177
322	11.1. Cryostat	177
323	11.1.1. Procurement and radiopurity control of the membrane cryostat components	177
324	11.1.2. Cryostat construction in Hall C at LNGS	178
325	11.2. Titanium Vessel	181
326	11.2.1. Procurement of radiopure Titanium	181
327	11.2.2. Ti vessel construction and installation	182
328	11.3. Cleaning of metallic parts	182
329	11.4. УAr Cryogenic system	182
330	11.5. Gadolinium-loaded acrylic mass production	183
331	11.5.1. Gd loaded PMMA quality control	184
332	11.6. Procurement, construction and test of the photo-detectors	185
333	11.6.1. Procurement of radiopure components	185
334	11.6.2. Work flow of the SiPM and electronics mass production	185
335	11.6.3. PDU+ assembly	187
336	11.6.4. SiPM and electronics test protocol and Quality Assurance	187
337	11.6.5. PDU testing and QA/QC in the INFN-Naples PDU test facility	190
338	11.6.6. Electronics for the Veto	191
339	11.7. Inner Detector	191
340	11.7.1. Activities in locations other than LNGS	192
341	TPC assembly and transportation handling system	192
342	Anode and cathode	192
343	Gd-PMMA Barrel panels	193
344	Wire grid	193
345	Reflector panels and field-cage resistor links	194
346	Calibration pipes	194
347	Outer cosmic Veto items	194
348	11.7.2. Preparatory operations at LNGS: cleaning and staging	194
349	11.7.3. TPC assembly activities in NOA CR2	195
350	11.7.4. Activities in Hall C	197
351	Power distribution and grounding	197
352	Hall C and cryostat preparation for detector final integration	198
353	Inner Detector final integration	200
354	11.8. Cryogenics commissioning	204
355	11.9. Detector commissioning	205
356	12. Validation of the Choices and Expected Performances	208
357	12.1. Monte Carlo results for TPC key performance parameters	208
358	12.1.1. TPC Light Yield	208
359	12.1.2. PSD performance	208
360	12.1.3. Position reconstruction resolution	210
361	12.1.4. Dynamic Range	210
362	12.2. Monte Carlo simulation results on neutron Veto performance	211
363	12.2.1. Neutron veto inefficiency	211
364	12.2.2. Dead-time induced by the neutron tagging strategy	214

365	12.3. Pile up rate in TPC and overall acceptance loss	215
366	12.4. Random pile up and dust background sources	216
367	12.5. Sensitivity Projections	218
368	12.6. Validation Studies for the DAQ system	220
369	12.6.1. TPC Readout Data Rates	220
370	12.6.2. Studies and test with DS-Proto0 data and other test data	222
371	Exponential Filter	222
372	Feature Extraction	223
373	12.6.3. Data compression in the frontend	224
374	13. Safety and Environmental Aspects	226
375	13.1. Italian and European and Regulations	226
376	13.1.1. Procedural Process Authorization	227
377	13.2. Work-site Organization and Preparation to Start	227
378	13.3. Information, Education and Training	227
379	14. Management	229
380	14.1. Summary of the available funding	229
381	14.2. INFN funds for DS-20k	230
382	14.3. Collaboration funds for DS-20k	231
383	14.4. Schedule	234
384	14.5. Commissioning of the detector	235
385	14.6. Memorandum of Understanding	235
386	14.7. Summary of the requests to the LNGS laboratory	236
387	References	237

388

LIST OF FIGURES

389	1	Top: CAD rendering of the DS-20k experiment in Hall C of LNGS showing the red ProtoDUNE like cryostat housing the detector and the cryogenics system and its support structure. Bottom Left: cross section showing the inner detector with the Gd-PMMA in green, the Titanium vessel in gray and right: external view of the TPC and Veto showing the full assembly features including VPDU+, Calibration, Optical planes and the Gd PMMA wall structure.	3
390	2	6
391	3	DS-20k materials database structure	10
392	4	Web interface of DS-20k materials database	10
393	5	Left panel: DCR as a function of temperature for the SF and LF versions at two values of excess bias. Right panel: AP probability as a function of excess bias at 77 K for the LF and LF-LowAP SiPMs. Reproduced from [1].	13
394	6	Rq boxplot LF	14
395	7	Rd spectrum	15
396	8	Aging trends	16
397	9	SiPM crack image after thermal cycle	16
398	10	Distribution of Measured R_d	17
399	11	Single Photon Electron (SPE) gain and charge as a function of the over voltage measured by several institutions. TRIUMF data is labeled as #1 while LNGS, INFN PISA and FBK data are labeled as #2, #3, and #4 respectively, when available. ..	18
400	12	Left: Breakdown voltage and single cell capacitance as a function of the SiPM temperature. The dashed region represents the uncertainty on the stabilisation temperature of the TRIUMF setup at 77 K (#1). Note as this quantity is not the statistical fluctuation on the temperature that was < 1 K. Right: Single cell capacitance extracted from the fit. The dashed region represents instead the acceptance requirement on the single cell capacitance, based on Table VII. TRIUMF data is labeled as #1 while LNGS, INFN PISA and FBK data are labeled as #2, #3, and #4 respectively, when available.	18
401	13	Charge distribution of first pulses following single PE trigger pulses as a function of the time difference with respect to their primary pulse	20
402	14	Left: Number of Correlated Delayed Avalanches (CDAs) per primary pulse within a time window of 5 μ s after the trigger pulse as a function of the applied over voltage for different SiPM temperatures. Right: Dark Noise (DN) rate normalized by the SiPM photon sensitive area as a function of the applied over voltage. TRIUMF data is labeled as #1 while LNGS, INFN PISA and FBK data are labeled as #2, #3, and #4 respectively, when available.	20
403	15	Left: Number of Additional Prompt Avalanches (APAs). Right: Direct Cross talk probability as a function of the over voltage. TRIUMF data is labeled as #1 while LNGS, INFN PISA and FBK data are labeled as #2, #3, and #4 respectively, when available.	21
404	16	PDE of the LFoundry DarkSide SiPM as a function of the over voltage for temperatures of 213 K and 100 K, under 420 nm light illumination. The 10 K in the 100 K TRIUMF measurement (#1) represents the uncertainty on the stabilisation temperature of the TRIUMF setup at 100 K. Note as this quantity is not the statistical fluctuation on the temperature that was < 1 K. TRIUMF data is labeled as #1 while LNGS, INFN PISA and FBK data are labeled as #2, #3, and #4 respectively, when available.	22
405	17	PDE of the LFoundry DarkSide SiPM measured as a function of the wavelength, for two over voltages, at 213 K. TRIUMF data is labeled as #1 while LNGS, INFN PISA and FBK data are labeled as #2, #3, and #4 respectively, when available. ..	22

439	18	PDE of the LFoundry DarkSide SiPM as a function of the wavelength, for two over voltages, at 100 K. The 10 K in the 100 K TRIUMF measurement (#1) represents the uncertainty on the stabilisation temperature of the TRIUMF setup. Note as this quantity is not the statistical fluctuation on the temperature that was < 1 K.	23
440	19	Tile configuration for the 4x2s3p (left) and 4s6p (right), see text for details. The intermediate voltage references are produced by a voltage divider based on 10 M Ω 1% resistors with PEN HV shunt capacitors.	24
441	20	Schematic of the transimpedance amplifier	25
442	21	Multi photoelectron plot ("finger plot") for matched filtered signals of single-channels tile #ML-13 with NUV-HD-Cryo from LFoundry read by a traditional FEB (4×2s3p) with SNR=27 and by a single TIA FEB (1×4s6p) with SNR=25.	26
443	22	CASTOR	27
444	23	Veto front end board	28
445	24	Veto FEB noise power spectrum	28
446	25	Veto Front End Board pulse example	29
447	26	Preliminary veto ASIC performance	29
448	27	Characterization of the differential transmission line. Left: 0.5 μ s long pulse after decreased the 10 meters cable at room temperature and in liquid nitrogen: due to the resistivity of copper the rise time changes from 10 ns to 3.7 ns 10-90 (and about 1.5 ns 20-80 at 77 K). Right: Bandwidth of the transmission chain: differential driver, cable (10 m in liquid nitrogen) and differential receiver (feedthrough absent). The system proves a bandwidth in excess of 200 MHz.	31
449	28	Left: The copper Motherboard of the PDUSlim. Right: Kapton strips.	32
450	29	Top Left: The steering module. Top Right: The 13 channels output driver. Bottom: The ASIC Front End Board (AFEB). The magnification shows the ASIC.	33
451	30	Left: A SiPM tile. Right: The first prototype PDUSlim fully populated with PDMs	34
452	31	IV curve at warm for PDUSlim	35
453	32	PDUSlim IV curve at LN temperature and signal pulse shape	35
454	33	PDUSlim single tile comparison	36
455	34	PDUSlim charge spectra vs OV	36
456	35	PDUSlim raw amplitude spectrum	37
457	36	PDUSlim timing performance	38
458	37	Tile+ design and test results. Top: Tile+ TF-253 top view (left) with 24 SiPMs and bottom view (right). The unit was produced with borders (5 mm) to simplify the testing (including a top acrylic frame), but the final version will be border-less with a total dimension of 49.5×49.5 mm ² . In the bottom view it is possible to see the TIA and the connector on the left side. Four 5×3 mm threaded pillars are soldered to the PCB to allow a reliable connection with the motherboard. Bottom Left: Finger plot of tile+ #TF-253 for filtered signals at 7 VoV with a SNR=25. Bottom Right: Noise power spectrum at 86 K of the 1-TIA amplifier connected to a Tile+ compared to the one of the 4 TIA (4 × 2s3p) scaled of 12 dBm/ \sqrt{Hz} (6 dBm/ \sqrt{Hz} are due to the 4 TIA configuration that exhibits a doubled noise while the remaining contribution is given by the summing and differential FEB stages and the differential to single-end converter). The curves are consistent within 20%. Such difference is explained with the different devices used to assemble the tiles (FBK SiPMs in Tile+ and LFoundry SiPMs in the 4 TIA).	39
459	38	Veto Tile+ spectrum	40

486	39	MB+ design and test result. Top Left: MB $\frac{1}{4}$ prototype assembly. In this setup three Tile+ are with the protection border to simplify the R&D. The final MB+ will assemble 16 tile+ without empty spaces. Top Right: Drawing of the PDU+ (made of four MB $\frac{1}{4}$ shown in the left plot) with the acrylic protection on the top. Bottom: Finger plot of Tile+ #TF-253 connected to a MB $\frac{1}{4}$ for filtered signals at 7 VoV with a SNR=25. In this measurement all the components of MB $\frac{1}{4}$ are connected and working (adder, differential transmitter, 10 m of cable but the LDO is disabled).	41
493	40	A pulse corresponding to a single photoelectron signal (average of many pulses) transmitted through a short and 10 meters cable in liquid nitrogen. No significant deformations of the pulse shape are present.	42
496	41	R&D work on the multilayered HV cable. Figure A shows the Heinzinger power supply together with an HV cable featuring an adapted plug (zoomed view in Figure C). This design features the cable core connected to the power supply plug via a crimped ferrule and a spring relieving all the mechanical tensions. The spring is encapsulated in a Faraday cage to ensure an electrically safe connection. Figure B shows the thread achieved on the end of the HV cable using the developed tapping device.	45
503	42	Hemispherical reflectivity measured at 7° angle of incidence with a spectrophotometer for: ESR, PEN air-coupled to ESR, TPB evaporated on ESR, TPB evaporated on ESR	47
506	43	2PAC setup consisting of two identical chambers, allowing for a simultaneous comparison of PEN/ESR and TPB/ESR performance with SiPM area coverage fraction comparable to that of the DarkSide-20k veto.	48
509	44	PMMA cylinder loaded with Gd ₂ O ₃ nano-grains. The sample has a 2% Gadolinium concentration.	53
511	45	5 cm thick PMMA samples loaded with Gd(acac): on the left the Gd concentration is 2%, on the right it is 0.5%.	54
513	46	The gadolinium-doped acrylic sample from Donchamp Acrylic Group	55
514	47	Elements of calibration system mock-up. (a) Stainless steel pipe (3m long). (b) Stainless steel tank; (c) Insulated tank; (d) The mock-up system: tank, pipe and instrumentation.	56
517	48	DS-20k UAr cryogenic system component fabrication and installation at CERN for testing.	58
519	49	DS-20k UAr cryogenic system testbed being prepared for operation at CERN.	58
520	50	Preliminary data from the DS-20k UAr cryogenic system testbed at CERN taken in July 2021. From left to right shows three nights of data. Respectively, from top to bottom shows the gas pressure, mass flow, and outgoing (warm) temperature for the nitrogen (solid blue lines) and argon (solid red lines) loops.	59
524	51	ER and NR PSD distribution vs recoil energy in DarkSide-50.	61
525	52	ER leakage probability in DEAP	62
526	53	ReD single-photon spectrum with Vinogradov distribution	64
527	54	Design of the inner detector showing the TPC, the Veto and the calibration pipes all contained in the titanium vessel which will host all the underground argon target for TPC and Veto.	65
530	55	Product Breakdown Structure (PBS) of the DS-20k experiment showing the three branches and sub-branches together with their names.	88
531	56	PBS of the membrane cryostat	89
532	57	ProtoDUNE cryostat operating at CERN.	90
534	58	3D view of the AAr cryostat	91
535	59	Detailed view of the cryostat seismic brackets.	92
536	60	Cryostat warm structure and top caps isometric view.	92
537	61	DarkSide-20k Cryostat front view dimensions	93

538	62	Top caps modules components.....	94
539	63	DarkSide-20k Inner Detector, Titanium vessel and Cryostat front view cut.....	95
540	64	Cryostat top caps penetrations.....	96
541	65	Conceptual schematics of the AAr cryogenic system	97
542	66	PBS of the TPC & Veto, showing details to level 5.....	98
543	67	Integrated TPC and Veto showing the top and bottom optical planes along with the connecting rods. The VPDU+s are also visible mounted on the external walls and on the top of the top optical plane, looking into the Veto region. The ESR and PEN reflector panels, mounted on the exterior, are suppressed for clarity. The mechanical anchor system is also shown which will mate with the titanium vessel and directly transfer the load to the hanger system (DSS) on the roof of the cryostat. Colors: blue - Clevios coating, pink - PMMA, green - Gd-loaded PMMA, yellow - photoelectronics (VPDU+s), gray - titanium or stainless steel.	99
551	68	Left: A cut-away view of the assembled TPC, emphasizing the corners, highlighting the component integration. Right: The spring assembly which will ensure the detector surfaces stay in contact when cooled to 87 K. A PTFE sleeve will be used to avoid friction during thermal contraction. The ESR and PEN reflector panels, mounted on the exterior, are suppressed for clarity.	100
556	69	PMMA anode plate. Left: Top view showing the concentricity guides. Right: View showing the diving bell structure which will contain the gas pocket. The additional holes located on the edges are for creating and maintaining the gas pocket.	101
559	70	PMMA cathode plate assembly. Left: Bottom view showing the upward slope from the center to the edges. Right: View showing the bonded barrel section with the Clevios coated field cage rings highlighted in darker blue. The concentricity guides are visible in both views.	102
563	71	The wire grid. Left: View showing the cross-section of the frame and a through-hole that one of the connecting rods will pass through. Right: A zoomed-in view showing how the individual wires attach to the frame.	102
566	72	The bubbler system. Top right: The bubbler with beveled bottom edges to allow efficient passage of the gas bubbles. Top left: The vertical tube is the gas inlet which feeds into a gas router. The router connects the gas pocket and bubbler volumes. Bottom: A side view showing where the gas/liquid interface is relative to the bubbler system.	104
571	73	The HHV port. Left: A cross-sectional view showing the HHV conductor cavity penetrating to the cathode. Right: The cathode plate assembly showing the HHV port.	104
574	74	Zoom-in of the one inside corners of the cathode barrel (left) and the Gd-loaded PMMA barrel (right). The resistor links are visible in both. Colors: blue - Clevios coated field cage rings, pink - PMMA, green - Gd-loaded PMMA.	105
577	75	Top: Resistor links. Bottom: The cathode plate assembly showing the resistor links on the barrel section.	106
579	76	Drift field uniformity in DS-20k. To ensure electrostatic field uniformity, a high voltage scheme that allows for independent control of the potentials on the top field cage ring (HV_r) and the wire grid (HV_g) will be used.	107
582	77	Different views of a reflector panel and components.	108
583	78	Left: Fully assembled reflector field cage. Right: Cross-sectional view of a lower corner of the TPC with the reflector panels visible. The PMMA standoffs are shown making contact with the areas of PMMA in between the field cage rings.	109
586	79	Pieces and partial assembly of an optical plane structure.	110
587	80	Left: Optical plane mechanical structure highlighting the eight through-holes for integration with the TPC barrel. Right: Zoom of one of the eight through-hole mounts. Welded inserts for the mounting of the VPDU+ plate are also visible at the intersections of the cross-pieces.	111

591	81	Details of the PDU+ mounting mechanism to the titanium holders which will be welded to the optical plane support structure.....	111
592	82	The PDU+ (left) and VPDU+ (right) holders highlighted in blue, welded to the support frame. The Gd-loaded PMMA blocks are also shown in green laid within the titanium frame.....	112
593	83	A fully assembled optical plane showing the TPC (left) and Veto (right) sides. The individual tile+s are visible in dark yellow. The ESR and PEN reflector panels, mounted on the exterior, are suppressed for clarity.....	112
594	84	The Gd-loaded panels and assembled barrel. Colors: green - Gd-loaded PMMA, blue - Clevios coating, gray - stainless steel angle brackets.....	114
595	85	Details of the VPDU+ mounting mechanism to the titanium holders which will be mounted to the Gd-loaded barrel wall panels.....	115
596	86	Different Gd-loaded components making up the endcaps of the DS-20k LAr TPC. To accommodate the cabling and to minimize the machining workload, the number of unique pieces has been kept to a minimum.....	115
597	87	Fully assembled Gd-loaded PMMA endcap. The grooves visible here will align with grooves in the titanium <i>x</i> and <i>y</i> cross-pieces such that paths for the cables will form that the cables can pass through. Keep in mind that the cables can weave into the <i>z</i> direction as well.....	116
598	88	The ESR and PEN reflector foil assembly. These panels will attach to the interior walls of the the titanium vessel with PTFE push-pins. A zoom-in of the panels highlighting the push-pins and the full panel assembly is shown on the left and right, respectively. Similar panels will attached to the exterior of the TPC walls.....	117
599	89	CAD design of the signals chimney. Open during installation (left), top view (middle) and isometric view (right). There are 5 feedthrough flanges on each chimney: one serves for veto readout and the other four for TPC readout. A large port on top is for easy access during cables installation. The gas extraction port is visible at the bottom.....	118
600	90	CF63 PCB flange: CAD design (left) and manufactured prototype at LNGS (right).	119
601	91	FEA results of the chimney PCB electrical feedthrough. Top left: deformation under vacuum and top right: stress under vacuum; bottom left: deformation with +0.35 barg pressure and bottom right: stress with + 0.35 barg pressure.	119
602	92	Titanium vessel cross section with markup of the main elements.	120
603	93	Titanium vessel FEA results	121
604	94	Detector Support System conceptual sketch.	122
605	95	Typical Detector Support System warm assembly.	123
606	96	Typical Detector Support System cold assembly.	123
607	97	PBS of the Outer Veto detector.	124
608	98	PBS describing the calibration item.	125
609	99	Schematic of the sources insertion system	128
610	100	Schematic representation of the calibration control system: the two motor boxes, one glove box and the two ropes to hold the source. The anchor points for the rope during physics data taking periods are shown. A picture of one motor is inserted.	129
611	101	PBS of the cryogenics in Hall C	130
612	102	Process and instrumentation diagram (P&ID) of the DS-20k UAr cryogenic system.	131
613	103	PBS for the readout and DAQ .	133
614	104	DAQ concept scheme	134
615	105	Distribution of the Clock and commands from the "Global Data Manager" to the Digitizers is done through a board dispatcher "Crate Data Manager". The Digitizers are using the same data path to return their information (Busy, Hit Map) to the GDM for run control and trigger generation.	137

642	106	Each digitizer has its own buffer marked with the common TSM marking the Time Slice duration boundaries. For each received buffer, a thread will apply a digital signal processing for data reduction/compression. Once complete, all the fragments of the same time slice are collected in a final buffer to the Time Slice transmission thread.	138
647	107	The figure shows the slicing of the timeline of the data flow. Tx refers to the FEPs and Rx to the TSPs. All the FEPs for a given Time Slice, send their data to a unique TSP. The subsequent time slice data will be directed to another idle TSP. In order to prevent analysis issues at the "boundary" of the slice split, a time overlap is to be present in both consecutive time slice (v mark)	139
652	108	The Pool Manager is acting as a proxy on behalf of all the TSPs for requesting all the time slice fragment for its segment processing.	141
654	109	PBS of the Data products.	142
655	110	Scheme of the PyReco package for the reconstruction of simulated and real data. PyReco is designed for DS-20k but can also serve ancillary apparatus such as ReD, prototypes and test setups.	142
658	111	PBS with details of the "Light Detectors" item.	145
659	112	Left: top view of the PDU+ showing 16 Tile+ mounted on the Motherboard+ (MB+) and covered by an acrylic sheet. Each Tile+ is made up of 24 SiPM. Right: bottom view of the PDU+ where the MB+ is shown with its electronic components.	146
662	113	Left: Top view of the Tile+ where the 24 SiPM are mounted in 4 rows x 6 columns. SiPM anodes are wire bonded to the tile along the two lines between rows 1 and 2 and between rows 3 and 4. Right: Bottom view with electronic components.	147
665	114	Left: Top view of the Motherboard+ showing the connectors for the 16 Tile+. Right: bottom view with electronic components and Motherboard+ connectors.	148
668	115	Schematics of the signal path of one MB+ channel. The signal from 4 Tile+ is actively summed by an adder and then transformed into a differential by a proper driver and transmitted via the SAMI cable. A sketch of the 5 V regulator with the virtual ground divider is also present.	149
671	116	Cross section of the cable used for power, bias, controls and signals of PDUs. All cables are stranded copper, AWG24 for power and AWG30 for all others. The insulation is in Siltem for radiopurity, with no dying, and a polyester mesh bundles together the cable. All five twisted pairs for command and signal have characteristic impedance $Z = 100 \pm 10\Omega$. The pairs are identified with the strand helicity and with a polyester fibre. The bias cable is identified with a slightly thicker insulation. An additional twisted pair may be added for voltage sensing.	150
678	117	Sketch of the PSU architecture	151
679	118	Block diagrams of Low Voltage and High Voltage channels: Left: Lo-V Right: Hi-V	151
680	119	PBS of the various support facilities.	153
681	120	Floor plan of the <i>Nuova Officina Assergi</i>	155
682	121	Simulation of the air flow in NOA	156
683	122	Simulation of Rn concentration in NOA. $1200 \text{ m}^3/\text{h}$ (left) and $600 \text{ m}^3/\text{h}$ (right) of Rn free make up air flow-rate	156
684	123	Left: the Naples 50 m^2 Clean Room layout. Right: the custom made Cryostat of the PDU Test Facility	157
685	124	Picture of the Naples Test Facility holding structure used in PDU+ cold test.	158
686	125	Amplitude spectra of PDU+, PDUSlim and the old design PDU (MB3) from the Napoli PDU Test Facility	160
689	126	The PHAEDRA veto PDM test platform.	161
691	127	False floor: the wooden blocks and plates protect the primary corrugations while the stainless steel lining ensures the dust cleanliness requirements.	164
693	128	Schematics of the setup for the optimization of the S2 signals	166
694	129	Picture of the mounted test TPC for the optimization of the S2 signals.	166

695	130	The DS-Proto cryostat and the layout of the complete test system at CERN.	168
696	131	Conceptual Design of the DS-Proto detector	169
697	132	Overall view of the DS-Proto mockup TPC and its supporting structure	169
698	133	DS-Proto mockup TPC section view and barrel parts	170
699	134	DS-Proto mockup TPC anode with features for confirming DS-20k design	170
700	135	PBS of Urania	172
701	136	Process Flow Diagram for the Urania UAr extraction plant	173
702	137	PBS of Aria.	175
703	138	The Seruci-0 cryogenic distillation column	175
704	139	Lowering test of an Aria module	176
705	140	Details of the cryostat installation sequence - I	179
706	141	Details of the cryostat installation sequence - II	180
707	142	Details of the cryostat installation sequence - III	181
708	143	Transportation of the titanium vessel barrel (a) and top dome (b) through the Hall C door.	182
709	144	Details of the Ti vessel installation sequence	183
710	145	PDU+ process flow overview. The work flow is divided into three main branches: SiPM testing and dicing; Tile+ production; MB+ production. Functional SiPMs are attached to working Tile+ PCB to form a Tile+ which, in turn, after being tested, is mounted on the MB+ to form the final PDU+ that will be tested in INFN-Naples.	185
711	146	MuGS multipurpose box with the Tile+	187
712	147	Pivoting support for MB+ assembly	188
713	148	Detail of the acrylic protection support	189
714	149	The PDU+ integration	189
715	150	veto Tile+ prototype produced in the UK and voltage vs. time waveform for veto Tile+ prototype in response to laser illumination, in UK cryogenic test	192
716	151	NOA CR2 3d view	195
717	152	Schematic of grounding and power distribution used at ProtoDUNE	199
718	153	Cryostat during final detector assembly: the cryostat top aperture.	199
719	154	Conceptual sketch of the soft wall clean room and temporary cover on top of the cryostat during the Inner Detector assembly. The pink panels are the air tight covers that can slide below the roof integrated with HEPA filters (orange panel) to allow clean insertion of large pieces inside the cryostat.	200
720	155	(a) Temporary support structure placed inside the cryostat. (b) Bottom Optical Plane (BOP) on top of the temporary support structure. (c) and (d) Details of the calibration pipes lower sections integration. (e) TPC acrylic vessel on top of BOP. (f) Top Optical Plane (TOP) on top of the TPC acrylic vessel.	202
721	156	(a) Integration of the 8 spring-loaded rods. (b) Integration of the Ti vessel top dome and of the lifting beam. (c) Lifting out of the detector integrated with Ti vessel top dome.	203
722	157	(b) Titanium vessel insertion. (c) Reflector foils mounting.	204
723	158	(a) Detector insertion inside the titanium vessel. (b), (c), (d) Cryostat top caps installation: at first the top caps are only bolted to the rest of the structure waiting for the warm test of the full electronics and DAQ chain.	205
724	159	(a) Chimney installation. (b) DAQ system installation. (c) Detector Support System (DSS) installation. (d) Detector lifting via DSS and removal of the temporary support structure and titanium vessel temporary feet. (e) Final piping connections. (f) Calibration equipment installation.	206
725	160	Photon detection efficiency as a function of the vertical position of a scintillation event. $z = 0$ corresponds to the TPC center, the LAr-GAr interface is at $z = 175$ cm.	209
726	161	NR acceptances for the 1x1, 2x1, and 2x2 configurations, assuming 7 Volt over voltage.	210
727	162	Number of collected photoelectrons in the Veto as a function of the z coordinate. The results are from 1 MeV electrons releasing all their energy in the UAr.	212

748	163	Relative increase of the neutron tagging inefficiency for neutrons from the Veto PDUs and from the TPC PDUs as a function of the Gadolinium doping concentration	213
749	164	Example of the hit finding algorithm developed for the veto	214
750	165	The distribution of energy deposited in LAr due to alpha decays within Gd-loaded PMMA dust particles of various radii. For each radius 10^6 events are simulated. For larger dust radii the number of alphas reaching the LAr decreases resulting in less entries in the histogram.	217
751	166	The distribution of energy deposited in LAr due to alpha decays within Norite dust particles of various radii. This plot is produced with the same level of statistics as Fig. 165.	217
752	167	The distribution of energy deposited in LAr due to alpha decays within copper dust particles of various radii. This plot is produced with the same level of statistics as Fig. 165.	217
753	168	Relative change of the discovery reach as a function of the sum of NR backgrounds for various WIMP masses.	219
754	169	Input data rate in input to Front End Processors	221
755	170	The effect of summing channels and varying the waveform segment extension criteria on the data rate. Also shown is the limit imposed by the 1 Gb connection on the digitizers. The uncertainty on the rates are calculated using the ToyMC procedure described in the text.	222
756	171	LNGS tile average signal and exponential filter	223
757	172	LNGS finger plot and exponential filter	223
758	173	LNGS timing with trapezoidal filter	224
759	174	Schedule of the construction of the DS-20k detector.	235
760			
761			
762			
763			
764			
765			
766			
767			
768			
769			
770			
771			

LIST OF TABLES

773 I	Approval History	iv
774 II	Version History	iv
775 III	Summary of DS-20k assays performed	9
776 IV	Specifications of the SiPMs	12
777 V	Summary of the backside options and issues	15
778 VI	Summary of the LFoundry SiPMs tested by several institution	18
779 VII	Summary of the breakdown voltages measured by several institutions extrapolated from the Single PhotoElectron (SPE) charge	19
780 VIII	Summary of the FBK NUV-HD-CRYO LFoundry SiPM specification	22
781 IX	Specifications driving the development of the cryogenic amplifiers. See [2] for the justification of most of them. Note that the some target parameters for the Veto are more relaxed than that needed for the TPC. (*) Contribution to the radioactivity background from all the installed amplifiers	23
782 X	Specifications of the TIA coupled to a tile with 24 SiPMs	24
783 XI	Parameters of the bare SiPMs and of the assembled tiles, with 4 TIA and 1 TIA configuration	26
784 XII	SNR for PDUSlim at 5, 7 and 9 VOV	37
785 XIII	Assay results of PEN samples for the DS-20k Veto with HPGe (top) and HR-ICPMS (bottom), both performed at LNGS	49
786 XIV	Target specification driving the R&D activity toward the development of the Gd loaded PMMA. (*) before the machining of the final pieces	50
787 XV	Assay results of pure Gd_2O_3 samples, performed by DS-20k collaborators with Germanium detector sensitive to the isotopes in the chains ^{238}U - ^{226}Ra and ^{232}Th - ^{228}Th	51
788 XVI	Results of calcinations performed on three samples of different dimensions and with different Gd_2O_3 concentrations. *2.3% of Gd_2O_3 corresponds to 2% of Gd, considering the molecular mass	52
789 XVII	TPC design parameters	66
790 XVIII	Ar properties. L_{eff} is the ratio between the scintillation efficiency for NR and ER	67
791 XIX	Photoelectronics specification parameters	69
792 XX	Specifications for wavelength shifters and reflectors	69
793 XXI	Outer cosmic veto requirements	70
794 XXII	Ar cryogenic system design specifications	71
795 XXIII	Calibrations system parameters and methods	71
796 XXIV	DAQ design parameters	72
797 XXV	Computing design parameters	72
798 XXVI	Backgrounds expected during the full DS-20k exposure	75
799 XXVII	Simulated radiogenic neutron rates	76
800 XXVIII	Simulated radiogenic neutron rates	77
801 XXIX	Simulated radiogenic neutron rates	78
802 XXX	Simulated radiogenic neutron rates	79
803 XXXI	Simulated radiogenic neutron rates	80
804 XXXII	Simulated radiogenic neutron rates	81
805 XXXIII	Simulated radiogenic neutron rates	84
806 XXXIV	Summary of the gamma activities used in the Monte Carlo simulation of gamma backgrounds, grouped by source category	86
807 XXXV	Total γ activity and γ interaction rates in the TPC and Veto, resulting from the total source activity (produced by summing the contributions of all chains in table XXXIV)	87
808 XXXVI	Fyostat design parameters	90
809 XXXVII	Ar cryogenic system design parameters	94
810 XXXVIII	cryogenics power consumption	97

824	XXXIV Chimney parameters	118
825	XL Titanium vessel parameters	120
826	XLI DAQ readout channels	135
827	XLII PDU+ performance parameters	146
828	XLIIISummary of the SiPM Requirements for the Darkside-20k SiPMs. SPE stands for Single Photon Electron	147
829	XLIVElectrical parameters of NUV-HD-LF Cryo SiPMs assembled in tiles with 1 TIA configuration (4s6p)	148
830	XLVThe NOA clean room sub-structures and destination.	152
831	XLVIcoating facility parameters	163
832	XLVIDS-Proto mockup TPC parameters.	168
833	XLVIIAr Production parameters	171
834	XLIXRadio-purity and composition specifications for the cryostat materials.	177
835	L Materials, interfaces and their modeling	209
836	LI Neutron Veto inefficiency from topical positions in the detector.	212
837	LII Compression for normal waveform	225
838	LIII Compression for signal waveform	225
839	LIV Compression for signal downsampled 2	225
840	LV Summary of the major financial contributions to the DS-20k experiments. In kind contributions are not reported.	230
841	LVI Distribution of the construction scope by funder: Detector Elements PBS branch, TPC & inner Veto items.	231
842	LVII Distribution of the construction scope by funder: Detector Elements PBS branch for items other than TPC & inner Veto.	232
843	LVIIIDistribution of the construction scope by funder: Photo-detectors PBS branch.	233
844	LIX Distribution of the construction scope by funder: Argon extraction and distillation PBS branch.	233
845	LX High level allocation of INFN-CIPE and PON funds	234
846	LXI Summary of the INFN-CSN2 funds.	234

853

1. EXECUTIVE SUMMARY

854 The Global Argon Dark Matter Collaboration (GADMC) aims to design, construct, assemble,
855 install, commission, and operate the DS-20k experiment in Hall C of the INFN-LNGS.

856 DS-20k is designed to observe dark matter particles scattering from argon atoms in the liquid
857 argon (LAr) target. The visible signal from Weakly Interacting Massive Particle (WIMP) dark
858 matter scattering is a nuclear recoil, depositing tens to hundreds of keV of energy in the argon.

859 The detector is designed to operate for a minimum of 10 years while maintaining negligible
860 instrumental background level in the WIMP search region of interest. The background to our dark
861 matter search is dominated by coherent neutrino-nucleus scattering interactions; thus the sensitivity
862 approaches the ‘neutrino floor’.

863 The core of the apparatus is a dual phase Time Projection Chamber (TPC) with 51.1 t LAr
864 mass, instrumented to detect both argon scintillation photons as well as ionization electrons. The
865 TPC is filled and surrounded by low-radioactivity underground argon (UAr) in which the level of
866 the β radioactive isotope ^{39}Ar is lower by more than a factor of thousand than the standard argon
867 of atmospheric origin (AAr), as demonstrated [3] by the predecessor experiment DS-50.

868 The TPC serves as both WIMP target and detector, with three dimensional spatial reconstruction
869 capability that permits the definition of an inner fiducial volume which excludes the wall surfaces.
870 Two planes of cryogenic SiPMs covering the top and the bottom faces of the TPC detect the light
871 signals produced by the scattering of a WIMP particle on an Ar atom. These signals are the prompt
872 scintillation produced in the liquid, termed S_1 , and the delayed light from electroluminescence
873 produced by the ionization electrons drifted up and extracted into the gas region, termed S_2 .

874 Trace radioactivity present in the materials used to build the detector or surrounding it are potential
875 sources of background. Gammas or neutrons from spontaneous fission and (α,n) interactions,
876 in particular, can produce background from more distant sites, while β and α particles produced
877 by a radionuclide decay can typically contribute to the background only if the nuclide is in contact
878 with the LAr target. In addition to this bulk contamination, background contributions come from
879 cosmogenic activation of materials and surface contamination, mainly due to radon diffusion and
880 plate-out of the radon daughters produced in the surrounding air during manufacturing or storing
881 and transportation.

882 A key feature of the detector is the pulse shape discrimination (PSD) capability of argon. Scintillation
883 light due to electrons or gamma energy deposits form the electronic recoil (ER) background
884 category, for which the bulk of the scintillation is emitted with a time constant of approximately
885 $1.5\ \mu\text{s}$. This is in stark contrast to the nuclear recoil signal (NR) expected from WIMP-nucleus scattering
886 in the argon, which is dominated by scintillation emission with a time constant of $\sim 6\ \text{ns}$.
887 The single phase DEAP-3600 experiment, described in section 4, has exploited this effect using
888 pulse shape discrimination to achieve ER background rejection of 2.4×10^8 [4, 5]. Pulse shape discrimination
889 in a dual phase argon TPC was demonstrated by the DarkSide-50 (DS-50) experiment,
890 described in section 4. Many fundamental design parameters for the DS-20k experiment are based
891 on the successful experience of the DarkSide Collaboration in constructing, commissioning, and
892 operating the DS-50 and DEAP-3600 detectors in a background-free mode. The technical details
893 can be found in [3, 6–18].

894 The PSD and the reduction of the ^{39}Ar in the UAr, together with a careful choice of the construction
895 materials and their handling, make the background induced by β and γ events negligible
896 within a time scale of 10 years. Neutrons undergoing an elastic scattering in the fiducial volume
897 of the LAr TPC are the most dangerous remaining instrumental background, as a single induced
898 nuclear recoil can fully mimic a WIMP event.

899 Neutron-induced nuclear recoils are rejected by identifying the presence of the neutron. The
900 DS-20k detector has a novel design in which the neutron veto and the TPC are integrated into a
901 single mechanical unit that sits in a common bath of low-radioactivity argon, separated from the
902 atmospheric argon in the main cryostat by a sealed titanium vessel, as shown in figure 1.

903 Gd-PMMA (Gadolinium-loaded polymethylmethacrylate), is the material of choice for the neu-

tron veto and layers of Gd-PMMA surround the entire TPC volume. Gd-PMMA is highly efficient at moderating and then capturing neutrons, the capture resulting in the emission of several γ s, with total energy 7.9 MeV. The thickness and Gadolinium concentration of the Gd-PMMA are set to achieve a neutron capture inefficiency of < 1 %. The thickness of the argon volume between the Gd-PMMA and the enclosing titanium vessel, 40 cm, is set to ensure the production of sufficient scintillation light from the capture γ -rays in the case that none of them pass into the TPC. The Gd-PMMA is arranged in an octagon of 8 vertical panels of thickness 15 cm and two end caps of thickness 15 cm. The 8 vertical panels also serve as the lateral walls of the TPC. It should be noted that the use of low-radioactivity argon in the veto region greatly simplifies the design of the neutron veto - which otherwise would have to cope with the high rate of ^{39}Ar decays.

All the surfaces in contact with the outer UAr volume (the outer surfaces of the Gd-PMMA itself and the inner surface of the titanium vessel) are covered in reflective foil and wavelength shifter. Arrays of SiPMs distributed over the surface of the Gd-PMMA detect the scintillation produced in the UAr volume between the Gd-PMMA and the titanium vessel.

The TPC volume itself is a right octagon with inscribed circle of diameter 350 cm and height 348 cm. Its walls, as mentioned, are formed by the vertical walls of the Veto the top and bottom caps of the TPC are pure, transparent, acrylic. The cathode, drift field and anode in the TPC are generated using Clevios, a transparent conducting polymer, as electrode material with coatings on the inside of the bottom cap for the cathode, on the inside walls for the field cage, and on the inside of the top cap for the anode. A gas phase with thickness (7.0 ± 0.5) mm where the electroluminescence (charge signal) is developed is maintained just below the anode. A skein of wires just below the liquid surface acts as an extraction grid. The inner walls are covered with high reflectivity reflectors and all the inner surfaces are coated with TPB to shift the native UV argon light to the visible.

Scintillation light generated inside the TPC volume is detected by planes of SiPMs just outside and completely covering the top and bottom caps. Just outside each SiPM plane and mechanically integrated with the SiPM structure are the end cap layers of gadolinium-loaded acrylic.

The detector is housed within a sealed, vacuum capable, titanium vessel immersed within a bath of liquid atmospheric argon (AAr) acting as shield and outer veto detector. The AAr is contained within a ProtoDUNE like membrane cryostat [19–21].

Figure 1 shows a CAD rendering of the cryostat and the related infrastructures in Hall C in LNGS (top), a cross view of the inner detector inside the cryostat (bottom left), and the TPC outside wall with veto light sensors and the titanium vessel top cover (bottom right).

The construction, installation and commissioning of the DS-20k detector in the Hall C of the INFN-LNGS laboratory depend on the availability of additional plants and infrastructures realized by the GADMC Collaboration and together they contribute to form the DS-20k experiment. We identify five main branches in the Product Breakdown Structure shown in figure 55 in section 6: the Urania and Aria facilities for the extraction and distillation of the UAr, two branches describing the DS-20k detector elements and the photo-detector system respectively and, finally, support facilities necessary during the various phases of the construction and assembly of the detector.

This document is a Technical Design Report (TDR) of the DS-20k detector and it describes in detail all the items in the two branches DS-20k detector elements and photo-detectors. Items belonging to the support facilities branch are discussed at a level of detail needed for understanding the DS-20k detector items production and integration. The branches related to the UAr will not be covered here in detail; only the interfaces with the DS-20k detector will be described. A more detailed description of Aria can be found in [22].

This document is organized as follows: section 2 briefly summarizes the physics case and shows the sensitivities for WIMP detection. Section 3 describes the R&D activities toward the design and construction of the detector, specifying the goals of the R&D and the results achieved. After a short review of previous results obtained by the GADMC with argon-based detectors in section 4, the detailed DS-20k detector design is described in section 5. The overview of the Product Breakdown Structure is presented in section 6, followed by detailed technical descriptions of all the parts of the detector and of the related infrastructure, in sections 7, 9 and 10. The assembly of the detector

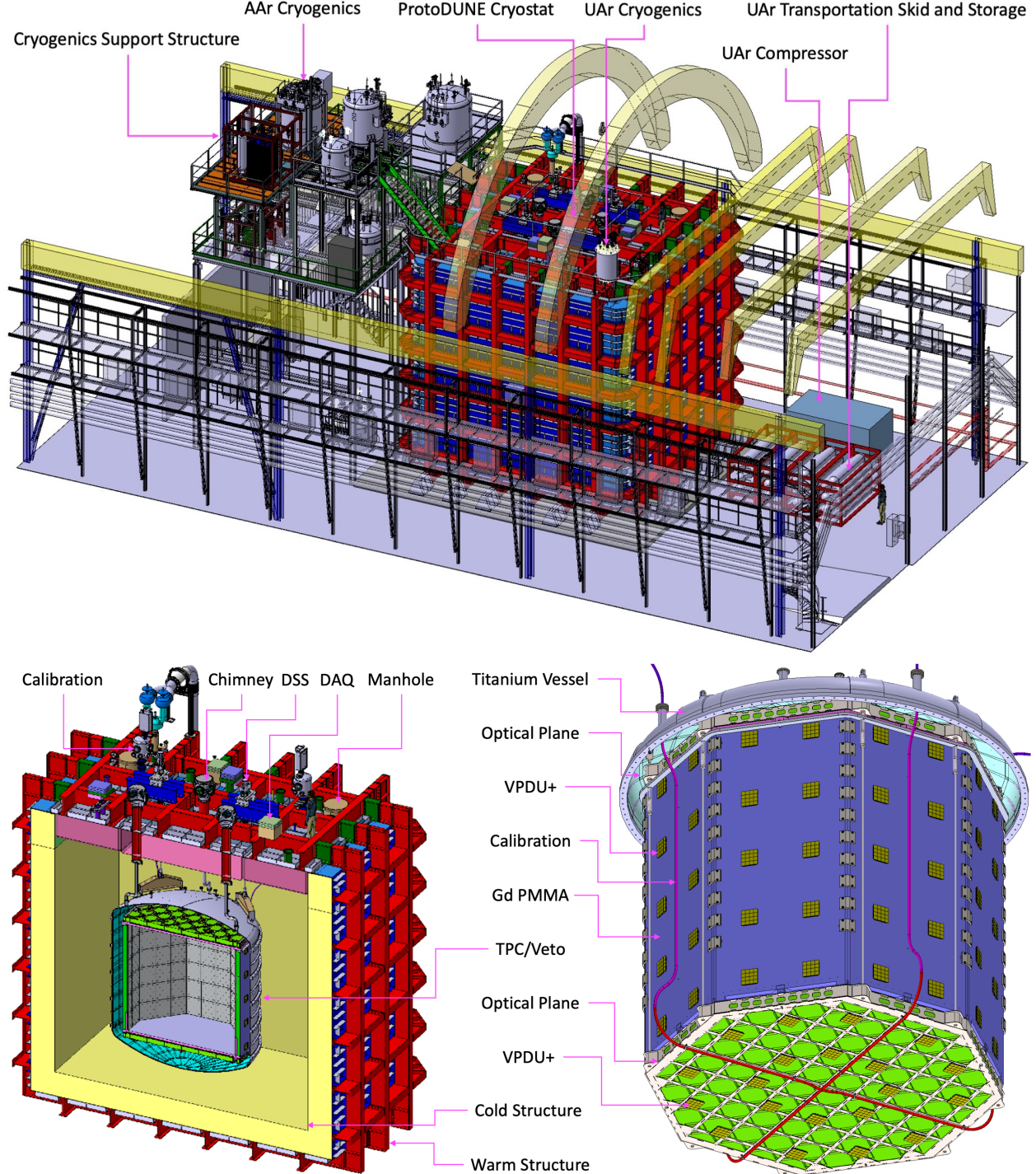


FIG. 1. **Top:** CAD rendering of the DS-20k experiment in Hall C of LNGS showing the red ProtoDUNE like cryostat housing the detector and the cryogenics system and its support structure. **Bottom Left:** cross section showing the inner detector with the Gd-PMMA in green, the Titanium vessel in gray and right: external view of the TPC and Veto showing the full assembly features including VPDU+, Calibration, Optical planes and the Gd PMMA wall structure.

957 is described in section 11, including procurement, construction, quality control and assurance and
958 handling of the various parts of the apparatus to reach the necessary levels of radiopurity and
959 cleanliness. The validation of the design choices, including both Monte Carlo evaluation and tests

960 with prototypes, are described in section 12. Health, Safety and Environment (HSE) aspects,
961 including description of relevant regulations and procedures, are presented in section 13. Section
962 14 covers management and organization, with details about funding, schedule and summary of
963 requests to LNGS.

964

2. SCIENTIFIC MOTIVATIONS

965 A body of astronomical observations, including galactic rotation curves, strong gravitational
 966 lensing, and the anisotropy of the cosmic microwave background, indicates that known matter
 967 only accounts for a small fraction of the mass-energy content of the Universe [xx]. The evidence
 968 is widely interpreted to imply that the missing dark matter is composed of as yet unidentified
 969 elementary particles [xx]. Direct detection of such particles would be an extraordinary discovery,
 970 opening a gateway to the investigation of the dark universe and understanding of physics beyond
 971 the Standard Model. One of the best motivated dark matter candidates is the weakly interacting
 972 massive particle (WIMP), a thermal relic of the Big Bang, which has a sub-electroweak scale
 973 interaction cross section and a mass in the TeV/c^2 -range. The WIMP dark matter hypothesis is
 974 also motivated by the ubiquity of WIMP-like particles in extensions to the Standard Model. The
 975 motion of galactic halo WIMPs relative to a detector on Earth could result in WIMP-nucleus elastic
 976 collisions detectable in a low-background, low-energy-threshold detector. Such a detector must be
 977 capable of unambiguously identifying a small number of nuclear recoils from WIMP interactions
 978 over the course of a very large exposure.

979 The observation of WIMPs with masses up to about $1 \text{ TeV}/c^2$ is a major objective of the exper-
 980 imental program at the High Luminosity Large Hadron Collider. Future high energy colliders like
 981 the FCC-*hh* (Future Circular Collider) will be able to extend these searches up to the $10 \text{ TeV}/c^2$
 982 mass range [23]. Direct and indirect dark matter detection techniques allow for a search program
 983 complementary to the LHC, capable of probing masses beyond the reach of colliders. While several
 984 early results from small direct detection detectors were consistent with a dark matter signal [xx],
 985 these have not been confirmed and are in tension with recent results [xx]. A convincing discovery
 986 will require detection with multiple targets, which will allow for more stringent constraints on dark
 987 matter particle properties despite the significant uncertainty of astrophysical parameters [xx].

988 The median sensitivity of the DS-20k experiment is calculated using a profile likelihood approach
 989 and is based on a comprehensive Monte Carlo simulation to predict the event rate in the WIMP
 990 region of interest. Systematic uncertainties affecting the various sources of backgrounds consid-
 991 ered in the likelihood analysis are propagated into rates and spectrum uncertainties. The present
 992 projection is based on a 10 yr run, corresponding to a fiducial volume exposure of 200 t yr. An
 993 analysis that considers the instrumental background in the full active volume of the DS-20k target,
 994 including its spatial distribution within the detector, would lead to an exposure of 500 t yr and
 995 increased sensitivity. The projected sensitivities of the full volume analysis are $4.6 \times 10^{-48} \text{ cm}^2$ for
 996 the 90% C.L. exclusion and $1.5 \times 10^{-47} \text{ cm}^2$ for the 5σ discovery of a $1 \text{ TeV}/c^2$ WIMP, well beyond
 997 any current or funded experiment as shown in Fig. 2. This will either lead to discovery, confir-
 998 mation, or exclusion of the WIMP-DM hypothesis, down to the level where coherent scatters from
 999 atmospheric neutrinos start contributing to the background rate. We further note that, thanks to
 1000 the low rate of irreducible background from coherent neutrino scatters (which is expected to be the
 1001 dominant background source), the DS-20k sensitivity continues to increase with exposure time. A
 1002 20 yr run would bring the sensitivity closer to the “neutrino floor” [24].

1003 As shown in Fig. 2, DS-20k results from an initial five year run, would cover and extend the mass
 1004 vs. cross-section range being explored by LZ and XENONnT for WIMP masses above $0.1 \text{ TeV}/c^2$.

1005 Should LZ or XENONnT measure a dark matter signal over the course of their nominal operating
 1006 lifetimes of 2.7 yr and 5 yr, respectively, DS-20k is the only planned detector that could promptly
 1007 confirm their result, and will do so using a different detector technology with different systematic
 1008 effects. This confirmation would be crucial in establishing the validity of a landmark discovery.
 1009 Additionally, a positive detection using an argon target combined with the xenon result will improve
 1010 the determination of the dark matter mass and coupling. See [25, 26] for details.

1011 The use of the ionization signal only enables extension of the DS-20k observation window to light
 1012 dark matter candidates and neutrinos. The ionization yield of NRs has recently been measured
 1013 to be about 7 e-/keVnr at 500 eVnr, which allows the detection threshold to be lowered to only
 1014 3 electrons extracted in the gas phase for the DS-50 experiment [31]. The high ionization yield
 1015 in addition to the favorable kinematics, which guarantee a higher transferred momentum than

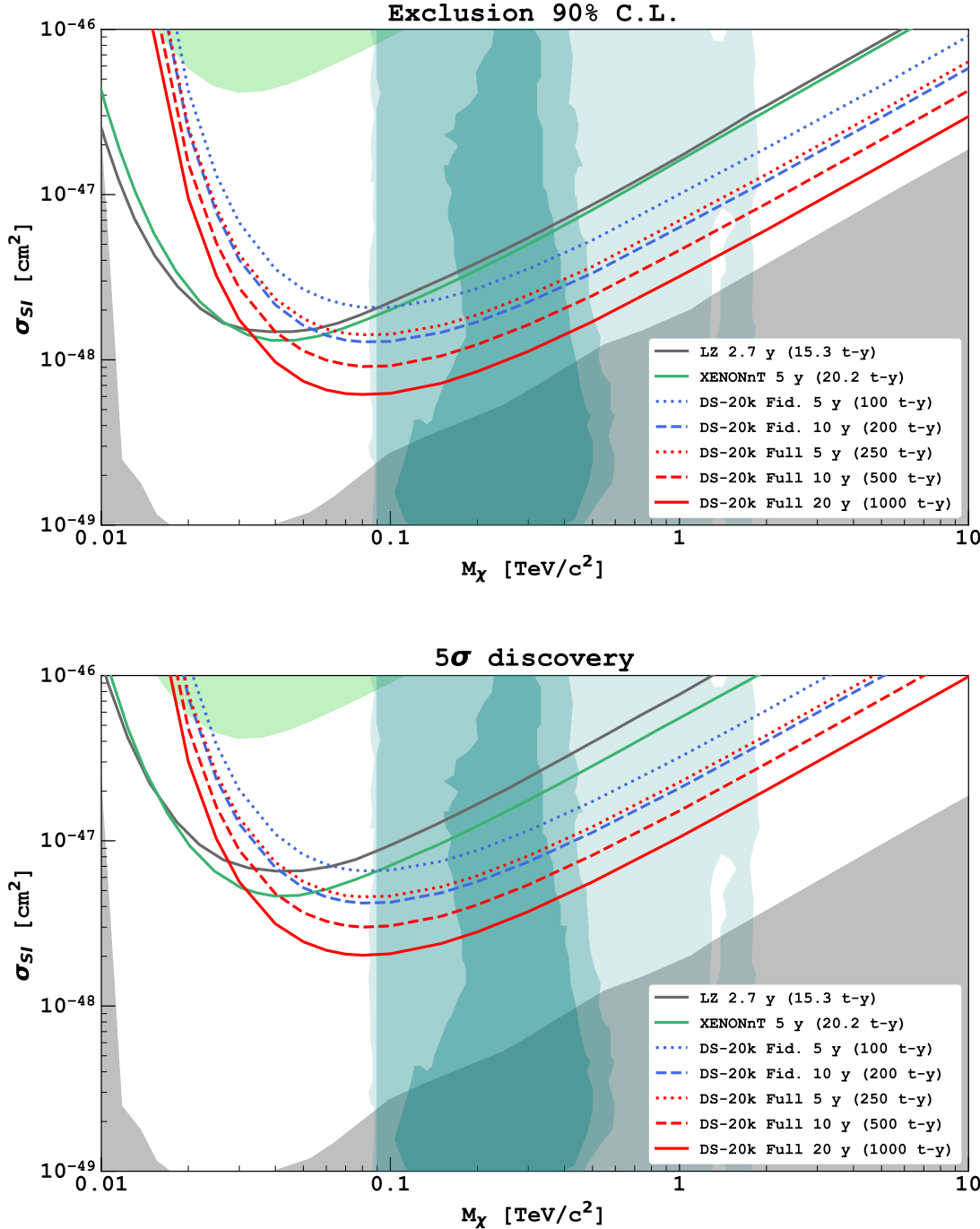


FIG. 2. The sensitivity of DS-20k to spin independent WIMPs (top: 90% C.L. exclusion; bottom: 5 σ significance) for different lengths of runs shown compared to the nominal sensitivity of currently funded experiments LZ (2.7 yr run, 15.3 t yr exposure [27]) and XENONnT (5 yr run, 20.2 t yr exposure [28]) that are expected to lead the field for high mass WIMPs searches in the next few years. The region excluded by XENON1T [29] is shown in shaded green, the “neutrino floor” for argon in shaded gray [24], and the turquoise filled contours represent the 1-, 2-, and 3- σ favored regions from the pMSSM11 model constrained by astrophysical measurements and the \sim 36 fbarn LHC data at 13 TeV [30]. (Note: the XENONnT 90% C.L. exclusion curve shown in these plots use a two-sided test statistic, leading to limits weaker by 30%, as described in [28].)

1016 in Xe thanks to the lower atomic number, allows to explore interactions from a number of dark
1017 matter candidates down to the sub-keV range. In particular, DS-20k will extend current limits
1018 from WIMP-nucleus, with and without Migdal effect, and WIMP-electron interactions for WIMP
1019 masses below $5 \text{ GeV}/c^2$, and from galactic and solar axion-like particles, and keV-mass scale sterile
1020 neutrinos.

1021 Beyond dark matter searches, the outstanding sensitivity to coherent nuclear recoils will enable
1022 DS-20k to detect a supernova neutrino burst coming from anywhere in the Milky Way Galaxy
1023 and, for a majority of the galaxy, clearly identify the neutronization burst. DS-20k would perform
1024 a flavor-blind measurement of the total neutrino flux and average energy, determining an overall
1025 normalization that is not affected by neutrino oscillations [32].

1026 DS-20k also has the potential to detect solar neutrinos, via elastic scattering, in the [0.6, 1.3] MeV
1027 range, beyond the energy region dominated by ^{39}Ar decay. In this energy window, about 1,000
1028 signal events are expected in a 100 tonne-year exposure [33]. DS-20k therefore can measure the
1029 rate of ^{7}Be neutrinos, which represent about 60% of the expected signal, with an uncertainty of
1030 less than 5%, improving upon the the most accurate measurement so far by Borexino [34].

3. R&D TOWARD THE DS-20K DETECTOR DESIGN

In this section we describe the subset of R&D activities related to the final detector design. In particular we will describe

- The material screening.
- The development of cryogenic SiPMs.
- The design and test of cryogenic amplifiers coupled to a SiPM tile (together comprising a Photo Detector Module, abbreviated PDM) and its compact version called Tile+.
- The design and test of the Photo Detector Unit (PDU), which integrates several PDMs in a large matrix.
- The development of radio-pure cables and connectors.
- The development of TPC components, including the design of the High Voltage cables, the electric field generation and simulation.
- The characterization of wavelength shifting films for the TPC and Veto.
- The development of a hybrid material made of PMMA loaded with Gd to form the TPC and Veto structure.
- The mock-up of the calibration system.
- The development and test of the UAr cryogenics system.

Each subsection of this chapter is organized as follows: specification of the goal of the R&D, report on the R&D activity, and summary of the results achieved and conclusions.

3.1. Material Assays

3.1.1. Goals of the R&D

The goals of this activity are

- to measure the concentration of radioactive contaminants in the materials to be used in the detector;
- to develop strategies for material selection and well-defined protocols for machining, storing, transporting, cleaning and assembling of the detector components; and,
- to develop tools to evaluate the neutron and γ background of the experiment.

3.1.2. Organization of the activity

We have developed a radio-purity assay program that takes advantage of facilities and experts in low background techniques and material assay methods throughout the collaboration. This program involves hundreds of assays, to identify radio-pure materials, screen all detector components, and develop and validate material cleaning and handling procedures. The collaboration has extensive and diverse assay capabilities that are sufficient to complete this program, with extra capacity to handle additional unforeseen assays.

The assay challenges are organized into six focus areas: mass spectrometry (ICP-MS), Rn emanation, direct gamma assay (HPGe), surface assays of α activity, cosmogenic activation and materials handling. The goal is to assay and approve *all* materials or items selected to reside within the cryostat, particularly by scrutinizing the entire ^{232}Th and ^{238}U decay chains. This strategy calls for multiple assays with multiple techniques for each sample, as different techniques are required to measure different parts of the chains.

ICPMS allows measurement of the ^{232}Th and ^{238}U concentrations at very low levels, typically $< 100 \mu\text{Bq}/\text{kg}$, allowing determination of the upper decay chains in a wide variety of samples. HPGe counting is used to measure the activity of U and Th daughters in the middle chains, as well as K-40 and all other relevant gamma emitters (for example ^{60}Co , ^{137}Cs , ^{235}U , etc.). Radiochemical techniques, e.g. chemical extraction of polonium [35], are used to measure the lower part

of the ^{238}U decay chain. The use of these three different techniques enables investigation of the entire decay chain, without assuming secular equilibrium, thus allowing a more precise calculation of the material-induced background.

^{232}Th , ^{238}U and ^{40}K contamination in the 1-10 Bq/kg range is tolerable in the parts of the detector farthest from the TPC, e.g. in the cryostat, due to gamma-ray attenuation in the argon buffer and neutron attenuation/detection in the Gd-loaded acrylic veto. Much more stringent radiopurity requirements are necessary for the TPC and veto materials: contamination $\ll 1 \text{ mBq/kg}$ may be required, depending on the mass of the component.

3.1.3. Radio-purity database

The need for fast access to, and exchange of, data within the collaboration is addressed by the DS-20k materials database (MDB). Information on the radioactive content of materials to be used for DS-20k construction is stored therein, including comprehensive information about samples: chemical composition, origin (production batch), data-sheets, pictures, location in the detector, history of assays, etc. MDB data on radioactivity content are carefully evaluated and included in the total background budget estimation of the experiment.

The database helps to systematize the radioactive background budget estimation, material selection and tracking, assay prioritization, and cleaning and handling methods. Rules for handling and cleaning of the samples, developed and verified during the screening process, are also stored in the database.

The MDB structure reflects the flow of the material assay process, aiding material selection as well as QA/QC processes during the construction phase of the experiment. The database consists of cross-related tables, holding information on the status of the assay requests, screening methods, samples, assay results and people/institutions involved (see Fig. 3). The MDB stores the history and the current status of any assay performed by the Materials Working Group. It also keeps track of the queues in different facilities, balancing the workload and assay resources between the facilities and institutions involved in this task. A convenient web-based interface is provided for users (see Fig. 4), dedicated to: submission of new assay requests from other DS-20k Working Groups; uploading, browsing and reporting of assay status and results; and, managing queues at different facilities.

Assay Method	Participating Institutions	Information	Typical detection limits	Number of assays
ICP-MS	LNGS, LSC, MSU, PNNL	Upper U and Th chains	$\approx 1\text{-}10 \text{ ppt}$ ($10\text{-}100 \mu\text{Bq/kg}$)	65
HPGe counting	Boulby, LNGS, LSC, SNOLAB, Temple	Middle U and Th chains Gamma spectroscopy	$\approx 100\text{-}200 \mu\text{Bq/kg}$	90
Chemical extraction of Po	Kraków	Lower U and Th chains	$\approx 10 \text{ mBq/kg}$	35
α 's counting	LSC, Kraków, SNOLAB	Surface α contamination	$\approx 1 \text{ mBq/m}^2$	5
Radon emanation	Kraków, Marseille		$\approx 20 \mu\text{Bq}$	5
Other				3

TABLE III. Methods used for the DS-20k assay campaign and participating institutions. Only the assays performed since 2017 in preparations of the DS-20k construction are reported in the last column. In the case of HPGe counting, the detection limits depend on the specific gamma line analyzed. The reported numbers refer to the main ^{228}Th , ^{226}Ra , ^{137}Cs lines for a some kg polyethylene sample.

More than 200 assays have been performed since the start of the campaign in 2017 (see Table III). Assay results obtained for the materials used for DS-50 were also imported to the MDB.

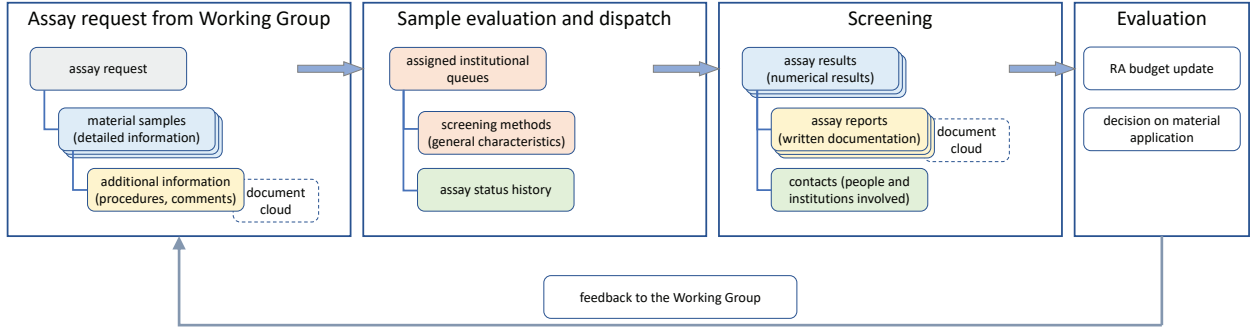


FIG. 3. A simplified DS-20k materials database structure. Information on each relevant aspect of the assay process is stored in the database, facilitating the management of the whole assay process.

Sample name Description Batch DS-20 reference Search ▾														
Show 25 entries Copy CSV Hide empty Show all Column visibility ▾														
ID	Report	Name	Reference	Method	Sample	Date	^{60}Co	^{137}Cs	^{40}K	^{234m}Pa	Pb	^{210}Pb	^{210}Po	^{226}Ra
1910	253	Capacitor 22pF	273 Non-satisfactory	PDM module	HPGe GeDSG (Matthias Laubenstein, LNGS, INFN),	complete	2018-12-13	<6 [mBq/kg] (3 sigma)	<6 [mBq/kg] (3 sigma)	1.5 ± 0.7 [Bq/kg] (1 sigma)	<1 [Bq/kg] (3 sigma)			<1 [Bq/kg] (3 sigma)
36	5	Panasonic SMD capacitors	5 Decision pending	PDM module	HPGe GeCris (Matthias Laubenstein, LNGS, INFN),	complete	2017-12-14	<2 [mBq/kg]	<4 [mBq/kg]	<1 [Bq/kg]	<2 [Bq/kg]			<6 [mBq/kg]
1854	246	Panasonic capacitors	57 More assays needed	PDM module	HPGe BEGe (Matthias Laubenstein, LNGS, INFN),	complete	2018-08-30	<7 [mBq/kg]	<5 [mBq/kg]	<2 [Bq/kg]	<7 [Bq/kg]			<0.2 [Bq/kg]

FIG. 4. Interface web page, presenting a selection of assay results for various types of capacitors. The database is also used to manage the assay process of each sample.

1107

3.1.4. Radioactivity budget

1108 Neutron-induced nuclear recoils can pose irreducible backgrounds to dark matter searches. The
 1109 most critical requirement in terms of radio-purity is given by the α activity, mainly caused by
 1110 the naturally occurring radioactive chains of ^{232}Th and ^{238}U , and potentially producing neutrons
 1111 through (α, n) reactions. Neutrons are highly penetrating and this demands severe radio-purity
 1112 constraints, not only to the materials close to the fiducial volume of the TPC, but also to external
 1113 materials.

1114 The radioactivity budget quantifies the expected neutron and γ background produced by all
 1115 components located within or around the cryostat, taking into account the assayed radio-purity,
 1116 mass, composition, shape, and location of each material. This budget is calculated by considering
 1117 the contribution of each individual detector material, using the inputs above together with the
 1118 Monte Carlo background rejection efficiency of the DS-20k detector for each component.

1119 We have developed online tools, available via a web interface to all collaborators, to evaluate the
 1120 neutron and γ background rates. The tool is continuously updated to reflect current assay results,
 1121 and it serves as a powerful instrument to monitor the expected background and identify potentially
 1122 dangerous contributions.

1123 The methodology employed for estimating (α, n) neutron production rates, energy spectra, cor-
 1124 related γ -rays, and the backgrounds these give rise to are described in section 5.8.3.

1125 *3.1.5. Surface contamination, material storage and cleaning*

1126 Exposure to environmental ^{222}Rn during fabrication, assembly, and installation of the experiment
 1127 can lead to build-up of ^{210}Pb on surfaces. ^{210}Pb , which has 22 yr half-life, can act as an
 1128 approximately constant source of radiation, from its own decays and from associated decays of ^{210}Bi
 1129 and ^{210}Po , throughout the full life of the experiment. In case of surface contamination, the alpha
 1130 decays are relatively easy to identify by their specific energies, e.g. 5.3 MeV for ^{210}Po . However,
 1131 in some cases the alpha peaks may be shifted to lower energies due to quenching effects or energy
 1132 losses if the source is located in a sub-surface layer (termed degraded alphas). Additionally, alpha
 1133 decays on the surfaces of materials that contain isotopes with high α -n cross sections can contribute
 1134 to the neutron background.

1135 Activities related to studies of surfaces contamination may be in general divided into two groups:
 1136 (i) Materials; and, (ii) Procedures. Materials activities include investigations of initial, post-
 1137 production surface contamination levels for most critical materials used in the experiment (acrylic,
 1138 ESR foil, titanium, copper). Under "Procedures" we include: investigations of handling procedures;
 1139 development of cleaning protocols for different materials; and, development of methods to protect
 1140 surfaces from contamination.

1141 The collaboration has established a dedicated research program for each group of activities within
 1142 Materials and Procedures, summarized below.

1143 Concerning materials, measurements of the cleanliness level of copper and ESR foil are currently
 1144 ongoing. Tests of Ti, stainless steel and PMMA/Gd-loaded PMMA are planned.

1145 With respect to handling procedures, we are now investigating the ESR film covered with a thin
 1146 layer of Clevios (described in section 3.6.4), which has been shown to contain very little $^{210}\text{Pb}/^{210}\text{Po}$
 1147 ($\sim 10 \text{ mBq/kg}$). The clean conductive layer on the ESR foil allows accurate measurements of con-
 1148 tamination of non-conductive surfaces, also highlighting any impurities introduced by the coating
 1149 procedure. The next tests will be performed for TPB coating of the ESR foil (combination to be
 1150 used in the detector) and PMMA coating with Clevios. To study materials and handling procedures
 1151 high-sensitivity instruments are necessary. For this, the collaboration has access to two screening
 1152 stations, large-surface ultra-low background alpha spectrometers, with detection limits at the level
 1153 of 1 mBq/m^2 .

1154 Concerning Procedures, in order to minimize the contamination of material surfaces with short-
 1155 and long-lived daughters of ^{222}Rn , specific surface cleaning protocols are being developed for the
 1156 most critical detector components. In general, to investigate cleaning protocols it is possible to
 1157 artificially contaminate the surface, then clean it, to measure reduction of radioactivity from the
 1158 protocol, thus standard semiconductor alpha spectrometers are usually sufficient. The DS-20k
 1159 copper cleaning protocol is developed at the Legnaro National Laboratories (LNL). The protocol
 1160 is an adaptation of the CUORE cleaning protocol [36] and it consists of 3 subsequent steps of
 1161 treatment:

- 1162 • Tumbling: it is a mechanical treatment of polishing and preparation of the surface, it removes
 1163 less than 1 μm of material.
- 1164 • Electropolishing: it is an electrochemical treatment acting on the metal surface, it removes
 1165 a thickness in the range of 100 μm of material on each surface. The electrochemical reaction
 1166 is driven by the current passing through the EP circuit.
- 1167 • SUBU: it is a chemical treatment acting on the metal surface, it removes a thickness in the
 1168 range of 5 μm of material on each surface. The reaction is driven by the temperature of the
 1169 solution ($72 \pm 1^\circ\text{C}$).

1170 Several tests have been already performed to verify the ^{210}Po removal efficiency from copper, demon-
 1171 strating reduction of surface specific activity by two orders of magnitude. Even if the described
 1172 procedure is simplified to remove less copper than the standard 100 μm (50 μm and 20 μm have
 1173 been tested), the reduction is similar. Cleaning protocols and tests are under development for Ti
 1174 and stainless steel.

1175 Following cleaning procedures, in order to avoid re-contamination, all relevant detector com-
 1176 ponents will be stored in a nitrogen atmosphere. Triple-layer (PE/PA/PE), radon impermeable

1177 plastic bags will be used to store components in vacuum or under neutral gas atmosphere. The
 1178 diffusion of Rn through these bags is currently being studied through dedicated R&D in order to
 1179 quantify the maximum safe storage time for these components. Dedicated boxes, air tight, will be
 1180 built to store and transport the assembled electronics. Similarly, the surfaces of acrylic plates will
 1181 be protected by bags immediately after production.

1182 It is foreseen that handling and installation of the critical detector's parts will be performed
 1183 in a Rn-reduced atmosphere, including mechanical cleaning if the exposure to normal air prior to
 1184 installation exceeds safe limits. Evaluation of the exposure limits, including the realistic surfaces
 1185 of the various part of the detector, are in section 5.8.4.

1186 3.1.6. R&D results and conclusions

1187 The software tools to record radioassay data and to evaluate the backgrounds, the selection of
 1188 the main materials, and protocols for handling materials have been developed. Three different
 1189 radioassay techniques have been used to assay the entire ^{238}U chain. Using this suite of tools, the
 1190 materials of the critical detector components have been selected on the basis of multiple analyses of
 1191 samples. Where suitable commercially available components were not found, dedicated R&D has
 1192 been completed in collaboration with industries in order to build radio-pure cables and connectors
 1193 (described in sections 3.5). The radioactive budget of the experiment is updated in real time with
 1194 the progress of the material assay campaign. New measurements will be performed on the final
 1195 production batches to confirm the results of the analysis of the samples used to select components.

1196 3.2. SiPMs

1197 3.2.1. Goals of the R&D

1198 This R&D aims to develop SiPMs suitable for use in a cryogenic environment, at 87 K, and to
 1199 transfer the SiPM technology to a company with the infrastructures suitable for the full production
 1200 for the DS-20k experiment. The total surface of SiPMs to be used in the DS-20k detector is more
 1201 than 25 m^2 . To minimize the number of readout channels, this R&D aims to develop arrays of
 1202 SiPMs assembled into a tile, coupled to a suitable amplifier in the cryogenic environment, with
 1203 a single signal output. Table IV reports the initial target specifications driving the development
 1204 activities. More detailed specifications (reported in Table XLIII) have been elaborated following
 1205 the results achieved by the R&D.

Parameter	Value
Stable operation at 87 K	
Single SiPM size	$\simeq \text{cm}^2$
Tile dimension	squared or rectangular, few cm edge
PDE at 420 nm at 77 [k] at 9 [V] of OV	>40 % (420 nm)
Dark noise rate at 77 [K] at 7 [V] of OV	< 0.01 Hz/mm ²
Dark noise rate at 77 [K] at 9 [V] of OV	< 0.1 Hz/mm ²
Total contribution to n background	< 0.01 neutrons/200 t yr after the analysis cuts

1206 TABLE IV. Specifications of the SiPMs
 1207

1208 3.2.2. Development of cryogenics SiPMs

1209 The SiPMs development enterprise started with a research activity involving Fondazione Bruno
 1210 Kessler -Trento, Italy (FBK) and the GADMC , who together identified the best technology, re-

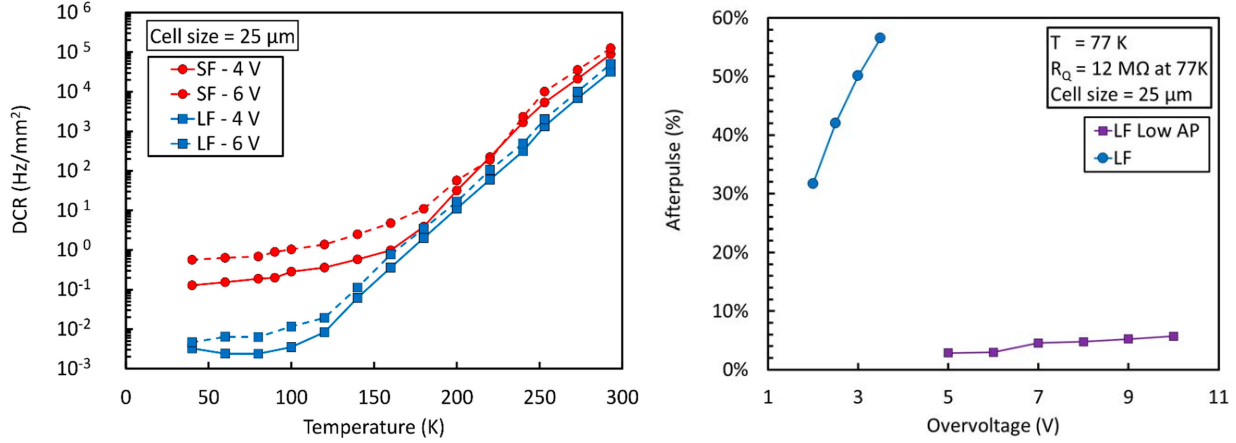


FIG. 5. Left panel: DCR as a function of temperature for the SF and LF versions at two values of excess bias. Right panel: AP probability as a function of excess bias at 77 K for the LF and LF-LowAP SiPMs. Reproduced from [1].

1211 ported in [2]. The enterprise continued with the technology transfer to LFoundry Srl-AQ, Italy
 1212 (LFoundry), a company with the infrastructures for the full production of the devices for DS-20k.

1213 First, two SiPM technologies already available at FBK were characterized in cryogenic conditions,
 1214 NUV-HD-LF and NUV-HD-SF. Both technologies have maximum detection efficiency at 410 nm
 1215 wavelength, in the near-ultraviolet (NUV), and feature high density (HD) of single photon avalanche
 1216 diodes (SPADs). "SF" refers to standard field, and "LF" to low field [37]. The two versions are
 1217 based on the same p-on-n technology and only differ in the doping profiles, such that the LF
 1218 version shows a lower peak value of the junction electric field at breakdown. For the same reason,
 1219 the breakdown voltage V_{BD} of the LF version is shifted to 32.5 V at room temperature, compared
 1220 to the 26.5 V of SF. Under cryogenic operation, the carrier mean free path increases, thus a lower
 1221 electric field is needed to reach the breakdown condition. For this reason, at liquid nitrogen (LN)
 1222 temperature V_{BD} is shifted to 21.4 V and 27.0 V for SF and LF, respectively.

1223 The main development activities towards selecting the technology were:

1225 • Reduction of Dark Count Rate (DCR) at cryogenic temperatures

1226 DCR is an important parameter because it contributes to the detector occupancy per event.
 1227 The left panel in figure 5 shows the dependence of DCR on temperature for SF and LF
 1228 devices, at two different biases above the breakdown voltage. While SF and LF show a
 1229 comparable DCR at room temperature, LF shows a lower plateau value at cryogenic tempera-
 1230 ture, when the main mechanism becomes direct band-to-band tunneling. Since tunneling
 1231 is field-dependent, the LF version benefits from a lower peak electric field, thus reaching a
 1232 typical value of few mHz/mm² at a temperature below 80 K. Based on this observation, LF
 1233 was chosen as the baseline platform for the development.

1235 • Reduction of Afterpulsing probability (AP) at cryogenic temperatures

1236 AP is an important parameter because it can impact particle identification using pulse shape
 1237 discrimination. At cryogenic temperature, typically below 150 K, the AP probability in-
 1238 creases rapidly in NUV-HD technologies (both SF and LF), reaching a maximum around
 1239 80 K [38]. This effect is attributed to a longer release time constant of carriers captured
 1240 by trapping centers at cryogenic temperatures. The increase of AP probability with bias
 1241 voltage limits the operating range of SiPMs, preventing exploitation of the increasing Photon
 1242 detection Efficiency (PDE) with larger excess bias. A specific process split was identified
 1243 to strongly suppress the increase of AP probability at cryogenic temperature. The resulting
 1244 technology is thus called LowAP. This process adjustment was applied to NUV-HD-LF leading
 1245 to a new technology named NUV-HD-CRYO. The right panel in figure 5 shows the AP

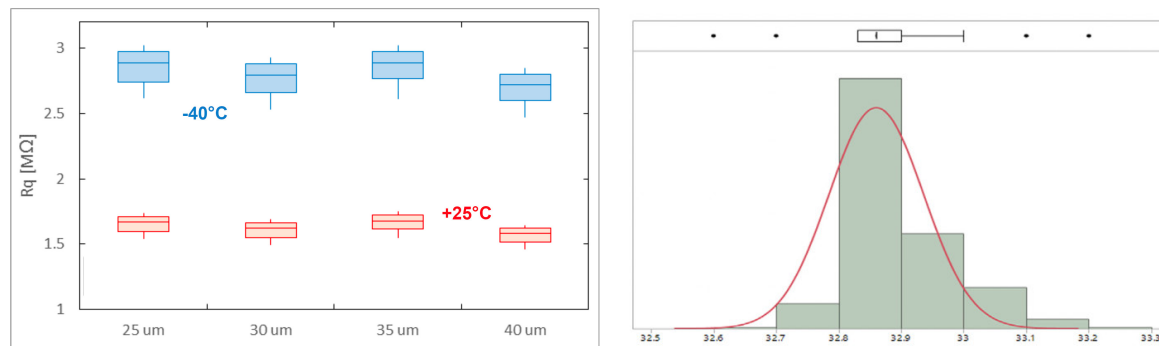


FIG. 6. Left: Quenching resistance by cell size at -40°C and 25°C . Sample size is over 4000 SiPM. Right: Breakdown Voltage distribution of about 20,000 SiPM, on different wafers.

1246 probability reduction of LowAP, compared to the conventional technology.

1247

- 1248 • **Stability of quenching resistance with temperature**

1249 In the standard fabrication process of SiPMs at FBK, the quenching resistor (R_q) is made
 1250 of polycrystalline silicon (poly-Si). This material exhibits a significant resistivity variation
 1251 with temperature: the standard R_q shows a 64 fold increase from 293 K to 77 K. As an
 1252 example, a resistor with a value of $\sim 6.5 \text{ M}\Omega$ at 77 K would have a value of $100 \text{ k}\Omega$ at room
 1253 temperature, preventing correct avalanche quenching above 2 V excess bias. This represents
 1254 an issue for characterization purposes, where SiPMs need to be functional both at room
 1255 temperature and in cryogenics. FBK developed a technology variant of the poly-Si resistor,
 1256 which allows operation of SiPMs at both room and cryogenic temperatures. This process
 1257 adjustment obtains a variation only of a factor 4 from room temperature to LN temperature.
 1258 This also allowed having a relatively fast recharge time constant of the microcell in cryogenic
 1259 conditions, below 300 ns with a 30 μm cell.

1260 3.2.3. *Technology transfer*

1261 The first process transfer started in 2016 with the NUV-HD technology. Later in 2018, the process
 1262 was tuned according to the NUV-HD-CRYO technology in order to meet the DS-20k requirements.

1263 Uniformity of SiPM performance is required by the experiment in order to achieve integration
 1264 into tiled arrays with a single output. SiPMs are assembled into a tile array, typically made up of 24
 1265 individual SiPMs. The individual SiPMs of a tile should have as much as possible uniform behavior
 1266 in terms of gain and pulse shape in order to preserve single photon resolution in the summed signal
 1267 output.

1268 Following the technology transfer, the quenching resistance was measured on more than 4000
 1269 SiPMs from 25 different wafers showing an interquartile range of 7% at both $+25^{\circ}\text{C}$ and -40°C
 1270 temperatures (See Fig. 6, left panel). The break-down voltage distribution at room temperature
 1271 showed a standard deviation of 0.2% (or 75 mV) over an average value of 32.8 V (see Fig. 6, right
 1272 panel). As illustrated in Fig. 21 this degree of uniformity is sufficient to achieve the signal-to-noise
 1273 requirement for single photon detection.

1275 3.2.4. *Backside metallization development*

1276 The SiPM wafers need a backside metallization to make a good cathode contact without affecting
 1277 the detector resistance (R_d) between the anode and the cathode of the tile. R_d is measured as the
 1278 slope of the IV curve in forward bias in the linear region. When SiPMs are tested individually, the
 1279 R_d is equal to the series resistance of: SiPM, wire bonding, backside contact resistance, connectors

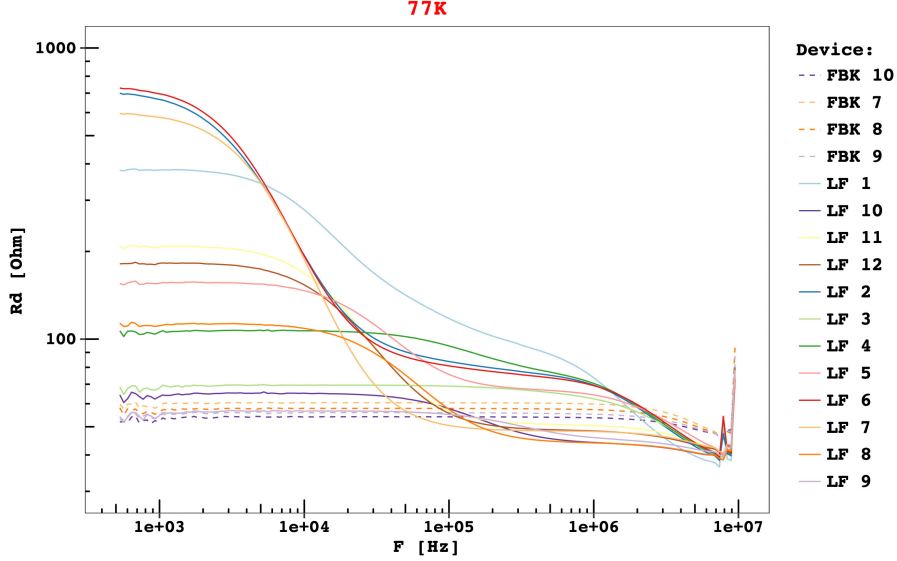


FIG. 7. Forward resistance vs frequency at 77K from both LFoundry (solid lines) and FBK (dashed lines). Similar behaviour was observed also at 300K.

and PCB tracks. The latter quantities are expected to be negligible with respect to the SiPM resistance, so that $R_d \approx R_{SiPM}$.

Stable results were obtained with a film stack of AlSi/Ti/TiN (in the order of deposition, so the AlSi is in contact with silicon) sputtered by FBK. LFoundry proposed a stack of AlCu/Ti/TiN since the AlSi was not available while AlCu is a standard production process. The first run, LFoundry-Run-1, showed a significant spread of the forward detector resistance R_d among SiPMs and higher values than FBK reference data, as shown in Fig. 7.

The issue was traced to the backside surface preparation before sputtering the AlCu/Ti/TiN stack, leading to a resistive interface between back metal and silicon. The modified process applied on LFoundry-Run-1b showed satisfactory results, so LFoundry-Run-2 and LFoundry-Run-3 (25 wafers each) were processed for further R&D to build new tiles.

Four months after the production of LFoundry Run-2, the tiles produced from Run-2 and Run-3 were measured again and showed an unexpected increase of the detector resistance by up to a factor of 2. The spread among the SiPMs increased as well. In order to identify the root cause of the resistance increase, Run-4 was processed with different backside processes, including AlCu/Ti/TiN, AlSi/Ti/TiN and Ti/Ni/Ag from LFoundry, as well as Au from FBK. Samples in LFoundry were also split with different surface roughnesses. TiN samples were bonded with silver epoxy glue while indium-based soldering was used for gold and silver. A summary of the backside film options and related deposition and bonding technologies is reported in Table V.

Film Deposition site	Deposition Technology	Bonding Technology	Issues
AlCu	LFoundry	Sputter (PVD)	R_d Aging, R_d spread
AlSi	LFoundry	Sputter (PVD)	R_d Aging
Au	FBK	Evaporation (e-beam)	No issues
Ag	LFoundry	Evaporation (e-beam)	SiPM cracks

TABLE V. Summary of the backside options and issues

Tiles were been built from these runs, using approximately 300 SiPMs, for which IV curves were collected twice a week at both LN and room temperature. After two months of tests, the increase of device resistance effect has been observed on all the tiles made with AlCu and AlSi, with an average growth rate of 0.5 Ω /week. Au and Ag backside samples have shown no aging over a testing period of 6 months. Au and Ag show the narrowest distributions of R_d , as shown in Fig. 10, which

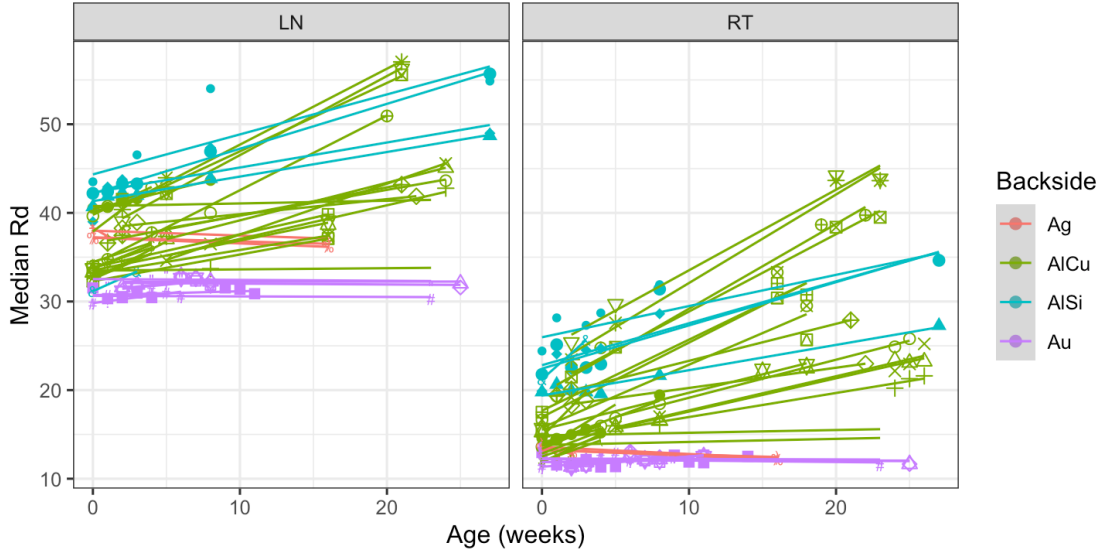


FIG. 8. Forward resistance vs. time of tiles with different backside films. Left panel: liquid nitrogen (LN) temperature measurements. Right panel: room temperature (RT measurements). Different symbols represent different tiles.

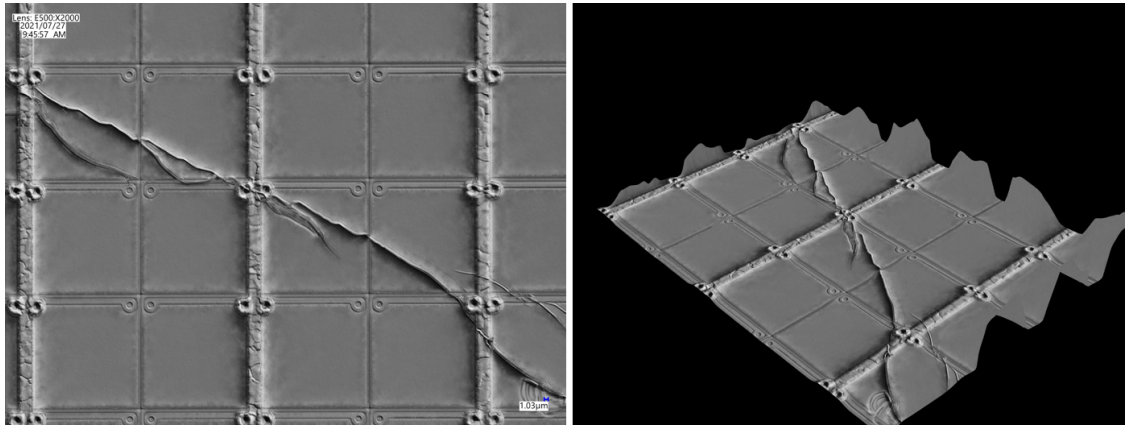


FIG. 9. Optical image of a SiPM with a 2000x magnification, showing a crack after a thermal cycle between room temperature and liquid nitrogen.

1307 compares the values measured vs. time since time zero (i.e. within 1 day from the tile assembly)
 1308 at both room and liquid nitrogen temperatures.

1310 After repeated temperature cycles, shorts between anode and cathode were observed in a large
 1311 fraction, up to 90%, of the Ag backside devices. This cause of the shorts was identified as cracking
 1312 in the silicon (see Fig. 9). The failure rate, which increased at each thermal cycle from room
 1313 temperature to liquid nitrogen, was studied against several parameters: quantity of soldering paste,
 1314 number of solder dots, silicon thickness and soldering temperature. The only significant effects were
 1315 obtained by reducing the quantity of soldering paste and the number of solder dots. However, the
 1316 best result was of 5% failure rate after 3 thermal cycles. This remains an unacceptably high risk.

1318 In conclusion, the backside metallization of choice is Au, the resistance of which shows the lowest
 1319 value, the narrowest distribution (within tile and tile-to-tile) (see Fig. 10) and after 14 thermal
 1320 cycles from room temperature to liquid nitrogen, over a sample of 13 tiles, has not shown any
 1322 failures.

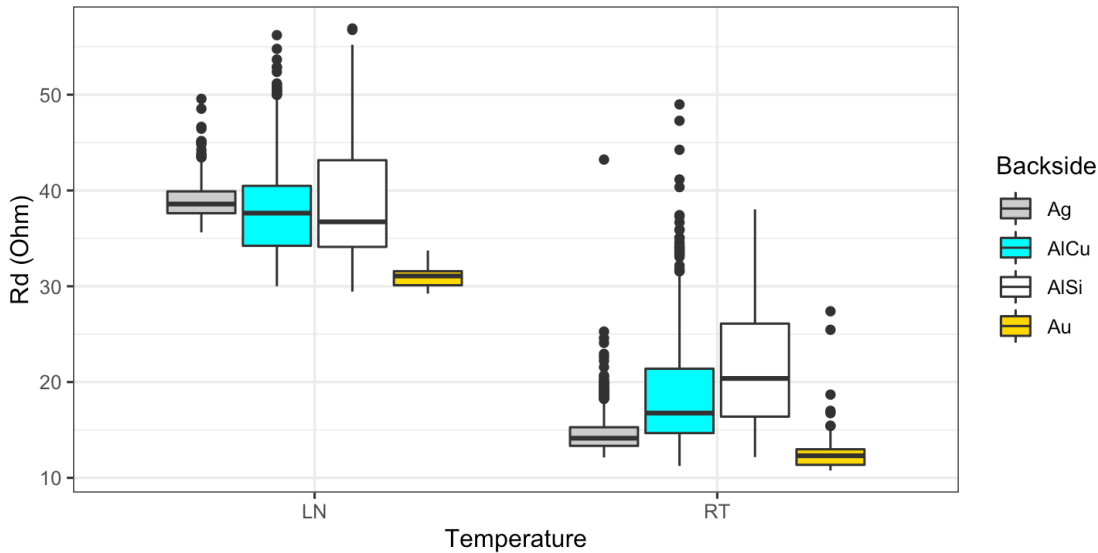


FIG. 10. Distributions of R_d measured at time zero, both at Room T and LN, from all the tiles with different backside films.

1323

3.2.5. Through Silicon Vias (TSV) development

1324 The option of TSV was considered in order to make both anode and cathode contacts from the
 1325 backside of the SiPM. This option is attractive as it would remove the need for wire bonding, and
 1326 as a result increase the fill factor via smaller die-to-die spacing and reduced pad area.

1327 The processes required to make TSV are not available in LFoundry. Commercial processes
 1328 are available to be subcontracted but the materials used are not suitable for DS-20k's radiopurity
 1329 requirements; most TSV suppliers use relatively radioactive borosilicate quartz wafers as mechanical
 1330 carrier wafers. Fused silica cannot be used as the coefficient of thermal expansion is far from that of
 1331 silicon, leading to cracks during the TSV processing. LFoundry engaged with an external partner
 1332 to do R&D to make TSV in DS-20k devices without carrier wafers. The activities have been run
 1333 over 2020 and the yield has been poor. Only 1 functional SiPM was obtained over 45 tested. All
 1334 the devices showed high leakage currents in reverse mode, which exceeded the current compliance
 1335 if tested again, suggesting a poor TSV isolation. Given the cycle time needed to further develop
 1336 the TSV process, this option has been rejected.

1337

3.2.6. Validation procedures development

1338 Beyond the quality assurance and quality control developments described above, a significant
 1339 R&D effort across the collaboration was dedicated to developing validation tools to measure the
 1340 SiPM performance parameters that impact upon the DS-20k physics programme. Table XLIII
 1341 summarizes the requirements that the SiPMs need to achieve to be compatible with the DS-20k
 1342 physics program.

1343 The program of testing and validation of the LFoundry SiPMs was carried out across several
 1344 institutions of the collaboration. Institutes tested tiles built with different backside metallization
 1345 options, and additionally TRIUMF and FBK tested individual SiPMs, not assembled in a tile.
 1346 Table VI summarizes the type of SiPM/tile measured by several institutions.

1347 *a. Single PE Gain and Breakdown Voltage* Single PE dark pulses are used to measure the single
 1348 PE SiPM gain ($G_{1\text{ PE}}$) as a function of the SiPM temperature as reported in Figure 11. From the
 1349 single PE gain it is possible to extrapolate the single PE charge, defined as $Q_{1\text{ PE}} \equiv q_E \times G_{1\text{ PE}}$
 1350 (with q_E elementary charge) reported in Fig. 11. The single PE charge, as a function of the bias
 1351 voltage, was then linearly fitted as $Q_{1\text{ PE}} = C_D \times (V - V_{BD})$, in order to extract: (i) the single

SiPM backside metallization-[Type]	Institution
Gold, AlSi/Ti/TiN, AlCu/Ti/TiN [individual SiPMs]	FBK
Gold-[Individual SiPMs]	TRIUMF
AlSi/Ti/TiN-[Tile]	LNGS
AlCu/Ti/TiN-[Tile]	INFN PISA

TABLE VI. Summary of the LFoundry SiPMs tested by several institution.

1353 SiPM cell capacitance C_D and (ii) the Breakdown Voltage V_{BD} defined as the bias voltage at which
 1354 the SiPM single PE gain (or charge) is zero. These two quantities are reported in Fig. 12, as a
 1355 function of the temperature. Table VII summarizes the breakdown voltages measured at 77 K.
 1356 Within statistical error, the breakdown voltages measured, both at the tile level and at the single
 1357 SiPM level, meet the specification of Breakdown Voltage at 77 K (SPE amplitude): 27.5 ± 0.2 V
 1358 (Table XLIII).

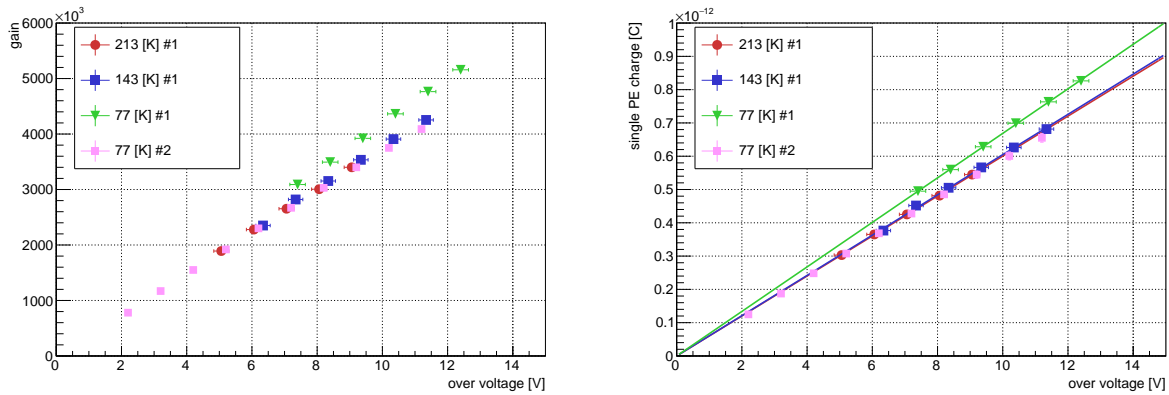
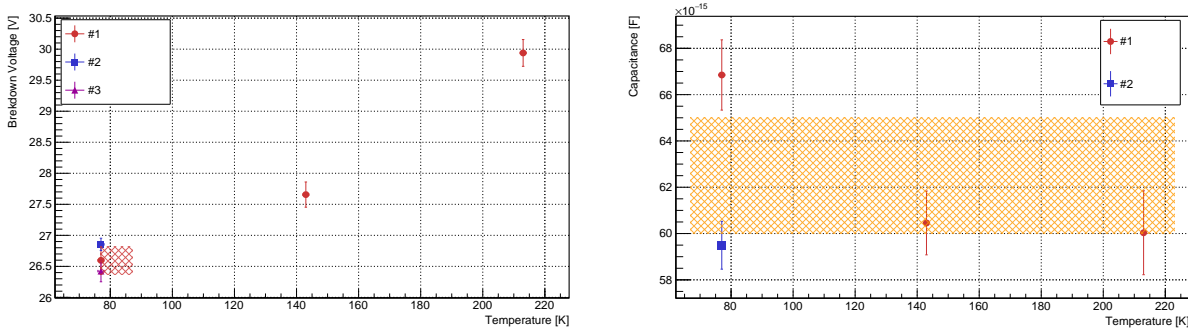


FIG. 11. Single Photon Electron (SPE) gain and charge as a function of the over voltage measured by several institutions. TRIUMF data is labeled as #1 while LNGS, INFN PISA and FBK data are labeled as #2, #3, and #4 respectively, when available.

1359
 1360 The dashed region in the capacitance vs temperature figure represents instead the acceptance
 1361 region on the single cell capacitance, accordingly to the requirement of Table XLIII. We note that
 1362 a requirement on the SPE charge automatically sets a requirement on the SPE gain.
 1363

FIG. 12. Left: Breakdown voltage and single cell capacitance as a function of the SiPM temperature. The dashed region represents the uncertainty on the stabilisation temperature of the TRIUMF setup at 77 K (#1). Note as this quantity is not the statistical fluctuation on the temperature that was < 1 K. Right: Single cell capacitance extracted from the fit. The dashed region represents instead the acceptance requirement on the single cell capacitance, based on Table VII. TRIUMF data is labeled as #1 while LNGS, INFN PISA and FBK data are labeled as #2, #3, and #4 respectively, when available.

1364

1365

Breakdown Voltage [V]	Institution
26.4 ± 0.2	TRIUMF
26.8 ± 0.2	LNGS
26.6 ± 0.2	Pisa

TABLE VII. Summary of the breakdown voltages measured by several institutions extrapolated from the Single PhotoElectron (SPE) charge.

1366 *b. Dark Noise Rate* SiPMnoise rates are among the crucial parameters that characterize
 1367 SiPMs, and the SiPM technology was purpose-optimized to suppress these rates. This, and the
 1368 subsequent sections, present the validation of the R&D results across multiple test stands.

1369 The measured DN rates are shown in the right panel of Fig. 14 as a function of the over voltage. To
 1370 meet SiPM specifications the dark noise rate needs to be smaller than 0.01 Hz/mm^2 and 0.1 Hz/mm^2
 1371 at 7 V and 9 V of over voltage, respectively. As shown in Fig. 14 both requirements are satisfied.
 1372 The dark noise rate of LFoundry SiPM exceeds the requirement with a rate that, up to 14 V of
 1373 over voltage, is below 0.1 Hz/mm^2 . More details on the measurement technique can be found in
 1374 [39, 40].

1375 *c. Number of Correlated Delayed Avalanches per Pulse* Correlated Avalanche (CA) noise is
 1376 due to at least two processes: the production of secondary photons during the avalanche in the
 1377 gain amplification stage detected in nearby cells, and the trapping and subsequent release of charge
 1378 carriers produced in avalanches. The latter process is usually referred to as afterpulsing (AP), while
 1379 the former is termed crosstalk. Crosstalk photons produce nearly simultaneous avalanches to the
 1380 primary one (Direct CrossTalk (DiCT)) or delayed by several ns (Delayed CrossTalk (DeCT)). In
 1381 general, the subset of the CAs constituted by afterpulses and delayed crosstalk events is named Cor-
 1382 related Delayed Avalanches (CDAs). Unlike CDAs pulses, dark noise pulses (DN) are uncorrelated
 1383 with a primary signal.

1384 Figure 13 shows an example of the charge distribution of first pulses following single PE primary
 1385 pulses as a function of the time difference with respect to the primary pulse, recorded at $T=77 \text{ K}$
 1386 and for an over voltage of $10.4 \pm 0.2 \text{ V}$. Afterpulses and delayed crosstalk are minimal compared
 1387 with direct crosstalk. In this distribution the SiPM noise was studied using dark data, that is,
 1388 taken with the SiPM shielded from any light source.

1389 DN and CDAs events can be distinguished by studying the time distribution of events relative to
 1390 the primary pulse. The measured average number of CDAs per pulse in the $5 \mu\text{s}$ window after the
 1391 trigger pulse is reported in the left panel of Fig. 14. Note that the CDA requirement is specified in
 1392 Table XLIII only at 9 V of overvoltage since it is intended to be a maximum tolerable level for the
 1393 experiment. The number of CDAs is well below the required 10% value in $5 \mu\text{s}$ window after the
 1394 trigger pulse (Table VII); it is at most 4.5% at 9.5 V of over voltage.

1395 *d. Number of Additional Prompt Avalanches* Based on the measured dark noise rate above,
 1396 and assuming Poisson statistics, the probability of having two dark noise pulses occurring within
 1397 few nano-seconds is negligible. Therefore, the collected dark data can be used to investigate Direct
 1398 CrossTalk (DiCT). The charge distribution of the prompt pulses obtained from the dark data can
 1399 be used to determine the mean number of Additional Prompt Avalanches (APA)s, N_{APA} , due to
 1400 Direct CrossTalk as [42]:

$$N_{\text{APA}} = \frac{1}{N} \sum_{i=1}^N \frac{A_i}{\bar{A}_{1 \text{ PE}}} - 1 \quad (1)$$

1402 where A_i is the charge of the prompt pulse i , $\bar{A}_{1 \text{ PE}}$ is the average charge of 1 PE pulses and N is
 1403 the number of prompt avalanches analyzed. The N_{APA} number, in unit of PE, as a function of the
 1404 over voltage and for different SiPM temperatures, is reported in the left panel of Fig. 15.

1405 Direct Crosstalk is often measured as a probability. In this case the DiCT probability is defined
 1406 as the ratio between the number of prompt pulses with an integrated charge bigger than 1.5 Photo-
 1407 electron Equivalent (PE) divided by the number of prompt pulses with an integrated charge bigger

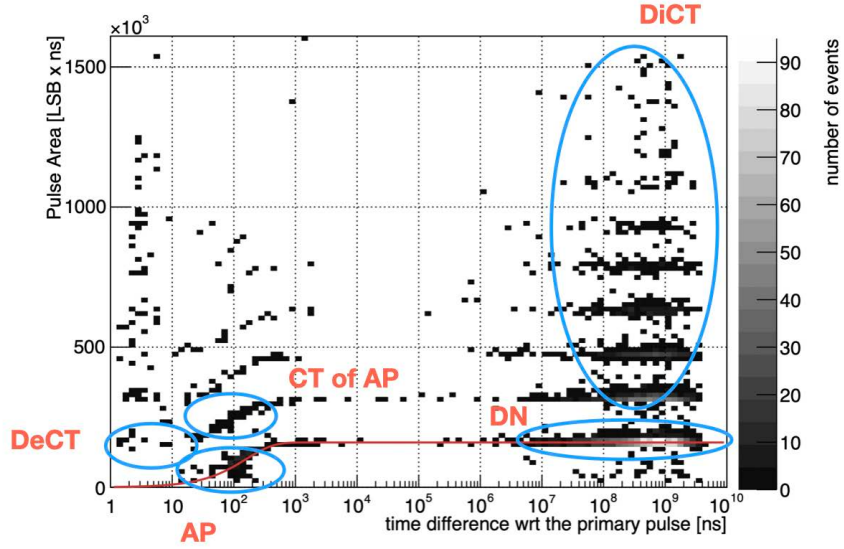


FIG. 13. Charge distribution of first pulses following single PE trigger pulses as a function of the time difference with respect to their primary pulse for $T=77$ K and for an over voltage of 10.4 ± 0.2 V. The gray scale represents the number of events in each bin on a logarithmic scale. The solid red line shows a fit of the afterpulsing events [41].

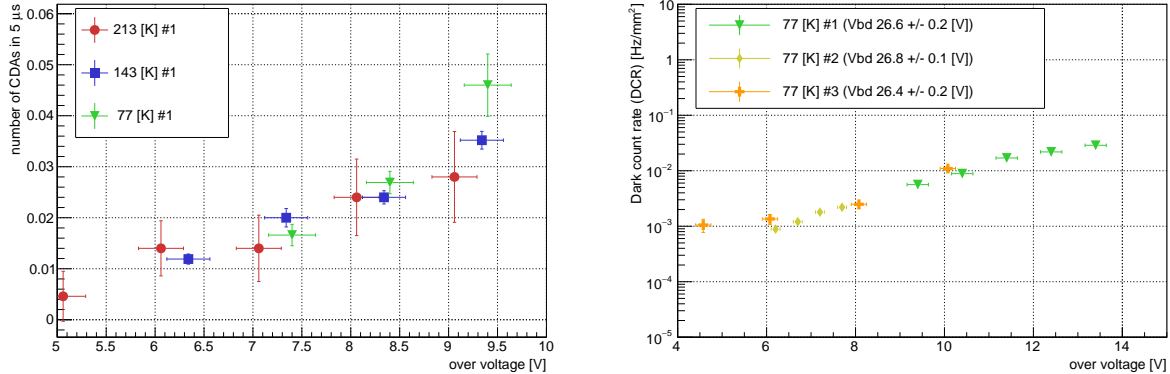


FIG. 14. Left: Number of Correlated Delayed Avalanches (CDAs) per primary pulse within a time window of 5 μ s after the trigger pulse as a function of the applied over voltage for different SiPM temperatures. Right: Dark Noise (DN) rate normalized by the SiPM photon sensitive area as a function of the applied over voltage. TRIUMF data is labeled as #1 while LNGS, INFN PISA and FBK data are labeled as #2, #3, and #4 respectively, when available.

than 0.5 PE as follows

$$P_{CT} = \frac{N_{A>1.5PE}}{N_{A>0.5PE}} \quad (2)$$

The DiCT probability is reported in the right panel of Fig. 15. The requirement for the Direct CrossTalk probability of the SiPMs is less than 33 % and 50 % at 7 V and 9 V of over voltage, respectively (Table XLIII). All the SiPMs tested meet the specification both at 7 V and 9 V of over voltage.

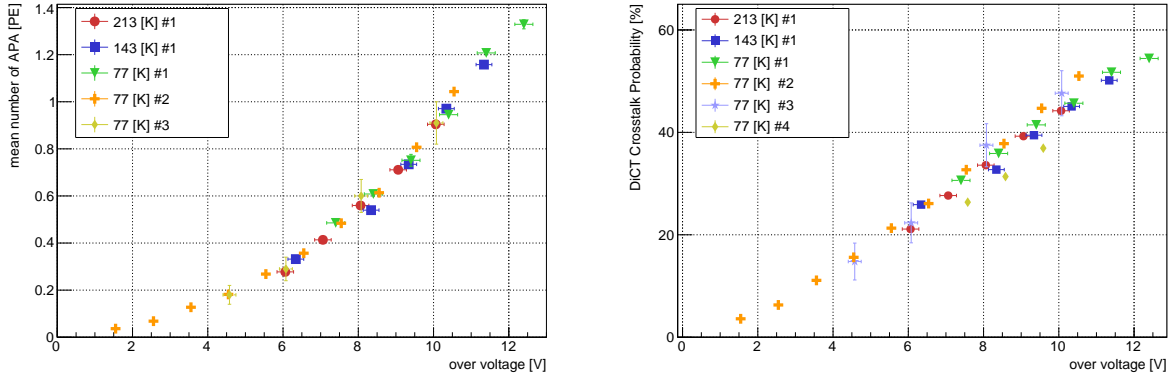


FIG. 15. Left: Number of Additional Prompt Avalanches (APAs). Right: Direct Cross talk probability as a function of the over voltage. TRIUMF data is labeled as #1 while LNGS, INFN PISA and FBK data are labeled as #2, #3, and #4 respectively, when available.

1414

3.2.7. Photon Detection Efficiency (PDE)

1415 An important question for DS-20k is the how the photon detection efficiency of the SiPMs varies
 1416 with temperature.

1417 The Photon Detection Efficiency (PDE) is the combined probability that a photon is absorbed
 1418 in the active volume of the SiPM and subsequently triggers an avalanche. The photon detection
 1419 efficiency was studied in a dedicated apparatus described in [42]. The SiPM PDE was studied
 1420 as a function of the temperature to investigate possible variation of the SiPM efficiency at liquid
 1421 nitrogen temperatures. The PDE at 420 nm is reported in Fig. 16 as a function of the applied over
 1422 voltage for 213 K and 100 K. The dashed region and the error bars in the points of the TRIUMF
 1423 measurement (#1) represent the systematic and statistical uncertainty, respectively. The figure
 1424 also reports the PDE measured by FBK at 420 nm and 290 K during the technological transfer to
 1425 LFoundry for the SiPM production (#4).

1426 At 420 nm the SiPM PDE shows a weak temperature dependence dropping of roughly 5% at
 1427 100 K if compared with the one measured at 213 K however at 9 V of over voltage is above the 40 %
 1428 requirement at 100 K. We note that the measurement temperature is higher than the one specified
 1429 in the requirement (77 K). However we do not differences in the measured PDE between 100 K
 1430 and 77 K to exceed those between room temperature and 100K; at 420 nm the SiPM PDE shows a
 1431 weak temperature dependence dropping of roughly 5% at 100 K compared with the one measured at
 1432 213 K. This is a preliminary measurement on a single device and more will be measured in the near
 1433 future, however this first measurement validates that the PDE is within specification: at 420 nm
 1434 the SiPM PDE at 9 V of over voltage is above the 40 % requirement at 100 K (Table XLIII).

1435 The wavelength dependence of the SiPM PDE is reported in Fig. 17 at 213 K, and in Fig. 18
 1436 at 100 K for two over voltages. The dashed and the error bars in the points of our measurement
 1437 (#1) represent the systematic and statistical uncertainty, respectively. This figure also reports the
 1438 wavelength dependence of the SiPM PDE measured by FBK at 290 K during the technological
 1439 transfer to LFoundry (#4).

1440 An interference pattern is clearly visible in the TRIUMF measurement compared with the FBK
 1441 one. This is due to a resin that FBK applied to the samples tested by them. This resin produces
 1442 a better match with the silicon dioxide index of refraction present on the SiPM Anti Reflective
 1443 Coating (ARC) surface coating structure, reducing therefore the interference of the incoming light
 1444 with the ARC and damping the oscillations. A similar behavior is expected to happen in liquid
 1445 argon due to a good match between the liquid argon and the silicon dioxide indices of refraction.
 1446 The samples measured by TRIUMF in vacuum were instead naked samples without the protective
 1447 resin and therefore present oscillations.

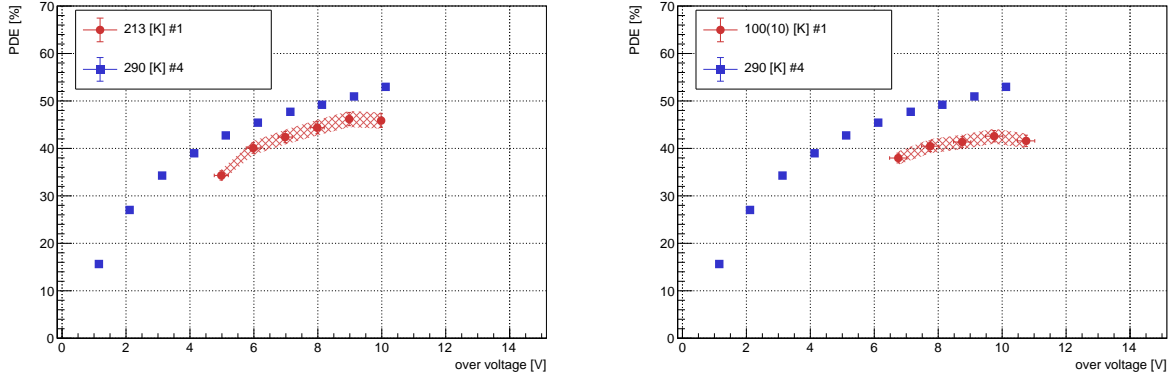


FIG. 16. PDE of the LFoundry DarkSide SiPM as a function of the over voltage for temperatures of 213 K and 100 K, under 420 nm light illumination. The 10 K in the 100 K TRIUMF measurement (#1) represents the uncertainty on the stabilisation temperature of the TRIUMF setup at 100 K. Note as this quantity is not the statistical fluctuation on the temperature that was < 1 K. TRIUMF data is labeled as #1 while LNGS, INFN PISA and FBK data are labeled as #2, #3, and #4 respectively, when available.

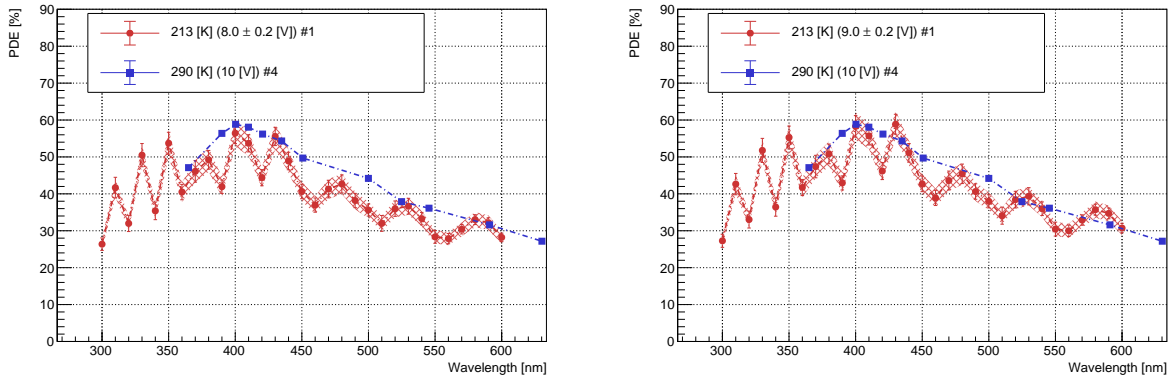


FIG. 17. PDE of the LFoundry DarkSide SiPM measured as a function of the wavelength, for two over voltages, at 213 K. TRIUMF data is labeled as #1 while LNGS, INFN PISA and FBK data are labeled as #2, #3, and #4 respectively, when available.

1448

3.2.8. R&D results and conclusions

1449 We have identified the technology NUV-HV-Cryo as the one suitable to produce large area
 1450 SiPMs working in cryogenic environment and satisfying the specifications listed in table [XLIII](#).
 1451 The SiPMtechnology, developed in collaboration with FBK, has been successfully transferred to an
 1452 industrial partner, LFoundry. The LFoundry SiPM characteristics, derived from devices produced
 1453 after the NUV-HD-CRYO technology transfer, are reported in Table [VIII](#). Based on an extensive

Parameter	LFoundry SiPMs
Pixel size	$30 \times 30 \mu\text{m}^2$
Fill Factor	76.6%
Active area single microcell	$689 \mu\text{m}^2$
Number of Cells (N_{cell})	94904
Total Area	$11.7 \times 7.9 \text{ mm}^2$
Expected Breakdown Voltage [87K]	[27-28] V

1454

TABLE VIII. Summary of the FBK NUV-HD-CRYO LFoundry SiPM specification.

1455

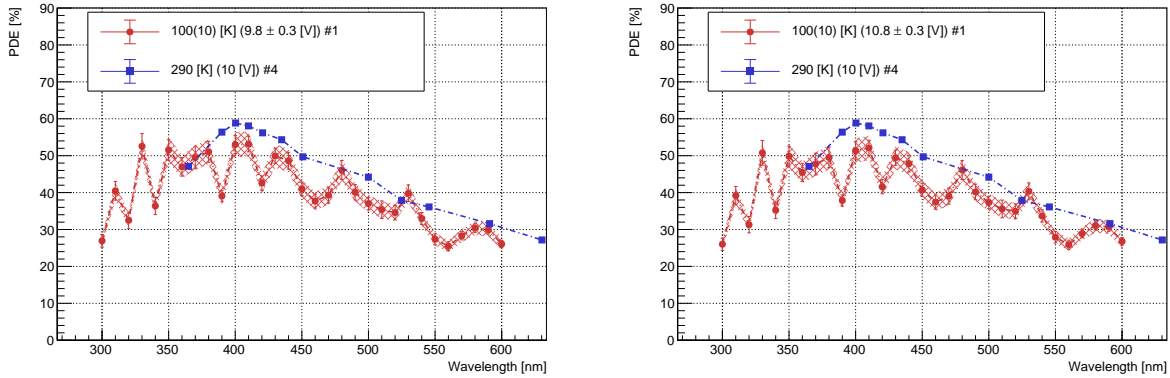


FIG. 18. PDE of the LFoundry DarkSide SiPM as a function of the wavelength, for two over voltages, at 100 K. The 10 K in the 100 K TRIUMF measurement (#1) represents the uncertainty on the stabilisation temperature of the TRIUMF setup. Note as this quantity is not the statistical fluctuation on the temperature that was < 1 K.

1456 campaign of device resistance measurements vs. time, involving an order of magnitude more thermal
 1457 cycles than expected in the lifetime of the experiment, we have selected gold as the material for the
 1458 back side metallization. We discarded TSV as the test results did not meet specifications. We have
 1459 measured the SiPM performance parameters relevant for the physics performance of DS-20k at
 1460 several institutions across the collaboration, and confirmed that the SiPMs meet our specifications.
 1461 The order for the full production of the SiPM wafers for the entire detector has been issued in
 1462 December 2021 by INFN.

1463 3.3. Tiles and Front End Amplifiers

1464 3.3.1. Goals of the R&D

1465 The goal of the activity is the development of a suitable amplifier working in cryogenic environment
 1466 coupled to SiPMs with the specifications listed in Table IX.

Parameter	Value (TPC amplifier)	Value (Veto amplifier)
Stable operation at 87 K	yes	yes
Time resolution, (1 PE, 7 VoV)	< 10 ns	< 30 ns
SNR (software filtered)	> 8 (87 K)	> 5 (87 K)
Dynamic range	> 50 simultaneous PE	> 50 simultaneous PE
power dissipation	< 250 mW/channel	< 250 mW/channel
radiopurity* (neutrons)	$<< 0.1$ neutrons/200 t yr	$<< 0.1$ neutrons/200 t yr
radiopurity* (γ)	< 40 Hz in the TPC	< 50 Hz in the Veto

1467 TABLE IX. Specifications driving the development of the cryogenic amplifiers. See [2] for the justification
 1468 of most of them. Note that the some target parameters for the Veto are more relaxed than that needed for
 the TPC. (*) Contribution to the radioactivity background from all the installed amplifiers.

1469 3.3.2. Tiles and transimpedance amplifiers

1470 The experiment foresees a photo-sensing area in excess of 25 m^2 . The choice of the number of
 1471 SiPMs that are combined into a tile and coupled to a single front end amplifier is a compromise
 1472 between limiting the number of readout channels and ensuring a sufficiently high signal-to-noise
 1473 ratio (SNR). The former favors assembling SiPMs into tiles of large dimensions. However, the

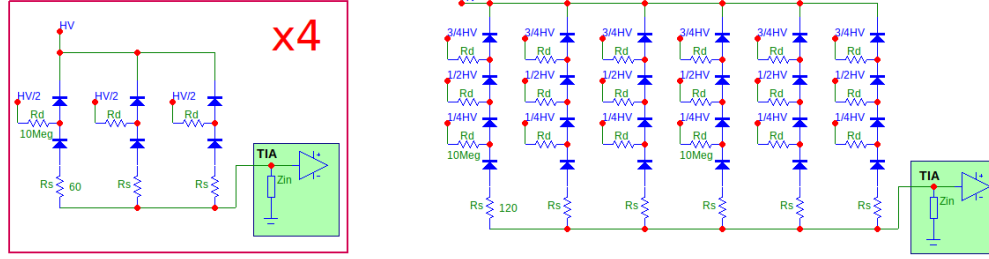


FIG. 19. Tile configuration for the 4x2s3p (left) and 4s6p (right), see text for details. The intermediate voltage references are produced by a voltage divider based on $10\text{ M}\Omega$ 1% resistors with PEN HV shunt capacitors.

1474 capacitance of SiPMs presents a challenge in readout, as it increases with the area of the sensor
 1475 and it affects the SNR. With the typical value of 50 pF/mm^2 , a single SiPM with only a $5\text{X}5\text{mm}^2$
 1476 surface area passes the nF scale for capacitance.

1477 The use of a transimpedance amplifier (TIA) is preferable to a charge integration amplifier, since
 1478 the latter's noise and rise time are very strongly affected by the large detector capacitance. With
 1479 this in mind, we have developed and optimized a TIA based readout. If all the SiPMs of a tile were
 1480 readout in parallel, the detector capacitance C_d would be the sum of the single SiPM capacities,
 1481 resulting in a tile with degraded SNR compared to that of a single SiPM. In addition, since the
 1482 bandwidth of the TIA amplifier is proportional to $1/\sqrt{C_d + C_f}$, where C_f is the parasitic
 1483 capacitance, increasing C_d may lead to significant reduction of the bandwidth, degrading the time
 1484 resolution of single photoelectron pulses. Our mitigation strategy is a hybrid readout scheme, with
 1485 parallel-series combinations of SiPMs. In this configuration, the output signal of an individual
 1486 SiPM is reduced by a factor equal to the number of SiPMs put in series, but this disadvantage
 1487 is offset by the attenuation of noise gain due to the reduction in the input capacitance, resulting
 1488 in the same SNR obtainable with a single device. The SNR is defined here as the ratio between
 1489 the single photoelectron peak in the amplitude (or charge) spectrum and the rms of the baseline.
 1490 Details of the hybrid scheme are reported in [2].

1491 Our final choice is a tile of $5\times 5\text{ cm}^2$ area, comprised of 24 SiPMs of $11.7\times 7.9\text{ mm}^2$ each. We
 1492 have tested 2 types of ganging, as shown in figure 19. The first has 4 identical quadrants each with
 1493 3 parallel branches of 2 SiPMs in series, whose signal is summed in a subsequent stage, the second
 1494 has 6 branches of 4 SiPMs in series and does not require further summing. We refer to them as
 1495 4x(2s3p) or 4s6p configurations, respectively.

1496 We have characterized at cryogenic temperature (INFN LNGS group) a high speed, ultra-low
 1497 noise amplifier fabricated with SiGe technology by Texas Instruments (LMH6629) and we have
 1498 developed a custom TIA based on the use of this device, following the design of figure 20. Details
 1499 are reported in [43]. The required specifications of the TIA coupled with a SiPM tile are listed in
 1500 table X.

Parameter	Value
Stable operation at 87 K	
Timing resolution	< 10 ns
SNR	> 8 (87 K)
power dissipation	< 250 mW/channel
radiopurity	< 0.01 neutrons/200 t x y after the analysis cuts

1501 TABLE X. Specifications of the TIA coupled to a tile with 24 SiPMs
 1502

1503 At the time of the design of the first tile coupled to the amplifier (called Photo Detector Module,
 1504 PDM), we were using SiPM developed during the R&D phase with FBK. We used the 4x(2s3p)
 1505 configuration in which we split the readout of the tile in four quadrants, each read by an independent
 1506 TIA, as shown in the left panel of figure 19. An active adder was summing the four amplified signals
 1507 to aggregate 24 SiPMs, in a single analog output. This choice was motivated by the low current

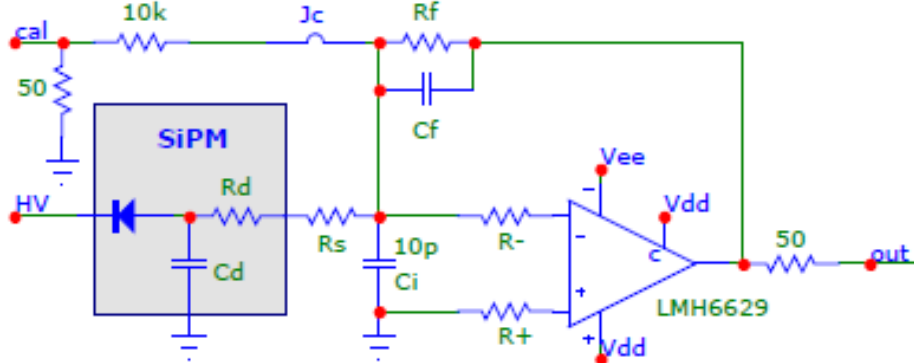


FIG. 20. Schematic of the transimpedance amplifier as described in [43]. The calibration input is disconnected during normal operation.

generated by the SiPM as result of the small cell size and high quenching resistor; higher order of ganging, with more devices in series, would have resulted in lowering the input current even further. We built two matrices of 25 PDMs each, called Photo Detector Units (PDU), and we have obtained an SNR value larger than 15 (25) for the first (second) PDU, in both cases above the specification in table X.

The second design iteration, made possible by the performance of the LFoundry SiPMs (see XI), implements the configuration shown in the right panel of Fig. 19 with six branches of four SiPMs in series read by a single TIA. The 1 TIA configuration has the advantages of reduced power dissipation in the liquid argon and a lower number of electrical components, reducing radioactivity and complexity.

In the 4s6p configuration the gains of the SiPMs are halved with respect to the 2s3p configuration, but the same occurs for the noise. In both cases we are in a quantum noise limited configuration: the electronic noise of the amplifier is negligible with respect to the Johnson noise of the resistors in the tile ($R_{TIA} = 20 \Omega$) [44]. The input equivalent thermal noise density for a generic configuration of active ganging with Q quadrants each with P branches of S SiPMs in series is:

$$I_n\{1MHz\} = \sqrt{\frac{Q \times 4k_B T}{(R_s + S \times R_q/N_c)/P + R_{TIA}}} + 2e^- \times Q \times I_{TIA} \quad (3)$$

For $R_s = 120 \Omega$ (where R_s is the series resistor shown in 19, right) the output overall noise of the 4s6p configuration is halved with respect to the 4x(2s3p) configuration (with $R_s = 60 \Omega$) and the TIA is configured with the same noise gain and bandwidth. In this case the SNR of the 1 TIA and 4 TIA scenarios is in principle the same.

With NUV-HD-Cryo SiPMs produced by LFoundry the input signal level is almost twice as large with respect to the level achieved in the FBK devices (50 nA/VoV vs 30 nA/VoV) even in the 4s6p configuration. Furthermore NUV-HD-Cryo SiPMs can be operated in stable conditions up to 9–10 VoV vs 6 VoV for older SiPMs. Overall we can feed a total of 450 nA in a single TIA vs 180 nA per TIA of the first 4-TIA tiles. Table XI reports the parameters of the NUV-HD-Cryo SiPM produced by LFoundry in comparison with the NUV-HD SiPM produced by FBK.

Fig. 21 reports a measurement for the same tile read in $4 \times 2s3p$ and in 4s6p. As expected, the gain of the second configuration is halved, but the SNR is nearly unchanged,¹ scaling from 27 to 25. This 10% decrease in SNR is expected when considering self-inductance. For this measurement the tile was operated in liquid nitrogen at 7 VoV in both configurations. Data are analyzed with digital filtering, typically matched filter, where the reference curve is computed averaging several acquired waveforms.

¹ SNR is calculated dividing the gain (from a linear regression of the peak position) and the average RMS-AC in the waveform pre-pulse (for a gate of 1 μ s)

Group	Parameter	NUV-HD-Cryo	LF	NUV-HD	MB-1
SiPM	Cell Unit Size (S_c)	30 μm		25 μm	
	Cell Capacity (C_d)	60 fF		40 fF	
	Number of cells (N_c)	100 k		150 k	
	Quenching Resistance (R_q)	3 M Ω		10 M Ω	
	Maximum Over-voltage (V_{oVMAX})	9 V		6 V	
	Primary Recharge Time ($R_q \times C_d$)	180 ns		400 ns	
Tile Classic (4x2s3p)	Recharge Time (τ)	300 ns		600 ns	
	Current Peak ($I_p = \frac{1}{2} C_d / \tau$)	100 nA / VoV		30 nA / VoV	
	Noise (see Eq.3 Q=4, S=2, P=3)	$18 \text{ pA} / \sqrt{\text{Hz}}$		$15 \text{ pA} / \sqrt{\text{Hz}}$	
	SNR with Matched Filter	$R_s = 60 \Omega$, $R_{TIA} = 20 \Omega$, $I_{TIA} = 20 \mu\text{A}$		$4 / \text{VoV}$	$4 / \text{VoV}$
Tile 1TIA (4s6p)	Recharge Time (τ^+)	350 ns			
	Current Peak ($I_p^+ = \frac{1}{4} C_d / \tau$)	50 nA / VoV			
	Noise (see Eq.3 Q=1, S=4, P=6)	$9 \text{ pA} / \sqrt{\text{Hz}}$		$R_s = 120\Omega$	
	SNR^+ with Matched Filter			$>3.6 / \text{VoV}$	

TABLE XI. Parameters of the bare SiPMs (NUV-HD used to assemble MB1 and NUV-HD-Cryo produced by LFoundry) and of the assembled tiles, both with classic 4 TIA configuration and with 1 TIA. The thermal noise is given at 86 K. The improved performance of the NUV-HD-Cryo SiPMs, in terms of gain and recharge time, corresponds to a signal (I_p) that is increased by a factor three over the NUV-HD devices, for the same over-voltage.

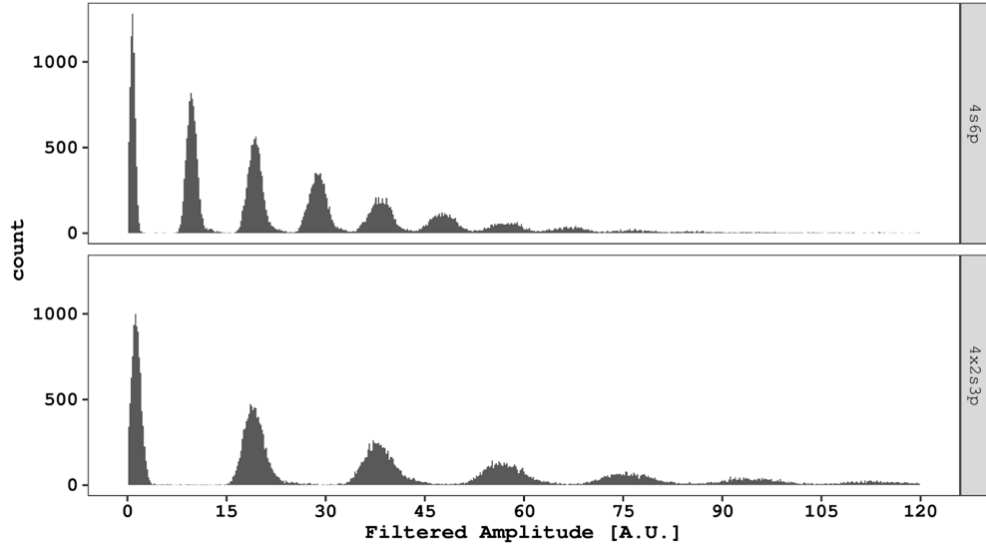


FIG. 21. Multi photoelectron plot ("finger plot") for matched filtered signals of single-channels tile #ML-13 with NUV-HD-Cryo from LFoundry read by a traditional FEB (4×2s3p) with SNR=27 and by a single TIA FEB (1×4s6p) with SNR=25.

1540

3.3.3. CMOS Integrated Electronics for SiPM Readout

1541 The Collaboration (INFN Torino) developed a custom CMOS integrated readout electronics optimised for the readout of large area SiPMs at cryogenic temperature. The ASIC is implemented in a
 1542 110 nm standard CMOS technology node and features the configuration with 4 TIAs with 4X(2s3p)
 1543 SiPM connection and a summing stage. Two options are available in the DS20k_V2/CASTOR chip:
 1544 190/110 ns rise time with a dynamic range of 100/170 charge-equivalent photo-electrons, with a de-
 1545 sign SNR of 16 and 13, respectively, at 8 VoV. The CAD layout of the 2.7 mm² ASIC is illustrated
 1546 in Fig. 22.
 1547

Possible ASIC ageing effects have been evaluated by means of a dedicated cryostat, hosting 21

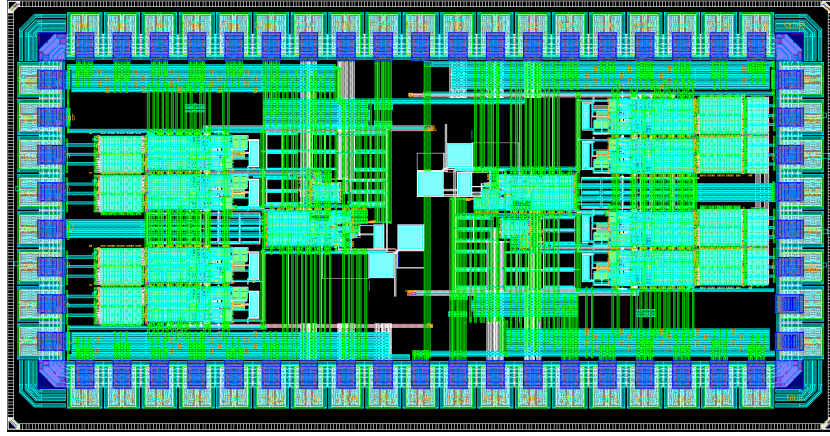


FIG. 22. CAD Layout of the CMOS analogue integrated electronics for SiPM readout.

1550 ASICs, in which we were able to periodically send a pulse to any of the ASICs and read the amplified
 1551 output back. In this way we monitored the functioning of all the ASICs. During the years 2020
 1552 and 2021 we performed about 10 thermal cycles for a cumulative time at LN temperature of about
 1553 7 months. None of the ASICs in the apparatus break or show malfunctioning.

1554 3.3.4. *Front end board amplifier for the inner Veto readout*

1555 The basic optical detector element is the same SiPM tile used in the TPC, but with a custom
 1556 ASIC (described in section 3.3.3) in the electronic amplification chain. The activity on design
 1557 of the readout of the Veto also provided tests and validation of the newly developed ASIC. We
 1558 have developed (INFN Genova) dedicated front end boards (FEB) realized with the version of the
 1559 custom ASIC with 190 ns risetime. We have coupled it to SiPM tiles (see Fig. 23) and operated
 1560 in liquid nitrogen. Laser pulses were used to illuminate the SiPMs. The ASIC showed a linear
 1561 behavior up to more than 700 mV and an RMS noise of 0.8 mV when coupled with the LFoundry
 1562 SiPM tile, both in excellent agreement with the values expected from simulations. With 9 V (6 V)
 1563 of over voltage applied to the tile, the measured mean peak amplitude of the single photoelectron is
 1564 9.7 mV (6.4 mV), translating to a linear dynamic range of 72 PE (109 PE). The signal-to-noise ratio
 1565 obtained in these conditions, defined as the ratio between the gain and the width of the baseline
 1566 noise peak, is 17 (11).

1567 The time resolution has been measured with a simple algorithm searching for the time when
 1568 single photoelectron SiPM pulses cross an amplitude threshold of $4 \times \sigma_{noise}$, where σ_{noise} is the rms
 1569 noise in absence of pulses. The measured rms timing resolution is 24.5/18.5/14.5 ns for 6/7.5/9
 1570 volts overvoltage.

1571 During the R&D phase, the PCB enabled the output of the ASIC to be connected to three drivers
 1572 for studying the optimal signal transmission strategy. These were:

- 1573 • single ended coaxial electrical transmission, mainly used for debug and lab measurements;
- 1574 • differential electrical transmission, configurable in voltage or current, to drive a twisted pair;
 1575 or,
- 1576 • optical transmission.

1577 While the results reported above were obtained with a double polarity power scheme for the
 1578 ASIC, we have realized a test board that can be powered using two possible schemes:

- 1579 • Single supply: (virtual) GND generated on-board
- 1580 • Dual supply: GND directly connected to the external low voltage power supply (LVPS)

1581 Using dual supply scheme, an additional wire (GND) must be carried out from the liquid nitrogen
 1582 test stand and the negative rail does not have a local regulator. In case of single supply scheme
 1583 the signal levels are referred to a virtual ground which is half of the supply. In both cases the local

¹⁵⁸⁴ LDO regulator can be bypassed if externally well-regulated supplies are used.

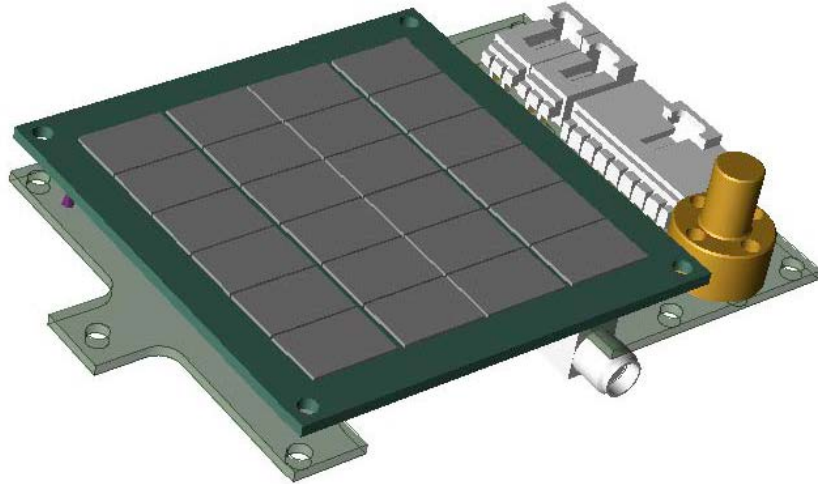


FIG. 23. Design of the test front end board coupled with the tile used in the test of the Veto readout. The test board has coaxial, differential and optical outputs for test purposes. Note the geometry for the coupling of the SiPMs tile to the front end board, with the two devices parallel for the veto detector, as opposed to the earlier design for the TPC where the SiPMs tile was perpendicular to the front end board.

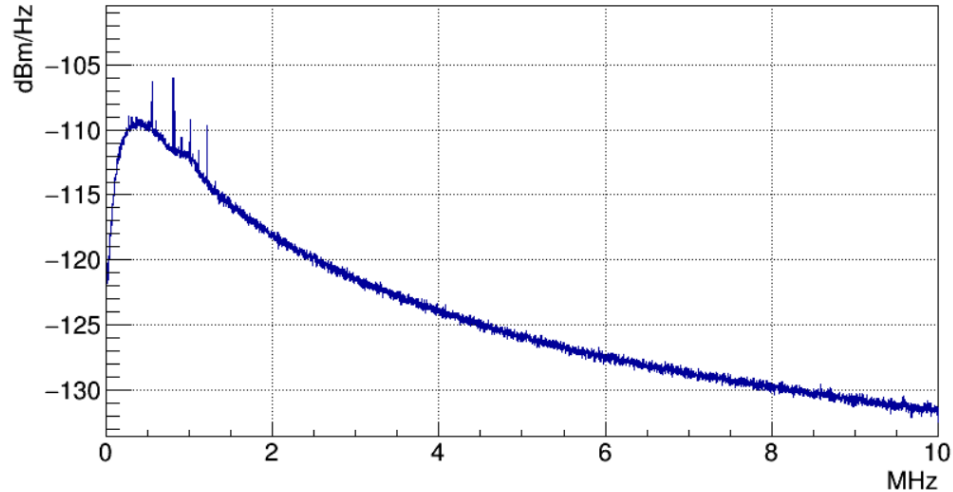


FIG. 24. Noise power spectrum measured with the veto FEB coupled to LFoundry SiPMs tile. SiPMs bias voltage was set to 20 V, which is well below the breakdown value. The spikes visible between 0.5 and 1.5 MHz are ascribed to external noise.

¹⁵⁸⁵ The noise spectrum measured with the veto tile and electronics described here is shown in Fig. 24.
¹⁵⁸⁶ A single photoelectron waveform from a veto tile illuminated by a laser is shown in Fig. 25.
¹⁵⁸⁷ The amplitude and charge spectra from this test board are shown in Fig. 26, demonstrating signal-to-noise ratio within specifications.
¹⁵⁸⁸

¹⁵⁸⁹ With respect to radioactivity, the substrate that will be used in the final veto tile PCB production
¹⁵⁹⁰ is ARLON 55NT, 4 layers, in the same material and stackup already adopted for the TPC tile PCBs.
¹⁵⁹¹ All the components have been selected from the already-assayed component list maintained by the
¹⁵⁹² DS-20k Materials Working Group.

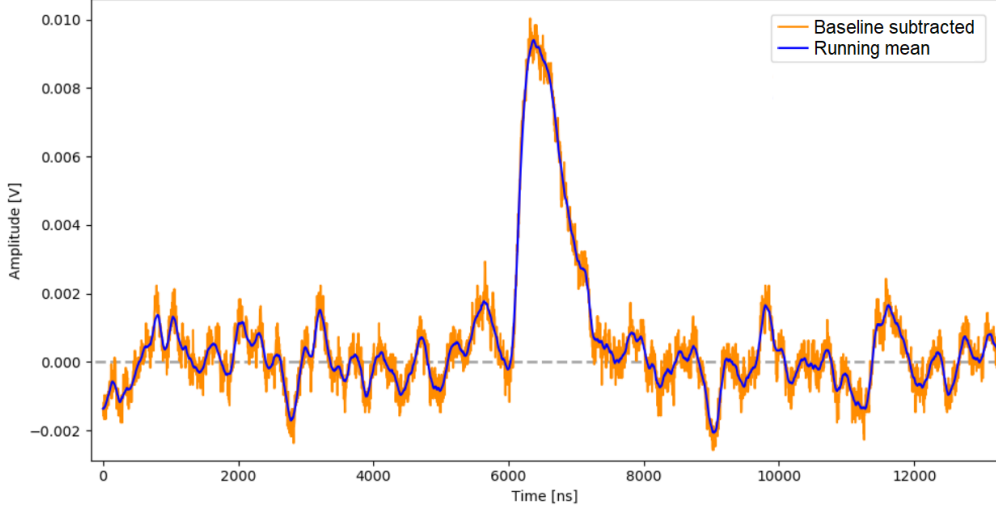


FIG. 25. Example of response to a laser pulse, acquired with the LFoundry SiPMs tile coupled to the veto FEB. The pulse amplitude of about 9.5 mV is compatible with the signal expected by a single photoelectron with 9 VoV.

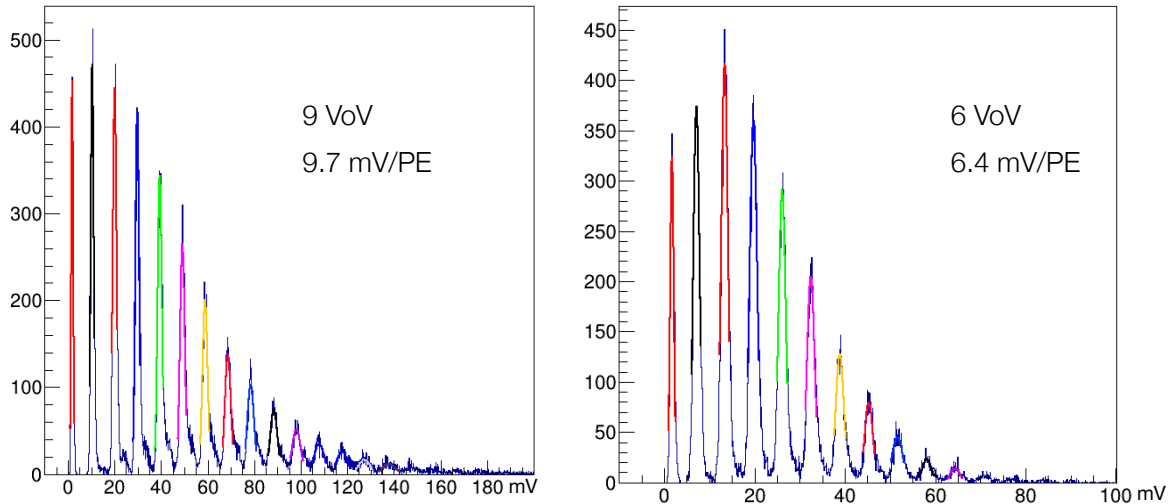


FIG. 26. Results of tests of the veto FEB prototype, equipped with the custom made ASIC and coupled with a LFoundry SiPMs tile. The data reported have been taken in liquid nitrogen with illumination by laser pulses. The figure shows the peak amplitude distributions for two values of over-voltage, with clearly resolved peaks corresponding to different photoelectron numbers.

1593

3.3.5. R&D results and conclusions

The TIA scheme is the choice selected for the entire detector. We have built and successfully operated TIAs realized with discrete commercial components coupled to SiPM with 2 different ganging topologies (4X(2s3p) and 4s6p), and a TIA realized with a custom ASIC coupled to SiPM in the 4x(2s3p) configuration. The baseline solution for assembling the photo-sensors in the detector reported in section 3.4.5 adopts the discrete elements TIA configuration in the TPC and the ASIC in the Veto. The use of the ASIC in the TPC is a possible option, as demonstrated by the test results shown in section 3.4.3.

1601 **3.4. Photo Detection Unit (PDU)**

1602 *3.4.1. Goals of the R&D*

1603 The goal of this activity is to design and test a device that allows mechanical assembly and
 1604 electrical integration of SiPM tiles into a suitable matrix to be mounted in the two optical planes
 1605 of the TPC and in the Veto. We call this assembly the Photo Detection Unit (PDU or vPDU when
 1606 referred to the Veto). The PDU and vPDU must provide the following functions:

- 1607 • include 16 PDMs and their amplifiers;
- 1608 • have a total height less than 2 cm;
- 1609 • dissipate less than 1.5 kW total power in the cryostat;
- 1610 • transmit the signal along a 10 m long cable;
- 1611 • distribute power to the PDMs and to the electronics;
- 1612 • include control signals to individually switch off noisy PDMs;
- 1613 • realize the sum of 2 or 4 amplified PDM signals to reduce the number of channels and the
 radioactivity associated with cabling;
- 1614 • meet the requirements of signal-to-noise ratio greater than 8 and timing resolution better
 than 10 ns for single photoelectrons (though a worse timing resolution has minimal impact
 on the PSD);
- 1615 • keep the radio-purity level below 100 mBq/PDU (except 500 mBq/PDU for the ^{210}Pb activi-
 ty).

1620 We have tested several solutions to assemble single PDMs into a PDU that meet these goals. The
 1621 solutions share the transmission strategy (section 3.4.2) but differ in the mechanical support and
 1622 production strategies. One solution implements the discrete components amplifier (section 3.4.4)
 1623 whilst the other employs the ASIC implementation (section 3.4.3).

1624 *3.4.2. Signal Transmission*

1625 Motivated by reducing the radioactivity associated with cables, we have performed an R&D
 1626 activity to develop analog optical transmission of the amplified PDU signals. This activity obtained
 1627 very good results during laboratory tests of limited number of channels. However, we have judged
 1628 that the progress of this solution in terms of channel-to-channel reproducibility, radio-purity of the
 1629 transmission LEDs, and long term aging of some components, still showed significant risks when
 1630 the results were extrapolated to the full scale production.

1631 These considerations, together with the positive results in the search for radio-pure cables and
 1632 tests of the integrity of the signal transmission through differential lines reported below, led us to
 1633 drop the option of the analog optical transmission and to adopt in the DS-20k detector electrical
 1634 differential transmission lines, both in the TPC and in the Veto.

1635 Designs for the first prototype PDUs used a low power differential amplifier, TI THS4521, to
 1636 transmit the signal of each PDM to the motherboard transmitter. At liquid argon temperature
 1637 this solution has a voltage swing of 2.6 V after the back-termination. Given the requirement to
 1638 sum 2 to 4 PDM channels, in order to maintain the dynamic range of the adder, even including
 1639 negative polarization, the photo-electron amplitude should be in the range of 4 mV. This value is
 1640 a bit low to transmit on a differential cable longer than 10 meters, as foreseen to route cables from
 1641 the bottom of the Veto to the cryostat exit flange.

1642 We tested an alternative based on the THS4541 differential amplifier. With this chip we are
 1643 able to achieve a voltage swing of 3.8 V with the back-termination and the supply at 5 V. With
 1644 this swing the photo-electron amplitude can be brought to 6.5 mV, with a dynamic range of 350
 1645 photo-electrons. Furthermore, this chip can drive a $50\ \Omega$ differential cable with the same output
 1646 swing: in such a case the transmitter feeds more power on the cable, almost doubling the immunity
 1647 to pick-up noise with respect to the standard $100\ \Omega$ cables.

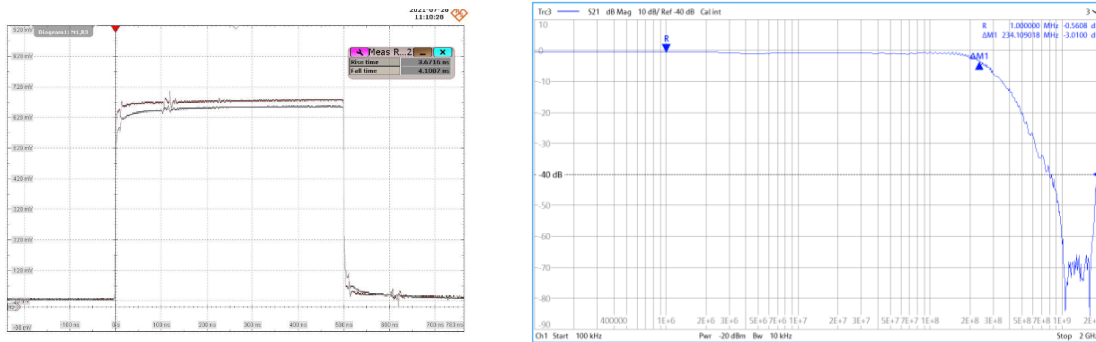


FIG. 27. Characterization of the differential transmission line. **Left:** 0.5 μ s long pulse after decreased the 10 meters cable at room temperature and in liquid nitrogen: due to the resistivity of copper the rise time changes from 10 ns to 3.7 ns 10-90 (and about 1.5 ns 20-80 at 77 K). **Right:** Bandwidth of the transmission chain: differential driver, cable (10 m in liquid nitrogen) and differential receiver (feedthrough absent). The system proves a bandwidth in excess of 200 MHz.

1648 A single custom composite cable will provide power for the electronics, bias for the SiPMs, and
 1649 control lines (see section 3.5.2). We are designing the cable including four differential lines for
 1650 transmission of the signal along the $\simeq 10$ m path from the cold region up to the room temperature
 1651 electronics. While the final cable has still to be produced, in the meantime we tested a version that
 1652 has only a fraction of the required conductors. The goal of the test was to measure the compatibility
 1653 of the differential line for transmission of the signal, focusing on bandwidth, attenuation and cross-
 1654 talk.

1655 Figure 27 reports the signal transmitted over 10 meters of the selected cable showing that no
 1656 significant attenuation is present in liquid nitrogen. The same figure also shows the bandwidth
 1657 of the differential transmitter plus cable, exhibiting a bandwidth of 200 MHz, more than suited
 1658 for the transmission of SiPM signals. Transmission of single photo-electron signals over this cable
 1659 was tested in the PDU+ scheme (section 3.4.4); figure 27 illustrates that the differential line is
 1660 correctly terminated for signals with a rise-time of 10 ns, consistent with our specification (while
 1661 for faster signals the reflection is of order 10%).

1662 3.4.3. PDUSlim: Design, Performances and Test Results

1663 The PDUSlim design is based on modularity, i.e. a detector assembled with different and re-
 1664 placeable PCBs. The building blocks of the PDUSlim are: PDMslims, composed of the tile PCB
 1665 and an amplifier front end board (AFEB); a copper mechanical support, termed motherboard; a
 1666 kapton strips PCB that routes PDM signals; a steering module PCB that distributes voltage and
 1667 control signals; and, an electrical transmission driver PCB.

1668 The PDUSlim is a design evolution of the first PDU prototypes delivered in September 2018,
 1669 August 2019 and August 2021, respectively. The PDUSlim retains the mechanics and the modu-
 1670 larity of the original PDU design, for which the assembly procedures and the mechanical reliability
 1671 have been proven in three full functional prototypes, all of them successfully shipped across three
 1672 institutions with no damages and operated in liquid argon (CERN) or liquid nitrogen (LNGS,
 1673 Naples). No mechanical failure was observed for any of them. Motivated by the need to satisfy the
 1674 specifications listed in section 3.4.1, the PDUSlim implements few improvements to reduce height
 1675 and dissipated power, and implements the ASIC front end amplifier.

1676 For the full-scale production the PDUSlim design is based on the splitting of the whole PDU
 1677 into five separate PCBs: this allows to parallelize the production, to speed up the QA/QC tests,
 1678 and to increase the global yield as each PCB can be easily replaced in case of a fault during the
 1679 massive production. These five components are implemented as follows.

1680 **The motherboard (MB)** 250 x 250 x 5 mm³ in the first PDU prototype design, is made of
 1681 pure (oxygen free) copper (see figure 28, left panel). The motherboard is a radiopure and reliable
 1682 mechanical structure for the PDU, providing a thermal path for the amplifier Front End Board
 1683 (AFEBS) components and a robust electrical grounding. The structure has open windows to allow
 1684 the Photo Detection Modules (PDMs) housing and to reduce the total weight (3.5 kg). On the top
 1685 side, PDM are anchored to the motherboard by acrylic screws. On the bottom side, the AFEBS
 1686 connectors insert into the kapton strip PCB, hosted by the motherboard.

1687 To remove radon the MB surface is cleaned with a chemical process that consists of 3 steps
 1688 which each act differently on the copper surface, removing part of the material. To improve
 1689 the erosion uniformity and guarantee the dimensional tolerances of the MBs are respected, two
 1690 different modifications of the electropolishing steps were studied, in particular we reduced the
 1691 surface material removal from 100 μ m/face to respectively 50 μ m and 20 μ m. Two different MBs
 1692 were treated with these modified protocols and validated from the point of view of the dimensional
 1693 tolerances. Two other copper plates were prepared with the same protocols and then measured:
 1694 the radioactivity results were similar to those with the initial protocol that foresaw 100 μ m of copper
 1695 removal. These results confirm that the MBs can be treated, removing less material, respecting the
 1696 dimensional tolerances and the background level requirements of the experiment.

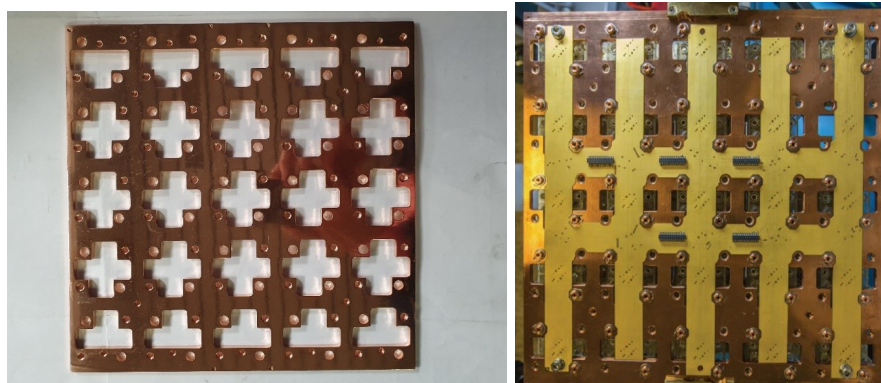


FIG. 28. **Left:** The copper Motherboard of the PDUSlim. **Right:** Kapton strips.

1697 **The kapton strip** is a multilayer printed circuit, mounted on the bottom side of the MB (see
 1698 figure 28, right panel). The kapton strip routes the SiPM differential signals to the electrical trans-
 1699 mission driver board and distributes the LV/HV generated by the Steering Module (described
 1700 below). On one side it has one connector for each PDM, while on the other side, 5 connectors
 1701 allow the output driver and the steering module insertion. The kapton strip feeds each PDM with
 1702 low voltage power supplies, high voltage for the SiPM biasing and the control signal to disable
 1703 the AFEBS. The stack-up ensures a controlled impedance (100 Ω) for the differential signal lines
 1704 and a cross talk between channels less than 1%. The signal planes are embedded in two ground
 1705 planes, electrically connected to the copper motherboard. The kapton strips have been successfully
 1706 tested in the previous prototypes. For the PDUSlim a minor modification is required by mounting
 1707 radiopure connectors on both sides.

1708 **The Steering Module** provides the Low Voltage (LV) for the ASIC and the microcontroller,
 1709 located on the AFEBS, and the High Voltage (HV) bias for the SiPMs. It should be noted that the
 1710 voltage values are not manipulated but are simply switched on/off. In this way, all PDMs will receive
 1711 only the voltage set on the power supplies. This is all done with an on-board microcontroller and a
 1712 setup that will be integrated in the slow control. The steering module is inserted to the bottom side
 1713 of the PDU through the kapton strip, next to the output driver. The power and communication
 1714 wires come in on a single cable, through a single connector. Two steering module prototypes were
 1715 successfully operated in the last two PDU prototypes, working at cryogenic temperatures.

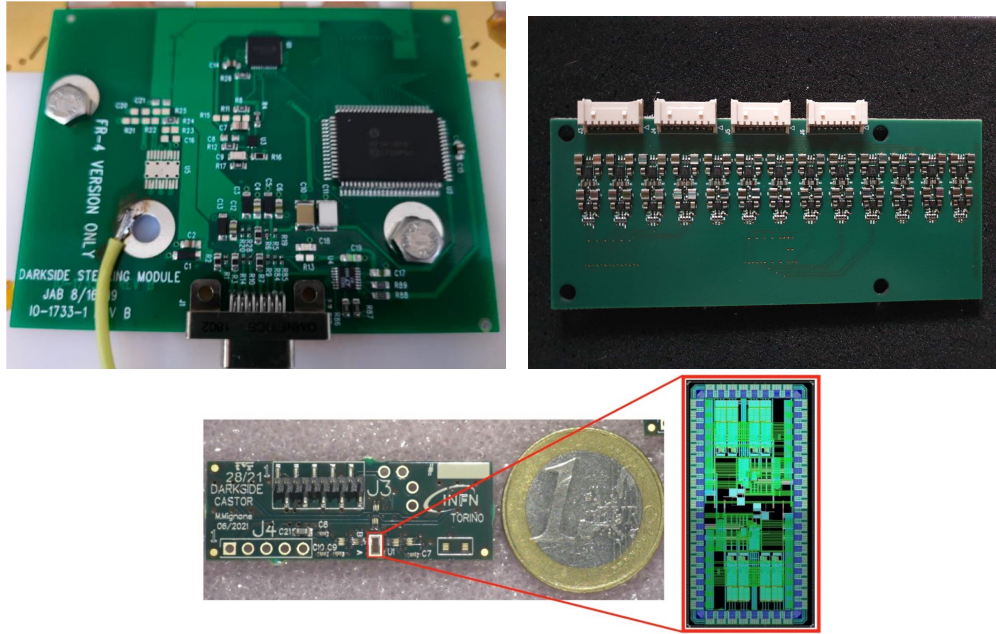


FIG. 29. **Top Left:** The steering module. **Top Right:** The 13 channels output driver. **Bottom:** The ASIC Front End Board (AFEB). The magnification shows the ASIC.

1716 **PDMslim** Each PDMslim (see figure30) is made of an acrylic cage, a SiPM tile and an AFEB.
1717 The AFEB is mounted on the bottom of the tile (figure30, right). The acrylic cage provides a
1718 reliable mechanical frame to connect the SiPM tile and the AFEB with the kapton strip. The
1719 acrylic cage is designed to protect the AFEB wire-bondings, allow safe handling of the tile, and
1720 provide the fitting into the rest of the mechanical and electrical structure. The acrylic plastic cage
1721 structure can withstand the thermal cycles from warm to cryogenic temperature envisaged for the
1722 testing, characterization and running phases of the experiment. The PDMslim will also provide an
1723 adequate thermal path from the AFEB active components, to mitigate bubbling in the LAr TPC
1724 as much as possible. The total PDMslim height is 10 mm.

1725 The $50 \times 50 \text{ mm}^2$ SiPM tile is built from an array of 24 SiPMs in the configuration 4X(2s3p)
1726 described in section 3.3. The four readout quadrant output signals are sent to the AFEB input.
1727 The back side of the tile PCB hosts the electrical connectors and four soldered profiles, suitable
1728 for a snap-fit joint with the plastic cage, devoted to the latching of the tile to the AFEB. The
1729 thermal contact is loose to avoid heat transfer from the AFEB to the SiPMsand to maintain their
1730 working temperature at 87 K. The snap-fit profile material in the present version is made of steel
1731 and will be preferably OFHC copper in the final version for its radiopurity and good soldering
1732 properties. The connectors mate with the AFEB providing some axial float (roughly 1 mm) to
1733 accommodate mechanical misalignment of the ASIC components and some radial float (roughly 0.5
1734 mm) to accommodate for mismatch in the thermal dilatation of different materials.

1735 The prototype of the AFEB is made of a 4-layer FR4 stack and hosts the CASTOR ASIC
1736 described in section 3.3.3. The total thickness is 1.2 mm. The top side of the board (39.75×3.72
1737 mm^2) is shown in Fig. 29, with a close-up of the 2.7 mm^2 ASIC CAD layout. The final AFEB will
1738 be made in ARLON 55NT.

1739 The off-chip biasing of the ASIC is implemented with a mesh of 5 voltage dividers, while the
1740 chip is powered with $+1.2\text{V}$ and -1.2V voltage supply, filtered in this prototype board with a set
1741 of 12 capacitors. The electronics for the PDUSlim features a 110 ns peaking time with a dynamic
1742 range of 170 photo-electrons and a SNR of 15 at 7.5 VoV. The ATTiny102 microcontroller and the
1743 SiPMsignal connectors are mounted on the back of board, while the innermost layers are used for
1744 power and ground planes.

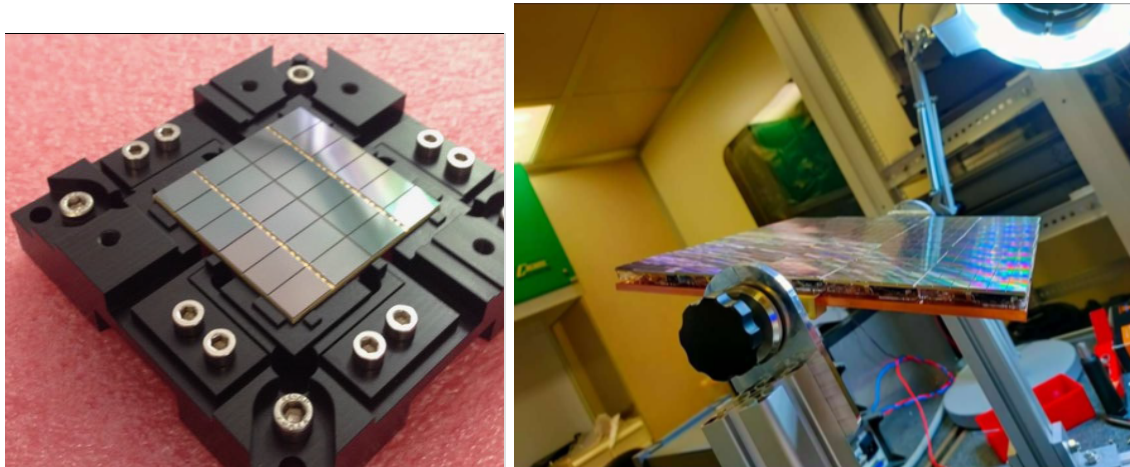


FIG. 30. **Left:** A SiPM tile. **Right:** The first prototype PDUSlim fully populated with PDMs

1746 **Output Driver** As discussed above, the PDUSlim design is driven by flexibility: the bottom
 1747 side of the kapton strip allows the insertion of a board to transmit the output signals, that may
 1748 implement different channel-sum schemes and can rely on the use of optical or copper transmission.

1749 The present output driver configuration foresees that a single output channel is associated to the
 1750 sum of the signals from two PDMslims. The schematics is based on the signal sum and transmission
 1751 scheme developed for the PDU+, described in section 3.4.2. The main differences are the 2x1
 1752 summing (with respect to the 4x1 in the PDU+) and the overall gain/bandwidth. The signal sum
 1753 relies on the OPA856 operational amplifier, suitable for cryogenic operations; the overall gain is set
 1754 to 6 dB and its bandwidth to 170 MHz. The maximum output swing for unipolar ground referred
 1755 input signals is limited to about 1.5V. To increase it, a -1 V offset is added to the input voltage
 1756 increasing the output swing to 2.5 V. The output is connected to a fully differential amplifier that
 1757 oversees the transmission. The transmitter chip is a THS4541 from Texas Instruments. Its typical
 1758 use is the feeding of an ADC differential driver, with typical input impedance of 500 Ω . In the
 1759 output driver, this component transmits the differential signal through a 10 m long cable, with 100
 1760 Ω impedance. By using an overall back termination of 200 Ω , thus increasing the load seen by the
 1761 chip to 300 Ω , a stable operating condition is achieved. The gain of the chip is set to 3 but, due
 1762 to the back-termination, the usable signal is 1/3 (100 Ω /300 Ω) of the total, for an overall gain
 1763 = 1. In this condition, the maximum output swing for unipolar ground referred input signals is
 1764 maintained to about 2.5 V. To avoid unnecessary electric and thermal load to the chip and cable,
 1765 an AC coupling is needed.

1766 The overall gain is set at 6dB and the bandwidth at 30 MHz. Considering the single photo-
 1767 electron level at 8 mV (as measured for LFoundry SiPMsat 7.5 VoV) the total dynamic range is
 1768 about 160 PEs (two channels). It is worth noting that the driver can be also operated without
 1769 the negative voltage bias, preserving a total dynamic range at about 100 PE, still within the
 1770 specifications.

1771 **PDUSlim assembly and preliminary tests** The PDUSlim was fully populated with 25 PDMs.
 1772 Three channels (ch 11, 14, 15 and 19) showed an acceptable performance (ch 19 was at the limit,
 1773 see below), allowing therefore a detailed analysis in terms of SNR and time resolution. As far as
 1774 ch15 is concerned, just one of the two tiles is operating: this allows to study the response of a single
 1775 tile in the channel, a situation foreseen in one of the 13 PDUSlim channels, although here the noise
 1776 is larger than expected when a single tile is connected physically to the output driver. It should be
 1777 noted that no one of these tiles have a quality comparable to that expected by the LFoundry final
 1778 production. Therefore, the obtained SNR and time resolution should be considered as lower limits
 1779 of what would be the production device.

1780 The first step of the test foresees the measurement of the photo-current of the single tiles at
 1781 warm temperature, with the supply voltages turned off. The expected current is few tens of

1782 μA with ambient light conditions. The next step is the measurement of the I-V curves at room
 1783 temperature. Figure 31 shows the I-V curves for the eight considered tiles. The absorbed current
 1784 is in line with the expectations.

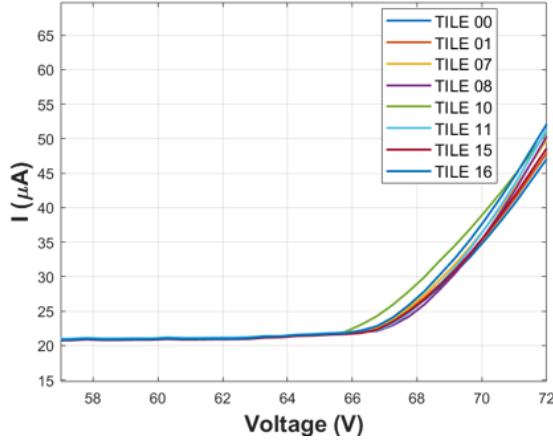


FIG. 31. I-V curves at room temperature for the 8 tiles tested.

1785 The low voltage power supply is then turned on (1.2 V), to measure the current absorption. The
 1786 measured value for the eight selected AFEBs was about 32 mA each. The noise spectrum was
 1787 recorded by mean of an oscilloscope to test the adder and the differential driver performance.

1788 **PDUSlim tests in the Napoli PDU Test Facility** Upon arrival few tests were performed to
 1789 check the PDUSlim integrity after the shipping: the photo-current and the power absorption were
 1790 measured, giving results compatible to those already reported in Pisa. Finally, the PDUSlim was
 1791 mounted in the liquid nitrogen dewar and cooled down at cryogenic temperature.

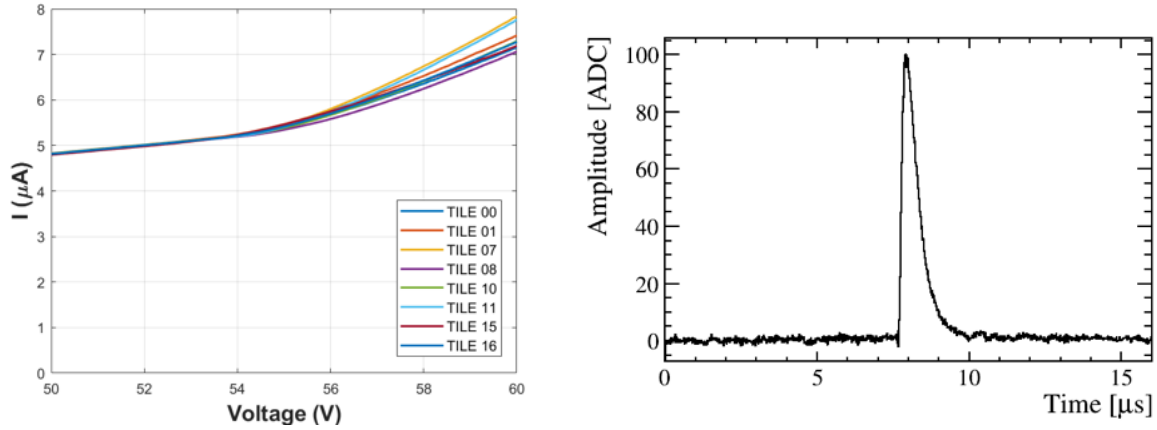


FIG. 32. **Right:** I-V curves measured in LN at the Napoli Test Facility; **Left:** PDUSlim tile signal.

1792 Cryogenic temperature I-V curves were measured, to test the homogeneity of the breakdown
 1793 voltage and the integrity of the bias voltage connections, and are shown in Fig. 32 (Left). A typical
 1794 PDUSlim tile signal at LN temperature is shown in Fig. 32 (Right).

1795 The breakdown voltage inferred from the I-V curve for ch11 and ch15 was (54.3 ± 0.2) V, cor-
 1796 responding to 27.15 V for the single SiPM tile. The breakdown voltage estimated as the intercept
 1797 ($Q=0$) of the collected charge integrated in a time window 1 μs , as a function of the voltage, gave

(54.2 ± 1.0) V, (54.1 ± 1.0) V, (53.8 ± 1.0) V, (54.6 ± 1.0) V for the channels 11, 14, 15 and 19, respectively. The uncertainty was estimated from the fit and varying the charge integration time by a factor of 2.

The DS-20k PDUs are fed with a single bias line, thus tile with similar breakdowns need to be paired. Since this operation was not possible for in this case the PDU prototype is not optimized. This is highlighted in Fig. 33, where the response of the two individual tile contributions to the ch11 signal is compared.

The power supply was set to operate at three different voltages, corresponding to 5, 7 and 9 VoV (Volt over Voltage) and few laser runs were collected. Data was collected in a low luminosity condition, to emphasize the single photo electron (SPE) analysis. The SPE signal amplitude at 7 VoV (9 VoV) is 7.6 mV (9.4 mV), offering a good safety margin from the pick-up noise in DS-20k. In the PDUSlim a SNR=8 can be maintained even with a noise as large as 1 mV. The amplitude spectrum was obtained after filtering the collected waveforms with a moving average filter, over a range of 400 ns. Fig. 34 shows the charge spectrum obtained for two of the four channels (ch15 and ch11) at VoV=5, 7, and 9, respectively.

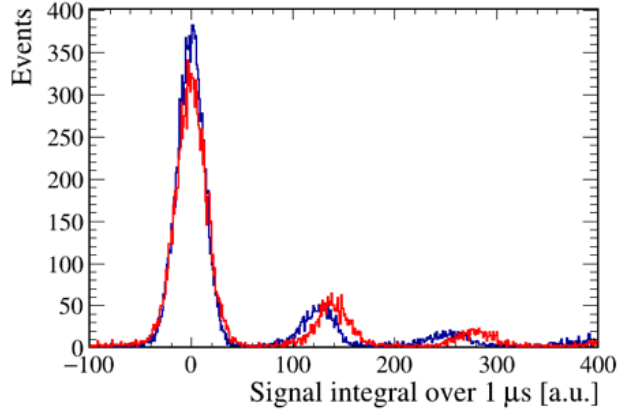


FIG. 33. The signal from channel 11 with the two tiles in the pair alternatively turned on (red: TILE01 on, TILE00 off; blue: TILE01 off, TILE00 on)

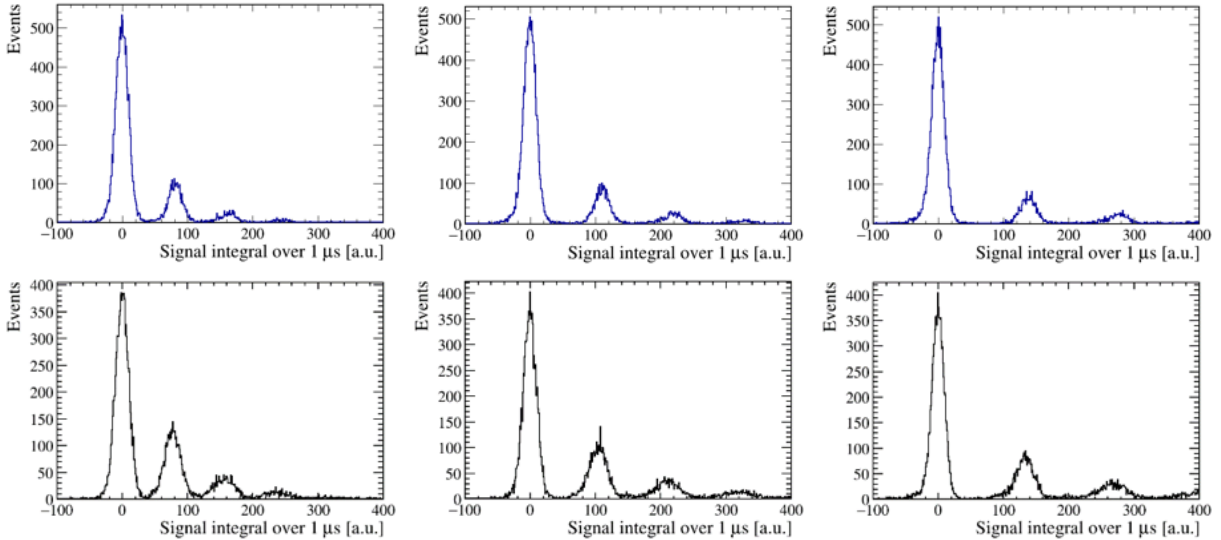


FIG. 34. Charge spectrum for ch15 (top) and ch11 (bottom), at 5,7 and 9 VoV.

1813 The analysis of the charge and amplitude spectra gave a SNR ranging from 9.1 to 19.0, depending
 1814 on the applied voltage for $\text{VOV} \geq 7$ V, as reported in Table XII. It is worth noting that even at
 1815 over-voltages as low as 5 V, half of the channels show a performance reaching or exceeding the
 1816 DS-20k specification (SNR=8), while the others are quite close to the specification, suggesting that
 1817 a $\text{VOV}=6$ V would be sufficient to meet this requirement. The result obtained at 9 VoV for channel
 1818 19 gives a very large SNR, taking advantage of the baseline low noise, although the SPE spectrum
 1819 shape fit is not very smooth. Since the baseline noise for channel 19 represents an outlier, we
 1820 consider only ch11, ch14 and ch15 in the following discussion of performances. In addition, the raw
 1821 amplitude spectrum without any filtering returned quite remarkable SNRs (for ch15 at 7 VoV (9
 1822 VoV) SNR=6.8 (8.4)), a feature that can be useful to simplify the trigger and to facilitate in situ
 1823 debug conditions. Similar results are obtained for ch14, where a SNR = 6.1 at 7 VoV is obtained
 1824 (see Fig. 35).

	SNR at 5VOV	SNR at 7VOV	SNR at 9VOV
Ch 11 (Charge Spectrum)	7.4	10.2	13.8
Ch 11 (Filtered Amplitude Spectrum)	7.3	10.0	13.0
Ch 14 (Charge Spectrum)	6.9	9.2	13.0
Ch 14 (Filtered Amplitude Spectrum)	6.7	9.1	12.0
Ch 15 (Charge Spectrum)	8.2	11.1	13.6
Ch 15 (Filtered Amplitude Spectrum)	9.5	13.0	17.0
Ch 19 (Charge Spectrum)	10.2	14.1	18.6
Ch 19 (Filtered Amplitude Spectrum)	11.0	14.0	19.0

TABLE XII. SNR for PDUSlim at 5, 7 and 9 VOV

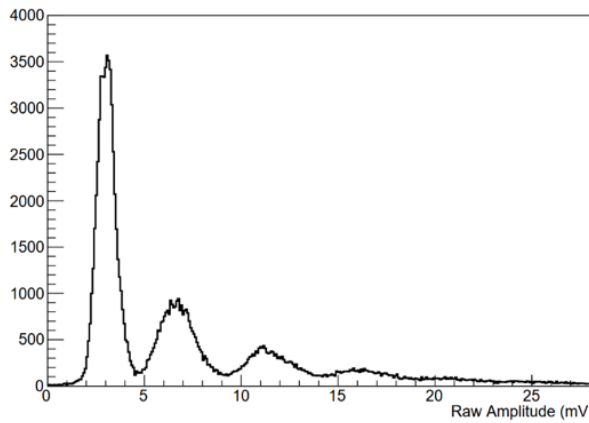


FIG. 35. Raw amplitude spectrum for channel 14 obtained at 7 VoV.

1825 Finally, the PDUSlim time resolution was estimated relying on a simple time difference between
 1826 the measured signal time and the laser start signal, sent to the DAQ. The time of the hit is obtained
 1827 using a cross-correlation with the template shown in Fig. 32 (Right). The measured resolution, σ_t ,
 1828 is 15 ns (18.6 ns) at 9 VOV (7 VOV) for ch15 and 20 ns(22 ns) at 9 VOV (7 VOV) for ch11. Fig. 36
 1829 shows the ch15 and ch11 signal time distribution at 7 VoV. Similar results were found in the other
 1830 channels. The contribution to the global time resolution due to the jitter of the laser start signal
 1831 as acquired by the DAQ is estimated to be about 2 ns. The result obtained with a simpler rolling
 1832 threshold method, that do not depend on the signal template, is only marginally worse (19.9 ns vs
 1833 18.6 ns).

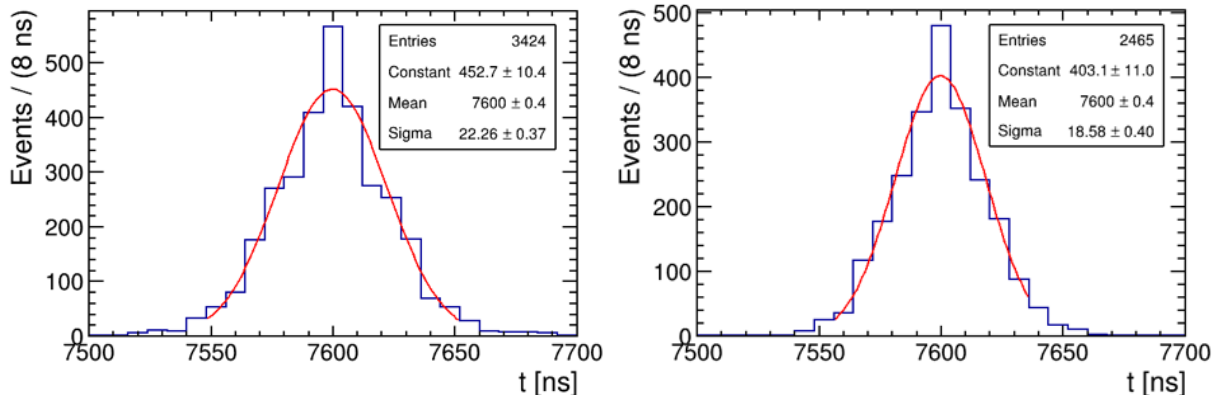


FIG. 36. Distribution of the time difference with respect to the laser time at 7 VoV using a cross-correlation method for single photo-electron signal of ch11 (left) and ch15 (right).

1834

3.4.4. PDU+: Design, Performances and Test Results

1835 The PDU+ is a compact design in which all the PDU functions are performed with a minimum
 1836 number of Printed Circuit Boards (PCBs), minimizing the number of connectors and cables. The
 1837 PDU+ builds on previous experience in developing single functions, keeping most of the basic
 1838 schematics and simply integrating them in a new compact layout.

1839 The components of the PDU+ are: Tile+, which is a single PCB that hosts both SiPMsand the
 1840 front end electronics; and, Motherboard+ (MB+), which distributes voltage and control signals,
 1841 sums Tile+ channels, and drives the electrical signal transmission. This section describes the
 1842 electrical performance; radiogenic backgrounds are described in section 12.2.

1843 **Tile+ and vTile+** A single PCB is used to mount the SiPMs and the amplifier, based on the
 1844 observation that a single trans–impedance amplifier (TIA) occupies about 7×16 mm² and can be
 1845 easily integrated into the printed circuit board (PCB) of the tile. This configuration removes the
 1846 necessity of using two boards (one for the SiPM and one for the amplifier) thus implementing a
 1847 complete photo–detector module in a single unit 1 cm tall, as opposed to the PDM design adopted
 1848 for the first PDU prototypes that used two PCBs, integrated in an object 5 cm tall and requiring a
 1849 plastic cage to keep the PCBs in place. Similar considerations hold for the ASIC based amplifier,
 1850 thus opening the possibility of adopting in the entire detector a single PDU design. We have tested
 1851 two flavors of the single PCB integrating SiPM and amplifier

- **Tile+:** with a 4s6p configuration and 1 TIA amplifier based on the LMH6629 described in section 3.3.2, to be used in the TPC;
- **vTile+:** with a 4X(2s3p) configuration and the ASIC amplifier described in section 3.3.3, to be used in the Veto.

1852 In both cases, 16 Tile+ (vTile+) are mounted on top of a second larger PCB, called MB+ (Mother
 1853 Board). A PDU+ (vPDU+) is then the full assembly of 16 Tile+ (vTile+) and 1 MB+ (vMB+).
 1854 Fig. 37 shows the first Tile+ prototype realized in FR4. While this device has borders for safe
 1855 handling, the final version will be border-less and made in Arlon–55NT. The tile+ sinks about 10
 1856 mA with a supply of 5.5 V; the power is dissipated by the LMH6629 operational amplifier. The
 1857 PCB has 4 active layers with blind vias and a buried ground plane. The top layer, where SiPMs
 1858 are bonded, is unaltered with respect to the tile developed for the first PDM prototypes, described
 1859 in section 3.3.2. Given the ganging topology, the SiPMnetwork requires a bias in excess of 130 V.

1860 The Tile+ units can be secured to a motherboard via four cylindrical pillars ($\phi=3$ mm $h=5$ mm)
 1861 with an internal thread for M1.6 screws. In the final version both the screw and the pillar will be
 1862 produced in clean copper and polished.

1863 The photoelectron spectrum measured with the prototype Tile+, operating at 7 VoV, is shown in
 1864 the bottom left plot of Fig. 37. A SNR of 25 is obtained for the matched filtered signals, consistent

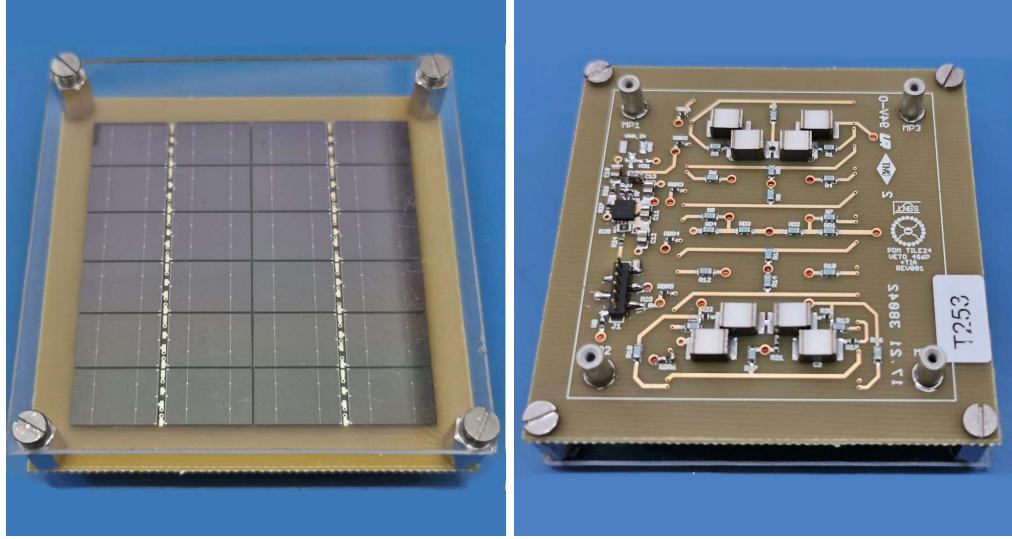


FIG. 37. Tile+ design and test results. **Top:** Tile+ TF-253 top view (left) with 24 SiPMs and bottom view (right). The unit was produced with borders (5 mm) to simplify the testing (including a top acrylic frame), but the final version will be border-less with a total dimension of 49.5x49.5 mm². In the bottom view it is possible to see the TIA and the connector on the left side. Four 5x3 mm threaded pillars are soldered to the PCB to allow a reliable connection with the motherboard. **Bottom Left:** Finger plot of tile+ #TF-253 for filtered signals at 7 VoV with a SNR=25. **Bottom Right:** Noise power spectrum at 86 K of the 1-TIA amplifier connected to a Tile+ compared to the one of the 4 TIA (4 x 2s3p) scaled of 12 dBm/ $\sqrt{\text{Hz}}$ (6 dBm/ $\sqrt{\text{Hz}}$ are due to the 4 TIA configuration that exhibits a doubled noise while the remaining contribution is given by the summing and differential FEB stages and the differential to single-end converter). The curves are consistent within 20%. Such difference is explained with the different devices used to assemble the tiles (FBK SiPMs in Tile+ and LFoundry SiPMs in the 4 TIA).

1869 with that shown in Fig. 21 with the traditional two PCB configuration developed for the first PDU
 1870 prototypes and 1 TIA.

1871 The photoelectron charge spectrum obtained with vTile+, again operated at 7 VoV, is reported
 1872 in Fig. 38. In this case the pulse charge is obtained by integrating over an interval of 1 μs , the single
 1873 photoelectron response is 900 $\text{pV} \cdot \text{s}$ and a SNR of 14.9 was obtained with no filtering procedure.

1874 **MB+** 16 Tile+ will be mounted on a single Arlon-55NT PCB called Motherboard+ (MB+).

1875 The MB+ board includes all the required components to provide the correct bias to the tiles,
 1876 four active adders to sum tile signals, and four high dynamic range differential transmitters. The

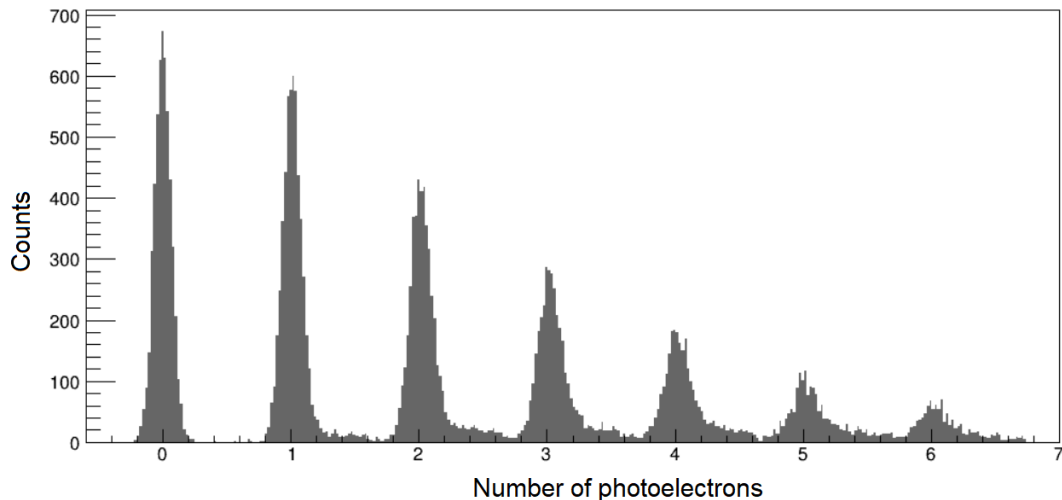


FIG. 38. Finger plot of vTile+ obtained with laser at liquid nitrogen temperature. Note that here the pulse charge, evaluated over an interval of $1 \mu\text{s}$, has been used in place of the pulse amplitude.

MB+ has 4 analog high dynamic range differential outputs corresponding, each, to the sum of 4 Tile+ units. The output signals are intended to travel on four twisted pairs in the same radio-pure cable providing the power to the unit, thus simplifying the cabling of the detector. A MB+ has a size of $200 \times 200 \text{ mm}^2$ with a thickness of 1.4 mm: the PCB is robust enough to provide support for the photo-detectors. This design strongly reduces the number of components required to assemble a PDM, as described in the next section, thus simplifying the production and the integration.

The first assembled and tested prototype of the MB+ is called $\text{MB}_\frac{1}{4}$, a PCB hosting 4 Tile+, one adder, one differential transmitter and the power supply regulator (LDO). The stackup of the board has all components on the bottom except the tile connectors that are on the top. A buried ground plane protects the TIA on the Tile+ from pickup by the $\text{MB}_\frac{1}{4}$ traces.

The $\text{MB}_\frac{1}{4}$ is fed with a single-ended supply of about 6 V. A voltage regulator (ADM7150ACPZ-5.0-R7) filters the line and provides a stable supply of 5 V. A local ground is reconstructed by a 1:1 resistive divider, properly shunted with tantalum and plastic (PPS) capacitors. The schematics are the same as those developed for the 4 TIA amplifier.

Experience with cryogenic adders has been developed during the work towards the original 4 TIA amplifier, where the sum of the four branches of SiPMs of the 4X(2s3p) configuration is performed. This design shares most of these technical details to implement the sum of four outputs of the already-amplified signals.

The original 4 TIA scheme implements a 4:1 adder to sum the TIAs connected to a single SiPM with the TI OPA838 operational amplifier. This amplifier works at cryogenic temperature but its performances are uneven between the chips. As a result, for some units, the bandwidth of the adder falls below the requirement of 30 MHz, bringing the rise-time of the FEB below the requirement of DS20k (10 ns 10-90%). Lowering the (noise) gain leads to instability and oscillation. As an alternative for the $\text{MB}_\frac{1}{4}$ we tested a new operational amplifier, OPA856, that is working in LN2, is stable at gain 1 and has a bandwidth larger than 100 MHz (in our configuration) with a voltage swing of 2.4 V. The OPA856 drains a bit more current than the OPA838: 8 mA vs 2 mA at 5V. In the $\text{MB}_\frac{1}{4}$ we implemented the adder based on this solution: to improve the dynamic range the adder is polarized at -1 V at rest, offering a dynamic range of 1.4 V, corresponding to about 350 photo-electrons at 7 VoV for the sum of four Tile+ units reaching the design goal of the experiment. A further improvement can be obtained configuring the amplifier in double gain with a diode feedback: the negative polarization of the output ensures that the first half of the dynamic range is completely free from aberrations.

A $\text{MB}_\frac{1}{4}$, is shown in Fig. 39 with three Tile+ mounted. In Fig. 39 (bottom plot) we show the

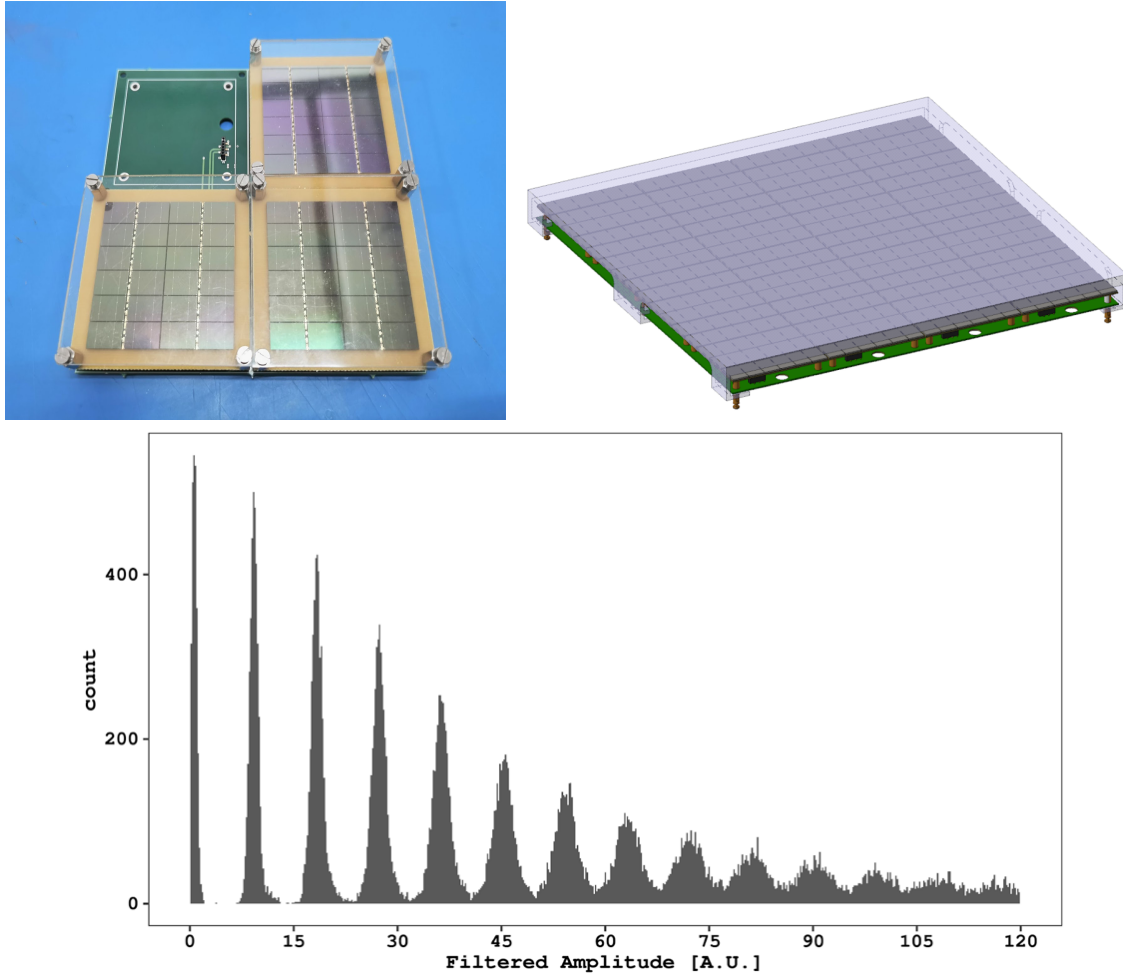


FIG. 39. MB+ design and test result. **Top Left:** MB $\frac{1}{4}$ prototype assembly. In this setup three Tile+ are with the protection border to simplify the R&D. The final MB+ will assemble 16 tile+ without empty spaces. **Top Right:** Drawing of the PDU+ (made of four MB $\frac{1}{4}$ shown in the left plot) with the acrylic protection on the top. **Bottom:** Finger plot of Tile+ #TF-253 connected to a MB $\frac{1}{4}$ for filtered signals at 7 VoV with a SNR=25. In this measurement all the components of MB $\frac{1}{4}$ are connected and working (adder, differential transmitter, 10 m of cable but the LDO is disabled).

1910 measurements done on the full system assembled with tile #TF-253. The differential transmission
 1911 is routed through 10 meters of cable, to simulate the real scenario. The results are identical to the
 1912 tests of the standalone Tile+ (shown in Fig. 37) confirming the performances of the MB $\frac{1}{4}$ design
 1913 and implementation meet the DS-20ks specifications.

1915 3.4.5. *R&D results and conclusions*

1916 Two solutions for the PDUs have been proposed by the Collaboration and are under active
 1917 consideration for the two optical planes: PDU+ and PDUSlim (see sections 3.4.4 and 3.4.3). The
 1918 Collaboration opted to setup a formal decision process for verification of the full compliance of the
 1919 two solutions to the technical specifications (listed in section 3.4.1). The steps of the review include
 1920 provision of comprehensive documentation, delivery of prototypes, operation of the prototypes in
 1921 the PDU test facility (described in section 9.2), analysis of data, and independent verification of
 1922 all previous steps by an internal review committee.

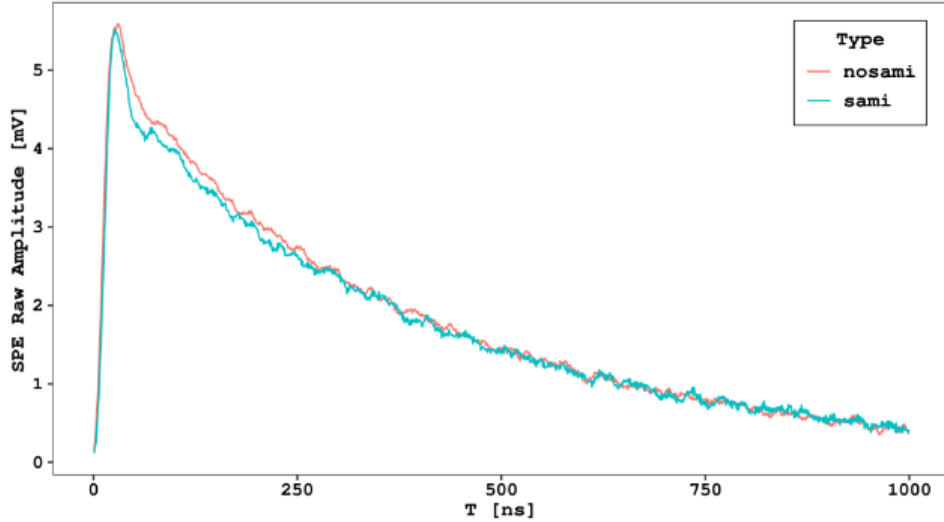


FIG. 40. A pulse corresponding to a single photoelectron signal (average of many pulses) transmitted through a short and 10 meters cable in liquid nitrogen. No significant deformations of the pulse shape are present.

1923 Review of the PDU+ has been successfully completed, and thus PDU+ is to be considered an
 1924 approved baseline solution. Testing of PDUSlim is complete, and review is ongoing. Work is ongoing
 1925 to guarantee mechanical and electrical compatibility with the PDU+ solution. A final decision is
 1926 expected upon receipt of the report on PDUSlim issued by the internal review committee.

1927

3.5. Cables and connectors

1928

3.5.1. Goals of the R&D

1929

The goal of this R&D activity is to select cables and connectors which are reliable in LAr and
 1930 which they are subdominant contributors in the background budget.

1931

3.5.2. Cables

1932

Cables are needed to power the front-end electronics and to send commands to the Photo Detector
 1933 Units. An R&D program to provide a low radioactive cable suitable for operation at cryogenic
 1934 temperature was established with the SAMI S.P.A industrial partner. While standard industrial
 1935 copper used for the cable core is adequately radiopure, the insulator plastic material can have
 1936 high neutron capture cross section and high γ activity. Various insulator materials were tested.
 1937 FEP (fluorinated ethylene propylene), a copolymer of hexafluoropropylene and tetrafluoroethylene,
 1938 was considered. Although it acts as an excellent insulator at low temperature, the presence of
 1939 fluorine increases the background due to high α,n cross section. PEEK (polyether-ether-ketone)
 1940 was also considered but, although potentially very radio-pure, produced a cable with unacceptable
 1941 rigidity. A resin commercially called SiltemTM, or polyetherimide-siloxane, was also considered.
 1942 This polymer is free of halogens and is very flexible, making it feasible for cryogenic usage. Both
 1943 the raw resin and a sample cable have been assayed following the protocols describe in Sec. 3.1.2
 1944 with satisfactory results, implying a subdominant contribution of the cables to the total background
 1945 budget.

1946

The sample cable consists of four twisted conductors pairs. The measured impedance of a twisted
 1947 pair is $(108 \pm 2) \Omega$ and compatible with the required $(100 \pm 20) \Omega$. Four such cables are bundled

1948 together. One pair uses AWG24 wire and is meant for powering the PDU. The other three use
 1949 AWG30 wire: one pair is used to carry the bias voltage for the SiPM and its return while the
 1950 remaining carry the control signal, with redundant connection for LV sensing. The cable is covered
 1951 in a polyester woven sheath, allowing flow when immersed in LAr. Two polyester wires are also
 1952 used to identify the signal twisted pairs.

1953 At the cryostat exit, where the signals are fed through the flange, the bundle is soldered to a
 1954 D50 connector. On the other side, connecting to the PDU, each cable is crimped to a sherlock-like
 1955 PCB to wire connector.

1956 3.5.3. Connectors

1957 The electrical and mechanical connection between the motherboard and the tile is presently
 1958 achieved with single-line pins. Similarly to cable insulation, the main source of radioactivity is
 1959 the plastic comprising the connector. Most commercial connectors are made with liquid crystal
 1960 polymers loaded with glass fiber to increase their resistance to high temperature. Initial prototype
 1961 tiles and motherboards have been produced and tested using standard connectors while searching
 1962 for radio-pure ones. We tried to involve several companies to produce prototypes with radiopure
 1963 materials. After a long search, a company was found (SHENZHEN FORMAN PRECISION
 1964 INDUSTRY CO., LTD) which could manufacture connectors with a nylon material which is potentially
 1965 radiopure. The initial assay on the material proved the absence of radioactive contaminant,
 1966 while Nylon PA66 is known to be suitable for cryogenic applications. A first batch of connectors has
 1967 been purchased and is being tested for radiation purity. The same prototyping and assay operation
 1968 is in progress for the radiopure version of a sherlock type connector from the radiopure cable to
 1969 the PDU. This connector is crimped to the cable, while the male is soldered at low temperature on
 1970 the PDU board. These connectors are packaged in a reel, to be manipulated by a pick and place
 1971 machine for automatic production of PCBs.

1972 3.5.4. R&D results and conclusions

1973 The R&D program on cables and connectors has occurred primarily through interaction with
 1974 companies. While the sources of radiopure cables were already known among some possible industrial
 1975 partners, for connectors we had to identify a company willing to change the composition of
 1976 their plastic enclosures. Unloaded radiopure plastic has the disadvantage of being more sensitive
 1977 to temperature, requiring low temperature soldering. This makes the radiopure connectors less
 1978 attractive for general use in the consumer market. We have identified the company for the production
 1979 of low radioactivity connectors. A feature of this R&D is that the prototype runs may cover
 1980 a considerable part of the final need of the experiment in terms of number of pieces: the minimum
 1981 order quantity is typically of the order of several thousand pieces. The sample connectors produced
 1982 by the company have been assayed, and have acceptable radiopurity (section 5.8.3).

1983 3.6. TPC design

1984 3.6.1. Goals of the R&D

1985 The DS-20k baseline design is a TPC constructed mainly with PMMA plates to form the trans-
 1986 parent anode and cathode and Gd-loaded PMMA panels to form the barrel. Following a highly
 1987 integrated design philosophy, the shape and size of all components are evaluated considering their
 1988 mechanical and thermal behavior, purity, multipurpose usage, and overall geometrical optimiza-
 1989 tion to create both a uniform electrostatic field in the entire active region of the TPC and a very

1990 uniform luminescence field in the gas pocket. The goal of the R&D is focused around achieving
 1991 these TPC scientific goals.

1992 The following activities are described below: the cathode HV delivery system and detailed meth-
 1993 ods for HV cable fabrication; design of the field cage and overall geometrical layout optimization
 1994 using FEA to achieve uniform field; and the procedure for conductive polymer coating and post
 1995 processing for both the field cage rings and the anode and cathode windows.

1996 *3.6.2. Electric field in the acrylic TPC*

1997 Electric field simulations were performed using the COMSOL Multiphysics™ [45] software em-
 1998 ploying detailed models of the full DS-20k detector both in 2-D and 3-D. This confirmed the
 1999 feasibility of achieving an uniform drift field in the active volume and only up to 0.5 % in a 1cm
 2000 region near the reflector walls and near the grid wires. This is also accomplished thanks to main-
 2001 taining the anode and the wire frame flat. FEA simulations confirmed that a perfectly flat anode
 2002 window will bow up to 0.54 mm at the center due to the fact that acrylic density is less than that
 2003 of liquid argon when operating in liquid argon with a gas pocket below. Moreover, wires will sag
 2004 by a maximum of 0.5 mm The mitigation of anode bowing will be accomplished by machining the
 2005 anode in a computed curved shape that will lead to a flat anode when in liquid and cold. This
 2006 activity is being worked out with FEA studies and actual lab test.

2007 *3.6.3. Cathode high HV cable*

2008 The delivery of the high HV (HHV) to the detector cathode is a critical issue of all noble gas
 2009 detectors. Members of the DarkSide team responsible for this activity have successfully built and
 2010 operated such system at voltage as high as 300 kV in liquid argon. The main component of the TPC
 2011 HHV system is the penetration from air to the argon volume using a high voltage feed-through
 2012 (HVFT). Our approach would be to use an alternate solution to safely provide HV delivery to
 2013 liquid noble gas TPC using a multilayered PE cable. A triple layered PE cable is commercially
 2014 available (Dielectric Sciences): it features a pristine PE as the insulator and a semi-conductive PE
 2015 (SCPE) as the core conductor and outer ground layer. R&D is ongoing to establish a practical way
 2016 of creating an additional semi-resistive (SR) layer in between the insulator and the ground. This
 2017 additional layer is only needed for the cathode HV connection to minimize electric fields near the
 2018 HV cable termination in LAr. The triple layered PE cable will be used for all initial tests in a HHV
 2019 mockup and DS-Proto while development of SR layer is ongoing.

2020 The HHV mockup is a scaled down version of the acrylic geometry with the same thickness as
 2021 in the actual DS-20k detector and it features all the electrodes, the integrated field cage rings,
 2022 and the resistor chains as in DS-20k. Together with the mockup, the following tests are planned:
 2023 1) establish the effective bending radius of the HV cable both at warm and cold, 2) develop a
 2024 procedure for HV cable annealing, and 3) test the HV connections and their long term stability.

2025 Since the triple layered PE cable is entirely made of plastic no soldering of the conductive core is
 2026 possible. A design of the plugs connecting the cable to the Heinzinger power supplies is completed
 2027 and prototypes are fabricated (see Fig. 41).

2028 The cold HV cable termination design features a smooth metal cap screwed at the end of the
 2029 cable. The internal pin of the cap embeds itself into the core of the PE cable and guarantees
 2030 electrical connection at cold temperatures. A prototype of a tapping die for the cable insulator has
 2031 been fabricated and tested (see Fig. 41). The cable is then plugged into the cold HV FT consisting
 2032 of a PMMA conical port (see Fig. 73 in Sec. 7.2.4) housing the metal receptor which is connected
 2033 to the cathode.

2034 Since plastic tends to exhibit increasingly hard, stiff, and brittle responses to mechanical loads
 2035 as it is cooled from room temperature toward cryogenic temperatures, the PE cable needs to be



FIG. 41. R&D work on the multilayered HV cable. Figure A shows the Heinzinger power supply together with an HV cable featuring an adapted plug (zoomed view in Figure C). This design features the cable core connected to the power supply plug via a crimped ferrule and a spring relieving all the mechanical tensions. The spring is encapsulated in a Faraday cage to ensure an electrically safe connection. Figure B shows the thread achieved on the end of the HV cable using the developed tapping device.

annealed. A preliminary design of an oven able to anneal the cable in various sections is done. It features a water bath concentric to a copper pipe to warm up the cable.

To achieve the SR layer different avenues were followed including carbon doped PE, ion implantation, and semiresistive epoxies. Among these methods carbon doped PE shows promising results. Different samples of PE loaded with different conductive materials (PE1296, and PE702-50) at different concentrations (25%, 33% , and 60% respectively) were acquired from a company (PreMix) and their resistivity assayed. These samples will help to tune more precisely the resistivity required by the SR layer since the dependence of the resistivity as a function of the carbon concentration is not linear. Once tuned, the material could be purchased and used to produce a new cable. We have already identified at least one company willing to co-extrude a PE cable with four different layers.

R&D for developing a stratified PE cable with metal wires fully embedded within the SCPE core is also planned. Finally, the backup option for HV cable is to use the triple layered PE cable but with an increased diameter which would also help to minimize the strength of the electric field near the termination of HV cable.

3.6.4. Field cage and Clevios tests

Generating the electric field within the acrylic TPC will be accomplished by coating the inner surfaces of the field cage, cathode and anode with Clevios FET conductive polymer from Heraeus. The polymer provides good surface conductivity, it bonds well to the acrylic surface, and for thin layers allows good optical transparency. We have tested various methods of application of the polymer to large-area surfaces, and found that spray-coated films with a surface resistivity of around $10\text{ k}\Omega/\text{square}$ will satisfy the requirements for the inner surfaces of the TPC anode and cathode, and will contribute to only minimal absorption of visible photons. We have studied the stability of the thin films, and found that they are stable and survive cryogenic cycling if excessive exposure to UV light or oxygen is avoided. We are currently assembling a prototype system with an x-y translation table that will be used to coat the anode and cathode surfaces of the prototype TPC. The system can be later scaled to the full-size required for DS-20k.

The field shaping rings inside the TPC barrel are not subject to the same stringent requirements for optical absorption as cathode and anode surfaces, so that a much thicker Clevios coating is allowed in these region. Such a coating is much less susceptible to degradation from air and UV exposure. At Carleton, we are starting a set of tests to finalize the procedure of coating the barrel sections.

3.6.5. R&D results and conclusions

Component tests for the high voltage system and the electrostatic field(s) creation have developed designs and fabrication methods that meet the requirements for DS-20k. Beyond the electrostatic

2071 field elements described here, every component design that will be used in the DS-20k TPC has
 2072 been tested in some form, and integrated tests have been carried out with DS-Proto0, see Section
 2073 [9.6.1](#).

2074 **3.7. Reflectors and wavelength shifters**

2075 **3.7.1. Goals of the R&D**

2076 Scintillation light from argon is peaked at 128 nm and a wavelength shifter (WLS) is required for
 2077 its efficient detection. The goals of the activity are to compare 1,1,4,4-tetraphenyl-1,3-butadiene
 2078 (TPB) with PolyEthylene Naphthalate (PEN) as wavelength shifters to develop the optimum sys-
 2079 tem for the TPC and Veto use, enabling design of the reflector system to maximize light yield
 2080 whilst minimizing material.

2081 **3.7.2. Description of the activity**

2082 All the inner surfaces of both the TPC and the Veto detectors are lined with a WLS material.
 2083 Since the energy threshold and the light yield are critical for the dark matter sensitivity, the TPC
 2084 uses vacuum-evaporated TPB coating, which has the highest wavelength shifting efficiency (WLSE).
 2085 The vacuum evaporation of TPB may become not practical when the surfaces are very large as in
 2086 the case of the Veto (174 m^2). The Veto light yield requirement is less stringent than that of TPC
 2087 thus allowing us to instead choose polyethylene naphthalate (PEN) in the Veto, available as a large
 2088 format polymeric film, which dramatically simplifies the production and installation. The decision
 2089 to use PEN was informed by an extensive survey of commercially available grades and successful
 2090 tests in a representative environment, described in more detail later in this section.

2091 Wavelength shifted blue light must be then collected in the photosensors, which cover only 3.2 %
 2092 of the Veto surface. To this end a highly efficient multilayer polymeric Enhanced Specular Reflector
 2093 film (ESR) from 3M is used, with a reflectivity of 98 % over the entire visible spectrum (400-1000
 2094 nm) for all angles of incidence [46]. The reflectivity is particularly important for the Veto, in which
 2095 photons reflect many times before reaching a SiPM. ESR is commercially available as $60 \times 60 \text{ cm}^2$
 2096 foils with $65 \mu\text{m}$ thickness. The foils are delivered with top and bottom $50 \mu\text{m}$ thick films for
 2097 protection against dust which, importantly for our case, also prevent plate out of Rn daughters.
 2098 ESR is state-of-the-art and well-proven in LAr detector applications.

2099 **a. TPB coated ESR for the TPC** We have tested coating TPB onto ESR films at Carleton
 2100 and found that the films are robust and survive cryogenic cycling. We will test the mechanical
 2101 robustness of the full procedure in the prototype TPC (section [9.6.2](#)). TPB-coatings on ESR will
 2102 be identical to those in DS-20k, with the exception of additional precautions on radon exposure
 2103 and radiopurity for the final films. The targeted TPB thickness is $3 \mu\text{m}$ with maximum thickness
 2104 variation of $\pm 20\%$.

2106 **b. ESR and PEN** PEN is chemically a cousin of the well known polyethylene terephthalate
 2107 (PET or Mylar). Because of its low oxygen permeability and convenient mechanical, electrical
 2108 and optical properties, it is industrially mass produced for applications in e.g. food packaging
 2109 or electronics. Although it is also one of the components of the ESR film and its fluorescence
 2110 properties have been known for a long time [47], it was only proposed as a scintillator in 2011 [48],
 2111 and then, recently, as a WLS particularly well suited for large scale LAr detectors [49]. While
 2112 ProtoDUNE-DP [50] performed a proof-of-principle test, using PEN foils as WLS installed in front
 2113 of a fraction of PMTs, the DS-20k Veto will be the first detector to use PEN on a $O(100 \text{ m}^2)$ scale.
 2114 Importantly, long history of use of PEN-containing ESR in cryogenic or LAr detectors shows no
 2115 evidence of leaching, or any other type of mechanical or optical degradation.

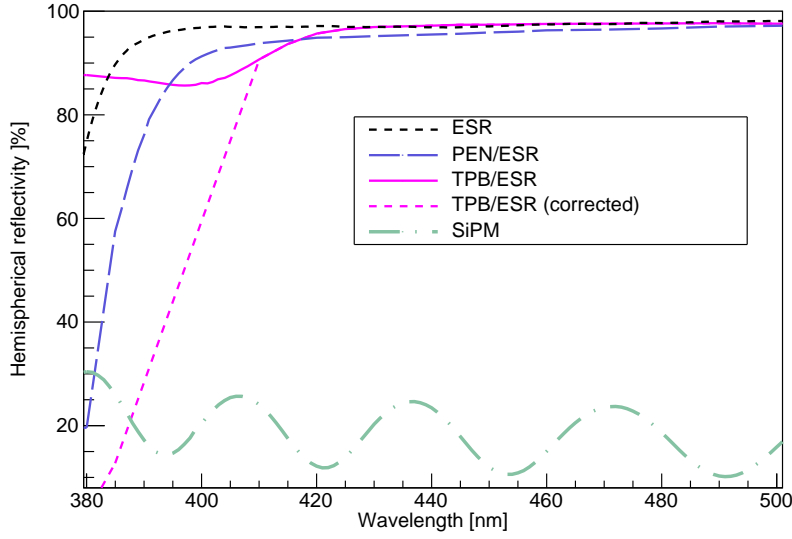


FIG. 42. Hemispherical reflectivity measured at 7° angle of incidence with a spectrophotometer equipped with an integrating sphere for: ESR, PEN air-coupled to ESR, TPB evaporated on ESR, TPB evaporated on ESR corrected for the spurious fluorescence component based on [52], and SiPMs (see legend).

2117 The main advantage of PEN is its scalability, ease of use and low cost. It appears that even
 2118 commercially produced off-the-shelf grades of PEN exhibit WLSE sufficient for use in the DS-20k
 2119 Veto (for more details on the Veto requirements, see Sec. 5.8.4). PEN is available in large format
 2120 rolls or sheets and can be easily used as a liner for even very large LAr tanks.

2121 The WLSE of PEN, relative to TPB, is a key parameter needed to evaluate the performance of
 2122 the veto. Significant R&D effort was invested into selecting the most promising PEN candidate
 2123 among the large number of available PEN grades, comparing their performance with TPB, and
 2124 verifying their suitability for the Veto detector with a full optical Geant4-based simulation. PEN
 2125 grades differ in crystallinity, as well as the amount and type of (proprietary) additives, which
 2126 affects the WLSE. Because WLSE is generally dependent on both the excitation wavelength and
 2127 the temperature it is critical to have such relative measurement performed in relevant conditions,
 2128 i.e. with 128 nm excitation and at 87 K. Since such measurements are very challenging, for initial
 2129 survey a large number of candidate grades and PEN-reflector laminates has been characterized
 2130 at near-UV using an integrating sphere at room temperature (University of Warsaw, Chemistry
 2131 Department), for chosen samples supplied then with a 128 nm excitation measurements at RT
 2132 (TUM). In general, samples performing better at near-UV did also exhibit higher emission also at
 2133 VUV, exceeding WLSE of 0.3 relative to TPB.

2134 The most promising candidate, Teonex Q51, was characterized in a vacuum monochromator
 2135 setup supplied with a cryostat at the Institute of Low Temperature and Structure Research of the
 2136 Polish Academy of Sciences, and, finally, with a direct comparison in LAr performed at LNGS. The
 2137 results of these point at WLSE of PEN relative to TPB of $47.2 \pm 5.7\%$ in the conditions of a LAr
 2138 detector, which exceeds results previously reported for other PEN grades [51].

2139 Because of limited photosensor coverage of surfaces in the Veto blue photons will bounce from
 2140 the walls on average 70 times prior to detection. Therefore, the final light yield will be proportional
 2141 to R^n , where n is the mean number of wall collisions. This makes R a key parameter for the
 2142 comparison of both options, in addition to WLSE. We have therefore characterized the reflectivity
 2143 of ESR as well as ESR with WLS, as shown in Fig. 42, which revealed that both WLS options had
 2144 comparable performance. Another conclusion from this study was a far worse reflectivity of PEN
 2145 laminated on ESR (later independently confirmed [51]). The 2PAC (2 Parallel Argon Cylinders)
 2146 setup, was designed and fabricated at AstroCeNT to test both WLS efficiency and reflectivity at
 2147 once, using separate TPB and PEN lined chambers in the same LAr bath. 2PAC with approx. 1%
 2148



FIG. 43. 2PAC setup consisting of two identical chambers, allowing for a simultaneous comparison of PEN/ESR and TPB/ESR performance with SiPM area coverage fraction comparable to that of the DarkSide-20k veto.

coverage fraction and 1 mm LAr gap between the PEN and ESR foils, measured a light yield of the PEN chamber relative to the TPB chamber of $39.4 \pm 0.4(\text{stat}) \pm 1.9(\text{syst})\%$ [53], giving a robust validation of the final achievable light yield in the Veto.

Based on the measurements so far, the most promising grade of PEN is 25 μm thick Teonex Q51, supplied by Teijin DuPont (in Europe represented by Inabata) in a range of widths and roll lengths (up to 2 km). The entire amount needed for the veto can be purchased as a single roll, leaving a generous amount of extra material for radiopurity assays. Cutting the film to the desired shape should happen in a cleanroom, although a Rn-reduced atmosphere is not necessary, as detailed below. The sheets will be bagged in batches until the installation time to prevent Rn daughters depositing on the surfaces, and stored in a dark environment. The AstroCeNT cleanroom (ISO 7) or LNGS is one of the possible locations available for this effort.

Currently, a cryogenic setup using poisoned gaseous Ar scintillation as the excitation is being developed at AstroCeNT with the goal of providing time-resolved measurements and to support rapid testing and quality control of multiple samples at the production stage.

While the commercially available grade is sufficient for the DS-20k Veto, further R&D is ongoing aimed at custom production of PEN with WLSE close to that of TPB; which would be a very compelling option for the next generation LAr detectors, including ARGO.

Simulation results: The Geant4-based optical simulation of the Veto using the measured reflectivity spectra from Fig. 42 and PEN WLSE extracted from the measurements with 2PAC predicts the light yield of 2000 PE/MeV for the DarkSide-20k Veto. The Monte Carlo results have been cross-checked against a simplified analytic model, described in [54]. Such light yield is sufficient for achieving the targeted performance (vetoing efficiency and introduced dead time) of the Veto.

Radiopurity assay results: The driving requirement on the veto WLS radiopurity is due to (α , n) neutrons; so both the primary chains and secondary contamination with Rn-222 during storage and installation have to be taken into account. The total mass of PEN to be used in the veto is 6 kg (assuming 25 micron thick grade), which based on the goal of having a contribution below 10^{-4} neutron interactions in the TPC after cuts in a 10 year exposure translates to the requirement of $< 17 \text{ mBq/kg}$ in U and Th subchains. The results of HPGe and HR-ICPMS assay of our sample of Teonex Q51 film are acceptable from the point of view of neutron backgrounds and with a generous safety margin.

The last concern is limiting the activity of out-of-equilibrium Po-210 from Rn-222 diffusion, implantation and surface deposition. Requiring for simplicity that the Po-210 background contribution not exceed that from the U-238 chain, we arrive at $< 90 \text{ mBq/kg}$ (total of 1.8 Bq) requirement for Po-210, which can also be translated to $152 \mu\text{Bq/m}^2$ (for $174 \text{ m}^2 \text{ m}^2$ of 25 μm film). The Rn

Sample	^{226}Ra [mBq/kg]	^{228}Th [mBq/kg]	^{40}K [mBq/kg]	^{228}Ra [mBq/kg]	^{235}U [mBq/kg]
Teonex Q51 (Inabata)	1.4(2)	<0.52	5(2)	<0.74	<0.41
Sample	U [ppt]	Th [ppt]	K [ppb]		
Teonex Q51 (Inabata)	88.6±26.4	75.3±22.5	1000±400		

TABLE XIII. Assay results of PEN samples for the DS-20k Veto with HPGe (top) and HR-ICPMS (bottom), both performed at LNGS.

2188 diffusion parameters of PEN are known [55], with the diffusion coefficient, D , $4.1 \times 10^{-4} \text{ m}^2\text{s}^{-1}$. Us-
 2189 ing the most conservative assumption that the roll of PEN is fully permeated by Rn, we arrive at
 2190 the exposure limit of 9 months. Using Rn activity of 10 Bq/m^3 , more typical for surface conditions
 2191 increases that time by an order of magnitude.

2192 It is desirable to limit exposure of PEN to high Rn activity air, however conservative estimates do
 2193 leave a reasonable time window for installation underground without additional extreme measures.
 2194 In addition to custom ordering a fresh batch, given the short diffusion length, as long as a large
 2195 roll is purchased (typically available in about 2 km long rolls), using the innermost layers should
 2196 guarantee negligible diffused in activity at the start, moreover edges of the roll can be trimmed off
 2197 (screening results will inform if this is necessary).

2198 Radon-borne contamination plated out on the surface from decays in the room atmosphere will
 2199 be prevented by covering/storing the PEN material in e.g. polyethylene bags except for the times
 2200 when it is handled.

2201 3.7.3. R&D results and conclusions

2202 While for TPC the standard ESR coated with TPB will be employed, the R&D described above
 2203 allowed us to achieve satisfactory light collection and radiopurity levels using PEN as wavelength
 2204 shifter in the Veto.

2205 3.8. Gd-loaded acrylic

2206 3.8.1. Goals of the R&D

2207 The goal of this activity is the development of a procedure to produce Poly(methyl methacrylate),
 2208 PMMA($C_5O_2H_8)_n$, loaded with a suitable gadolinium (Gd) compound. This hybrid material will
 2209 be used in the construction of the integrated structure that makes up the DS-20k TPC outer wall
 2210 and Veto inner wall. This material is employed to thermalize neutrons, via collisions with the
 2211 Hydrogen in PMMA, and then enhance the capture and detection probability thanks to the high
 2212 Gd neutron capture cross section and the subsequent emission of an easily-detectable high energy
 2213 γ ray cascade. Multiple γ s emitted from Gd reach energy up to 8 MeV [56, 57], while the capture
 2214 of neutrons on Hydrogen produces 2.2 MeV single γ s.

2215 PMMA has been selected as base material because it can be produced with an excellent degree
 2216 of radio-purity through a casting process, polymerizing its liquid monomer (methyl methacrylate,
 2217 MMA) [58]. The Juno Collaboration reported extremely clean acrylic, with $(3.58 \pm 0.62) \times 10^{-3}$
 2218 mBq/kg of ^{238}U and $(2.20 \pm 0.73) \times 10^{-3}$ mBq/kg of ^{232}Th [59].

2219 Table XIV summarizes the target specifications. The guideline for establishing the Gadolinium
 2220 concentration is to load the PMMA with Gadolinium such that the (n,γ) process on Gadolinium
 2221 dominates over the same process on Hydrogen, in order to ensure high efficiency in detecting the
 2222 (n,γ) event. Considering all the seven Gd isotopes, the thermal neutron capture on Gadolinium
 2223 σ_{Gd} is 4.9×10^4 barns, while the capture cross section on Hydrogen, σ_H , is 0.3326 barns. The

2224 thermal neutron capture cross section on Carbon, σ_C , is three orders of magnitude lower than σ_H ,
 2225 thus the Carbon contribution to thermal neutron capture is negligible. Given these cross sections,
 2226 for the probability of a thermal neutron to capture on Gd to be ~ 100 times greater than on H,
 2227 the Gd concentration in mass needed is $\sim 1\%$ with respect to the PMMA mass. A concentration
 2228 between 0.5% and 1% still ensures a large safety margin on the capture ratio, and this range of
 2229 concentration allows to tolerate a grade of non-uniformity in the Gd distribution up to 50%, i.e.
 2230 having a nominal concentration of 1% with a 50% non-uniformity means that everywhere there
 2231 is at least 0.5% of Gd, so in every point of the material the capture on Gadolinium is dominant.
 2232 Detailed Montecarlo simulations, developed considering the full detector design and capture gamma
 2233 detection efficiency, confirm this rough estimate (see Sec. 12.2.1 for details) and the possibility to
 2234 allow a 50% non-uniformity, without affecting the neutron rejection efficiency.

2235 The walls of the inner detector must be 15 cm thick once finished, therefore the rough slabs,
 2236 before mechanical processing, must have a thickness of about 17 cm. This presents a requirement for
 2237 developing the Gadolinium mixing procedure and subsequent polymerization, as the solidification
 2238 times, and consequently any non-uniformity in the distribution of Gd, depend on the thickness of
 2239 the final object.

2240 Approximately 20 t of material are needed before all the machining to form the integrated TPC
 2241 and veto structure, thus the procedure must be scalable to an industrial environment.

Parameter	Value
Gd concentration (weight)	$0.5\% < \text{Gd} < 1\%$
Gd homogeneity	$\simeq 50\%$
Transparency of the hybrid material	not necessary
Machinable	yes
Glass transition temperature	compatible with pure PMMA - 110 °C
Young module	compatible with pure PMMA - 3100 MPa
Resistant at 87 K	yes
Thickness	~ 17 cm
Maximum size	sheets of ~ 3.5 m \times 2 m
U,Th contamination	$<< 0.1$ n-induced bkg events in 200 t · yr
Amount needed*	about 20 tonnes

TABLE XIV. Target specification driving the R&D activity toward the development of the Gd loaded PMMA. (*) before the machining of the final pieces.

2242 3.8.2. Development of the material

2243 We have studied two possible Gadolinium compounds, taking into account the radio-purity and
 2244 the ease of the mixing in acrylic: Gadolinium oxide (Gd_2O_3) in the form of nano-grains or a
 2245 Gadolinium β -diketonate. The two solutions - with very different chemical characteristics - have
 2246 advantages and disadvantages that make them both interesting for our purpose.

2247 3.8.3. Gadolinium oxide nano-grains dispersion

2248 The first step of the R&D (developed by INFN Genoa) was to select radio-pure commercial
 2249 Gadolinium oxide. After screening several samples of material available on the market, we have
 2250 found that commercial Gd_2O_3 delivered by the Shin-Etsu company has the lowest radioactive
 2251 contaminants. The results of the HP-Ge detector screening, done on three different samples, are
 2252 reported in table XV.

Sample	^{238}U [mBq/kg]	^{232}Th [mBq/kg]	^{40}K [mBq/kg]
Shin-Etsu 1	13.6 ± 3.0	<27	< 37
Shin-Etsu 2	6.6 ± 1.8	<19	< 23
Shin-Etsu 3	2.68 ± 0.47	2.31 ± 0.68	< 13

TABLE XV. Assay results of pure Gd_2O_3 samples, performed by DS-20k collaborators with Germanium detector sensitive to the isotopes in the chains ^{238}U - ^{226}Ra and ^{232}Th - ^{228}Th .

Gadolinium oxide is not miscible with liquid MMA, so it is necessary to make a mechanical dispersion in order to mix them together. To obtain a uniform distribution of Gd we decided to use Gd_2O_3 in the form of nano-particles, with an average diameter of 30 nm.

Ultra pure acrylic is usually manufactured by casting the liquid monomer, MMA, mixed with initiators and possibly other additives into a form or mold, made from two sheets of glass. Then the polymerization can be performed in several ways: in a warm water bath, in an oven or in an autoclave, depending on the requirements of the final product. To mix the Gd_2O_3 we make a uniform colloidal dispersion of Gadolinium oxide nano-grains in the monomer, before the final polymerization occurs.

The strategy adopted to minimize the clustering of nano-grains and consequent deposition of the Gadolinium oxide on the bottom of the mold during the polymerization process is to treat the particle surfaces. The procedure developed consists of a first phase during which the nano-grains are treated with a commercial surfactant (Igepal-CO 520, CAS: 68412-54-4) in a non-aqueous solvent (2-butanone, CAS: 78-93-3). This is done through a molecular functionalization of the surface of the nano-particles, aimed at creating repulsive electrostatic forces and steric hindrance factors, which favor the stabilization of the dispersion in MMA. The second phase is the polymerization procedure, which has been optimized to produce samples up to 20 cm in thickness. The polymerization time depends not only on the type and quantity of initiators used, but also on the polymerization temperature and the thickness of the sample to be obtained. The curing time increases non-linearly with increasing plate thickness. This fact is a key point of the mixing procedure, because increasing the time that the monomer takes to solidify also increases the probability of forming aggregates of nano-particles and consequently a Gd_2O_3 deposit is more likely to form. This effect required fine tuning of the polymerization temperature, but also of the quantities of chemical initiators used. We developed a two-step radical polymerization, using two different initiators. During the first step the MMA- previously mixed with the suspension of treated nano-grains, surfactant and solvent - is heated up to the boiling point, in order to both start the pre-polymerization and let the solvent evaporate. During the second phase, the syrup obtained is inserted in a glass mold and the final polymerization is done in an oven for 24 hours.

After polymerization, the hybrid material is therefore a PMMA polymeric matrix with Gadolinium oxide nano-grains and surfactant. Consequently, after developing this procedure it became necessary to measure the radio-purity of the surfactant also. Germanium screening revealed a potassium contamination that needs to be reduced in order to limit the gamma background. Laboratory tests are underway to minimize the amount of surfactant required, currently the best result is 0.1% in mass with respect to the Gadolinium oxide. In parallel it is envisaged to carry out purification tests of the surfactant using a cation exchange resin.

At present the tests done at laboratory scale, both on mixing and polymerization, have given very good results. We obtained uniform samples with a concentration up to 2 % Gd by weight, reaching a thickness of 22 cm, as can be seen in Fig. 44. We have largely achieved both the requirements in terms of thickness of the samples and Gadolinium concentration, reaching even the double of what is necessary. Reproducibility tests have been performed and they show compatible results, so we can consider the procedure solid and reliable.

A quantitative characterization has been developed, in order to evaluate both the Gd_2O_3 uniformity and the quality of the final material from the mechanical point of view. Thus far we have measured the Gd_2O_3 concentration in ten different samples, of various thicknesses and with different Gd loading. We have measured the content of Gadolinium oxide in different portions of the

2299 same sample exploiting two different thermal treatments: thermo-gravimetric analysis (TGA) and
 2300 calcination. Due to the small mass of the samples used for TGA, of the order of 10 mg, and the
 2301 oxide concentrations to be measured, we consider calcination measurements to be more reliable.
 2302 Calcination refers to heating a solid chemical compound to high temperatures, generally for the
 2303 purpose of removing impurities or volatile substances and/or to incur thermal decomposition. In
 2304 our case we performed thermal cycles up to 600°C in order to remove all the organic fraction of the
 2305 sample and then measure the inorganic residual, that corresponds to the Gd_2O_3 .

Sample	Section	Section weight	Residual weight	Gd_2O_3 percentage
1% _w Gd_2O_3 4 cm height	bottom	7.1594 g	0.0683 g	1.11%
	middle	7.1988 g	0.0492 g	0.91%
	top	7.5977 g	0.0764 g	1.50%
1% _w Gd_2O_3 7 cm height	bottom	9.3122 g	0.0910 g	1.15%
	middle 1	7.2555 g	0.0648 g	1.01%
	middle 2	7.2828 g	0.0593 g	1.00%
	top	7.4754 g	0.0739 g	1.07%
2.3% _w * Gd_2O_3 12 cm height	bottom	5.1411 g	0.1265 g	2.66%
	middle 1	7.3345 g	0.1815 g	2.77%
	middle 2	7.0346 g	0.1578 g	2.60%
	middle 3	5.7850 g	0.1411 g	2.27%
	top	5.5834 g	0.1310 g	2.61%

TABLE XVI. Results of calcinations performed on three samples of different dimensions and with different Gd_2O_3 concentrations. *2.3% of Gd_2O_3 corresponds to 2% of Gd, considering the molecular mass.

2306 For all the samples screened so far the Gd_2O_3 distribution was very uniform along the entire
 2307 height, Table XVI reports the results for three samples. The residual is almost always higher than
 2308 the initial concentration in weight, but this is expected because during the polymerization process
 2309 some of the MMA evaporates. This is due to the fact that in the laboratory we do not have the
 2310 possibility to perform polymerization in sealed molds, but it will not be an issue using professional
 2311 casting molds. In conclusion we consider the homogeneity requirement fully met.

2312 Concerning the mechanical properties of the hybrid material, we performed differential scanning
 2313 calorimetry (DSC) to check the glass transition temperature. The data show that the Gd-loaded
 2314 sample has a glass transition temperature compatible with the one of pure PMMA, this meaning the
 2315 hybrid polymer should behave as the pure one. We are also performing stress-strain measurements
 2316 and testing the rheological properties of several samples. Finally, some of the samples have been
 2317 annealed in order to remove eventual mechanical tensions and cooled to 77 K. The cooling in liquid
 2318 nitrogen did not affect the status of the samples, as expected. We have also measured the Young's
 2319 module after four thermal cycles in liquid nitrogen, the results obtained are compatible with the
 2320 one measured prior to thermal cycling. We can conclude that our hybrid material meets also the
 2321 requirement of being resistant at 87 K.

2322 The next step is to integrate the described procedure in an industrial line suitable for the full
 2323 production of the plates for the detector. In view of this step, a special safety data sheet for the
 2324 hybrid material developed by the company MSDS Europe was compiled and certified. In conclusion
 2325 it should be noted that gadolinium oxide is a stable and well known compound, available in large
 2326 quantities with good radiopurity and at a cost of 490 USD/kg.

3.8.4. Gadolinium β -diketonate solution

2328 An alternative approach is based on the formation of a real solution of a Gd-based compound
 2329 in MMA. In particular, it may be a dissolution of a complex compound from the Gadolinium
 2330 β -diketonates: the two possible compounds under consideration are Gadolinium acetylacetone



FIG. 44. PMMA cylinder loaded with Gd₂O₃ nano-grains. The sample has a 2 % Gadolinium concentration.

2331 Gd(C₅H₇O₂)₃ and Gadolinium tetramethylheptanedionate Gd(C₃₃H₅₇O₆). In both cases the com-
2332 plex would be added in the initial MMA monomer, followed by the polymerization step.

2333 Commercial Gadolinium acetylacetone (Gd(acac)₃) is expensive (order of 10 keuro/kg), so
2334 our strategy is to directly synthesize the compound. The production is articulated and quite
2335 delicate and consists of several different steps under development by the IHEP group. The main
2336 phases would be to obtain gadolinium chloride (GdCl₃) from commercial gadolinium oxide (Gd₂O₃),
2337 then purify the GdCl₃, synthesize Gd(acac)₃ and finally perform a second purification. The two
2338 purification phases, done at laboratory scale by the Russian group, obtained a radioactivity level of
2339 2.3 mBq/kg for U and 3.3 mBq/kg for Th. The polymerization procedure was done using standard
2340 chemical initiators. The final samples, shown in Fig. 45, have a Gd concentration of 2 % and 0.5 %
2341 respectively. Their radio-purity level is 0.22 mBq/kg for U and 0.10 mBq/kg for Th. To analyze
2342 chemical purity of Gd-based preparations it was used inductively coupled plasma mass spectrometry
2343 with preliminary transfer of the solid sample to the liquid phase. Gd-concentration distribution
2344 inside Gd-doped hybrid material was measured by a scanning electron microscope equipped with an
2345 energy-dispersive unit. The mechanical characterizations of these samples were carried out using an
2346 Instron 5882 testing machine at room temperature and at 77K, the results obtained are acceptable
2347 at both temperatures.

2348 3.8.5. *Gd-loaded acrylic towards the final production*

2349 The DS-20k detector requires around 20 tonnes of gadolinium-doped acrylic before machining of
2350 the final pieces. Considering as a baseline 1% Gadolinium mass fraction and taking into account
2351 the Gadolinium oxide molecular mass, this leads to about 230 kg of gadolinium oxide needed. We
2352 started a collaboration with the Chinese prime producer (DonChamp Acrylic Group) of ultra-high
2353 purity PMMA that is producing all the acrylic for the Juno collaboration. A production test of 1
2354 m² sample, 5 cm thick done simply mixing Gd₂O₃ (without any treatment) and liquid MMA using
2355 one standard industrial line of this company has been performed, demonstrating the feasibility of
2356 the collaboration with the industrial partner in performing a non standard industrial procedure.
2357 Figure 46 shows the first test sample of the gadolinium-doped acrylic from DonChamp Acrylic



FIG. 45. 5 cm thick PMMA samples loaded with Gd(acac): on the left the Gd concentration is 2 %, on the right it is 0.5 %.

2358 Group.

2359 The developed pre-treatment of Gd_2O_3 nano-grains for the full scale production could be either
 2360 performed at the company site or elsewhere. In this last case, the company would receive the
 2361 functionalized nano-grains, ready to be incorporated in MMA. We are currently evaluating with
 2362 the company all the details in order to make the mixing procedure scalable to large quantities
 2363 and compatible with their industrial production procedures. An administrative issue in testing the
 2364 complete Gd_2O_3 mixing procedure with DonChamp is that the company currently does not have
 2365 the authorization to use non-polar solvents needed for the nano-grains surface treatment. We are
 2366 interacting to solve this, and in parallel are performing a test with the company Europrod s.r.l.
 2367 (Italy). We have screened with ICP-MS a sample of MMA prior to the test and obtained upper
 2368 limits of 0.12 mBq/kg for U and $4.06 \times 10^{-2} \text{ mBq/kg}$ for Th. We have sent the functionalized
 2369 nano-grains in order to produce 15 kg of Gd-doped PMMA. The company will both test the two-
 2370 step polymerization procedure developed during the R&D phase and use the treated nano-grains
 2371 to perform their standard polymerization procedure.

2372 In case we will not be able to achieve the uniformity needed, we continue to develop the
 2373 β -diketonate method, in which about 2 tonnes of gadolinium β -diketonate are required for 1 %
 2374 gadolinium mass fraction. The candidate institute is presently optimizing the recipe of gadolinium
 2375 β -diketonate mass production, to increase the chemical stability of the organic compounds, since
 2376 the stability of gadolinium β -diketonate could affect its solubility in liquid MMA. Solubility tests,
 2377 as well as radioactivity assays, will be implemented in the process of development.

2378

3.8.6. R&D results and conclusions

2379 We have successfully demonstrated two possible approaches to produce PMMA loaded with
 2380 gadolinium, both matching the radiopurity levels required. Collaboration with an industrial partner
 2381 (DonChamp Acrylic Group) available for the full scale production has been established. This
 2382 company has developed ultra-clean production infrastructures in the context of the furniture of
 2383 the acrylic vessel of the Juno experiment, and has produced 5 cm thick slabs of Gd-loaded PMMA
 2384 for us, demonstrating the feasibility of industrial scale production. We continue developments to
 2385 improve the uniformity of the Gd loading in the industrial process in thicknesses up to 17 cm.



FIG. 46. The gadolinium-doped acrylic sample from Donchamp Acrylic Group

2386 The final recipe will be based on the ease of production and outcome of the process optimization
 2387 for the uniformity. The baseline is the method demonstrated at industrial scale at DonChamp,
 2388 using Gd_2O_3 , which is commercially available at reasonable costs however requires the treatment
 2389 described above before mixing to achieve uniform loading. To mitigate this risk, we carry forward
 2390 the development of a promising alternative, a β -diketonate compound method, which is easy to
 2391 mix with MMA, but requires establishment of a semi-custom production line, as it is not available
 2392 on the market with accessible costs. The procedure for getting the MSDS of the Gd_2O_3 loaded
 2393 PMMA has been concluded and the documentation is available.

2394

3.9. Calibration system mock-up

2395

3.9.1. Goals of the R&D

2396

The calibration system is described in section 7.4. The main concern is its operation at liquid
 2397 argon temperature and the risks associated with ice formation; the system has to guarantee the
 2398 safe inclusion and extraction of the radioactive sources and their smooth movement inside the
 2399 calibration pipes. In order to study the critical aspects of the system, a cryogenic mock-up has
 2400 been built.

2401

3.9.2. Mock-up construction

2402

A mock-up has been built at CPPM (Marseille-France). It consists of a stainless steel tank (1800
 2403 x 90 x 10 mm³) insulated with polystyrene, and a 3 m long 30 mm diameter and 1.5 mm thickness
 2404 stainless steel pipe. The pipe is shaped as a U and has two vertical sections of 600 mm, two curved
 2405 sections with a radius of curvature of 400 mm (as foreseen for the experiment) and an horizontal
 2406 section of 600 mm (see Figure 47). The pipe is equipped with temperature and strain sensors which
 2407 are read out via National Instruments modules. A humidity sensor is also present. Figure 47 shows

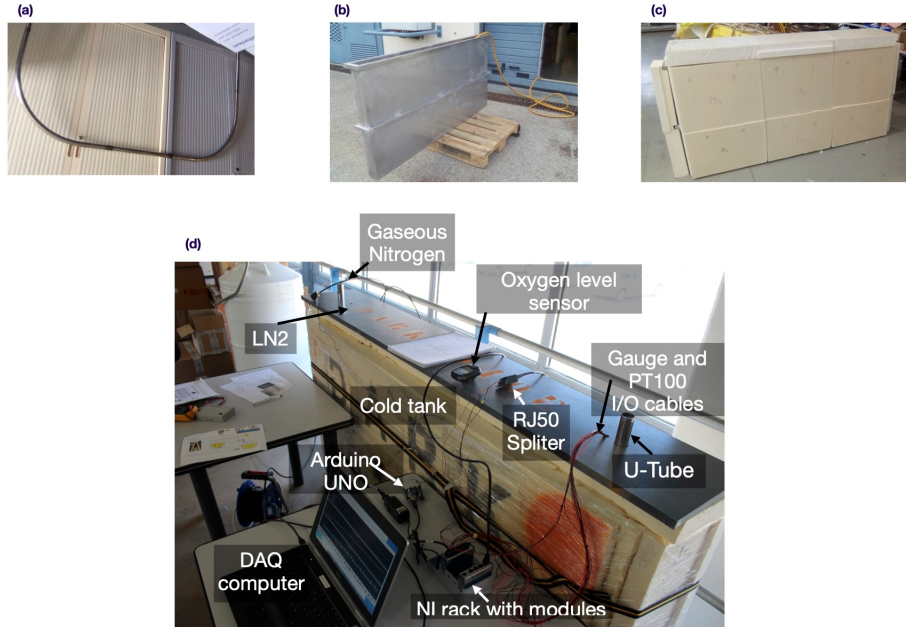


FIG. 47. Elements of calibration system mock-up. (a) Stainless steel pipe (3 m long). (b) Stainless steel tank; (c) Insulated tank; (d) The mock-up system: tank, pipe and instrumentation.

2408 a picture of the mock-up system during data taking. A first test with liquid nitrogen took place
 2409 in July 2021, with the aim to check all the procedures involving LN2 and measuring temperature,
 2410 deformation and humidity. Nitrogen gas was flushed inside the pipe only for a fraction of the time.

2411 3.9.3. *R&D results and conclusions*

2412 A visual inspection at the end of test, accomplished by introducing a small camera in the pipe,
 2413 revealed the probable presence of small ice blocks. For the next sets of tests, the pipe will be flushed
 2414 and kept under nitrogen gas. The next step for the mock-up is to equip each extremity of the pipes
 2415 with a motor box composed of pulleys, load cells and a motor and operate a rope between the two
 2416 sides. The motor systems have been designed and built at Queen's University and are based on
 2417 the one operated for SNO+. A new pipe made of titanium, will be built.

2418 **3.10. UAr cryogenic system component testing at CERN**

2419 3.10.1. *Goals of the R&D*

2420 The goal of this work is to validate the novel cryogenic system design, and validate it under
 2421 operation. Briefly, the UAr cryogenic system uses a closed argon loop which comes into thermal
 2422 contact with liquid nitrogen via a sophisticated heat-exchanging network. The parameters that
 2423 require experimental verification include the cooling power, pressure stability, and the nitrogen
 2424 consumption.

2425 3.10.2. *Construction of the UAr system at CERN*

2426 A full-size prototype LAr condenser, the core component of the UAr cryogenic system, has been
 2427 already built and tested at UCLA, and a cooling power of 2.2 kW (latent heat only) was verified.

2428 This is nearly twice that needed for the DS-20k. The DS-20k UAr cryogenic system condenser
2429 box design was finalized, approved, and the welding of the large pneumatic cryogenic valves and
2430 auxiliary components was completed during the summer of 2019, see Fig. 48. During 2020 and the
2431 beginning of 2021, the cryostat, cryogenic transfer lines, and all of the electrical components were
2432 installed (Fig. 49) and approved for operation by CERN. In addition, a commercial compressor
2433 was procured and tested at CERN. The Celeroton² pump is a turbo centrifuge pump with digital
2434 control of the rotor speed and, hence, the flow rate. The rotor is suspended with gas bearing and
2435 requires no lubricant, no service and maintenance free. It was also integrated, and the first full
2436 system tests were performed in July 2021.

2437 In addition to the Celeroton pump, another design has been fabricated based on the successful
2438 demonstration of the gas circulation pump in DS-50, providing a speed up to 50 std L/min. This
2439 pump design relies on two main components: 1) Linear motors and 2) Reed valves. The linear
2440 motors, consisting of a piston and pair of cylinders, provide adjustable pumping power. The reed
2441 valves act as guides for the flow of gas as the linear motors cycle. Two linear motors are placed
2442 face-to-face such that they operate out of phase and keep vibrations minimal. This combination
2443 of linear motors and reed valve allows the pump to operate with no contacting surfaces, which
2444 results in a long lifetime. A full-size prototype circulation pump was fabricated at UCLA and
2445 Princeton, and passed initial tests. It was shipped to CERN and is awaiting EU safety requirement
2446 certification.

2447 3.10.3. R&D results and conclusions

2448 Fig. 50 shows the first (preliminary) data from the DS-20k UAr cryogenic system. Three nights
2449 of data are shown from left to right with gas pressure, mass flow, and temperature displayed
2450 respectively from top to bottom. Data for nitrogen (solid blue lines) and argon (solid red lines)
2451 are shown in all panels. The gas pressure of the argon is taken from the cryostat volume, i.e. the
2452 gas pocket. The temperatures are taken from the ‘warmest’ points on the outgoing lines, meaning
2453 that these temperatures can be used to determine the heat exchanging efficiency of the system.
2454 There are three notable points: 1) The stability of the argon gas pressure within the cryostat. 2)
2455 The minor change in LN₂ consumption following a significant change in the argon loop flow, which
2456 signals a highly efficient system. 3) The clear outgoing temperature response to the change in argon
2457 flow, which shows that system is removing more heat in both lines in response to the added heat
2458 from the increased argon flow. This, again, highlights the efficiency of the system.

² Celeroton web site: <https://www.celeroton.com/en/products/compressors.html>

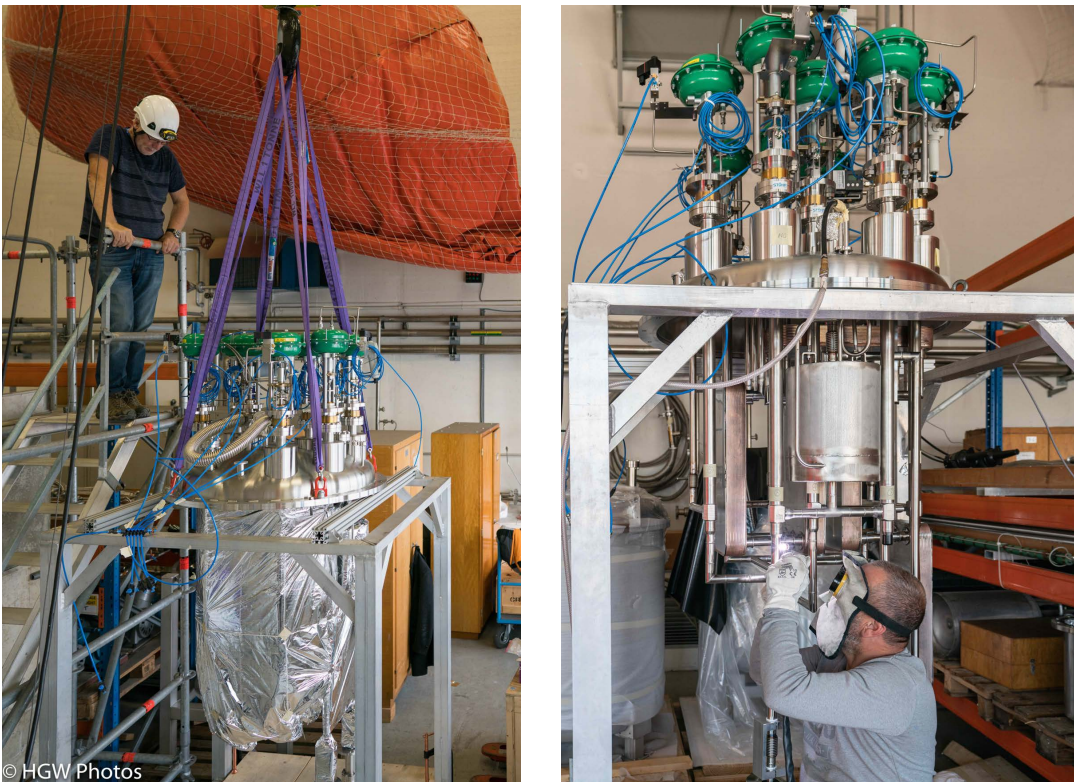


FIG. 48. DS-20k UAr cryogenic system component fabrication and installation at CERN for testing.

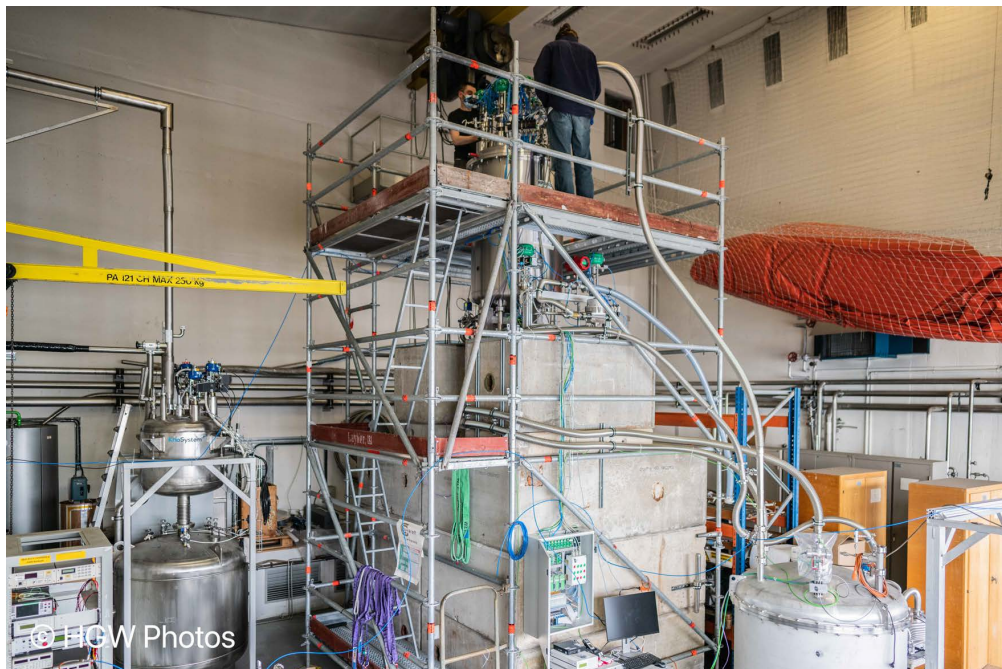


FIG. 49. DS-20k UAr cryogenic system testbed being prepared for operation at CERN.

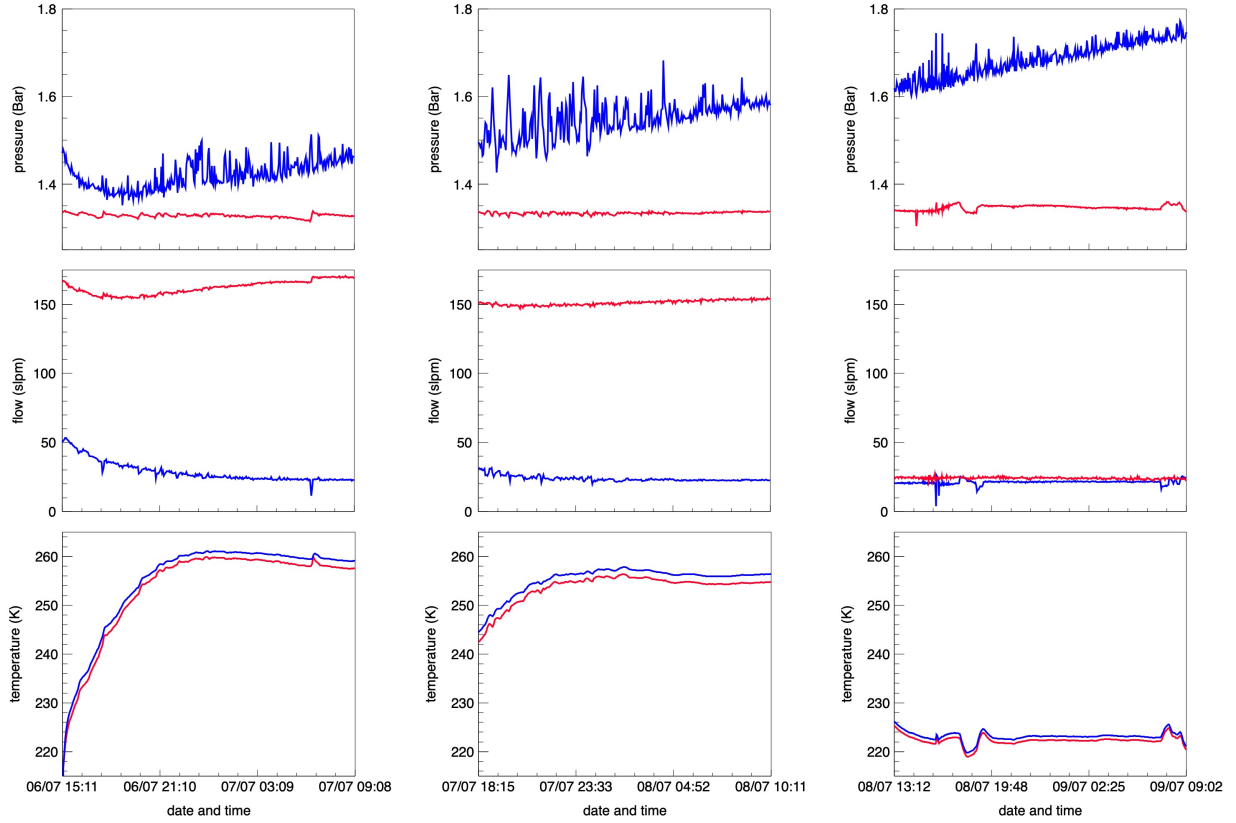


FIG. 50. Preliminary data from the DS-20k UAr cryogenic system testbed at CERN taken in July 2021. From left to right shows three nights of data. Respectively, from top to bottom shows the gas pressure, mass flow, and outgoing (warm) temperature for the nitrogen (solid blue lines) and argon (solid red lines) loops.

2459 4. PREDECESSOR EXPERIMENTS RELEVANT FOR THE DS-20K DESIGN

2460 The Global Argon Dark Matter Collaboration (GADMC) draws scientists from all of the major
 2461 groups currently using LAr to search for dark matter, including ArDM, DS-50, DEAP-3600, and
 2462 MiniCLEAN, with the objective of designing and constructing the DS-20k two-phase LAr detector.
 2463 The key experiences with DS-50 and DEAP-3600 experiments that lead to the current DS-20k
 2464 design are described in this section, as well as the results from the characterization of a very first
 2465 miniature detector built and operated by members of the collaboration, the ReD experiment TPC,
 2466 that employs some of the key features of the DS-20k design.

2467 In particular DS-50 demonstrated the feasibility of background free operation with a LAr TPC
 2468 and the more than 1000-fold reduction in the rate of ^{39}Ar in underground argon from CO₂ wells
 2469 in Colorado. A series of ancillary experiments, SCENE and ARIS, provided a body of crucial
 2470 measurements that form the basis for our LAr response modeling. The DEAP-3600 experiment
 2471 demonstrated the feasibility of constructing large, extremely radio-pure PMMA vessels, a key capa-
 2472 bility for the realisation of the DS-20k design, and reached world best ER background rejection
 2473 using pulse shape discrimination. The ReD experiment characterized the light and charge response
 2474 of a LAr TPC to neutron-induced nuclear recoils, using the tiled SiPM array photon detector
 2475 technology developed for DS-20k.

2476 4.1. The DarkSide-50 experiment

2477 The DS-50 experiment conducted a direct search for WIMPs using a two-phase LAr TPC with
 2478 an active mass of (46.4 ± 0.7) kg of LAr. The LAr TPC is surrounded by a 4.0 m-diameter borated-
 2479 liquid-scintillator neutron veto (LSV), which is in turn surrounded by a 1-kton water Cherenkov
 2480 muon veto (WCV). The experiment ran at LNGS from 2013 until 2020.

2481 In 2015, WIMP search results from the first physics run were published, from an exposure of
 2482 47.1 live-days using AAr as the active target material [6]. In April 2015, a second physics run
 2483 begun, using a fill of UAr. The first goal of the second run was to determine the activity of the
 2484 UAr, as only upper limits on which were possible with smaller, higher-background detectors. We
 2485 found that the level of ^{39}Ar in the UAr was a factor of 1400 ± 200 lower than that in AAr. The
 2486 initial WIMP search with UAr using 70.9 live-days of data [9] was published in 2016.

2487 Following the analysis of the 70.9 live-days data set, DS-50 collected an additional 532.4 live-days
 2488 of blinded UAr data. Before un-blinding the high-mass WIMP region of interest, an exhaustive
 2489 simulation and analysis campaign was completed to make reliable predictions of all backgrounds
 2490 and to design analysis cuts that reduced the total predicted background below <0.1 events in the
 2491 full exposure. The outcome of this high-mass WIMP dark matter search is a null result (see Fig. 51),
 2492 delivering on the promise of zero-background and producing the best limit with an argon target at
 2493 the time of publication [3] (later improved by DEAP-3600 [5]).

2494 The extremely low background, and the ability to trigger on the S2 signal from a single electron,
 2495 allowed us to extend the analysis threshold to 100 eV_{ee} (600 eV_{nr}). Two dark matter searches were
 2496 performed using this technique. The first, an S2-only nuclear-recoil dark matter search, published
 2497 [17], it presently remains the world's most sensitive limit in the mass range from $1.8\text{ GeV}/c^2$ to
 2498 $3.5\text{ GeV}/c^2$. The second search used the S2 signal to constrain the rate of dark matter scattering
 2499 on electrons [18].

2500 Critical for the blind analysis of 532.4 live-days of UAr data was the completion of several calibra-
 2501 tion campaigns, performed either by injecting sources directly into the LAr via the cryogenics and
 2502 gas handling system or by positioning sources against the LAr TPC cryostat with a deployment
 2503 device reaching through the water tank and neutron veto [14]. These calibration campaigns have
 2504 also enabled a rich set of detector-performance analyses. For instance, an americium-beryllium
 2505 neutron source was deployed for several campaigns. $^{241}\text{AmBe}$ neutrons gave us our first direct look
 2506 at WIMP-like NRs in the LAr TPC and neutron capture signals in the neutron veto. Figure 51
 2507 (right) shows the f_{90} response of the LAr TPC to NRs and ERs induced by neutrons and γ -rays,

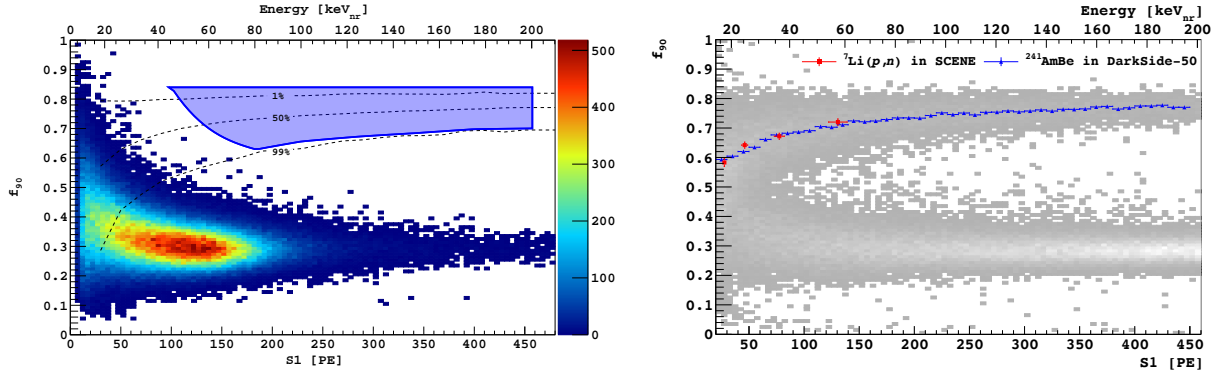


FIG. 51. **Left:** Results from a run of DarkSide-50 with a UAr fill for a 532.4 live-days livetime. The plot shows the distribution of events in the main pulse shape discriminant, f_{90} (the fraction of the primary scintillation pulse in its first 90 ns) vs. the total integral of the primary scintillation pulse, S_1 (measured in photoelectrons, PE), after application of the standard analysis cuts that maximize the DS-50 sensitivity. The dashed lines identify the lower boundaries of nuclear-recoil signal regions having the indicated acceptances. The shaded blue region above the blue line is the WIMP search box. The NR energy scale relevant for WIMP scattering is shown across the top axis. **Right:** f_{90} vs. S_1 distribution for NRs (WIMP-like) and ERs (background) from $^{241}\text{AmBe}$ calibration data. The scatter of events between the bands is due to $n+\gamma$ mixed events from the source. Our measurements of the median of the NR band are compared to those from SCENE, which cover only the low energy range. In both plots, the NR energy scale relevant for WIMP scattering is shown on the top axis.

2508 respectively, from the $^{241}\text{AmBe}$ source. It also shows the median f_{90} response of NRs as extrapolated
 2509 from our independent calibration experiment, SCENE [60], and that the two measurements
 2510 are in good agreement with each other.

2511 External calibration campaigns have provided data critical to the optimization of the DS-50
 2512 detector and the extraction of its scientific results. The two major calibration efforts that have
 2513 been completed are:

- 2514 • **SCENE:** The first measurement of the low-energy light (10.3 keV_{nr} to 57.3 keV_{nr}) and charge
 2515 (16.9 keV_{nr} to 57.3 keV_{nr}) yields for NRs as a function of drift field was performed in the SCENE
 2516 experiment [60, 61], led by members of the DarkSide-50 collaboration. The choice of a standard
 2517 drift field value of 200 V/cm for DS-50 was based on the SCENE results and motivated by the
 2518 need to minimize the loss of scintillation light for NRs at higher drift fields. The NR energy
 2519 scale and NR acceptance curves used in the DS-50 science papers [6, 9] were also determined
 2520 using the SCENE data. Finally, the SCENE experiment hinted at a directional signature in the
 2521 scintillation response of 57.3 keV_{nr} NRs, which has recently been further investigated with the
 2522 ReD experiment (Sec. 4.3)
- 2523 • **ARIS:** The ARIS experiment also provided light yield measurements for NRs as a function of the
 2524 drift field and did so with much higher precision and spanning a larger energy range (7.1 keV_{nr} to
 2525 117.8 keV_{nr}) than SCENE. Additional ARIS results include measurements of the recombination
 2526 probability of electron-ion pairs as a function of energy and applied electric field for both ERs
 2527 and NRs and the confirmation of the light yield linearity of the LAr ER response. These results
 2528 are important in the construction and calibration of models that predict the behavior of LAr
 2529 to recoiling electrons and nuclei. The Precision Argon Response Ionization and Scintillation
 2530 (PARIS) model has been developed to describe the LAr response inside the DarkSide LAr TPC
 2531 detectors [13]. We plan to use ARIS data in combination with further data from ReD or other
 2532 future calibration campaign to further improve the PARIS model, a crucial tool for predicting
 2533 the sensitivity of future large LAr detectors in the search for dark matter.

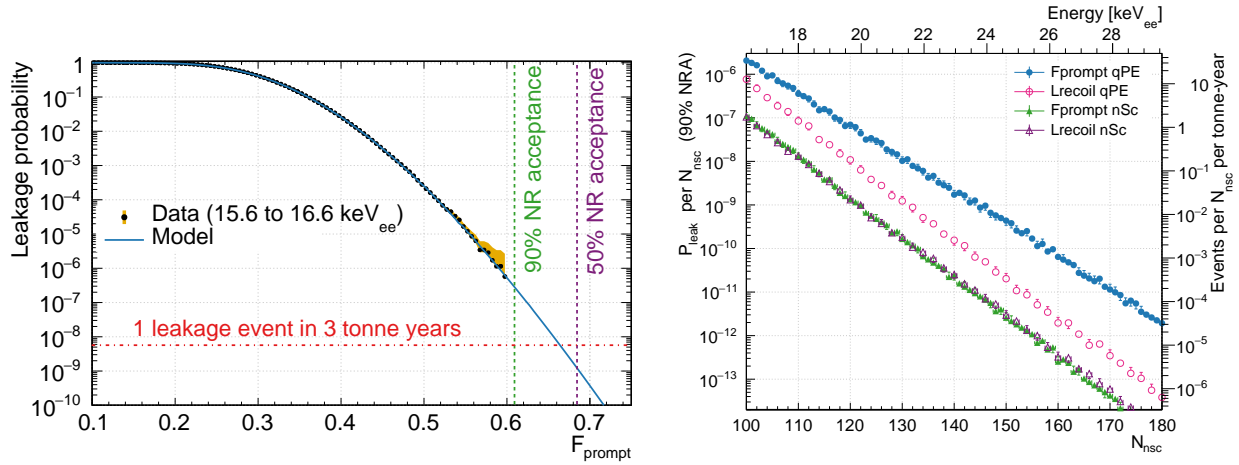


FIG. 52. **Left:** Probability of an ER being detected above a given PSD parameter value in the lowest 1 keVee bin in the WIMP-search region of interest in DEAP-3600 [5]. For comparison, vertical lines show the values above which 90% or 50% of nuclear recoils are expected to be found. **Right:** The leakage probability as a function of the number of the observed scintillation photo-electrons (N_{nsc}) at 90% nuclear recoil acceptance [64].

2535

4.2. The DEAP-3600 experiment

2536 The DEAP-3600 experiment conducted a direct search for WIMPs using a single phase detector
 2537 with an active mass of 3279 kg of LAr. The LAr is surrounded by a water Cherenkov muon veto.
 2538 The experiment has been taking data at SNOLAB since 2016, and continues to run.

2539 The LAr in DEAP-3600 is held within a PMMA vessel, and thus the DEAP-3600 collaboration
 2540 has developed extensive experience in constructing large, radio-pure PMMA vessels [4, 58, 62]. This
 2541 technology will be used to assemble the large cathode and anode optical aperture and build the
 2542 vessel for the DS-20k LAr TPC. The PMMA vessel will also reduce the complexity of the TPC
 2543 assembly. The requirements on superficial contamination of the inner surface in contact with the
 2544 active LAr volume are being developed also on the basis of the experience gained in achieving the
 2545 excellent value of $200 \mu\text{Bq}/\text{m}^2$ registered for the inner surface of the DEAP-3600 PMMA vessel.

2546 With the largest AAr dark matter target operated to date, DEAP-3600 has integrated unpreced-
 2547 ented statistics to quantify the power of particle identification in LAr. LAr is a particularly
 2548 favorable target for the detection of WIMPs thanks to its excellent event discrimination capa-
 2549 bilities. Scintillation light initiated by particles recoiling from atomic electrons (ERs), the most
 2550 numerous potential source of background in a WIMP direct detection experiment, is dominated by
 2551 a component with a time constant of 1445 ns[63]. This is in stark contrast to the nanosecond-scale
 2552 time constant of scintillation light that dominates the emission initiated by recoiling nuclei (NRs),
 2553 as expected in a WIMP-Ar scattering interaction. The DEAP-3600 experiment has exploited this
 2554 effect via pulse shape discrimination (PSD) to achieve ER background rejection of 2.4×10^8 [4, 5]
 2555 whilst retaining 90% efficiency for NRs. This world-leading particle identification result, in any
 2556 dark matter detector, underpins DEAP-3600's WIMP search result, the best in a LAr target at
 2557 high mass. Detailed investigation of different PSD algorithms performance in DEAP-3600 has been
 2558 recently published [64]. Figure 52 shows the leakage probability at the lower energy boundary of the
 2559 region of interest for the DEAP-3600 WIMP search [5] and its dependence on the recoil energy [64].

2560

4.3. The ReD experiment

2561 The ReD project aims to characterize the light and charge response of a LAr TPC to neutron-
 2562 induced nuclear recoils, especially at low energy, and to explore for the possible directional de-

pendence suggested by the SCENE experiment [60, 61]. Since the ReD TPC uses many of the innovative features of the DS-20k design, in particular the readout based on SiPMs and the cryogenic electronics, the outcome of the characterization campaign is an important underpinning series of measurements for DS-20k.

The first phase of ReD, tailored to the directional dependence, consisted in the irradiation of a miniaturized LAr TPC with a neutron beam at the INFN, Laboratori Nazionali del Sud (LNS), Catania. The measurement was performed in February 2020 with 70 keV Ar recoils only. The preliminary results are compatible with the absence of a directional sensitivity of the LAr TPC detector at this energy [65].

Prior to the deployment on the beam line at LNS, the ReD TPC underwent a detailed characterization campaign with laser, external γ -sources, an internal ^{83m}Kr source which generates a uniform distribution of mono-energetic events and neutrons, in order to characterize the detector performance and stability over several months. A detailed report of the results is given in [66].

The second phase of the ReD scientific program, which is characterizing the response of a LAr TPC to few-keV nuclear recoils, is in progress and data taking is foreseen in early 2022. Neutrons for this measurement will be produced by a ^{252}Cf fission source.

The core detector of ReD is a custom-made TPC with similarities to the LAr TPC of DS-20k. The TPC is a cube with size of about 50 mm. An acrylic vessel defines the active volume. The top and bottom acrylic windows are coated with a conductive layer of ITO (indium-tin oxide), to allow for the application of the electric field, and the side ESR-acrylic sandwich reflection panels to maximize the reflectivity of the chamber. All of the internal surfaces are coated with TPB to wavelength shift the argon scintillation light. The drift field is kept uniform along the drift coordinate by means of the field shaping rings, deposited by thin-coating the walls of the acrylic vessel with ITO. The drift length, extraction length and electroluminescence length of the ReD TPC are 5 cm, 3 mm, and 7 mm, respectively. We used $50 \times 50 \text{ mm}^2$ tiles produced by FBK during the R&D phase for DS-20k photo-sensors, each made by 24 rectangular SiPMs. The tile on the top of the LAr TPC has a custom-made 24-channel readout, in order to improve the $x - y$ sensitivity, necessary at the small scale of ReD while the bottom tile has a standard DS-20k4-channel readout.

The Single Electron Response (SER) of the SiPMs was studied in regular calibration runs taken with a pulsed diode laser at 403 nm. Figure 53 (left panel) displays a typical charge distribution obtained for a bottom SiPM in a laser run, already calibrated in photoelectrons. The standard deviation σ_1 of the single-photon peak is 0.16 (0.20) PE for the charge distribution of bottom (top) channels³. Due to the effect of the afterpulsing and cross-talk, the probability to detect N photoelectrons does not follow the Poisson distribution, but it is instead described by the Vinogradov model [67]. If p is the probability for a primary photon to trigger a secondary emission in the SiPM, one can define the coefficient of duplication $K_{dup} = \frac{p}{1-p}$, so that $(1+K_{dup})$ represents the total number of photoelectrons detected for each primary photon incident on the SiPM. Typical values of K_{dup} obtained for the individual channels range between 0.31 and 0.37. The relative fluctuation of the SER values, calculated from all 42 laser calibrations taken during 165 d of uninterrupted operation, was 0.7% (1.0%) rms for bottom (top) channels. Variations of the SER between consecutive laser calibrations were well below 2% for all channels. The relative fluctuations on K_{dup} over time was 3.0% (3.6%) rms for bottom (top) channels and it is of the same order of magnitude as the typical statistical uncertainties of the individual fits.

The (S1) scintillation yield at null field, measured with 59.5 keV γ -rays from ^{241}Am is (9.80 ± 0.13) PE/keV. The corresponding energy resolution σ/μ achieved with charge integration is 6.4%; it can be improved to 5.4% by using dedicated algorithms for digital filtering of the waveforms. The time stability of the S1 response of the ReD TPC was verified using four ^{241}Am calibrations taken in equivalent conditions throughout the operational period. The position of the full-energy ^{241}Am peak was found to be stable to within 2%.

Regarding stability, an electron lifetime larger than $> 1 \text{ ms}$, i.e. much longer than the maximum drift time in the TPC (about 60 μs at 200 V/cm drift field), was achieved within two weeks from

³ A significantly better resolution ($\sigma_1 = 0.06 - 0.08$ PE) can be achieved by using more refined and CPU-intensive digital filtering techniques.

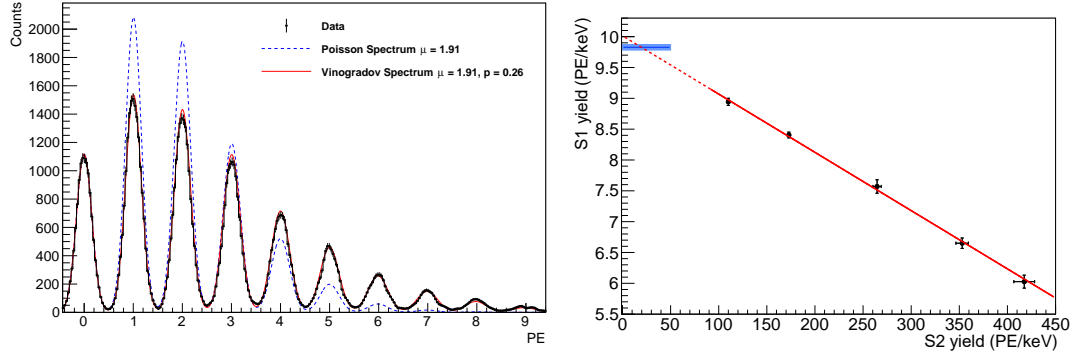


FIG. 53. **Left:** A typical charge distribution, in number of photoelectrons, for a bottom channel of ReD (black histogram), superimposed with a pure Poisson distribution with mean $\mu = 1.91$ (blue dashed line) and a Vinogradov distribution [67] with $\mu = 1.91$ and $p = 0.26$ (red solid line). **Right:** S1 vs. S2 yields for ^{241}Am calibration runs taken in double-phase mode from 75 V/cm to 1000 V/cm [66]. The red line is the best linear fit according to the procedure of [60]. The horizontal blue band shows the S1 yield measured at null field ($9.80 \pm 0.05_{\text{stat}}$) PE/keV, where the measurement of the S2 yield is not possible due to the absence of a drift field.

2615 the initial cool-down and re-circulation; it showed no hints of degradation in time throughout the
2616 rest of the operational time.

2617 The TPC was also irradiated with 2.4-MeV neutrons produced by a deuterium-deuterium generator.
2618 The dispersion σ/μ in S_2/S_1 was measured to be about 12 % for nuclear recoils of approximately
2619 60 keV_{nr} to 90 keV_{nr}. This can be compared with 18 % dispersion measured for electron recoils from
2620 ^{241}Am , depositing 60 keV of energy.

2621 As expected, anti-correlation between the scintillation and ionisation yields S_1 and S_2 has been
2622 detected. Results with drift fields from 75 V/cm to 1000 V/cm are displayed in figure 53 (right
2623 panel). The scintillation gain g_1 and the ionisation amplification g_2 were derived using the fit
2624 procedure described in [60]: the output parameters are $g_1 = (0.195 \pm 0.018_{\text{stat+sys}})$ PE/photon and
2625 $g_2 = (20.7 \pm 1.6_{\text{stat+sys}})$ PE/e⁻. The measured g_1 of ReD is higher than the corresponding values
2626 from DarkSide-50, 0.157 ± 0.001 PE/photon [13], and from SCENE, 0.104 ± 0.006 PE/photon [60].
2627 The ionisation amplification of ReD g_2 , is comparable to that of DarkSide-50, 23 ± 1 PE/e⁻ [17],
2628 and significantly higher than SCENE, 3.1 ± 0.3 PE/e⁻ [60].

2629 **5. DETECTOR DESIGN AND SPECIFICATIONS**

2630 The achievements of the R&D described in section 3, the results obtained with DarkSide-50
 2631 DEAP-3600 and ReD reported in section 4, and the ability to scale up the procurement of argon
 2632 depleted from its radioactive isotope (UAr) to the hundred-tonne scale lead the GADMC Collabora-
 2633 tion to define the design of the DS-20k experiment.

2634 The primary scientific goal of DS-20k is to detect dark matter by observing the signals generated
 2635 by the scattering of WIMPs. In a detector where the background from any radioactive contaminants
 2636 is suppressed to less than <0.1 events in the total exposure of 10 yr, considering only Poisson
 2637 fluctuations of the number of counts, just 5 WIMP-like events can be statistically significant enough
 2638 to claim a detection at the 5σ level. The discovery power and the sensitivity of the detector,
 2639 including the background due to ν -induced nuclear recoils is presented in section 2. Detector design
 2640 specifications, described in this section, flow from this primary goal. The technical description of
 2641 all the detector parts is given in section 7.

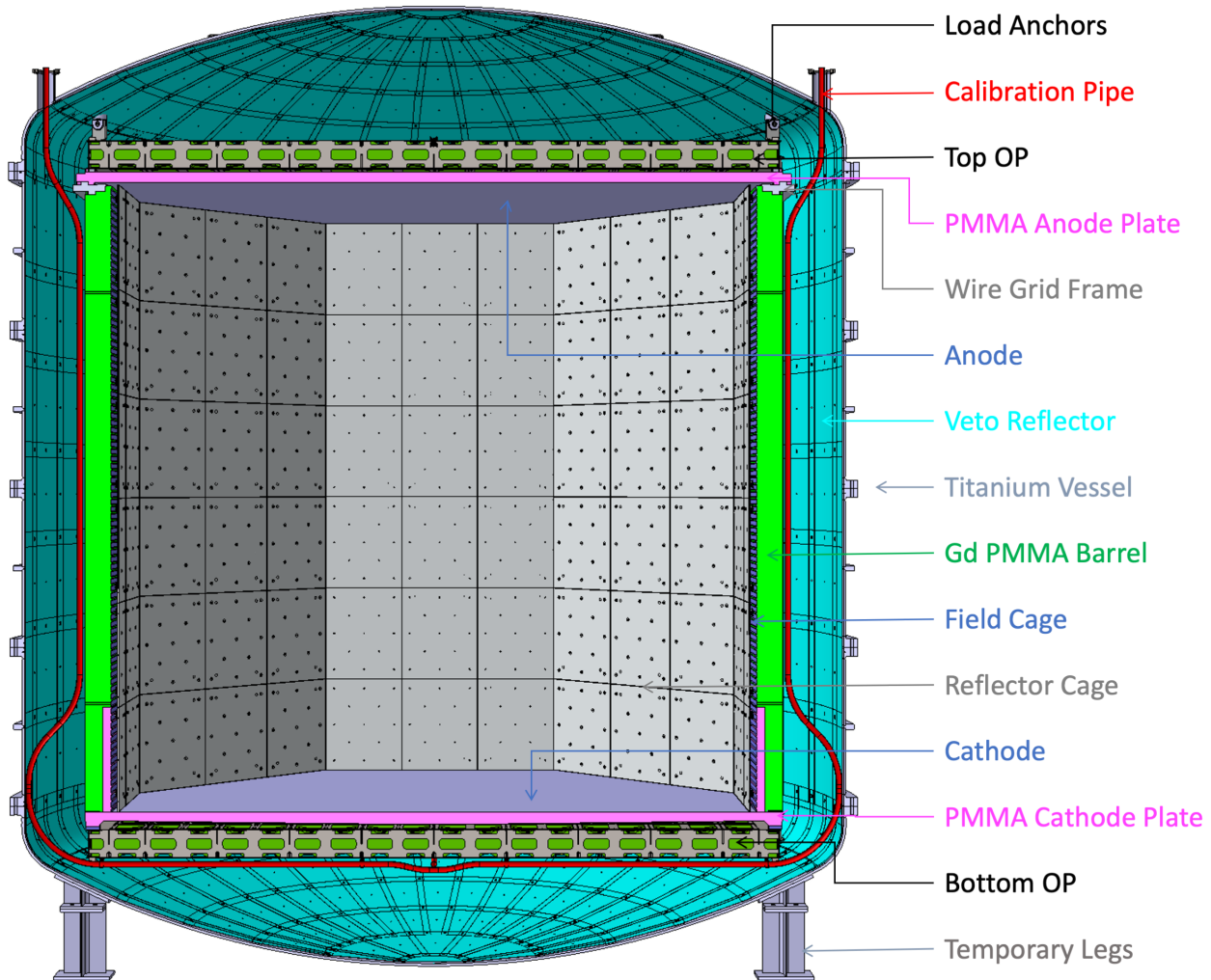


FIG. 54. Design of the inner detector showing the TPC, the Veto and the calibration pipes all contained in the titanium vessel which will host all the underground argon target for TPC and Veto.

2642

5.1. TPC and inner Veto

2643 The detector is fully based on the use of liquid argon: 99.2 t of UAr is used in the core of the
 2644 apparatus and it fills a dual phase LAr TPC (49.7 t active) which is the WIMP target and detector.
 2645 The UAr also forms a layer of 32 t that surrounds the TPC, this inner Veto region operates as a
 2646 single phase detector. The LAr TPC and the inner Veto, together referred to as the inner detector,
 2647 are designed with the goals of

- 2648 • minimizing the amount and type of passive materials;
- 2649 • meeting the requirement of highly efficient detection of WIMP signals in the TPC; and,
- 2650 • meeting the requirement of highly efficient rejection of backgrounds—mostly neutrons—
 2651 through synergistic use of the signals originating in the TPC and in the inner Veto.

2652 Figure 54 shows a view of the inner detector, and table XVII reports the specifications of the inner
 2653 detector.

TPC Parameter	Value
TPC drift length	348 cm
Octagonal inscribed circle diameter (87 K)	350 cm
UAr mass in TPC	51.1 t
Active LAr mass	49.7 t
Vertical fiducial cut (nominal)	70 cm
Radial fiducial cut (nominal)	30 cm
Fiducial UAr mass	20.2 t
Drift field	200 V/cm
Extraction field	2.8 kV/cm
Luminescence field	4.2 kV/cm
Cathode operating voltage	-73.38 kV
Extraction grid operating voltage	-3.78 kV
Anode operating voltage	ground
Field cage ring vertical spacing	4 cm
Gas pocket thickness	(7.0 ± 0.5) mm
Anode flatness	<0.1 mm
Grid optical transparency	97 %
Electron drift lifetime	>5 ms
Projected light yield at null field (S1)	10 PE/keV _{ee}
S2 yield	>20 PE/e ⁻
xy resolution	<5 cm
z resolution	1 mm
Veto Parameter	Value
Active mass	32 t
Light yield	2000 PE/MeV
Light yield uniformity	3.0 %
Reflective surface	174 m ²
SiPM geometrical coverage	3.2 %
Gd concentration in PMMA	0.5% -1% in weight
Ti vessel Parameter	Value
Vessel inner diameter	4650 mm
Vessel total internal volume	80 m ³
Total UAr (with TPC installed)	99.2 t

TABLE XVII. TPC and inner VETO design specifications.

2654 The UAr is contained within a sealed titanium vessel, and immersed within a bath of 700 t of
 2655 atmospheric liquid argon, AAr. The titanium vessel separates the two volumes of UAr and AAr.
 2656 The AAr acts as a buffer and shield from external radiation and, when instrumented, as a muon
 2657 and cosmogenic neutron Veto(outer Veto). A membrane cryostat similar to the ones built for
 2658 ProtoDUNE contains the entire detector.

The AAr is intrinsically radioactive at a rate of 1 Bq/kg, and the operation of the detector described above is only possible because of the discovery of low radioactivity argon in underground CO₂ wells (UAr) with an activity 1400 (or more) times lower than AAr.

Liquid argon is the material chosen as the target for the dark matter search because of several attractive features. Liquid argon has a reasonably high specific density of 1.4; it emits a burst of light (S1) whenever an interaction deposits energy in it, and ionization electrons produced in an interaction can be drifted many meters under the influence of a moderate electric field. Energy deposits in the LAr target result in the production of excited and ionized argon atoms, in different ratios depending on the electronic- or nuclear-recoil (ER or NR) nature of the interaction. Excited argon atoms, formed either directly or by recombination of ionization charge, lead to an efficient formation of excited argon excimers. They decay via the emission of scintillation light characterized by two decay time constants, one of the order of nanoseconds (spin singlet state), the other of microseconds (spin triplet state). The two components combine to yield a prompt light signal, called S1. Ionization electrons escaping recombination are drifted to the top of the LAr by an applied electric field, where an electric field, stronger than the field applied to drift the electrons, extracts them into the gas region above the liquid. Here the strong field accelerates the electrons enough for them to excite (but not ionize) the argon gas, producing a secondary scintillation signal S2, proportional to the ionization charge extracted at the liquid surface. Table XVIII shows selected relevant properties of liquid Argon.

Parameter	Value
Scintillation wavelength	128 nm
Liquid density	1.4 g/cm ³
Boiling point	87.3 K
Average work function	19.5 eV
Scintillation photon yield	51 ph/keV
Singlet de-excitation time	6 ns
Triplet de-excitation time	1.5 μ s
singlet/triplet for ER	0.3
singlet/triplet for NR	0.7
L_{eff} for 40.5 keV NR (null field)	0.286
typical ³⁹ Ar activity in AAr	1 Bq/kg
³⁹ Ar depletion factor in UAr	(1.4 ± 0.2) · 10 ³
³⁹ Ar Qvalue	565 keV

TABLE XVIII. LAr properties. L_{eff} is the ratio between the scintillation efficiency for NR and ER.

Photo-sensors placed on top and bottom of the TPC, read out both scintillation signals (S1 and S2) of each event.

The S1 signal provides two pieces of information. It provides the event energy and it further provides powerful event-type identification through its pulse shape in time (pulse shape discrimination, (PSD)). This latter feature is a powerful property of argon where the ratio of the fast to slow light in the S1 signal depends on whether the light comes from a recoiling electron or from a nuclear recoil.

S2 similarly provides two pieces of information. It provides energy information and also the 3D position measurement of the event. The vertical coordinate of the interaction is inferred from the time between S1 and S2, and the horizontal coordinates using the distribution of light from the S2 pulse in the top photosensors (the design resolution goals are 10 mm in horizontal direction and 1 mm on the vertical one).

The TPC mechanical structure is realized with an innovative design which uses only PMMA-based materials and it benefits from the excellent radio-purity properties of PMMA. The anode and cathode require high light transparency, as the light sensors are mounted above and below it, respectively. The anode and cathode are thus realized with pure PMMA. The lateral walls are made of a new hybrid material, which is PMMA loaded with Gd (Gd-PMMA) developed during

2697 our R&D activity. This material acts as an efficient neutron moderator, thanks to the high content
 2698 of Hydrogen in PMMA, and the Gd captures neutrons releasing high energy γ s, enabling efficient
 2699 tagging. Additional Gd-PMMA is located on top and bottom of the light sensors thus surrounding
 2700 the TPC in all directions.

2701 Neutrons that scatter elastically only once in the fiducial volume of the LAr TPC can mimic
 2702 a WIMP event, and thus are the most dangerous background for the experiment. However these
 2703 background events will be identified and rejected if the TPC signal is accompanied a subsequent
 2704 neutron capture signal producing scintillation in the UAr of either the TPC and inner Veto. The
 2705 analysis cuts that identify and reject those neutrons include a spatial cut, eliminating events too
 2706 close to the Gd-PMMA wall that forms the border of the TPC (see section 5.8.4). This defines the
 2707 TPC fiducial volume reported in table XVII. The shape of the TPC is an octagonal prism, with a
 2708 height of 348 cm and a distance between parallel walls of 350 cm.

2709 To shape the electric field, conductive rings are formed by painting the inner walls of the
 2710 Gd-PMMA with a conductive material (Clevios), avoiding the insertion of a metal field cage struc-
 2711 ture and thus minimizing the types, and amount, of passive material. Clevios painting is also used
 2712 for the cathode and anode.

2713

5.2. Light detection

2714 SiPMs are used as light sensors for both the TPC and Veto signals. Our R&D has resulted in the
 2715 development of, and in a full production chain for, cryogenic large-area SiPM tiles as light sensors
 2716 with superior efficiency, and of cryogenics electronics with a bandwidth appropriate for pulse shape
 2717 discrimination. The same type of SiPMs are used to detect both the LAr TPC and the Veto light.
 2718 The TPC light sensors are located above and below the anode and cathode planes and the sensors
 2719 of the inner VETO are placed on the external walls of the TPC. The names PDM and vPDM
 2720 refer to the photon detector module in the TPC and Veto respectively. The size of the individual
 2721 light sensors is a compromise between the practical advantages in minimizing the number of DAQ
 2722 channels and reaching an adequate transverse resolution to identify multiple scattering of neutrons,
 2723 define event positions and set fiducial volume boundaries in TPC. The Veto is less demanding and
 2724 it adopts the same choices of the TPC to simplify the production and testing of the photo-sensors.

2725 Each photon detector module is composed of a SiPM tile coupled to its cryogenic amplifier. The
 2726 SiPMs, $7.9 \times 11.7 \text{ mm}^2$ each, are realized with the NUV-HD-Cryo technology discussed in sec. 3.2.
 2727 An array of 24 of these SiPMs is used to build the tile that reads out both the TPC and Veto light.

2728 We adopt in the TPC and Veto readout the same technology to integrate single PDMs (vPDMs)
 2729 into a larger matrix, called Photo Detector Unit (PDU), containing 16 tiles, amplifiers, bias and
 2730 control signals, a summing stage and the signal transmitter.

2731 The TPC and Veto amplifiers are optimized for their specific needs, leading to the choice of
 2732 discrete elements 1 TIA schematic for the TPC with 4s6p SiPMs ganging and to the use of the
 2733 custom ASIC for the Veto with 4X(2s3p) SiPM ganging, both described in section 3.3.

2734 Summed signals from each of the four tiles making up a PDU+ (vPDU+) quadrant are amplified
 2735 and transmitted through a differential line to feedthroughs at the top of the cryostat. Thus each
 2736 PDU+ (vPDU+) comprising 16 individual tiles has 4 DAQ channels. The modularity of the
 2737 PDUSlim differs, with a sum of two tiles only foreseen.

2738 PDUs are mounted with a spacing of $\sim 5 \text{ mm}$ to form the top and bottom TPC optical planes,
 2739 thus achieving a geometrical coverage of $\sim 97.5\%$. In the Veto they are sparser, with a geomet-
 2740 rical coverage of 3.2 %, determined based on simulation studies of neutron tagging performance
 2741 (described in section 12.2.1).

2742 High level specification parameters for the TPC and Veto photo-sensor systems are reported in
 2743 Table XIX. Detailed specifications for individual components of these systems are given in section 8.

2745

Parameter	Value
Number of Tiles in the TPC	8448
Number of Tiles in the Veto	1920
Area covered by PDU+s (TPC) and VPDU+s (Veto)	25.92 m^2
SiPM dimensions	$7.9 \times 11.7 \text{ mm}^2$
PDU dimensions	$20 \times 20 \text{ cm}^2$
number of summed PDM signals	4
number of readout channels	2592
PDM overall photon detection efficiency	45 %
PDM fill factor	88 %

TABLE XIX. Photoelectronics specification parameters.

5.3. Reflectors and wavelength shifters

Due to the deep UV nature of the argon scintillation light, around 128 nm, which is absorbed by most materials, a thin layer of wavelength shifter covers all exposed surfaces to convert the photons to visible wavelengths for detection by our photosensors. Measurements of the parameters of our wavelength shifters are reported in section 3.7. Specifications for the wavelength shifters and reflectors are listed in table XX.

The TPC and Veto are optically isolated. We use TPB evaporated on ESR to cover the inner lateral walls of the TPC and ESR wrapped with PEN with a thin layer of Argon in between, to cover the external walls of the TPC and all the inner walls of the titanium vessel. ESR reflectors, also discussed in section 3.7, ensure that visible light hitting the walls is efficiently reflected. This light is then trapped within the TPC or Veto regions respectively, and it bounces back and forth until it reaches a light sensor. The geometrical coverage in the Veto is only 3.2 % and the optical photons are detected after several tens of reflections on average. The nominal ESR reflectivity of 98%, and its implementation in the Veto design, ensure that any dark area is minimized. The light collection uniformity in the Veto relies on the multiple reflections and also on the careful choice of the position of the photo-sensors.

Parameter/Method	Value
Area to be covered by wavelength shifter + reflector in TPC	43.2 m^2
Area to be covered by wavelength shifter + reflector in veto	174 m^2
Area of each ESR sheet	$26\text{in} \times 26\text{in}$
Number of ESR sheets needed	672
ESR reflectivity	98%
Minimum PEN re-emission efficiency	30%
Assumed TPB re-emission efficiency in simulation	100%

TABLE XX. Specifications for wavelength shifters and reflectors.

5.4. Outer Cosmic Veto

The LAr volume inside of the cryostat serves as an outer cosmic veto, targeting muons and their associated shower products, which may include high-energy neutrons. Simulations show that in order to decrease cosmogenic backgrounds to a negligible rate, DS-20k must veto events in which 50 MeV or more is deposited in the outer cosmic veto. This occurs when a muon traverses a chord shorter than 25 cm through the LAr, or if it misses the outer cosmic veto and only its shower products enter.

This threshold is achieved by instrumenting the AAr buffer with strings of photo-sensors, held in place through a set of flanges at the top of the cryostat. The photo-sensors for the outer cosmic veto employ the same technology as in the inner Veto, with specification parameters reported in Table XXI. The faces of these sensors in the outer cosmic veto are coated in TPB so that they

2773 can detect scintillation light from the AAr. To increase the light collection efficiency given the low
 2774 optical coverage, the cosmic veto will be lined with two layers of reflective Tyvek 4077D foil and
 2775 PEN wavelength-shifting foil.

Parameter/Method	Value
Minimum light yield for MIP detection	1 PE/MeV
Minimum number of VPDU's to reach threshold	24
Tyvek-4077D sheet area (3 layers)	1106 m ²
Tyvek-4077D reflectivity (450 nm)	>92%
PEN area	444 m ²

TABLE XXI. Specifications for the outer cosmic veto.

2776

5.5. Cryogenics

2777 There are two major independent cryogenic systems: one for the AAr inside the cryostat and
 2778 one for the UAr in the titanium vessel for the LAr TPC. The AAr cryogenics system is the same
 2779 as the demonstrated ProtoDUNE system already built twice at CERN, one for the ProtoDUNE
 2780 single phase and one for the ProtoDUNE dual phase detector. The cryostat specifications are listed
 2781 in table [XXVI](#).

2782 The UAr cryogenic system design is derived from the successful scheme of the DS-50 cryogenics
 2783 and gas handling system. Its basic operating principle is a recirculating system in which UAr
 2784 gas is extracted from the TPC volume and purified. A steady supply of LN is then used to cool
 2785 and re-condense the UAr gas into liquid as efficiently as thermodynamically allowed. The main
 2786 parameters of the UAr cryogenics system are given in Table [XXII](#).

2787 The long-term TPC pressure stability, an essential parameter for S2 resolution, has been achieved
 2788 in DS-50 with remarkable success, with fluctuations of only 160 pbar RMS. A drift electron lifetime
 2789 of ≥ 5 ms was also achieved, equivalent to an oxygen contamination in LAr of less than 0.06 ppb.
 2790 This is greatly beneficial for low energy signals and is absolutely essential for efficient collection of
 2791 the S2 signal over the long drift distance of 348 cm in DS-20k.

2792 The UAr handling system delivers the clean radon-free UAr from its initial storage location,
 2793 in the storage system which utilizes the UAr transportation skid described in section [10](#), to the
 2794 DS-20kdetector.

2795 The UAr purification system purifies the argon in gas phase during the circulation. A commercial
 2796 Zr-based getter system has already been proven to work well in DS-50 and an identified model with
 2797 increased circulation capability will be used in DS-20k.

2798 The custom cold-box assembly containing the condenser and heat exchangers has been fabricated,
 2799 built and commissioned at CERN and during summer 2021 as detailed in Sec. [7.5](#), together with a
 2800 custom gas circulation pump, fabricated at UCLA, and a commercial alternative.

2801

5.6. Calibrations

2802 A high sensitivity search for dark matter particles in a wide mass range requires a multifaceted
 2803 calibration program for TPC and the inner Veto detectors that includes:

- 2804 • measurement of the detector response for both ER and NR with energies as low as 0.05 keV
 2805 and 0.5 keV respectively;
- 2806 • measurement and calibration of the detector response uniformity throughout LAr TPC and
 2807 Veto;
- 2808 • validation of the pulse shape discrimination of NR vs ER with a variety of calibration sources;
- 2809 • monitoring the detector response over the lifetime of the experiment which is expected to
 2810 operate for a decade or longer.

Parameter	Value
Total UAr mass filled during normal operation	99.2 t
Purification system cooling power	500 W
Purification system gas-phase circulation rate up to	1000 std L/min
Purification system gas-phase turnover time	40 d
Single GAr circulation pump flow rate	500 std L/min
Pressure stability	160 μ bar (RMS)
Heat exchangers recovery efficiency	>95 %
LN ₂ storage	30 t
Rn concentration limit activated charcoal trap	<2 μ Bq/kg after trap
Maximum allowed helium leak rate at all welds and joints	2×10^{-9} std cm ³ /s

TABLE XXII. UAr cryogenic system design specifications.

Calibrations for both the TPC and the inner Veto detectors range from low-level calibration of detector response, such as the single-photoelectron response of individual photosensors, to high-level physics calibration like the acceptance as a function of energy for nuclear recoils. A combination of radioactive sources, a neutron generator, and light sources ensures a robust calibration plan to enable DS-20k to achieve its science goals. Table [XXIII](#) gives the list of the specifications of the calibration system that flow from these requirements.

Parameter/Method	Value
TPC and Veto source deployment system number of ports	4
TPC and Veto source deployment system number of pipes	2×20 m U-shaped
TPC and Veto source deployment pipe diameter	30 mm
Voltage for the DD neutron generator	10 kV
Full TPC volume light yield calibration	^{83m} Kr and ²²⁰ Rn
TPC neutron recoil calibration	²⁴¹ AmBe, ²⁴¹ Am ¹³ C, and ²⁴¹ AmLi
TPC energy scale calibration	⁵⁷ Co, ¹³³ Ba, ¹³⁷ Cs, and ⁶⁰ Co
Veto light yield calibration	⁵⁷ Co, ¹³³ Ba, ¹³⁷ Cs, and ⁶⁰ Co
Veto neutron tagging efficiency calibration	²⁴¹ Am ¹³ C

TABLE XXIII. Calibration systems parameters and methods.

2817
2818

2819

5.7. DAQ and Data Management

The current design for the DS-20k data acquisition system (DAQ) integrates the readout of the TPC, Inner Veto and Outer Veto photo-sensors in a unique and uniform system, providing digitized data for subsequent data analysis. The main challenge that the DAQ system has to face is the large number of readout channels for SiPM sensors covering the cathode and anode optical planes of the TPC, the long drift-time (the maximum expected electron drift time is 4 ms), coupled with the need for sensitivity to single photo-electron scintillation signals in the WIMP dark matter search region of interest (ROI). The long drift time and the large number of channels makes it impractical to record full waveforms for events, even for low energy events within the WIMP ROI.

Thus the design that will be described in Sec. [7.6](#) is based on the following principles:

- digitization of the SiPMs signals is performed with a sampling rate matched to the front-end amplifiers of the different detectors;
- noise at the single channel level is minimized by digital signal processing in firmware at the level of the digitizer electronics, which, for this purpose, will host a powerful Field Programmable Gate Array (FPGA);
- individual channel thresholds are set to record single photo-electron signals with high efficiency (ideally > 99%);
- waveform fragments of variable length are selected based on suitable algorithms also implemented in the FPGA, accounting for the possibility of multiple photo-electrons close in time

- (e.g. ionization signals, S2) and queued to the output of the digitizer;
- synchronization of all the digitizers is ensured by distributing a common clock signal from a centralized source;
 - in normal conditions the system is operated in trigger-less mode to ensure flexibility in the selection of interesting events and information to be saved for offline analysis;
 - individual channel pulses are analyzed online in a first stage of software processing (Front End Processors, FEPs) to allow a reasonable amount of information to be sent to the event building stage;
 - event building and selection is performed in software on a second stage of processing (Time Slice Processors, TSPs) where multiple servers analyse pre-defined time intervals where data from all detectors are available with the proper time-stamp; and,
 - data transfer is managed internally on a private 10 Gb/s ethernet network with a large switch at its core connecting FEPs and TSPs.

The key specification parameters guiding the design of the DAQ system are reported in Table [XXIV](#). It is assumed that the ER-induced event rate discussed in Sec. [5.8.6](#) will be the largest fraction of the trigger rate in DM search mode, but we account for an extra conservative margin of about 50% to allow for contingency, acquisition of events triggered only by the Veto systems and other special needs.

A fully fledged data-management plan is still to be completed. The current plan foresees to have a disk buffer to store onsite raw-data corresponding to a week of operations. At the specified data logging rate reported in Table [XXV](#) 40 TB would be sufficient, at the maximum design data logging rate this increases to about 120 TB of short term disk onsite. The data buffered locally will be copied at off-site computing centers for long term storage, reprocessing and offline analysis. At the nominal logging rate, including a typical 95% uptime, secondary dataset and MC simulations we estimate, very preliminarily, a need for about 20 PB of long term data storage for the nominal 10 yr length of the proposed run.

Centralized data management at CNAF is a natural option, but a further copy of all the relevant data should be stored for safety reasons at a second computing center offered by the international partners, yet to be defined. Secondary data sets, useful for user data analysis, will be distributed widely throughout the network of international partners with computing resources made available by partner institutions.

Parameter	Value
Typical trigger rate in DM search mode	120 Hz
Maximum design trigger rate	200 Hz
Network band width from digitizer to front end CPU	1 Gbit/s to 10 Gbit/s
Network band width from front end CPU to event builder	10 Gbit/s
Design average event size	0.5 MB
Maximum sustainable average event size	1 MB
Maximum sustainable logging rate	200 MB/s

TABLE XXIV. DAQ design parameters.

Parameter	Value
Expected data logging rate in DM search mode	60 MB/s
Short term data storage at experimental site	120 TB
Expected DS-20k total data volume	20 PB

TABLE XXV. Computing design parameters.

2869 **5.8. Materials and Radiopurity**

2870 The specifications for the radiopurity of detector materials flow from the ultra-low background
 2871 requirements of the dark matter search. In this section, we first specify the characteristics of
 2872 expected WIMP dark matter-induced signals, then categorize the background sources, describe
 2873 the methodology for evaluating background contributions given the measured specific activity of
 2874 detector materials from the radioassay campaign, and finally quantify the expected material-related
 2875 background contributions in table [XXXIII](#).

2876 **5.8.1. Expected signals**

2877 WIMP-induced nuclear recoils in the DS-20k TPC are identified as having a single reconstructed
 2878 interaction site in the active volume of the TPC be reconstructed as a NR-like event not rejected by
 2879 PSDand with as S1 scintillation signal falling within a predefined region of interest for WIMP-like
 2880 dark matter candidates (DM ROI). Additionally the single interaction vertex may be required to
 2881 lay within the fiducial volume. Single sited interactions are characterized by one S1 and only one
 2882 S2 in the acquisition window. The DM ROI is defined as the [30,200] keV_{nr} energy range. NR and
 2883 ER interactions are distinguished based on the S1 time profile, as discussed in [7.7](#).

2884 The event position is reconstructed using the time difference between S2 and S1, proportional
 2885 to the drift distance, and the S2 light distribution on the top arrays of photo-detectors. The FV
 2886 is defined as the volume contained by a surface of 30 cm removed from the lateral boundary and
 2887 70 cm from the top and bottom surfaces of the active UAr target.

2888 The S2 signal, proportional to the drifting ionization electrons, benefits from a multiplication
 2889 factor, thanks to the electroluminescence in the gas ($>20 \text{ PE/e}^-$). Therefore, low-energy recoils
 2890 will generate S2 events if S1 is vanishing. Low-energy searches using only the ionization signal,
 2891 such as the ones performed by DarkSide-50 [[17](#), [18](#)], reached single electron sensitivity.

2892 **5.8.2. Sources of background**

2893 In absence of a specific signature of a single WIMP scattering event, every interaction in the
 2894 detector resulting in detected signals equivalent to that of a single nuclear recoil (NR) is a potential
 2895 source of background.

2896 Sources of NR background events include neutron interactions, predominantly due to radiogenic
 2897 neutrons produced by (α,n) reactions induced by contaminants of the detector materials - (α,n)
 2898 from ^{232}Th , ^{235}U , ^{238}U chains - and spontaneous fission of ^{238}U . The typical energy of these
 2899 neutrons is in the $\simeq \text{MeV}$ region and their elastic scattering on Ar nuclei in the TPC can produce
 2900 NR with an energy in the same range of the WIMP signal.

2901 Additional NR backgrounds events come from the random coincidence of Cherenkov light or
 2902 α -decays on the inner TPC surface with unrelated S2 signals. Degraded α -decays originated from
 2903 dust inside the fiducial volume can mimic WIMP signals (See Sec. [12.4](#)).

2904 In addition, cosmogenic neutrons are produced due to spallation reactions of muons on nuclei in
 2905 the detector or surrounding cavern. These high energy neutrons may be moderated in detector
 2906 materials, and can produce hadronic showers containing low energy neutrons, allowing the background
 2907 events in the WIMP signal energy range to be produced.

2908 Sources of electronic recoil (ER) background events are β and γ decays of residual radioactive
 2909 contaminants in the UAr and γ decays of contaminants of the materials used to build the detector
 2910 or originating from the surrounding cavern.

2911 While comparing the energy of background sources, the quenching of NRs must be properly
 2912 accounted for. The same energy deposit due to NRs or ERs induces different atomic mechanisms
 2913 triggered by details of the specific energy loss. The scintillation efficiency for NR is typically reduced

2914 compared to that of ER by a factor depending on the energy and the value of the electric field in
 2915 the TPC. A reference value at null field is reported in table XVIII.

2916 *5.8.3. Evaluation of the expected background rates*

2917 To ensure that DS-20k achieves its science goals, a detailed detector model has been built using
 2918 the G4DS Monte Carlo simulation package [13], which is based on the Geant4 framework. This
 2919 model is used in particular to study the NR backgrounds in the detector and the γ rate. Additional
 2920 simulation tools have been developed to include detailed SiPM response.

2921 Accurate estimates of (α, n) neutron production rates, energy spectra, and correlated γ -rays
 2922 are fundamental to understanding our background. The yield of neutrons from this reaction is
 2923 calculated using NeuCBOT [68] and SaG4n [69]. NeuCBOT is a code developed for DarkSide-50 which
 2924 calculates the yield in a fast way using TALYS [70] provided the chemical composition of the material.
 2925 TALYS is versatile but is based on theoretical calculations and it has improvable accuracy for some
 2926 relevant cases. Also, in its current configuration, it only accounts for homogeneous materials with a
 2927 defined proportion of chemical elements (and isotopes). We consider that this can be an important
 2928 limitation to estimate the total neutron yield with the required accuracy, so a new code, SaG4n,
 2929 has been developed in the context of the DS-20k assay campaign, with the goal of reducing our
 2930 systematic uncertainty.

2931 SaG4n is a Geant4-based code and has two major advantages compared to similar codes: first, ar-
 2932 bitrarily complex geometries can be defined, with different volumes having different compositions.
 2933 Second, any ENDF-6 format library of choice can be used as input for the cross sections, so experi-
 2934 mental values can be used where available, the JENDL/AN-2005 library being an example. The code
 2935 uses biasing techniques (enhancement of the relevant cross sections) to reduce the computing time
 2936 significantly, as required to make such detailed simulations viable.

2937 *5.8.4. Nuclear Recoil-background rates*

2938 Neutron-induced NR events are rejected by a combination of analysis cuts involving TPC and
 2939 Veto signals. The background rejection of the combined TPC and Veto selection is studied with the
 2940 Monte Carlo simulation, first generating millions of neutrons with accurate initial energy spectra
 2941 and positions in the detector, then counting the number N_s of neutron-induced events surviving
 2942 the following analysis cuts:

- 2943 • detection of a WIMP-like event in the TPC namely a single sited NR with S1 energy in the
 range $[30,200]$ keV $_{NR}$. All the NRs in this energy window are conservatively accounted for
 as a background event, neglecting the acceptance loss due to PSD, discussed later in Section
 12.1.2. Neutrons typically generate multiple scatter events in the TPC which are rejected by
 the requirement of a single scatter identified by a single S2 signals following the Wimp-like
 S1.
- 2949 • the NR event position is required to be at least 70 cm distance from the anode and cathode
 in the z direction and 30 cm distance from the lateral TPC walls in the x-y plane. These cuts
 define the fiducial volume mass.
- 2952 • no detection of any event in the Veto with energy above the threshold $E_{VETO}^t = 200$ keV, in
 a 800 μ s time window following an S1 signal in the TPC. This window length is optimized
 from simulation; the average capture times are found to be 35 μ s for captures on Gd, and
 200 μ s for captures on Ar.
- 2956 • no detection, within the same time window of 800 μ s, of any event in the TPC with energy
 above the threshold $E_{TPC}^t = 50$ keV.

2958 The inefficiency is $\epsilon = N_s/N_g$, where N_s is the number of events surviving these cuts and N_g is the
 2959 number of generated neutrons. In general, the inefficiency varies with the position of the neutron
 2960 capture.

Radiogenic neutrons The expected number of residual radiogenic neutrons, surviving the cuts above, is obtained by scaling ϵ by the number of neutrons produced during the entire exposure of the detector. This requires the estimation of the radioactive contamination, the knowledge of the (α,n) cross sections and of the composition of the materials.

The neutron vetoing procedure has a high efficiency, however, given the experiment's stringent requirements on NR backgrounds, it is necessary to aggressively minimize the radiogenic neutron production rate. This process includes selecting materials that have low (α,n) cross sections and are ultra-low in uranium and thorium contamination. The (α,n) yield of a material strongly depends on the α -particle's energy, making the assessment of the activity in the lower sections of the ^{238}U and ^{232}Th decay chains particularly important. In DS-20k three different assays techniques have been used to measure ^{238}U , ^{235}U , ^{232}Th , and their decay products in the detector materials (Sec. 3.1). By doing so, the contamination levels of many radioisotopes within each decay chain are measured, allowing departures from secular equilibrium to be measured.

In addition to U and Th contamination, precise knowledge of the chemical composition of the material is mandatory to accurately calculate of the (α,n) yield. The DS-20k assay campaign is now complemented with an elemental analysis campaign to minimize uncertainty due to the material composition.

The detailed inputs to the radiogenic neutron NR background estimates for the 200 t yr exposure of DS-20k are summarized in Tables XXVII – XXXII. Table XXVI summarizes the resulting NR background by source, described in detail in the rest of this section. The total estimated NR background in this exposure is 9.5×10^{-2} . The error on this background is being evaluated. It depends largely on detailed knowledge of the material composition of the internal detector components and on the uncertainty of the cross section (α,n) . The last one in particular can be as high as 50 % in the case of materials for which few experimental data are available. We estimate that a conservative overall error on the (α,n) background of the order of 50 % has a negligible impact on the physics reach of the experiment.

Background type	Bg events in ROI [200 t yr] ⁻¹
(α,n) neutrons from U and Th	9.5×10^{-2}
Fission neutrons from U-238	$<2.3 \times 10^{-3}$
Neutrons from Rn-222 diffusion and surface plate-out	$<1.4 \times 10^{-2}$
Cosmogenic neutrons	$<6.0 \times 10^{-1}$
Neutrons from the lab rock	1.5×10^{-2}
Random surface α decay + S2 coincidence	$<5.0 \times 10^{-2}$
Correlated ER + Cherenkov	$<1.8 \times 10^{-2}$
Uncorrelated ER + Cherenkov	$<3.0 \times 10^{-2}$
ER	$<1.0 \times 10^{-1}$

TABLE XXVI. Nuclear recoil (NR) backgrounds expected during the full DS-20k exposure, based on current data and Monte Carlo simulations. The right column is the total number of events surviving the veto cut, fiducial volume cut, and PSD.

Fission neutrons from ^{238}U ^{238}U spontaneous fission generates multiple neutrons and MeV-scale γ -rays. The multiplicity of these decay products significantly enhances the probability that the fission-induced NRs can be tagged and rejected using the neutron veto or multiple-scattering cuts. The inefficiency in discriminating this background, calculated via a Monte Carlo simulation, is >15 times smaller than that of neutrons produced via (α,n) . Preliminary results constrain the rate of spontaneous fission neutron-induced background events to $<2.3 \times 10^{-3}$ in the full 200 t yr. This contribution is negligible with respect to the one previously discussed.

Cosmogenic neutrons Simulations were performed of 30.6 years of cosmogenic muon showers in

Detector element	Material	Mass [kg]	^{238}U		^{238}U lower		^{232}Th		^{235}U		Neutron tagging inefficiency after cuts [n/10 yr]	Neutrons [n/10 yr]	Bkg fraction [%]
			Activity [mBq/kg]	Activity [mBq/kg]	Activity [mBq/kg]	Activity [mBq/kg]	Activity [mBq/kg]	Activity [mBq/kg]	Yield [n/decay]	Yield [n/decay]			
TPC													9.5×10^{-3}
Ultrapure acrylic	1.978.0		3.7×10^{-3}	1.2	1.2	2.4×10^{-3}	1.7×10^{-4}	4.5×10^2	5.8×10^{-6}	2.6×10^{-3}		2.7	
PMMA windows (anode & cathode)	TPB	9.2×10^{-2}	9.1×10^{-8}	3.4	5.0	5.5×10^{-7}	8.8×10^{-8}	8.8×10^{-7}	9.0×10^{-7}				
Conductive polymer Clevios (PEDOT)		8.0	8.6×10^{-8}	1.4	10.0	5.6×10^{-7}	1.0×10^{-8}	0.48	6.4×10^{-2}	19	5.8×10^{-6}	1.1×10^{-4}	0.12
Gd oxide	3860.0		8.5×10^{-8}	5.5×10^{-7}	1.2	5.5×10^{-8}	8.8×10^{-7}	9.0×10^{-7}	1.1×10^{-2}	1.2×10^3	6.7×10^{-7}	7.9×10^{-4}	0.83
Gd-acrylic	38.6		2.7×10^{-8}	1.2×10^{-7}	6.2	2.7	27.0	2.3	0.29	17	6.7×10^{-7}	1.1×10^{-5}	1.2×10^{-2}
Sulfactant IGEPAL Co-520		3.9	8.2×10^{-8}	5.5×10^{-7}	6.2	2.7	27.0	2.3	0.29	70	6.7×10^{-7}	4.6×10^{-5}	4.8×10^{-2}
Optical plane structure	Titanium	928.0		8.0	0.12	80.0	0.12	0.37			6.7×10^{-7}	1.1×10^{-6}	1.2×10^{-3}
Wire frame & grid	Stainless steel	703.0	3.9×10^{-10}	5.8×10^{-7}	0.4	0.4	0.8×10^{-2}	1.8×10^{-2}	4.6×10^{-7}	4.1×10^2	5.8×10^{-6}	2.4×10^{-3}	2.5
TPC rods	Titanium	52.0	4.9×10^{-9}	2.6×10^{-6}	8.0	2.6×10^{-6}	1.6×10^{-8}	6.5×10^{-6}	2.6×10^{-6}	56	5.8×10^{-6}	3.2×10^{-4}	0.34
Barrel brackets	Stainless steel	352.0	3.9×10^{-10}	5.8×10^{-7}	0.4	0.4	0.8×10^{-2}	1.8×10^{-2}	4.6×10^{-7}	2.1×10^2	5.8×10^{-6}	1.2×10^{-3}	1.3

TABLE XXVII. Simulated radiogenic neutron rates from the detector materials over the full 200 t yr fiducial volume exposure.

Detector element	Material	Mass [kg]	^{238}U		^{238}U		^{232}Th		^{235}U		Number of neutrons [n/10 yr]	Neutron tagging inefficiency	Neutrons after cuts [n/10 yr]	Bkg fraction [%]
			upper	middle	Activity [mBq/kg]	Activity [mBq/kg]	Activity [mBq/kg]	Activity [mBq/kg]	Yield [n/decay]	Yield [n/decay]				
TPC														
														9.5×10^{-3}
														10.0
ESR reflector Vikuiti (PET, Laysan)		3.1		1.6		1.6		0.9		7.4 $\times 10^{-2}$		2.1		5.8 $\times 10^{-6}$
Panels, spacers, reflectors and WLS in the inner TPC barrel	TPB	8.8×10^{-2}	3.4	5.0	8.0	1.9	0.16	0.18				1.2 $\times 10^{-5}$		1.3 $\times 10^{-2}$
Conductive polymer Clevios (PEDOT)		1.0	1.4	10.0	10.0	0.48	6.4 $\times 10^{-2}$					1.0 $\times 10^{-6}$		1.05 $\times 10^{-3}$
Acrylic		264.1	0.25	1.2	1.2	0.24	1.1 $\times 10^{-2}$					1.3 $\times 10^{-5}$		1.4 $\times 10^{-2}$
Nylon 66		3.1	5.0	5.0	5.0×10^2	8.0	0.23					1.3 $\times 10^{-5}$		
Copper		0.17	0.33	1.6	16.0	1.0 $\times 10^{-2}$	1.5 $\times 10^{-2}$					4.7 $\times 10^{-4}$		0.49
Resistors		7.1×10^{-3}	3.7×10^3	7.0×10^3	8.2×10^3	9.7×10^2	$7.1 \times 10^{+2}$					2.3 $\times 10^{-4}$		0.24
Field cage Resistors solder		4.9×10^{-3}	28.0	7.2×10^2	7.2×10^2	28.0	1.3					2.0 $\times 10^{-8}$		2.1 $\times 10^{-5}$
PCB substrate Arlon 55NT		6.6×10^{-2}	53.0	53.0	1.28×10^2	70.0	2.4					1.5 $\times 10^{-6}$		1.6 $\times 10^{-3}$
Nylon 66		1.1	5.0	5.0	5.0×10^2	8.0	0.23					2.1 $\times 10^{-5}$		2.2 $\times 10^{-2}$

TABLE XXVIII. Simulated radiogenic neutron rates from the detector materials over the full 200 t yr fiducial volume exposure.

Detector element	Material	^{238}U			^{238}U			^{232}Th			^{235}U			Neutron tagging inefficiency	Neutrons after cuts [n/10 yr]	Bkg fraction [%]
		upper	middle	lower	Activity [mBq/kg]	Activity [mBq/kg]	Activity [mBq/kg]	Activity [mBq/kg]	Yield [n/decay]	Yield [n/decay]	Yield [n/decay]	Yield [n/decay]	Yield [n/decay]			
Veto																
															1.63 × 10⁻²	17.2
TPC Barre	Acrylic	7400.0	0.25	1.2	8.5×10^{-8}	5.5×10^{-7}	5.5×10^{-8}	8.8×10^{-7}	0.24	1.1×10^{-2}	9.0×10^{-7}	2.3×10^3	5.8×10^{-6}	1.32×10^{-2}		13.9
	Gd oxide	74.5	6.2	2.7	2.7×10^{-8}	1.2×10^{-7}	1.5×10^{-8}	1.9×10^{-7}	2.3	0.29		32.5	5.8×10^{-6}	1.9×10^{-4}	0.20	
	Gd-acrylic	74.5	6.2	2.7	8.2×10^{-8}	5.5×10^{-7}	5.5×10^{-8}	8.7×10^{-7}	2.3	0.29		1.35 × 10 ²	5.8×10^{-6}	7.8×10^{-4}	0.82	
	Sulfactant	0.12	1.20	1.2×10^1	8.0×10^{-8}	5.5×10^{-7}	5.5×10^{-8}	8.8×10^{-7}	4.1	10^{-2}	5.5×10^{-3}	3.2	5.8×10^{-6}	1.9×10^{-5}	2.0×10^{-2}	
IGEPAL Co-520	IGEPAL Co-520	7.45	8.0×10^{-8}	5.5×10^{-7}	5.5×10^{-8}	8.8×10^{-7}	8.8×10^{-7}	8.8×10^{-7}								
	ESR reflector	1.6	1.6	1.6					0.9	7.4×10^{-2}						
	Vikuiti (PET, Laysan)	13.5										9.2	8.8×10^{-7}	8.1×10^{-6}	8.5×10^{-3}	
	Wavelength shifter	5.1	0.93	1.4					7.8	0.36×10^{-2}	1.0×10^{-6}	3.0	8.8×10^{-7}	2.7×10^{-6}	2.8×10^{-3}	
Reflectors and WLS in the Top, Bottom and outer TPC barrels	PEN	9.3	10^{-8}	6.4×10^{-7}	6.3×10^{-8}	1.0×10^{-6}	1.0×10^{-6}	1.0×10^{-6}								
	ESR reflector	22.4	1.6	1.6					0.9	7.4×10^{-2}						
	Vikuiti (PET, Laysan)	9.2	10^{-8}	6.1×10^{-7}	6.1×10^{-8}	9.7×10^{-7}	9.9×10^{-7}	9.9×10^{-7}								
	Wavelength shifter	9.0	9.3×10^{-8}	6.4×10^{-7}	6.3×10^{-8}	1.0×10^{-6}	1.0×10^{-6}	1.0×10^{-6}								
Reflectors and WLS in the inner titanium vessel walls	PEN															
	Titanium	300.0	8.0	0.12	80.0	0.12	0.36	4.3×10^{-2}	0.12	0.37×10^{-2}	1.0×10^{-6}	5.3	2.4×10^{-7}	1.3×10^{-6}	1.4×10^{-3}	
	Vessel support structure															
	Titanium	8230	8.0	0.12	80.0	0.12	0.12	2.6×10^{-6}	6.5×10^{-6}	2.6×10^{-6}	2.6×10^{-6}	3.2	2.4×10^{-7}	7.6×10^{-5}	8.0×10^{-2}	
Vessel																

TABLE XXIX. Simulated radiogenic neutron rates from the detector materials over the full 200 t yr fiducial volume exposure.

Detector element	Material	^{238}U		^{238}U		^{232}Th		^{235}U			
		upper	middle	lower	Activity [$\mu\text{Bq}/\text{PDM}$]	Activity [$\mu\text{Bq}/\text{PDM}$]	Activity [$\mu\text{Bq}/\text{PDM}$]	Activity [$\mu\text{Bq}/\text{PDM}$]	Number of neutrons [$n/10 \text{ yr}$]	Neutron tagging inefficiency after cuts	Neutrons [$n/10 \text{ yr}$]
		Mass [g/PDM]	Yield [n/decay]	Mass [g/PDM]	Yield [n/decay]	Mass [g/PDM]	Yield [n/decay]	Mass [g/PDM]	Yield [n/decay]	Mass [g/PDM]	Yield [n/decay]
TPC photoelectronics w/o transmission											
528 PDU+	SiPM tile+ and MB+	157.5 304	8.4×10^4	1.7×10^4	3.0×10^5	2.0×10^4	3.9×10^3	1.6×10^4	2.2×10^{-6}	3.47×10^{-2}	36.6
Veto photoelectronics w/o transmission											
120 vPDU+	Veto SiPM tile+	24.0 200	5.8×10^4	1.8×10^4	6.2×10^5	1.8×10^4	3.1×10^3	5.1×10^3	8.8×10^{-7}	4.5×10^{-3}	4.7
	Veto MB+	13.4 112	4.4×10^4	9.9×10^3	2.4×10^5	1.1×10^4	2.1×10^3	1.6×10^3	8.8×10^{-7}	1.4×10^{-3}	1.5

TABLE XXX. Simulated radiogenic neutron rates from the detector materials over the full 200 t yr fiducial volume exposure.

Detector element	Material	Mass [kg]	Activity [mBq/kg]	Activity [mBq/kg]	Activity [mBq/kg]	Activity [mBq/kg]	Number of neutrons [n/10 yr]	Neutron tagging inefficiency after cuts	Neutrons [n/10 yr]	Bkg fraction [%]
			Yield [n/decay]	Yield [n/decay]	Yield [n/decay]	Yield [n/decay]				
TPC transmission										
Cathode HV cables	Copper	4.24	0.33	1.6	16.0	1.5×10^{-2}	1.5×10^{-2}	8.85×10^{-2}	5.8×10^{-6}	5.1×10^{-7}
LV, HV, control cables	SAMI cable	92.1	5.4	5.4	1.1×10^2	6.1	0.25	60.3	5.8×10^{-6}	2.4×10^{-7}
	Copper	0	3.8×10^{-8}	0	3.1×10^{-7}	1.8×10^{-8}			2.1×10^{-4}	0.22
	SAMI cable	28.0	3.8×10^{-8}	1.2×10^{-6}	6.7×10^{-8}	2.0×10^{-6}	1.6×10^{-6}	2.4×10^2	5.8×10^{-6}	8.3×10^{-4}
	Silitem								2.4×10^{-7}	0.87
Calibration fiber	Core	3.0×10^{-3}	8.0	8.0×10^3	8.0	0.37	0.13	5.8×10^{-6}	7.7×10^{-7}	8.1×10^{-4}
	Fused silica		8.0×10^{-8}	8.5×10^{-7}	6.0×10^{-8}	1.4×10^{-6}	1.3×10^{-6}			
Jacket PEEK	Jacket	1.9×10^{-2}	7.0	7.0×10^1	1.0×10^3	0.10	0.32	6.70×10^{-1}	5.8×10^{-6}	3.9×10^{-6}
	PEEK	9.5×10^{-8}	6.6×10^{-7}	6.4×10^{-8}	1.1×10^{-6}	1.1×10^{-6}				4.1×10^{-3}
Veto transmission										
LV, HV, control cables	SAMI cable	21.3	5.4	5.4	1.1×10^2	6.1	0.25	14.0	2.4×10^{-7}	6.7×10^{-7}
	Copper	0	3.8×10^{-8}	0	3.1×10^{-7}	1.8×10^{-8}			8.8×10^{-7}	8.1×10^{-3}
	SAMI cable	5.4	5.4	1.1×10^2	6.1	0.25	54.6	2.4×10^{-7}	6.7×10^{-7}	3.0×10^{-5}
	Silitem	6.5	8.3×10^{-8}	1.2×10^{-6}	6.7×10^{-8}	2.0×10^{-6}	1.6×10^{-6}	8.8×10^{-7}	3.15×10^{-2}	
3.8 × 10⁻⁵ 4.0 × 10⁻²										

TABLE XXXI. Simulated radiogenic neutron rates from the detector materials over the full 200 t yr fiducial volume exposure.

Detector element	Material	Mass [kg]	^{238}U		^{238}U		^{232}Th		^{235}U		Number of neutrons [n/10 yr]	Neutron tagging inefficiency	Neutrons after cuts [n/10 yr]	Bkg fraction [%]
			upper	middle	lower	Activity [mBq/kg]	Activity [mBq/kg]	Activity [mBq/kg]	Yield [n/decay]	Yield [n/decay]				
Cryostat														
														2.74×10^{-2}
														28.9
Stainless steel for the cryostat	6.6 × 10 ³	48.8	27.3	1.1 × 10 ³	3.9	2.2	4.6 × 10 ⁻⁶	4.6 × 10 ⁻⁷	5.4 × 10 ⁴	2.2 × 10 ⁻¹⁰	1.2 × 10 ⁻⁵	1.3 × 10 ⁻²		
Stainless steel Beams & shell	3.9 × 10 ⁻¹⁰	5.8 × 10 ⁻⁷	9.25 × 10 ⁻¹⁰	2.0 × 10 ⁻⁶	4.6 × 10 ⁻⁷	1.8 × 10 ⁶	2.2 × 10 ⁻¹⁰	4.0 × 10 ⁻⁴	4.0 × 10 ⁻⁴	4.0 × 10 ⁻⁴	4.0 × 10 ⁻⁴	0.42		
Plywood	12.3 × 10 ³	5.3 × 10 ²	5.3 × 10 ²	1.5 × 10 ⁴	5.1 × 10 ²	24.4	1.0 × 10 ⁻⁶	9.7 × 10 ⁻⁷	6.9 × 10 ⁶	2.2 × 10 ⁻¹⁰	1.6 × 10 ⁻³	1.7		
Reinforced polyurethane foam	27.9 × 10 ³	1.1 × 10 ³	1.1 × 10 ³	2.2 × 10 ³	1.5 × 10 ³	50.7			4.9 × 10 ⁷	2.2 × 10 ⁻¹⁰	1.10 × 10 ⁻²	11.6		
Rigid barrier	550	1.2 × 10 ⁴	1.2 × 10 ⁴	1.2 × 10 ⁵	2.7 × 10 ⁴	5.5 × 10 ²	5.3 × 10 ⁻⁶	5.8 × 10 ⁻⁶	4.6 × 10 ⁷	2.2 × 10 ⁻¹⁰	1.04 × 10 ⁻²	11.0		
Flexible barrier	183	9.9 × 10 ³	9.9 × 10 ³	9.9 × 10 ⁴	1.9 × 10 ⁴	4.6 × 10 ²	6.1 × 10 ⁻⁶	6.4 × 10 ⁻⁶	1.3 × 10 ⁷	2.2 × 10 ⁻¹⁰	2.8 × 10 ⁻³	2.95		
Mastic rope	12.0 × 10 ³	3.8 × 10 ²	3.8 × 10 ²	3.8 × 10 ³	1.8 × 10 ²	17.3			2.8 × 10 ⁶	2.2 × 10 ⁻¹⁰	6.3 × 10 ⁻⁴	0.66		
Aluminum foil	20	2.0 × 10 ³	4.1 × 10 ²	4.1 × 10 ³	6.0 × 10 ²	92.2								
Polyurethane foam for the roof	2.3 × 10 ³	1.1 × 10 ³	1.1 × 10 ³	2.2 × 10 ³	1.5 × 10 ³	50.7			2.1 × 10 ⁶	2.2 × 10 ⁻¹⁰	4.7 × 10 ⁻⁴	0.49		
Total										1.2×10^8	9.49×10^{-2}	100		

TABLE XXXII. Simulated radiogenic neutron rates from the detector materials over the full 200 t yr fiducial volume exposure.

2995 Hall C in order to determine the expected number of backgrounds arising from cosmogenic neutrons
 2996 scattering in the TPC, using the FLUKA software package. Before applying cuts using the outer
 2997 cosmic veto, an expected background rate of (0.43 ± 0.10) events/yr is predicted. After vetoing
 2998 events in which at least 50 MeV is deposited in the outer cosmic veto, this prediction is reduced to
 2999 a 90 % CL upper limit of <0.06 events/yr in the fiducial volume, limited by the currently available
 3000 MC statistics. Work is in progress to reduce the statistical error of this prediction. It is to be
 3001 noted that further rejection against this class background can be obtained by identifying multiple
 3002 scatterings of the neutrons within the TPC volume which is not considered in this estimate.

3003 **Radiogenic neutrons from the rock** Large statistics simulations of neutrons from the walls
 3004 of the Hall C were performed in order to estimate the resulting background rate. These neutrons
 3005 are mainly due to (α, n) reactions in the rocks and in the concrete, and their energy spectrum and
 3006 flux have been calculated in [71].

3007 The simulation strategy consists of performing two subsequent steps with the Geant4-based G4DS:
 3008 the first step estimates the probability that rock and wall neutrons from outside the ProtoDUNE
 3009 cryostat reach the outer boundary of the Veto. Position, direction and kinetic energy of neutrons
 3010 reaching that boundary are saved and used for input for the second simulation step. The surviving
 3011 fraction is $< 10^{-4}$, due to the effect of the cryostat itself as a moderator.

3012 The second step of the simulation consists of simulating neutron transport inside the boundary
 3013 of the Veto. The size of the population surviving the first simulation step is large enough to be
 3014 considered representative of the predicted neutron flux at the Veto boundary. Each event from the
 3015 named population is thus simulated many times ($\sim 10^3$), in order to reach a statistics equivalent
 3016 to 10^4 years of run of DS-20k.

3017 The same selection criteria described above are applied to determine the rate of surviving
 3018 neutrons: $(1.5 \pm 0.4 \pm 0.5) \times 10^{-2}$ in the full 200 t yr. This contribution is subdominant with respect
 3019 to the (α, n) background.

3020 **Neutrons from ^{222}Rn diffusion and surface plate-out** Radon progeny may plate-out on de-
 3021 tector materials exposed to air when ambient radon decays above or in contact with them. Charged
 3022 radon daughters that deposit on material surfaces can then induce (α, n) reactions, increasing the
 3023 neutron background. In particular, the long half-life of ^{210}Pb allows it to remain out of secular
 3024 equilibrium with the rest of the decay chain, and it may accumulate after prolonged exposures
 3025 to air. The presence of ^{210}Pb will eventually give rise to an equal activity of ^{210}Po , which may
 3026 α -decay during the experiment's operation. Additionally, the diffusion of ^{222}Rn inside of a material
 3027 strongly depends on the material's porosity. While this process is usually subdominant compared
 3028 to plate-out, ^{222}Rn can diffuse several microns into a material, while nuclei that have plated-out
 3029 typically only implant up to depths on the order of 100 nm. These background levels depend on
 3030 factors including the ^{222}Rn concentration in the air, the temperature and humidity at the time of
 3031 exposure, and the properties of the exposed material.

3032 Table XXXIII reports the surface of each component of the detector and the expected number
 3033 of neutrons due (α, n) reactions induced by the decay of ^{210}Po accumulated on the surface during
 3034 a reference exposure time of one month in regions with different Rn concentration. We have
 3035 considered a typical Rn concentration measured in an underground laboratory of 135 Bq/m^3 ,
 3036 normal air with 15 Bq/m^3 and a room with a Rn abatement system able to reach 0.1 Bq/m^3 . All
 3037 the materials are in contact with liquid argon when installed in the detector, and thus we have
 3038 considered both the α interaction with the material itself and with argon, which typically dominates.
 3039 Given the half life of ^{210}Po of 138 days, the resulting background is roughly proportional to the air
 3040 exposure time, unless it becomes significantly longer than $\simeq 100$ days. Assuming a linear relation
 3041 with the exposure time provides a conservative estimation. The plate-out velocity depends linearly
 3042 on the Rn concentration when other ambient conditions, such as humidity and ventilation, are kept
 3043 fixed.

3044 Limits for the exposure time of the various surfaces are derived by scaling the numbers in the
 3045 table and requiring that the neutron-induced background be well below our maximum allowed

3046 reference number of 0.1 events/200 t yr. The analysis reported in table XXXIII, shows that the
 3047 assembly of the detector could be done in an environment with Rn activity \simeq Bq/m³, assuming a
 3048 maximum exposure time of 6 months. More stringent limits for the exposure of the inner surfaces
 3049 of the TPC are derived from considering the pile-up events described in section 5.8.5 and also
 3050 including proper safety margins in this evaluation.

3051 Between production and installation/assembly, materials will be stored in a radon-free atmo-
 3052 sphere and subjected to material-specific surface cleaning protocols. Further details of this plan are
 3053 discussed in Sec. 11.

3054 **Atmospheric Neutrino-induced Nuclear Scatters** Coherent elastic neutrino-nucleus scat-
 3055 tering has been observed for the first time on an argon target by the COHERENT collaboration [72].
 3056 This process produces single-site nuclear recoils uniformly in the detector. We expect 3.2 neutrino
 3057 induced coherent nuclear scattering events during the 200 t y exposure. While these events will
 3058 represent an irreducible background to the WIMP search, their observation by DS-20k will con-
 3059 stitute the first measurement of coherent nuclear scattering of atmospheric neutrinos, representing
 3060 a significant milestone. Because this background is ultimately irreducible, it is not included in
 3061 Table XXVI, although it has been taken into account in the calculation of the sensitivity of the
 3062 DS-20k experiment reported in section 2.

3063 5.8.5. *Backgrounds from uncorrelated and correlated coincidences*

3064 **Uncorrelated surface α -decay and S2 coincidences**

3065 An α -decay occurring on the inner surface of the TPC may result in an S1-only NR if the
 3066 scintillation is produced on the TPB and/or ESR or if non-uniformities in the drift field cause a
 3067 loss of drifting electrons suppressing the associated S2 signal near the TPC walls. Totally unrelated
 3068 low-energy ERs in the LAr TPC may be mis-reconstructed as S2-only signals if they occur near
 3069 the top of the TPC and the S1 and S2 signals appear within \sim 1 μ s of each other and therefore
 3070 completely overlap. The random time between these uncorrelated events may allow them to appear
 3071 to come from the fiducial volume, and mimic the expected WIMP signals.

3072 The rate of these background events is proportional to the activity of α -emitting radioisotopes
 3073 on the TPC inner surfaces and to the rate of ERs near the LAr surface, dominated by γ -rays
 3074 emitted by radioactivity in the detector materials. Offline rejection techniques can be implemented
 3075 to suppress these backgrounds, and dedicated studies have been performed to assess their rejection
 3076 power. For example, longitudinal diffusion of the ionization cloud allows the time profile of the
 3077 S2 pulse to be used to infer with sufficient precision the position of the energy deposit along the
 3078 drift direction [16]. A detailed MC study has demonstrated that this technique can be used to
 3079 efficiently distinguish events originating at the top of the TPC (unresolved S1+S2) from those
 3080 with longer drift-times that were genuinely produced in the fiducial volume even in the low energy
 3081 range characteristic of WIMP-like signals, rejecting at least 90% of this class of background for
 3082 99% signal acceptance. Improved pattern recognition algorithms have been successfully developed
 3083 on simulated pulses that could potentially reject more than 75% of the overlapping pulses for drift
 3084 times as low as 0.75 μ s, however this is not considered here further.

3085 Based on these simulation results, the expected background rate from the current material ra-
 3086 dioactivity budget as detailed in Sec. 5.8.6, and the requirement to maintain a background ex-
 3087 pectation of <0.05 events for this class of background in the full 200 t yr exposure, specifications
 3088 of the maximum tolerable surface α contamination for the inner parts of the TPC have been de-
 3089 rived. The most stringent of those, 30 μ Bq/m², is placed on the ESR foils surface (see additional
 3090 discussion in Sec. 12.4). To reach and maintain these levels of contamination, protocols to ensure
 3091 cleanliness and to prevent Rn plate-out through the assembly of the detector in the dedicated clean
 3092 room have been developed (Sec. 11.7), and the maximum allowed Rn concentration is determined
 3093 to be 100 mBq/m³ assuming plate out rate as measured at SNOLAB on polyethylene and copper

Material	Surface [m ²]	inefficiency [n/alpha]	yield average [Bq]	activation [nAC]	bkg [Bq]	activation [nAC]														
Ti Vessel (in + out)	209	2.40E-7	1.63E-7	2.61E+1	3.22E-4	2.90E+0	3.58E-5	1.94E-2	2.39E-7											
ESR on Ti	263	2.40E-7	1.86E-7	1.94E+1	2.73E-4	2.16E+0	3.04E-5	1.44E-2	2.02E-7											
PEN on Ti	263	2.40E-7	1.86E-7	1.94E+1	2.74E-4	2.16E+0	3.05E-5	1.44E-2	2.03E-7											
PEN on TPC (for veto)	161	8.80E-7	1.86E-7	1.19E+1	6.16E-4	1.32E+0	6.84E-3	8.82E-3	4.56E-7											
ESR on TPC (for veto)	161	8.80E-7	1.86E-7	1.19E+1	6.13E-4	1.32E+0	6.81E-5	8.82E-3	4.54E-7											
PCB Veto (Arlon)	15	8.80E-7	1.82E-7	1.11E+0	5.59E-5	1.23E-1	6.21E-6	8.21E-4	4.14E-8											
SiPMs veto	5	8.80E-7	1.83E-7	6.25E-1	3.18E-5	6.95E-2	3.54E-6	4.63E-4	2.36E-8											
Acrylic barrel ext	46	5.81E-6	1.83E-7	3.40E+0	1.14E-3	3.78E-1	1.26E-4	2.52E-3	8.43E-7											
Ti structure SiPMs	92	2.22E-6	1.63E-7	1.15E+1	1.31E-3	1.28E+0	1.46E-4	8.52E-3	9.73E-7											
Acrylic bricks	80	2.22E-6	1.83E-7	5.91E+0	7.56E-4	6.57E-1	8.40E-5	4.38E-3	5.60E-7											
PCB (Arlon)	63	2.22E-6	1.82E-7	4.66E+0	5.92E-4	5.17E-1	6.58E-5	3.45E-3	4.39E-7											
SiPMs	21	2.22E-6	1.83E-7	2.63E+0	3.37E-4	2.92E-1	3.75E-5	1.95E-3	2.50E-7											
Acrylic plates A+K out	23	2.22E-6	1.83E-7	1.70E+0	2.17E-4	1.89E-1	2.41E-5	1.26E-3	1.61E-7											
Acrylic plates A+K in	23	2.22E-6	1.83E-7	1.70E+0	2.17E-4	1.89E-1	2.41E-5	1.26E-3	1.61E-7											
Clevios A+K	23	2.22E-6	1.83E-7	1.70E+0	2.21E-4	1.89E-1	2.45E-5	1.26E-3	1.63E-7											
TPB A+K	23	2.22E-6	1.85E-7	1.70E+0	2.21E-4	1.89E-1	2.45E-5	1.26E-3	1.63E-7											
Acrylic barrel int	44	5.81E-6	1.83E-7	3.25E+0	1.09E-3	3.61E-1	1.21E-4	2.41E-3	8.06E-7											
Clevios barrel	8.8	5.81E-6	1.83E-7	6.51E-1	2.18E-4	7.23E-2	2.43E-5	4.82E-4	1.62E-7											
Acrylic holding plate	88	5.81E-6	1.83E-7	6.51E+0	2.18E-3	7.23E-1	2.42E-4	4.82E-3	1.61E-6											
ESR out	44	5.81E-6	1.86E-7	3.25E+0	1.11E-3	3.61E-1	1.23E-4	2.41E-3	8.20E-7											
ESR in	44	5.81E-6	1.86E-7	3.25E+0	1.11E-3	3.61E-1	1.23E-4	2.41E-3	8.20E-7											
TPB in	44	5.81E-6	1.85E-7	3.25E+0	1.11E-3	3.61E-1	1.23E-4	2.41E-3	8.19E-7											
Grid	5	2.22E-6	1.55E-7	6.25E-1	6.81E-5	6.95E-2	7.56E-6	4.63E-4	5.04E-8											

TABLE XXXIII. Simulated radiogenic neutron rates from surface Rn-222 daughters plate-out over the full 200 t yr fiducial volume exposure. The Rn concentration is 135 Bq/m³ (UG exposure), 15 Bq/m³ (Surf. exposure) and 0.1 Bq/m³ (Rn abated exposure). The exposure time is 1 month. The residual neutron background in 200 t yr, obtained summing all the contributions, is reported in the first row of table, in bold characters.

3094 surfaces [73], and allowing for up to six months of exposure time during TPC construction.

3095 **Correlated ER + Cherenkov coincidences** High-energy γ -rays emitted by detector components
 3096 may induce Cherenkov radiation in the LAr or in the transparent anode and cathode windows
 3097 of the TPC. The time profile of the Cherenkov emission is compatible with the fast component of
 3098 LAr scintillation (~ 10 ns). Thus, the combination of a regular ER S1 signal with some Cherenkov
 3099 light will boost the prompt fraction for the reconstructed signal, potentially causing the event to fall
 3100 in the NR expectation region. Monte Carlo simulations including Cherenkov radiation show that
 3101 the single γ -ray from the dominant emitters ^{208}Tl and ^{40}K in the photodetectors have negligible
 3102 probabilities to both induce a single-sited ER in the Fiducial Volume (FV) and to generate the
 3103 necessary Cherenkov emission to shift the event into the NR expectation band. A FV cut of 70 cm
 3104 from the top and bottom of the detector efficiently removed these events, after which <0.018 events
 3105 are expected to be found in the DM ROI in the 200 t yr exposure.

3106 **Uncorrelated ER + Cherenkov coincidences** Additional studies estimate the probability of
 3107 an accidental coincidence between an ^{39}Ar decay inducing an ER in the FV and a γ -ray interaction
 3108 in the TPC windows producing Cherenkov light without scintillating in the LAr. Based on a
 3109 ± 150 ns coincidence window and the current radioactivity budget, the rate of coincidence events
 3110 mis-reconstructed as NRs is expected to be <0.03 events in the 200 t yr exposure.

3111 5.8.6. Electron Recoil-background rates

3112 DS-20k will suppress the rate of ER-induced backgrounds (from β and γ) by using a UAr target
 3113 that is depleted in ^{39}Ar , employing strict material qualification standards to reduce the material
 3114 induced background, and utilizing a dual-phase LAr TPC, in order to detect multi-site interactions.

3115 The total rate of ER-like events is the sum of several contributions: ^{39}Ar , cosmogenic activation,
 3116 and γ radioactivity, discussed in what follows.

3117 **^{39}Ar** The ^{39}Ar activity of the UAr is assumed to be (0.73 ± 0.11) mBq/kg, as measured in DS-50.
 3118 Given the total mass of UAr 50 t in the TPC and 32 t in the veto, this contributes 36 Hz to the
 3119 ER rate in the TPC and 26 Hz to the ER rate in the veto.

3120 **Cosmogenic activation** Cosmogenic activation of the UAr is evaluated assuming a realistic
 3121 exposure history for the Ar extraction, storage and transportation. We consider that the UAr
 3122 extracted at the Urania plant in Colorado (USA) will first be shipped to the Aria facility In
 3123 Sardinia (Italy) for purification and then to LNGS for storage and detector filling. Air transport
 3124 will be avoided in all such transfers. A total of 134 days of exposure at different altitudes and
 3125 locations are considered. Production rates of ^{39}Ar and ^{37}Ar estimated in [74] for neutrons, protons,
 3126 muons and gamma rays are used, including correction factors for different altitudes and locations
 3127 obtained following the method proposed in [75]. In these conditions, the ^{39}Ar activity is calculated
 3128 to be (0.0190 ± 0.0016) mBq/kg, which is 2.6 % of the activity measured in DS-50 for UAr. The
 3129 rate of cosmogenic production of ^3H in Ar is estimated to be about 9 $\mu\text{Bq}/\text{kg}$ for the same exposure.
 3130 It can be concluded that, in the realistic exposure history considered, the cosmogenic production
 3131 of ^{39}Ar is not an issue for DS-20k. Activation yields of other cosmogenic isotopes induced in argon
 3132 have also been considered, although in general they have shorter half-lives.

3133 For copper and titanium the production rates of the cosmogenic isotopes can be estimated by tak-
 3134 ing into account the measurements or calculations available in the literature. Then, the cosmogenic-
 3135 induced activity is computed assuming various scenarios for the exposure history. Considering the
 3136 half-lives of the different cosmogenic products, the most relevant isotopes, generating gammas
 3137 around the DS-20k active volume, are estimated to be ^{57}Co and ^{60}Co in copper and ^{46}Sc in tit-
 3138 anium. Even assuming a conservative long exposure on the surface of 10 years, the activity of copper

Source	Mass [kg]	^{238}U up [Bq]	^{238}U mid [Bq]	^{238}U low [Bq]	^{232}Th [Bq]	^{235}U [Bq]	^{137}Cs [Bq]	^{60}Co [Bq]	^{40}K [Bq]	^{54}Mn [Bq]	^{176}Lu [Bq]	^{46}Sc [Bq]
PDUs and cables	193	45	12	214	11	2.5	0.4	0.6	130	0	0	0
vPDUs and cables	42	12	3.2	95	3.5	0.6	0.2	0.2	34	0	0	0
Gd-PMMA	$1.2 \cdot 10^4$	3.5	14	23	3	0.2	2.8	2.6	404	0	0.25	0
Ti vessel	$8.2 \cdot 10^3$	65	0.9	568	0.9	3.0	0	0	4.9	0	0	26
Cryostat	$2.8 \cdot 10^5$	$6.4 \cdot 10^4$	$5.9 \cdot 10^4$	$5.7 \cdot 10^5$	$7.3 \cdot 10^4$	$2.9 \cdot 10^3$	$1.2 \cdot 10^4$	$6.6 \cdot 10^3$	$3.5 \cdot 10^5$	0	0	0

TABLE XXXIV. Summary of the gamma activities used in the Monte Carlo simulation of gamma backgrounds, grouped by source category.

would be at the level of 10 Bq. For titanium, the saturation activity of ^{46}Sc is estimated, following different approaches, to be around 4 mBq/kg, in agreement with available measurements; then, for a foreseen mass of 9.3 t a total activity of ≈ 37 Bq is expected. Other Sc isotopes have very short half-lives.

For stainless steel, the cosmogenic activities are estimated as 50 Bq per tonne, for 1 yr of exposure; ^{54}Mn has been identified as a potential relevant contributor to background. However, given the mass of stainless steel in the detector, the corresponding expected contribution to the γ rate is negligible compared to the overall rate in the TPC.

The possible cosmogenic activation of acrylic and gadolinium compounds is being explored, although no hint of cosmogenic radioisotopes has appeared when assaying samples of these materials with HPGe crystals.

As table XXXV summarizes, the background produced by the cosmogenic activation of the most massive detector components is small in comparison to the overall rate expected from gamma-ray activity (described in the next section), which allows us to relax additional limitations on the surface residency time of these materials and requirements for storage and transportation during the detector construction and operation.

Gamma backgrounds in the TPC and in the inner Veto Gamma rays emitted from the bulk of materials are relevant for assessing the overall performance of DS-20k since these can induce acceptance losses via ER + NR pile-up in the TPC or accidental coincidence between the Veto and TPC signals that mimic the neutron capture signature. Detailed Monte Carlo simulations of γ s from the full set of detector components and chains were performed in order to estimate the γ background rates in the TPC and in the Veto. The simulation inputs are the γ activities of all components, estimated from the radioassay campaign, for the chains reported in table XXXIV. Gamma activities are reported in table XXXIV grouped by detector components. The category "PDUs" corresponds to activity evaluated for all components in the 8280 PDMs that instrument the TPC, read out with 1 TIA FEBs, hosted in the baseline PDU+ design. Similarly, the category "vPDUs" corresponds to the 1920 PDMs that instrument the Veto, also hosted in the baseline vPDU+ design, read out with ASIC. These reported activities also include cables. The Gd-PMMA category refers to the activity of the 11 ton of Gd-loaded acrylic as evaluated from assay campaign, including the contribution from surfactant using during the production. The cosmogenics activation is also included in the budget. This contribution is dominated by ^{46}Sc produced in the titanium vessel, as described in above.

The expected γ event rates reported in table XXXV are computed as the rate of γ interactions producing any energy deposition greater than zero in the TPC and Veto in G4DS simulations of the gamma activities in table XXXIV. The total γ rate, summing over all contributions in table XXXV, is 52 Hz in the TPC and 135 Hz in the Veto.

Summary of the ER background rates

The total rate of ER-like events, summing ^{39}Ar , cosmogenic activation, and γ activity, described in detail in this section, is estimated to be 88 Hz in the TPC and 161 Hz in the inner Veto.

The expected ER background event rate surviving fiducialization and rejection of multi-site interactions, in the [10, 50] keV_{ee} energy range, is dominated by ^{39}Ar and corresponds to 1.2 Hz,

Source	Total source activity [Bq]	TPC rate [Hz]	Veto rate [Hz]
PDUs	420	29	11
vPDUs	150	2.3	47
Gd-PMMA	450	20	40
Ti vessel	760	0.5	35
Cryostat	$1.2 \cdot 10^6$	0.03	2.6

TABLE XXXV. Total γ activity and γ interaction rates in the TPC and Veto, resulting from the total source activity (produced by summing the contributions of all chains in table [XXXIV](#)).

3182 or 4×10^8 events in the full 200 t yr exposure. Those are efficiently suppressed by many orders of
 3183 magnitude using Pulse Shape Discrimination (PSD) [76]. This background discrimination technique
 3184 allows the WIMP search region of interest to be defined such that <0.1 ER backgrounds are expected
 3185 in the full 200 t yr exposure. Details of the pulse shape discrimination analysis are reported in
 3186 Sec. [12.1.2](#).

3187 Given these rates, the dead time, defined as the probability to tag a ^{39}Ar /gammas as neutron in
 3188 a time coincidence window of 800 μs , is 6.1% from TPC given an energy threshold of 50 keV_{ee} and
 3189 it is 7.6% from veto given an energy threshold of 200 keV_{ee}. Details about dead time estimation
 3190 and pile-up mitigation are reported in sections [12.2.2](#) and [12.3](#) respectively.

3191

6. THE PRODUCT BREAKDOWN STRUCTURE

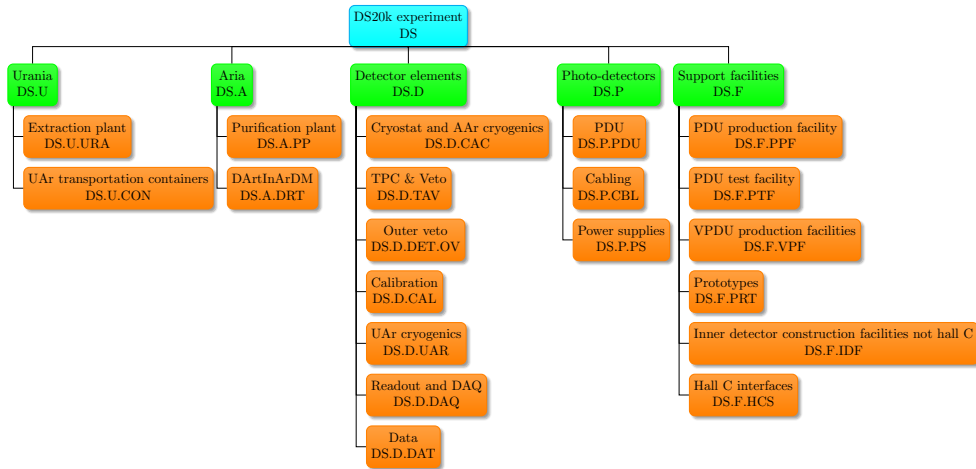


FIG. 55. Product Breakdown Structure (PBS) of the DS-20k experiment showing the three branches and sub-branches together with their names.

3192 The product breakdown structure (PBS) of the DS-20k experiment is shown in figure 55. We
 3193 identify five main branches of products (with green boxes on top): the first two branches refer to
 3194 the extraction (Urania) and distillation (Aria) of the UAr. The next two describe the parts of
 3195 the DS-20k Detector installed in the Hall C of LNGS. In particular "Detector elements" represents
 3196 all the mechanical parts of the detector and of the cryogenics systems while "Photo-detectors"
 3197 includes SiPMs and electronics up to the connection to the data acquisition system. The remaining
 3198 item, Support facilities, describes facilities used to construct, test or assemble parts of the detector.
 3199 Support facilities may be located in various Institutions of the collaboration. Items related to the
 3200 interfaces to Hall C in LNGS are part of this branch. Finally we include here the DS-20k prototypes.
 3201

3202 The orange boxes detail the parts and sub-parts making up each specific object. The next three
 3203 sections are devoted to a detailed technical description of each green branch and their sub-branches.
 3204 Two further levels, detailing the items shown in orange, are introduced where necessary. Section 11
 3205 describes the activities related to the construction, installation and commissioning of the DS-20k
 3206 Detector. The items of the branches DS.U, DS.A and DS.F are functional to this goal.

3207 The naming scheme of each product is DS.X.YYY.ZZZ.KKK, where X stands for U, A, D, P or F
 3208 indicating Urania, Aria Detector elements, Photo-detectors or Facilities. YYY is a three character
 3209 label of the orange product, ZZZ and KKK refer to the two additional sub levels, not shown in
 3210 figure 55 that will be introduced in the following chapters when necessary to describe details. A
 3211 maximum of 5 levels are considered.

7. TECHNICAL DESCRIPTION: DS-20K DETECTOR

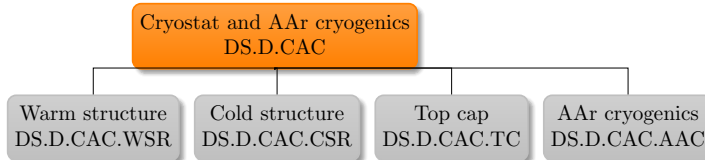
3211 PBS Item: DS.D

3212 This section provides a detailed description of all the parts of the DS-20k detector (DS.D) following the PBS shown in Figure 55. In the following subsections details up to level 5 are included where necessary.

3217 7.1. Membrane Cryostat and AAr cryogenics

3218 PBS Item: DS.D.CAC

3219 Figure 56 shows the branch of the PBS with the membrane cryostat. The DS-20k cryostat is
 3220 based on the successful experience of the deployment of two large membrane cryostats at CERN in
 3221 support of the ProtoDUNE project. The membrane cryostat technology in use was initially developed
 3222 for overseas transport of liquefied natural gas (LNG). The specific membrane technology is
 3223 developed by the French engineering firm Gaztransport & Technigaz (GTT). CERN has executed
 3224 a collaboration agreement with GTT to develop and adapt its MarkIII membrane cryostat technology
 3225 for particle physics detectors. This technology is owned by GTT and protected by Intellectual
 3226 Property regulations.



3228 FIG. 56. PBS of the membrane cryostat

3229 The DS-20k cryostat will retain all major elements of the ProtoDUNE cryostats, namely a stain-
 3230 less steel inner cold membrane in contact with the cryogenic liquid, the foam insulation panels
 3231 and a warm steel supporting outer structure. The cold membrane tank is made of a stainles-
 3232 steel, 1.2 mm thick leak-tight liner that contains the cryogenic liquid. This membrane liner has a
 3233 special corrugation that allows it to expand and contract in both transverse directions to provide
 3234 mechanical relief to strains resulting from temperature changes.

3235 The insulation is composed of two layers of polyurethane, providing a thermal barrier between the
 3236 membrane at the liquid cryogen temperature and the support structure at ambient temperature.
 3237 A secondary barrier, located between the layers of insulation, is a physical protection providing
 3238 secondary containment for the liquid cryogen in case of a failure of the first membrane.

3239 A warm steel structure, consisting of vertical and horizontal beams and a carbon steel tertiary
 3240 membrane, surrounds the insulation and provides mechanical support.

3241 The main components of the MarkIII GTT technology are visible in Fig. 57 (right panel). Fig.
 3242 57, left panel shows a view of the internal part of one of the two ProtoDUNE cryostats at CERN.

3243 Two cryostats of the same size as the one proposed here have been built at CERN and brought
 3244 into successful operation, one in the second half of 2018 and one in 2019. The experience gained
 3245 in the design, construction and operation will be fully translated to the DS-20k project. For this
 3246 reason, the same mechanical constraints, dimensions and thermal properties have been kept. A
 3247 Memorandum of Understanding between CERN and INFN is presently in advanced discussion.
 3248 It is aiming at regulating the role of CERN and INFN in the process of the construction of the
 3249 cryostat and of the AAr cryogenic system. Funds for both the two items are provided by INFN.

Parameter	Value
Nominal cryostat internal width	8548 mm
Nominal cryostat internal length	8548 mm
Nominal cryostat internal height	7900 mm
Maximum filling level	96 %
Nominal AAr mass	700 t
Steel Mass	217 t
Insulation Mass	62 t

TABLE XXXVI. Cryostat design parameters.

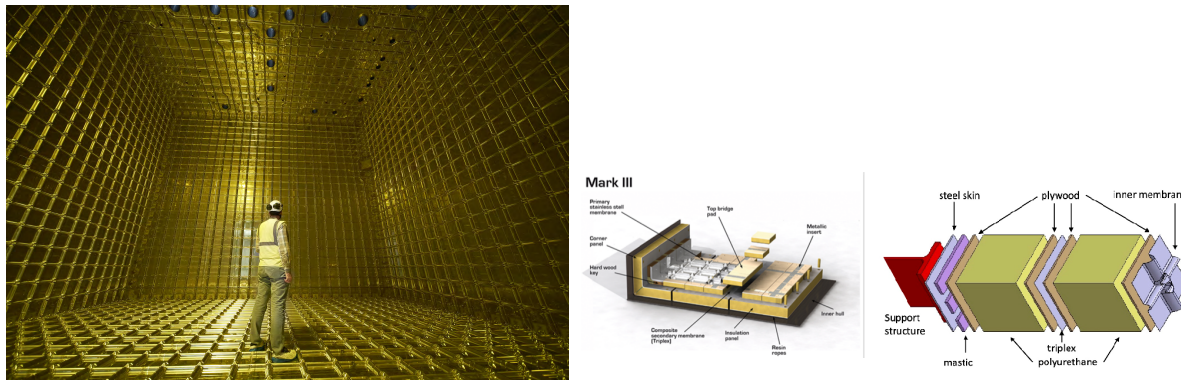


FIG. 57. **Left:** A view from inside of one of the ProtoDUNE cryostat operating at CERN. **Right** Membrane cryostat components (MarkIII technology from GTT) with a cross-section of the containment system and cold membrane.

3251 A 3D external view of the cryostat being planned for DS-20k is shown in Fig. 58.

3252 *7.1.1. Warm Structure*

3253 PBS Item: DS.D.CAC.WSR

3254
 3255 The outer warm structure, which provides the mechanical support for the membrane and its in-
 3256 sulation, consists of a net of vertical and horizontal IPEV600 profiles. The overall outer dimensions
 3257 are: width 11 410 mm, length 11 410 mm, height 10 760 mm. This outer structure is designed to
 3258 withstand the hydrostatic load of the liquid argon, the pressure of the gas volumes and all possible
 3259 external constraints (e.g., gravitational, seismic, etc.). The structural beams are made of a special
 3260 carbon steel alloy (S460ML 1.8838), able to maintain its mechanical properties down to 220 K.
 3261 Inside the beam structure, a skin of carbon steel plates with reinforcement ribs is welded to provide
 3262 an additional barrier to the outside. The cryostat is simply supported on a dedicated reinforced
 3263 concrete basement (13.8 m x 13.8 m) that will be built on top of the present Hall C floor. In the
 3264 case of seismic event, the cryostat is constrained laterally by 24 custom designed brackets bolted
 3265 to the concrete basement, as shown in Fig. 58. The brackets, shown in detail in Fig. 59, are also
 3266 manufactured in S460ML. The warm structure and top caps isometric view are shown in Fig. 60.

3267 All structural analyses required in support of the construction are already available, including a
 3268 current seismic analysis, which takes into account the particular conditions of LNGS. This latter
 3269 has been submitted to the local authorities responsible for seismic authorization procedures and
 3270 approved in June 2021.

3271 The entire vessel will be filled to the 96th percentile of its volume with liquid argon, requiring a
 3272 fill of approximately 700 t. The remaining 4 % of the volume will be filled with gaseous argon, at a
 3273 pressure ranging from 50 mbar to 70 mbar above atmospheric pressure. The vessel is protected by
 3274 a suitably-sized relief valve, opening at an over pressure of 350 mbar.

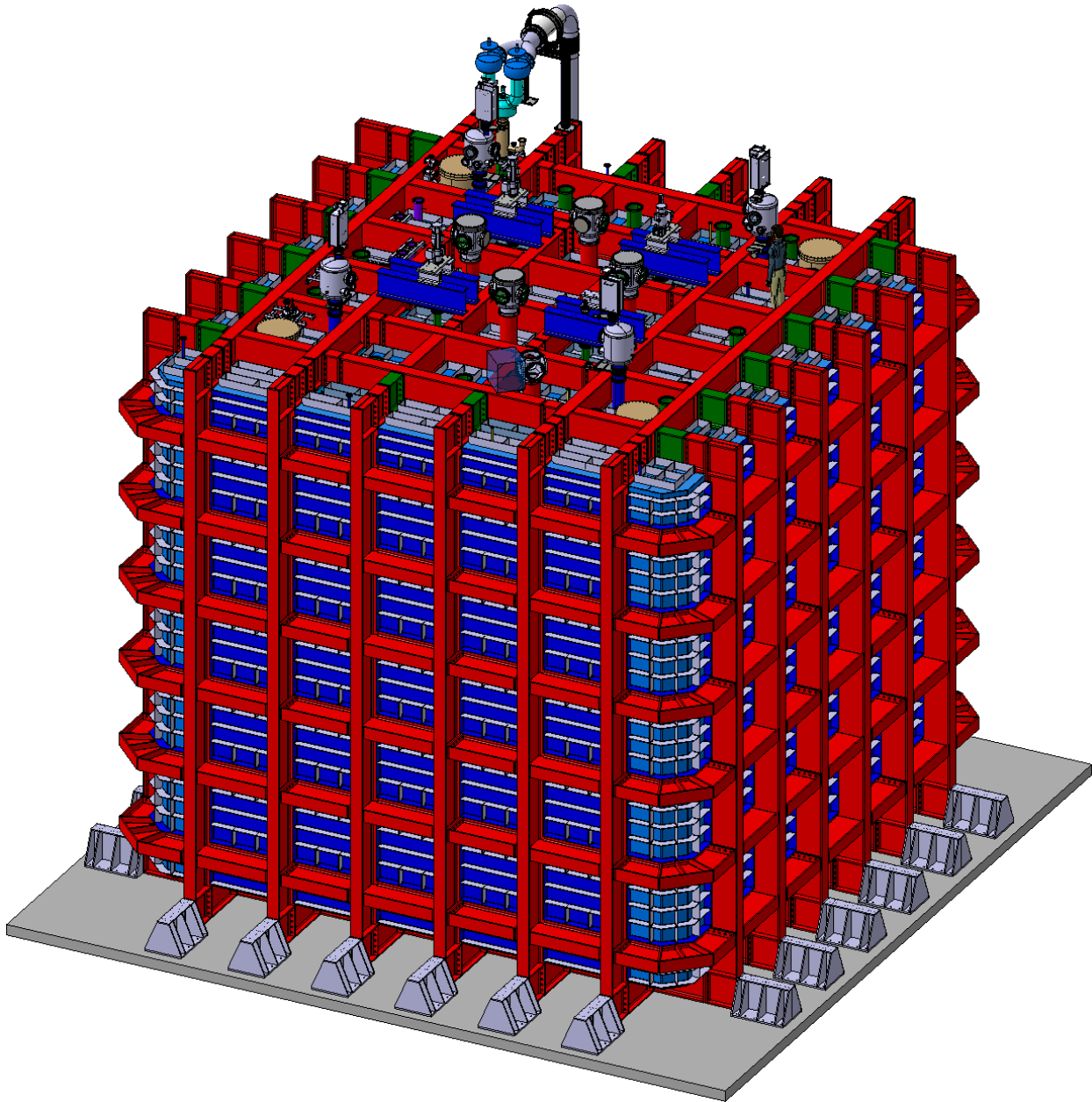


FIG. 58. 3D external view of the DS-20k AAr cryostat. The concrete basement and the seismic brackets are also shown.

3275

7.1.2. Cold structure

3276

PBS Item: DS.D.CAC.CSR

3277

3278 The cold vessel is installed inside the warm support structure. It consists of a primary corrugated
 3279 stainless steel membrane in contact with the liquid, two layers of thermal insulation, a secondary
 3280 membrane which provides secondary liquid containment and four layers of plywood to support
 3281 the foam. Thermal requirements determine the minimum thickness of insulation. A carbon-steel
 3282 skin, just outside the insulation, provides an effective gas enclosure, permitting proper handling
 3283 of the argon atmosphere inside the cryostat. While the liquid argon is contained by the primary
 3284 stainless steel corrugated membrane, the second membrane is present as a safety backup should

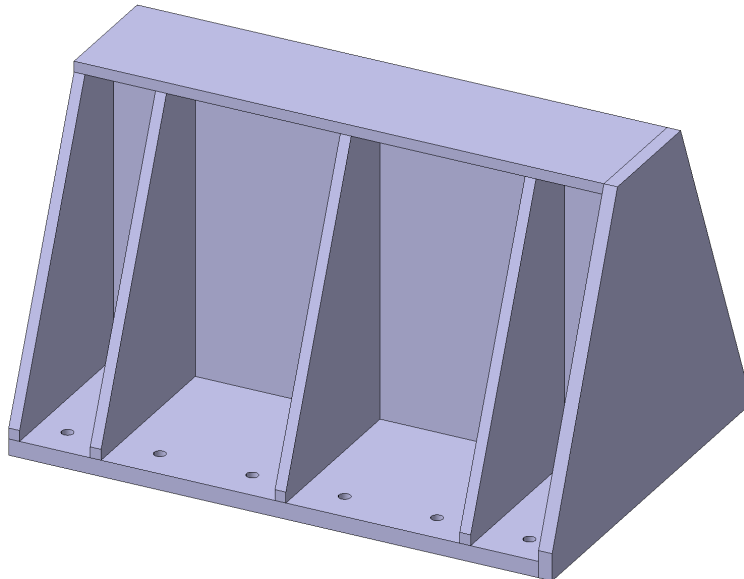


FIG. 59. Detailed view of the cryostat seismic brackets.

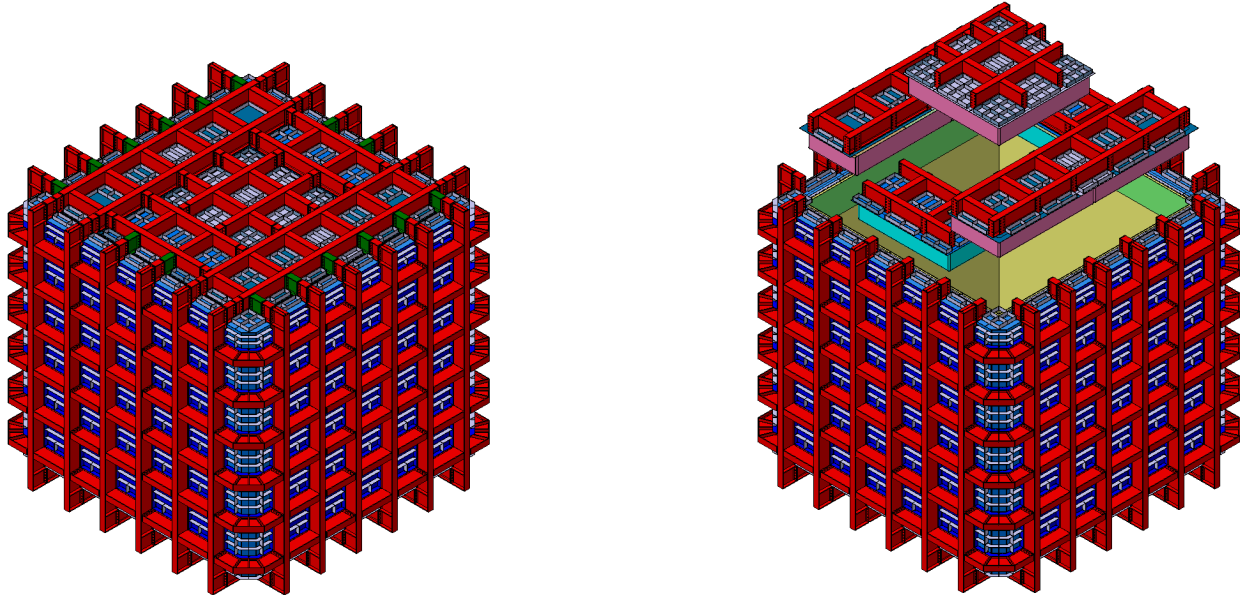


FIG. 60. Cryostat warm structure and top caps isometric view.

3285 the innermost membrane experience a leak. The volume of the insulation is operated in a nitrogen
 3286 atmosphere, at a pressure of a few mbar above atmospheric pressure. A 10 mm thick carbon steel
 3287 plate attached to the outermost structural beams seals the insulation space on the outside and acts
 3288 as a *de facto* tertiary membrane.

3289

7.1.3. Top caps

3290 PBS Item: DS.D.CAC.TC

3291

3292 The roof structure is composed of five pre-assembled modules called “top caps”: one central

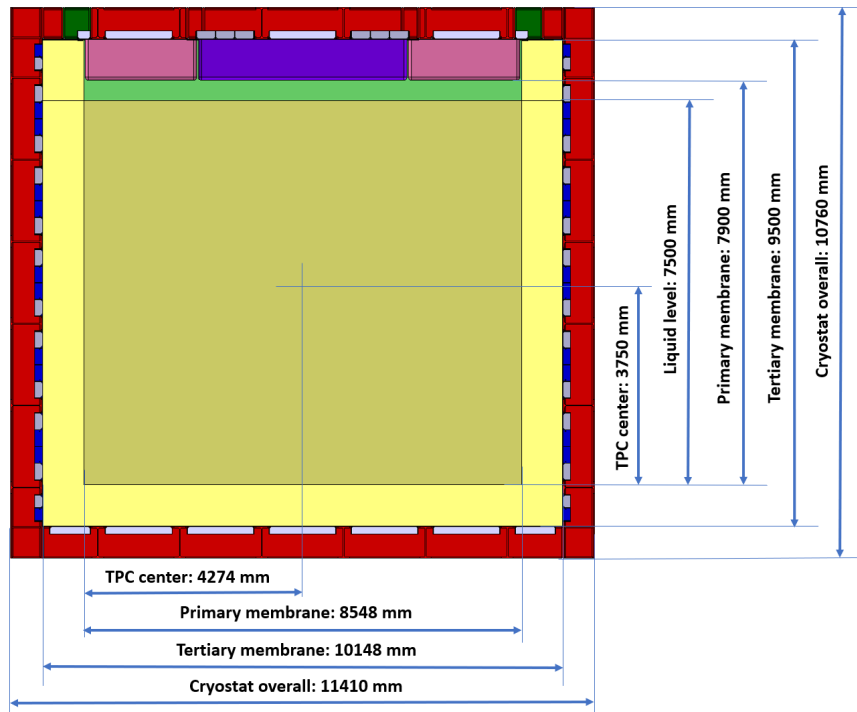


FIG. 61. DarkSide-20k Cryostat front view cut with dimensions. The membrane internal dimension does not include the space used by the corrugation.

3293 top cap ($4.1 \times 4.1 \text{ m}^2$) and four lateral top caps of two different shapes and sizes. These top caps
 3294 will be bolted together and to the lower vessel through several roof link modules, and eventually
 3295 shims will ease the installation phase. Each top cap consists of the steel IPEV600 beam frame, the
 3296 10 mm thick steel plate (warm skin), the thermal insulation and a thin metallic plate to support
 3297 the insulation (primary membrane), pipes and flanges for penetrations, welded to the warm skin.
 3298 Executive design and manufacturing of the the top caps cold part will be carried out at CERN.
 3299 The top caps allocate the support structure to which the detector will be hung, as shown in Fig.
 3300 63. A picture of the five top cap modules connected through the link modules is shown in Fig. 62.

3301 The modules are designed to be transportable and liftable using the available lifting equipment
 3302 in the Hall C. The top caps, once assembled to the rest of the warm structure, will be able to safely
 3303 support the dry static weight of the full assembled detector inside the titanium vessel, before the
 3304 filling phase. The design of the primary membrane will safely withstand all the existing mechanical
 3305 loads while minimizing the thermal link between cold and warm surfaces. The top caps will host all
 3306 the required penetrations for services and readout cables; the list of penetrations, their dimensions
 3307 and positions is shown in Fig. 64.

3309 7.1.4. AAr cryogenics

3310 PBS Item: DS.D.CAC.AAC

3311
 3312 The AAr cryogenics system combines the expertise of ProtoDUNE and DarkSide-50 experiments.
 3313 The system uses liquid nitrogen as refrigerant to cool and liquefy AAr. After purification in the
 3314 gas phases, the argon in the re-circulation is collected in the phase separator and then returned to
 3315 the cryostat via a guide system designed to achieve the desired temperature uniformity across the
 3316 entire volume. Radon emanated from warm components, like the chimney feedthroughs on the roof
 3317 of the cryostat, is captured by an active charcoal-based cold radon trap in argon gas re-circulation
 3318 loop, prior to its liquefaction and re-injection in the cryostat.

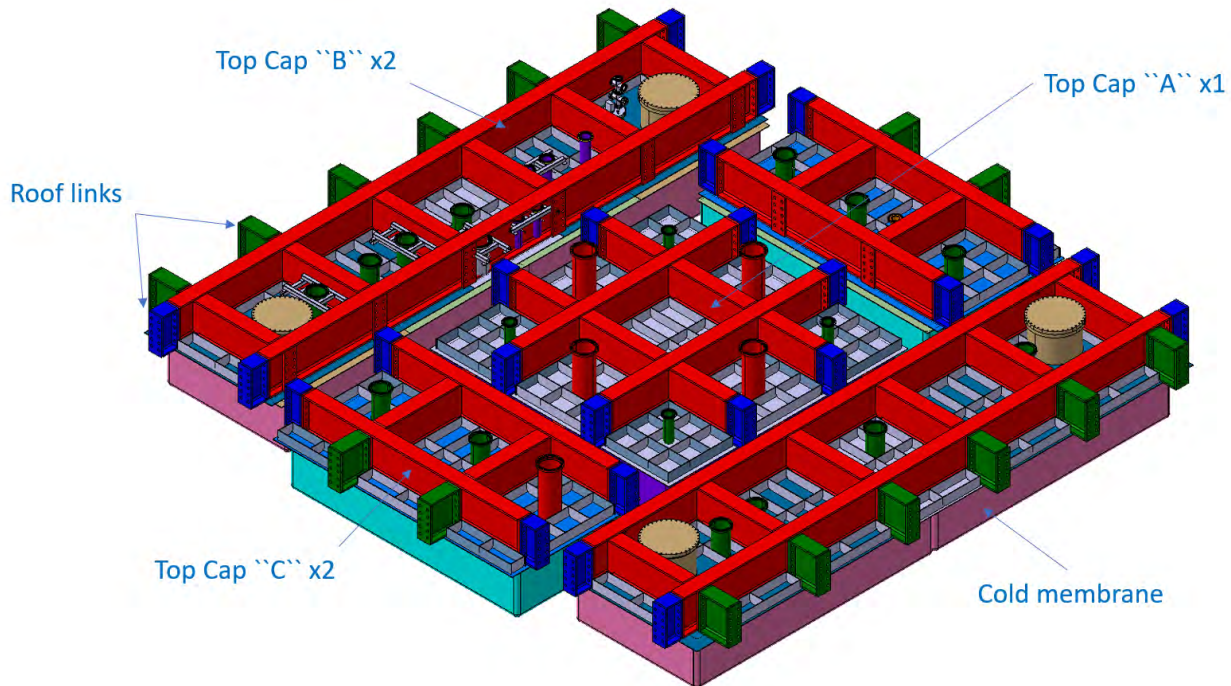


FIG. 62. Top caps modules components.

The AAr cryogenics system not only handles the AAr, but also functions as a thermal bath surrounding the titanium vessel filled with the UAr volume and containing the inner detector. The pressure of the AAr and UAr baths must be always balanced and controlled synchronously in all operation conditions, including emergency mode with total power failure, in order to ensure stable operations of the TPC, as well as the safe accommodation of UAr. Detailed requirements for the AAr cryogenics system are listed in Table XXXVII. In particular, Table XXXVII specifies the net available cooling power for the AAr cryogenics, once the heat loads from the detector have been subtracted from the cooling power that will be available in LNGS Hall C for DarkSide-20k. All argon filled into the cryostat must pass first through a hot zirconium getter and then through an activated charcoal trap operating near liquid argon temperature. A viable alternative could be a cold filter made of oxygen-free high conductivity copper (OFHC) pellets, whose operation would need to be demonstrated through suitable R&D program. Based on past operational experience the use of cold filters based on molecular sieves and/or alumina pellets covered by copper is disallowed on the basis of contamination from ^{222}Rn . General cryogenic system slow control will be included. QA sampling on levels of contamination of O_2 and N_2 , filled or circulated, will be done online.

Fig. 65 shows the conceptual schematic of the AAr cryogenic system during operation. The paths highlighted refer to the operation phase, with liquid circulation, but no purification. Purple lines are for liquid argon, the one in dark and light pink are for cold and warm argon gas.

Parameter	Value
Static heat load from the cryostat	6 kW
Maximum AAr circulation mass flow	300 g/s
Turnover time at maximum circulation	27 days
Minimum AAr heat exchanger efficiency	95 %
Nominal absolute operating pressure	1075 mbar
Maximum relative operating pressure	200 mbarg
Pressure regulation stability	1 mbar

TABLE XXXVII. AAr cryogenic system design parameters.

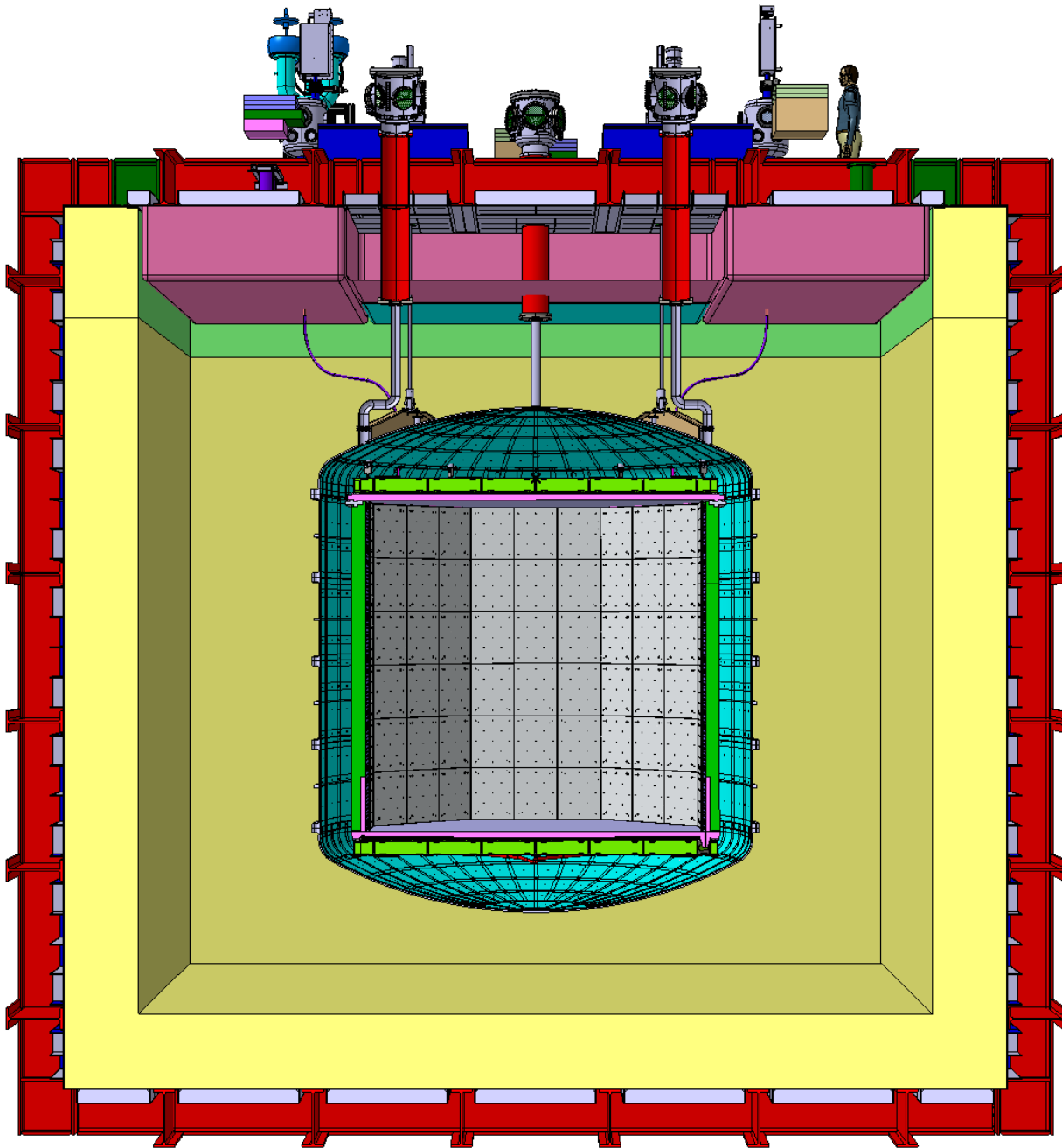


FIG. 63. DarkSide-20k Inner Detector, Titanium vessel and Cryostat front view cut.

3337

7.1.5. Total cryogenics power consumption

3338 Table [XXXVIII](#) shows the total cryogenics power consumption, including the contribution from
 3339 the cryostat and that of the detector. The last line reports the cooling power available today
 3340 in Hall-C assuming realistic estimation of the LN_2 recovery. A new closed circuit LN_2 recovery
 3341 system, serving all the experiments in LNGS, is foreseen during the time of the commissioning and
 3342 operation of DS-20k. Details of the inner detector heat load are described in section [7.5](#).



FIG. 64. Cryostat top caps penetrations.

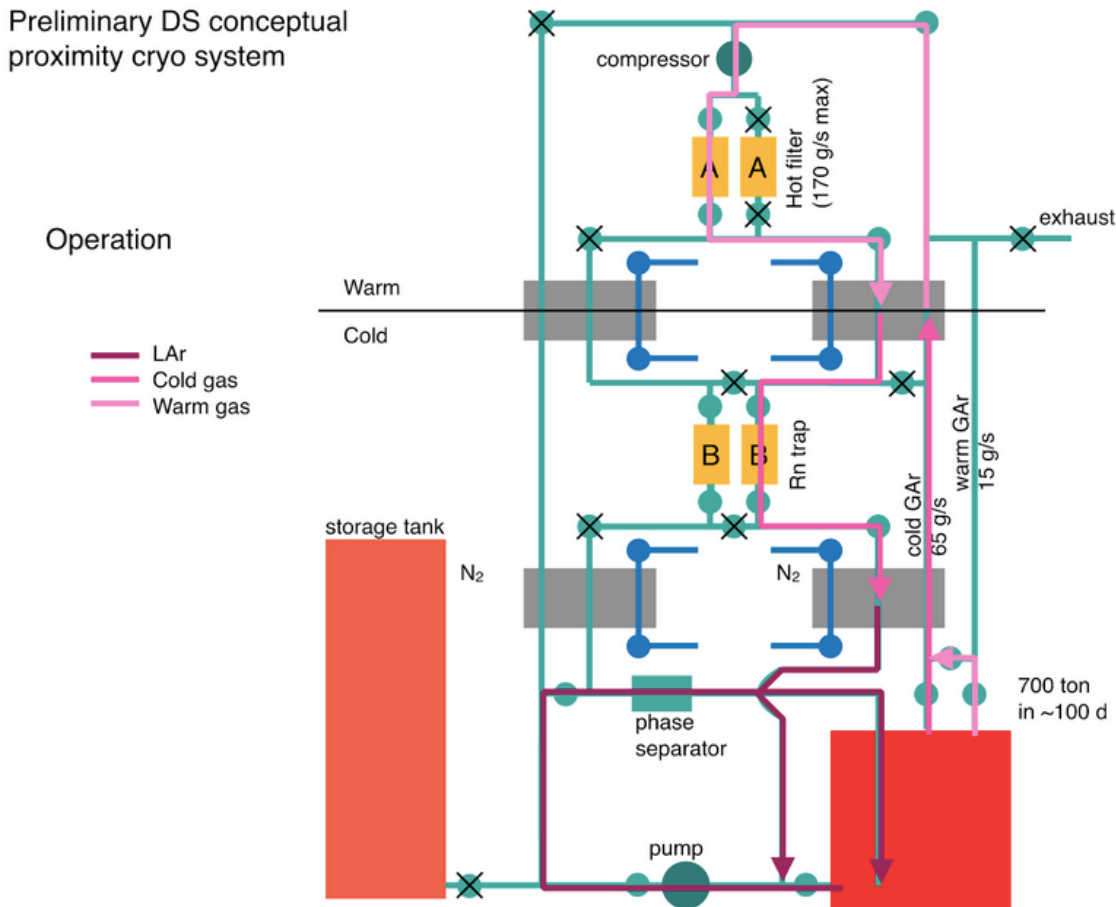


FIG. 65. Conceptual schematics of the AAr cryogenic system during operations of the detector.

Parameter	Value
Heat load from the cryostat walls	5.0 kW
Heat load from the cryostat roof	1.0 kW
Heat load from AAr cryogenics liquid recirculation	2.0 kW
Gas argon circuit (transfer lines and heat transfer inefficiencies)	1.0 kW
Outer Veto electronics 0.1 kW	
Total uncertainty	1.0 kW
Total cryostat heat load (with liquid recirculation)	10 kW
Total cryostat heat load (no liquid recirculation)	8 kW
Inner detector heat load from TPC electronics including cables	1 kW
Internal detector heat load from Veto electronics including cables	0.35 kW
Gas pocket generation	0.5 kW
UAr circuit	0.4 kW
Total inner detector heat load	2.25 kW
Total cryostat and inner detector heat load (no liquid recirculation)	10.5 kW
Today available Hall-C cooling power including LN₂ recovery	10.3 kW

TABLE XXXVIII. AAr cryogenics power consumption.

3343

7.2. TPC and inner Veto

3344

PBS Item: DS.D.TAV

3345

The overall motivations driving the design of the DS-20k inner detector are compactness and simplicity while addressing all of the challenges present in a large underground, low-background experiment. Fig. 66 shows the branch of the PBS detailing the components of the TPC + Veto assembly, which is referred to as the *inner detector*. These considerations have led to a high degree of integration among the detector components. The panels forming the barrel of the TPC will use the same ultra-pure PMMA as the anode and cathode plates, but doped with 1% gadolinium to form the neutron capture target for the Veto. The assembled barrel will serve as core of the inner detector design providing overall mechanical support, field cage functionality, well-defined grounding for the electrostatic fields, neutron moderation and capture, differential thermal contraction management, support for the wire grid frame, UAr flow control, and mounting support for the resistor links, reflector panels, and VPDU+s. It should be noted that this all accomplished without additional hardware or many dedicated sub-systems.

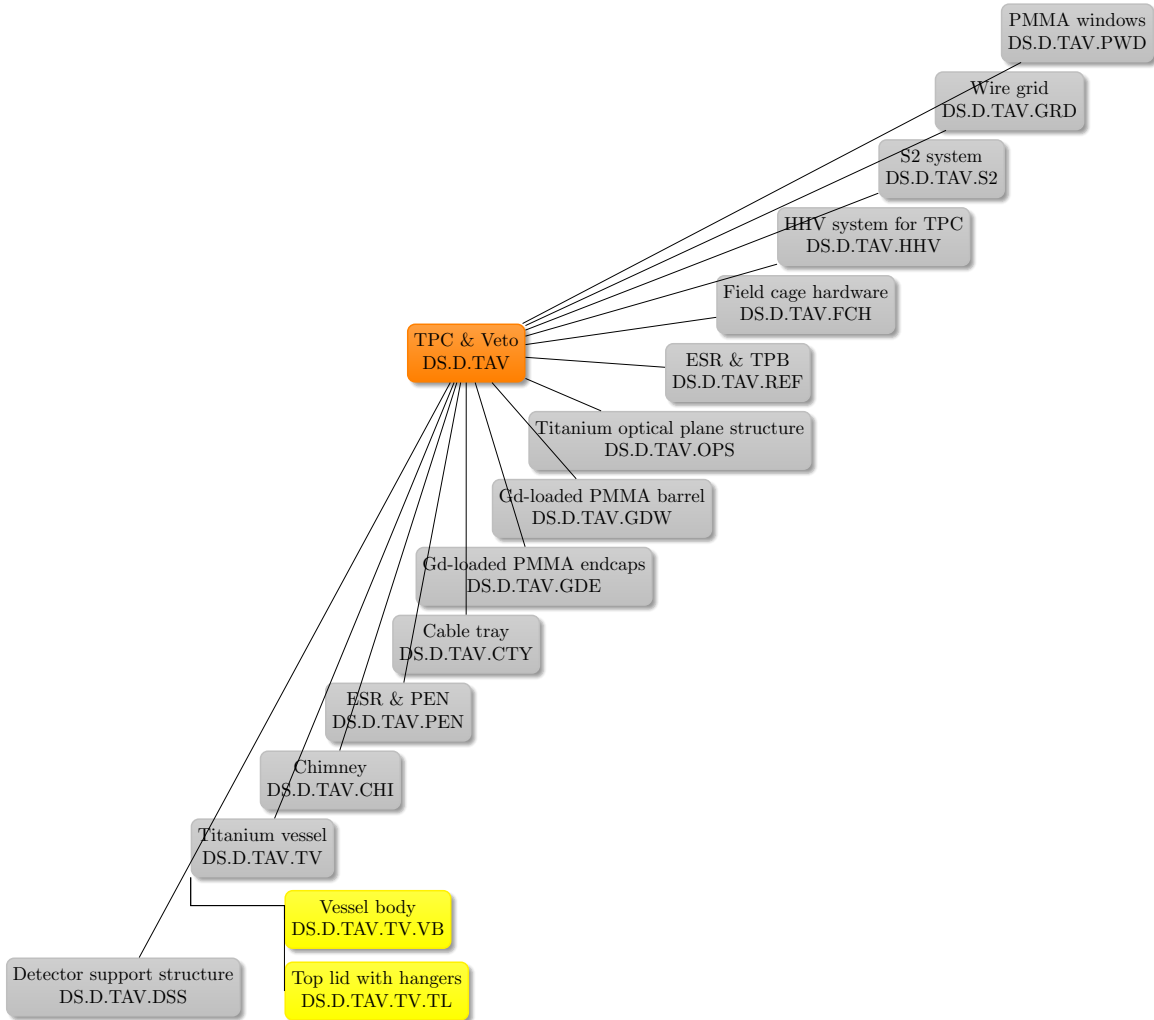


FIG. 66. PBS of the TPC & Veto, showing details to level 5.

The left panel of Fig. 68 shows a cut-away view of the assembled TPC, emphasizing the corners, and this helps highlight the degree of integration in the design. The wire grid and optical plane structures are made of stainless steel and titanium, respectively, while ultra-pure PMMA is used for the anode and cathode plates. When the TPC is assembled, these components will be in contact with each other as the detector is cooled to 87 K. To accommodate this differential thermal

3363 contraction safely, *concentricity guides* have been implemented throughout the design. These guides
 3364 will allow the different materials to pass by each other in a controlled manner, and will ensure that
 3365 the PMMA does not become stressed. In areas where friction is a concern, PTFE inserts will be
 3366 placed for relief. The right panel of Fig. 68 features the spring assembly which will accommodate
 3367 the thermal contraction along the drift direction. The assembled TPC will shrink by ≈ 4 cm along
 3368 the drift direction when cooled to 87K, and the spring assembly will ensure that there is adequate
 3369 force to keep all of the surfaces in contact.

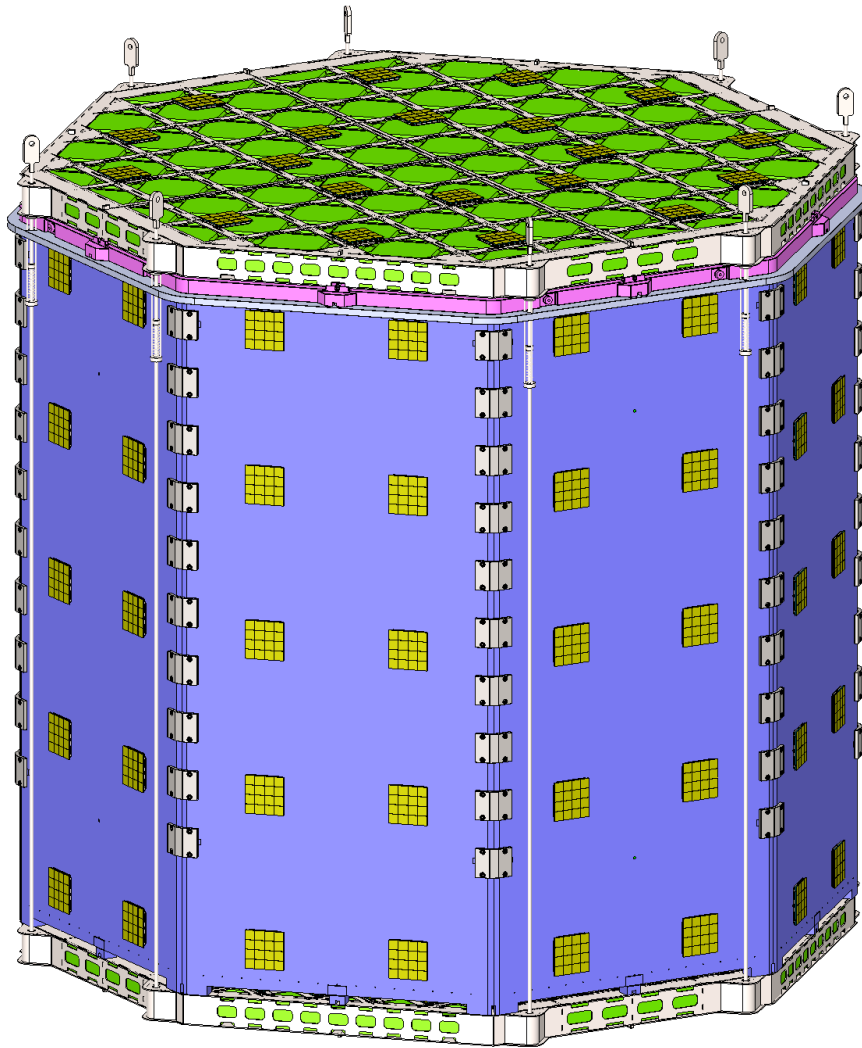


FIG. 67. Integrated TPC and Veto showing the top and bottom optical planes along with the connecting rods. The VPDU+s are also visible mounted on the external walls and on the top of the top optical plane, looking into the Veto region. The ESR and PEN reflector panels, mounted on the exterior, are suppressed for clarity. The mechanical anchor system is also shown which will mate with the titanium vessel and directly transfer the load to the hanger system (DSS) on the roof of the cryostat. Colors: blue - Clevios coating, pink - PMMA, green - Gd-loaded PMMA, yellow - photoelectronics (VPDU+s), gray - titanium or stainless steel.

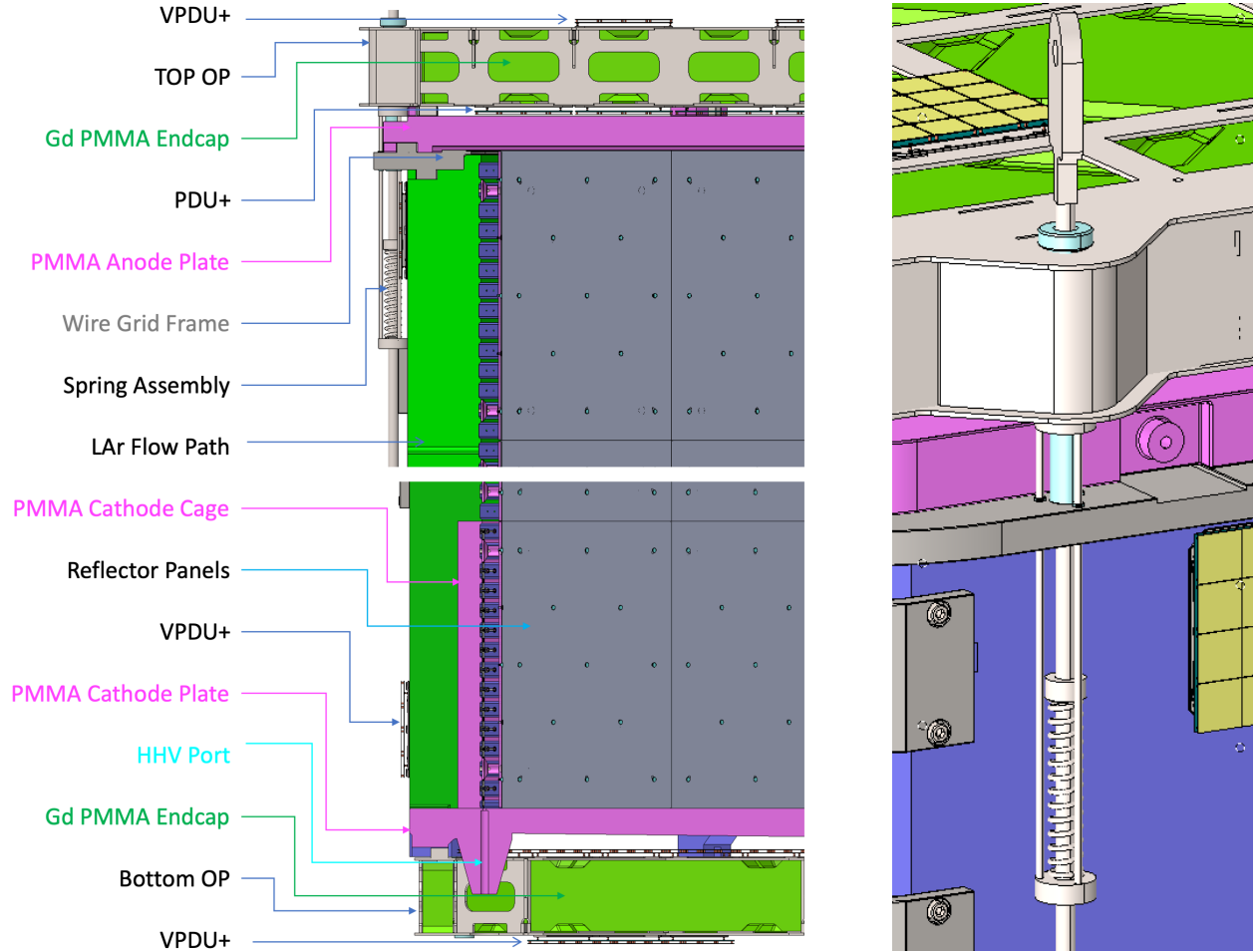


FIG. 68. Left: A cut-away view of the assembled TPC, emphasizing the corners, highlighting the component integration. Right: The spring assembly which will ensure the detector surfaces stay in contact when cooled to 87 K. A PTFE sleeve will be used to avoid friction during thermal contraction. The ESR and PEN reflector panels, mounted on the exterior, are suppressed for clarity.

3370

7.2.1. PMMA windows

3371 PBS Item: DS.D.TAV.PWD

3372

3373 The *anode plate* and *cathode plate*, shown respectively in Figs. 69 and 70, refer to the PMMA
 3374 pieces that the anode and cathode will be fabricated onto. Clevios will be applied to the PMMA
 3375 surfaces where a defined potential is required, and this is indicated by different shades of blue
 3376 in Figs. 69 and 70. Because the anode and cathode plates must also act as windows for the
 3377 argon scintillation light, the uniform application of Clevios on these surfaces is crucial. A coating
 3378 thickness of 5 μm is anticipated, and both surfaces will also be coated with TPB ($200 \mu\text{g}/\text{cm}^2$) to
 3379 serve as the wavelength shifter. The walls and edges are a darker shade of blue to indicate that a
 3380 thicker coating of Clevios will be applied to ensure good conductivity for the ground potential, and
 3381 where transparency is not required. The distance from opposing octagonal faces of the reflector
 3382 panels, see Section 7.2.6, at 87 K will be 350 cm, and the dimensions of the anode and cathode
 3383 plates account for this. Each will have concentricity guides in the form of small PMMA standoffs
 3384 with machined grooves allowing for thermal contraction along the radial direction, which will align
 3385 with corresponding posts on the titanium optical plane structures. The standoffs will be bonded
 3386 PMMA pieces strong enough to withstand the assembly sequence, which may eventually require

3387 rotating the plates (current sequence is described in section 11). This solution has been analysed
 3388 with FEA to confirm the strength requirements of the PMMA bonded standoffs.

3389 The anode plate will feature a diving bell shape with thickness of 5 cm and a 13 mm lip to contain
 3390 the gas pocket. The lip will rest on the wire grid frame, and only the surface facing the gas pocket
 3391 will be coated with Clevios which will be held at ground potential. In addition, an upward buoyant
 3392 force will exist across the anode due to the difference in densities between PMMA and LAr. The
 3393 anode plate must also remain parallel with respect to the wire grid when cooled to 87K. It is
 3394 anticipated that these issues will be taken care of during the manufacturing process. For instance,
 3395 machining of the level anode plate could take place under the same buoyancy conditions of the
 3396 running experiment. Then, once submerged in LAr, the anode plate will become parallel to the
 3397 wire grid.

3398 Both the bottom and inner surfaces of the cathode plate will be coated with Clevios, and they
 3399 will be held at ground potential and -73.38 kV respectively. To avoid trapping bubbles beneath,
 3400 the cathode plate will not have a uniform thickness. While the inner surface will be machined flat
 3401 for the electrostatic drift field, the center of the cathode plate will be 7 cm thick and will taper to
 3402 5 cm at the edges. This is illustrated in the left panel of Fig. 70 by the triangular sections which
 3403 meet at the low point in the center. To avoid any issues with splitting the drift field between two
 3404 objects at the high potential near the cathode, a section of the barrel will be manufactured from
 3405 PMMA and bonded to the cathode plate. This assembly, shown in the right panel of Fig. 70, will
 3406 fit into the bottom of the Gd-loaded PMMA barrel.

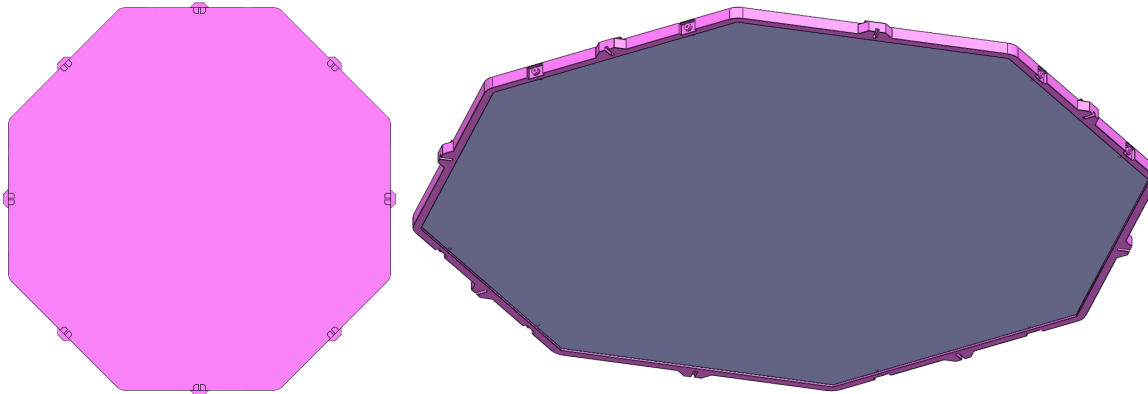


FIG. 69. PMMA anode plate. Left: Top view showing the concentricity guides. Right: View showing the diving bell structure which will contain the gas pocket. The additional holes located on the edges are for creating and maintaining the gas pocket.

3407

7.2.2. Wire grid

3408 PBS Item: DS.D.TAV.GRD

3409 The wire (extraction) grid is directly beneath the liquid surface, shown in Fig. 71. The wire
 3410 grid is composed of $150\text{ }\mu\text{m}$ parallel stainless steel wires with 3 mm spacing held in place by small
 3411 posts, which are set into a stainless steel frame. The most critical feature of the wire frame is the
 3412 uniformity of the electric fields (extraction and electroluminescence) that it creates. Since the entire
 3413 surface of the UAr is flat with respect to the ground by definition, a stringent requirement exists for
 3414 the flatness of the wires. Since the lip of the anode plate will rest directly on the frame, a stringent
 3415 requirement exists for the flatness of the frame as well. To this end, a tension of 2 N is required
 3416 in all of the wires and, to accomplish this, the wire grid frame must be 185 mm wide and have a
 3417 thickness of 35 mm. This design will keep deformation (sagging) of the wires and the frame within
 3418

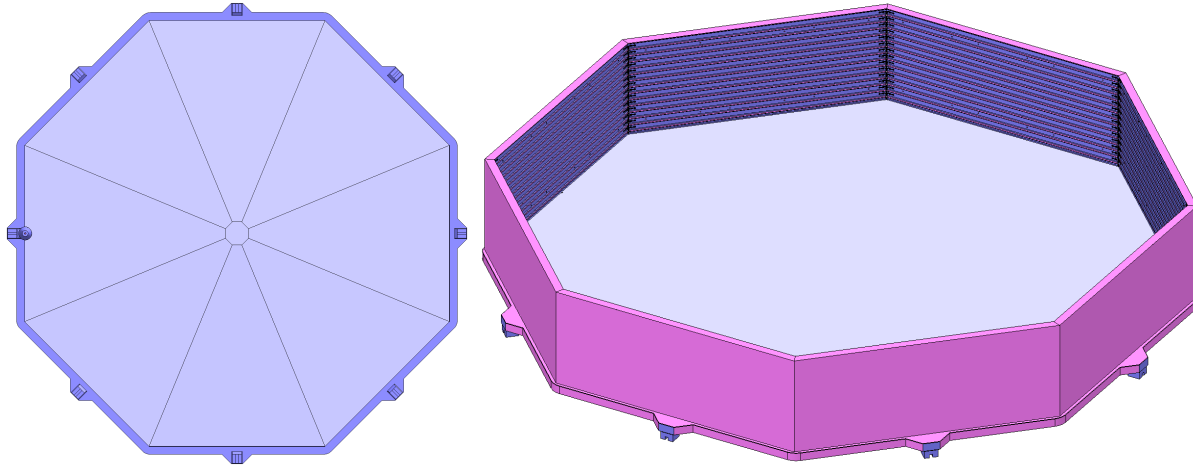


FIG. 70. PMMA cathode plate assembly. Left: Bottom view showing the upward slope from the center to the edges. Right: View showing the bonded barrel section with the Clevios coated field cage rings highlighted in darker blue. The concentricity guides are visible in both views.

3419 a fraction of 0.5 mm across the entire surface. Thus the grid frame will extend radially beyond the
 3420 anode plate and barrel walls, i.e. the anode plate will not be in contact with the barrel walls. This
 3421 is illustrated in Fig. 67 and the right panel of Fig. 66. Posts machined onto the wire grid frame
 3422 will slide within the grooves of the concentric guides machined into the anode plate, allowing for
 3423 the differential thermal expansion referenced to a common point. To ensure the tension integrity
 3424 of the wires over the lifetime of the experiment, they will be wire-wound onto each pin as shown in
 3425 the right panel of Fig. 71. Also note the ridge on the stainless steel frame which is outside of the
 3426 wire mounting posts. This ridge is designed to be at a height slightly above the liquid surface in
 3427 order to collect any excess charge, not extracted from the surface, before it can reach any insulating
 3428 surface where it could be collected causing field distortion.

3429 A smaller version of the frame has been successfully fabricated and deployed in previous detector
 3430 prototypes, while fabrication and operation of the grid for the DS-Proto detector will confirm
 3431 the final engineering details of the DS-20k extraction grid. These prototyping tests, along with
 3432 simulation studies, have resulted in a feasible design for the wire grid. The final engineering along
 3433 with a full FEA analysis have been completed, and production will be the next step.

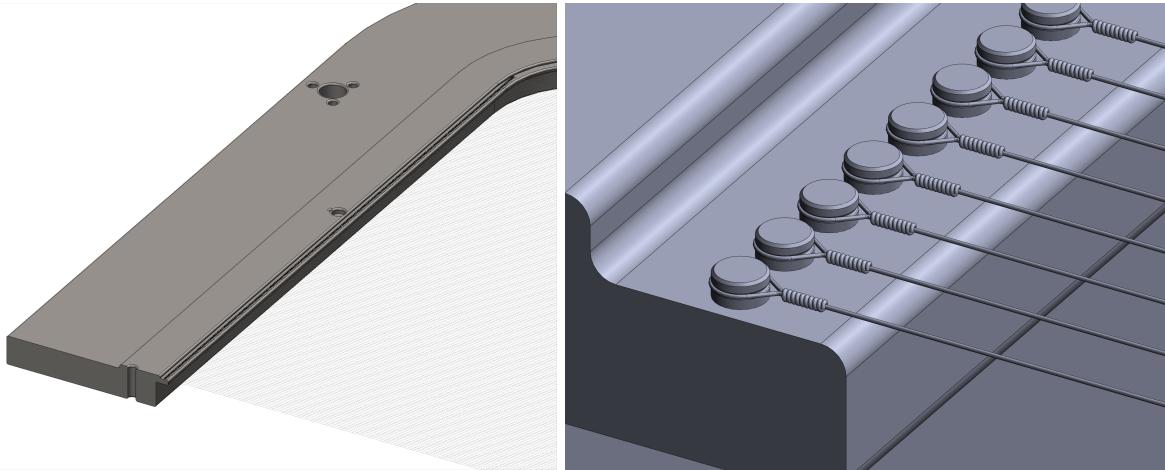


FIG. 71. The wire grid. Left: View showing the cross-section of the frame and a through-hole that one of the connecting rods will pass through. Right: A zoomed-in view showing how the individual wires attach to the frame.

3434

7.2.3. S₂ system

3435 PBS Item: DS.D.TAV.S2

3436

3437 S₂ signals in the DS-20k LAr TPC are generated after electrons are extracted from the liquid
 3438 surface and accelerated into the gaseous argon pocket by the electroluminescence field, and they are
 3439 used for various data quality assurance selections. The magnitude of the S₂ signals scales with the
 3440 gas pocket thickness and the magnitude of the reduced electroluminescence field, E/p , where p is
 3441 the gas pressure. Any factor that contributes to either the electric field strength, the gas pressure,
 3442 or the gas pocket thickness must be stringently controlled and any unspecified deviations must be
 3443 minimized. These considerations put a stringent requirement on the thickness and the uniformity
 3444 of the gas pocket. Based on previous experience with DarkSide-50, the shape of the S₂ signals can
 3445 be used to determine the thickness to within $\approx 50\ \mu\text{m}$.

3446 By definition, the surface of the liquid under the anode plate is level. Using precision machining
 3447 techniques, the anode plate will also be flat within the specification given in table XVII. The *bubbler*
 3448 system, pictured in Fig. 72, is the device that will control the amount of gas located between these
 3449 two surfaces, i.e. the gas pocket. Fundamentally, the bubbler system is a gas flow control system
 3450 consisting of an inlet and an outlet. The inlet is connected to the vertical PTFE tube visible in
 3451 Fig. 72. The outlet is the bottom edge of the device pictured in the top left panel of Fig. 72, i.e.
 3452 the *bubbler*. The bubbler will be mounted to the wire grid frame with a gap at a specified height,
 3453 and routed to a PTFE gas inlet router (top right panel of Fig. 72) with long, thin PTFE tubes to
 3454 allow for differential thermal contraction. The gas router will also be mounted to the previously
 3455 mentioned through-hole machined into to the lip of the anode plate. Thus the gas pocket volume
 3456 will be connected with the volume of the bubbler. Assuming that the gas flow is low enough such
 3457 that the pressure is in continuous equilibrium within both volumes, excess gas will ‘bubble’ out
 3458 from the gap at the bottom of the bubbler. This action will result in a gas/liquid interface, hence a
 3459 gas pocket thickness, that is well-defined. To avoid excessive gas flow across the gas pocket volume,
 3460 there will be eight inlet ports machined into the anode plate lip which will all be connected in
 3461 parallel. Four of these are visible in Fig. 69. One connection will be to the UAr cryogenic loop
 3462 (inlet) and all of the ports will route to one bubbler (outlet).

3463

7.2.4. HHV system for TPC

3464 PBS Item: DS.D.TAV.HHV

3465

3466 The HHV cable will penetrate through the warm HV cable feedthrough (FT) at the top of the
 3467 cryostat and will pass through the veto. Both the HV cable and the HV cable FT will be within
 3468 the UAr volume. As shown in Fig. 73, the HHV port is a conical piece of PMMA extending below
 3469 and bonded to the cathode plate assembly. The HHV port will fit within a special penetration in
 3470 the titanium optical plane structure, while its size and shape take into account that the electric
 3471 potential must go to ground on the external surface and the differential thermal contraction of the
 3472 materials.

3473

7.2.5. Field cage hardware

3474 PBS Item: DS.D.TAV.FCH

3475

3476 With the exception of the wire grid, Clevios will be used to define all of the electric potentials
 3477 for the DS-20k TPC. This eliminates the need for more massive metallic materials for the rings

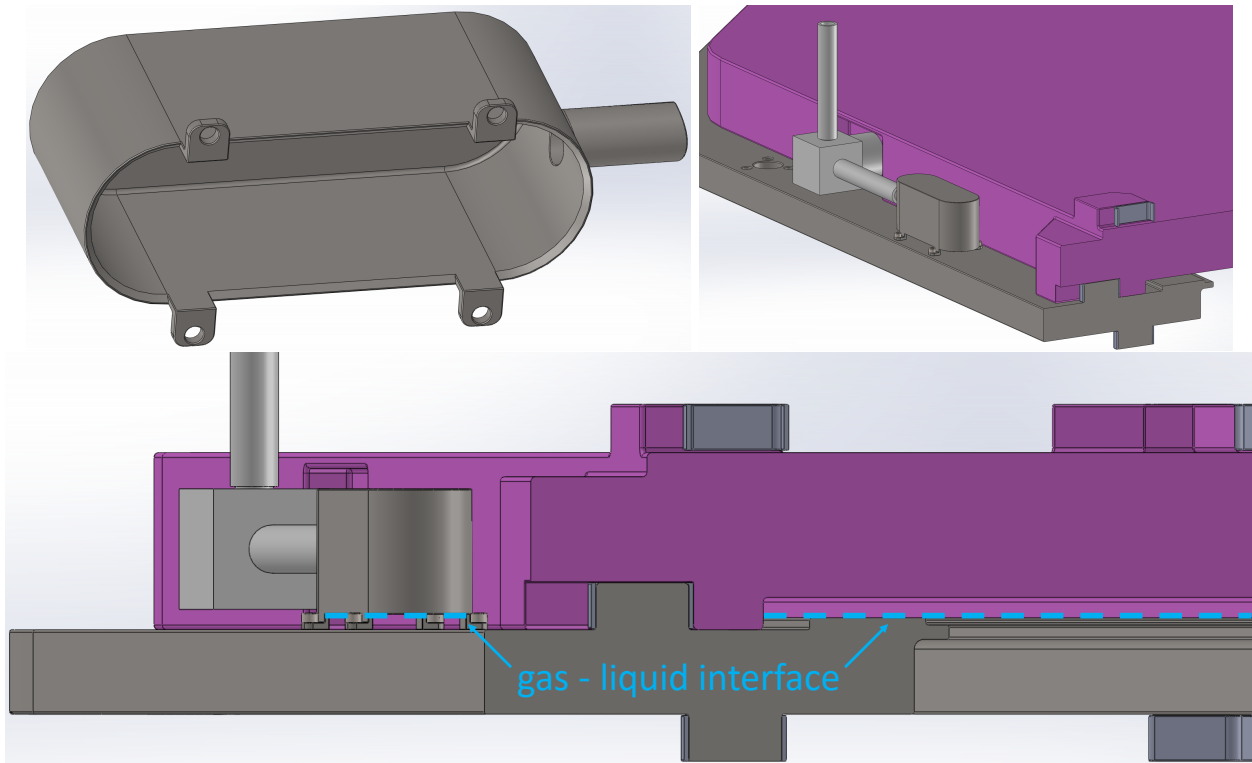


FIG. 72. The bubbler system. Top right: The bubbler with beveled bottom edges to allow efficient passage of the gas bubbles. Top left: The vertical tube is the gas inlet which feeds into a gas router. The router connects the gas pocket and bubbler volumes. Bottom: A side view showing where the gas/liquid interface is relative to the bubbler system.

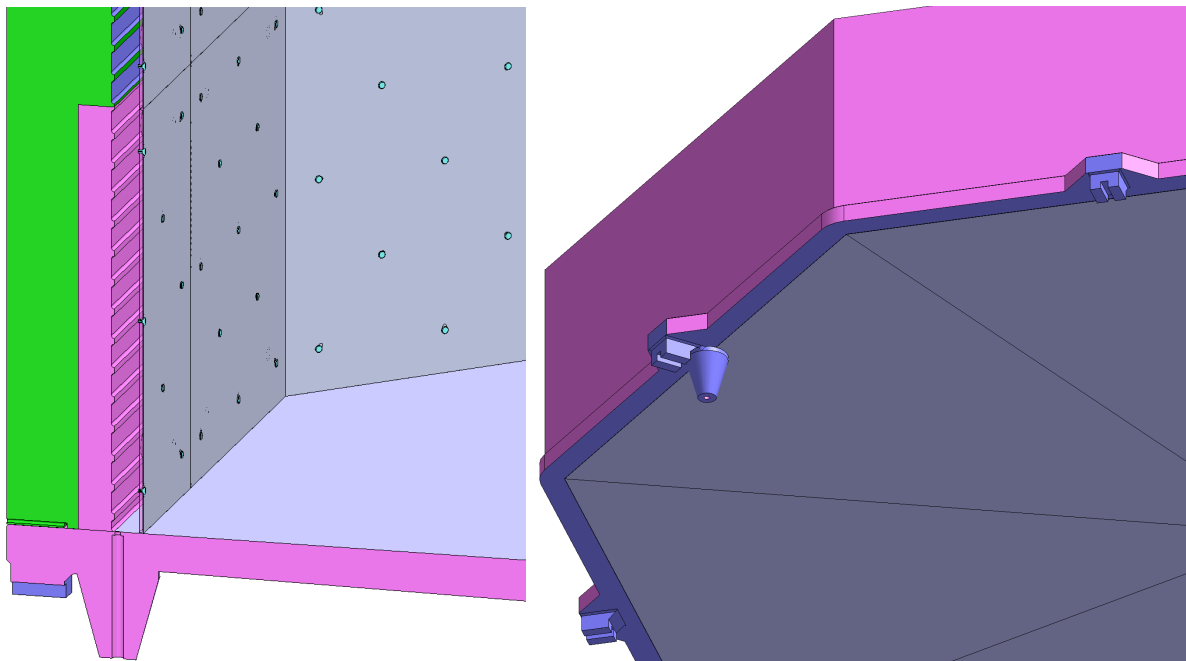


FIG. 73. The HHV port. Left: A cross-sectional view showing the HHV conductor cavity penetrating to the cathode. Right: The cathode plate assembly showing the HHV port.

and supporting structure, traditionally present in TPC design. Two critical factors determine the

3479 global uniformity of the drift and luminescence fields: 1) That the field cage ring profiles have an
 3480 80% ‘ring’ area and a 20% gap between the rings. This is important because it suppresses the
 3481 influence of the high-field near the cathode leaking into the sensitive volume and distributing the
 3482 uniformity. 2) That the wire grid covers the entire active area of the TPC. This is important
 3483 because it ensures that fields are uniform all the way to the edges of the TPC active area.

3484 The field cage rings will be hemispherical-like sections machined into the barrel walls of the
 3485 PMMA and the Gd-loaded PMMA. Fig. 74 shows the field cage rings colored in blue to indicate
 3486 the extent of the Clevios coating. They will measure 40 mm in height with a 24.9 mm flat section in
 3487 the middle, with a maximum depth 4 mm. The circular cuts into the PMMA at the top and bottom
 3488 of each ring will measure 4 mm along the drift coordinate, and the rings will be separated by 8 mm
 3489 sections of non-coated PMMA, which is visible in pink (PMMA) or green (Gd-loaded PMMA).

3490 The top panels in Fig. 75 show the resistor links which will form the resistive divider chain
 3491 delivering the different potentials to the field cage rings. Fig. 75(b) shows the side of the link
 3492 which will make contact with the Clevios coating. Two sets of mounting holes will be used for
 3493 redundancy, and PTFE screws will be used to anchor the resistor links to the PMMA. The links
 3494 feature a modular design fabricated onto a flexible copper-Kapton-copper substrate. Since the
 3495 eight walls of the barrel will be coated with Clevios independently, links will be fixed in each corner
 3496 where the sections join providing electrical contact between them. For added redundancy, four
 3497 of the chains will have resistive dividers, while the other four will only provide a conductive path
 3498 around the ring. Thus, for an entire ring to fail, four resistors on four separate links of the same
 3499 ring would need to fail. Similarly, for one-eighth of a ring section to fail, two conductive paths,
 3500 each with two contact points, would need to fail.

3501 To ensure that the electrostatic fields are uniform within the entire active volume, DS-20k will
 3502 employ the high voltage scheme depicted in Fig. 76(a). By decoupling the drift field from the
 3503 wire grid, compensation for the leak field can be implemented by altering the potentials set on the
 3504 top field cage ring (HV_r) and the wire grid (HV_g). Full 3d simulations have been carried out to
 3505 verify this concept and some results are shown in Fig. 76(b). Specifically, these figures show the
 3506 top corner of the drift field region near the wire grid and barrel wall. The uncompensated (left
 3507 panel) configuration, near the top of the reflector panel (vertical black lines), shows some slight
 3508 non-uniformity. While not drastic, this non-uniformity could cause charge-up issues over time.
 3509 By compensating the potentials (right panel), the non-uniformities within the active region are
 3510 essentially unnoticeable and should remain so over the lifetime of the experiment.

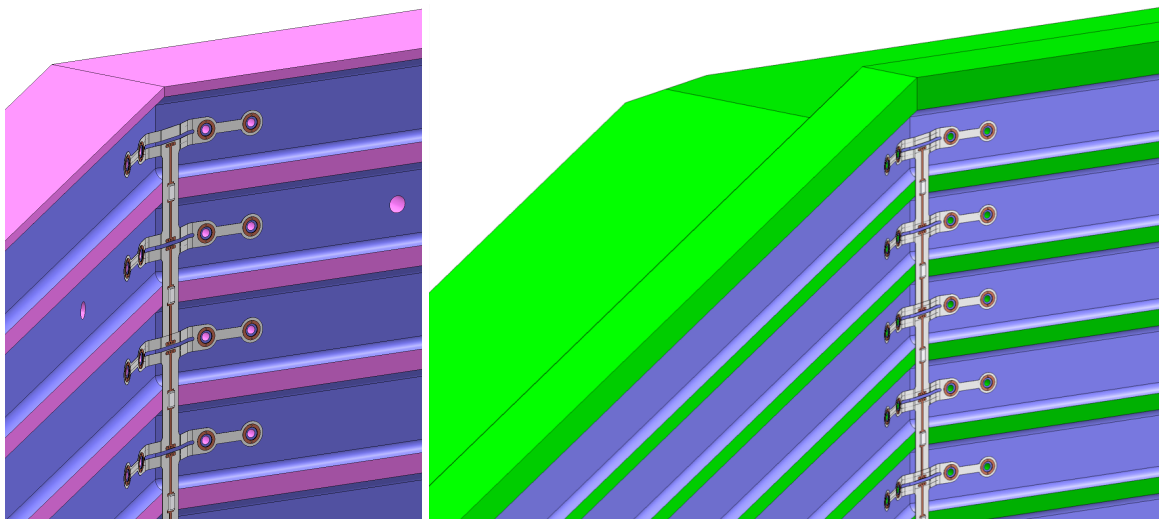


FIG. 74. Zoom-in of the one inside corners of the cathode barrel (left) and the Gd-loaded PMMA barrel (right). The resistor links are visible in both. Colors: blue - Clevios coated field cage rings, pink - PMMA, green - Gd-loaded PMMA.

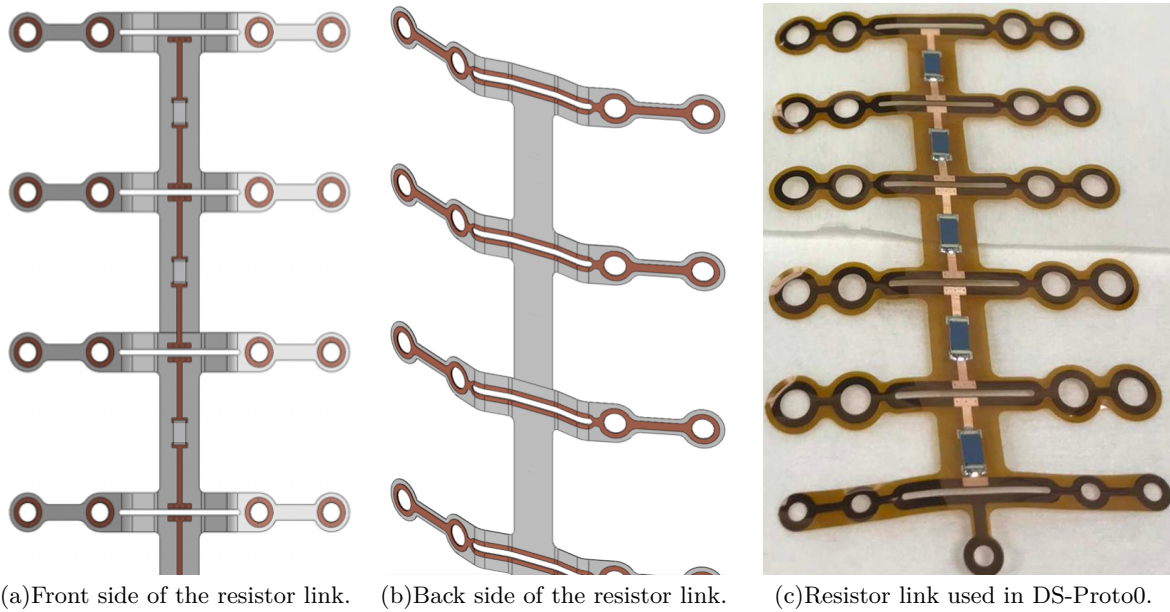


FIG. 75. Top: Resistor links. Bottom: The cathode plate assembly showing the resistor links on the barrel section.

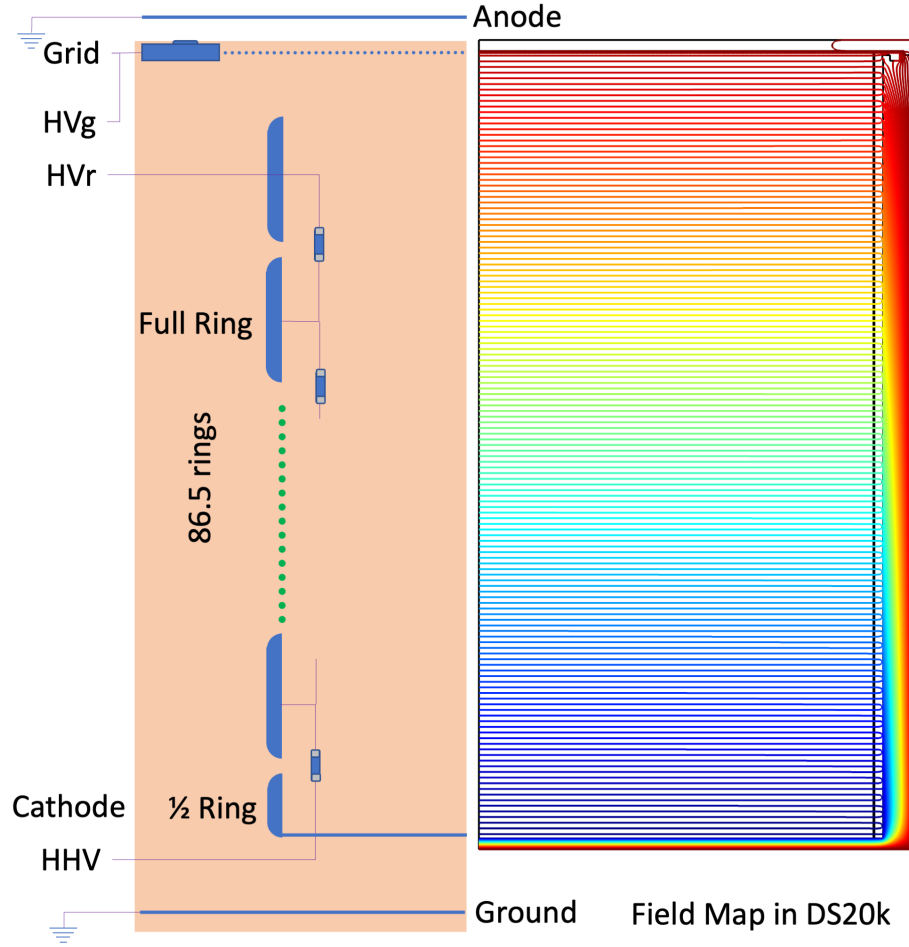
3511

7.2.6. ESR & TPB

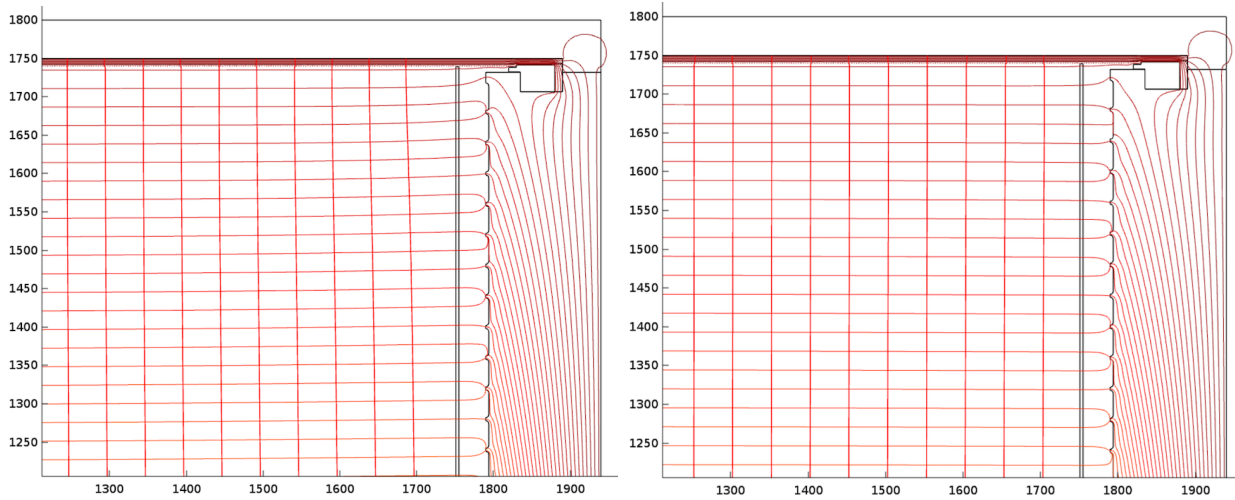
3512 PBS Item: DS.D.TAV.REF

3513

3514 To reduce the neutron background and Cherenkov light produced by conventional reflectors
 3515 manufactured with PTFE, the DS-20k TPC will use Enhanced Specular Reflector (ESR) foils for
 3516 light reflection. ESR is a high-performance, non-metallic, 50 μm thick foil with a reflection efficiency
 3517 of 98 % for 420 nm light. The ESR foils will be secured to 4 mm thick PMMA backing sheets with
 3518 PTFE push-pins, which will ease installation, and a cross-section view can be seen in Fig. 77(a).
 3519 These assemblies are referred to as *reflector panels*, Fig. 77(c), and once attached to the walls of
 3520 the TPC, they will form the *reflector cage* which is shown in the left panel of Fig. 78. The PMMA
 3521 sheets will be mounted to four PMMA standoffs which will make contact with the non-Clevios-
 3522 coated PMMA spacing between the field cage rings. This is shown in the right panel of Fig. 78.
 3523 The surface of each ESR foil facing the active LAr volume, along with the heads of the push-pins
 3524 which comprise ≈ 0.23 % of the total reflection surface, will be coated with TPB ($200 \mu\text{g}/\text{cm}^2$, the



(a) Cartoon of the field cage and high voltage scheme (left) alongside a contour mapping with the compensated potentials (right). Note that the resistors are not within the active TPC volume, i.e. they lie behind the reflector panels.



(b) Zoom-in of the upper corner of the drift field region for the uncompensated (left) and compensated (right) leak field.

FIG. 76. Drift field uniformity in DS-20k. To ensure electrostatic field uniformity, a high voltage scheme that allows for independent control of the potentials on the top field cage ring (HV_r) and the wire grid (HV_g) will be used.

3525 same amount as the PMMA windows). This will provide a highly-efficient wavelength shifting and
 3526 light reflection surface.

3527 To anticipate the differential thermal contraction between PMMA and ESR, the ESR foils will
 3528 feature elongated laser-cut holes for the push-pins which will align to the center of each foil. In
 3529 addition, small TPB-coated ESR washers will be placed underneath the foils at each push-pin
 3530 location. This will allow the PMMA sheets to thermally contract while not damaging the ESR
 3531 foils and keeping them flat, all while maximizing the light reflection efficiency. Another result of
 3532 the thermal contraction is that foils will all move away from one another, which could create gaps
 3533 in the reflection surface. To combat this, all of the ESR foils will be sized to overlap each other,
 3534 so that no gaps will appear at 87 K. Fig. 77(b) shows an ESR foil extending beyond the PMMA
 3535 sheet. This configuration also ensures that any Cherenkov light produced by the acrylic sheets, or
 3536 other materials outside, will be blocked by the ESR foils.

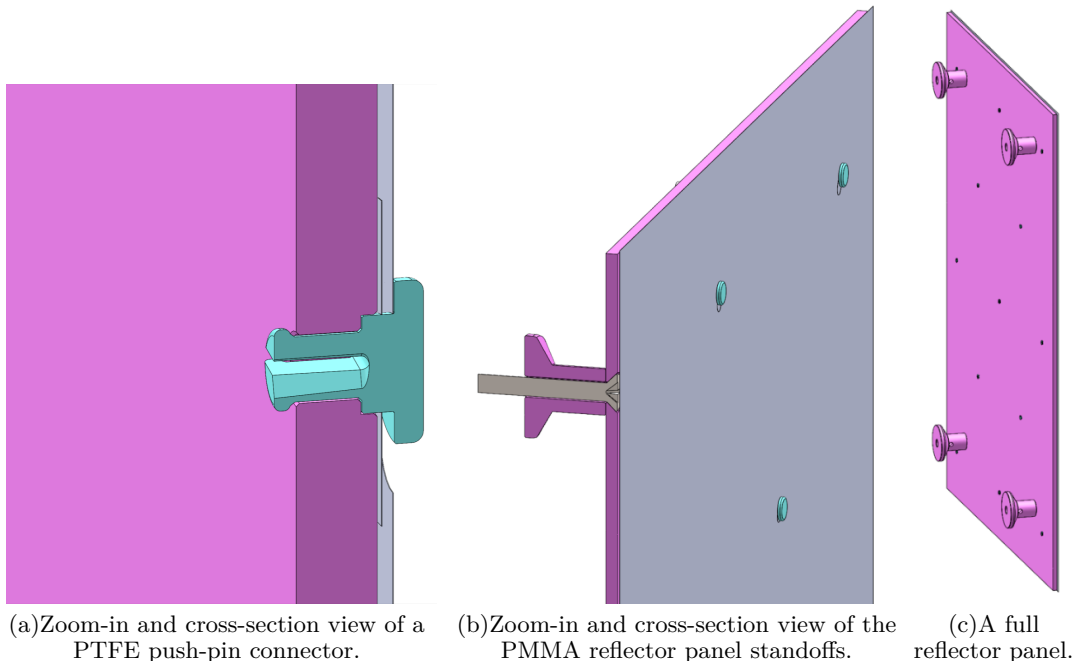


FIG. 77. Different views of a reflector panel and components.

3537

7.2.7. Titanium optical plane structure

3538 PBS Item: DS.D.TAV.OPS

3539
 3540 *Optical plane* is the name given to the fully assembled light detection surfaces which will be
 3541 installed both above the anode plate and below the cathode plate. The titanium optical plane
 3542 structures are the mechanical foundations of the optical planes, and are critical features in the
 3543 mechanical design of the TPC.

3544 Figs. 79(a) and 79(b) show both the x and y 156 mm-tall titanium pieces that perpendicularly
 3545 interlock to form the mechanical support structures of the optical planes. Respectively on the
 3546 bottom and top of Figs. 79(a) and 79(b), thin grooves are visible into which the other piece slides.
 3547 After these cross-pieces are fit together, they will mate with the PDU+ plate assembly. One quarter
 3548 of this plate assembly is pictured on the left of Fig. 79(c). The pattern of the grooves visible in the
 3549 PDU+ plate match the 3 mm protruding pieces that will form from fitting the titanium cross-pieces

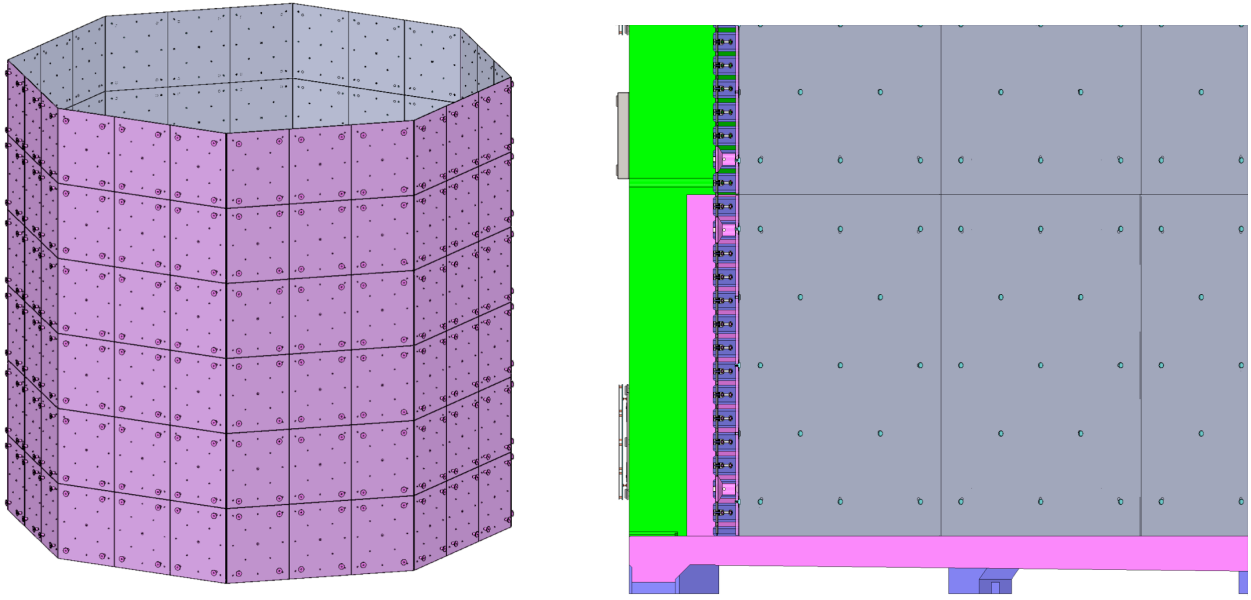


FIG. 78. Left: Fully assembled reflector field cage. Right: Cross-sectional view of a lower corner of the TPC with the reflector panels visible. The PMMA standoffs are shown making contact with the areas of PMMA in between the field cage rings.

3550 together. After the 3 mm pieces of titanium are fit into the grooves, they will be welded together
 3551 and the result is pictured in Fig. 79(d).

3552 As part of the integrated neutron veto, 15 cm thick Gd-loaded PMMA blocks, highlighted in green
 3553 in Fig. 80, will be inserted into the open spaces within the titanium structure. The Gd-loaded
 3554 PMMA endcaps are described in section 7.2.9. After the Gd-loaded PMMA blocks are placed, the
 3555 VPDU+ plate grooves will be aligned with the 3 mm pieces of titanium as on the PDU+ side. One
 3556 quarter of the VPDU+ plate is pictured on the right of Fig. 79(c), and grooves similar to those on
 3557 the PDU+ side are visible. At the intersections of the interlocking cross pieces, there will be tapped
 3558 inserts welded into place. One of these inserts is visible on the right of Fig. 80. The VPDU+ plates
 3559 will be bolted into place using these tapped inserts, completing the mechanical structure for the
 3560 optical plane.

3561 Once the mechanical structure is completed, the photoelectronics will be installed. Fig. 81(a)
 3562 shows the holder for the PDU+s along with the mounting mechanism. A small copper pin will be
 3563 fixed on each corner of the PCB of the PDU+s and VPDU+s. These pins will insert into holes
 3564 machined into the holders where a locking slide-mechanism will slide against the pins, fixing them
 3565 in place. A tool is being designed which will engage/disengage the slide mechanism. In addition,
 3566 this tool will allow for handling and installing the PDU+s without the need for screws or other
 3567 loose parts. Fig. 81(b) shows front and rear views of four PDU+s mounted to a holder, however
 3568 the holders will be welded to the titanium frame during the actual assembly.

3569 Highlighted in blue in Fig. 82 are the PDU+ (left) and the VPDU+ holders. The VPDU+ are
 3570 mounted singly, thus the holder is one-quarter of a PDU+ holder. Part of the ‘cable trays’ will be
 3571 formed by welding the PDU+ titanium plate assemblies and the PDU+ and VPDU+ holders into
 3572 place. Cables will then be routed and tested. Following this, the titanium frame will be rotated
 3573 such that the PDU+s and VPDU+s can be placed one-by-one with the silicon facing down to avoid
 3574 working over the sensitive surface. Fig. 83 shows a fully assembled optical plane with the individual
 3575 tile+s as the smallest squares.

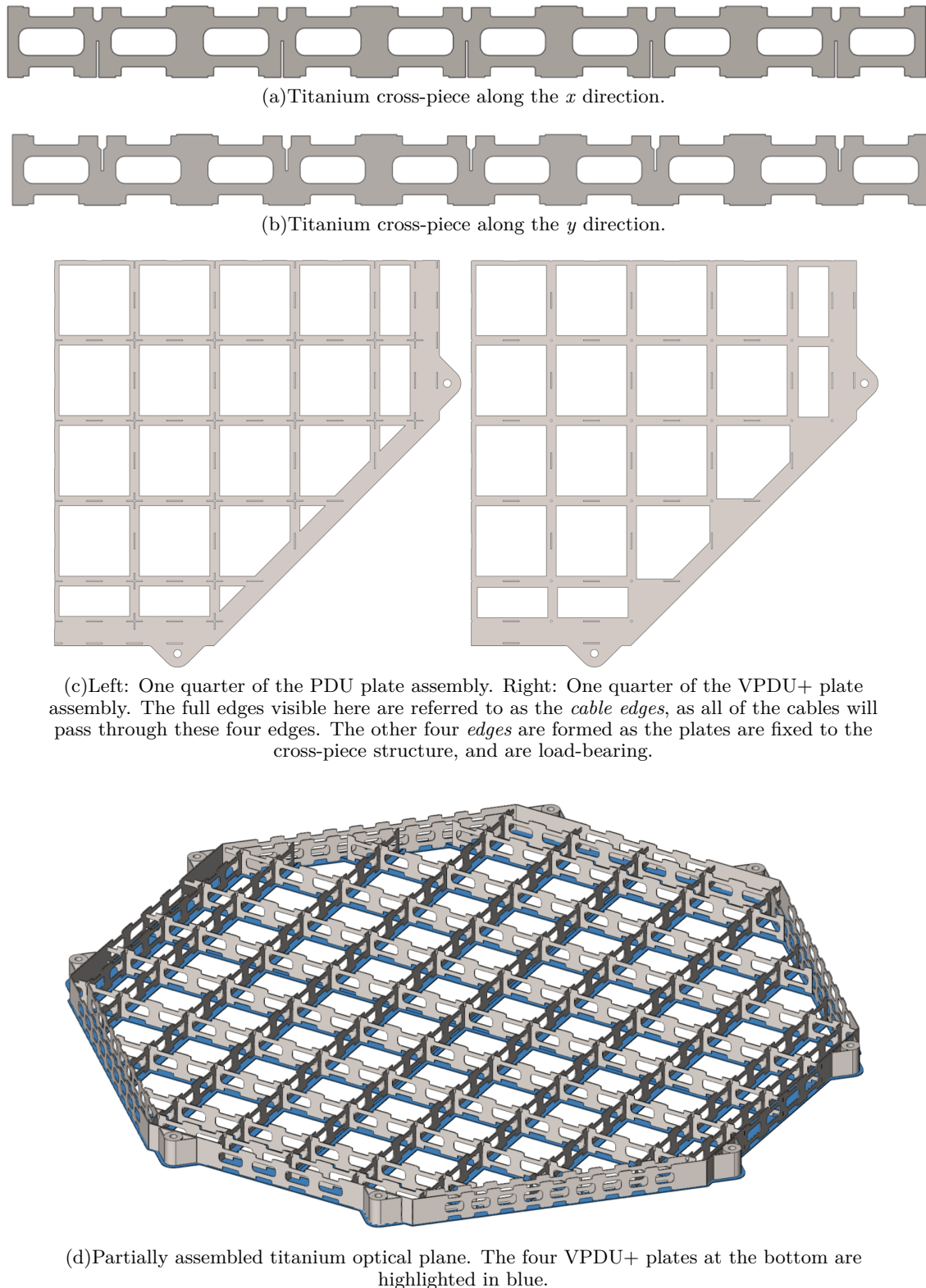


FIG. 79. Pieces and partial assembly of an optical plane structure.

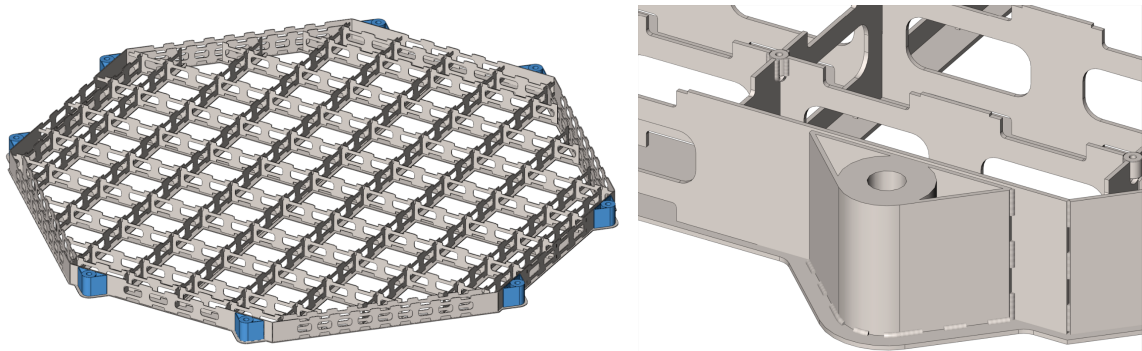
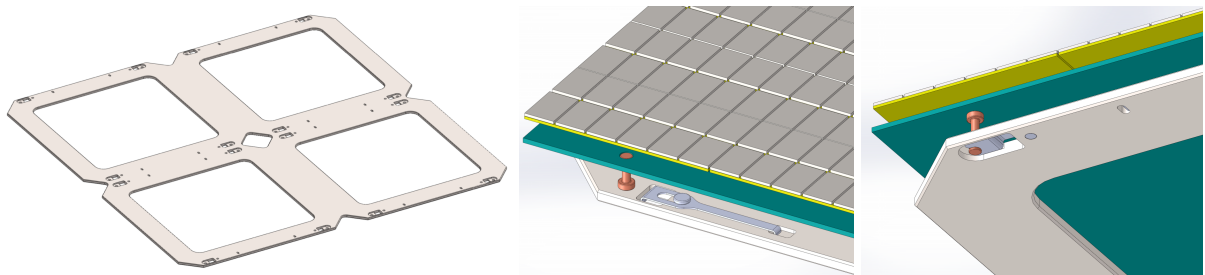
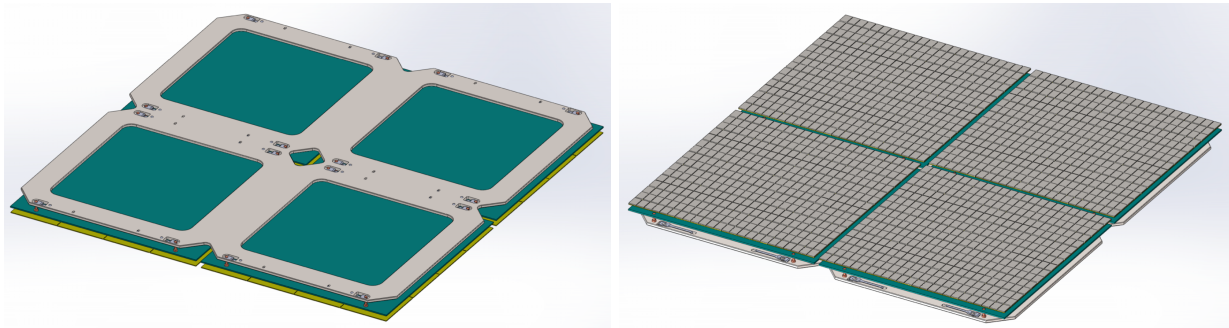


FIG. 80. Left: Optical plane mechanical structure highlighting the eight through-holes for integration with the TPC barrel. Right: Zoom of one of the eight through-hole mounts. Welded inserts for the mounting of the VPDU+ plate are also visible at the intersections of the cross-pieces.



(a)Left: A titanium PDU+ holder. Center and right: Views showing the locking mechanism to fix the PDU+ to the holders.



(b)Backside (left) and front-side (right) of a PDU+ to its holder. Four PDU+s will mount to a single holder.

FIG. 81. Details of the PDU+ mounting mechanism to the titanium holders which will be welded to the optical plane support structure.

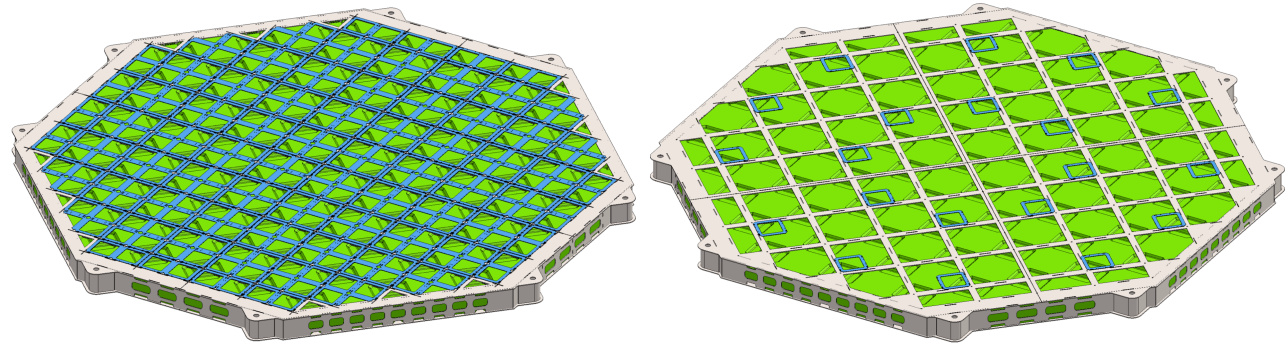


FIG. 82. The PDU+ (left) and VPDU+ (right) holders highlighted in blue, welded to the support frame. The Gd-loaded PMMA blocks are also shown in green laid within the titanium frame.

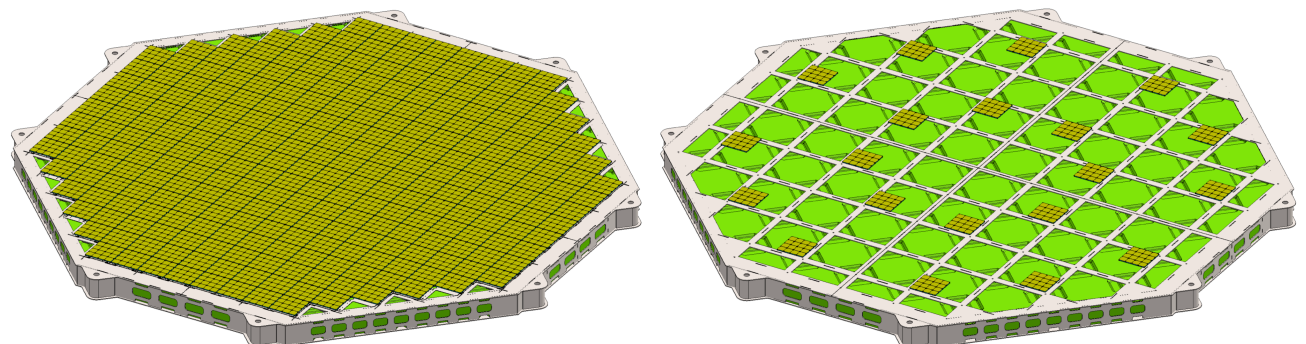


FIG. 83. A fully assembled optical plane showing the TPC (left) and Veto (right) sides. The individual tile+s are visible in dark yellow. The ESR and PEN reflector panels, mounted on the exterior, are suppressed for clarity.

3576

7.2.8. Gd-loaded PMMA barrel

3577 PBS Item: DS.D.TAV.GDW

3578

The body of the TPC will be formed by joining eight Gd-loaded PMMA panels measuring 163 cm wide and 365 cm tall, including the concentricity guides (feet). The panels will measure 10 cm thick near the bottom up to where the cathode barrel will fit, and 15 cm thick above. Fig. 84(a) shows a zoom-in view of the top corner of a panel with the Clevios field cage rings visible in blue, and Fig. 84(b) shows the inside view of an entire panel. The flat section at the bottom colored in green is the area that the cathode barrel will occupy. The individual panels will be held together by 2 cm thick stainless steel angle brackets, which are visible in Fig. 84(c) along with the fully assembled Gd-loaded PMMA barrel. The concentricity guides and load bearing points are also visible at the bottom, along with the cutouts where the cathode plate concentricity guides will fit. The dimensions of these cutouts are such that the load of the TPC will be supported by the Gd-loaded panels, and not transferred to the cathode plate. Once assembled, the anode and cathode plate and the barrel wall panels will form a virtually sealed volume allowing for the proper flow control of argon along with a positive gas pressure to protect the TPB and Clevios layers against oxidation during the transportation and assembly phases.

The VPDU+s will also mount on the outside of the barrel. The titanium mounting brackets for the VPDU+s can be seen in Fig. 85(b). They will be fixed to the Gd-loaded PMMA panels with PTFE push-pins as used for the reflector panels. Copper standoffs located on the VPDU+ PCB will attach via locking mechanisms, also visible in Fig. 85(b), to the titanium brackets. Fig. 85(a) shows the backside of an assembled VPDU+ with the push-pins inserted. To accommodate the thermal contraction of the Gd-loaded PMMA, the mounting holes in the titanium frames will be elongated towards the center of each frame, which are also visible in Fig. 85(b). Fig. 85(c) shows a VPDU+ fully assembled and mounted.

3601

7.2.9. Gd-loaded PMMA endcaps

3602 PBS Item: DS.D.TAV.GDE

3603

Like the walls of the TPC, the top and bottom must also be covered with ≈ 15 cm of Gd-loaded PMMA to complete the neutron Veto. However, the optical planes are on the top and bottom of the TPC, and a different scheme must be employed. In order to minimize the dead space of the UAr, the Gd-loaded PMMA should be as close to the PDU+s as possible. To accomplish this the optical planes are designed to hold both the PDU+s and the Gd-loaded PMMA endcaps.

Fig. 86 shows every component that will comprise the Gd-loaded PMMA endcaps. Once the titanium PDU+ plates are welded into place, these Gd-loaded pieces will be inserted into their respective positions. They are purposefully not fixed into place to avoid any thermal contraction issues. The Gd-loaded PMMA pieces measure 146 mm thick, many with 15 mm deep grooves machined into them. These grooves measure ≈ 8 cm wide and, when combined with the grooves in the titanium cross-pieces (Figs. 79(a) and 79(b)), will form part of the ‘cable trays’. A fully assembled Gd-loaded PMMA endcap is visible in Fig. 87.

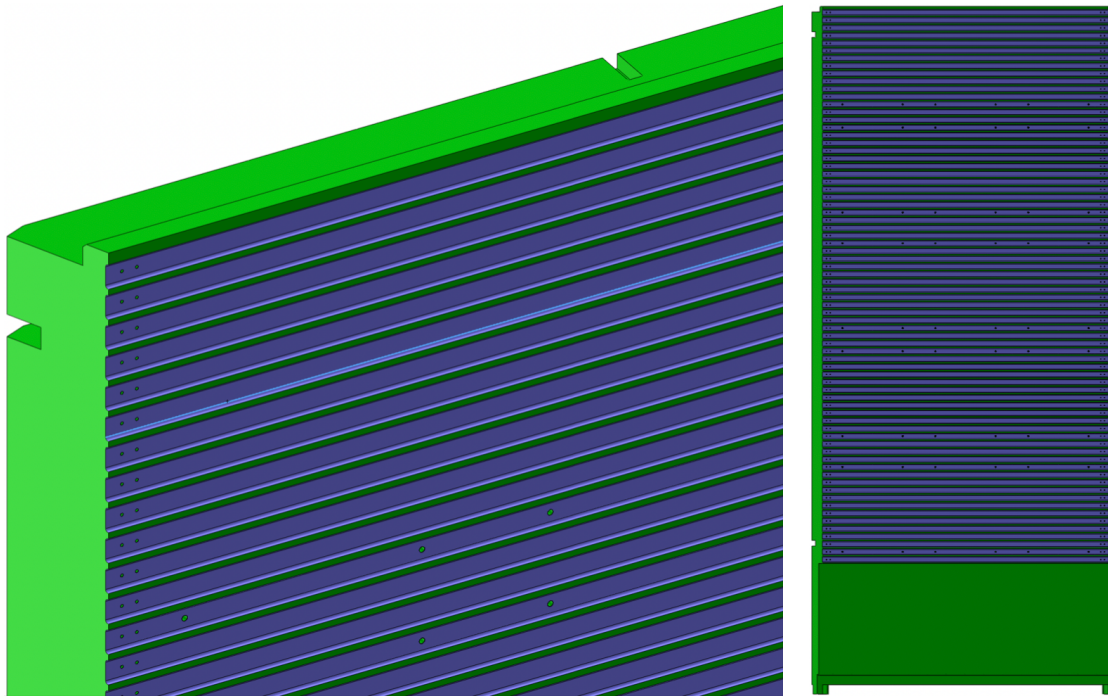
3616

7.2.10. Cable trays

3617 PBS Item: DS.D.TAV.CTY

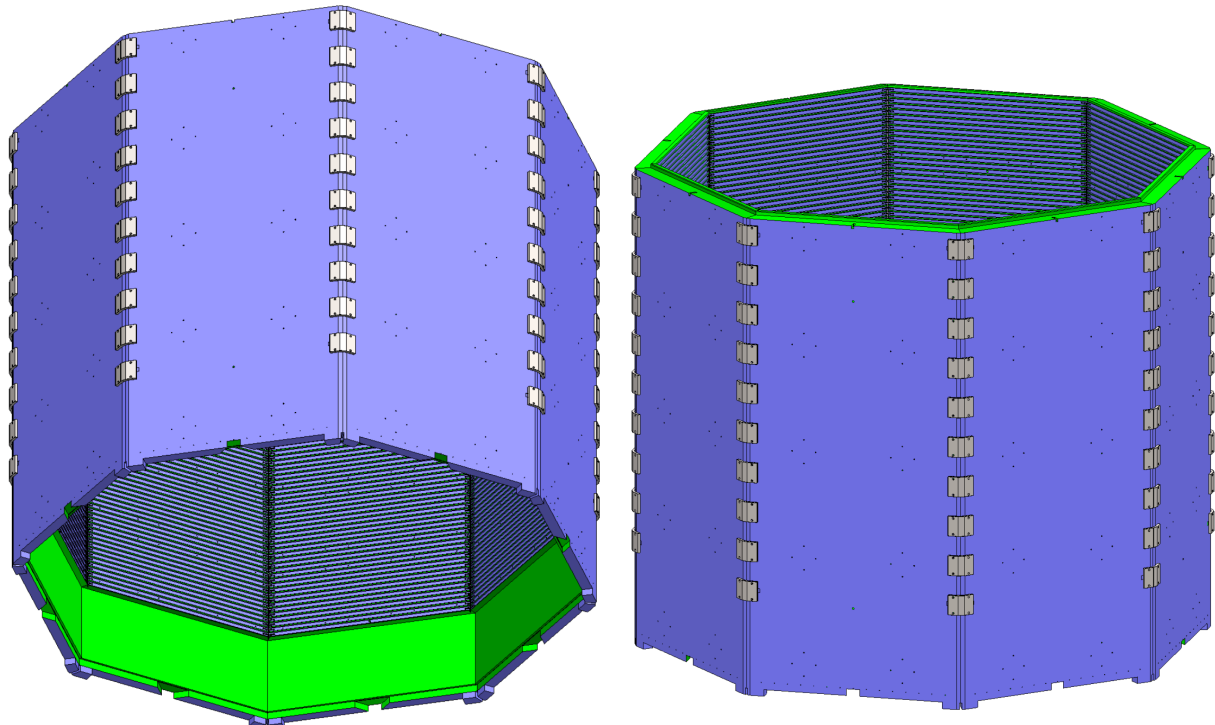
3618

As part of the integrated design, much of the cable routing for DS-20k has been built into the existing components, removing the need for a dedicated structure. Before the PDU+s and



(a) Zoom-in of a Gd-loaded PMMA barrel wall panel with the field cage rings colored in blue.

(b) A Gd-loaded PMMA barrel wall panel. The flat area at the bottom is where the cathode barrel will fit.



(c) Different views of the fully assembled Gd-loaded PMMA barrel with the steel angle brackets and load-bearing feet/concentricity guides visible.

FIG. 84. The Gd-loaded panels and assembled barrel. Colors: green - Gd-loaded PMMA, blue - Clevios coating, gray - stainless steel angle brackets.

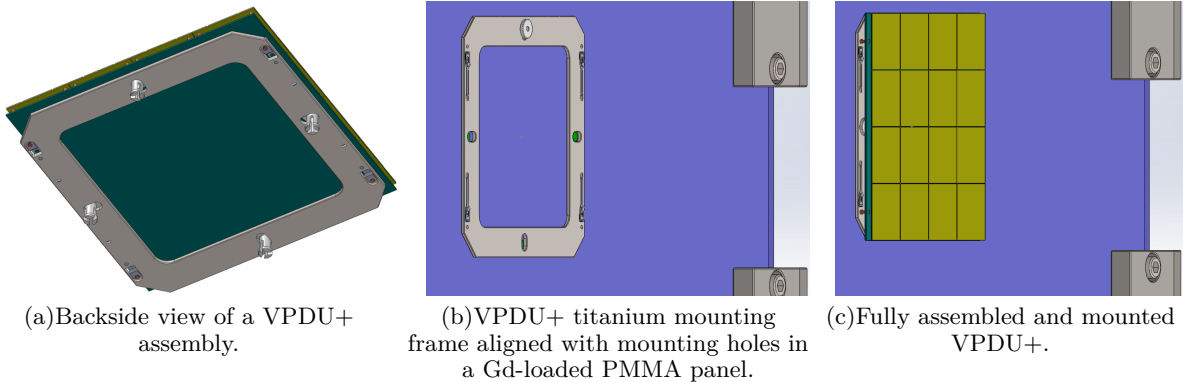


FIG. 85. Details of the VPDU+ mounting mechanism to the titanium holders which will be mounted to the Gd-loaded barrel wall panels.

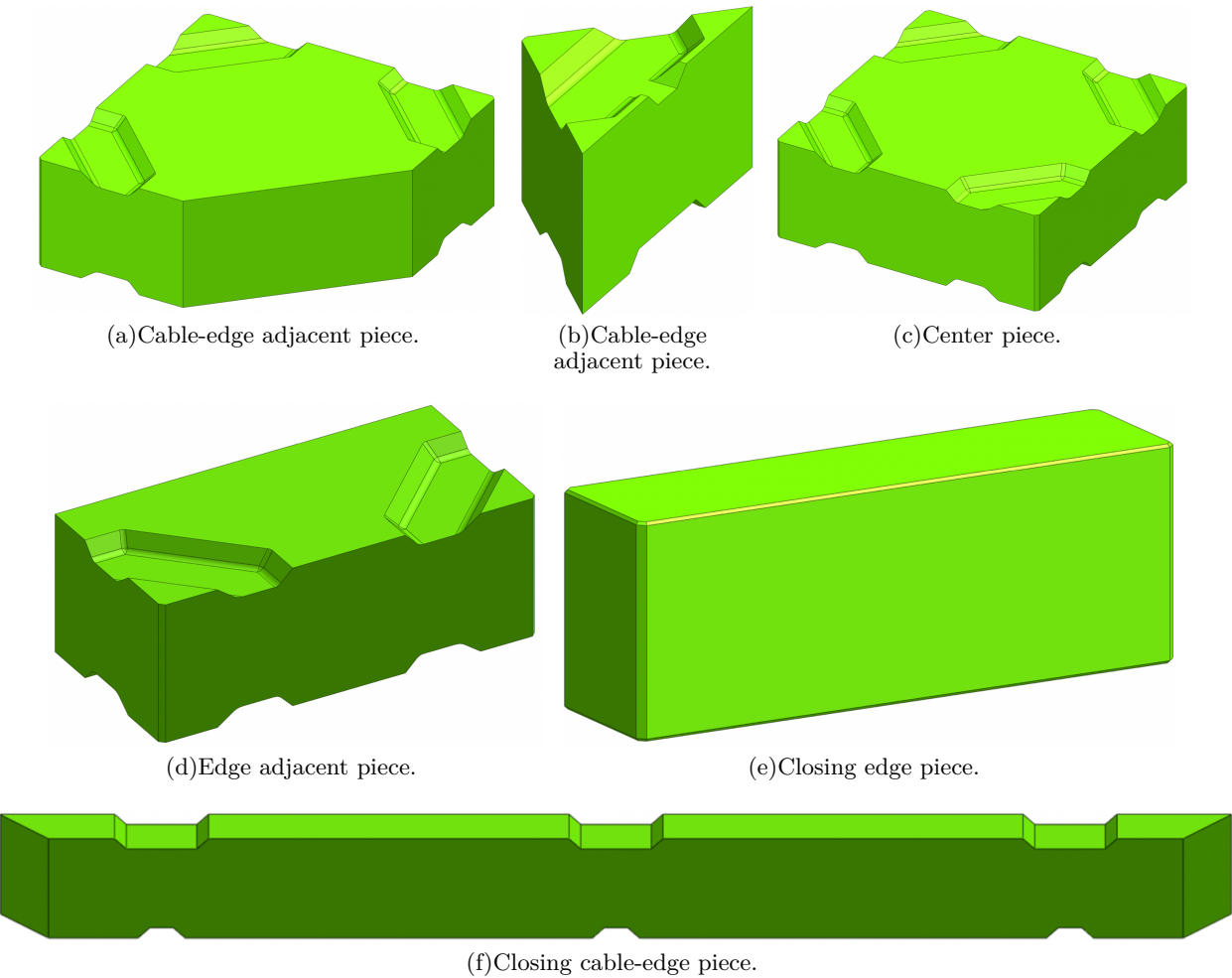


FIG. 86. Different Gd-loaded components making up the endcaps of the DS-20k LAr TPC. To accommodate the cabling and to minimize the machining workload, the number of unique pieces has been kept to a minimum.

3621 VPDU+s are installed, the connectors will be mounted and the cabling will be routed within
 3622 the optical plane structure, weaving in and out of the grooves of the Gd-loaded endcaps. This
 3623 will allow for cable testing before any photo detectors are installed along with the possibility to

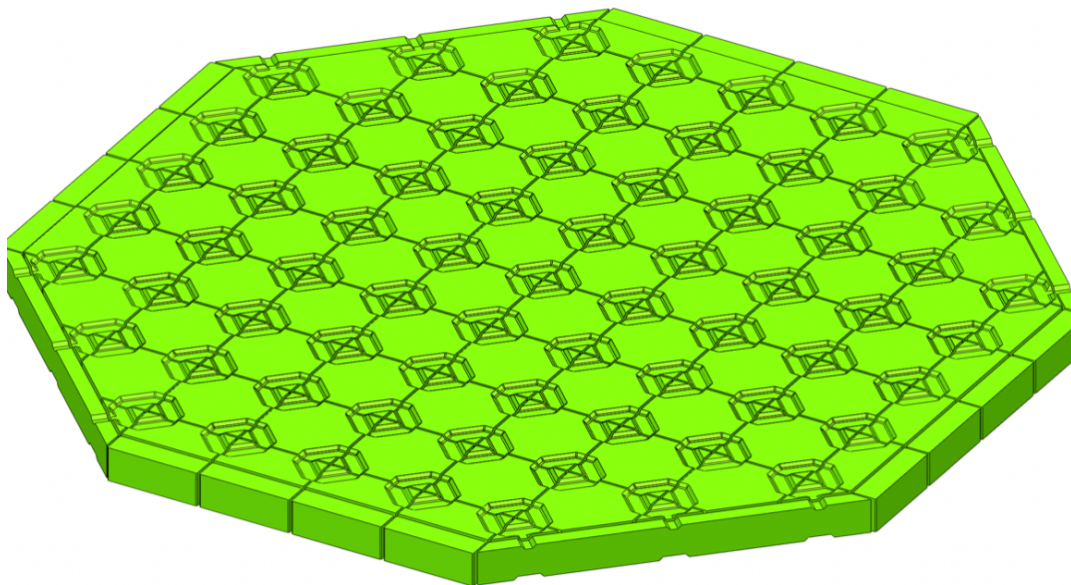


FIG. 87. Fully assembled Gd-loaded PMMA endcap. The grooves visible here will align with grooves in the titanium x and y cross-pieces such that paths for the cables will form that the cables can pass through. Keep in mind that the cables can weave into the z direction as well.

3624 remove/replace individual PDU+s if necessary.

3625 Given the octagonal design with eight joining edges of the barrel walls, the cables will be grouped
 3626 into eight bundles. The bottom optical plane will have the 264 TPC and 20 Veto cables routed to
 3627 the four cable-edges (see Fig. 79(c)). From here, each quadrant will be split into two bundles of 35
 3628 and 36. Each bundle will be routed and secured along a steel angle-bracket holding two of the walls
 3629 panels together. As the bundle moves up the wall, cables from the ten wall-mounted VPDU+s will
 3630 join. Similarly, the eight bundles from the top optical plane will group one-to-one with the existing
 3631 bundles and route to the top flange.

3632 The eight cable groupings will be brought through the titanium vessel to the four chimneys
 3633 located on the roof of the cryostat via flexible bellows. The bellows will serve three functions: 1) cable guides; 2) isolation between the UAr and AAr volumes; and, 3) continuous movement of the
 3634 gas outward to the purification system. As demonstrated with DarkSide-50, the third function is
 3635 crucial. The out-gassing from the cabling must not be allowed to flow into the clean UAr volume,
 3636 so the bellows will be sized such that a high flow rate is maintained away from the clean argon
 3637 volume.
 3638

3639

7.2.11. ESR & PEN

3640 PBS Item: DS.D.TAV.PEN

3641

3642 To efficiently collect the scintillation light generated within the Veto, all of the surfaces have
 3643 to be covered with a reflector and a wavelength shifter. As in the TPC, ESR foils will be used.
 3644 However, given the ease of procurement, handling, and the less stringent requirements of light
 3645 collection in the Veto, PEN foils will be used for the wavelength shifter. The ESR and PEN foils
 3646 will be secured to the exterior of the TPC barrel walls, to the top and bottom optical planes, and
 3647 to the inner surface of the titanium vessel with PTFE push-pins. The pins will be inserted in holes
 3648 machined into the TPC barrel walls and the titanium optical plane structure. To attach the foils
 3649 to the interior surface of the titanium vessel, a dedicated set of tapped inserts will be welded onto
 3650 the vessel. Fig 88 shows the a zoom-in view (left) of the panels and push-pins, and the panels

3651 fully assembled (right) to mount to the titanium vessel. As in the TPC, the ESR and PEN foils
 3652 will feature elongated push-pin holes which will point to the center of each foil. This will allow for
 3653 the differential thermal contraction without damaging any components, and the ESR foils will be
 3654 slightly over-sized to avoid any gaps in coverage at 87 K.

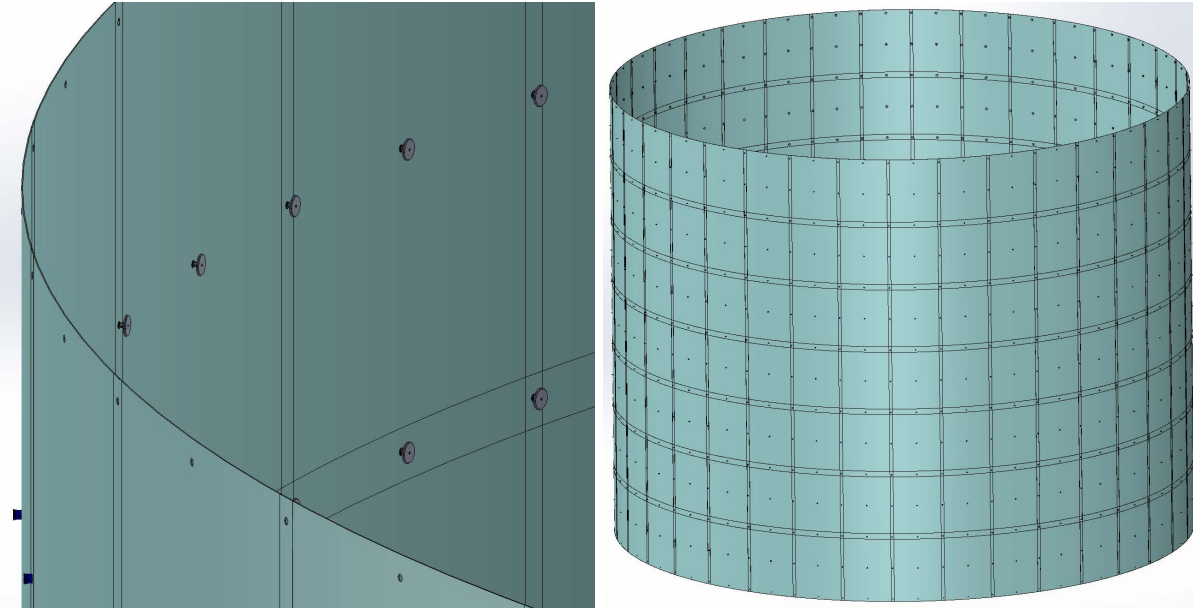


FIG. 88. The ESR and PEN reflector foil assembly. These panels will attach to the interior walls of the the titanium vessel with PTFE push-pins. A zoom-in of the panels highlighting the push-pins and the full panel assembly is shown on the left and right, respectively. Similar panels will attached to the exterior of the TPC walls.

3655

7.2.12. Chimneys

3656 PBS Item: DS.D.TAV.CHI

3657

3658 The cryostat central top cap is equipped with four DN300 penetrations for chimneys, which host
 3659 both the Veto and TPC signals and power supplies. The design of the chimney is shown in Fig.
 3660 89. Each chimney is equipped with total of 5 identical DN 250 CF feedthrough side ports, four of
 3661 which are for the TPC and one for the Veto. A large DN 450 CF wire sealed top blank flange is
 3662 used for view and easy access during installation. This volume is linked directly to the UAr gas
 3663 volume. A small gas extraction port is added to each chimney and linked to the UAr cryogenic
 3664 system so that a positive flow of argon gas up through the *cable tray* bellows prevent the dirty gas
 3665 back-diffusion from the warm space down to the clean space. In total 16 feedthrough flanges for
 3666 TPC can host up to the required 2112 TPC channels + 192 spares; 4 feedthrough flanges for Veto
 3667 can host up to the required 480 veto channels + 96 spares. Parameters of the chimney connections
 3668 are reported in table XXXIX.

3669 The flanges of the chimneys will be equipped with FR4-based feedthroughs. LNGS already
 3670 demonstrated the capability of designing and producing such PCBs, capable of a leak rate lower
 3671 than 10^{-9} mbar/s on CF63 flanges. Fig. 90 shows the CAD design and the CF63 PCB flange
 3672 manufactured at LNGS. This technology uses multi-layer FR4 with staggered blind vias between
 3673 layers. To withstand the pressure a total thickness of 4 mm is required with a longitudinal stainless
 3674 steel reinforcement on the flange. The PCB is bonded to the flange with an indium seal between
 3675 the stainless steel compression ring and an annular trace on the FR4. To avoid the formation of

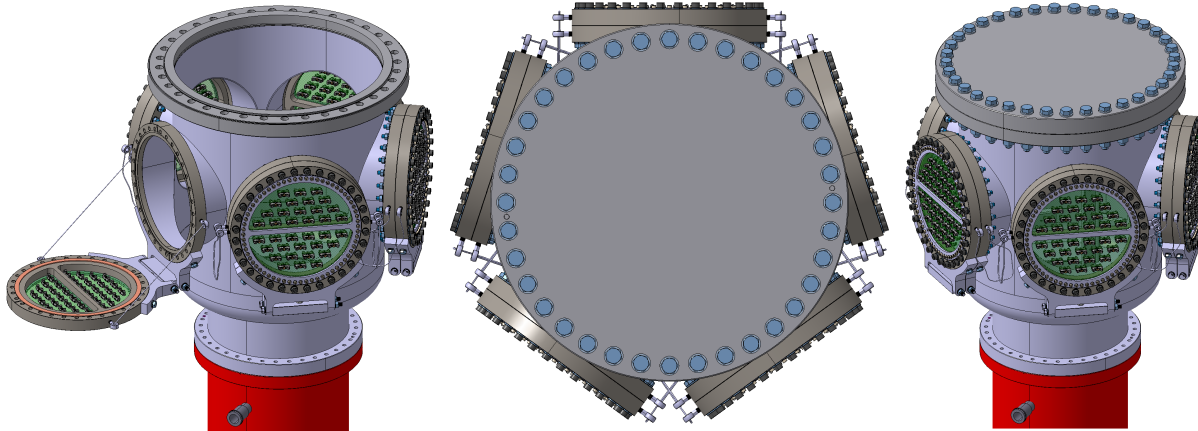


FIG. 89. CAD design of the signals chimney. Open during installation (left), top view (middle) and isometric view (right). There are 5 feedthrough flanges on each chimney: one serves for veto readout and the other four for TPC readout. A large port on top is for easy access during cables installation. The gas extraction port is visible at the bottom.

Parameter	Value
Total number of chimneys on the cryostat	4
Number of TPC feedthrough flanges per chimney	4
Number of Veto feedthrough flanges per chimney	1
Total number of TPC channels	2112
Total number of Veto channels	480
Total number of TPC PDU+ connectors	528
Total number of Veto PDU+ connectors	120
Minimum required number of PDU+ connectors per TPC flange	33
Minimum required number of PDU+ connectors per Veto flange	30
Actual number of PDU+ connectors per flange	36
Actual number of channels hosted by TPC feedthrough flanges	2304
Actual number of channels hosted by Veto feedthrough flanges	576

TABLE XXXIX. Chimney parameters.

3676 weak inter-metallic bonds with indium, the PCB traces are plated with gold; this also simplifies
 3677 soldering of the components. The connectors are surface mounted (vertically), a latching system
 3678 provides the retention of the cable. On the inner side the connector provides 16 conductors with 2
 3679 mm pitch, matching the mating part on the SAMI cable. On the external part the same connectors
 3680 will be mounted: a double RJ45 cable will mate to the feedthrough connectors, with separate paths
 3681 for the signals and for the power. This solution is both cheap and flexible. A total of 36 connectors
 3682 are mounted in each flange, serving an equivalent number of PDU+. The flange is equipped with
 3683 a hinge and a mechanical stop to guarantee safe and efficient cabling. The PCB can be produced
 3684 externally at vendors that can provide filled blind vias, a common technique. The connectors can
 3685 be mounted as service at the same company. The CF250 flanges will have to be custom machined
 3686 to host the PCB and the indium seal.

3687 FEAs have been carried out to check the PCB against the maximum expected internal pressure
 3688 and vacuum condition. Results are shown in Fig. 91.

3689 PBS Item: DS.D.TAV.TV

7.2.13. The titanium vessel

3690 PBS Item: DS.D.TAV.TV

3691 The TPC and veto are hosted inside a titanium vessel, which acts as a separator between the UAr
 3692

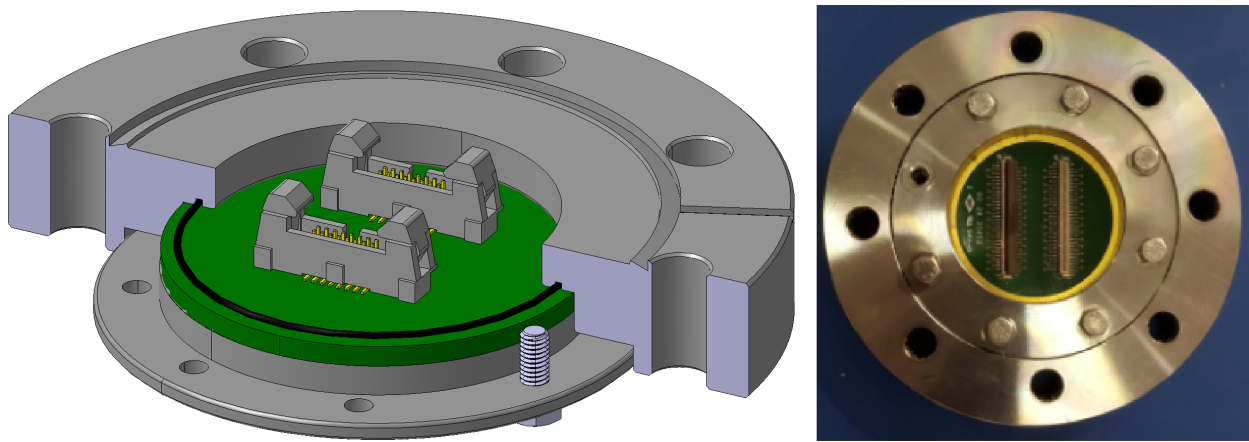


FIG. 90. CF63 PCB flange: CAD design (left) and manufactured prototype at LNGS (right).

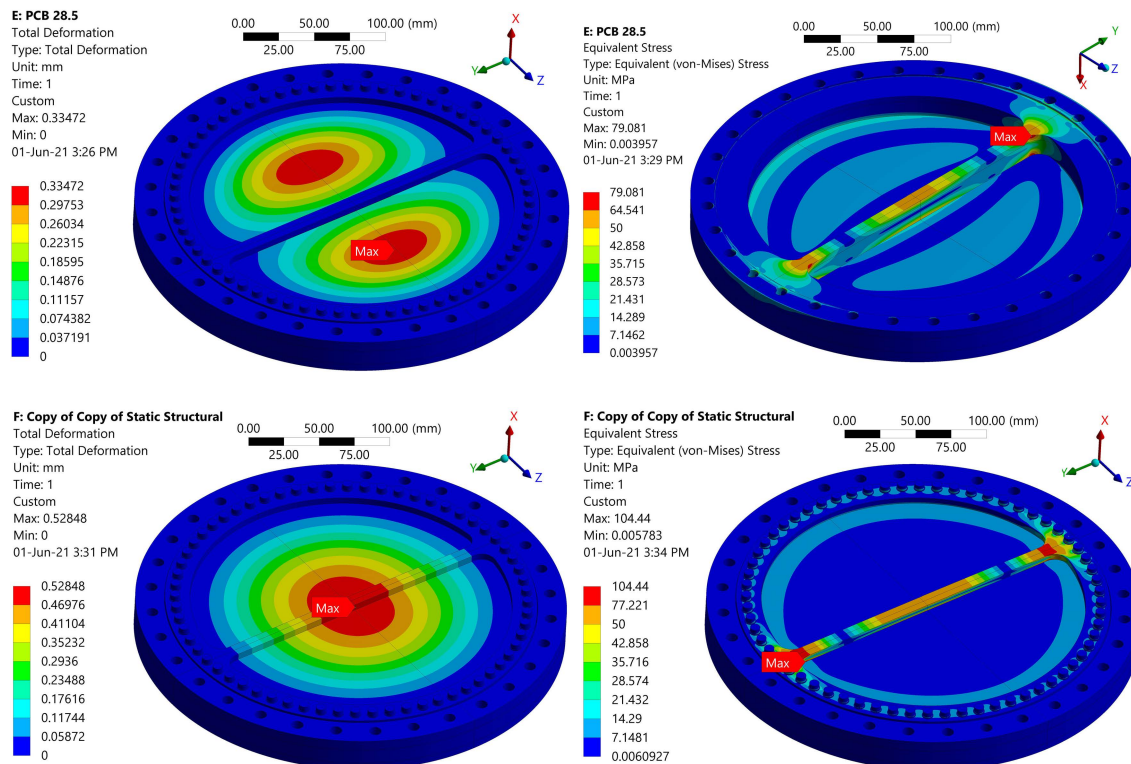


FIG. 91. FEA results of the chimney PCB electrical feedthrough. Top left: deformation under vacuum and top right: stress under vacuum; bottom left: deformation with +0.35 barg pressure and bottom right: stress with + 0.35 barg pressure.

and AAr volumes. The ability to evacuate the inner volume hosting the Inner Detector immersed in UAr is a key point in the design, as this will significantly ease the installation and commissioning phases, with respect to earlier designs where this operation was not possible. The Ti vessel cross section, with the main elements highlighted, is shown in Fig. 92. The parameters of the vessel are reported in Table XL.

Several FEA checks have been performed to validate the mechanical design while minimizing the mass for radiopurity requirements. Different load cases have been considered, such as the maximum expected operational positive pressure differential, vacuum, TPC lifting and TPC plus vessel self

Parameter	Value
Vessel inner diameter	4650 mm
Vessel total internal volume	80 m ³
Total UAr mass (with Inner Detector inside)	99.2 t
Vessel weight	8300 kg
Modules	2 x torispherical domes + 4 x barrel modules
Top dome seal	Indium and o-ring seals
Barrel modules seal	Welded seal
TPC and veto signals ports	4 x DN CF 100
Calibration pipes ports	4 x DN CF 100
Cryogenics ports	8 x DN CF 63
HHV and LHV ports	3 x DN CF 63

TABLE XL. Titanium vessel parameters.

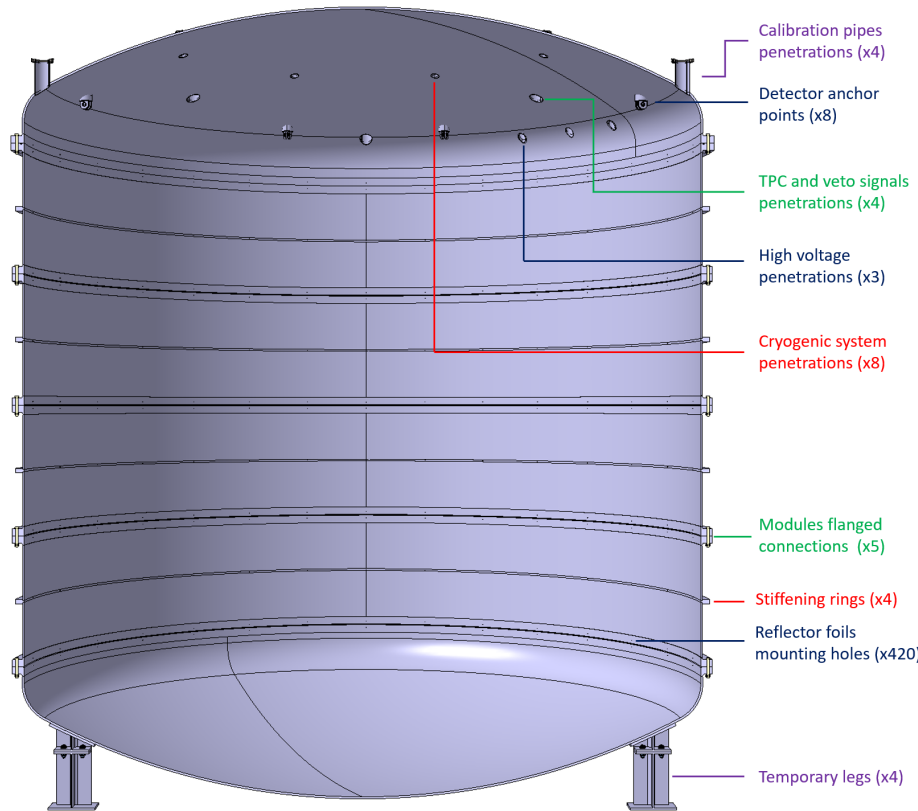


FIG. 92. Titanium vessel cross section with markup of the main elements.

3701 weight. Both the scenarios in which the vessel is hanging on the Detector Support Structure
 3702 (DSS) and sitting on the temporary legs have been taken into account (i.e. installation/operation
 3703 configuration). Combinations of different cases has been checked as well, if relevant. Buckling
 3704 analyses have been carried out for the relevant load cases. For brevity, here only results for the
 3705 vacuum plus gravity load case, while the vessel is hanging on the DSS, are reported in Fig. 93.

3706

Vessel body

3707 PBS Item: DS.D.TAV.VB

3708

3709 The vessel fabrication strategy takes into account LNGS transportation and handling limitations,

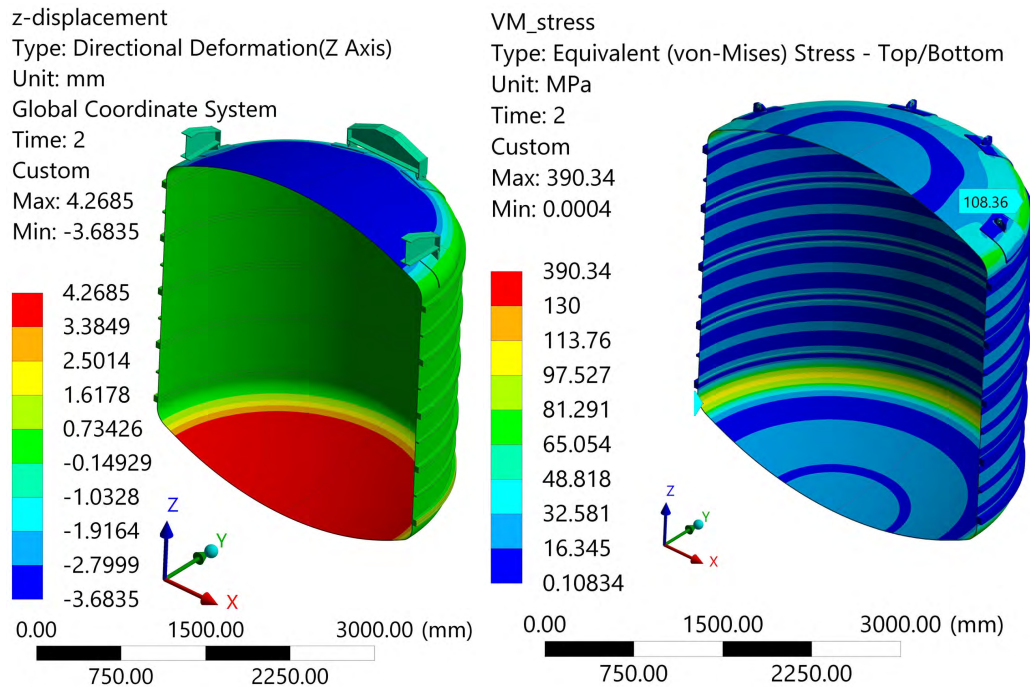


FIG. 93. Titanium vessel FEA results for the vacuum plus gravity load case. The vessel is hanging on the DSS. Left: z axis deformation; Right: VM stresses.

3710 including the Hall C door size and crane capacities. The vessel barrel is split into 4 identical modules
 3711 that are to be manufactured in the workshop and assembled on site, where they are bolted together.
 3712 The barrel modules seal is done via an on-site welding. In order to increase buckling resistance
 3713 against vacuum, stiffening rings are welded to the barrel. The stiffening rings and the internal
 3714 surfaces of the flanges are built with integrated holes for mounting the ESR and PEN foils. In
 3715 addition, a number of dedicated stubs are placed on the vessel internal surface where the foils are
 3716 attached and held in place with custom made push-pins. During the installation phase, the vessel
 3717 is sitting on temporary legs that can be unbolted once the detector is lifted by the detector support
 3718 system.

3719 *Top dome*

3720 PBS Item: DS.D.TAV.TL

3721
 3722 The top dome hosts all the required penetrations for the signal cables, calibration system, cryo-
 3723 genic system, detector support system and high voltage, as shown in Fig. 92. The 8 supporting
 3724 lugs are integrated to the top dome and the positioning is such to minimize the dome stress when
 3725 supporting the TPC weight. The top dome flange design provides the possibility to use either an
 3726 indium or o-ring seal for repair and quick access. The top dome is equipped with the same systems
 3727 as on the barrel to hold the reflector foils in place.

3728 *7.2.14. Detector Support System*

3729 PBS Item: DS.D.TAV.DSS

3730
 3731 The detector, integrated with the titanium vessel, is supported and leveled via the Detector

3732 Support System (DSS). The load is transferred to the cryostat roof warm structure by 4 identical
 3733 assemblies, comprising a warm and a cold part. The warm part, placed on top of the cryostat
 3734 roof, includes the following elements: a lifting jack is used to adjust the vertical position; a load
 3735 cell monitors the load on each assembly; 2 connection beams link the system to the cryostat roof;
 3736 an internal bellow separates the AAr volume from the external atmosphere and accommodates
 3737 vertical and horizontal adjustments; a mechanical stop is integrated in the support rod as a backup
 3738 safety feature and an external bellow accommodates installation misalignments. The lifting jack is
 3739 a commercially available stepper motor assembly, equipped with a speed reducer, limit switches as
 3740 a first layer safety feature and position sensors. The load and the position of the single rod assembly
 3741 are continuously monitored. A full manual leveling system is also being evaluated. Four DN150
 3742 penetrations on the cryostat central top cap are dedicated to the DSS. A conceptual drawing of the
 3743 DSS warm part is shown in Fig. 94. The typical DSS warm assembly connected to the cryostat
 3744 roof beam structure is shown in Fig. 95.

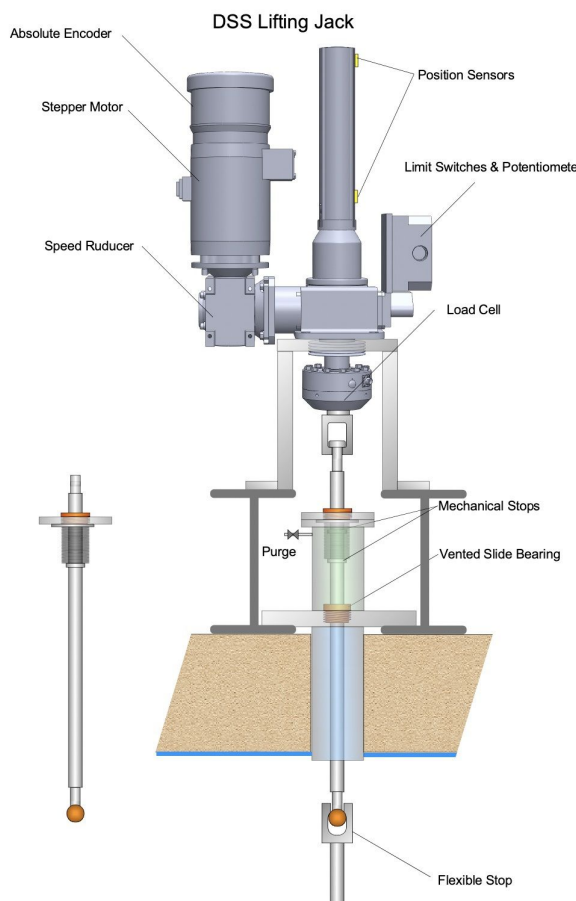


FIG. 94. Detector Support System conceptual sketch.

3745 The typical DSS cold assembly is shown in Fig. 96: the support rod is connected to a titanium
 3746 beam through a clevis pinned connection. The titanium beam is used both as a lifting jig during
 3747 detector installation and as a permanent link between the rod and the titanium vessel, through
 3748 two pinned connections. The design of the titanium beam minimizes the vertical space occupied
 3749 during installation and the support system permanent mass while ensuring the required mechanical
 3750 strength.

3751 The DSS executive design is currently under finalization; all the required analyses to check the
 3752 mechanical integrity of the apparatus and the ability to level the detector at the desired accuracy
 3753 are ongoing.

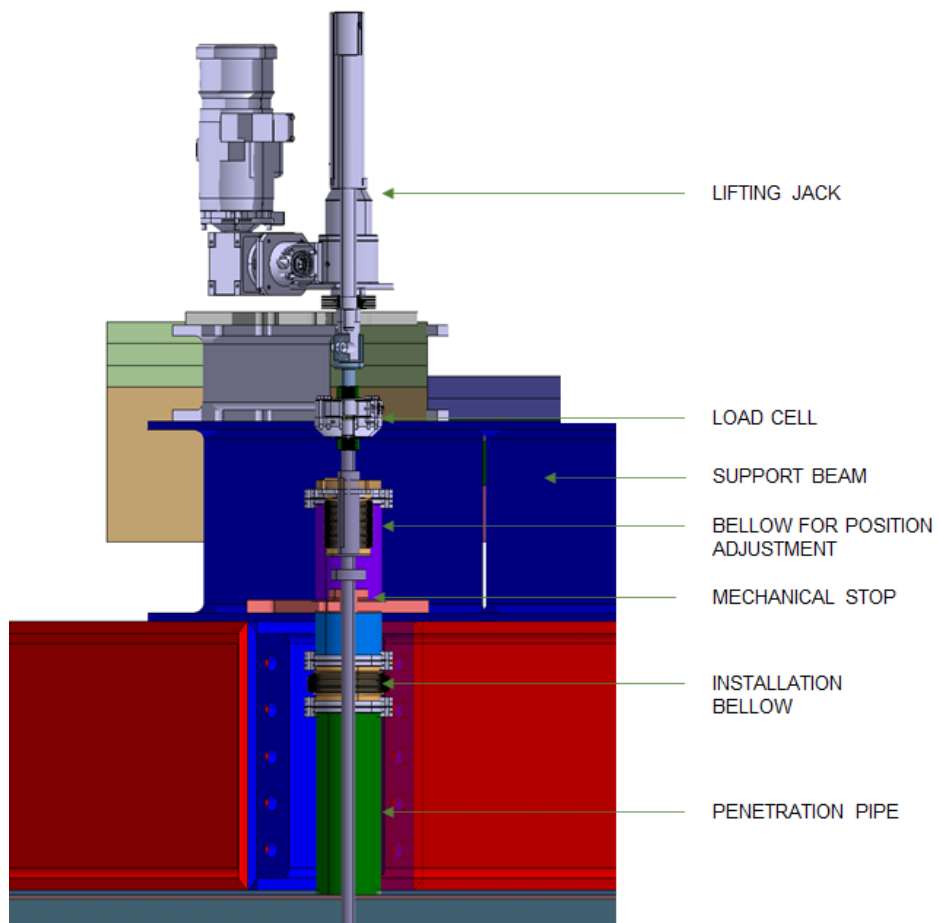


FIG. 95. Typical Detector Support System warm assembly.

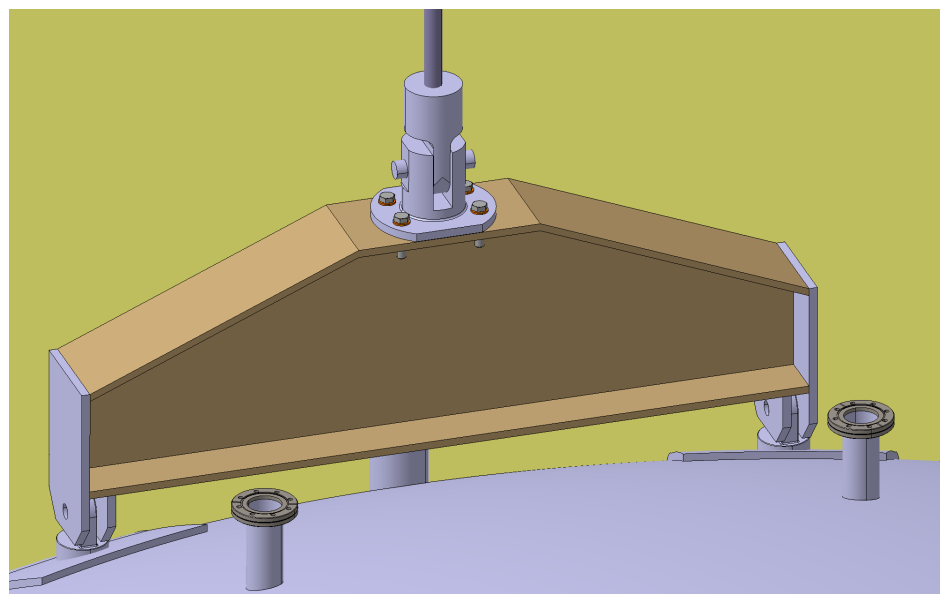


FIG. 96. Typical Detector Support System cold assembly.

3754

7.3. Outer Cosmic Veto Detector

3755

PBS Item: DS.D.OV

3756

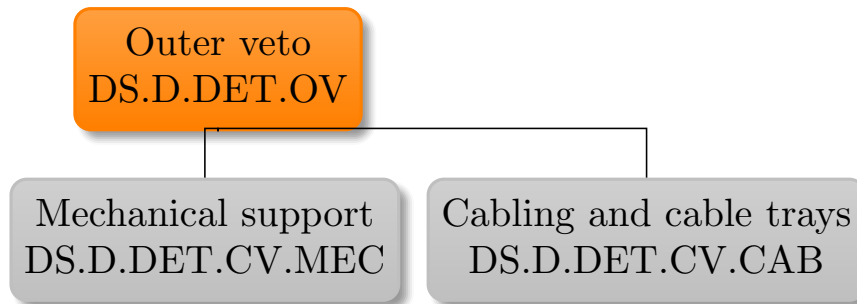


FIG. 97. PBS of the Outer Veto detector.

3757 The outer veto detector is designed to tag cosmogenic muons and shower products correlated
 3758 with cosmogenic neutrons which may produce backgrounds in the TPC. This is achieved by in-
 3759 strumenting the outermost LAr volume in the cryostat. Its PBS is shown in Fig. 97.

3760 Depending on the wafer yield of the SiPM production and the results of quality assessment tests,
 3761 up to 512 $50 \times 50 \text{ mm}^2$ tiles may be available for this purpose. Since these tiles will be used for
 3762 measuring higher energies and do not require precision, the quality control requirements for the tiles
 3763 used in the outer veto will be lower than for the inner veto and TPC. In particular, higher noise
 3764 rates and lower timing resolution are acceptable in the outer veto photoelectronics. These tiles will
 3765 be arranged into up to 32 VPDU, the faces of which will be coated in an evaporated layer of TPB.
 3766 Depending on the wafer yield of tile production for the inner Veto and TPC, fewer tiles may be
 3767 available for the outer veto; in this case, the number of VPDU will be adjusted accordingly, down
 3768 to a minimum of 24 VPDU, as required to meet the minimum light yield in optical simulations of
 3769 the outer veto.

3770 Photo-sensor arrays will be lowered into the AAr cryostat through a set of dedicated flanges on
 3771 the top of the cryostat, spaced evenly around the perimeter, inset 20 cm from the inner wall. Glove
 3772 boxes will sit on top of each flange, so the photo-sensor arrays can be placed in position through
 3773 each flange either before or after the outer veto has been filled with LAr.

3774 Assuming 32 VPDU are available for the outer veto, 4 VPDU will be lowered down each flange.
 3775 In the case that fewer tiles are available, channels will be distributed as uniformly as possible coming
 3776 from each flange. Each VPDU will be mounted on a $25.4 \text{ cm} \times 25.4 \text{ cm}$ stainless steel plate, using
 3777 mounting holes in the back of the PCB. Four holes are drilled into these plates, two spaced 22.7 cm
 3778 apart on both the top and bottom, allowing each plate to be attached to the ones above and below
 3779 it using Kevlar 49 rope, which has been successfully used at cryogenic temperatures in CUORE.
 3780 Two eye bolts in the flange will allow the top VPDU to attach to it. Each VPDU mount plate will
 3781 attach to the plate or flange above it with a 331 cm-long segment of rope, crimped to itself with
 3782 9.6 cm of overlap to form a loop, connecting the upper holes in one plate to the lower holes in the
 3783 plate beneath it. Doing so leaves 138 cm between each VPDU, leaving them approximately evenly
 3784 spaced along the vertical length of the outer veto. To dampen motion, a 20 kg stainless steel bar
 3785 connects to the bottom VPDU plate via a pair of eye bolts and a 115 cm-long loop of rope, leaving
 3786 a 30 cm gap between it and the lowest plate. The use of two ropes per flange is meant to prevent
 3787 twisting of the VPDU array. Cables from each VPDU will run up the length of the rope, behind
 3788 the VPDU faces, and connect to a 16-pin connector on the bottom of the flange.

3789 To compensate for the low optical coverage ($\sim 0.25\%$), the AAr volume will be lined with
 3790 wavelength-shifting and reflective foils. This surface will consist of three layers of Tyvek 4077D

3791 reflector beneath a layer of PEN foil, which will shift incident VUV photons to visible wavelengths
 3792 at which the Tyvek will reflect them with 96 % reflectivity. Tyvek 4077D is used in the outer veto
 3793 due to its relatively low cost and availability in large rolls, suitable for covering large surface areas
 3794 with minimal intermediate support. A protective titanium-oxide coating maintains Tyvek 4077D's
 3795 reflectivity while submerged in liquid, but imposes a cutoff at wavelengths shorter than 400 nm,
 3796 mitigated by the PEN layer. The use of three layers protects against degradation of the reflectiv-
 3797 ity over time despite the protective coating. These wavelength-shifting and reflective foils will be
 3798 arranged in overlapping strips. These foils will be cut into 1 m-wide strips: each lateral wall will
 3799 have 9 800 cm-long strips of PEN, and the 9 stacks of Tyvek 4077D strips (27 in total because of
 3800 triple layering) will be 830 cm long. These lengths allow the foils to thermally contract when the
 3801 outer veto is filled with LAr, while maintaining a few centimeters of overlap between neighboring
 3802 strips, ensuring complete coverage without disrupting fluid flow.

3803

7.4. The Calibration System

3804 PBS Item: DS.D.CAL

3805

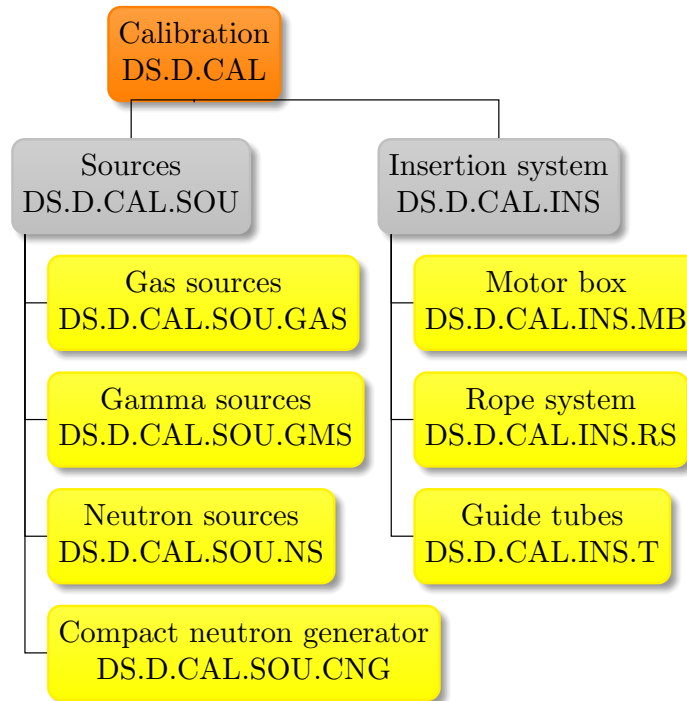


FIG. 98. PBS describing the calibration item.

3806 Calibrations for both the TPC and the veto detector range from low-level calibration of detec-
 3807 tor response, such as the single-photoelectron response of individual photosensors, to high-level
 3808 physics calibration like the acceptance as a function of energy for nuclear recoils. A combination
 3809 of radioactive sources, a neutron generator, and light sources ensures a robust calibration plan to
 3810 enable DS-20k to achieve its science goals. Figure 98 shows the PBS.

3811

7.4.1. Calibration pipes system

3812 The baseline for the calibration system of the TPC consists in two U-shaped pipes of 3 cm
 3813 internal diameter and 1.5 mm thickness. The diameter is sufficient for radioactive sources and may
 3814 need to be enlarged in order to accept DD-gun as a neutron generator. The preferred material
 3815 for the pipes is Titanium. Screening of the raw material is required in order keep the background
 3816 contributions from the pipes to less than few percent of the global level of estimated background of
 3817 0.10 events in 200 tonne×year exposure. The surface of the pipes will be covered with a reflector
 3818 in the optical volume of the Veto. The pipes follow a routing along and below the TPC which is
 3819 illustrated in Figure 99. Each pipe goes vertically along a lateral face of the TPC, then reaches
 3820 the bottom following a bending of 40 cm curvature radius, goes to the opposite side passing by the
 3821 center and finally (after a second bending) goes up vertically along the opposite lateral face of the
 3822 TPC. A further set of bends is necessary for each pipe to go out through the two exits on the roof
 3823 of the cryostat, away from the detector support system.

3824

7.4.2. Calibration control system

3825 PBS Item: DS.D.CAL.INS

At the location of one of the two exits (per pipe), a glove box will be installed, on top of the smaller flange, for the insertion and fixation of the source to the rope which goes inside the pipe. This box will be followed by a motor box allowing the motion of the rope thanks to a set of pulleys, drum, motor and encoders, based on the SNO+ motor system. The four motor boxes have been built and are currently being tested (see Figure 100). The design of the glove box has started. The operation of the calibration system at LAr temperature is being tested and validated with a mock-up system equipped of one U-pipe immersed in a tank of liquid nitrogen. The pipe will be equipped with a glove box, a pair of motor boxes and a rope, and will be filled with nitrogen gas to prevent any ice formation inside. Deformation, humidity, temperature are monitored during tests. The movement of a dummy source, inside the two 40 cm diameter bends will also be tested.

3836 During operation of the DS-20k detector, outside calibration runs, valves will be closed below
 3837 the motor boxes; the pipes will be either evacuated or filled with LN2.

3838

7.4.3. Gas Sources

3839 PBS Item: DS.D.CAL.SOU.GAS

3840 Full volume calibration of the TPC will be achieved with distributed gas sources: ^{83m}Kr and ^{220}Rn .
 3841 Gas sources are simple to implement, since they are added to the argon re-circulation stream and
 3842 feature short half lives, decaying quickly to negligible levels. The mono-energetic decays of ^{83m}Kr ,
 3843 distributed through the active volume of the TPC, can give a key calibration point in the WIMP
 3844 recoil energy region. The 3D reconstruction of events in the TPC allows the full mapping of position-
 3845 dependence of the light yield using the ^{83m}Kr source. This means that, while broad dissemination
 3846 through the active volume is important, a uniform distribution is not required.

3847 The ^{83m}Kr decays quickly ($\tau=2.64\text{ h}$) to a stable nuclide and causes no long-term contamination or
 3848 background to the WIMP search. The DS-20k ^{83m}Kr source is based on the source used successfully
 3849 in DS-50. A tiny droplet of a solution of ^{83}Rb ($\tau=124.4\text{ d}$) is adsorbed into a piece of charcoal; after
 3850 drying the charcoal is placed between two particulate filters in a branch of the argon re-circulation
 3851 system which is normally isolated and can be pumped separately to vacuum. In DS-50, an initial
 3852 8.5 kBq of ^{83}Rb gave a ^{83m}Kr trigger rate of hundreds of Hz, even though the flow subsequently
 3853 passed through a cooled radon trap. In DS-20k, the challenge will be to get the ^{83m}Kr broadly
 3854 distributed in the 49.7 t active mass before it decays. To further this, LAr will be returned to the
 3855 TPC after re-purification via numerous tubes whose endpoints will be distributed over the surface

3856 area of the TPC side panels.

3857 ^{220}Rn and its short-lived daughters produce several γ -rays, β 's, and α 's of various energies,
 3858 making it an attractive distributed calibration source. It can be implemented in a similar manner
 3859 as the ^{83m}Kr source, except that the charcoal trap needs to be bypassed to avoid trapping the Rn.
 3860 The ^{220}Rn source may be prepared as a ^{228}Th electroplated on stainless steel or copper, enclosed in
 3861 a small metal-sealed and vacuum-tight volume equipped with a VCR/CF port. The use of a ^{220}Rn
 3862 source has many potential advantages:

- 3863 • ^{220}Rn and its daughters are short-lived (the longest half-life in the chain is 10.6 h for ^{212}Bi)
 3864 and so the activity introduced into the detector will disappear after a few days;
- 3865 • there are several high energy α 's emitted by ^{220}Rn and daughters in the chain (at 6.05 MeV,
 3866 6.09 MeV, 6.29 MeV, 6.78 MeV, and 8.78 MeV);
- 3867 • the presence of the coincident ^{220}Rn - ^{216}Po and ^{212}Bi - ^{212}Po decays allows study of the actual
 3868 source distribution and the LAr flow patterns including potential “dead volumes” that are
 3869 not affected by the LAr circulation;
- 3870 • the emitted radiation also allows study of the drift of the charged ions inside the LAr volume
 3871 (which interesting also with respect to Po isotopes from the ^{222}Rn chain);
- 3872 • last, but not least, low-energy β 's appearing in the chain may be used for calibrations of the
 3873 low-energy response of the detector.

3874 7.4.4. Gamma-ray Sources

3875 PBS Item: DS.D.CAL.SOU.GMS

3876 The γ -ray sources, ^{57}Co (122 keV), ^{133}Ba (356 keV), ^{137}Cs (662 keV), and ^{60}Co (1.33 MeV), are
 3877 planned for use in an external guide system that passes around the TPC . The combination
 3878 of these sources in the absence of ^{39}Ar gives an excellent calibration of the electron recoil PSD
 3879 band and detector energy scale near the TPC wall and fiducial volume boundary. In addition,
 3880 external γ -ray sources provide valuable data for tuning of the detector response in the Monte Carlo
 3881 simulation. The γ -ray sources were chosen to span the energy range of interest in combination
 3882 with the distributed ^{83m}Kr and ^{220}Rn sources, while providing the additional penetrating power
 3883 with ^{60}Co MeV source. The sources will be miniature in size to allow insertion inside the source
 3884 guide tubes. An overall view of the design is shown in Fig. 99. Due to the large detector size,
 3885 γ -ray sources will probe the edge of the fiducial volume of the TPC and the veto, complementing
 3886 the coverage of the distributed sources that will probe the full volume, albeit with limited energy
 3887 range.

3888 7.4.5. Neutron Sources

3889 PBS Item: DS.D.CAL.SOU.NS

3890 Neutron sources are of particular interest for calibration of the nuclear recoil PSD band and for
 3891 measurement of the efficiency of the neutron veto, key features of the DS-20k design. To these
 3892 ends, small (α,n) sources such as $^{241}\text{AmBe}$, $^{241}\text{Am}^{13}\text{C}$ and $^{241}\text{AmLi}$ will be fabricated to fit into
 3893 the guide tube system. $^{241}\text{AmBe}$ is used as a tagged neutron source utilizing the 4.4 MeV γ -ray
 3894 emitted in 56 % of all cases. $^{241}\text{Am}^{13}\text{C}$ can serve as a γ -ray-free neutron source for veto calibration
 3895 by moderating alphas from the ^{241}Am such that the (α,n) reaction cannot reach the first state of
 3896 the daughter ^{16}O nucleus. The $^{241}\text{AmLi}$ source features a 1.5 MeV neutron energy end point, well
 3897 below average energy of $^{241}\text{AmBe}$ neutrons.

3898 While the $^{241}\text{Am}^{13}\text{C}$ source represents the best choice for calibration of the neutron detection
 3899 efficiency, radioactive decays from activity present in the source holder and detector material, un-
 3900 correlated with the AmC (α,n) reaction itself, may produce random backgrounds that can interfere
 3901 with the characterization of nuclear recoils in LAr. The $^{241}\text{AmBe}$ source was shown to be more
 3902 suitable for this calibration. The 4.4 MeV γ -ray is promptly emitted in the $^9\text{Be}(\alpha,\text{n})^{12}\text{C}$ nuclear

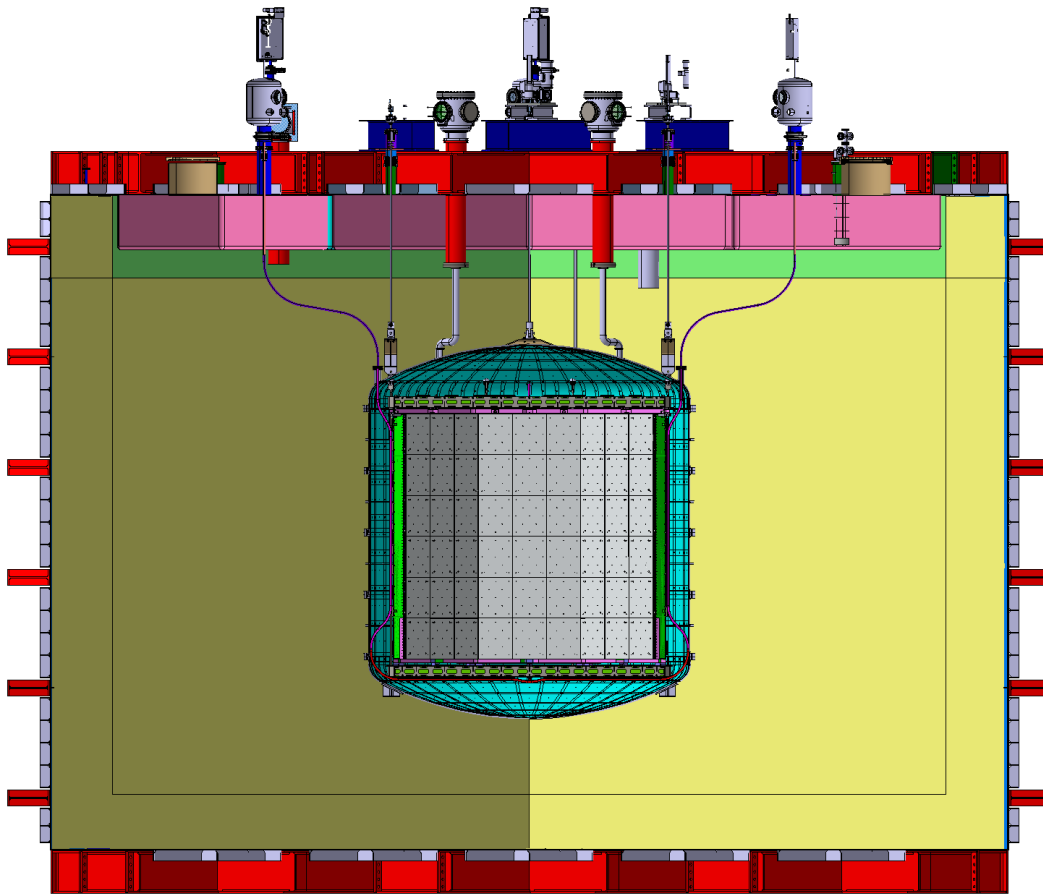


FIG. 99. Schematic representation of the system of guide tubes for insertion of sources. The four colours (pink, purple, magenta and red, from top to bottom) indicate the four portions of the pipes which will be welded or connected via a flange.

reaction in about 56 % of cases. By tagging the 4.4 MeV γ -ray in the Veto in a very tightly constrained time interval prior to the signal in the TPC, a very pure sample of nuclear recoils is obtained. The $^{241}\text{AmBe}$ calibration in DS-50 provided the best available nuclear recoil calibration of the DS-50 TPC *in situ*, and was in excellent agreement with the nuclear recoil calibration from the stand-alone SCENE experiment [60].

Due to the presence of Gd loaded acrylic between the TPC and the neutron sources, the rate of neutrons reaching the TPC volume is rather low and thus able to reach only the volume near the insertion point. The possibility to reduce the thickness of the loaded acrylic for a limited region may be considered, to increase the neutron rate inside the TPC.

3912

7.4.6. DD Neutron Generator

3913 PBS Item: DS.D.CAL.SOU.CNG

3914 Compact neutron generators (CNG) are promising devices for TPC calibration as neutrons are
 3915 generated one at a time without any accompanying γ -rays and the neutrons have a relatively
 3916 high energy which ensures a better penetrating power. These devices often consist of miniature
 3917 cylindrical vacuum chambers with a characteristic length of 5 cm and a diameter of 4 cm in which
 3918 a DD reaction takes place. In the DD reaction, an accelerated deuterium ion collides with a
 3919 deuterium target, resulting in the production of ^3He and a 2.45 MeV neutron. The deuterium ions
 3920 are produced as a result of ionization of the residual gas D₂, which fills the chamber at a pressure
 3921 of a few mTorr. The accelerating voltage required is several tens of kV and efforts are underway

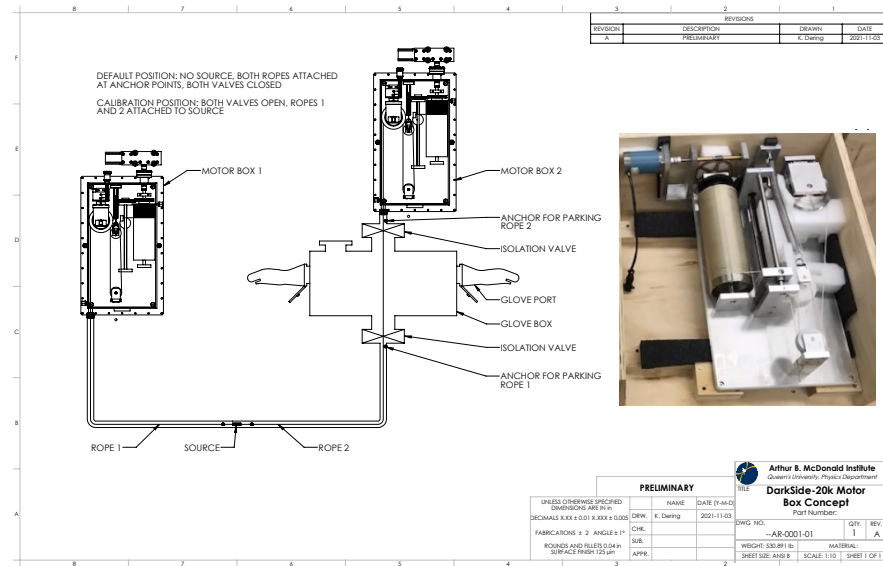


FIG. 100. Schematic representation of the calibration control system: the two motor boxes, one glove box and the two ropes to hold the source. The anchor points for the rope during physics data taking periods are shown. A picture of one motor is inserted.

3922 to achieve autonomous power generation. The expected yield is 10 n/s to 10^3 n/s depending on the
3923 applied high voltage.

3924 DS-20k is developing a novel compact high voltage neutron generator (HVNG) based on a carbon
3925 nanotube ionizer. In the HVNG, the electrical field is created in an oil-filled HV power supply.
3926 The device produces continuous neutron radiation and generates only a modest amount of heat.
3927 This reusable source is well suited to periodic or routine calibration modes. The HVNG can be
3928 controlled via adjustment of the high voltage value remotely. The design of HVNG, small enough
3929 to be circulated inside the calibration pipes is in progress.

3930

7.5. UAr Cryogenics

3931 PBS Item: DS.D.UAR

3932

3933 To isolate the UAr from the AAr, two separate cryogenics systems will be employed (refer to the
3934 PBS in Fig. 55). One system will handle the AAr in the ProtoDUNE cryostat, which is described
3935 in Sec. 7.1.4, and the other will handle the UAr in the titanium vessel for the LAr TPC embedded
3936 in the ProtoDUNE cryostat. The PBS for the UArcryogenics is shown in Fig. 101.

3937 The DS-20k UAr cryogenic system will build on the successful operation of DS-50 cryogenic
3938 and gas handling systems, which has operated for eight years without issue. Key parameters from
3939 DS-50 which serve as baselines for DS-20k, include: 1) The long-term TPC pressure stability,
3940 160 μ bar RMS, which is essential for S2 resolution. 2) The lifetime of drift electrons, ≥ 5 ms. This
3941 is equivalent to a LAr oxygen contamination LAr < 0.06 ppb, which is greatly beneficial for low-
3942 mass dark matter searches [17, 18]. 3) Total power failure immunity (including UPS system failure).
3943 This has been tested in the commissioning phase and recently verified by a total blackout at LNGS.
3944 This demonstrates the safety of the entire LAr TPC and, especially, of the valuable UAr. Lab tests
3945 performed over the previous six years have demonstrated the additional features required for the
3946 performance of the control system and the safety of the large amount of UAr in the DS-20k system,
3947 which are detailed below. The critical parameters of the UAr cryogenic system are listed in Table
3948 XXII, and the full P&ID is shown in Fig. 102.

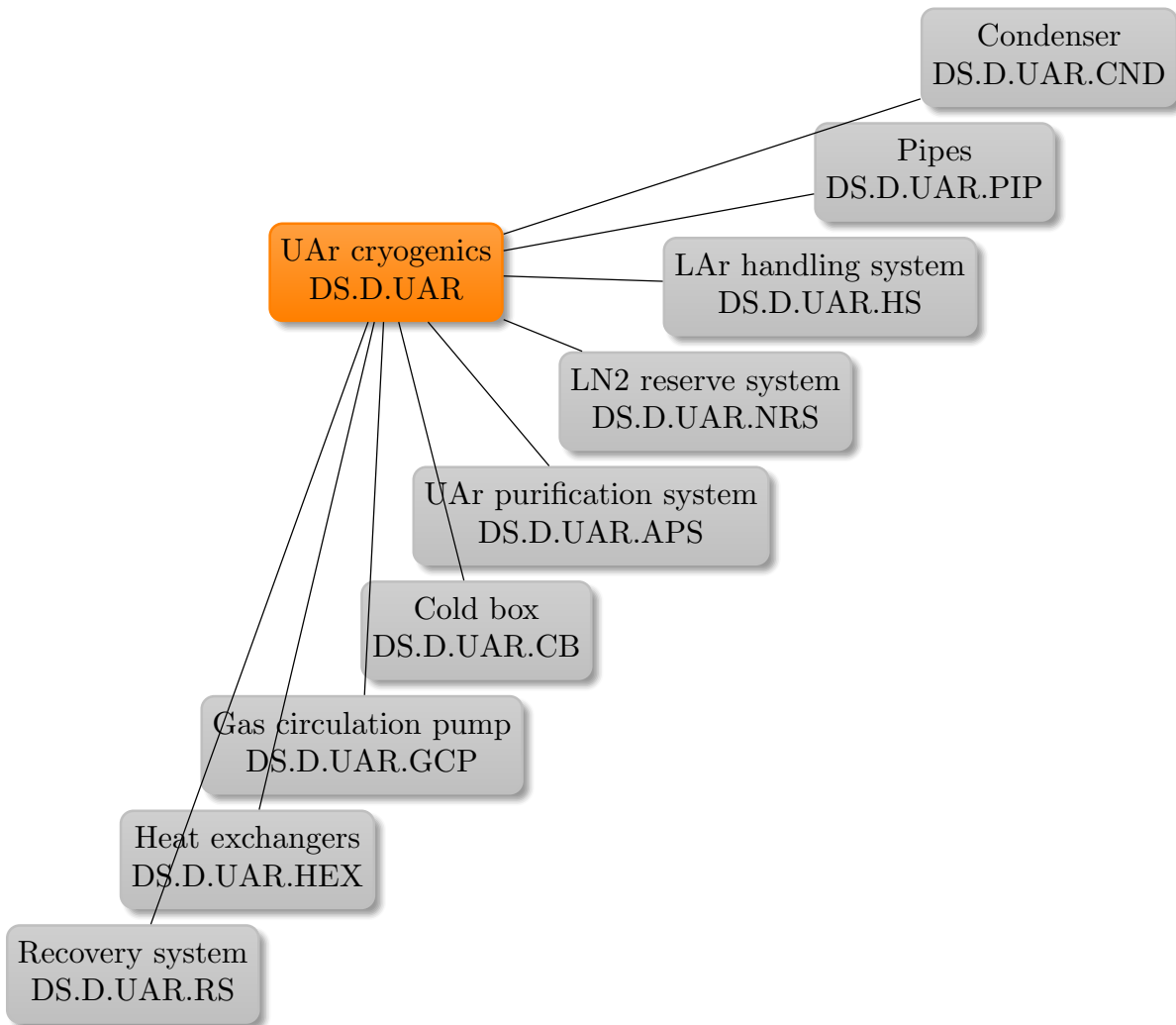


FIG. 101. PBS of the cryogenics in Hall C

3949 In addition to the above guidelines, efficiency is a driving factor in the UAr cryogenic system de-
 3950 sign. The basic operating principle is to use a steady supply of liquid nitrogen to cool and condense
 3951 underground argon gas into liquid as efficiently as thermodynamically allowed. To accomplish this,
 3952 a liquid nitrogen volume will be continuously maintained in the event of a power failure and, it
 3953 is important to note, the ProtoDUNE cryostat thermal load does not depend on electrical power.
 3954 Heat exchangers will be strategically placed throughout the system for LAr filling and removal at
 3955 the required speeds for the different operational modes. To maintain the UAr purity, the con-
 3956 tinuous gaseous circulation will be performed with a set of specialized pumps, developed by the
 3957 collaboration working in conjunction with industry partners.

3958 One major improvement over the DS-50 system is the increase of the circulation speed to
 3959 1000 std L/min. DS-20k requires this speed to reach the LAr purity requirement in a couple of
 3960 turn-over times of 40 d. The other major improvement is the increase in total cooling power of
 3961 the cryogenic system to handle the heat load from the cold electronics power dissipation, the
 3962 inefficiencies of the heat exchanger system, and the higher circulation speed. When combined
 3963 with the integrated heat exchangers, the system can handle high circulation rates, mass flow \approx
 3964 1000 std L/min UAr. The UAr system can draw either, or both, liquid and gaseous phase argon to
 3965 effectively remove electronegative impurities, e.g N₂, CO₂, and O₂, via a SAES hot-getter. This,

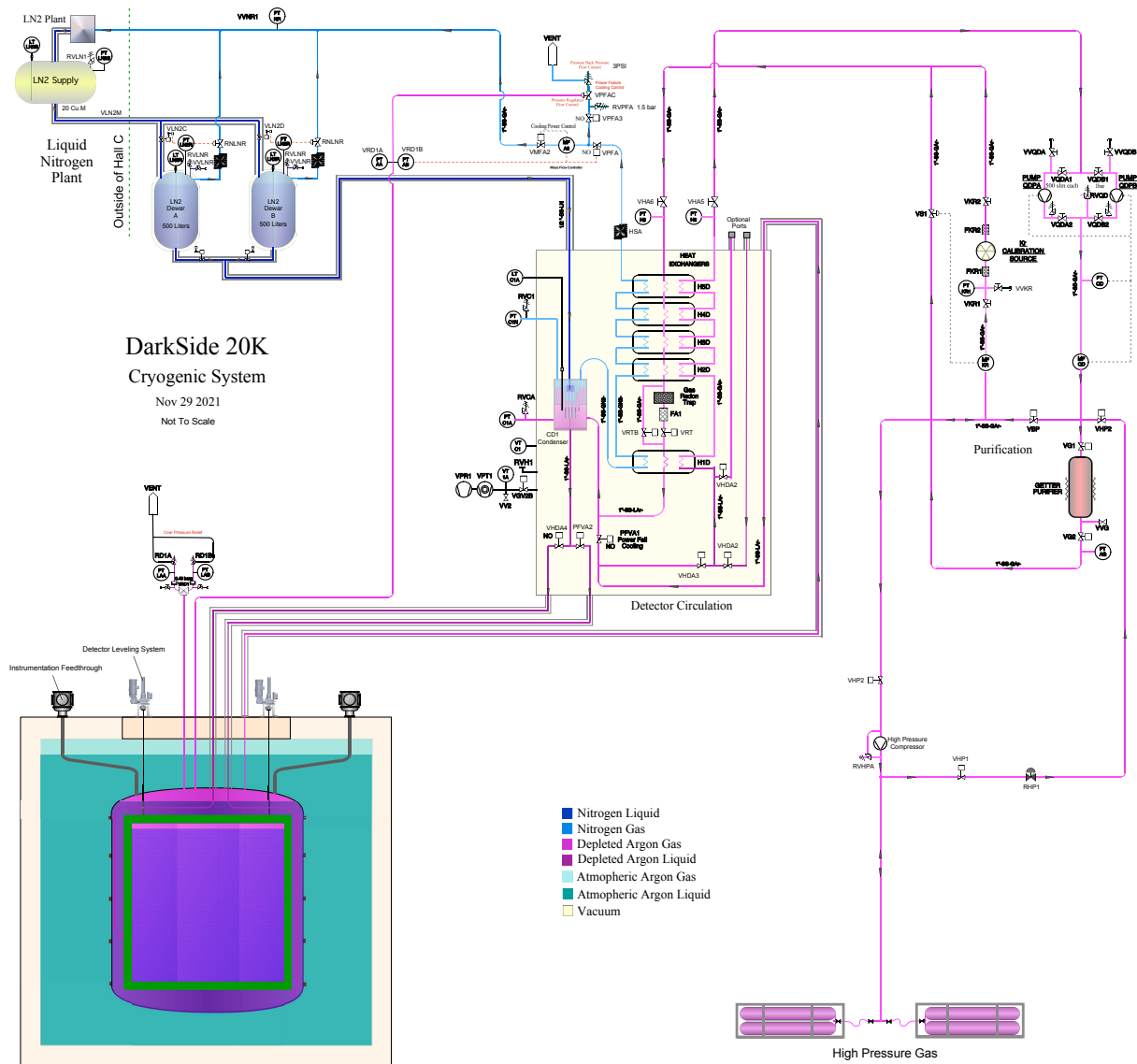


FIG. 102. Process and instrumentation diagram (P&ID) of the DS-20k UAr cryogenic system.

along with the UAr purification system, cold box, gas circulation pump, integrated heat exchange systems (both in the cold box and close to the TPC), UAr recovery and storage system, and the inline radon trap are all shown in Fig. 102. Details of the sub-systems follow:

Condenser (DS.D.UAR.CND): The core of the system, the stainless steel LAr condenser, consists of 127 0.5" OD tubes, closed on the top end. These tubes are optimally arranged and welded at the bottom end to a base-plate which provides good thermal conductivity. Thus the condenser separates the nitrogen volume on the top from the argon volume on the bottom and, as it condenses on the inner walls of the tubes, the liquid argon falls down into the cryostat. A so-called *chicken feeder* is mounted at the end of the liquid nitrogen delivery tube to maintain a flow of liquid nitrogen on a as-needed basis.

Cold box (DS.D.UAR.CB): The cold box, Fig. 48, contains all of the major cryogenic handling components. Apart from the condenser, the cold box contains five tri-flow heat exchange modules to efficiently cool the gaseous argon with the cold gas return from the cryostat, and the cold nitrogen gas after its latent heat exchange with argon in the condenser. This technique reduces

3980 the required cooling power dramatically. To maximize efficiency of radon removal, in gaseous phase
 3981 near 100 K, the radon trap will be placed between the two coldest heat exchange modules. To ac-
 3982 commodate the argon circulation speed, 1000 std L/min, tube sizes are chosen as 1" OD stainless
 3983 steel. Eight cryogenic valves and several temperature and pressure sensors are also installed to
 3984 control and monitor the system. The flow of the evaporated nitrogen gas is monitored by a mass
 3985 flow meter and adjusted by a control valve, both located at ambient temperature. The control
 3986 valve uses the LAr TPC pressure from UAr ullage as a feedback signal to automatically adjust the
 3987 evaporated nitrogen gas flow rate, which is directly coupled to the cooling power of the condenser.
 3988 This action maintains the LAr TPC pressure at a desired set point.

3989 **Heat exchangers (DS.D.UAR.HEX):** There are a total of three heat exchange systems in
 3990 the DS-20k UAr system. 1) Within the cold box, as mentioned in the preceding paragraph, to
 3991 increase the system efficiency. 2) Outside of the titanium vessel, near the level of the gas pocket
 3992 in the LAr TPC, to ensure gaseous argon is continuously created for circulation. 3) At the bottom
 3993 of the titanium vessel for quick recovery when the liquid is removed. Regarding 2), this system
 3994 acts as one large parallel plate heat exchanger. Outgoing liquid will absorb heat from the incoming
 3995 liquid-gas mixture, boil off into gas, and enter the circulation loop. This system will be located
 3996 near the level of the gas pocket to avoid a large head height which could result in an argon pressure
 3997 below its triple point somewhere in the loop, which would cause it to freeze. Regarding 3), this
 3998 heat exchange system will completely passive during normal operation, and would be used only
 3999 during the draining phase. Both 2) and 3) will be immersed in a thermal bath of LAr within the
 4000 ProtoDUNE cryostat.

4001 **Gas circulation pump (DS.D.UAR.GCP):** As discussed in Section 3.10.2, two pump de-
 4002 signs have been considered for DS-20k. The compactness and ease of use of the Celeroton makes it
 4003 a clear favorite, and further long-term testing with the UAr system at CERN will confirm its even-
 4004 tual use in DS-20k. The pump is required to achieve a circulation speed equivalent to 1000 std L/min
 4005 and it is anticipated that two pumps will be arranged in parallel to distribute the flow requirement
 4006 and for redundancy. After the initial circulation period for purity is finished, the pump speed(s)
 4007 can be lowered to counter only the heat load from the cold electronics and to maintain the UAr
 4008 purity.

4009 **UAr purification system (DS.D.UAR.APS):** The UAr purification system purifies the ar-
 4010 gon in gaseous phase during circulation. A commercial Zr-based getter system has already proven
 4011 successful in DS-50. A similar model with increased circulation capacity, an Entegris MegaTorr®
 4012 Rare Gas Purifier (model PS5-MGT100), will be used in DS-20k. A radon trap, similar to the one
 4013 used in DarkSide-50, will also be installed in the DS-20k coldbox along with a 0.003 μm Entegris
 4014 Wafergard® bulk in-line gas filter (model SI2N0100B) to remove any residual dust particles entering
 4015 the UAr volume.

4016 **LAr handling system (DS.D.UAR.HS):** The LAr handling system delivers the clean radon-
 4017 free UAr, initially stored in the high pressure storage system, which is capable of storing the entire
 4018 target volume of UAr for DS-20k. The recovery system will utilize the high pressure transportation
 4019 skids with a compressor to refill the gas bottles.

4020 **LN₂ reserve system (DS.D.UAR.NRS):** The LN₂ reserve system is a closed loop with a
 4021 LN₂ plant located outside of Hall C along with a couple of liquid nitrogen Dewars. The system
 4022 will deliver liquid nitrogen to the condenser of the UAr cryogenic system, and will recuperate the
 4023 boiled-off nitrogen gas to liquefy it back into the LN₂ system.

4024 **UAr storage and recovery system (DS.D.UAR.RS):** The UAr recovery and storage sys-
 4025 tem consists of a set of the transportation skids used to transport the UAr for its source. They will
 4026 be grouped together as the storage and recovery system upon arrival at LNGS. To secure all of the
 4027 UAr, the recovery rate must be synchronized with the rate of emptying the ProtoDUNE cryostat.
 4028 This will ensure that the thermal load applied to the titanium vessel is never higher than it can
 4029 withstand. A compressor system similar to that used in Urania and Aria will be used at LNGS for
 4030 recovery together with the storage bottles.

4031

7.6. Readout and Data Acquisition System

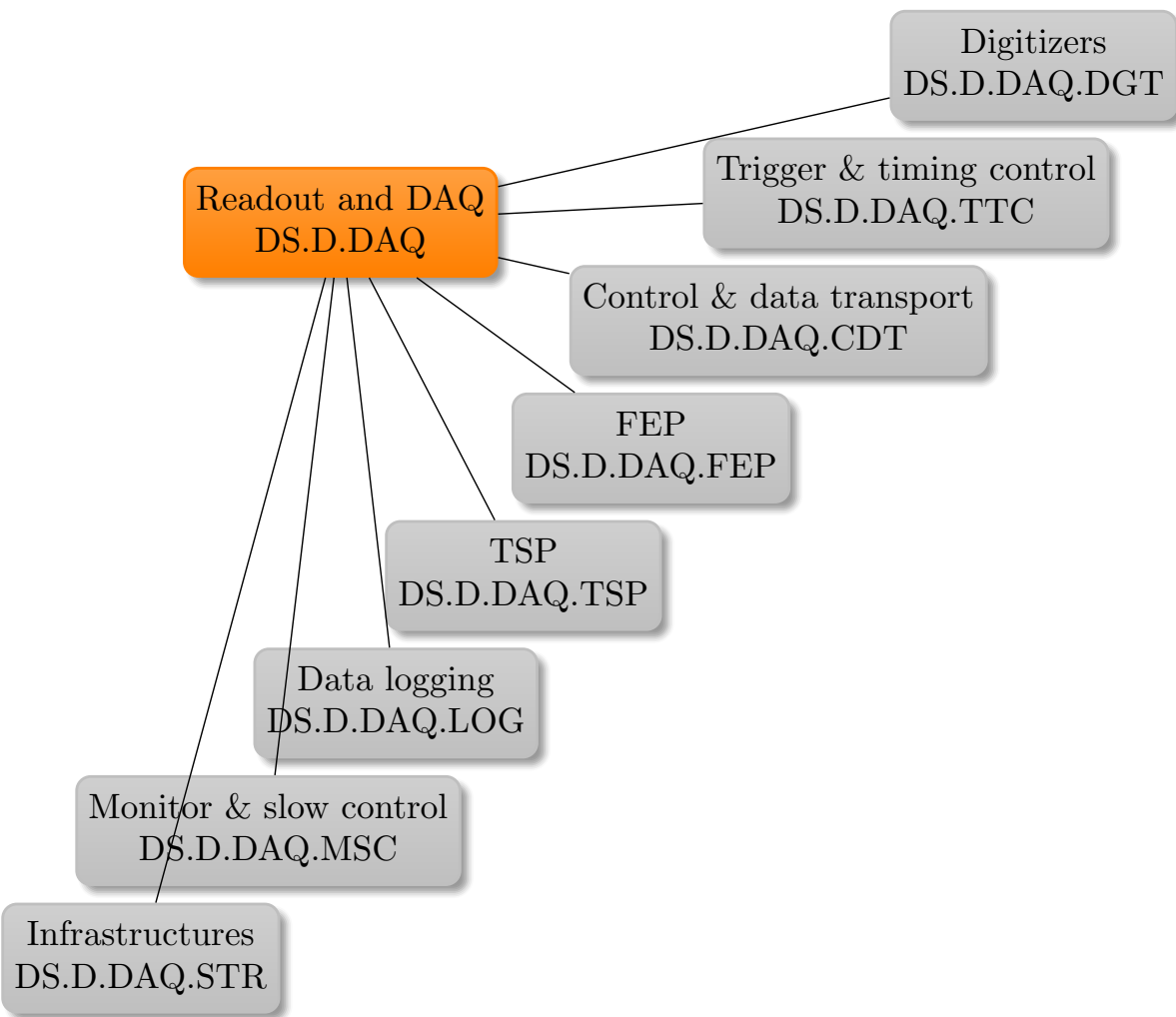


FIG. 103. PBS for the readout and DAQ .

4032

PBS Item: DS.D.DAQ

4033

4034

4035

4036

4037

4038

4039

4040

4041

4042

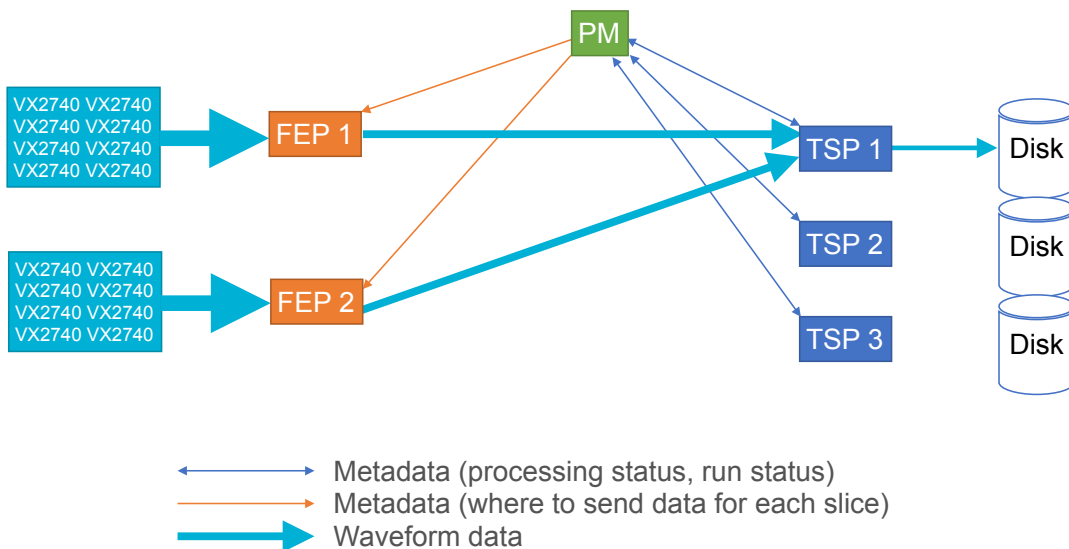
4043

4044

4045

The basic scheme for the readout of all DS-20k detectors foresees a differential transmission line, arriving at the feedthrough flanges on the chimneys on the top of the AArc cryostat roof. Signals are then routed to a custom patch panel with only passive components that will provide correct termination on the differential lines, adjust the dynamic range of the differential transmitter to the proper range (2V) for the digitization hardware in use in the system, and provide the signals on cables with proper connectors and ordering to feed into digitizer inputs. The ADC in the selected digitizer boards (see Sec. 7.6.1) are connected to large Field Programmable Gate Arrays (FPGA). The digital filtering capability within the digitizer board will allow the discrimination of single photo-electron signals and a first determination of the time and charge of the individual channel pulses. For large and slow signals, such as the S2 ionization-born pulses in the TPC, or the typical signal of interest for Veto, the digitizer board would provide a down-sampled waveform matching the expected signal bandwidth of a few MHz.

The combination of the data processing in the digitizer board and in the first stage of the DAQ system CPU will provide the needed data reduction to allow trigger-less operation of the readout for the TPC and Veto detectors. Digitized waveform data around the location of the signal pulses in the TPC and Veto detectors will be transferred to the front-end data processing units (Sec. 7.6.3)) where further data reduction is performed. Finally, the data will be passed to an online event building processor (called in the following Time Slice Processors) that will select interesting events and write them to permanent storage (Sec. 7.6.4)), performing additional data reduction to save finally on permanent storage a suitable small set of data for each event without compromising physics performances. The actual event data structure to be saved is under active study and preliminary estimations are consistent with the target specifications of Table XXIV. A sketch of the system is presented in Fig. 104.



In normal data-taking mode, an energy deposit in the TPC might be identified by a coincidence of hits within a specified time window. The specification for the light sensors for DS-20k ensures full efficiency for WIMP-like signals with negligible contribution from fake hits from noise or dark rate coincidences in the detector.

The event building and software trigger stage is realized with modern commodity CPUs and connected via Ethernet with the front-end DAQ processors. Given the low expected rate, the trigger-less option is foreseen to be feasible to implement. The expected combined event size for the TPC and Veto detectors is projected to be well below 1 MB.

Synchronization between the TPC and Veto DAQ is fundamental for the effectiveness of the design, and will be provided and maintained during the data taking. A central clock source will be used as reference and digital signals (like GPS time stamps or trigger IDs) will be generated to uniquely identify each event regardless of the trigger origin or the detector. A preliminary design of custom hardware, that in addition will also deliver some fast trigger capability, is described in Sec. 7.6.2.

The DS-20k specific DAQ software will be developed within the framework of the MIDAS DAQ

4072 package (MIDAS [77] stands for “Maximum integrated Data Acquisition System”). This software
 4073 package includes a range of applications for integrating the slow control and monitoring of the
 4074 detector in the system (Sec. 7.6.7).

4075 The DAQ system will be located near the penetrations on the roof of the AAr cryostat, with the
 4076 exception of the event builder and logger stage that will be located in the counting room formerly
 4077 in use by the DS-50 experiment. The arrangement will allow personnel access while minimizing
 4078 the length of the differential lines to transmit the data from the feedthrough to the digitizers
 4079 (Sec. 7.6.8).

4080 The total number of readout channels in the DS-20k design is shown in Table XLI. As shown
 4081 in figures 40 and 25, the signals from the TPC and Veto detectors will have significantly different
 4082 shape and may require different signal processing. For this reason we are assuming for now not
 4083 to mix signals from different detectors in the same ADC board. We plan to group digitizers in
 4084 VME crates located close to the 4 chimneys carrying the electrical feedthroughs, setting in this way
 4085 to a minimum the cable lengths from the feedthrough to the ADC to minimize electromagnetic
 4086 noise pickup. These considerations drive the minimum number of digitizer boards reported in
 4087 Table XLI. It is to be noted, however, that due to the large area (100 cm) covered by a single
 4088 PDU+ and VPDU+ channel, the hit rate might be high enough to be a concern for the capability
 4089 of the system to extract digitized data from the digitizer boards. A mitigation strategy that we
 4090 consider to counter this risk is to populate a smaller number of ADC channels per board. To
 4091 accommodate a conservative safety margin, we consider a system with up to 64 in total.

Parameter	Value
Total number of readout channels in TPC detector	2112
Total number of readout channels for inner Veto detector	480
Total number of readout channels for outer Veto detector	128
Minimum number of digitizer boards for TPC readout	36
Minimum number of digitizer boards for inner and outer Veto readout	12

4092 TABLE XLI. Readout channels and minimum number of CAEN Vx2740 units needed, neglecting bandwidth
 limitation issues.

4093
 4094 The product breakdown structure for the readout and DAQ is shown in Fig. 103, and the following
 4095 paragraphs give further details on the various items.

4096 7.6.1. Digitizer Boards.

4097 PBS Item: DS.D.DAQ.DGT

4098
 4099 The Commercial CAEN Waveform Digitizer model VX2740 is selected to convert all the analog
 4100 sensor signals to digital form. The VX2740 Digitizer is a 64-channel digital signal processor in a
 4101 VME64X form factor, that has been designed and implemented by CAEN in close collaboration
 4102 with DS-20k. Each channel of the module digitizes the analog input on 16 bit at 125 Msps over
 4103 a 2Vpp. While several method are available for extracting the data (USB, CONET), we selected
 4104 the Ethernet. Currently 1GbE is available but development is in progress for the implementation
 4105 of 10GbE. However it is to be noted that even using the 10 GbE line the output bandwidth will be
 4106 limited by the maximal internal throughput and only up to 300 MB/s (2.4 Gbps) can be extracted
 4107 from each digitizer board.

4108 Custom Firmware Specification

4109 This CAEN module has been designed in such a way that the end-user has the ability to upload
 4110 custom firmware code into a reserved area of the FPGA (OpenFPGA).

4111 This permits access to the digital raw data flow in order to apply custom data processing such
 4112 as triggering scheme, data filtering or data compression. As long as the data output from the
 4113 "OpenFPGA" section is returned as a valid CAEN data block format, the transmission will be
 4114 carried further by the WFD CAEN core application.

4115 This custom firmware development comprises the following.

- 4116 • Custom board management: this section covers all the board infrastructure in the DS-20k
 4117 context. It has to manage in real-time dedicated incoming data packets issued from a cen-
 4118 tralized hardware module providing the global synchronization clock and the real-time com-
 4119 mands, discussed later. This is separate from the board configuration which is done through
 4120 a network link from a software application.
- 4121 • I/O interface to the "OpenFPGA" section: this covers the all the necessary connections and
 4122 configuration as well as the operation status of the user code.
- 4123 • Individual channel self-triggering: at the individual channel level, the signal is forked in two
 4124 paths. In one, the data is delayed until the data in the second path went through a dedicated
 4125 signal processing algorithm to filter the data in order to better capture the characteristics of
 4126 the signal and trigger validity of the raw data from the first path.
- 4127 • Data compression: additional data processing of the accepted data can be expected and the
 4128 CAEN data block header is untouched allowing a smooth data transfer off the board.

4129 7.6.2. Trigger and Clock Module

4130 PBS Item: DS.D.DAQ.TTC

4131
 4132 The DS-20k experiment is foreseen to have up to 64 waveform Digitizer (WFDs). The data
 4133 acquisition is expected to be operated in a "Triggerless" or "Self-triggered" mode (based on an
 4134 individual signal). To ensure that all the WFD's data produced during a given physics event in
 4135 the detector is meaningful, every piece of the data (individual WFD data) is to be stamped with
 4136 an identical time mark across all the digitizers. This information is the pillar for the physics event
 4137 reconstruction analysis. This time synchronization is provided by a unique time source distributed
 4138 to every piece of electronics equipment involved in the data acquisition. The WFD sampling clock is
 4139 125 MHz, and the distributed clock is 62.5 MHz. Beside the reference clock distribution, additional
 4140 information is to be communicated to all the WFDs in real-time such as:

- 4141 • Reset signal to initialize the internal counters (time, scalers) at the beginning of a run (time
 4142 synchronization)
- 4143 • Trigger, trigger type and/or trigger region: while the experiment is triggerless, optional
 4144 external or "periodic" triggers are necessary to collect specific data such as calibration data
 4145 based on laser or radioactive sources, regional test data for mapping verification, detector
 4146 noise evaluation, etc.
- 4147 • "Time Slice Marker": periodic signal generating a WFD event slicing the overall data flow
 4148 to support the "Time Slice" acquisition mode (with period in the second range).
- 4149 • "Enable/Disable": global and synchronized acquisition signal to throttle the data flow. The
 4150 input signals for that decision come from all the elements of the DAQ chain.
 - 4151 – Busy signal from each WFD reflecting output buffer level.
 - 4152 – Acquisition computers FEPs (Frontend Processors) reflecting event processing backlog.

4153 While all the above communications are directed towards the WFDs, the digitizers themselves do
 4154 generate control data that are valuable when gathered to a common location. There are two types
 4155 of information that need to be collected:

- 4156 • The individual digitizer module busy (logical signal) informing the level of the memory usage.
 4157 This signal is used to act upon the acquisition control of the entire DAQ system.
- 4158 • The digitizer module hit map (logical signals of grouped or consecutive channels per board).
 4159 These logical signals when collected provide a hit map image of the entire detector and can

be used in real-time to independently trigger the full or partial detector. This mode of trigger is particularly useful during commissioning or during calibration.

The information-mentioned above composes the core of the communication between a single board - GDM “Global Data Manager” to the digitizers. Given the large number digitizers in play, several “crates” (4 VME, at a minimum) are necessary to house the WFDs modules. Each crate handling up to 16 WFDs, we foresee this communication to be done in 2 stages.

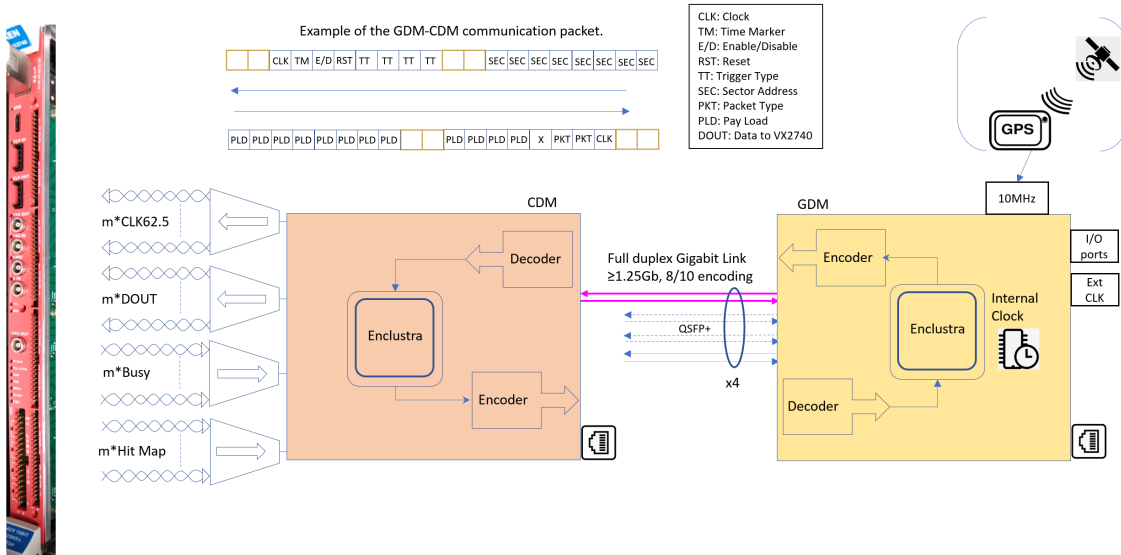


FIG. 105. Distribution of the Clock and commands from the “Global Data Manager” to the Digitizers is done through a board dispatcher “Crate Data Manager”. The Digitizers are using the same data path to return their information (Busy, Hit Map) to the GDM for run control and trigger generation.

1. From a unique module (GDM) to a “Crate Data Manager” module (CDM)
2. From the CDM to all the local WFDs of its crate.

The first stage communication is through a full-duplex optical link at a speed of 1.25GHz or higher. This provides a 1Gb/s data transfer from each individual CDM or in other word the total bit rate from the 16 WFDs. The second stage connectivity will match the WFDs I/O requirements and is based on a 125MHz clock due to some hardware limitation of the WFD.

For the communication to the WFD, we foresee a physical “bus” of 8 lanes handling the traffic in both direction. One dedicated lane (CDM to WFD) provides the 62.5 MHz as the main reference clock. The other 7 lanes are split in 2 for in/out from the CDM to the WFDs. Presently 2 lanes are allocated for the commands to the WFDs and 5 lanes for the “Hit Map” and Busy from the WFD to the CDM. While the command communication to the WFD is based on the 125MHz, and the composition of the command requires a minimum of 16 bits, the WFD can be updated faster (64 ns) than the expected external trigger rate (5 ms) as well for the DAQ throttling.

7.6.3. Front-End Processors

PBS Item: DS.D.DAQ.FEP

The Front-End Processors (FEPs) receive the digitized waveform signals of the detector, apply smoothing and/or compression filters, group them into time slices, then send them to Time Slice Processors (TSPs). Each FEP is responsible for configuring and reading out waveforms from several digitizers, and is connected to them using ethernet over a private network.

4188 During each experimental run, the Pool Manager (see Sec. 7.6.5) informs the FEPs where the
 4189 data for each slice should be sent, based on which Time Slice Processors are available for work.
 4190 Time Slice Markers in the data stream ensure that all FEPs know when each slice ended, and that
 4191 the data from all FEPs for slice N is sent to the same TSP.

4192 The FEP application is extremely multi-threaded to maximize usage of CPUs and network band-
 4193 width. Separate threads are used for reading the data from each digitizer, applying filters to the
 4194 data from each digitizer, accumulating the data into time slices, and sending the data from each
 4195 slice to the Time Slice Processors. The design of the program allows different filters to be easily
 4196 integrated and tuned, to allow rapid development during the prototyping and commissioning stages
 4197 of the experiment. It is foreseen that the FEPs would significantly reduce the data rate into the
 4198 Time Slice Processor by extracting from filtered waveforms time and charge of single photo-electron
 4199 signals in all detectors discarding the corresponding raw waveform from the data stream, excepting
 4200 a small fraction used for monitoring performances of the photo-sensors in situ.

4201 As well as handling the main data flow, the FEP application also configures the digitizers before
 4202 the start of each experimental run based on settings specified in the Midas database. It also
 4203 periodically reads metadata such as temperatures and buffer status from each digitizer, and reports
 4204 this to Midas.

4205 The number of FEPs has not yet been completely finalized, but it has to be adjusted to the
 4206 expected data rate from the digitizer and the complexity of the data processing that is expected
 4207 to occur at this level of the processing. A preliminary estimate of 16 FEP nodes for the TPC and
 4208 4 for the Veto has been made based on current simulations. We note that the data rate does not
 4209 depend, to a large extent, on the option of summing the signals of several tiles in the TPC and
 4210 VetoPDUs.

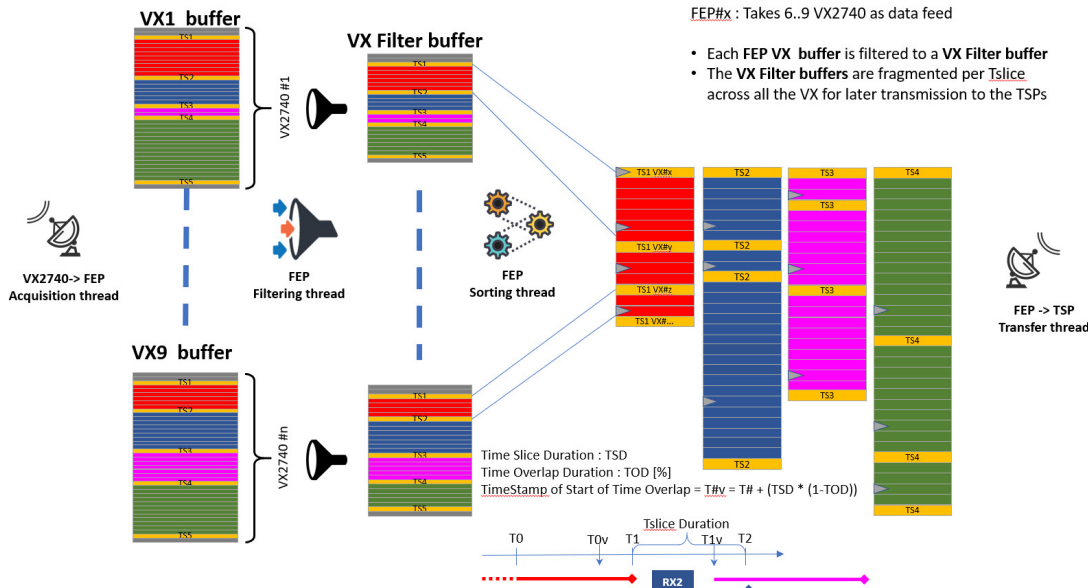


FIG. 106. Each digitizer has its own buffer marked with the common TSM marking the Time Slice duration boundaries. For each received buffer, a thread will apply a digital signal processing for data reduction/compression. Once complete, all the fragments of the same time slice are collected in a final buffer to the Time Slice transmission thread.

The detector event analysis is to be performed on fully assembled data collected from all the waveform digitizers over a time period that is specific to the detector characteristics, such as the maximal electron drift time through the TPC (about 4 ms) or the relevant coincidence time between TPC and Veto signals (about 1 ms). Due to the large data size and complexity of the analysis, the continuous stream of data is segmented in time and each consecutive segment is assigned to a given analysis computer node (Time Slice Processor or TSP). This "segment" of data is referred as "Time Slice", while the individual WFD data collected from a given digitizer for that Time Slice is referred as "Fragment". In other words, the Time Slice Processor (TSP) is to receive all the WFDs fragments prior the start of the segment analysis for a given time slice. The slicing in time of the data flow from all the digitizers is achieved by insertion of a "Time Slice Marker" (TSM) sent from a unique hardware module to the digitizers. This TSM part of the digitizer data-stream is used to locally pre-assemble all the data fragments in each FEP concurrently and make them available to the TSP once a TSP is available for the analysis of a newly formed segment, as sketched in figure 107.

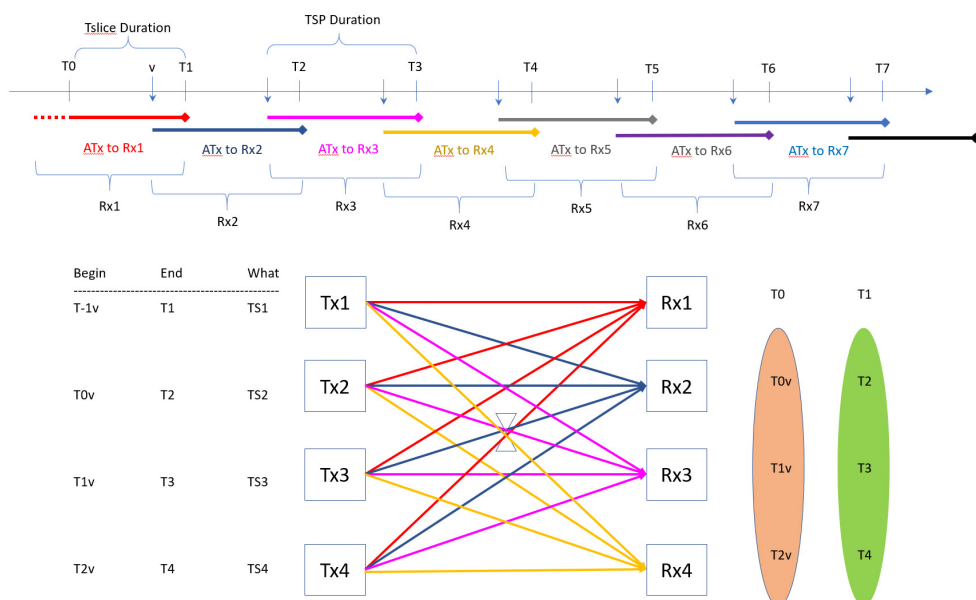


FIG. 107. The figure shows the slicing of the timeline of the data flow. Tx refers to the FEPs and Rx to the TSPs. All the FEPs for a given Time Slice, send their data to a unique TSP. The subsequent time slice data will be directed to another idle TSP. In order to prevent analysis issues at the "boundary" of the slice split, a time overlap is to be present in both consecutive time slice (v mark)

4228

4229

4230

Trigger Algorithms

The TSPs will first have to reconstruct valid pulses from data of the entire detector, by clustering signals in time from individual readout channels of the TPC. For both S1 and S2 pulses this will involve collecting precise timing information from single photo-electron signals as determined during the filtering stage in the Front End Processor together with waveform segments, possibly downsampled, for very large signals or S2 pulses.

Once a list of pulses is available, several trigger algorithms can be run in parallel. Each algorithm may apply a selection on pulse size, location in the detector or other characteristics to determine the interesting seed signals in the time slice. A typical WIMP selection at the TSP level may involve selecting low energy S1 that are followed by at least a valid S2 signal within one maximal drift time with respect to the selected S1. This may start the process of collecting all the detector

4241 signals relevant for further analysis. This includes, for example, the inner Veto and outer Veto
 4242 signals within a predefined time window relative to the timing of the seed S1, to allow studying
 4243 the neutron-induced or cosmogenic-induced background and eventually rejecting it. Concurrently,
 4244 other trigger algorithms may look, for example, for high energy γ signals in the TPC to be used for
 4245 calibration purposes, or any other seed signals of interest. Once all the algorithms have concluded
 4246 the analysis of the time slice, assembled events are pushed to the Data Logger stage for saving to
 4247 permanent storage.

4248 The number of TSPs will be finalized once a more precise estimate of the latency added to the system
 4249 for the complete analysis of a single time slice will be available. The current design is based
 4250 on 72 TSPs nodes in total, which would allow several second processing, on average, for every event
 4251 at the expected maximum event rate.

4252 7.6.5. Flow Control and Data Transport

4253 PBS Item: DS.D.DAQ.CDT

4254

4255 Communication between the FEPs and the digitizers uses a proprietary C++ library provided
 4256 by CAEN. The industry-standard ZeroMQ library is used for communication between the Pool
 4257 Manager and the FEPs. A raw TCP socket is used to transmit the large volume of data between
 4258 the Front-End Processors and Time Slice Processors, to maximize the performance of this link.

4259 The coordination of the transmission of the FEPs fragments to individual TSP is managed
 4260 by the "Pool Manager" (PM), see Figure 108. The PM is in direct communication with all the
 4261 parties and therefore receives individual notifications of availability from free (idle) TSPs. This
 4262 notification information contains the TSP destination address as well as previous Time Slice Status
 4263 results. While the Time Slice status result is collected and sent to the Midas Acquisition system
 4264 for monitoring purpose, the notification is queued in the PM and passed to all the FEP's Transfer
 4265 Thread. On reception of the PM information, every FEP transfer thread will send the corresponding
 4266 Time Slice buffer to the provided TSP destination address. On completion of the transfer from *all*
 4267 the FEPs, the TSP starts the data analysis of its Time Slice Segment. Once completed, the TSP
 4268 notifies the PM of its availability, again by sending the status of the last data transfer and data
 4269 analysis. This new Time Slice segment request is not necessarily the next slice in time. Therefore
 4270 the data collected/analyzed at the TSP level is composed of a collection of non-contiguous Time
 4271 Slices. A list of which Time Slice each TSP has processed is maintained by the Pool Manager and
 4272 reported to the overall Data Acquisition system.

4274 7.6.6. Data Logger

4275 PBS Item: DS.D.DAQ.LOG

4276

4277 Events identified and assembled by the TSP are assigned to different streams and transferred to
 4278 the data logger. Depending on design and optimization choices, this can happen either through
 4279 network or simply by using temporary files on network attached disks. The task of the data logger
 4280 is to collect data from the various TSPs in the system, potentially identify the possible duplicate
 4281 events occurring in the small time-overlap between one time slice and the next one, and write on a
 4282 large pool disk the data in the final raw data format. Files will be assigned to a given run for later
 4283 retrieval in the offline reprocessing stage in the experiment database. The data logger will also
 4284 initiate, and keep track of, the transfer of the raw data off-site at CNAF and at other international
 4285 data centers. A local pool of disk of about 120 TB is expected to be enough to store the raw data
 4286 corresponding to 1 week of operations in normal conditions. This is considered enough to allow
 4287 for the occasional down time of the link to the above-ground INFN network, while preserving the
 4288 regular operations of the experiment.

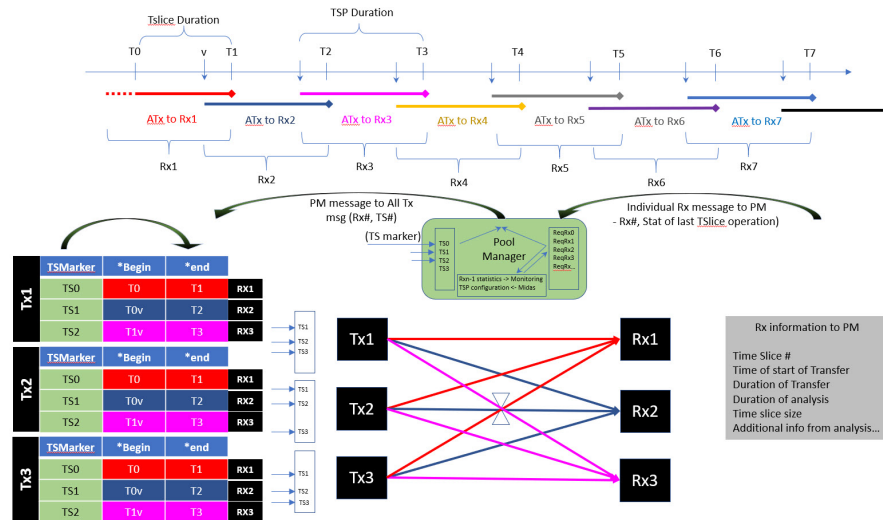


FIG. 108. The Pool Manager is acting as a proxy on behalf of all the TSPs for requesting all the time slice fragment for its segment processing.

4289

7.6.7. Online Monitoring

4290 PBS Item: DS.D.DAQ.MSC

4291

4292 Online monitoring is implemented in MIDAS. The MIDAS software package has been developed
 4293 over the last 25 years specifically for the physics community. It is based on C, C++, with de-
 4294 pendence to standard libraries. Current experiments using Midas are: T2K, MEG, ALPHA-II,
 4295 ALPHA-G, DEAP. Its implementation provides all the expected features required for control and
 4296 monitoring of a mid-range physics experiment, including full remote control through web interface.
 4297 It includes custom or root-based online data monitoring/analysis and slow control/monitoring such
 4298 as: High Voltage, frontend electronics, crates U/I, temperature. The system is modular and flexible
 4299 to easily allow integration of specific software readout or control using any type of communication
 4300 channels.

4301 Physics-level monitoring of the status of the DS-20k detector will be performed on a fraction
 4302 of the data flowing through TSPs which will also be available, in addition, to the pool manager
 4303 (Sec. 7.6.5). Pulse shape and gain monitoring of the individual readout channel response will be
 4304 available continuously by analyzing a specialized data stream that will include an unbiased sample
 4305 of signals above threshold that will be transported unaltered through the system up to the local
 4306 data storage.

4307

7.6.8. Infrastructure

4308 PBS Item: DS.D.DAQ.STR

4309

4310 Digitizer and FEPs will be located in racks located very close to the position of the chimney on
 4311 AAr roof top cap. We plan to use commercial ventilated racks. These racks will host at least one
 4312 VME rack for digitizer and CDM units, a patch panel for line termination and correct signal routing,
 4313 a 10Gbps network switch and at least 5 FEPs (4 for the TPC and 1 for the Veto). A dedicated UPS
 4314 unit will also be located nearby for providing emergency power to preserve equipment integrity.

4315 Power for this equipment will be delivered through the specially designed detector electrical
 4316 power network described in Sec. 9.5.3.

4317 Cable trays will need to be installed on the AAr roof top cap for holding the network cables
 4318 connecting the FEPs to the TSPs through the main network switch. The TSPs and the network

switch are expected to be located in the designated control room (see Sec. 9.5.4), which is located approximately 50 meters away from the cryostat.

The existing control room will be refurbished and equipped with a more powerful cooling system to sustain the power dissipated by the TSPs computers and related equipment.

7.7. Data

PBS Item: DS.D.DAT

The PBS of the data products is shown in figure 109.

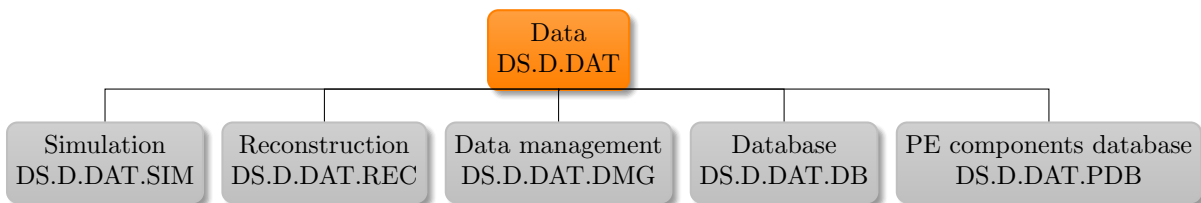


FIG. 109. PBS of the Data products.

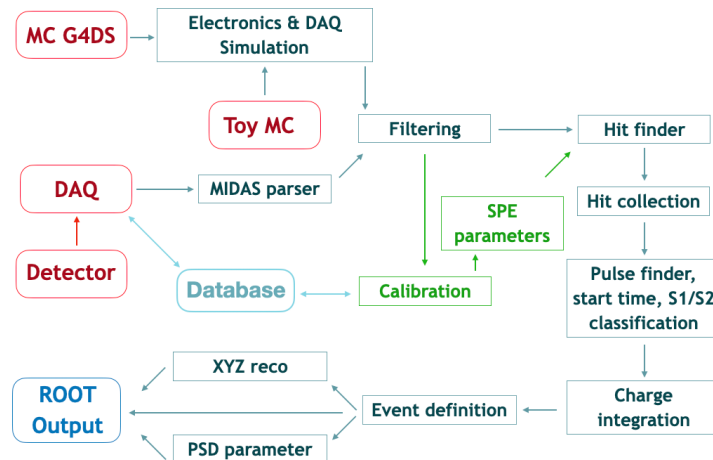


FIG. 110. Scheme of the PyReco package for the reconstruction of simulated and real data. PyReco is designed for DS-20k but can also serve ancillary apparatus such as ReD, prototypes and test setups.

The DarkSide Geant4-based particle tracking simulation package, G4DS is designed with a modular architecture in order to include a full description of all the detectors belonging to the DarkSide program: DS-10, DS-50 DS-20k and Argo. G4DS has been extensively validated on DS-50 data, demonstrating the high accuracy required to optimize the geometry and establish the performance of the TPC DS-20k and the neutron and muon vetoes. The code provides a detailed description of geometry and materials. Great efforts have been devoted to the description of the physical properties of materials, especially the optical ones, exploited by G4DS to track each photon. Optical parameters of materials new to DarkSide-50, such as acrylic, have been integrated primarily through measurements and models used for (and validated with) DEAP-3600. The LAr scintillation and ionization processes are simulated with the custom PARIS model, validated on SCENE and ARIS data, and recently improved thanks to the ReD data analysis.

4339 A spatial event generator is implemented for each detector material in order to generate and
 4340 track particles emitted by radioactive decays and to assess its impact on the DS-20k background.
 4341 In addition, we implemented an (α, n) event generator, based on the TALYS package, to study
 4342 the impact of the neutron background on the final sensitivity. Cosmic muons and cosmogenic
 4343 activations can be simulated with both G4DS and FLUKA packages. In the latter case, G4DS uses the
 4344 output as an event generator to track the particles in the DS-20k geometry.

4345 The Monte Carlo chain is completed by the electronics simulation. This is embedded in the
 4346 PyReco package, which also allows the reconstruction of both the simulated data and the data
 4347 acquired so far through the ReD and DS-Proto0 detectors, as shown in the scheme of Fig. 110.
 4348 The SiPM time response is applied to each photoelectron simulated with G4DS using parameters
 4349 measured in the mentioned detectors and/or in dedicated LN test setups. The dark count rate
 4350 is also modelled from the results of measurements described in section 3.2. The simulation of
 4351 internal cross-talk (CTs) and afterpulses (APs) takes into account the statistics dictated by their
 4352 recursive nature (CT/AP can induce in turn CT/AP). For the APs, the time response, critical for
 4353 the PSD, is modelled with an exponential decay. External CTs require special handling since they
 4354 are generated at the electronics level and then must be optically tracked: for this reason, we placed
 4355 a toy Monte Carlo for an effective modeling of external CTs, between the output of G4DS and the
 4356 input of PyReco.

4357 For each DAQ channel, we simulate a waveform with the sum of all SiPM responses and white
 4358 noise, normally distributed. A dedicated task force is currently working to refine the noise sim-
 4359 ulation, incorporating measured noise spectra. The waveforms can eventually be stored on disk.
 4360 However, this solution is impractical, because it requires significant disk space and non-negligible
 4361 amount of time for writing and reading large amount of data by PyReco. The alternative, and
 4362 primarily used, approach lies in processing each simulated waveform on-the-fly.

4363 The reconstruction code first filters the waveform with the matched filter. A custom-made peak
 4364 finder is applied to the filtered waveform to identify individual hits. The peak finder returns quality
 4365 parameters that allow suppressing fake hits due to waveform fluctuations. The most recent peak
 4366 finder version has shown the ability to achieve a high hit identification efficiency ($\sim 97\%$) and also
 4367 a high level of sample purity ($\sim 99\%$). Several studies have shown that these performances have
 4368 a low dependence on the SiPM response function template used in the matched filter. This is an
 4369 important result, because although a system is provided to monitor the SiPM time constants, slight
 4370 non-uniformities in the responses of SiPMs of the same PDU, which are modelled with a unique
 4371 set of parameters, do not alter the performance of the peak finder.

4372 The collection of hits from all waveforms is then processed by the pulse finder which clusters hits
 4373 into pulses and, based on the pulse shape, classifies these into S1 or S2. For each pulse, we identify
 4374 its start time and apply a standard algorithm of baseline subtraction and charge integration on each
 4375 individual waveform. This information is important in regimes of high photoelectron occupancy
 4376 on single channels, on the time scale of a few hundreds of nanoseconds, a regime in which the peak
 4377 finder efficiency decreases. Once an S2 pulse is identified, we reconstruct its xy position. PyReco
 4378 already embeds a number of xy reconstruction algorithms, among which two machine learning
 4379 ones. The currently implemented Pulse Shape Discrimination (PSD) algorithm is the same one
 4380 adopted in DarkSide-50, based on the fraction of hits detected in a prompt gate. Machine learning
 4381 algorithms based on the pulse shape identification are in preparation but not yet operational. The
 4382 output of PyReco is a ROOT file with a single tree containing reconstructed variables and Monte
 4383 Carlo truth ones if the data sample is simulated.

4384 The study of the nuclear recoil acceptance region and of the exclusion curve to limit electron
 4385 recoil leakage requires distinct treatment. The number of expected ERs events from ^{39}Ar and
 4386 from γ 's originating from the material surrounding the TPC ($\sim 1.3 \times 10^9$ in 100 t yr in [30, 250]
 4387 keV $_{nr}$) is too large for performing full optical simulations. A toy MC approach was developed
 4388 in order to build NR acceptance and ER exclusion curves, accounting for the scintillation pulse,
 4389 the photon propagation in the TPC, and for all the electronics and reconstruction effects. The

4390 obtained acceptance region is finally used in the “high-mass” code, which uses RooFit⁴. It is
4391 designed to determine the final sensitivity of DarkSide-20k by applying a Profile Likelihood Ratio
4392 approach, using three binned observables: S1, xy and the drift time. The high-mass code includes
4393 the irreducible backgrounds from neutrons and neutrinos via coherent scattering off nuclei, using
4394 G4DS samples to account for the spatial distributions.

4395 Additionally, we also developed the “low-mass” simulation and analysis code, dedicated to the
4396 search for light dark matter particles through the analysis of the ionization signal only. The low-
4397 mass package includes models for WIMP scattering off electrons and scattering off nuclei, also
4398 including the Migdal effect (ionization and excitation of bound electrons induced by the recoiling
4399 nucleus), solar and galactic axion-like particles (ALPs) via axioelectric effect, and sterile neutrinos.
4400 Special tools have been developed for establishing the sensitivity to neutrinos from supernova core-
4401 collapse and from the Sun.

⁴ RooFit is a toolkit integrated with the ROOT environment used for modeling the distribution of events in a physics analysis

8. TECHNICAL DESCRIPTION: LIGHT DETECTORS

4402 PBS Item: DS.P

4403

4404
4405 In this section the structure and function of the photo-detectors are described in terms of the
4406 Photo-Detection Units (PDU), cabling and power supplies. The PBS is shown in figure 111.

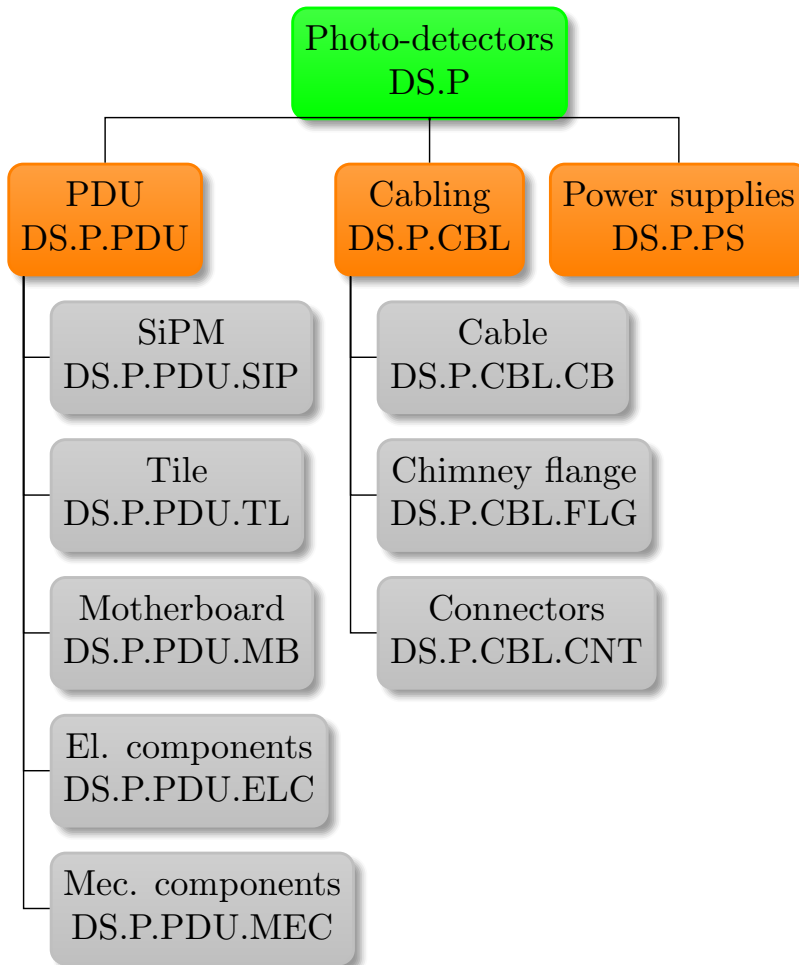


FIG. 111. PBS with details of the "Light Detectors" item.

8.0.1. PDU+

4407 PBS Item: DS.P.PDU

4408

4409
4410 The basic element of the SiPM readout and bias structure for DS-20k is a photo-detector unit
4411 (PDU+) featuring the Silicon PhotoMultiplier technology developed by FBK designated by the
4412 name NUV-HD-Cryo (section 3.2). Each PDU+ is a 20 cm × 20 cm area object that hosts by 16
4413 tiles (called Tile+) and a motherboard PCB (called MB+). The MB+ distributes voltages and
4414 control signals, and transmits the summed SiPM signals towards the DAQ system. A rendering of

4415 the PDU+ is shown in Fig. 112. A detailed description of the PDU+ electronics design is given
 4416 in section 3.4.4. Parameters of the PDU+ are listed in Table XLII. The results achieved in the
 4417 testing program reported in Table XLII meet the specifications set out in section 3.4.1.
 4418

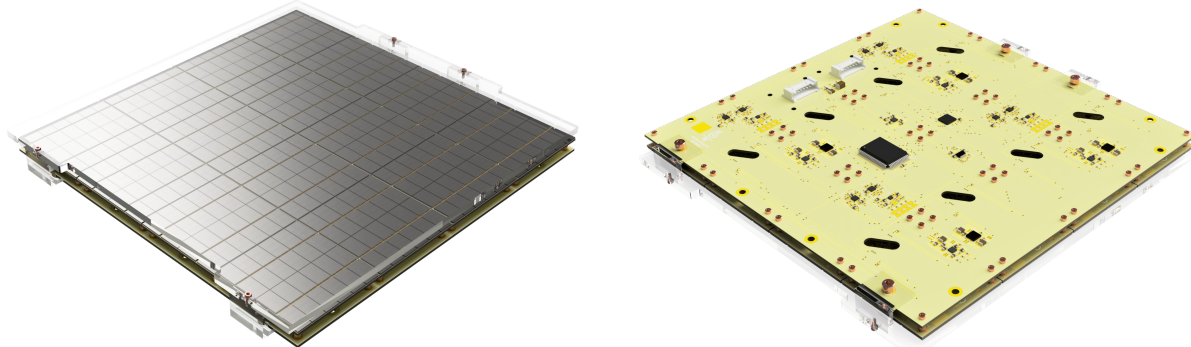


FIG. 112. Left: top view of the PDU+ showing 16 Tile+ mounted on the Motherboard+ (MB+) and covered by an acrylic sheet. Each Tile+ is made up of 24 SiPM. Right: bottom view of the PDU+ where the MB+ is shown with its electronic components.

Parameter	Value
Dimension	200 x 200 x 25 mm ³
Total mass	~350g (~550 g with protection)
Dissipated power	1.7 W
Number of output signal channels	4 (100x100 mm ² each)
SPE signal amplitude (@ 7 VoV)	10.5 mV differential (after back-termination)
Dynamic range	300 PE
SPE signal rise time	8 ns (20-80)%
SPE signal recharge time	350-400 ns
SNR (@ 7 VoV) ^a	> 12 with matched filter
Time jitter (@ 7 VoV)	< 10 ns

^a The Signal to Noise Ratio (SNR) was defined in Sec. 3.3.2 and is the ratio between the single Photo-Electron peak in the charge spectrum and the RMS of the baseline.

TABLE XLII. PDU+ performance parameters.

4419 a. *SiPM* PBS Item: DS.P.PDU.SIP

4420
 4421 The NUV-HD-Cryo devices, developed for the DS-20k requirements, are described in detail in
 4422 the section 3.2. The characteristics of these SiPMs are reported in the Table VIII. The SiPMs are
 4423 designed to minimize dark noise and afterpulsing while exhibiting a uniform and stable quenching
 4424 resistance at cryogenic temperature. The peak photon detection efficiency is in the blue region of
 4425 the spectrum, matching the TPB wavelength shifter emission spectrum. Table XLIII summarizes
 4426 the requirements that the SiPMs have to achieve to be compatible with the DarkSide-20k physics
 4428 program.

4429 The SiPM requirements are specified in Table XLIII at 77 K, liquid nitrogen temperature, which
 4430 is straightforward to achieve in test stands as tiles can be directly immersed in liquid nitrogen. No
 4431 significant difference of the SiPM performance is expected between 77K and the 87K temperature
 4432 of liquid argon. This assumption was specifically verified in dedicated measurements at TRIUMF
 4433 of the LFoundry SiPMs characteristics as a function of the temperature, in the apparatus described

Parameter	7 V of OV	9 V of OV
Internal Cross Talk probability at 77 K	< 33 %	< 50 %
Dark noise rate at 77 K	< 0.01 Hz/mm ²	< 0.1 Hz/mm ²
Afterpulse probability at 77 K [within 5μs]	-	< 10 %
PDE at 420 nm at 77 K	-	>40 %
Breakdown Voltage at 77 K (SPE charge)	26.8 ± 0.2 V	
Breakdown Voltage at 77 K (SPE amplitude)	27.5 ± 0.2 V	
Single Cell Capacitance (from SPE charge)	62.5 ± 2.5 fF	

TABLE XLIII. Summary of the SiPM Requirements for the Darkside-20k SiPMs. SPE stands for Single Photon Electron.

in [78]. Requirements are specified for two different over voltages that represent a range of possible operating voltages during detector operation. Section 3.2.6 demonstrates in detail that the SiPMs meet these requirements.

4437

4438 b. Tile+ PBS Item: DS.P.PDU.TL

4439

4440 Each Tile+, as shown in Fig. 113, is composed of a 5 × 5 cm² PCB hosting 24 SiPMs on the top
 4441 side, ganged in the 4s6p configuration described in Sec. 3.3, and the front-end electronics, based
 4442 on a single trans-impedance amplifier (TIA), on the bottom side. A single TIA occupies about
 4443 7 × 16 mm² of the PCB area and can be directly soldered on the Tile+ PCB.

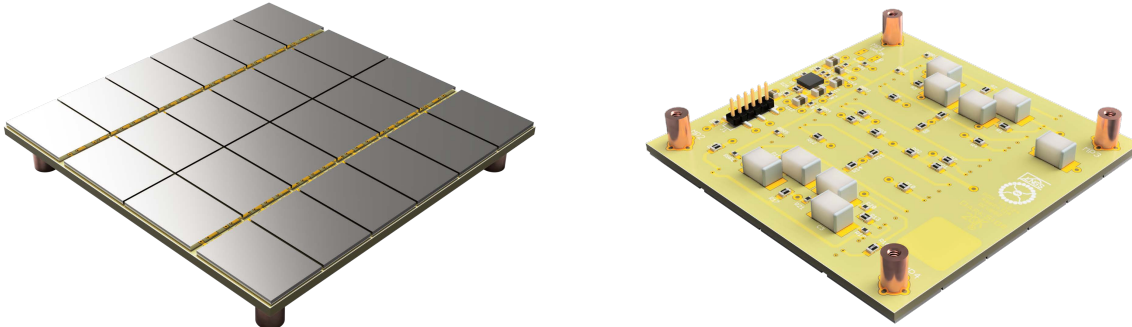


FIG. 113. Left: Top view of the Tile+ where the 24 SiPM are mounted in 4 rows x 6 columns. SiPM anodes are wire bonded to the tile along the two lines between rows 1 and 2 and between rows 3 and 4. Right: Bottom view with electronic components.

4444 The Arlon-55NT PCB is a sandwich of 4 active layers with blind vias and a buried ground plane.
 4445 Wire bondings on the top layer are placed such that they avoid the tile edge, to mitigate mechanical
 4446 risks. The bottom layer of the PCB hosts the SiPM ganging circuit and the cryogenic pre-amplifier.
 4447 An 8 × 8 mm² pad has also been added for the laser engraving of a unique QR-code on each Tile+,
 4448 for tracking of assembly and QA/QC test information in the production data base.

4449 Table XLIV reports the signal and noise parameters measured in a Tile+.

4450 The Tile+ sinks about 11 mA with a supply of 5 V in liquid nitrogen; the power is mainly
 4451 dissipated by the LMH6629 operational amplifier, the core of the TIA. Given the ganging topology,
 4452 the SiPM network requires a bias in the range between 108 V and 150 V. Power lines, power down,
 4453 bias and signal are routed on a 6 pin female socket. The signal has a back-termination of 300 Ω.
 4454

4455 The bias is split by a passive divider implemented with 10 MΩ resistors, properly shunted with
 4456 100 nF PEN capacitors. Each SiPM is then connected to the divider nodes with a further 10 MΩ
 4457 resistor. In this configuration, a current leakage of 1 nA from one SiPM will unbalance the bias of

Parameter	Value
Recharge Time (τ^+)	350 ns
Current Peak ($I_p^+ = \frac{1}{4} C_d / \tau$)	50 nA / VoV
Noise	9 pA / $\sqrt{\text{Hz}}$ / $R_s = 120\Omega$
SNR^+ with Matched Filter	>3.6 / VoV

TABLE XLIV. Electrical parameters of NUV-HD-LF Cryo SiPMs assembled in tiles with 1 TIA configuration (4s6p)

4458 the other SiPMs connected in the branch by about 20 mV. The gain spread introduced by such
 4459 effect, amounting to about 1%, has a negligible impact on the single photo-electron resolution.

4460 The veto Tile+ has a geometry similar to the one developed for the TPC: on one side the board
 4461 hosts the 24 SiPMs, the other side hosts the SiPM bias network in 2s3p configuration, the Castor
 4462 chip-on-board ASIC, the power down switch and a single 6 pin I/O connector. The board has the
 4463 same interface as the TPC Tile+ so it can use the same MB+, power supply, and cabling.

4464

4465 c. *Motherboard+* PBS Item: DS.P.PDU.MB

4466

4467 Sixteen Tile+ are mounted on a single Arlon-55NT PCB called Motherboard+ (MB+). The
 4468 MB+ board will include all the required components to provide the correct bias to the tiles, four
 4469 active adders and four high dynamic range differential transmitters (see Fig. 114).

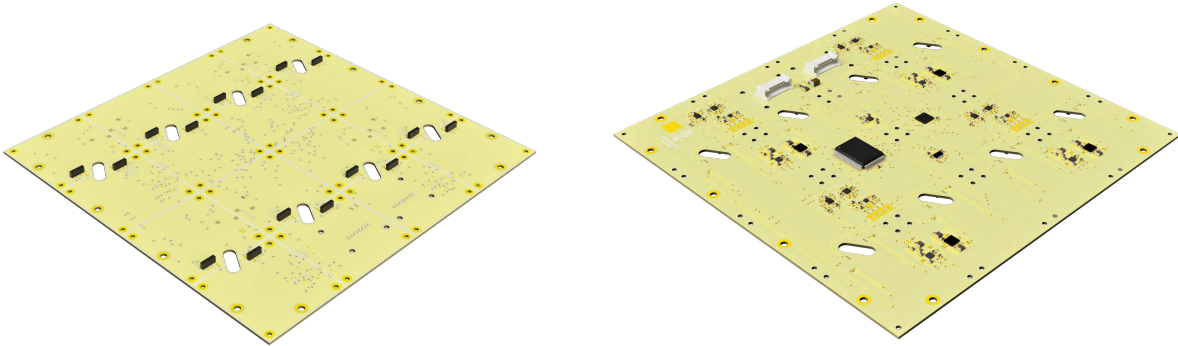


FIG. 114. Left: Top view of the Motherboard+ showing the connectors for the 16 Tile+. Right: bottom view with electronic components and Motherboard+ connectors.

4470 The active adder sums the signals of four Tile+ into a single channel before transmission: the
 4471 single photo-electron (SPE) from each Tile+ has an average amplitude of 3.5 mV at 7 VoV. The
 4472 MB+ has 4 analog high dynamic range differential outputs corresponding, each, to the sum of 4
 4473 Tile+ units. The MB+ is fed with a single-ended supply of about 6 V. For each channel, a voltage
 4474 regulator (model ADM7150ACPZ-5.0-R7) filters the line and provides a stable supply of 5 V. A
 4475 local virtual ground is reconstructed by a 1:1 resistive divider, properly shunted with tantalum
 4476 and plastic (PPS) capacitors. Optionally, a second voltage regulator (model TPS7420) provides
 4477 2.5 V necessary to operate the Castor ASIC, as planned for the veto Tile+. The output signals are
 4478 intended to travel on four twisted pairs in the same radio-pure SAMI cable providing the power
 4479 to the unit, thus simplifying the cabling of the detector. A schematic diagram showing the signal
 4480 path for one channel is shown in Fig. 115.

4481 **Power Module** The Power Module is similar to the Steering Module described in section 3.4.3
 4482 and is implemented with the same functionalities in the MB+ providing the control signals and the

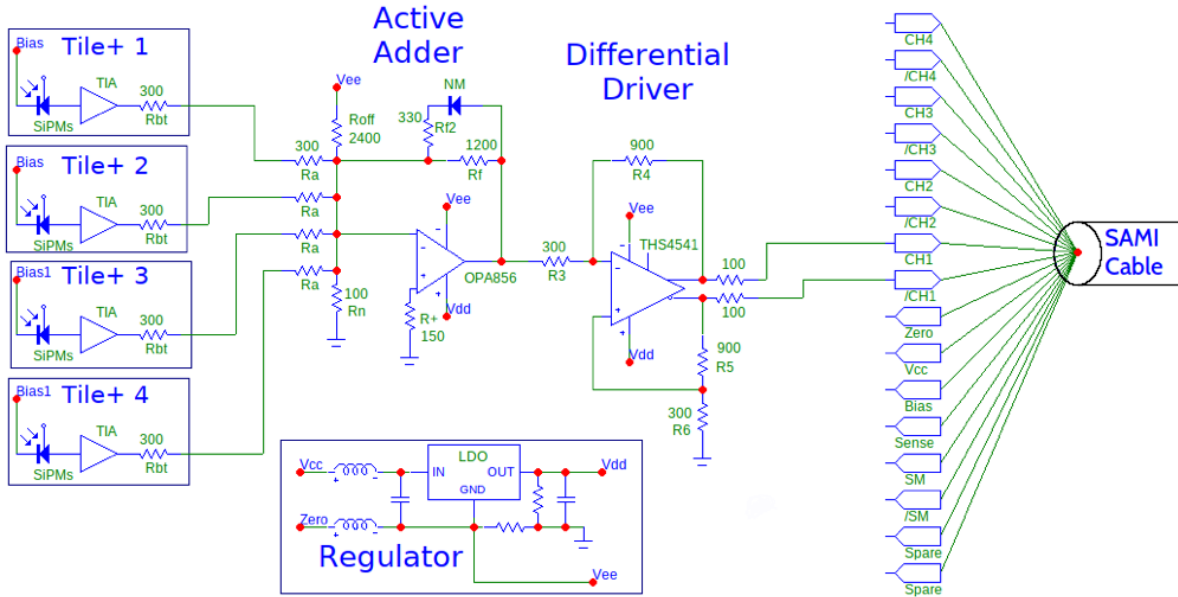


FIG. 115. Schematics of the signal path of one MB+ channel. The signal from 4 Tile+ is actively summed by an adder and then transformed into a differential by a proper driver and transmitted via the SAMI cable. A sketch of the 5 V regulator with the virtual ground divider is also present.

4483 power management. The high voltage (HV3418) and low voltage (HV5523) serial switches have
 4484 been added to the MB+ in a very similar configuration, including the SPI communication interface
 4485 (LTC6820). The MB+ can:
 4486

- individually enable/disable the bias of the 16 Tile+ units
- individually enable/disable the TIA of the 16 Tile+ units
- individually enable/disable the low voltage for the four channels

 4489 The last option effectively turns off the 4 TIAs, the adder and the differential transmitter of the
 4490 selected channel, but not the bias to the SiPMs.
 4491

4492 8.0.2. Cabling

4493 PBS Item: DS.P.CBL

4494
 4495 This section describes the cabling used to control the PDU, supply the power to the front-end
 4496 electronics, bias the SiPM and read the signals.

4497
 4498 a. *Cable (PBS Item: DS.P.CBL.CB):* the power to each PDU+ is delivered through a twisted
 4499 pair of AWG24 stranded copper wires, isolated with Siltem (STM1500), a polymer (polyetherimide-
 4500 siloxane) which has proven to be compatible with cryogenics and radiopure. In the same cable
 4501 bundle are six other pairs, all with AWG30 stranded copper wires, using the same Siltem insulation.
 4502 One pair provides the bias voltage for the SiPM; A second pair, with nominal impedance of 100Ω ,
 4503 is for the command to the PDU; the analog signals are carried by four similar pairs of AWG30
 4504 wires, with $100 \pm 10\Omega$ impedance and Siltem insulation; a spare pair could be used for voltage
 4505 sensing. The cables are bundled together with a mesh made of polyester. The cable weighs about
 4506 30 g/m. Left-handed and right-handed twisting of the stranded copper wires, together with the use
 4507 of polyester fibers, are used to identify the signal pairs. The bias cable, instead, can be identified
 4508 by a thicker insulator. The cross section of the cables is shown in Fig. 116.

4509

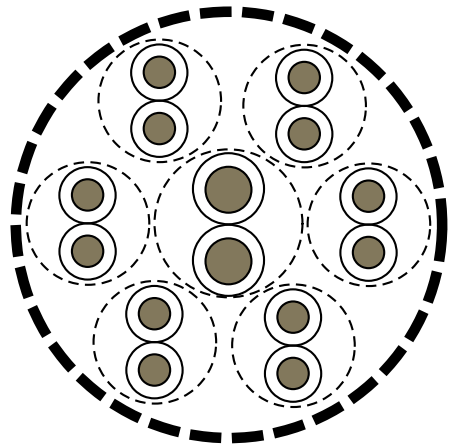


FIG. 116. Cross section of the cable used for power, bias, controls and signals of PDUs. All cables are stranded copper, AWG24 for power and AWG30 for all others. The insulation is in Siltem for radiopurity, with no dying, and a polyester mesh bundles together the cable. All five twisted pairs for command and signal have characteristic impedance $Z = 100 \pm 10\Omega$. The pairs are identified with the strand helicity and with a polyester fibre. The bias cable is identified with a slightly thicker insulation. An additional twisted pair may be added for voltage sensing.

4510 *b. Chimney Flange (PBS Item: DS.P.CBL.FLG):* The chimney flange is described in detail
4511 in section 7.2.12.

4512 *c. Connectors (PBS Item: DS.P.CBL.CNT):* connectors for these cables are surface mounted
4513 on the PDU+ board, using low temperature soldering. They are made with nylon PA66 with no
4514 fiberglass filling, for lowered radioactivity. Two additional soldering points hold the male connector
4515 to the board. Ad-hoc connectors have been developed, similar to the Sherlock connectors. The
4516 pitch is 2mm, to minimize cross talk. On the cable side, the female connectors are crimped to
4517 the single wires and are then inserted in the nylon body, which latches on the connector which is
4518 soldered on the board. Two connectors, each with eight pins, are used, separating the signals from
4519 the power, bias and control signals.

4520

4521 8.0.3. Power Supply

4522 PBS Item: DS.P.PS

4523 The Power Supply Unit (PSU) is a post regulated custom design based on low noise channels
4524 each providing both the low and high voltage to a single PDU+ according to specific requirements:

4526 1. Low Voltage Channels

- 4527 (a) 6 V fixed stabilized output voltage
- 4528 (b) 2 A maximum current capacity (500 mA needed)
- 4529 (c) 1 mA current resolution

4530 2. High Voltage Channels

- 4531 (a) programmable stabilized output voltage in a range 0-190 V (160 V needed)
- 4532 (b) 3 mA maximum current (500 μ A needed)
- 4533 (c) 100 nA-1 μ A current resolution

4534 Each PSU channel has to provide voltage and current measurement and also supply a very low
4535 noise, < 1 mV. The PSU architecture is shown in Fig. 117. The design is based on multiple,
4536 modular channels managed by a Master Control Unit (MCU) which on one side communicates

4537 with the Channel Control Unit (CCU) by means of an Ethernet and on the other side sends data
 4538 to a PC via USB port. The CCU handles either the high-voltage (Hi-V) or low voltage distribution
 4539 (Lo-V), constantly monitoring the output voltage and current for the nth channel. Both Hi-V
 4540 and Lo-V channels need to be stabilized with a minimum ripple of a few mV. The In-channel and
 4541 CCU-to-channel communications use common chip-to-chip serial protocols, such as SPI and I²C
 4542 (Inter Integrated Circuit).

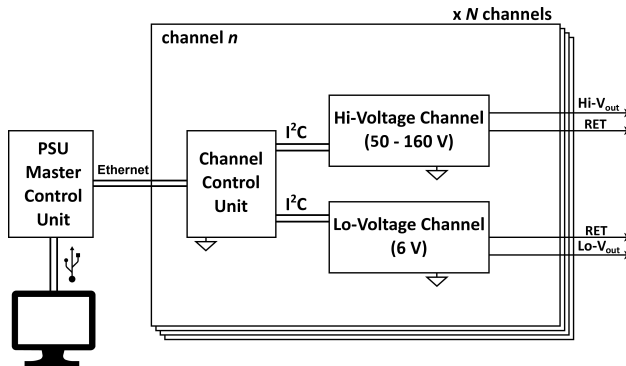


FIG. 117. Sketch of the PSU architecture

4543 *a. Low Voltage channel specifications:* a block diagram for the Lo-V channel is reported in
 4544 Fig. 118, left. A DC-DC buck converter is used to step-down the voltage from a 24 V value
 4545 provided by an internal bus to a lower level with high efficiency. Hence the LDO voltage regulator
 4546 eliminates the DC-DC ripple and provides the required voltage to the load (i.e. 6 V in the condition
 4547 of no voltage drop on the cables). Both the DC-DC and LDO are controlled by two references thus
 4548 allowing to set the DC-DC output a little higher than the LDO's one, reducing the voltage drop
 4549 on the LDO (which has a lower efficiency than the buck converter). Both output voltage and
 4550 current are monitored by means of a microcontroller that consequently controls DC-DC and LDO
 4551 references. Since the output current is quite high, the voltage drops could not be negligible, thus
 4552 a voltage feedback could be used by the microcontroller to properly control the DC-DC and LDO
 4553 references.

4554 *b. High Voltage channel specifications:* the block diagram of the Hi-V channel is sketched in
 4555 Fig. 118, right. A DC-DC boost converter provides an output voltage up to 190 V from a smaller
 4556 reference value (i.e. 24 V). As in Lo-V channel, the LDO is needed to eliminate the voltage ripple.
 4557 Both DC-DC and LDO references are varied together to reduce the power dissipation, stepping-up
 4558 the voltage at the minimum level required from LDO to work (i.e the desired output summed to the
 4559 dropout). Since the output current is quite small, the voltage feedback from load can be omitted
 4560 and the current measure can be done on the low-end of the output.

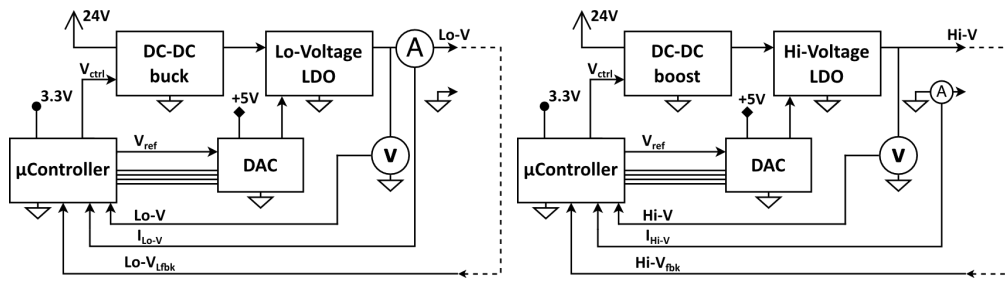


FIG. 118. Block diagrams of Low Voltage and High Voltage channels: **Left:** Lo-V **Right:** Hi-V

9. TECHNICAL DESCRIPTION: SUPPORT FACILITIES

4561 PBS Item: DS.F

4562

4563 The construction and installation of the DS-20k detector involves a number of support facilities
 4564 as shown in figure 119. During the test and R&D phase we have set up additional infrastructures
 4565 and facilities in various laboratories of the Institutes of the Collaboration that will not be discussed
 4566 here. Small scale prototypes of the DS-20k detector, aiming at testing, verifying and establishing
 4567 experimental procedures about particular technical aspects of the final detector design, are also
 4568 included in the branch Support Facilities.

4569 The DS-20k SiPM packaging foresees the production of more than 8448 PDMs for the TPC
 4570 (table XIX). This remarkable effort requires a large clean room, relying on cutting edge technology
 4571 equipment and trained personnel. We selected for the DS-20k SiPM packaging facility a clean room
 4572 inside the LNGS surface laboratory in the so-called *Hall di Montaggio* (Assembly Hall), with a total
 4573 area of $\simeq 420 \text{ m}^2$. The area occupied by the structure is of about $\simeq 460 \text{ m}^2$ divided into 5 main
 4574 sub-structures, as shown in table XLV.

Name	m^2	Destination
CR1	15	Dressing area-air shower
CR2	65	Inner detector assembly
CR2-IS	3.4	Air shower and pass box
CR3	338	Photo-detector assembly
HVAC	42	Service area

TABLE XLV. The NOA clean room sub-structures and destination.

4575 The clean room will satisfy the ISO Class 6 standard, it has fully metal walls to ensure low
 4576 Radon emanation and it is designed to allow for very low level of Rn concentration ($<50 \text{ mBq/m}^3$)
 4577 once equipped with proper filters and a Rn abatement system. The tender for the construction
 4578 was finalized in Nov. 2019 and, at the time of writing this document, it is in an advanced stage of
 4579 implementation with access to the room expected by the end of Feb. 2022.

4580 The clean room together with its infrastructures is called NOA (Nuova Officina Assergi).

4581 The NOA clean room is formed by two main rooms (see table XLV, called CR2 and CR3, devoted
 4582 to the assembly of parts of the inner detector (CR2, PBS item DS.F.IDF.CR2) and to the packaging
 4583 of the SiPMs and electronics (CR3, PBS item Ds.F.PPF.CR)).

4584 The DS-20k SiPM packaging foresees the production of more than 1920 PDMs for the Veto
 4585 (table XIX). The veto DS-20k SiPM packaging will be done in the UK (DS.F.VPF), within the
 4586 Liverpool Semiconductor Detector Centre (LSDC), in collaboration with a consortium of 13 Uni-
 4587 versity Particle Physics groups and the STFC Interconnect facility. The LSDC clean room, with
 4588 an area of 450 m^2 , has been in operation since 2003.

4589 Tests of the PDUs will be performed in a dedicated facility (DS.F.PRO.PTF) in Naples (Univer-
 4590 sita' Federico II and INFN).

4591 With reference to figure 119, the item DS.F.IDF.CF describes large evaporators located at the
 4592 University of Alberta in Canada, in a radon-abated cleanroom, for TPB coating of the anode,
 4593 cathode and ESR foils of the TPC. Finally, the item "Hall C interfaces", DS.F.HCS, groups several
 4594 infrastructures located in Hall C that are necessary during the installation and commissioning of
 4595 the detector.

4596

9.1. PDU production facility

4597 PBS Item: DS.F.PPF

4598

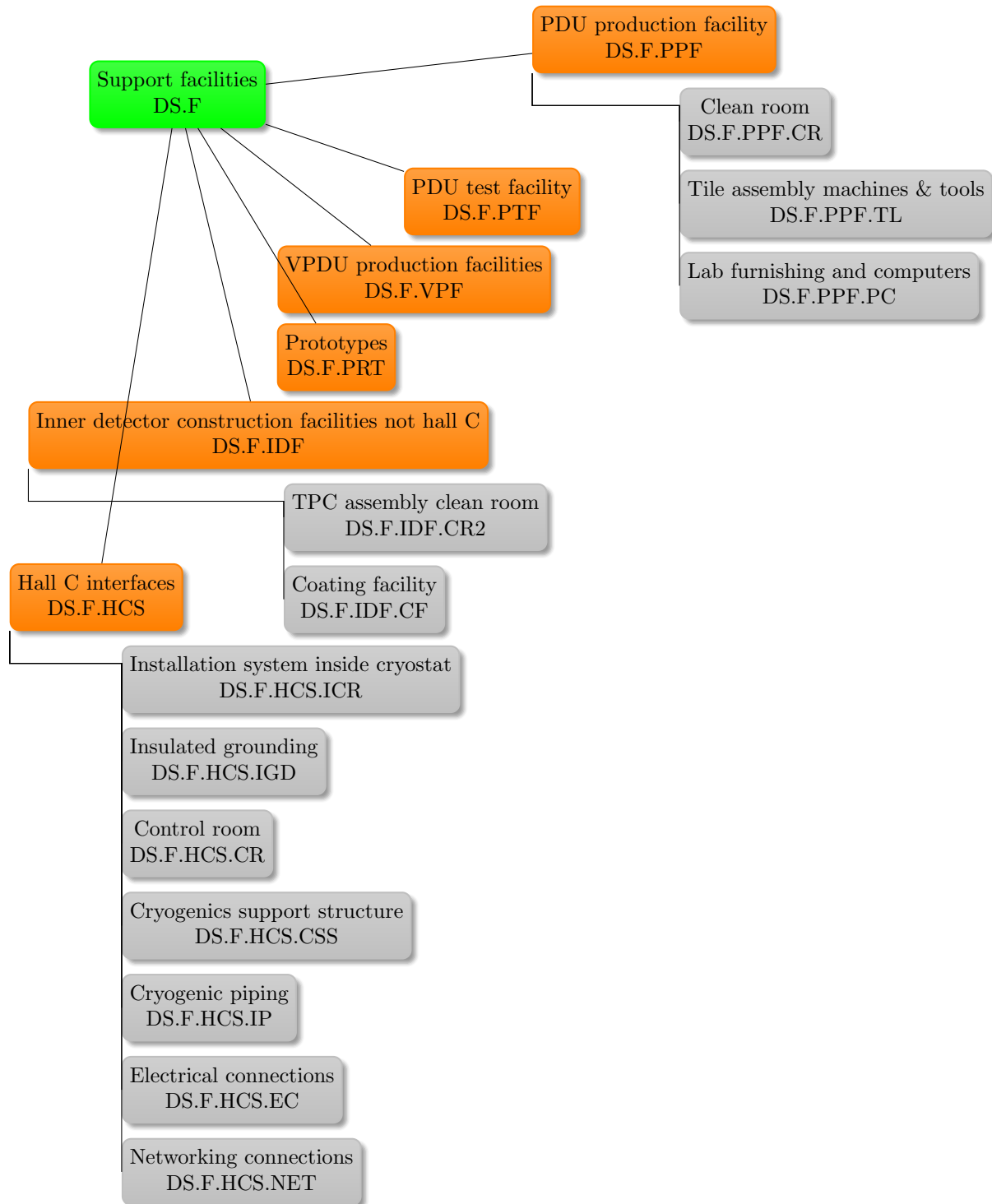


FIG. 119. PBS of the various support facilities.

4600 A layout of the NOA facility is shown in Fig. 120. The major equipment that will be installed
 4601 in CR3 are a cryogenic silicon wafer probe, a flip-chip bonder and a full surface mount technology
 4602 (SMT) reflow system.

4603 We foresee 26 workstations, each equipped with low pressure nitrogen (around 1,5 barg), oil-free
 4604 compressed air, vacuum < 1 mbarA, electrical power both from normal supply and from UPS, data
 4605 and phone. The total UPS power capacity is 80 kVA, and the electrical plant is designed to ensure
 4606 the feasibility of installing a second unit with the same power in the future.

4607 Following the evaluation shown in table XXIII, we do not require a Rn abatement system for
 4608 the SiPM and electronics during assembly. The exposure to air of SiPM and electronics components
 4609 will be reduced to a minimum during the mounting operations, with components stored prior to
 4610 assembly in proper Rn-tight packaging and sealing (described in section 3.1.5). Similarly, Rn-tight
 4611 packaging of the PDU will be used during the transportation to and from the PDU Test Facility
 4612 and during the storage time before the final assembly.

4613 The NOA air handling system is design to provide 50 exchanges/day of the full air volume
 4614 according to ISO-6 classification standards. This requirement is accomplished by combining the
 4615 air flux provided by the Unit for the air treatment, which is about 28.000 - 30.000 m³/h, and
 4616 the air flux coming from the 41 Fan Filter Units placed on the roof which provide the remaining
 4617 re-circulation flux of about 40.000 m³/h. The same system has been designed and constructed
 4618 to provide and guarantee a total flux of make-up air of about 7.800-8.000 m³/h. These numbers
 4619 describe the operation without an additional Rn abatement system. Fluid dynamic simulations
 4620 have been carried out in order to study the air streams inside the clean room: these analyses have
 4621 been very useful in order to detect any possible stagnation zones. This allowed identification of
 4622 the best position of the HEPA filter units in order to guarantee the ISO-6 classification standards.
 4623 Simulations also provided useful information that led to some adjustments of the air-duct design
 4624 and configuration, thus optimizing the air handling plant and system. The results are shown in
 4625 figure 121.

4626 A Rn detector with a special air sampling system will be installed inside the CR to constantly
 4627 monitor the Rn concentration in air. In particular, the fluid dynamic simulations performed have
 4628 identified three air points where Rn concentration is higher than the mean value. In these points
 4629 an air sampling system has been designed and implemented. A fourth sampling point is planned
 4630 for future installation, to measure air at the exit of the Rn reduction plant, in order to provide a
 4631 reference value for the Rn concentration level. Two different Rn free make-up air flow-rates have
 4632 been studied: 1200 m³/h, which would allow for about 24 people present in NOA at the same time,
 4633 and 600 m³/h, which wouls allow for 12 people at the same time. Results of this optimization
 4634 are in figure 122 and they show that both configurations allow compliance, with one order of
 4635 magnitude safety factor, with the maximum Rn concentration allowed during the TPC assembly
 4636 (set to 100 mBq/m³in section 5.8.5).

4637 The air handling system can be arranged in a “reduced energy” mode, which means that the
 4638 plant is running with a reduced make-up air flow-rate, compatible with the “Rn free” operating
 4639 mode. In the “reduced energy” mode the Fan Filter Units also run at a lower velocity. These
 4640 two features allow the reduction of the total electrical power supply requested by the room, whilst
 4641 keeping the ISO-6 classification standards during stand-by periods.

4642 The air handling system allows running CR2 and CR3 separately, both in “normal” and in ”Rn
 4643 free” mode. The air configuration system, following the latest design implementations, foresees the
 4644 following operating modes, (both with and without Rn abatement system active):

- 4645 • CR2 working, CR3 not working - CR2 ON; CR3 OFF
- 4646 • CR2 not working, CR3 working - CR2 OFF; CR3 ON

4647 An “air lock” has been constructed in order to allow access to CR2 in a clean condition, with the
 4648 CR3 off. This “air lock” is also provided with an auxiliary door with the function of a “pass box”.

4649 The DS-20k detector assembly, as described in detail in Sec. 11, requires the implementation of
 4650 an additional auxiliary area adjacent to CR2 to function as a staging area (marked with dashed
 4651 lines in Fig. 120 since it is not part of the current NOA plan). The collaboration will provide the
 4652 resources for the design and construction of this additional temporary infrastructure; discussion

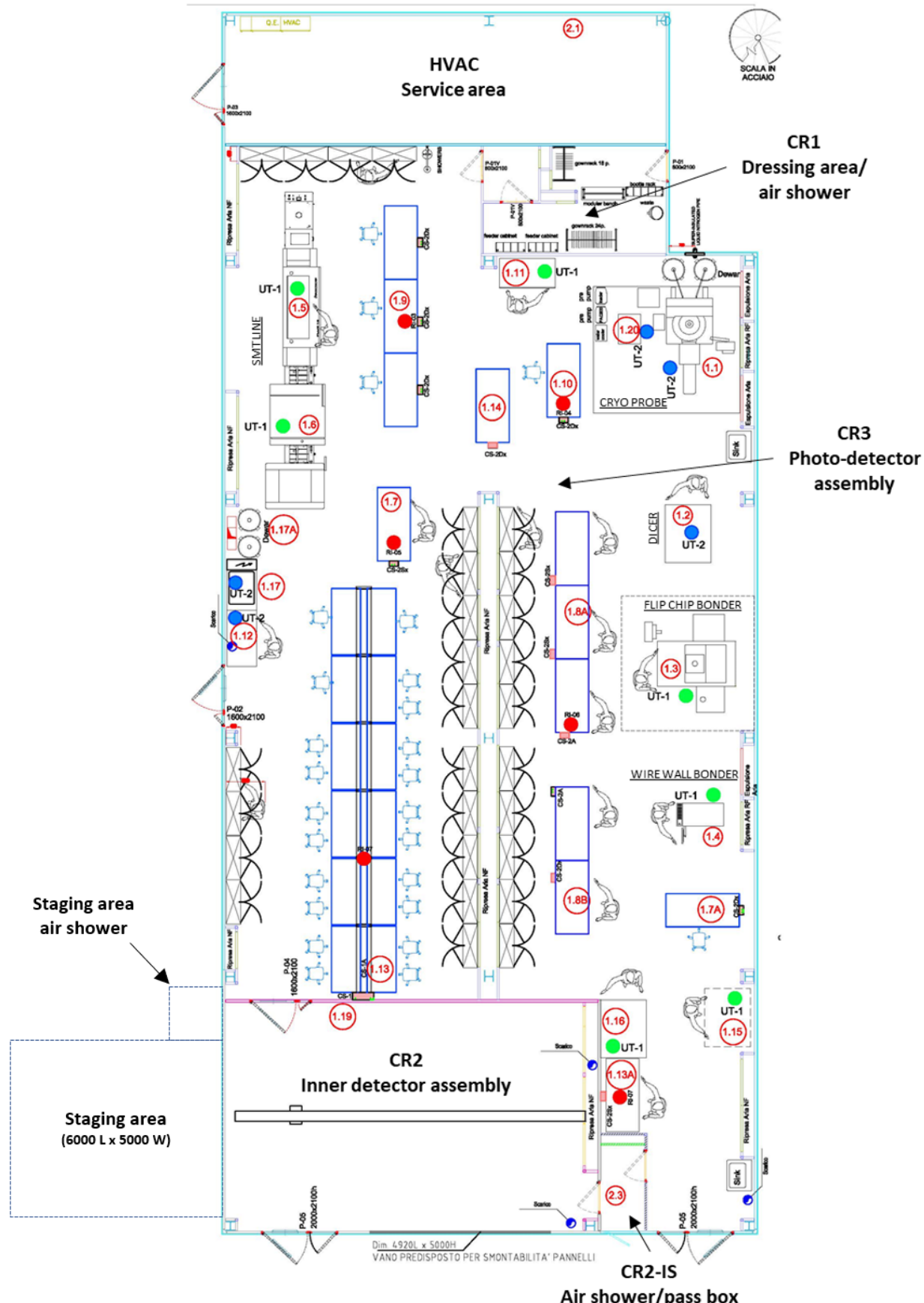


FIG. 120. Floor plan of the NOA clean room in the *Hall di Montaggio* of the LNGS surface laboratory¹⁵⁵, showing designated position of equipment and working and storage areas. At the bottom left the detector assembly staging area that will be implemented by the collaboration is visible.

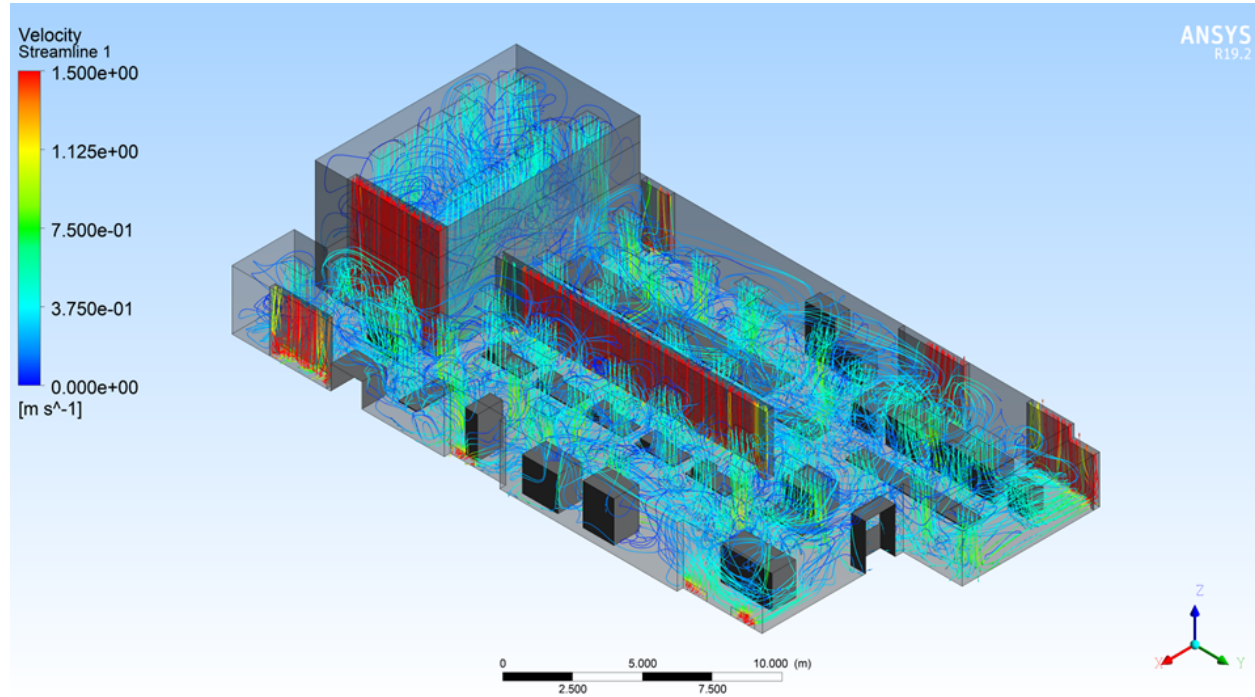
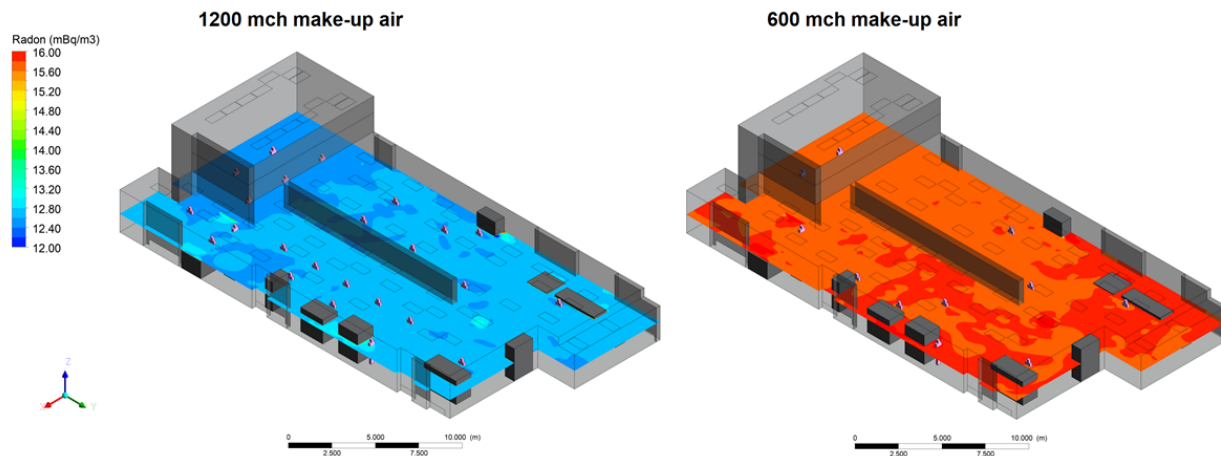


FIG. 121. Simulation of the air flow in NOA

4653 with the NOA group has already started in order to address the mechanical and HVAC interfaces
 4654 with the NOA facilities. This intermediate clean volume, with a footprint of $\sim 5 \times 6 \text{ m}^2$, is necessary
 4655 to control the radon and dust contamination whenever any of the large detector parts need to be
 4656 inserted into the CR2. The staging area walls will be constructed in suitable materials for a clean
 4657 environment. The access to CR2 will be implemented through removable panels with dimensions
 4658 of width 5.15 m \times height 5.70 m.

FIG. 122. Simulation of Rn concentration in NOA. 1200 m³/h (left) and 600 m³/h (right) of Rn free make up air flow-rate

4659

9.2. PDU Test Facility

4660 PBS Item: DS.F.PTF

4661

4662 The Naples PDU Test Facility is a dedicated installation assembled inside the Naples Cryolab
 4663 cleanroom, comprising 50 m² working area (see figure 9.2, left) at ISO Class 6. The facility was
 4664 designed specifically for the cryogenic test in liquid nitrogen of the Photo Detecting Units (PDU)
 4665 produced in NOA.

4666 The goal for the test rate of the facility is 12 PDUs per week.

4667 *Facility Cryogenics overview* The PDU Test Facility cryogenic system is composed of two sub-
 4668 systems:

- 4669 • an external plant with 3000L LN storage tank that provides liquid and gas Nitrogen at the
 4670 operation pressure of 2.5 bar; and,
- 4671 • the clean room cryogenics composed of the custom-made PED certified cryostat (see figure
 4672 9.2, right) and the filling station comprising bi-directional vacuum insulated transfer line,
 4673 custom made cold box with manual and pneumatic cryogenic valves and the vent collector
 4674 to collect and expel the Nitrogen gas outside.

4675 The clean room is also equipped with high (up to 10 bar) and low (up to 2.7 bar) pressure Nitrogen
 4676 gas lines. The high pressure is used for valve control, while the low pressure is used to drain the
 4677 facility cryostat.

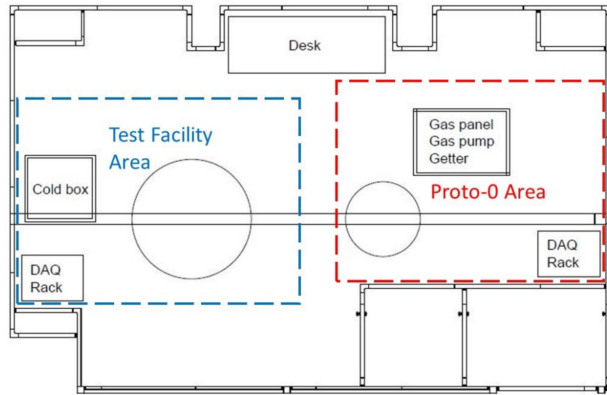


FIG. 123. **Left:** the Naples 50 m² Clean Room layout. **Right:** the custom made Cryostat of the PDU Test Facility

4678

The cryostat is a 1.57 m high double wall vacuum insulated vessel, coupled with a 1.15 m diameter
 4679 and 0.26 m high single wall domed flange. It is equipped with nine PT100 level meter sensors, a
 4680 pressure transducer and an analog pressure indicator in order to monitor and maintain stable
 4681 conditions inside during the test. The domed flange has a number of CF flanges of different sizes
 4682 for electrical feedthroughs (to extract signals and provide power lines), for the optical feedthrough
 4683 (to deliver pulsed laser signals) and for all other needs foreseen in the test protocol. The double
 4684 wall vessel has two vacuum insulated side ports with female bayonets, one for the LN inlet and
 4685 one for the cold gas vent. The LN supply port allows filling the vessel from the bottom. A rubber
 4686 O-ring is used in order to seal the vessel. The maximum allowed pressure in the cryostat is 3 barA,
 4687 the pressure above this value will be released by relief valves to the vent line. The key features
 4688 of the cryogenic system, such as the status of proportional and automatic valves, as well as the
 4689 operating parameters, such as the temperature and the LN level inside the cryostat, are controlled
 4690 by a National Instruments PXI computer and LabView-based slow control program.

4691 The facility cryostat is connected with the external LN storage tank by a dedicated vacuum
 4692 insulated transfer line. Inside the clean room the flexible line links the cryostat to the cold box.
 4693 After the cold box the rigid insulated line exits the clean room and continues outside to the storage
 4694 tank. This transfer line is used in both directions; from the tank to the cryostat during the filling
 4695 phase, and from the cryostat towards the tank during the draining phase.

4696 Before the actual fill the cryostat has to be flushed with N₂ gas in order to remove moisture.
 4697 During the flush and fill the output vent line from the cryostat for the cold N₂ has to be opened;
 4698 it is closed at the end of fill when the desired level is reached. After filling, the pressure inside the
 4699 cryostat is maintained at a constant value of 1140 mbar by the inline relief valve. In order to drain
 4700 the cryostat, over-pressure is created in order to push the LN away through the supply line. Instead
 4701 of being collected back to the storage tank, the LN passes through a dedicated aluminum passive
 4702 evaporator and gets vented outside. At the pressure level of 2.3 barA the fully loaded cryostat can
 4703 be drained in 25-30h. The cryogenic system was fully assembled and successfully commissioned in
 4704 the beginning of August 2021.

4705 *a. PDU holding structure* In order to accommodate 12 PDUs, a three plane mechanical structure
 4706 is designed to be installed inside the cryostat. Each plane hosts four PDUs. Every PDU will be
 4707 coupled with a light distribution plane equipped with laser fibers and teflon diffusers to distribute
 4708 light for the laser calibration runs.

4709 The holding structure is designed to be easily decoupled from the domed flange and then secured
 4710 on the dedicated working table, in order to load and unload the PDUs in stable and secure way.



FIG. 124. Picture of the Naples Test Facility holding structure used in PDU+ cold test.

4711 *b. Laser calibration system* The Light pulses provided by the Hamamatsu laser head PLP
 4712 C8898 will be delivered inside the cryostat by means of the 16 individual optical feedthroughs
 4713 mounted on the CF100 flange. The primary fiber that drives the light pulse from the laser head
 4714 will be split into 12 fibers and then connected to 12 ports on the optical feedthrough mounted on
 4715 the top domed flange. Inside the cryostat from the feedthrough 12 SMA-SMA fibers of 2 m (one
 4716 for each PDU) will be further split into 4 in order to provide four fibers per PDU. An example of
 4717 the two plane structure used in the PDU+ cold test is shown in figure 124.

4718 c. *Electronics and read out* The Naples Test Facility will use the low and high voltage power
4719 supplies, power line filter boxes and digitizers following the recommendations provided by the
4720 Photo-electronics Working Group. Accordingly, at present, we are equipped to provide the low
4721 voltage with 2 CAEN A2518 modules, and the high voltage bias with one CAEN A1619 module.
4722 All power supply boards will be powered by the dedicated CAEN mainframe SY2527. In order
4723 to distribute the low and high voltage between the individual PDU channels, a dedicated Steering
4724 Module, mounted locally on the PDU will be used, and its power provided by the CAEN power
4725 supply A2518.

4726 In order to deliver the high and low voltage to the PDUs inside the cryostat, the DS-20k SAMI
4727 cable will be used, provided by INFN Milano.

4728 Five new 64-channel CAEN ADC boards VX2740, which are the selected digitizers for the DS-20k
4729 DAQ, are present in the facility, and two boards are already in use for the test of PDU+ and
4730 PDUSlim. DB50 connector feedthroughs are used to deliver the signals from the PDU inside the
4731 cryostat to the ADC mounted in the rack outside. Inside the cold volume the SAMI cable delivers
4732 the signals from the PDU to the feedthrough, outside the cryostat, a dedicated PCB adapter with
4733 DB50 connector on one side and seven RJ45 connectors on the other side is employed. From
4734 this adapter board to the ADC boards, a standard Ethernet cable (four twisted pairs) with RJ45
4735 connector is used, with one pair per channel. The ADC front panel employs a second adapter that
4736 couples the arriving RJ45 connectors with the standard header connectors of the VX2740 board.
4737 This configuration, based on two adapters and the Ethernet cable in between, was proposed by
4738 the Naples SER team, built and successfully tested in the Test Facility during the cold tests of the
4739 PDUSlim.

4740 d. *DAQ and Data Handling* Naples facility relies on a dedicated Data Acquisition System
4741 consisting of two server machines and over 600 TB of storage. The waveforms from 12 PDUs will
4742 be digitized by CAEN 64-channel VX2740 boards, and sufficient channels for this are available
4743 in the facility now. In addition, the facility has 4 V1725B boards, each with 16 channels for a
4744 total of 64 channels, presently in use for the LN test of the MB-3 PDU prototype used to study
4745 SiPM performance and stability. The process of data taking is automatized and governed by the
4746 MIDAS-based acquisition code developed by TRIUMF group specifically for this purpose.

4747 e. *Slow control* The test facility is controlled by a National Instruments PXIE-8861 based Slow
4748 Control system. The data flow provided by Labview is also supplied to the MIDAS based DAQ.
4749 The key features of the Slow Control are: monitoring of the temperature sensors and pressure of
4750 the cryostat, monitoring of liquid level and the pressure in external LN2 tank, monitoring of the
4751 vacuum in the cryostat insulation jacket, control of the filling and draining processes by regulating
4752 the proportional valve apertures; and, control of the CAEN boards to deliver the low and high
4753 voltages needed. The slow control web page is based on the NI LabView framework, similarly to
4754 DS-50 and ReD experiments.

4755 f. *Present Status* The PDU Test Facility has been active since mid-September 2021. On
4756 September 13th the original version of the PDU (MB-3) arrived in Naples and was successfully in-
4757 stalled inside a dedicated system equipped with standalone electronics and DAQ (ADC, differential
4758 to single end converters, power supplies and filters). It was filled with LN on September 17th and
4759 since then has been continuously taking data. This test, 10 weeks thus far, is the longest cold test
4760 the collaboration performed to date with the SiPMs. In addition, the main facility cryostat was
4761 used to test the other two prototype versions of the PDUs: the PDU+ (which arrived to Naples on
4762 September 28th and was tested in LN for 20 days) and the PDUSlim (which arrived to Naples on
4763 November 10th, and since 19th is under test in LN).

4764 While detailed analysis for long term stability of the quality of the signals is still underway, we
4765 show in the plots in Figure 125 sample amplitude spectra in the same conditions for all the three
4766 devices tested so far, that demonstrates the quality of the signals obtained in the PDU test facility
4767 and its versatility.

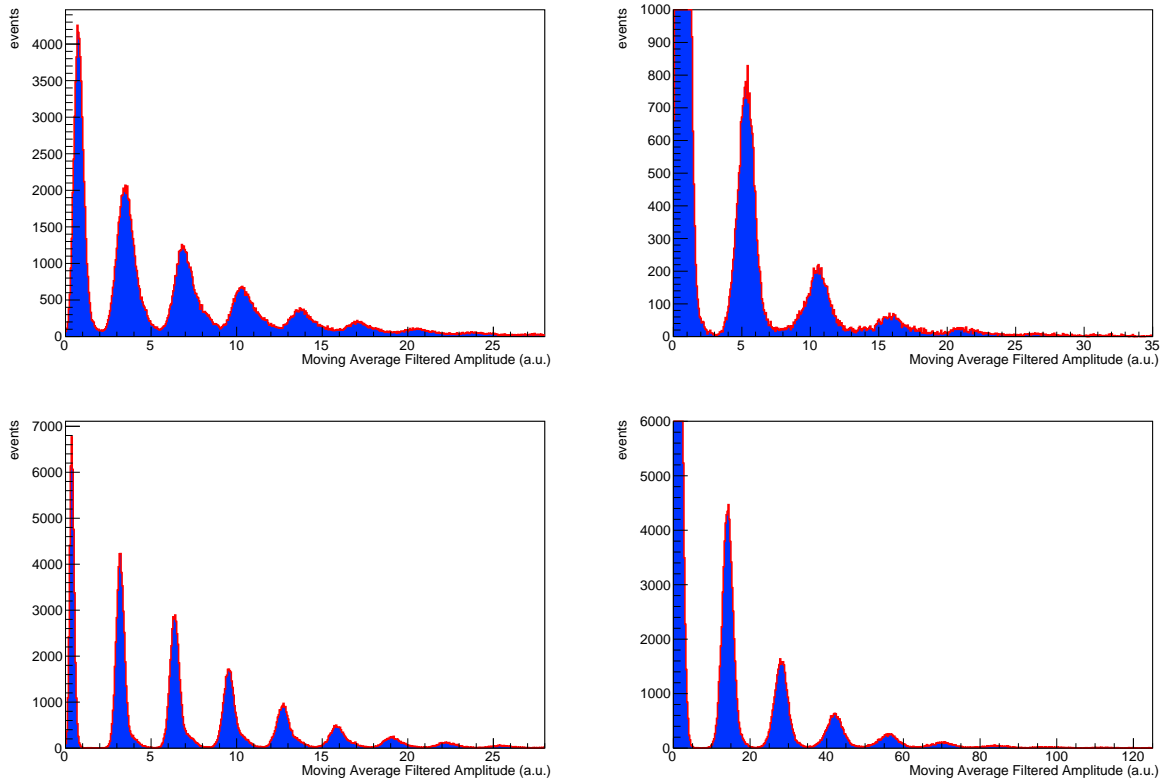


FIG. 125. Amplitude spectra under laser illumination for the PDU+, PDUSlim and MB3 photo-detection units. In all cases the maximum of the waveform averaged in a 400 ns moving window around the expected arrival time of the laser pulse is taken. This choice does not necessarily maximize signal to noise ratio (SNR) for any of the device tested and is adopted for illustrative purposes only. In all cases the SiPMs were operated at 7VOV. **Top left:** PDU+ with 4 Tile+ summed (SNR=8.5); **Top right:** PDUSlim with 2 Tiles summed (SNR=13); **Bottom left:** PDU+ with only 1 Tile+ (SNR=16); **Bottom right:** MB3 typical channel (SNR=19),

4768

9.3. vPDU Production Facilities

4769

PBS Item: DS.F.VPF

4770

The veto PDMs will be built in the UK, with the production of tiles at the LSDC facility at the University of Liverpool, supported by the STFC Interconnect facility at the Rutherford Appleton Laboratory, and population of tile substrate PCBs at the BILPA facility at the University of Birmingham.

4775

The LSDC facility cleanroom site comprises over 100 m² working area at ISO Class 5, and roughly 250 m² at ISO Class 7. It is re-certified annually by an external ISO approved inspector. The LSDC has previously hosted the construction of high-profile detector assemblies such as the ATLAS SCT Endcap C, LHC VELO1, and VELO2, T2K ND280 ECAL, NA62 KTAG and g-2 straw trackers. The LSDC is equipped with comparable (and in some cases identical) equipment to NOA for the glue/solder dispense and reflow parts of the production process, and hosts 2 Hesse & Knipps BJ820 wire bonding machines with working speed of 5 wires/second that will be used for the DS-20k veto PDM production wire-bonding assembly, as well as XYZtec Condor 100 pull tester for bond qualification and smartscope for post-production metrology.

4784

4785

4786

The STFC interconnect facility will collaborate in the development of the UK production work flow. STFC Interconnect is a detector assembly facility that moved into a purpose-built building on the UK STFC Rutherford Appleton Laboratory campus in 2019. STFC Interconnect has delivered

4787 major silicon detector components for ATLAS detector upgrade, and deployed flip chip assembly
 4788 processes at large scale together with ASIC integration for the European XFEL Large Pixel Detec-
 4789 tor. STFC Interconnect hosts comparable equipment for wafer dicing, glue dispensing, reflow and
 4790 wire bonding/testing to NOA as well as high rate flip chip bonding capability with Dr Tresky die
 4791 placer FC150 Flip chip and FC300 Flip chip machines.

4792 The BILPA facility at the University of Birmingham will populate the veto tile PCBs with
 4793 components. BILPA is a 200 m² clean room facility hosted by the Particle Physics group for the
 4794 High-Luminosity upgrade of the LHC (HL-LHC), generic R&D on semiconductor detectors for
 4795 future international collider experiments, and medical application of particle physics technology.

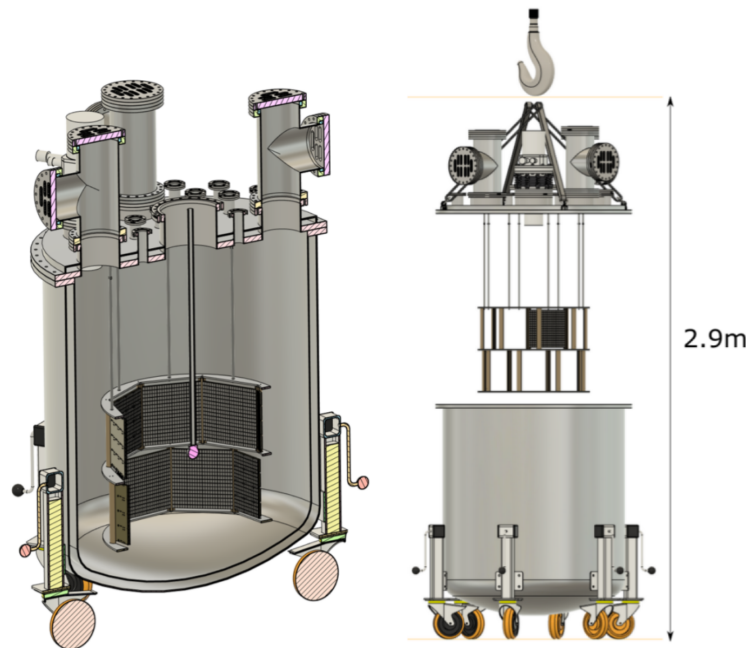


FIG. 126. The PHAEDRA veto PDM test platform.

4796 Veto PDMs built in the UK will be characterized at LAr temperature in Liverpool, which hosts
 4797 an established LAr facility. The facility develops innovative technologies for future LAr detectors in
 4798 Neutrino and Dark Matter experiments and other applications such as medical imaging and security.
 4799 The facility houses ARIADNE, a tonne-scale dual phase LAr detector for the development of optical
 4800 camera TPC readout technologies for LAr TPCs. The facility is building a sister platform of similar
 4801 scale (PHAEDRA, PHoton detection module Assembly cryoGenic DaRkside Apparatus) whose
 4802 design shown in Fig. 126, for cryogenically testing the veto PDMs produced in the UK. Smaller
 4803 test stands to support vPDU testing, similar in scale to figure 128, are also under construction at
 4804 Astrocent (Warsaw) and the University of Edinburgh.

4805 9.4. Inner detector construction facilities not in Hall C

4806 9.4.1. TPC assembly clean room

4807 PBS Item: DS.F.IDF.CR2

4808 As described in section 11, part of the the assembly of the inner detector will begin in CR2 and
 4809 then will be completed inside the membrane cryostat in Hall C. Removable panels, of 5.15 m wide ×
 4810 5.7 m tall, will be placed on the West side wall of CR2 allowing large objects, e.g. the acrylic pieces

4812 making up the TPC barrel, to move into CR2. A staging area, with a temporary infrastructure,
4813 will be organized in front of the West side of CR2, using the space previously allocated to the
4814 DS-20k experiment for the installation of an annealing chamber. The assembly of this temporary
4815 structure is responsibility of the DS-20k collaboration.

CR2 features an overall height of 7m and the floor is designed to support up to 2 ton/m². Following the results of the studies reported in section 5.8.5, a radon abatement system capable of reducing the Rn concentration to 100 mBq/m³, is planned to be used in CR2 during the assembly of the TPC. The collaboration will equip CR2 with the required infrastructures for the application and curing of the Clevios coating, and all assembly operations.

9.4.2. Coating facility

4822 PBS Item: DS.F.IDF.CF

The DS-20k TPC acrylic anode and cathode need to be coated with TPB after the Clevios deposition, to convert the VUV LAr scintillation light to optical wavelengths. A dedicated, large TPB coating facility has been designed for this purpose and will be built at University of Alberta, in Canada. It will be made of a stainless steel vacuum chamber with ~ 420 cm diameter and ~ 100 cm height, with a total volume of ~ 14 m 3 . The top flange of the chamber can be lifted and removed with the aid of a crane. The chamber will be equipped with a turbo-pumping station composed of one 200 m 3 /h dry pump and one ~ 1200 l/s turbomolecular able to achieve a vacuum level of $\sim 10^{-6}$ mbar. The turbomolecular pump will be connected to the bottom side of the chamber through a remotely operated gate valve. Vacuum gauges to monitor the vacuum level will be placed on the bottom flange. While inside the evaporator, the anode and cathode will be held stationary, and after outgassing of the acrylic pieces to reach sufficiently low vacuum pressure, uniform TPB deposition will be achieved on the surfaces through a set of stationary evaporation boats. Details of the crucible material and geometry are being defined, but the design calls for a set of crucibles with a volume of ~ 100 cm 3 able to host ~ 20 g of TPB each and equipped with a remotely operated shutter to be opened once the vacuum level of $\sim 5 \times 10^{-5}$ mbar is reached and the temperatures of the cell are at about 220 °C. A series of thermocouples are used to monitor the crucible temperatures, while a PID (Proportional Integral Derivative) controller ensures the stability of the temperatures during the whole of the coating process. Four quartz sensors will be used to monitor the thickness of the coating to determine the start and end of the evaporation process. A gaseous nitrogen line, connected to the coating system though valves, is used to fill the chamber at the end of the evaporation process. A small rack containing all the elements of a simple slow control will be implemented to manage the control of pumps, gate valves and crucible shutters as well as to monitor the vacuum level, the temperatures and the quartz during the operations. The TPB deposition goal is to have a surface coating density of about 200–300 µg/cm 2 . Preliminary coating tests will be performed in order to determine the time necessary to reach the desired vacuum level and surface TPB coating density.

In addition to the large evaporator, a smaller coating system will be used at Carleton University in Canada for TPB coating of the ESR reflective foils. The foils will be coated in batches, then stored in Rn-tight transportation vessels for shipping to LNGS and installation into the TPC.

4853 The large evaporation facility will be serviced by a crane that permits lifting and moving both
4854 the acrylic planes and the top flange of the chamber. The holding structure hosting the acrylic
4855 connects to tracks in the bottom part of the evaporation chamber. The sequence of operations to
4856 be performed for the TPB coating process is:

- Mount the acrylic anode/cathode on the holding structure
 - Open the top flange of the chamber with the crane
 - Open the crucibles shutters to fill the crucible with TPB
 - Close the crucibles shutters

- Inspect the gate valves
 - Insert the holding structure in the chamber
 - Close the chamber with the top flange
 - Open the gate valves
 - Turn on the pumping station
 - Check the pressure level and operate the vacuum system as required to outgas the acrylic
 - Turn on the crucible heaters
 - Open the crucibles shutters one the temperatures of the furnaces is around 220 °C
 - Start the TPB evaporation
 - Monitor all the parameters and in particular the quartz sensors
 - Close the crucibles shutter after no further rise or value is reported on the quartz sensors
 - Turn off the crucibles
 - Close the gate valves
 - Turn off the pumping station
 - Open the nitrogen gas valves and fill the chamber with nitrogen
 - Open the chamber once the pressure reaches the ambient pressure
 - Lift and move the top flange
 - Lift and move the acrylic holding system

4880 Technical specifications for the coating facility are shown in table **XLVI**.

Parameter	Value
Chamber inner diameter	420 cm
Chamber height	100 cm
Chamber weight	N/A
Ultimate vacuum pressure	$\sim 1 \times 10^{-6}$ mbar
Number of CF250 ports	2
Number of CF100 ports	12
Number of CF40 ports	12
Primary dry pump	1 - 200 m ³ /h - Ultimate pressure < $2 \times 1 \times 10^{-2}$ mbar
Turbomolecular pump	1 - 1200 l/s - Ultimate pressure $\sim 1 \times 10^{-8}$ mbar
Number of crucibles	6 on CF100 flange
Crucible material	TBD
Crucible single power	1,2 kW
Total estimated system power	15
TPB per crucible	5 g
Amount of TPB per process	30 g

TABLE XLVI. Coating facility parameters for anode and cathode coating.

9.5. Hall C interfaces

PBS Item: DS.F.HCS

9.5.1. Installation system inside the cryostat

To safely install the detector without risking damage to the primary membrane floor corrugations, a false floor with wooden blocks and wooden plates will be installed. The false floor enables resting the detector on the floor, on a temporary structure, while completing the installation. The wooden floor will be lined with a thin stainless steel plate in order to avoid dust contamination. A load-spreading system will be installed to comply with the loading capacity of the cryostat insulation system. Fig. 127 shows the false floor concept.

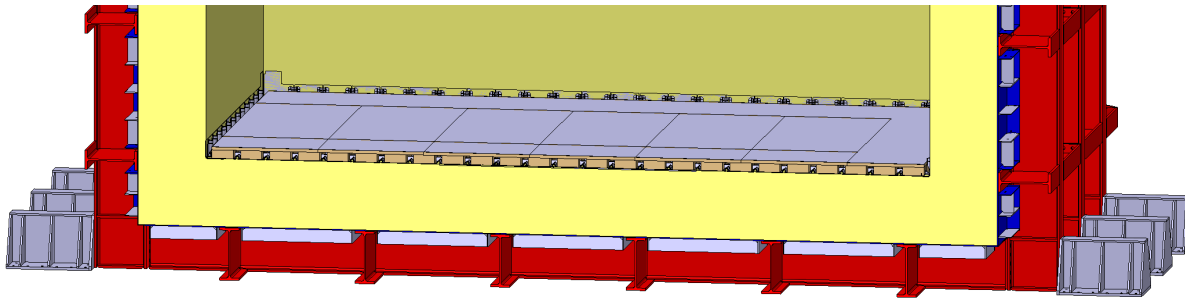


FIG. 127. False floor: the wooden blocks and plates protect the primary corrugations while the stainless steel lining ensures the dust cleanliness requirements.

4891 To complete the detector installation, scaffolding is needed. Scaffolding will be designed for
 4892 removal of all its elements via a DN700 flange on the top of the cryostat once installation is
 4893 finished.

4894 *9.5.2. Cryogenics support structure*

4895 The AAr cryogenic system will sit on top of a dedicated metallic structure, designed to guarantee
 4896 optimal relative height of the system with respect to the cryostat. The structure, shown on the top
 4897 of Fig. 1, will include the necessary stairways, entrances, egresses and emergency links to safely
 4898 access the cryogenic system and the roof of the cryostat. The vertical clearance below the structure
 4899 will serve for the insertion and operation of the UAr storage skids below the structure itself.

4900 A preliminary design has been drafted based on the ProtoDune cryogenic system geometrical and
 4901 process requirements. The executive design will be finalized once the AAr cryogenic system design
 4902 is frozen. An authorization procedure with the competent authorities will follow upon completion
 4903 of the design.

4904 *9.5.3. Detector electrical power, grounding and shielding*

4905 It is calculated that the power required by the electronics inside and immediately adjacent to the
 4906 cryostat is **????? watts**. This power will be provided by a dedicated transformer effectively isolated
 4907 from the building power while maintaining proper safety ground.

4908 The preservation of the integrity of the signals generated in the detector requires: 1) carefully
 4909 designed and implemented schemes for the distribution of electrical power; 2) the implementation of
 4910 techniques to avoid introducing external noise into the cryostat [79]; and, 3) a design of the detector
 4911 electronics themselves that avoids internally generated noise affecting the outputs. Furthermore,
 4912 even after implementing best practices everywhere, experience shows that some changes in the
 4913 connection of grounds may be required to achieve optimum performance. Such a flexibility will be
 4914 built into all feedthroughs. Experience also shows that to exploit such flexibility effectively requires
 4915 a system where all the penetrations have been documented. To this end, a team of engineers,
 4916 physicists and technicians will be in charge of ensuring that all systems which involve connection to
 4917 the interior of the cryostat are documented, reviewed and implemented with best practices. Such
 4918 a process was successfully used for the protoDUNE NP04 detector at CERN [80]. This detector
 4919 used a similar cryostat to DS-20k and may serve as an example installation.

4920 *9.5.4. Control room*

4921 The DS-50 control room will be refurbished to host the off-detector electronics for the DS-20k
 4922 detector. These include slow control computers as well as all equipment described in Sec. 7.6 that

4923 are not located near the signal chimneys on the cryostat roof. In particular, the control room will
 4924 host network apparatus, the TSP farm, and the data logger disk that will temporarily store the
 4925 DS-20k raw data before they are transferred to outside computing centers. The size of the required
 4926 computer farm necessary for online reconstruction and event selection and data storage in the final
 4927 format is not yet finalized, however we base our estimate on the presence of 72 worker nodes in
 4928 total for the TSPs farm and about 120 TB of disk space. The DS-50 floor plan is adequate to host
 4929 such equipment, but the room needs to be revamped taking into account the much larger power
 4930 consumption needed for the DS-20k experiment and the need for further cooling power of about 90
 4931 kW to keep the equipment safe.

4932 9.6. Prototypes

4933 PBS Item: DS.F.PRT

4934
 4935 The DarkSide-Proto project aims at constructing and operating prototype detectors of interme-
 4936 diate size, incorporating the new DS-20k technologies for their integration and full validation. The
 4937 scale of DarkSide-Proto detectors is chosen to allow for a full validation of the major innovative
 4938 technical features of DS-20k, including the mechanical and cryogenic design, the integration of the
 4939 custom photodetector modules and the full read-out electronics and data acquisition chain.

4940 DarkSide-Proto is not intended to replace validation and tests made in laboratories, but rather
 4941 to complement them with an integration test. This will also help to verify the production readiness
 4942 of the different institutions and to help the integration of the various teams working on the different
 4943 DarkSide sub-systems.

4944 9.6.1. DS-Proto0

4945 DS-Proto0, the first prototype built in the R&D phase, was designed for the specific purpose of
 4946 validating the bubbler mechanism for generating the gas pocket (described in section 7.2.3) and
 4947 optimizing the S2 signals.

4948 DS-Proto0 is a small TPC with reduced drift length (12 cm) to avoid pile-up (see Fig. 128). The
 4949 TPC can be equipped with up to 2 PDUs, one on the top and the other on the bottom plane.

4950 Full tests of the S1 response and therefore of the SiPM readout chain can be obtained by switching
 4951 off the electroluminescence field. The configuration of the gas pocket, both geometry and field, can
 4952 be varied by changing the distance between the anode and the wire grid, the width of the gas
 4953 pocket, and the electro-luminescence field. The S2 pulse shape can be precisely studied along with
 4954 different gas pocket configurations. This set-up also allows for early studies of the S2 formation
 4955 and readout, carried out while the pre-production of the PDUs is ongoing. The S2 shape analysis
 4956 is an important component of calibrating the DS-20k detector uniformity, by means of a binned
 4957 likelihood fit of the pulse shape, taking into account the drift across the gas pocket and the electron
 4958 diffusion. The final set-up is shown in Fig. 128, equipped with two PDUs.

4959 An early version of the DS-Proto0 TPC, equipped with only one PDU above the anode (see
 4960 Fig. 129) and no reflector on the walls, was operated at CERN in the second half of 2019. Results
 4961 of this commissioning run were used to tune the readout electronics and the reconstruction software
 4962 (some results are reported in section 12).

4963 The DS-Proto0 detector is now located at INFN Naples, preparing for future tests. It is currently
 4964 being installed into a dedicated cryogenic system equipped with argon condensation, recirculation
 4965 and purification loops.

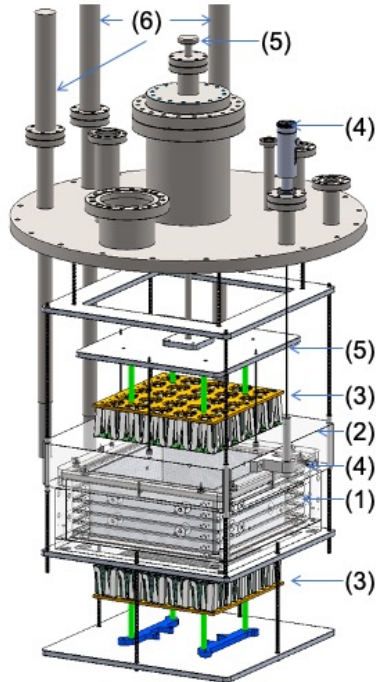


FIG. 128. Schematics of the setup for the optimization of the S2 signals. 1, TPC field cage; 2, movable anode and diving bell; 3, PDU; 4, motion feedthrough adjusting gas pocket thickness; 5, motion feedthrough adjusting PDUposition; 6, HV feedthroughs.

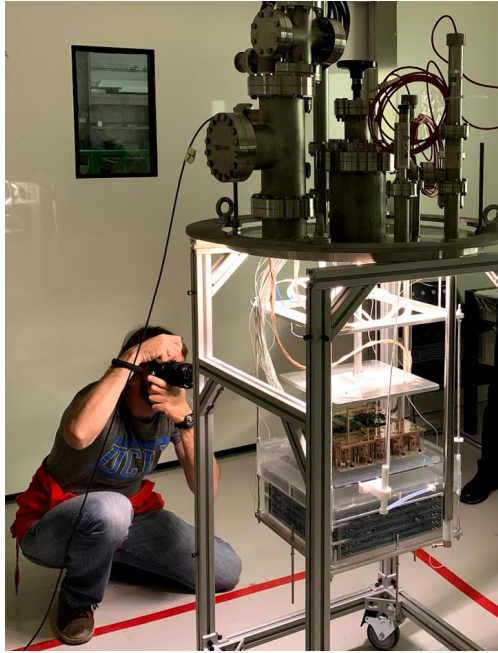


FIG. 129. Picture of the mounted DS-Proto0 TPC for the optimization of the S2 signals.

4966

9.6.2. Prototype for validation of the TPC mechanical design

4967

The next step in the DarkSide-Proto program is the construction of a scaled down version of the
4968 DS-20k TPC (DS-Proto).

4969

Aspects of the design of the TPC presented in section 7.2 will be validated by building and testing

4970 the mechanics of an acrylic dual phase mockup TPC of 56 cm drift length. The characteristics of
4971 the DS-Proto mockup TPC are listed in table [XLVII](#).

4972 In order to perform the tests in LAr a cryostat of $\sim 1\text{ t}$ size was built by Tecno Alarm s.r.l., Roma,
4973 and delivered to CERN in August 2018, where it was used for the validation of the cryogenic system
4974 design described in section [3.10](#). The schematic representation of the system and a photograph of
4975 the cryostat are shown in figure [130](#).

4976 Figs. [131](#), [132](#), [133](#), and [134](#) show the integrated DS-Proto mockup TPC and its optical planes.
4977 These parts have the same feature geometry as DS-20k except that the overall size is smaller to fit
4978 in the DS-Proto cryostat. Many parts of the DS-Proto mockup TPC, such as the reflector panels
4979 push-pin and HHV features, are identical to that of DS-20k in order to conduct a realistic test. The
4980 LAr cryogenic system to host the DS-Proto mockup TPC is built and operational. It was tested in
4981 July 2021.

4982 The operations to be validated include:

- 4983 • coating of the side panels with Clevios to produce a field cage;
- 4984 • coating of the PMMA cathode and anode windows with Clevios;
- 4985 • installation of the eight acrylic panels onto the cathode assembly;
- 4986 • installation of resistor links on the inner walls of the TPC and check of the connectivity;
- 4987 • installation of the wire grid;
- 4988 • installation of the anode assembly;
- 4989 • installation and checks of all service electrical connections;
- 4990 • TPC installation into the DS-Proto cryostat and mechanical checks at room temperature;
- 4991 • cool-down and filling of the cryostat with liquid argon using the existing DS-20k cryogenics
4992 system at CERN,
- 4993 • generation of the gas pocket and confirmation of the power requirement to maintain the gas
4994 pocket;
- 4995 • confirmation of the expected level control accuracy;
- 4996 • monitoring of the gas pocket size with time, allowing to compute the exact gas flow parameters
4997 to be used in DS-20k;
- 4998 • confirmation of the leveling of the anode to better than $100\text{ }\mu\text{m}$ via capacitive measurements;
- 4999 • setting of the high voltage to its nominal value of -15.0 kV on the cathode;
- 5000 • confirmation that the high voltage can be brought to the full DS-20k value of -73.38 kV and
5001 held at this value for a long term stability check;
- 5002 • opening of the cryostat, visual inspection of the TPC and confirmation of the mechanics after
5003 thermal cycling or HHV issue after HHV test.

5004 The acrylic panels for the DS-Proto mockup TPC will be built at University of Alberta (Canada)
5005 and IHEP Beijing (China) and assembled at CERN in Q1 of 2022. The specification for anode
5006 flatness at better than $100\text{ }\mu\text{m}$ as in the DS-20k design will have to be respected. The mechanical
5007 tests will be made in Q2 and Q3 of 2022. Tests of the mechanical insertion of PDUs onto the
5008 prototype optical planes may take place in Q4 of 2022 when PDUs will be available.

Parameter	Value
DS-Proto TPC Dimensions	
TPC Drift Length	56 cm
Total LAr Mass	760 kg
Active LAr Mass	57 kg
Nominal TPC Fields and Settings	
Drift Field	200 V/cm
Extraction Field	2.8 kV/cm
Luminescence Field	4.2 kV/cm
Cathode Voltage	-15.0 kV
Extraction Grid Voltage	-3.78 kV
Anode Voltage	ground
Gas Pocket Thickness	(7.0 ± 0.5) mm
Grid Wire Spacing	3 mm
Grid Optical Transparency	97%
SiPM tiles and PDU+	
Number of PDU+ slots on top optical plane	9
Number of PDU+ slots on bottom optical plane	8

TABLE XLVII. DS-Proto mockup TPC parameters.

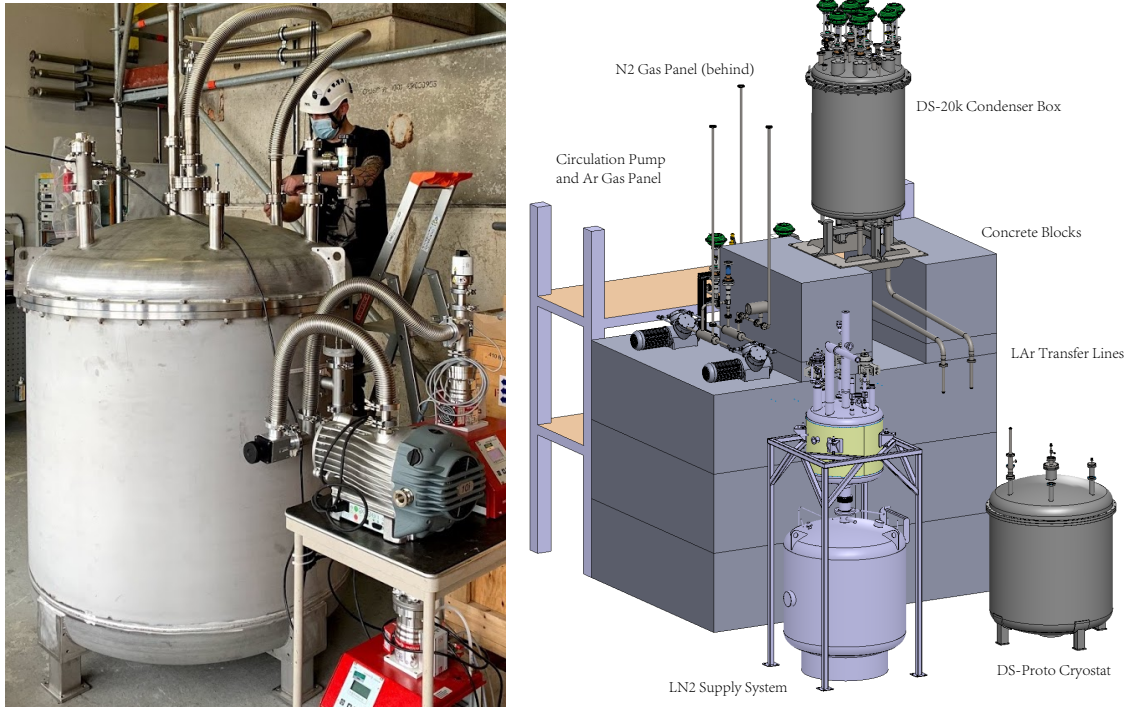


FIG. 130. The DS-Proto cryostat and the layout of the complete test system at CERN.

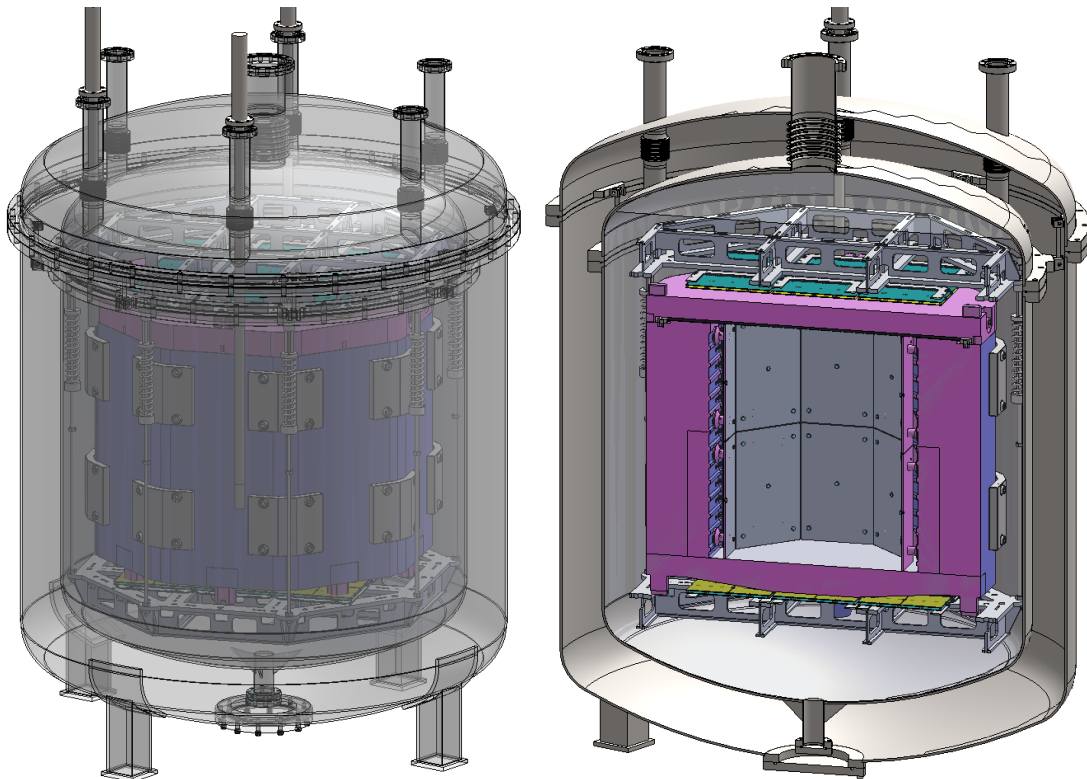


FIG. 131. Conceptual Design of the DS-Proto detector.

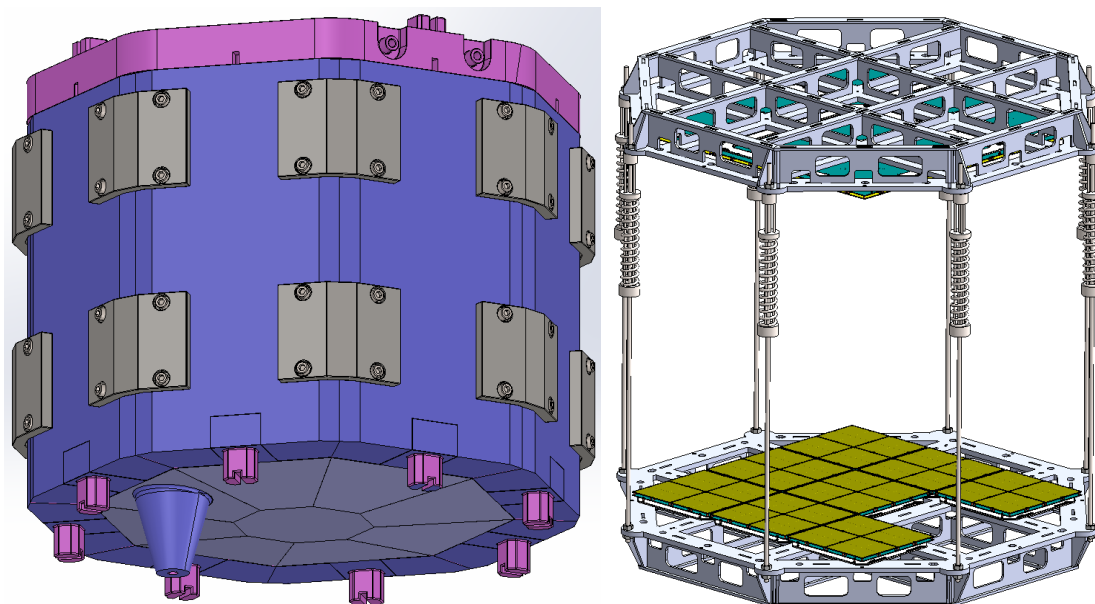


FIG. 132. Overall view of the DS-Proto mockup TPC, the existing internal optical readout supporting structure to be tested in the existing cryostat. Each square on the optical plane represents one of the four readout channels on a PDU+.

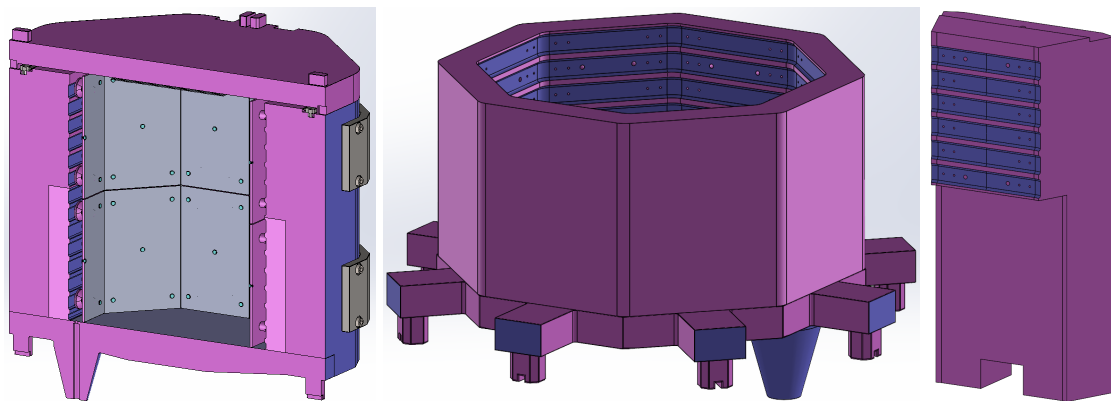


FIG. 133. DS-Proto mockup TPC section view and barrel parts.

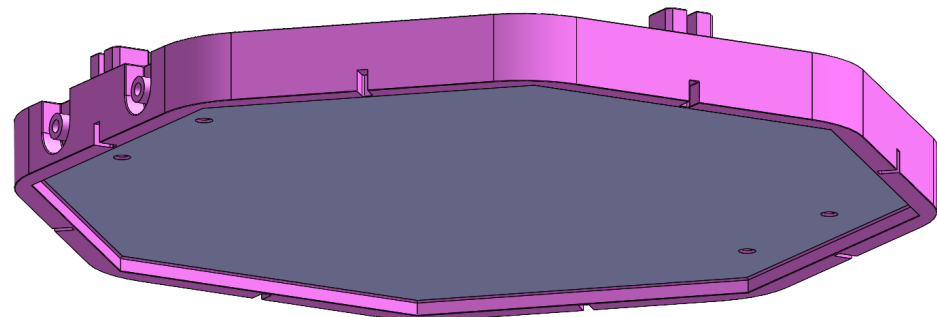


FIG. 134. DS-Proto mockup TPC anode with features for confirming DS-20k design.

5009 10. TECHNICAL DESCRIPTION: URANIA AND ARIA

5010 10.1. Procurement of the low-radioactivity Argon

5011 Low-radioactivity argon is key to the DS-20k scientific goals and a broad strategy has been
 5012 developed to achieve the production of the UAr necessary for DS-20k, as well as lay the groundwork
 5013 for UAr procurement into the future for larger argon-based detectors such as Argo. We have
 5014 developed three projects, Urania, Aria and DArTInArDM, whose joint operation will ensure the
 5015 procurement of UAr for DS-20k with the necessary purity and low concentration of ^{39}Ar . In detail:

- 5016 • The Urania facility will extract and purify the UAr from the CO₂ wells at the Kinder Morgan
 5017 Doe Canyon Facility located in Cortez, CO, at a maximum production rate of 330 kg/d, from
 5018 the same source of UAr that was used for the DarkSide-50 detector.
- 5019 • Aria will further chemically purify the UAr to detector grade purity using a cryogenic distil-
 5020 lation column called Seruci-I,
- 5021 • DArTInArDM will measure the ^{39}Ar depletion factor in the UAr as it is produced, thus
 5022 providing a means of quality assurance for the UAr sent to Aria and then to LNGS.

5023 The shipment of the UAr from Colorado to Sardinia will be done by boat in order to minimize
 5024 the cosmic activation of the argon (described in section 5.8.6), as well as conserve costs. For the
 5025 shipment of the UAr from Colorado to Sardinia, and then from Sardinia to LNGS, the current
 5026 baseline design is to ship the UAr in commercially available high-pressure (up to 450 bar) gas
 5027 cylinders that are organized into skids capable of containing 2 t of UAr each. Exact logistics within
 5028 each of the locations are being further developed within the assigned working groups, however, the
 5029 skids would be loaded into shipping containers and shipped in batches of up to three at a time,
 5030 providing shipments of 6 t.

5031 Table XLVIII gives the important parameters related to the extraction, purification and procure-
 5032 ment of the UAr .

Parameter	Value
UAr extraction rate at Urania	330 kg/d
UAr purity from Urania	99.99 %
Total UAr extracted by Urania	120 t
Total UAr in the detector	100 t
Seruci-I column diameter	0.3238 m
Seruci-I column height	350 m
Seruci-I number of modules	30
UAr purity from Aria	detector grade
Seruci-I chemical purification rate	$\text{O}(1 \text{ t/d})$
DartInArDM active mass	$\sim 1 \text{ Kg}$
DartInArDM ^{39}Ar depletion factor sensitivity	U.L 90% CL. 6×10^4
^{39}Ar depletion factor measured in DarkSide-50	$(1.4 \pm 0.2) \times 10^3$
Capacity of each transportation vessel	2 t
Total mass of each shipment	6 t
Number of transportation vessels	60

TABLE XLVIII. UAr production parameters.

5033 10.1.1. *Urania*

5034 PBS Item: DS.U

5035
 5036 Argon from the active CO₂ wells in southwestern Colorado have been found to contain very
 5037 low levels of the radioactive isotope ^{39}Ar , with the concentration shown to be a factor of
 5038 $(1.4 \pm 0.2) \times 10^3$ below that of argon derived from the atmosphere [9]. In an effort lasting more than

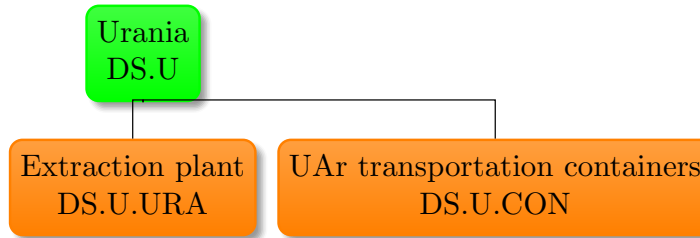


FIG. 135. PBS of Urania

5039 5 years, GADM collaborators at Princeton and Fermi National Accelerator Laboratory (FNAL)
 5040 extracted and purified (156 ± 1) kg of UAr, slightly more than the (153 ± 1) kg needed for the
 5041 target material in the DarkSide-50 detector.

5042 The opportunity to build Urania grew from the strong relationship between the DarkSide Col-
 5043 laboration and the Kinder Morgan Corporation. Based on gas analysis of the gas stream provided
 5044 to Kinder Morgan by the DarkSide Collaboration during the extraction of the DarkSide-50 UAr
 5045 target, a major industrial partnership between Kinder Morgan and a third party was established
 5046 in order to extract helium from the CO₂ at Kinder Morgan's Doe Canyon facility. The helium
 5047 extraction plant began operation in July 2015 and makes up 15 % of the production rate of helium
 5048 in the United States.

5049 The GADM Collaboration reached an agreement with Kinder Morgan to feed the Urania plant
 5050 with a small fraction of the gas stream returned to Kinder Morgan after helium extraction. This
 5051 gas stream holds two significant advantages over the gas stream used to extract the UAr for
 5052 DarkSide-50: it is completely dehydrated, and it contains only trace amounts of helium. These
 5053 features greatly simplify the process for UAr extraction by the Urania plant, while ensuring the
 5054 same radioactivity levels, or better.

5055

5056 PBS Item: DS.U.URA

5057

5058 The Urania feed stream is \sim 95 % CO₂, plus a few percent of N₂, one percent CH₄, 430 ppm
 5059 of UAr, and traces of higher hydrocarbons. The processing scheme of the UAr extraction plant
 5060 is optimized for this feed composition in order to achieve an UAr purity of better than 99.99 %.
 5061 As shown in Fig. 136 the UAr extraction plant consists of three gas-processing units, for the
 5062 separation of raw UAr, followed by a purification unit, based on cryogenic distillation technology.
 5063 The gas-processing units are two CO₂ liquefier/strippers followed by a pressure swing adsorption
 5064 unit (PSA). The purification units is a sequence of two pairs of cryogenic distillation columns. The
 5065 first liquefier accepts gas at (49 ± 1) bar, with a flow rate of 20 000 std m³/h and a temperature of
 5066 5 °C. At these conditions, the CO₂ partially condenses and the stream is separated into 2-phases
 5067 (gas/liquid) as it goes to the first stripper. In the column a controlled quantity of heat is given
 5068 by a hot fluid working between the chiller condenser and the column reboiler. The light products
 5069 are vaporized and recovered from the top of the column in gas phase. The heavy products (mainly
 5070 CO₂) are collected from the bottom, compressed to 50 bar and returned to Kinder Morgan as a
 5071 gas. The light products coming from the column head are cooled down to approximately -50 °C
 5072 and sent to the second stripper. The first column produces 3300 std m³/h of product flow, a factor
 5073 of 5 reduction in the amount of gas to be processed by the more complex downstream units.

5074 The second liquefaction and stripping unit further reduces the CO₂ content, in a similar process
 5075 as the first stripping unit. The separated CO₂ is joined with that from the first unit and returned
 5076 to Kinder Morgan. The product gas from the second stripper is re-heated in a heat exchanger
 5077 and delivered to the PSA unit, which separates the light fractions, including the argon, from the
 5078 remaining CO₂. The PSA is composed of four adsorption beds to allow continuous operation with
 5079 short time adsorption cycles. Desorption of CO₂ is made by decreasing the pressure of the bed.
 5080 The sorbent material is a commercial synthetic zeolite, also known as Kostrolith - NaMSXK. To

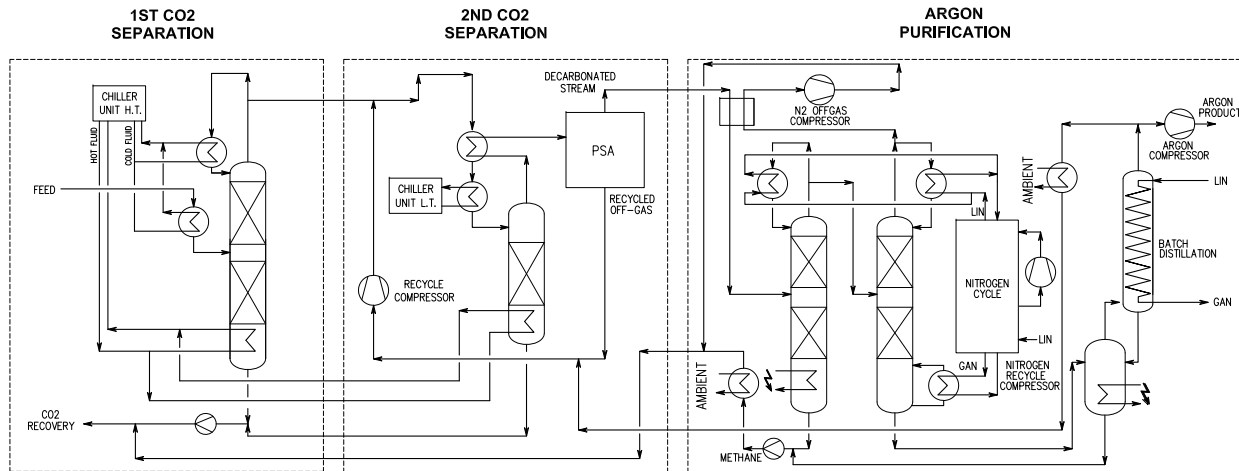


FIG. 136. Process Flow Diagram (PFD) for the Urania UAr extraction plant.

5081 optimize the performances, the operation of the adsorbers are combined by coupling the purge and
 5082 pressure swing phases. At the outlet of the PSA adsorption tanks, the presence of two buffer tanks
 5083 dampen process fluctuations and allow for continuous operations of the final purification section.
 5084 The PSA off-gas is delivered to a recycle compressor and sent back to the second CO₂ stripper
 5085 inlet for reprocessing. The PSA is a critical unit of the entire process since the dynamic adsorption
 5086 conditions are the most difficult to simulate and predict. For this reason, sorbent selection and
 5087 identification of the operational parameters have been identified experimentally with a PSA pilot
 5088 plant at Università degli Studi di Napoli “Federico II”.

5089 The UAr purification unit consists of four cryogenic distillation columns. The CO₂-free product
 5090 coming from the PSA plant is pre-cooled and sent to the first column, which works at a lower
 5091 pressure (~9 barg) for the removal of CH₄. The second column is used to remove the remaining
 5092 light fractions from the resulting N₂-rich stream. The UAr collected from the bottom of the second
 5093 distillation column is sent to a sister pair of distillation columns where CH₄ and N₂ are further
 5094 separated to increase the purity of the UAr obtained. In addition to removing the CH₄ and N₂,
 5095 any ⁸⁵Kr present in the stream will also be removed by this series of cryogenic distillation columns.
 5096 The CH₄-rich and N₂-rich wastes are returned to Kinder Morgan along with the CO₂. The final
 5097 product of the Urania processing plant is 99.99 % pure UAr that will be taken in liquid form from
 5098 the bottom of the last column and collected into a tank to check the quality of the argon. The UAr
 5099 will be sent to Sardinia, where it will undergo final chemical purification by the Seruci-I column.

5100 Construction of the Urania plant has been completed. Leak testing will be performed in the
 5101 next months at Polaris premises under the supervision of the Collaboration. The current plan is
 5102 to finish installation and commissioning of the plant approximately 1-year after delivery, allowing
 5103 for extraction of the 120 t of UAr approximately 2-years after delivery. The preparation of the
 5104 extraction site is being planned now via a specifications document that will be submitted for a
 5105 Request for Tender (RFQ), and will ultimately be managed by the collaboration with help from
 5106 the Kinder Morgan CO₂ Company and the contractors hired to carry out the work who will be
 5107 performing the major tasks. Site preparations for developing the facility before the arrival and
 5108 installation of the plant will begin as soon as the necessary land development permits have been
 5109 secured and the RFQ process has been completed, this is expected to proceed during the second
 5110 quarter of 2022.

5111

10.1.2. UAr transportation vessels

5112

PBS Item: DS.U.CON

5113

5114 Underground argon gas extracted from the Urania facility in Colorado will be stored in high-
5115 pressure gas cylinder skids for shipping to ARIA in Sardinia where it will undergo chemical purifi-
5116 cation to less than ppm-level impurities, and ultimately be shipped to LNGS for filling the DS-20k
5117 TPC.

5118 The gas will be pressurized to 450 bar and stored in high-pressure skids holding a total of
5119 approximately 2 tonnes of argon each. The skids have dimensions of L 147" x W 54" x H 78",
5120 an empty weight of 4.5 tonnes, and can be stacked up to two high. With the expected sustained
5121 Urania argon extraction rate of 250 kg per day, it will take approximately 8 days to fill each skid,
5122 and a total of 16 months to extract all 120 tonnes that will be shipped to ARIA in Sardinia. The
5123 120 tonnes of extracted argon are allocated as follows: 100 tonnes needed for filling the DS-20k
5124 TPC, 4 tonnes used during conditioning and purging the cylinder skids, 4 tonnes of argon left in
5125 ARIA after purification, and 12 tonnes for contingency.

5126 We will batch three skids for each shipment from Colorado to Sardinia, with each trip expected
5127 to take approximately 74 days; this prompt shipping schedule out of Colorado mitigates the cosmic-
5128 ray activation of argon, which is particularly problematic at Urania due to the high altitude. Once
5129 in Sardinia, the skids will be stored near ARIA and the argon will be accumulated for processing.
5130 It will be batch processed through ARIA in two separate runs of 60 tonnes each, with each of those
5131 runs taking approximately 60 days. After each of the two batches through ARIA, the purified
5132 (now grade 5) underground argon will be stored locally in Sardinia (the authorization for possible
5133 temporary underground storage in Sardinia is under investigation), until needed for filling into
5134 DS-20k.

5135 Once the detector fill is underway, we anticipate shipping 12 tonnes at a time (in a total of six
5136 skids), approximately weekly, and staging those in or near Hall C. The precise size and schedule of
5137 each shipment depends on available local storage at LNGS; storage for the full argon skids, with
5138 an overburden of at least 10 metres, would simplify shipping logistics. Two skids will be connected
5139 to the inlet of the DS-20k UAr purification system and gas will be extracted from one skid until
5140 empty, then the purification inlet connection will be switched to the second skid while the first is
5141 changed for a full one. In that way we anticipate having only two skids at a time connected to the
5142 purification and filling system of DS-20k, and on average between six and twelve full skids on site
5143 staged for filling. We anticipate storing the empty skids, after the argon has been filled into DS-20k,
5144 local to LNGS until the experiment has been filled and commissioned (expected to take a total of
5145 approximately 8 months). The skids can be stored locally in essentially any convenient location,
5146 which does not need to be underground. In case the argon needs to be removed at any time during
5147 the filling or commissioning process, we plan to make use of the large noble gas compressor system
5148 that will be available at LNGS, to extract argon at the nominal boiloff rate (approximately 100
5149 tonnes per 60 days) and pressurize it back to 450 bar in the gas cylinders, with a process and
5150 staging similar to that used during filling.

5151

10.1.3. *Aria*

5152 PBS Item: DS.A

5153
5154 The Aria plant was conceived and designed to perform the final chemical purification of the UAr
5155 extracted by Urania, and to test a method for active depletion of ^{39}Ar from the UAr to possibly
5156 provide DAr targets for future larger LAr dark matter detectors. Aria consists of a 350 m tall
5157 distillation column, Seruci-I, capable of separating isotopes by cryogenic distillation.

5158

10.1.4. *Purification plant*

5159 PBS Item: DS.A.PP

5160

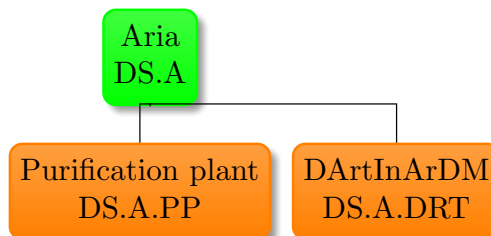
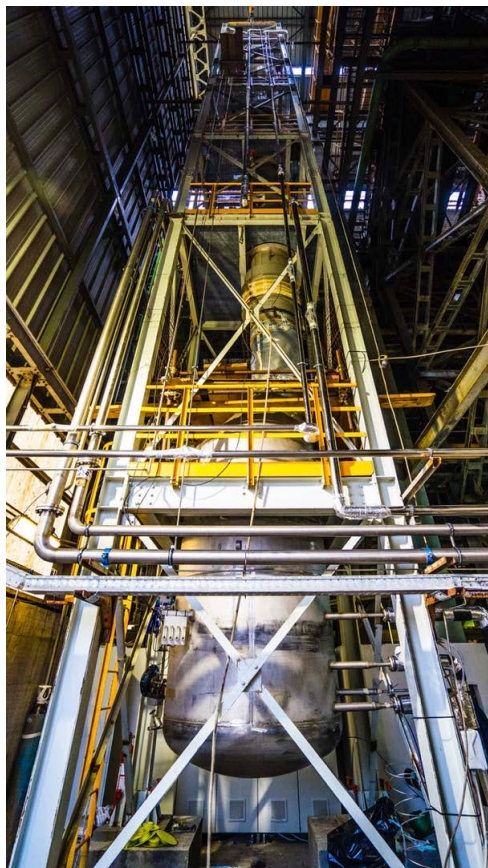


FIG. 137. PBS of Aria.

5161 The Aria plant is being installed in a vertical shaft of 5 m diameter and 350 m depth, located at
 5162 the Seruci mine campus of CarboSulcis, a mining company owned by the Regione Autonoma della
 5163 Sardegna (RAS). Seruci-I will consist of 28 modules of 12 m height, plus a top module (condenser)
 5164 and a bottom module (reboiler). Calculations indicate that Seruci-I will be able to process UAr at
 5165 a rate of $O(1 \text{ t/d})$, removing chemical impurities with a separation power better than 10^3 per pass.

5166 All modules for Seruci-I have already been built and passed a series of quality assurance checks.
 5167 During the first check, the process column and all the service pipes were individually checked for
 5168 leaks at room temperature. Then, the pipes were wrapped with super-insulation and everything
 5169 was assembled into the cold box. The second check was a full module check.

5170 Seruci-0 is a test column made by top (condenser) and bottom (reboiler) modules and a single
 5171 central module and is installed in an outdoor hall at the mine site, see Fig. 138.



5172 FIG. 138. The Seruci-0 cryogenic distillation column, installed in the *Laveria* building of CarboSulcis in
 Nuraxi Figus, Sardinia, Italy.



FIG. 139. Lowering test of an Aria module inside the shaft during April 2021.

5175 During the months of July/August 2019 and then again in October 2019 the test column was
 5176 operated with nitrogen both as refrigerant and liquid to be distilled. Stable distillation conditions
 5177 were reached for more than two weeks of operation time and the distillation performance was found
 5178 in broad agreement with expectations. A detailed account of the plan design, expected performance
 5179 for isotopic distillation and results of the isotopic distillation test run with nitrogen of Seruci-0 can
 5180 be found in [22]. A run with argon is foreseen to take place as soon as the COVID-19 pandemic
 5181 will allow it.

5182 Concerning the installation of Seruci-I, all the support platforms were delivered. Installations of
 5183 the first set of ten platforms has been completed, and all platforms have successfully passed the
 5184 load tests. Figure 139 shows a successful lowering test of an Aria module inside the shaft during
 5185 April 2021.

5186

5187

10.1.5. DArTInArDM

5188 PBS Item: DS.A.DRT

5189

5190 The DArTInArDM experiment at Laboratorio Subterraneo de Canfranc (LSC), Spain, aims at
 5191 measuring UAr to ^{39}Ar depletion factors of the order of 1000 with 10% precision in one week of
 5192 running. A full description of the apparatus and of its expected performance can be found in [81].
 5193 The detector re-uses the infrastructure of the ArDM experiment at LSC with some modifications.
 5194 DArTInArDM is a single-phase liquid argon detector, with an active volume of approximately one
 5195 litre, that will be filled with underground argon samples from Aria or Urania. The light produced
 5196 by ionizing radiation in the active volume will be readout by two 1 cm^2 SiPMs procured from the
 5197 DarkSide-20k production and packaged with the cryogenic readout electronics. DArTInArDM will
 5198 be housed at the centre of the 1 tonne LAr ArDM detector, which, after the replacement of the
 5199 PMT's with new ones, will serve as an active veto to tag both internal and external radiation.

11. PROCUREMENT, CONSTRUCTION, INSTALLATION

We provide in this section a detailed description of the procurement, construction, integration and installation of the DS-20k detector. In particular we describe the major steps leading to the mass procurement of the detector parts. We also discuss the procedures that we are adopting to meet the necessary cleanliness requirements and to ensure that proper quality control and assurance (QA/QC) standards are satisfied.

11.1. Cryostat

11.1.1. Procurement and radiopurity control of the membrane cryostat components

Cryostat procurement is defined in detail in the INFN-CERN Memorandum of Understanding under preparation.

Cryostat Materials Radio-purity	
For all Cryostat candidate materials	At least one sample for each material must be provided in time for radio assay and elemental analysis and approval from the Collaboration before final procurement
Radiopurity of warm structural beams and skins (150 tons + 67 tons)	$^{238}\text{U} < 2.5 \text{ mBq/kg}$; $^{232}\text{Th} < 7.5 \text{ mBq/kg}$.
Radiopurity of cold membrane stainless steel (4.2 tons in body + 1.2 tons in roof)	$^{238}\text{U} < 5 \text{ mBq/kg}$; $^{232}\text{Th} < 9 \text{ mBq/kg}$.
Paints used for steel or any structural material:	Type should be chosen with the Collaboration and be radio assayed
Composition of Rigid barrier material (glass fiber + Al + glass fiber, total mass 550 kg)	Elemental composition must be provided. Mass fractional limits: Al < 5.3 %. B < 2 %. F < 0.5 %. Be and Li < 0.1 %.
Radio-purity of rigid barrier material	< 5 Bq/kg
Flexible barrier material (<i>i.e.</i> , glass fiber + elastomer + Al + elastomer + glass fiber, for a total mass 183 kg)	Elemental composition must be provided. Minimize the use of Al and Mg for structural materials. Li, Be and B free components. Fractional limits in mass must be: F < 0.5 %. B < 2 %. Be and Li < 0.1 %. Al < 5.3 %. Na < 0.5%. Mg < 1%.
Radio-purity of flexible barrier material	< 5 Bq/kg
Insulating foam material (reinforced PU foam with 10% mass glass fiber)	Elemental composition must be provided. Limits in mass must be: F < 0.1 %. B < 0.3 %. Be and Li < 0.1 %. Al < 1.1 %.
Insulating foam material (for a total mass 28 tons)	$^{238}\text{U} < 1.1 \text{ Bq/kg}$; $^{232}\text{Th} < 1.5 \text{ Bq/kg}$.
Rest of components (for 12.3 tons plywood, 10 tons mastic, 2.3 tons roof PU)	$^{238}\text{U} < 0.8 \text{ Bq/kg}$; $^{232}\text{Th} < 0.8 \text{ Bq/kg}$; $^{210}\text{Pb} < 2.0 \text{ Bq/kg}$.
Fiberglass materials	Minimize use of fiberglass. No fiberglass with Boron is allowed.
Barriers materials	Use of fluorine free elastomer for flexible barriers
Structural materials	Minimize use of Al and Mg
If any material that will be used in the cryostat contains Be, B, F, Li, and Na:	Its elemental composition must be provided to the collaboration

TABLE XLIX. Radio-purity and composition specifications for the cryostat materials.

The primary responsibility of the GADMC in procurement is to make the necessary radio-purity measurements and calculate the impact of the cryostat contamination on the background of the experiment. Although the cryostat is far from the active volume, its large mass compared to the other detector components makes it necessary to carefully assess the contamination of the

5216 materials prior to its construction. The specifications of cryostat, summarized in the INFN-CERN
5217 Memorandum of Understanding under preparation, include that samples of the cryostat's candidate
5218 materials will be provided for radio-assay before construction. Detailed specifications are reported
5219 in table [XLIX](#). Once the suitable material has been identified as specified, it will be necessary to
5220 use only that material from that manufacturer, ensuring the use, when possible, of materials from
5221 the same production batch.

5222 *11.1.2. Cryostat construction in Hall C at LNGS*

5223 The cryostat is the first element of the experiment to be constructed underground. In this section
5224 the step-by-step operation list for the cryostat construction is reported:

- 5225 • Concrete basement construction (not shown in the pictures): removal of the existing resin
5226 coating (2 cm thick) on the area below the cryostat (13.8 m x 13.8 m); scarification of the
5227 surface of the existing foundation (6 cm thick); removal of the anchor bolts in the area of
5228 intervention, currently embedded in the existing slab; creation of the new reinforced concrete
5229 foundation with a height of 20 cm above the existing floor.
- 5230 • Floor preparation: survey network installation, floor planarity survey, marking the floor for
5231 the footprint of the cryostat, positioning of shims and the rubber pads for electrical isolation
5232 (Fig. [140\(a\)](#)).
- 5233 • Floor structure integration: 3 pre-assembled floor modules are assembled (bolted) together
5234 with link beams. The entire floor quadrant now sits on the prepared shims, lined with a layer
5235 of G10 electrical isolation. At this point a survey of the flatness is performed and if needed
5236 corrections are made (Fig. [140\(b\)](#) - Fig. [140\(g\)](#)).
- 5237 • First wall installation: additional 3 pre-assembled wall modules are positioned, bolted to
5238 the floor module and interconnected through link beams. Proper stabilizers to the floor
5239 structure are added to ensure stability during all the installation phase. Each of these steps
5240 requires detailed survey work to ensure perpendicularity between the cryostat floor and wall
5241 (Fig. [140\(h\)](#) - Fig. [140\(l\)](#)).
- 5242 • Second wall installation: similar activity as in the previous point. An additional inter-wall
5243 stabilizer is added on the corner position (Fig. [140\(m\)](#) - Fig. [140\(q\)](#)).
- 5244 • Successive walls installation: similar activity as in the previous point (Fig. [140\(r\)](#) - Fig. [141\(i\)](#)).
- 5245 • Corner module installation: the pre-assembled corners are installed. At this point geometrical
5246 corrections are made with shims as needed. Once done, all stabilizers are removed and roof
5247 link beams are installed (Fig. [141\(j\)](#) - Fig. [141\(m\)](#)).
- 5248 • Seismic brackets installation (not shown in the pictures): the 24 seismic brackets are bolted
5249 to the reinforced concrete basement.
- 5250 • AAr cryogenics support structure assembly on site: the AAr cryogenics support structure,
5251 along with the stairway to access the top of the cryostat, handrails and egresses, are assembled
5252 on site (Fig. [141\(n\)](#)).
- 5253 • Steel strips installation: thin steel strips are installed on the inner faces of the beams, prior
5254 to the installation of the warm skin plates (Fig. [141\(o\)](#)).
- 5255 • Cryostat warm skin installation: the 10-mm thick warm skin steel plates, pre-assembled with
5256 the reinforcement ribs, are welded together. At every step planarity and leak tightness checks
5257 are performed (Fig. [141\(p\)](#) - Fig. [142\(c\)](#)).
- 5258 • Cold cryostat installation: at this point the cold cryostat installation starts. The two layers
5259 of insulation, the secondary and the primary membrane are put in place. QA checks are
5260 required at every step. This is a several months process (Fig. [142\(d\)](#)).

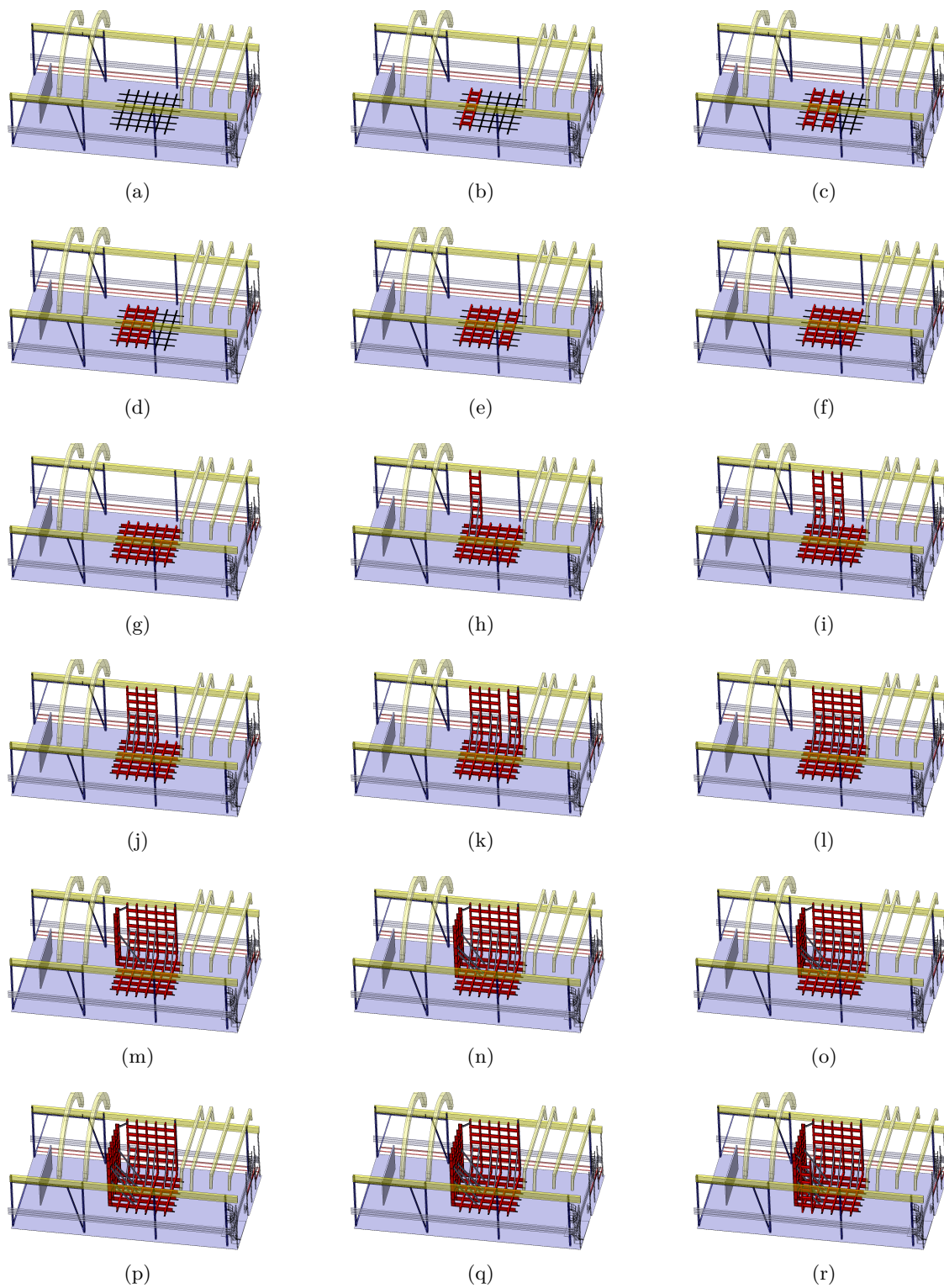


FIG. 140. Details of the cryostat installation sequence - I

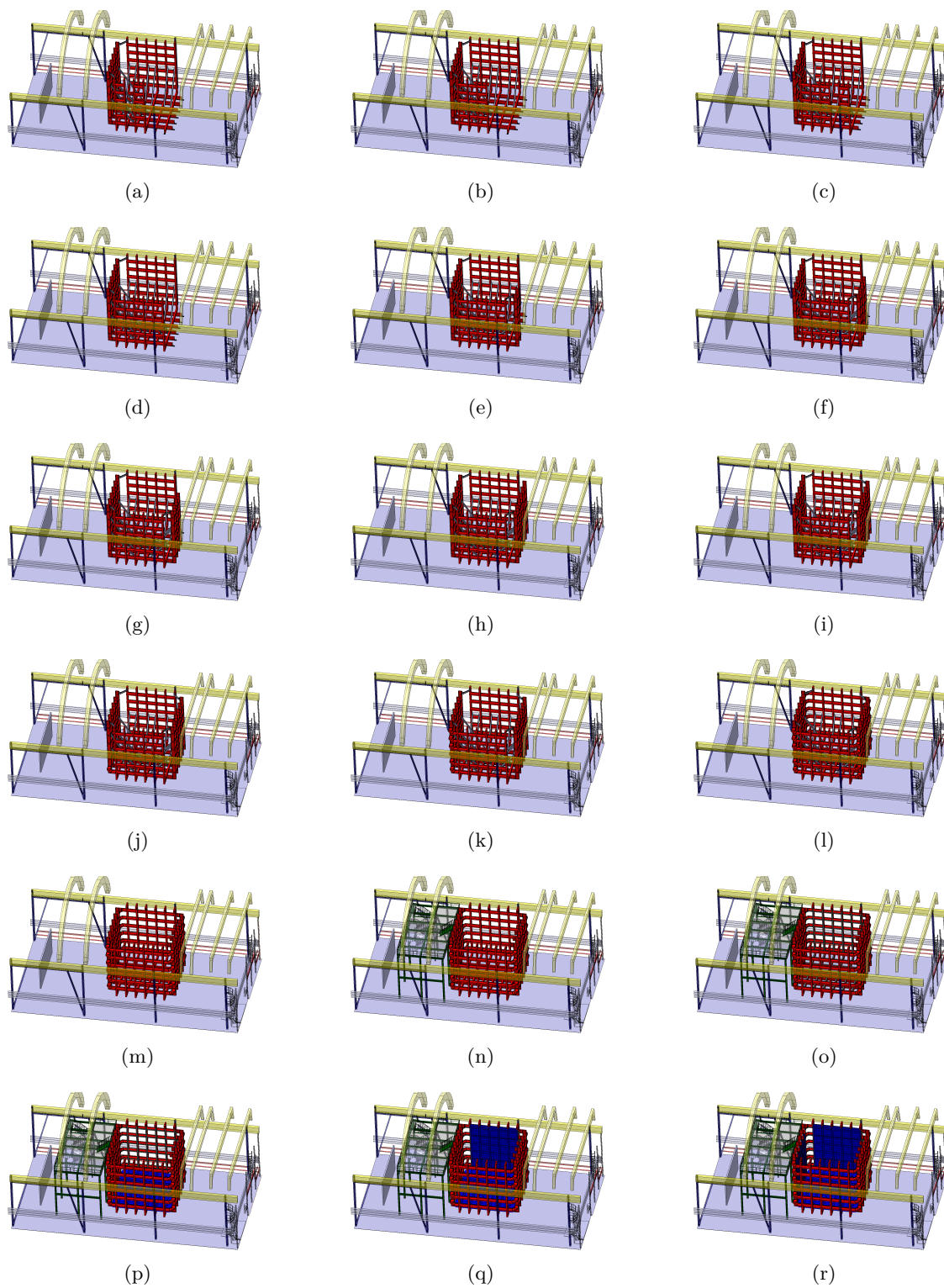


FIG. 141. Details of the cryostat installation sequence - II

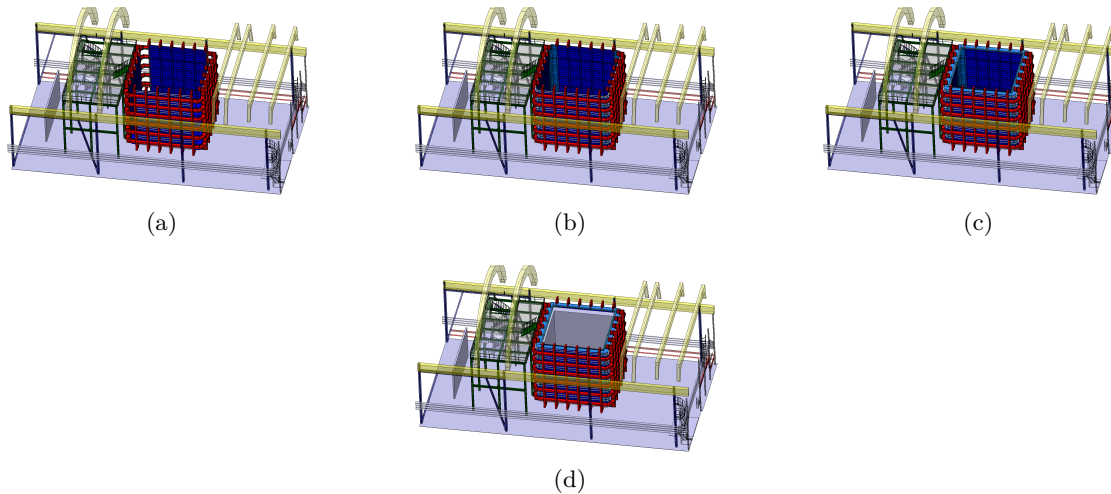


FIG. 142. Details of the cryostat installation sequence - III

5261

11.2. Titanium Vessel

5262

11.2.1. Procurement of radiopure Titanium

5263 Manufacturing the DarkSide-20k titanium vessel, and the TPC optical plane structures, requires
 5264 the procurement of low-background Titanium with a total mass of 19 tons in the form of various
 5265 types of titanium rolled products - sheets, bars and pipes.

5266 Reference numbers about the radioactive contamination of titanium are in table [XXXII](#). While
 5267 the radiogenic neutron-induced background is small, about 2% of the total, as shown in section
 5268 [5.8.6](#), the γ background rate in the inner Veto induced by the titanium radioactive contamination
 5269 is estimated to be 28 Hz. This is a sizable fraction of the total acceptable γ rate in the Veto
 5270 (about 150 Hz) to achieve dead time below 10%. This γ background sets the scale of the titanium
 5271 radioactivity requirement.

5272 In the framework of preliminary studies, it was shown that in order to ensure a low background,
 5273 it is necessary to avoid the use of titanium scrap and ligatures, which can be sources of uncontrolled
 5274 radioactive background. Thus, all low-background titanium ordered should be of VT1-00 grade.

5275 Low-background titanium rolled products will be made from low-background titanium sponge.
 5276 The production of such a quantity of low-background titanium rolled products requires about
 5277 40 tons of titanium sponge. Preliminary experiments carried out within the framework of the
 5278 collaboration showed that it is critical to manufacture rolled titanium products from titanium
 5279 sponge with a level of radioactive contamination no worse than the final rolled products. It has
 5280 been also confirmed that the industrial process used for making titanium sponge can provide the
 5281 required radiochemical purity.

5282 The order for low-background titanium is planned to be placed at VSMPO-AVISMA, which has
 5283 a full cycle of titanium product production from raw materials to final high-precision products for
 5284 companies such as Boeing and Airbus. Within the framework of a special agreement concluded by
 5285 the participants in the collaboration with VSMPO-AVISMA, research and development work will
 5286 be continued towards preparing production of a batch of low-background titanium in such a way
 5287 as to exclude, as much as possible, re-contamination of titanium at all stages of the production
 5288 cycle. A preliminary agreement has been reached with the titanium manufacturer on sampling
 5289 at all stages of the titanium production process in order to control possible sources of secondary
 5290 contamination. These measures should ensure the original low level of contamination from the
 5291 beginning through the end of the production cycle.

5292

11.2.2. *Ti vessel construction and installation*

5293

Given the dimensions of the titanium vessel, as described in Section Sec. 7, transportation and assembly constraints have been carefully considered in the design, in particular, insertion into Hall C. Fig. 143 shows one of the barrel modules and the top dome being inserted through the Hall C door.

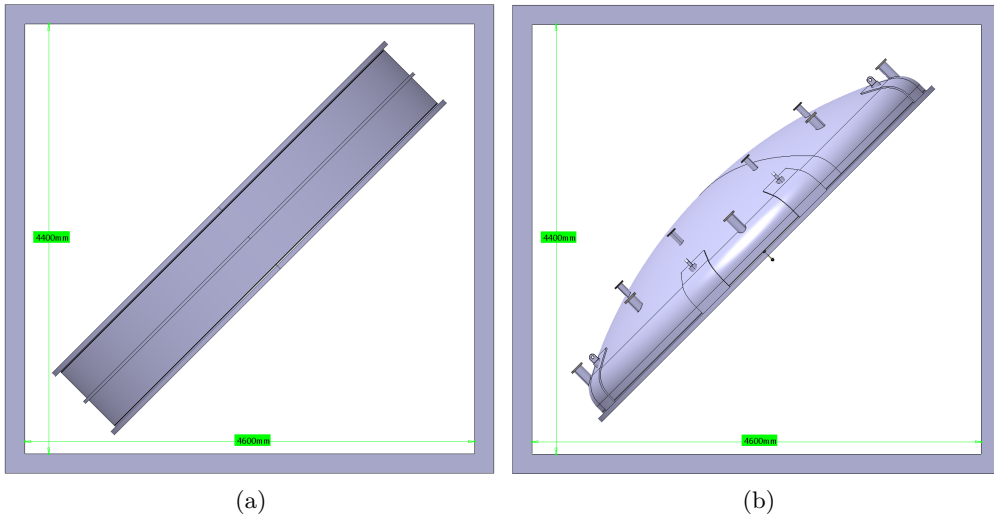


FIG. 143. Transportation of the titanium vessel barrel (a) and top dome (b) through the Hall C door.

5297

The vessel barrel is split into 4 identical modules that will be manufactured by an external company and assembled on site, by bolting the barrel flanges. The seal of the barrel modules will be guaranteed via on site welding. The construction sequence of the Ti vessel in Hall C is shown in Fig. 144.

5301

11.3. Cleaning of metallic parts

5302

A precision cleaning is required to leave the surfaces free of any dust, dirt or oxide particles. The desired cleanliness standard for the entire detector is MIL STD 1246 Level 50, which defines limits on the residual particulate size distribution. This goal assumes the argon causes particulate wash-off similar to water, and that Class 50 is the acceptable level for the argon, assuming the remaining particulates have a radioactivity similar to dust. The second assumption is pessimistic, as the remaining particulates are mostly metallic which are less radioactive than dust, resulting in very conservative specifications for the lines. The procedure is to first clean all lines and/or vessels with detergent, followed by rinsing, to remove many traces of dirt, grease and solvents prior to pickling. The final precision cleaning uses ultrapure water with sufficient flow to ensure turbulent flow for efficient removal of particulates. As regard as the inner surfaces of the Cryostat, the use of a sprayball system with detergent followed by water rinsing will be the best method to withstand the cleaning specifications, before starting the detector assembly.

5314

11.4. UAr Cryogenic system

5315

Procurement of the UAr cryogenic system components has already been completed. As discussed in Section 3.10.2, the condenser box assembly has been tested at CERN and is ready for use at LNGS with minor modification. To avoid contamination during testing at CERN, the inline radon

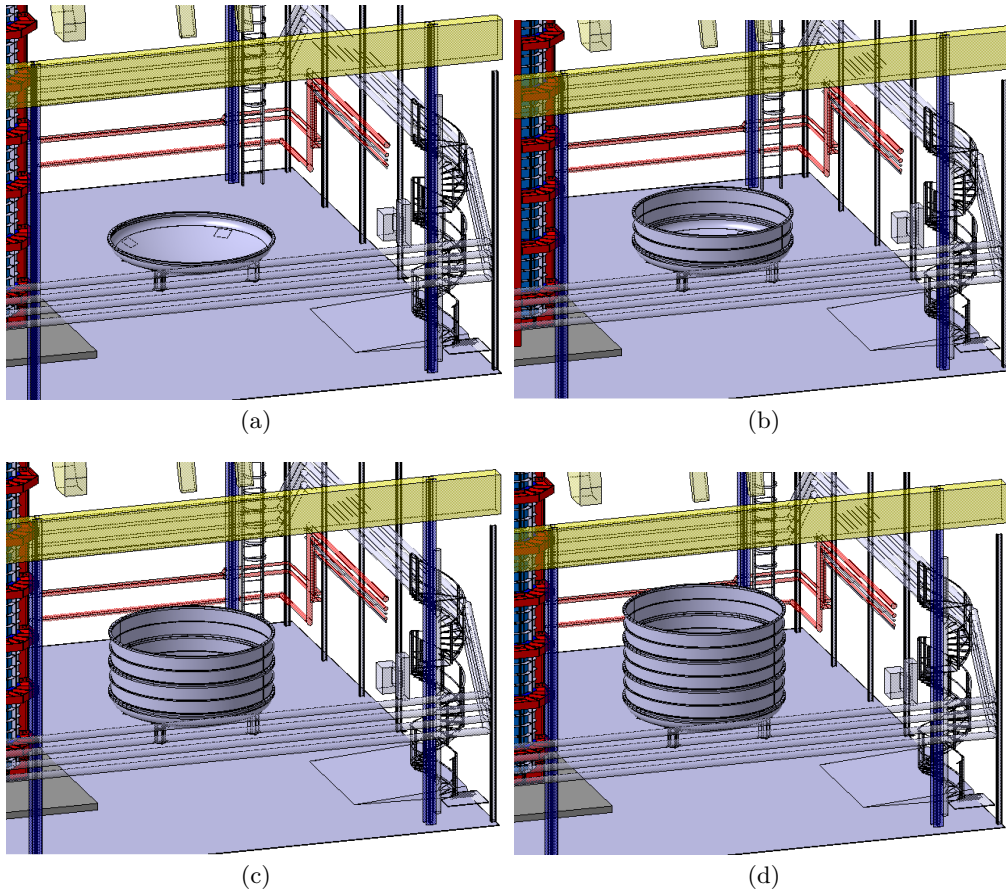


FIG. 144. Details of the Ti vessel installation sequence

trap and particulate filter following it have not been installed. These minor modifications will be performed at LNGS, and service LN₂ lines will need to be installed as part of the general facilities. The installation of the UAr cryogenic system will start after the TPC is installed, and after the ProtoDUNE cryostat roof is completed. Cryogenic service lines and the heat exchangers nearest the detector will be installed and connected to the top penetrations on the ProtoDUNE cryostat. The DS-20k condenser, along with the LN₂ buffer volumes, will be installed on the cryogenics support structure near the cryostat roof. Finally, the connection to the facility LN₂ system will be made.

5325 11.5. Gadolinium-loaded acrylic mass production

5326 The mass production of the gadolinium-loaded acrylic includes: procurement of the full amount
 5327 of gadolinium compounds, mass production of gadolinium-loaded acrylic panels, machining of
 5328 gadolinium-loaded acrylic panels, surface cleaning, annealing, and packaging.

5329 Approximately 20 tonnes of gadolinium-loaded acrylic is required to build the inner detector bar-
 5330 rel panels and the endcaps, including the material discarded during the machining. The production
 5331 process steps are:

- 5332 1. Mass production of gadolinium compounds.

5333 Baseline plan: In case of gadolinium oxide ~ 230 kg are necessary to reach 1% gadolinium
 5334 mass fraction. We have verified that this quantity of material is available on the market with
 5335 a delivery time of three months. The work flow is:

- 5336 (a) procurement of gadolinium oxide and of the surfactant from the producers selected
 5337 during the material screening activity.
 5338 (b) Measurement of the concentration of the radioactive contaminants of the materials.

- (c) Preparation of the pre-solution with the nano-particles functionalized. This work may happen in our laboratory or directly in the company site.
 - (d) Packaging and shipment to Donchamp Acrylic Group.

Risk mitigation plan (described in section 3.8): In case of Gadolinium β -diketonate, 1 tonne of gadolinium β -diketonate is required to reach 1 % gadolinium mass fraction in the gadolinium-loaded acrylic. The entire mass production of gadolinium β -diketonate will take approximately 6 to 8 months. The detailed work flow is:

 - (a) procurement of gadolinium chloride and the relevant organic ligand.
 - (b) Synthesis of gadolinium β -diketonate.
 - (c) Purification of the produced gadolinium beta-diketonate.
 - (d) Measurement of the radioactive contaminants.
 - (e) Packaging and shipment to Donchamp Acrylic Group.

2. Mass production of gadolinium-loaded acrylic panels. In this step, four gadolinium-loaded acrylic panels will be produced. The size of each panel is 800 cm by 320 cm by 17 cm. The entire production will take approximately 4 months at Donchamp. The detailed work flow is:

 - (a) mix the gadolinium beta-diketonate or the functionalized dispersion of Gd oxide with MMA liquid during the pre-polymerization procedure.
 - (b) Inject the mixed pre-polymerized liquid into a glass mold for the final polymerization, this step will take around two months at Donchamp.

3. Machining of TPC barrel panels and endcaps. In this step, the produced gadolinium-loaded acrylic will be machined to 8 inner detector barrel panels and 176 endcaps which will be inserted in the optical planes. The panels and the bricks used in the endcaps will be machined by the producer. The approximate machine time is 2 months. The detailed work flow is:

 - (a) Machine the inner detector barrel panels and endcaps to the shape.
 - (b) Anneal the machined parts in an oven under nitrogen.
 - (c) Pack with protection bags and ship to LNGS.
 - (d) A subsequent step at NOA is hand polishing to remove a thin layer (few hundreds μm) of material to clean the surface and remove surface contamination in the Rn-abated environment.

11.5.1. Gd loaded PMMA quality control

Two factors have to be taken into account for the gadolinium-loaded acrylic quality control: the radiopurity and the mechanical properties.

The radiopurity is dominated by that of the gadolinium compounds. A procedure for quality control has been developed.

In case of the choice of the commercially available Gadolinium oxide, the radioactivity of samples of material will be measured. A producer providing material satisfying our need has been identified (see section 3.8). We note that during the R&D phase three samples, purchased in 3 different times from this producer without tracking the original material batch, satisfied the radiopurity specifications. This producer ensured that the full amount of gadolinium oxide necessary for the experiment will be obtained from the same raw batch of material. This ensures that the measurements made on a sample will be representative of the values over the entire quantity.

In case of β -diketonate, during its production all the ingredients (gadolinium chloride and relevant organic ligand) will be sampled and measured by ICP-MS to understand the ^{232}Th and ^{238}U level. Only the qualified ingredients will be used for the production. Different batches of the produced gadolinium β -diketonate will be also sampled for the radiopurity measurement.

After the four gadolinium-loaded acrylic panels and endcaps are made, the leftover will be screened by a HPGe counter, in order to measure the ^{232}Th , ^{238}U and ^{40}K contamination. The leftover will also be machined into parts for measurement of the mechanical properties.

5387 **11.6. Procurement, construction and test of the photo-detectors**

5388 *11.6.1. Procurement of radiopure components*

5389 The components that must be procured for the PDU+ and vPDU+ are:

- 5390 • SiPMs: the contract for their production between LNGS and LFoundry was signed on 4th
October 2021 for 1400 wafers with 268 SiPM each. Wafers will be metallized with a gold
5391 backside. The delivery will start on January 2022.
- 5392 • Standard components that have been selected after radiopurity assays. These components
will be ordered via the standard vendors (RS/Mouser/Digikey).
- 5393 • Custom components: these include the radiopure pillar/screw sets and the acrylic protection.
5394 We are now contacting industrial machine shops capable of producing these parts.
- 5395 • Printed Circuit Boards: we have already identified an industrial partner capable of producing
5396 PCBs compatible with the required radiopurity levels.
- 5397 • ASIC: the production of the integrated electronics for the SiPM readout will be done using a
5398 Multi-Project Wafer or Engineering Run at UMC. The production and procurement will be
5399 handled by IMEC through Europractice.

5400 The tender processes for all these steps will finish not later than April 2022 in order to be able to
5401 start the production in June 2022.

5404 *11.6.2. Work flow of the SiPM and electronics mass production*

5405 The process flow for the production of the PDUs is summarized as a flowchart in Fig. 145.

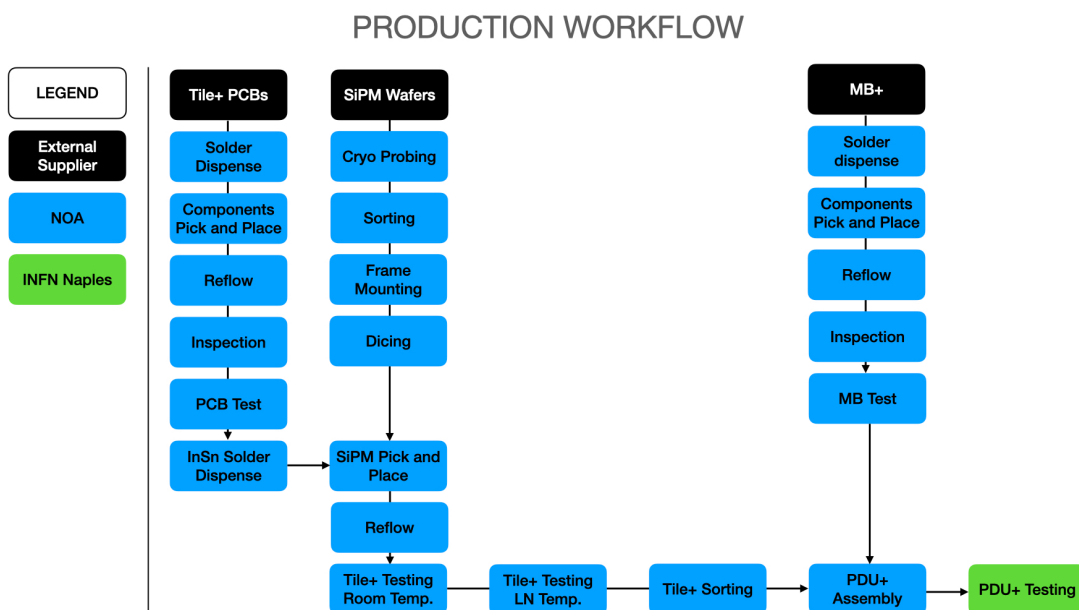


FIG. 145. PDU+ process flow overview. The work flow is divided into three main branches: SiPM testing and dicing; Tile+ production; MB+ production. Functional SiPMs are attached to working Tile+ PCB to form a Tile+ which, in turn, after being tested, is mounted on the MB+ to form the final PDU+ that will be tested in INFN-Naples.

- 5406 1. Wafers from the foundry are probed in a custom cryogenic wafer probe tool to sort devices
5407 based on their resistance, breakdown voltage and leakage current at liquid nitrogen temper-

- 5408 ature. Parameters are recorded for each die, indexed by wafer number and position. Wafers
 5409 are then diced and stored on the tape.
- 5410 2. Preparation of the MB+ PCB using standard SMT assembly line processes. These include the
 5411 application of solder with an automatic stencil-based dispenser, positioning of components
 5412 with a fully automated high speed pick-and-place machine and reflow of the solder in a multi-
 5413 zone nitrogen atmosphere conveyor oven. The production line includes an automated optical
 5414 inspection to verify that all the previous steps concluded successfully. A low temperature
 5415 solder (Bi-Sn T3 from CHIP QUIK [82]), will be used: this will allow a reflow process
 5416 compatible with the thermal requirements of the nylon connectors and of the PEN capacitors.
 5417 3. Testing the MB+ will be carried out using a custom probe-card: this unit will connect the
 5418 standard testing equipment (VNAs and oscilloscopes) with the 16 inputs and 4 outputs.
 5419 Thanks to RF switching matrices it will be possible to address each single Tile+ and each
 5420 single quadrant (signal from each adder that sums the signal of four Tile+), verifying that
 5421 the required performances (in terms of bandwidth, dynamic range, noise levels) are met.
 5422 This test will also verify that the power module unit is capable of disabling the high and low
 5423 voltages. These tests will be performed in liquid nitrogen.
- 5424 4. The preparation of the PCB of the Tile+ will follow the same processes described for the
 5425 MB+. Groups of 8 Tile+ will be processed at a time.
- 5426 5. The testing of the Tile+ will be carried out via a specific probe-card capable of reaching all
 5427 the relevant electrical elements of both the divider (to probe the divider) and the TIA. The
 5428 amplifier will be characterized in terms of dissipated power, noise level and bandwidth.
- 5429 6. Working Tile+ PCBs will be installed in groups of 16 into carriers compatible with the die
 5430 bonder (Amicra NOVA *PLUS*) [83]. The machine will then take care of applying the In-Sn
 5431 1E-T4 solder paste from Indium Corporation [84], via an Auger valve on the PCBs. The
 5432 machine will automatically pick up the SiPMs from the grip rings containing the diced wafers
 5433 and place them in the right location onto the Tile+ PCBs. Once the process is finished
 5434 the carrier with the Tile+ units will be positioned on the oven conveyor for reflowing the
 5435 solder. The In-Sn solder reflows 12 °C below the Bi-Sn solder: this allows safe operation in
 5436 this second step.
- 5437 7. To support the Tile+ during wire-bonding, the Tile+ will be installed in the MuGS
 5438 multipurpose box compatible with the pillars (see Fig. 146). Before populating the MuGS each
 5439 Tile+ unit will be equipped with mounting rods. A specific plier will be custom designed
 5440 to hold on one or two rods during the manipulation. The SiPMs on each Tile+ are wire-
 5441 bonded with a Bondjet BJ855 tool from Hesse Mechatronics [85], capable of fully automated
 5442 operations.
- 5443 8. Each Tile+ will be tested at room temperature and in liquid nitrogen. The protocol includes
 5444 the validation of SiPMs according to the detailed sequence of operations described in 11.6.4.
- 5445 9. The Tile+ units will be assembled on the MB+ PCB according to the integration procedure
 5446 described in 11.6.3.
- 5447 10. PDU+ will be tested at room temperature and in liquid nitrogen for a cryogenic characteri-
 5448 zation of Tile+ performance as described in 11.6.5.

5449 For the TPC Tile+, all the steps through 9 will be performed in the NOA clean room, while step
 5450 10 will take place in the PDU Test Facility (described in Sec. 9.2). Each production step will be
 5451 documented for every component by populating the construction database: automated tools are in
 5452 preparation for this.

5453 For the veto Tile+, steps 1 through 3 are performed in NOA, then the unpopulated Veto Tile+
 5454 substrates together with probed, diced dies are shipped on wafer tape to the UK. Following
 5455 room-temperature acceptance tests, the commensurate series of production steps described in 11.6.6
 5456 will be performed in the UK. Qualified devices are then shipped to Italy for assembly into veto
 5457 PDU+.

5458 The ASIC readout will be tested at wafer level, in case of a production handled through a
 5459 dedicated Engineering Run, or on packaged devices in case we opt for a production using a Multi-
 5460 Project Wafer shuttle run.

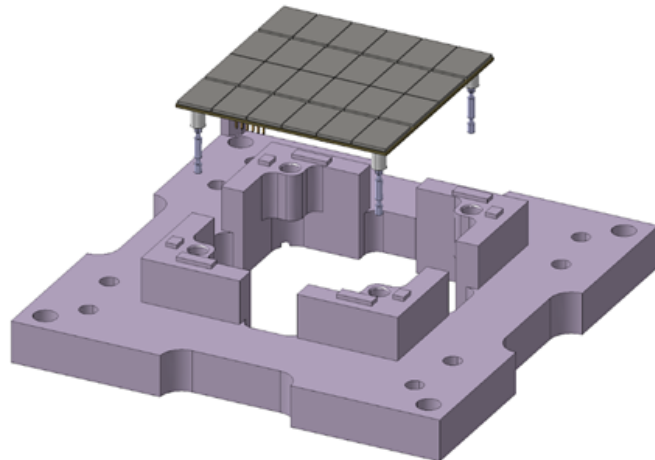


FIG. 146. MuGS multipurpose box with the Tile+.

5461 The production working packages have been defined, most group leaders have been hired or
 5462 identified, and we are working to define the procedures for the operators. The remaining operators
 5463 required for the 18 month production will be hired when appropriate.

5464

11.6.3. PDU+ assembly

5465 After the test phase both Tile+ and the MB+ will be integrated in a PDU+. The integration
 5466 procedure is similar to what has been developed for the first PDU prototypes. The steps of the
 5467 procedure are:

- 5468 • The MB+ will be installed on a pivoting support (Fig. 147) that will allow an access on both
 5469 front and back side.
- 5470 • The first step is the installation of the stands for the acrylic protection. An acrylic 4 mm thick
 5471 panel is intended to be mounted on the PDU+ as protection for the wire bonding during the
 5472 subsequent operations, as shown in Fig. 112, left. The design allows the removal of the front
 5473 panel after the optical planes are assembled. The supports of the protection require 5 mm of
 5474 dead space in one direction, while another 5 mm (in the other direction) will be required to
 5475 access the mounting clip on the titanium structure.
- 5476 • Then, the Tile+ will be ejected in a safe way from the MuGS by means of an ejector that
 5477 eventually will disengage the tile pushing the mounting rods from below.
- 5478 • The Tile+ is aligned to the mounting holes using the custom plier. While an operator holds
 5479 the Tile+ in position another one intercepts the mounting rods from the backside of the MB+
 5480 (see Fig. 149).
- 5481 • The Tile+ is slid into position on the MB+ using the guide provided by the rods and then
 5482 plugged into the MB+ connector.
- 5483 • The rods are replaced with the final screws.
- 5484 • The acrylic protection is mounted with screws, shown in Fig. 148. Figure Fig. 148 shows the
 5485 detail of the first prototype in production at CERN that will be available for the tests in the
 5486 INFN-Naples facility.
- 5487 • Finally, the PDU+ can be dismounted from the pivoting support.

5488

11.6.4. SiPM and electronics test protocol and Quality Assurance

5489 A portion of the NOA clean room has been designated to test all the PCBs and the tiles for
 5490 quality assurance during the production. At each stage of production and testing, information is

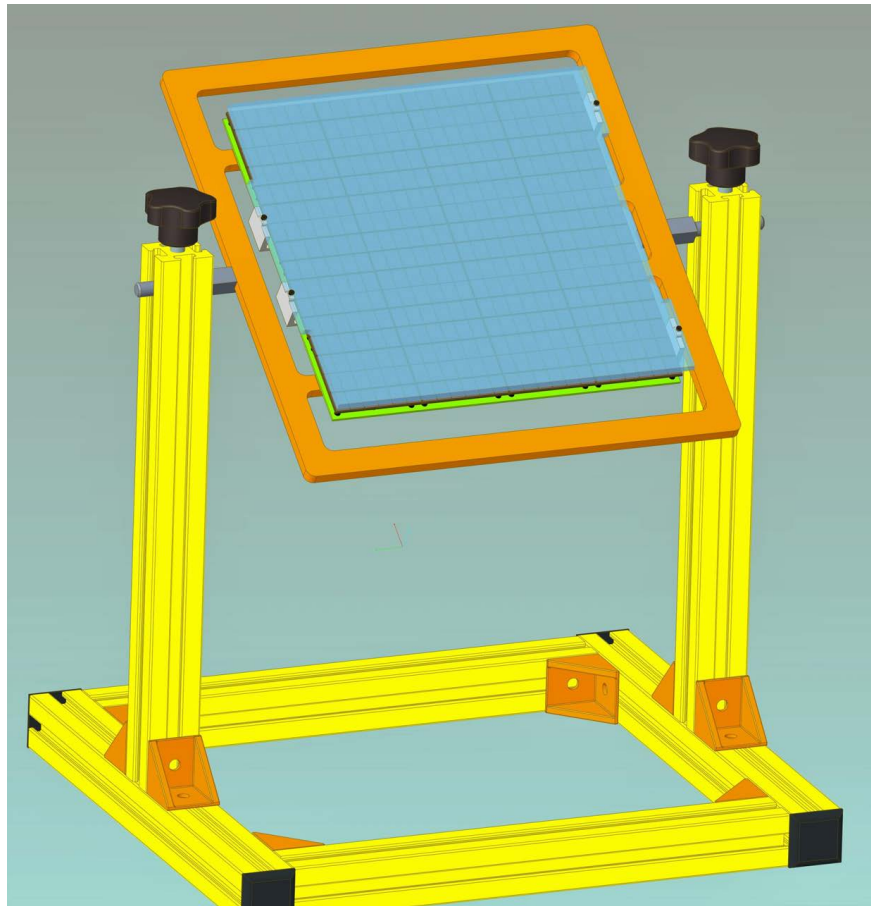


FIG. 147. Pivoting support for MB+ assembly.

5491 stored in a custom DarkSide photoelectronics construction database.

5492 *a. Tile PCB test* The PCB test starts with a visual inspection, to spot faulty components,
 5493 broken traces, and blown capacitors. If the visual inspection passes, the unit under test is powered
 5494 up, then, the relevant voltages and resistances are probed through the test points in the board.
 5495 The current absorption on the Vbias line at 150V is probed and also the TIA test is performed by
 5496 checking the power consumption at ± 2.5 V, the FFT response, the noise RMS at 200 MHz and the
 5497 output offset.

5498 *b. MB+ PCB test* The MB+ test starts with a visual inspection, to check the status of the
 5499 components. Then, dummy loads are mounted instead of the Tile+ units, and the MB+ is powered
 5500 on. The Power Module is tested through the serial communication, testing the power consumption
 5501 of the four quadrants. Each of the 16 channels are switched off and on singularly, to test the ability
 5502 to switch off every single channel on demand. In each quadrant the electrical response to a test
 5503 pulse of each channel is checked. The noise power spectra for each of the 4 outputs are acquired.

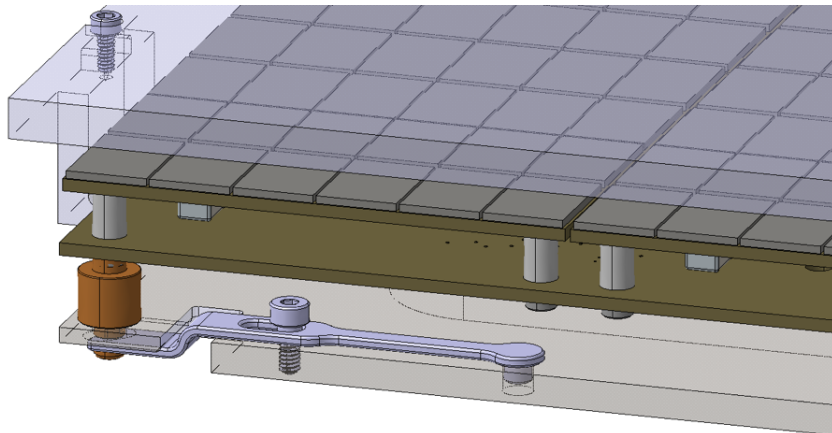


FIG. 148. Detail of the acrylic protection support. The front panel can be disengaged by removing the screws. The insertion clamp on the titanium structure is also visible

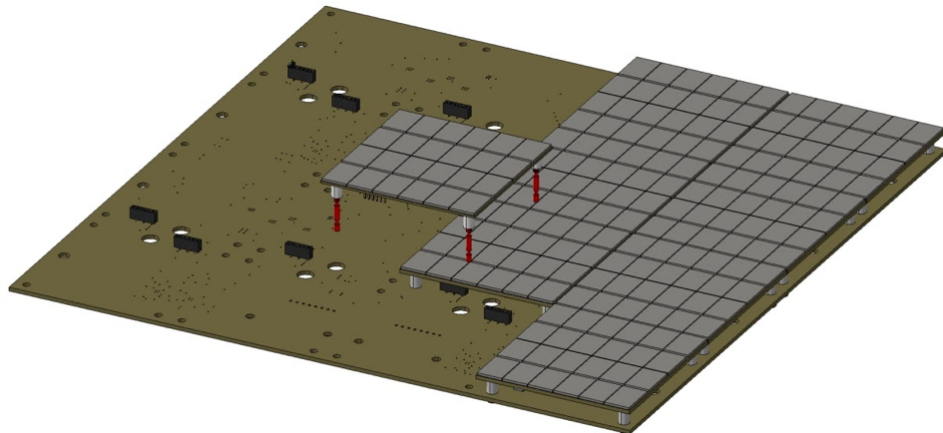


FIG. 149. The PDU+ integration. One Tile+ on the mounting rods (in red) can be seen.

5504 *c. Tile+ test* The tile operation and its uniformity are fundamental characteristics that can
 5505 be verified in terms of noise, breakdown voltage, and gain stability.

5506 All the tiles undergo an extensive test procedure defined in LNGS for which a dedicated set up
 5507 has been assembled and installed in a flanged dewar. The top flange provides the input for a fiber
 5508 laser and up to 4 vacuum tight feedthroughs for the electrical connections. Each tile is tested inside
 5509 the multipurpose box in order to keep the wire-bondings safe during all operations.

5510 After a first visual inspection to check the components, the soldering and the connectors, the
 5511 tile is mounted on a testing plate held by a tower structure that can be lowered in the dewar. The
 5512 protocol for the single tile characterization foresees two cycles only: the first at room temperature,
 5513 the second in liquid nitrogen (-196°C). Both cycles include measurements of the noise power
 5514 spectra and the IV reverse curves, and at cryogenic temperature the charge spectra are acquired
 5515 to extract a gain measurement. Then a set of several thousands of waveforms is acquired by the
 5516 digitizer to perform an offline analysis on the reconstructed and filtered data to estimate the SNR.

5517 *d. Logging test results in a production database* The test measurements and results are stored
 5518 in the DarkSide photo-electronics construction database, which is a service hosted at INFN-CNAF.
 5519 INFN-CNAF maintains the database infrastructure and is in charge of the development. Command
 5520 line APIs permit access to the database for insertion and retrieval of data. A web interface permits
 5521 data visualization, along with a data download utility. The database is used for the tracking of
 5522 the components during the construction and assembly of each Tile+. Moreover, the database will

5523 store the position of the Tile+ once assembled and keep inventory of the spares.

5524 Each *component*, present in the database in separate sets of tables, is an independent element
 5525 which is uniquely identified and will undergo stand-alone tests (e.g. wafers, ASICs, SiPMs, PCBs,
 5526 tiles, motherboards). The database contains both the TPC and Veto Tile+ order to permit recon-
 5527 struction of the whole production and test measurement stages. The set of tables are, in detail:

- 5528 • Components identification: a table for each component with an unique identifier and produc-
 5529 tion details;
- 5530 • Components assembly: components assembled to form a macro-component (e.g. 16 tiles and
 5531 1 motherboard form 1 veto PDU);
- 5532 • Components location during production: details about where I can find, in space and time,
 5533 a component around the world and what it is doing there (e.g. a vPDU+ in Manchester
 5534 University undergoing cold tests);
- 5535 • Components measurements: lower and higher level (DAQ and online in place) in warm and
 5536 cold environment;
- 5537 • Components measurements limits: used to assign a quality flag to each measurement;
- 5538 • Components location after installation: position of the Tile+ in the detector and location of
 5539 the spare components.

5540 11.6.5. PDU testing and QA/QC in the INFN-Naples PDU test facility

5541 As mentioned in section 9.2 the PDUs validation process in INFN-Naples Test Facility will
 5542 consist of several steps. Once the modules undergo a visual inspection, to check the components,
 5543 the soldering, and the connectors, they can be installed in the dedicated holding structure and all
 5544 external connections are made and verified. Finally the cryostat get closed. At this point the warm
 5545 test measurements can begin. If no issue is observed, the cryostat can be filled with liquid nitrogen
 5546 and the cold tests will take place. The list of tests foreseen and their duration is following:

- 5547
- 5548 • Warm test (1 day):
 - 5549 1. LV-HV single tile current measurement (during the massive testing the obtained val-
 5550 ues should be compared with registered at production site and stored at dedicated
 5551 production DB).
 - 5552 2. IV curves (reverse bias) measurement. Similar to the previous test, using the dedicated
 5553 software for the Power Module control and perform a one by one measurement for the
 5554 individual tile within the PDU (obtained results should be compared with the related
 5555 records in the production DB).

- 5556 • Cold test (1-2 days):

5557 With laser:

- 5558 1. IV curves (reverse bias) measurement (as in warm test).
- 5559 2. Pulse Shape measurement obtained with acquisition of the wave forms during the reg-
 5560 ular data taking with ADC boards.
- 5561 3. Signal to Noise ratio (SNR) at different Vov (regular data taking).
- 5562 4. Stability test (periodic data taking runs of 5-10 minutes over 24-48 h time period).
- 5563 5. Time resolution (regular data taking).

5564 Without Laser:

- 5565 1. Dark Count Rate and correlated noise, Cross Talk and After-Pulse (at different Vov).
 5566 Self trigger configuration (can also be measured in the pre-trigger part (few μ s) of the
 5567 acquisition window during the Laser calibration runs).

5570

11.6.6. Electronics for the Veto

5571 The photoelectronics system for the veto is being constructed in the UK facilities described in
 5572 Sec. 9.3. The work flow for the UK production starts on step 4 of the procedures detailed in
 5573 Sec. 11.6.2. The quality assurance testing steps are those described in Sec. 11.6.4.

5574 The set of construction steps prior to shipping to NOA are:

- 5575 1. LSDC receives probed, diced wafers from NOA in 8" Ultron grip rings in grip ring shippers.
 Dies are identified by die position and orientation in the wafer map from the NOA cryoprobe
 in the production database (output of step 1 in section 11.6.2).
- 5576 2. STFC Interconnect receives tile substrates and components for 2000 veto tiles + 20% spares
 (totaling 2400) and 140 MB+ for veto from central LNGS order, and acceptance tests fol-
 lowing the protocol described in section 11.6.4.
- 5577 3. STFC Interconnect laser engraves QR code on each substrate for subsequent component
 identification in the construction database.
- 5578 4. STFC Interconnect delivers labelled tile substrates to BILPA, labelled MB+ PCBs to Uni-
 versity of Manchester.
- 5579 5. BILPA mounts components on tile substrates and refows in class 7 clean room with contin-
 uous Rn monitoring, in dedicated reflow oven in N₂ environment.
- 5580 6. BILPA acceptance tests completed veto tile PCBs with dummy load, updates production
 database.
- 5581 7. BILPA delivers accepted veto tile PCBs to LSDC for tile mounting.
- 5582 8. LSDC acceptance tests veto tile PCBs on arrival.
- 5583 9. LSDC mounts SiPMs on tile PCBs, updates production database.
- 5584 10. LSDC delivers tile PCBs for warm testing at Manchester University.
- 5585 11. Manchester University does warm QA/QC of tiles and mounts on MB+ into PDU+ units as
 described in section 11.6.3, updates production database.
- 5586 12. Manchester University does warm QA/QC of assembled PDU+ units as described in sec-
 tion 11.6.5.
- 5587 13. Manchester University delivers warm-tested veto PDU+ units to Liverpool Argon facility.
- 5588 14. Liverpool Argon facility tests veto PDU+ units in liquid nitrogen, 16 veto PDU+ per cycle,
 for QA/QC as described in section 11.6.5.
- 5589 15. UK groups deliver QA/QC analysis report on warm- and cryogenic veto PDU+ tests, updates
 production database.
- 5590 16. Liverpool Argon facility packages tested, accepted veto PDU+ in dry-N₂ shipping/storage
 boxes .
- 5591 17. veto PDU+ ship in consignments to NOA, update production database.

5605 The UK construction project funding began in June 2021. First prototypes Tile+ for the veto have
 5606 been produced and tested in the UK, in collaboration with LNGS and Genova groups, following
 5608 the steps of this work flow, see figure 150.

5609

11.7. Inner Detector

5610 In this section the full process of construction of the Inner Detector is described, including all
 5611 the steps required for the TPC, Veto and optical planes integration.

5612 The overall strategy is to exploit the Rn-abated NOA CR2 for the assembly process of the TPC
 5613 acrylic vessel and inner components and for the integration of the two optical planes. The final
 5614 integration of the acrylic vessel together with the two optical planes will take place inside the
 5615 DS-20k cryostat. The inside of the cryostat will be connected to an existing Rn abatement and
 5616 ventilation system in Hall C, providing an air flux of 230 m³/h, so that the cryostat inner volume
 5617 will be transformed into a clean room with Rn-abated air.

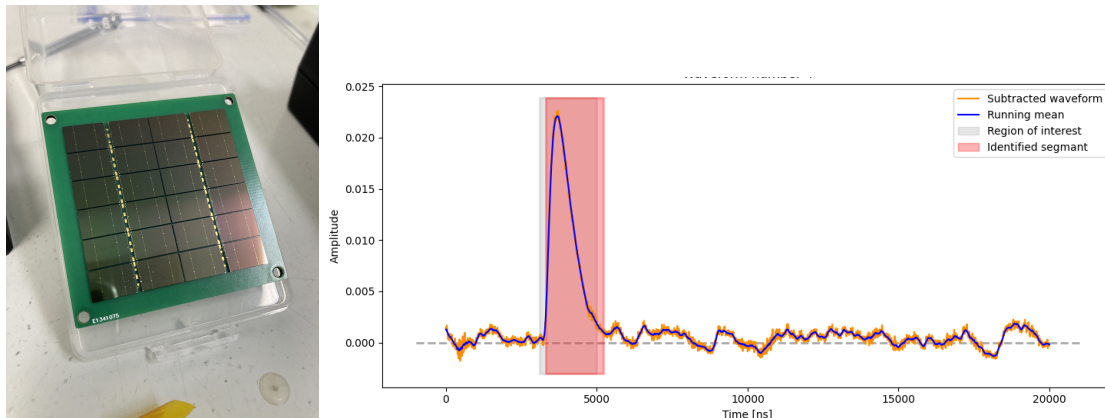


FIG. 150. Left: veto Tile+ prototype produced in the UK. Right: voltage vs. time waveform for veto Tile+ prototype in response to laser illumination, in UK cryogenic test.

5618

11.7.1. Activities in locations other than LNGS

5619 Preparatory activities for the Inner Detector, taking place in locations other than LNGS, include
 5620 construction and/or procurement of the following items:

- 5621 • TPC assembly and transportation handling system
- 5622 • Anode and cathode
- 5623 • Gd-PMMA Barrel panels
- 5624 • Titanium optical plane support structure (discussed in Sec. 7.2.7)
- 5625 • TPC full integration hardware (discussed in Sec. 7.2)
- 5626 • Wire grid
- 5627 • Reflector panels and field-cage resistor links (PCB)
- 5628 • Electronics for the Veto (discussed in Sec. 11.6.6)
- 5629 • Calibration pipes
- 5630 • Outer muon veto items

5631 These are briefly detailed below.

5632

TPC assembly and transportation handling system

5633 The TPC handling system is a custom fixture that is required for the construction of the TPC
 5634 in NOA CR2 and its transportation to underground Hall-C. It provides a rigid exoskeleton, onto
 5635 which each of the individual PMMA parts (anode, cathode, and 8 barrel pieces) can be rigidly
 5636 attached and have their position adjusted precisely to enable integration and to ensure that the
 5637 anode can remain flat. In addition, it enables vertical positioning of the assembly, and rotations.
 5638 The exoskeleton is positioned on a support structure in NOA CR2 for TPC assembly operations,
 5639 and it will be also used as a transportation cage for the TPC (without optical readout planes yet)
 5640 to underground Hall-C for final inner detector assembly. The structure is fabricated from painted
 5641 carbon steel members, with particular emphasis on components that are straightforward to clean
 5642 before bringing into CR2. The TPC handling system will be specified and fabricated by a bid
 5643 process from the University of Alberta, and will be shipped to LNGS with the PMMA components
 5644 from Canada (anode and cathode). The plan for TPC assembly is discussed in detail in 11.7.3.

5645

Anode and cathode

5646 The anode and cathode are both bonded and fabricated from several pieces of PMMA sheet from
 5647 Donchamp. This will happen at RPT in normal air, but annealing will happen under nitrogen.

5648 The fabricated components will be shipped to the University of Alberta (UofA). Note that all
5649 PMMA pieces used in the TPC construction are all machined at a predetermined temperature in
5650 a climate-controlled environment to ensure that the specifications match the final assembly site at
5651 LNGS.

5652 The construction steps at UofA in Radon free/clean air are:

- 5653 1. Sand all faces to remove plated out radon daughters. Clean pieces in a apparatus in which
5654 one circulates water through filter; repeating until the rinse water is dust free.
- 5655 2. Ensure anode is flat within tolerances (measure/correct with either machining or sanding).
- 5656 3. Do spray-coating of anode/cathode/lower barrel with Clevios.
- 5657 4. Bake (going through an acrylic annealing cycle).
- 5658 5. Coat anode and cathode with TPB in coating vacuum chamber. (The knee wall would be
5659 masked off during coating).
- 5660 6. Bake (going through annealing cycle).
- 5661 7. Cover/bag and ship to NOA.

5662 *Gd-PMMA Barrel panels*

5663 The barrel panels are made of gadolinium-doped PMMA. Eight pieces of barrel panels are re-
5664 quired to construct the octagonal shape TPC. The baseline scenario is that the barrel panels and
5665 all the GdPMMA pieces will be machined by the same company producing them The work flow is:

- 5666 1. Dope the gadolinium compounds into the MMA liquid during the pre-polymerization proce-
5667 dure of the acrylic production. This step is operated in a class 10000 cleanroom.
- 5668 2. Final polymerization in a temperature-controlled water bath.
- 5669 3. Machine each panel details in a climate-controlled machine shop.
- 5670 4. Anneal the machined barrel panels in an oven under nitrogen.
- 5671 5. Final mechanical inspection and pre-assembly test.
- 5672 6. Clean, bag and ship to NOA.

5673 *Wire grid*

5674 The 150 μm wire will be procured by the University of Houston group from the California Fine
5675 Wire Company, as they have provided for the smaller prototype detectors. A final order will be
5676 placed with this company, and a large batch will be counted to ensure the radioactive requirements
5677 of the wire. The group at University of Houston has produced a wire-winding machine that is
5678 capable of making the wire-to-pin attachment needed for the DS-20k installation. This machine
5679 has been used to produce wires with lengths up to 1.5 m, tensions controlled within 0.01 N, with
5680 length tolerances within 0.1 mm. The future upgrade that is planned for the machine will enable it
5681 to still provide the same precision on each of the parameters, while extending the length capability
5682 up to 4 m, as required for DS-20k. For DS-20k, the wires will be produced at University of Houston
5683 and then shipped to the assembly site of the inner detector in spools that allow for their indexing
5684 and insurance of safety. The wire frame itself will be produced at a company in Europe who has the
5685 capability of fabricating the frame out of a single piece and ensuring the flatness of the frame across
5686 all directions within specifications (given in section 7.2.2), and will also deliver to the assembly site
5687 of the inner detector. At that site, the wires will be inserted into the frame in a pre-defined order,
5688 and with a pre-loading of the frame, to ensure the final precision in the geometry of the wire grid
5689 is met.

5690 *Reflector panels and field-cage resistor links*

5691 The ESR reflector in the form of 26 in x 26 in foils will be acquired from a 3M retailer (American
 5692 Polarizer Inc.) which offers the possibility of laser cutting the panels to the desired design and
 5693 specifications. The foils will be shipped in radon impermeable plastic bags to Carleton for TPB
 5694 coating. TPB coatings with $200 \mu\text{g}/\text{cm}^2$ thickness with maximum thickness variation of $\pm 20\%$ will
 5695 be vacuum evaporated in several batches and shipped to LNGS, respecting precautions on radon
 5696 exposure.

5697 The resistor links will be produced by the CERN electronic shop given the satisfactory experience
 5698 with ProtoZero. The selected, cleaned resistors and solder will be shipped to the shop for assembly.
 5699 The completed resistor links will be shipped in radon impermeable plastic bags to LNGS.

5700 *Calibration pipes*

5701 The calibration pipes described in section 7.4.1 will be fabricated by the Marseille laboratory
 5702 (CPPM). Each one of the two 8-meter long titanium pipe will be built in seven sections and then
 5703 transported to LNGS. The sequence of operations for installation around the TPC at LNGS is
 5704 described in section 11.7.4.

5705 *Outer cosmic Veto items*

5706 The outer cosmic Veto will be achieved by instrumenting the AAr volume contained in the
 5707 cryostat with photosensors and Tyvek reflector foil sheets. Photosensor arrays, reflectors and
 5708 wavelength-shifting PEN sheets will be prepared outside of LNGS. The work flow is:

- 5709 1. Spare tiles from the inner veto and TPC, will be assembled in PDUs at NOA for use in the
 5710 outer veto.
- 5711 2. PDUs will be sorted into 8 groups, matching performance as evenly as possible.
- 5712 3. PDUs in each array will be mounted on stainless steel plates, which will be connected by
 5713 loops of Kevlar rope.
- 5714 4. Readout cables will be measured to span from each PDU to the flange at the top of its
 5715 corresponding array.
- 5716 5. PDUs and cables will be packaged together in radon-scrubbed nitrogen bags in preparation
 5717 for transport underground to LNGS Hall C.
- 5718 6. Reflector and PEN foils will be cut to the appropriate sizes in a clean room environment.
- 5719 7. Holes will be punched in the foils, and then reinforced with stainless steel grommets.
- 5720 8. Foils will be packaged in radon-scrubbed nitrogen bags and sent to LNGS in preparation for
 5721 transport underground to LNGS Hall C.

5722 *11.7.2. Preparatory operations at LNGS: cleaning and staging*

5723 To ensure control of radon levels within CR2, a staging area will be developed near the W side
 5724 entrance, as described in Sec. 9. The anode and cathode plates will arrive already coated with
 5725 Clevios and bagged from the Canadian site, but the remaining acrylic will be coated in CR2 and
 5726 must be cleaned before entry. The Gd-loaded PMMA barrel wall panels and endcap pieces are the
 5727 main considerations here. The pieces will arrive at LNGS already fully fabricated and annealed
 5728 into their final shapes, so no further mechanical work will be necessary at LNGS. Upon arrival at
 5729 NOA, the pieces will be unpacked in the staging area and hand-polished to remove a very thin layer
 5730 containing any radon or dust that accumulated during transport. Immediately after polishing, the
 5731 pieces will be sent through an assembly line containing a high-pressure water-jetting with de-ionized
 5732 water, and then into a custom low-temperature drying oven. After this, the pieces will move into

5733 an airlock to be flushed with dry radon-abated air before moving into CR2 for coating with Clevios.
 5734 Once the Clevios is applied, the pieces will again be placed in the drying oven, and then stored in
 5735 the radon-abated air of CR2 until the TPC assembly phase. The estimated surface area required
 5736 for this operation is $\sim 5 \times 6 \text{ m}^2$. The collaboration is foreseen to provide the oven and water-jet
 5737 bath.

5738 *11.7.3. TPC assembly activities in NOA CR2*

5739 The complete NOA infrastructure floor plan, including the detector assembly clean room CR2 and
 5740 staging area, is shown in Fig. 120. Fig. 151 shows a 3d view of CR2 with the internal dimensions
 5741 for the TPC assembly. This phase includes the mounting of the Gd-loaded PMMA barrel, cathode,
 5742 field cage resistor links, TPC reflector panels, wire grid frame and anode. In addition, the two
 5743 optical planes will be assembled in CR2 along with the PDU+, VPDU+, and Veto reflector panels.

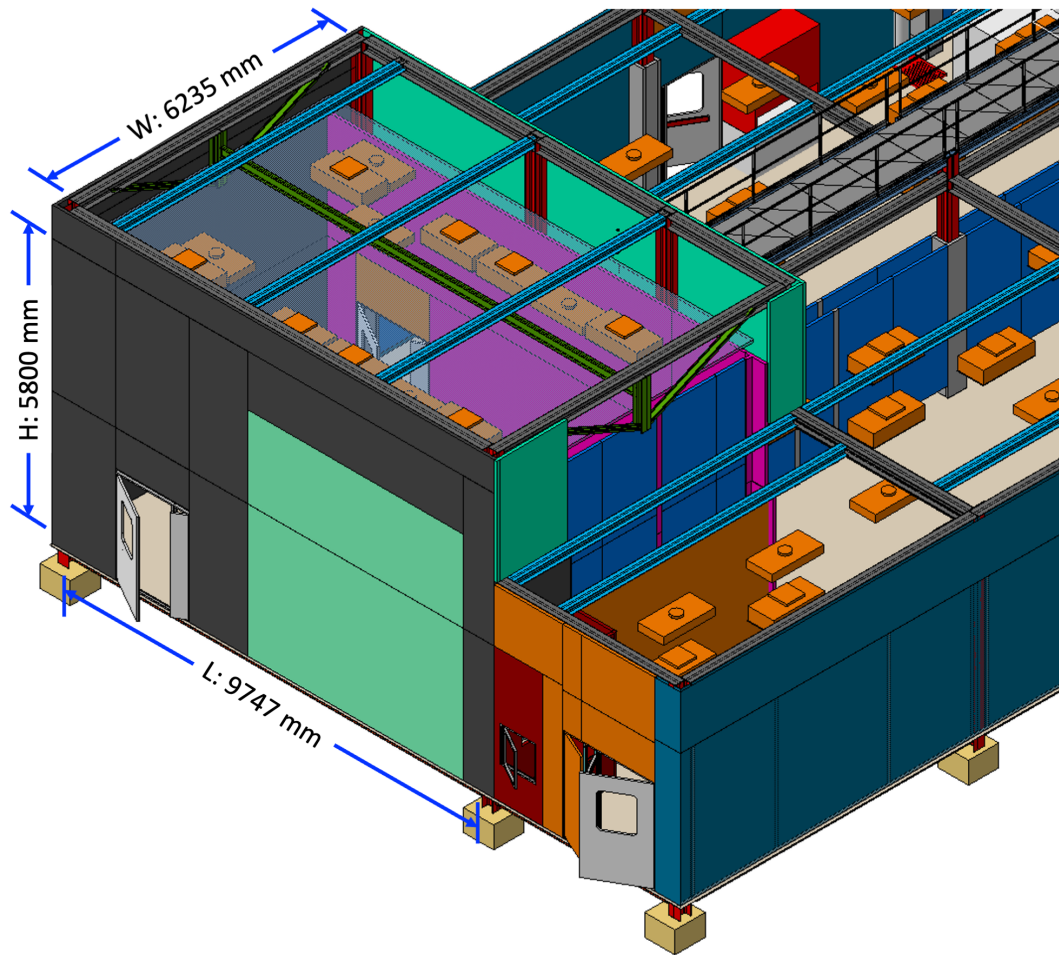


FIG. 151. The assembly clean room (CR2) within the NOA infrastructure.

5744 Upon completion of the preparatory operations described above, all necessary TPC parts will be
 5745 stored in the staging area or in CR2. At this point, personnel will only be able to enter through
 5746 the air-shower airlock door, and no additional large components will enter through the removable
 5747 panels. This is critical for controlling the dust and radon contamination levels.

5748 The activities to be carried out in NOA CR2 include:

- 5749 • TPC assembly handling system installation

- 5750 • TPC Gd-loaded PMMA barrel assembly
 - 5751 – mount all Gd-loaded PMMA panels onto the handling system, align and secure
 - 5752 – mount resistor links to connect the top 72 field cage rings
 - 5753 – mount reflector panels covering the top 72 field cage rings except the ones near the cathode and barrel junction
 - 5755 – prepare cathode assembly with lower 14 field cage rings connected with resistor links and reflector panels
 - 5757 – mount cathode from bottom to the barrel assembly
 - 5758 – make final connection between the barrel and the cathode junction
 - 5759 – mount last reflector panels
 - 5760 – mount wire grid
 - 5761 – mount anode
 - 5762 – check all connections
 - 5763 – pack with radon impermeable material
 - 5764 – install positive high purity N₂ gas flow to avoid any possibility of dust and air contamination during transport
- 5766 • Optical planes assembly
 - 5767 – mount already unpacked and cleaned optical plane structure on TPC assembly handling system
 - 5768 – set the structure at an appropriate height with the PDU+ facing downward orientation
 - 5769 – mount Veto Gd-loaded PMMA pieces in the empty spaces of the structure
 - 5770 – close the top with the prepared VPDU+ plate and secure it
 - 5771 – integrate the PDU+ and VPDU+ interface plates
 - 5772 – install all signal/power cables for both TPC and Veto
 - 5773 – check all cables with dedicated connectivity instrument
 - 5774 – install PDU+ from under side (connect cables, check, then secure in place)
 - 5775 – repeat for all PDU+
 - 5776 – repeat VPDU+ at the current orientation
 - 5777 – repeat check of all PDU+ connections
 - 5778 – pack cables but keep all connectors accessible for future checking during each of the following steps
 - 5780 – pack the full assembly for shipping to Hall-C.

5782 The main consideration while mating the anode and cathode plates with the TPC barrel is the
 5783 settling of dust and radon on exposed components. We foresee a procedure where the resistor
 5784 links and reflector panels are installed under a temporary barrel cover, or the already installed
 5785 anode plate. Once the internal components are installed and connected, the cathode plate will be
 5786 positioned under the barrel, uncovered, and moved into place. No rotation of the barrel is foreseen
 5787 in CR2; however, this remains an option. Temporary support structures will be placed in the optical
 5788 plane positions, and the entire assembly will be held together with connecting rods for movement
 5789 underground. Once anode and cathode plates are in place, a constant flow of dry nitrogen will be
 5790 supplied throughout the inner volume until enclosed within the titanium vessel and evacuated.

5791 The assembly of the optical planes is discussed in Section 7.2. The titanium structure, the Gd-
 5792 loaded PMMA endcaps, and the cable management are detailed respectively in Sections 7.2.7, 7.2.9,
 5793 and 7.2.10. The same TPC assembly handling system used for the TPC barrel construction will
 5794 be used for these operations, allowing for rotation of the planes with minimal additional hardware.
 5795 This will ensure that the delicate operation of handling the PDU+s and VPDU+s is done always
 5796 without the risk of damage from dropping objects. After the optical planes are assembled, they
 5797 will be placed within a dedicated transport structure and moved to the underground laboratory. A
 5798 portable testing device is foreseen for the PDU+s and VPDU+s during these processes. The device
 5799 will confirm that the PDU+ channels are operational and if a replacement is necessary. Various
 5800 testing periods will be defined with the acknowledgment that replacement becomes more difficult
 5801 as the assembly advances.

5802

11.7.4. Activities in Hall C

5803 Final detector integration is expected to happen in the DS-20k cryostat; the foreseen activities
 5804 in Hall C are:

- 5805 • Installation of electrical power
- 5806 • Hall C and cryostat preparation for Inner Detector final integration
 - 5807 – Cryostat false floor and scaffolding installation
 - 5808 – Cryostat clean room hardware installation and connection to the DS-50 Rn abatement
 system
 - 5810 – Soft-wall clean room installation
- 5811 • Inner detector final integration
 - 5812 – Bottom Optical Plane (BOP) insertion
 - 5813 – TPC acrylic vessel insertion
 - 5814 – Top Optical Plane (TOP) insertion
 - 5815 – TPC mechanical linkage hardware integration
 - 5816 – Barrel VPDU+ installation
 - 5817 – Calibration pipes integration
 - 5818 – Ti vessel top dome integration
 - 5819 – Detector + Ti vessel top dome bagging and removal
 - 5820 – Ti vessel bottom part insertion
 - 5821 – Reflector panels installation
 - 5822 – Detector insertion
 - 5823 – Top caps installation (bolting)
 - 5824 – Chimney installation
 - 5825 – Cables routing
 - 5826 – UAr cryogenics and service lines installation
 - 5827 – Pumping and leak check the UAr volume
 - 5828 – DAQ installation
 - 5829 – Full integrated warm test of electronics and DAQ
 - 5830 – Final top caps welding
 - 5831 – DSS installation
 - 5832 – DSS commissioning and detector lifting
 - 5833 – Final piping connections
 - 5834 – Temporary support structure removal
 - 5835 – Scaffolding and false floor removal
 - 5836 – Calibration equipment on top of the cryostat roof installation.

5837 These are each briefly detailed below.

5838

Power distribution and grounding

5839 The preservation of the integrity of the signals generated in the detector requires carefully de-
 5840 signed and implemented schemes for the distribution of electrical power, implementation of rules
 5841 for the avoidance of the introduction of external noise into the cryostat, and a design of the detector
 5842 electronics themselves that avoids unwanted noise from the detector electronics themselves affecting
 5843 their outputs. Furthermore, even after implementing best practices everywhere, experience shows
 5844 that some flexibility is required in the installation to achieve optimum performance. Experience
 5845 also shows that in order to exploit any flexibility effectively requires a system where all the power,
 5846 signal and return paths have been documented. A team of engineers and physicists will be in charge
 5847 of ensuring that all systems which involve connection to the interior of the cryostat are documented
 5848 and reviewed.

5849 We give as an example the arrangement used at CERN for the protoDUNE single-phase DUNE
 5850 prototype, protoDUNE-SP, which used an essentially identical cryostat structure to the DS-20k

5851 cryostat and was rather successful in terms of the noise levels achieved. The implementation at
 5852 LNGS will, of course, be subject to the rules and regulations at LNGS but we model our grounding
 5853 plan based on the system developed at CERN:

- 5854 • There were two distinct ground systems: Detector Ground and Building Ground.
- 5855 • A safety ground, consisting of a saturable inductor, connected the two ground systems and
 5856 maintained a low impedance current path for equipment short circuit and ground fault cur-
 5857 rents. This ensured personnel safety by limiting equipment/equipment and equipment/-
 5858 ground touch potentials.
- 5859 • Detector Ground was the steel containment vessel enclosing the cryostat, the cryostat, and
 5860 all metal structures attached to or supported by the detector vessel. Dielectric breaks were
 5861 required on all cryo piping and any other metal structures which were connected to Building
 5862 Ground.
- 5863 • Building Ground was a network of grounding bus bars and inter-connected rebar.
- 5864 • An insulating barrier, 2 mm of G10, was installed between the floor of the facility and
 5865 the bottom of the cryostat containment structure to reduce low frequency ground and noise
 5866 currents conducted between Building and Detector grounds.
- 5867 • Detector Readout racks were located on or near the top of the cryostat so that all the readout
 5868 racks can be on a common Detector ground system and cable runs minimized.
- 5869 • All cable trays from the racks to the feedthrough ports were solidly connected to the top
 5870 plate reference ground and treated as part of Detector ground.
- 5871 • All cryogenic and gas piping was connected to Building ground at intervals before arriving at
 5872 the cryostat. These pipes are required to have dielectric breaks located near the top of the
 5873 cryostat. A capacitance of 10pF or less at each dielectric break was required.
- 5874 • A 400/230 VAC, double shielded, isolation transformer was, located close to the cryostat.
 5875 The service panel from this transformer was provided with surge protection.
- 5876 • All connections between the detector racks (Detector ground) and the Control room/barracks
 5877 (Building ground) were by optic fiber.
- 5878 • The top plate of the cryostat served as the signal reference plane and Detector ground. A
 5879 copper grid, solidly connected to all feedthroughs and to the electronics racks was provided.
- 5880 • All local detector racks were solidly connected to the platform and to the cryostat top refer-
 5881 ence grid/plane representing Detector Ground.
- 5882 • Copper grounding bus bars were provided near the racks and any other equipment mounted
 5883 on the cryostat to aid in maintaining the low-impedance inter-connections to Detector ground.

5884 Fig. 152 is a schematic of the implementation at CERN.

5885 *Hall C and cryostat preparation for detector final integration*

5886 To complete the Inner Detector integration, the transformation of the ProtoDUNE cryostat into
 5887 a temporary Rn-suppressed clean room is foreseen. The air supply will be produced by the existing
 5888 DS-50 Rn-abatement system, capable of delivering approximately $230 \text{ m}^3/\text{h}$ with a Rn reduction
 5889 factor of greater than 1000. The stainless steel internal walls of the cryostat (primary membrane)
 5890 are suitable to constitute the lateral walls of the clean room.

5891 A false floor with wooden blocks and plates will be installed with the goal of protecting the
 5892 primary membrane floor corrugations while the detector is sitting on the temporary structure
 5893 awaiting assembly. The design of the false floor is discussed in Section 9.5.1 and Fig. 127 shows
 5894 the false floor concept.

5895 Before the final detector assembly, only one of the cryostat top cap modules (the N side) will be
 5896 mechanically connected to the rest of the warm structure. This will allow for the installation of
 5897 the AAr internal cryogenic components, while ensuring the availability of an aperture of $\approx 6.4 \text{ m}$
 5898 $\times 8.7 \text{ m}$ for the temporary cover of the cryostat during the final assembly of the detector, as shown
 5899 in Fig. 153.

5900 The top of the cryostat aperture will be equipped with a temporary soft wall clean room, large

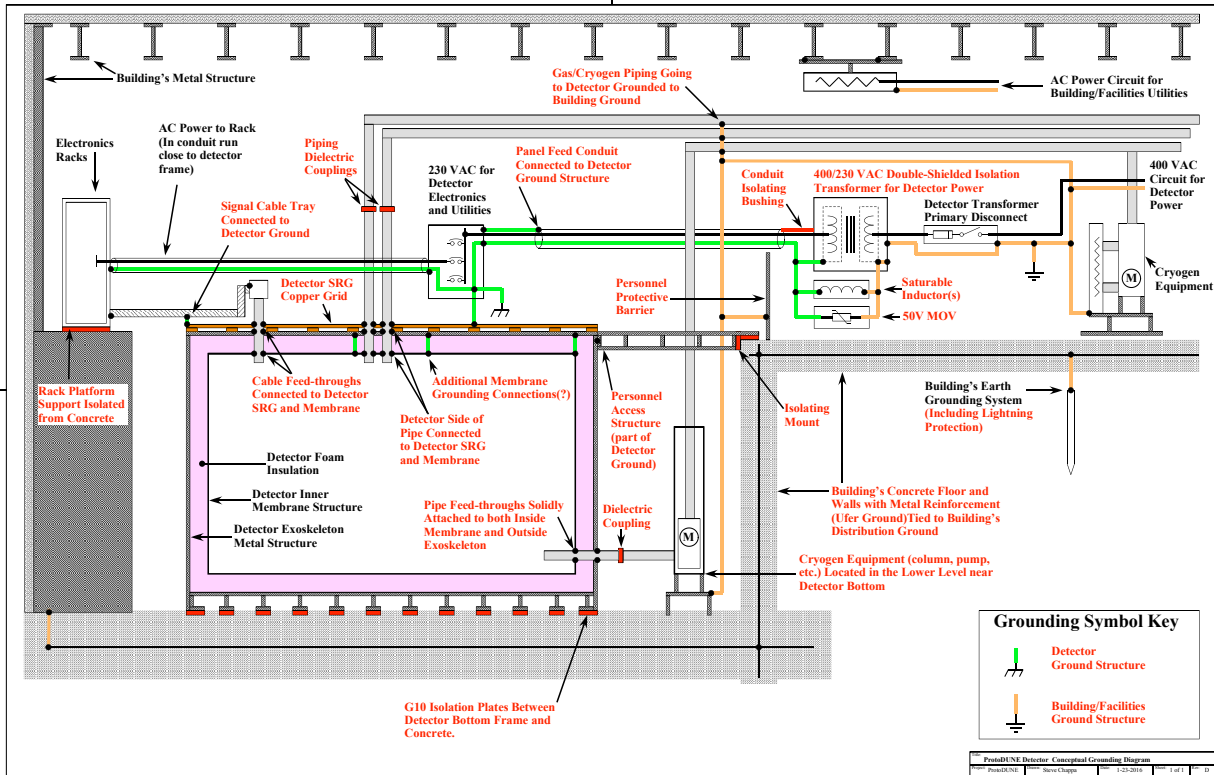


FIG. 152. Schematic of grounding and power distribution used at ProtoDUNE

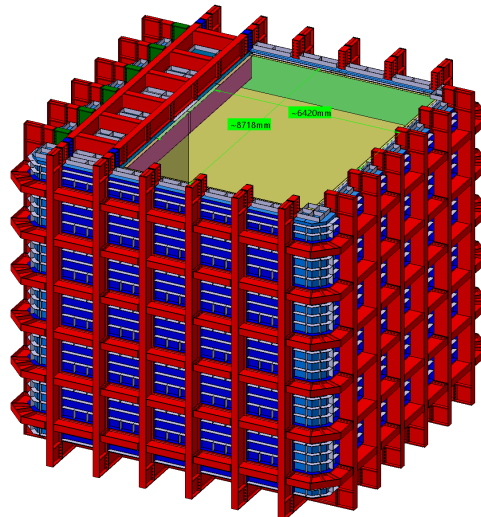


FIG. 153. Cryostat during final detector assembly: the cryostat top aperture.

enough to host the Inner Detector already assembled with the Ti vessel top dome ($6.6\text{ m} \times 5.2\text{ m} \times 5.5\text{ m}$). The goal is to provide an intermediate space acting as an airlock system whenever an object needs to be inserted or removed from the cryostat during installation. An airlock for personnel will also be installed. The volume of the cryostat will be separated from the clean room with dedicated air tight covers, while the remaining section will be equipped with HEPA filters integrated into the roof, an air plenum, and a supply fan for air circulation. A mechanical system for the covers to slide below the HEPA filters in order to allow aperture of the temporary cover while not spoiling

5908 the cryostat air purity is being designed. Specifications for the air circulation and filtration system
 5909 to achieve cleanliness class 1000-10000 are under study. A conceptual sketch of the assembly is
 5910 shown in Figs. 154(a) and 154(b).

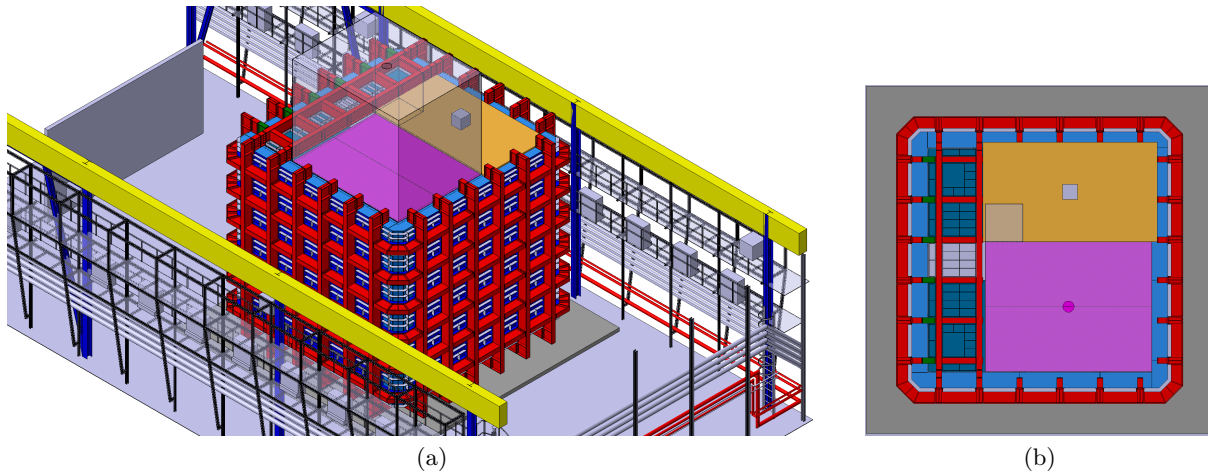


FIG. 154. Conceptual sketch of the soft wall clean room and temporary cover on top of the cryostat during the Inner Detector assembly. The pink panels are the air tight covers that can slide below the roof integrated with HEPA filters (orange panel) to allow clean insertion of large pieces inside the cryostat.

5911 In order to satisfy the stringent cleanliness requirements, a strict procedure will be in place for
 5912 movement of large items needs into (or out of) the cryostat volume. 1) Two of the clean room
 5913 soft walls are dismounted. 2) The item is inserted inside the clean room. 3) The soft walls are
 5914 re-mounted. 4) Air is circulated for a few hours. The top wall is designed in two pieces that can
 5915 be easily disassembled, with a central pocket which allows the crane hook to move through. Once
 5916 the complete volume of air is exchanged, the air tight covers will be slid below the roof integrated
 5917 with HEPA filters, and the item can finally be inserted inside the cryostat clean room.

5918 By the time the cryostat is transformed into a clean room environment, the outer veto Tyvek
 5919 reflector foils can be installed around the lateral walls.

5920 The other important aspect concerning Hall C preparation for detector final integration is the
 5921 removal of one of the two flat cranes currently available in Hall C, in order to extend the area of
 5922 action of the 20 + 20 t arc crane, needed for the insertion and extraction operations.

5923 *Inner Detector final integration*

5924 The final integration of the Inner Detector will take place in the cryostat clean room. A temporary
 5925 support structure will be installed on top of the cryostat false floor, which will support the load of
 5926 the integrated Inner Detector along with the titanium vessel. This temporary structure will be built
 5927 such that it can be quickly dismounted as the detector is lifted by the Detector Support System
 5928 (DSS) and removed through the manhole penetrations. A conceptual design of the structure is
 5929 shown in Fig. 155(a). All of the movement of components into and out of the cryostat will be
 5930 done using the arc crane in Hall C. The following is the sequence of installation steps within the
 5931 ProtoDUNE cryostat for DS-20k:

- 5932 • The bottom optical plane (BOP) will be removed from its transport structure and will be
 5933 the first component inserted into the cryostat, this is shown in Fig. 155(b). The fully
 5934 assembled BOP weighs approximately 2.5 tonnes and will be lifted by the eight attachment
 5935 points highlighted in Fig. 80 with the Hall C arc crane.
- 5936 • Once the BOP is placed, the lower sections of the calibration pipes will connected to the
 5937 BOP titanium structure with dedicated fixtures, i.e. the pipe collars will connect to stand-

- offs integrated into titanium structure using vented screws to avoid trapped air. The lower calibration pipe placement is shown in Figs. 155(c) and 155(d).
- Next, the PMMA barrel assembly will be inserted into the cryostat along with the transportation exoskeleton and protective bag. This assembly weighs approximately 12 tonnes and the transportation exoskeleton will also be used as anchor points for the lifting operation. The barrel assembly will now be sitting on top of the BOP, as shown in Fig. 155(e).
 - The top optical plane (TOP) will be removed from its bag and inserted in the same manner as the BOP.
 - The three main components of the Inner Detector will now be fixed together using the eight connecting rods and spring assemblies. This is shown in Fig. 156(a).
 - Cables from the BOP are routed and bundled with the Veto and TOP cables, and placed on the TOP awaiting extraction.
 - VPDU+s are installed on the exterior barrel walls and tested. These are the final photo detectors that will be mounted on the Inner Detector.
 - The top dome of the titanium vessel will be inserted. Reflector foils will have already been fixed to the interior walls of the titanium vessel, and this assembly weighs approximately 3.8 tonnes. This is shown in Fig. 156(b). For this operation a special lifting tool is being designed and, to connect the Inner Detector to the top dome, a scissor lift or a dedicated scaffolding will be needed.
 - The cables will be routed through the titanium vessel top dome, and a few final connections and checks will be performed before moving the assembly:
 - The middle sections of the calibration pipes will be connected to the flanges on the top dome and welded to lower sections. The welding will be done with an orbital welding machine, and there exists expertise within the collaboration on this topic.
 - The UAr lines will be connected to flanges on the top dome.
 - Final check of the gas pocket hardware.
 - Final check of the HHV system and connections.
 - Installation of any final instrumentation such as temperature or pressure sensors.
 - The entire assembly will then be bagged, lifted out of the cryostat, and placed outside, as shown in Fig. 156(c).
 - In parallel, the bottom section of the titanium vessel will be assembled and, once the Inner Detector is removed, it will be placed inside the cryostat using the same support structure as shown in Fig. 157(a)
 - The reflector foils will be installed covering the inner wall of the titanium vessel. The bottom part of the PEN reflector cage is shown in Fig. 157(b).
 - The indium seal will be prepared on the top flange.
 - The Inner Detector assembly, attached to the titanium vessel top dome, is carefully moved and inserted into the bottom of the titanium vessel and bolted together. This is shown in Fig. 158(a). Part of the lifting structure will also be removed at this point, while part of it will remain as the DSS.
 - Once the titanium vessel is sealed, the soft-wall clean room and temporary cover can be removed, and the cryostat can be temporarily closed. The top cap IPEV600 beams will be bolted together using link modules and, eventually, shims. This is shown in Figs. 158(b), 158(c), and 158(d).
 - The lower and outer Veto PDM strings will be installed, and secured to dedicated flanges on the top caps.
 - The TPC and Veto chimneys will be bolted to dedicated CF flanges on the central top cap, as shown in Fig. 159(a).
 - The bellows will be installed and the cables will be routed up to the chimneys. The UAr cryogenic pipes and service lines will be installed and the titanium vessel will be evacuated and leak checked. The DAQ system will also be installed at this point, as shown in Fig. 159(b).
 - Before the cryostat is sealed, a warm test of the electronics and DAQ chain will be performed.

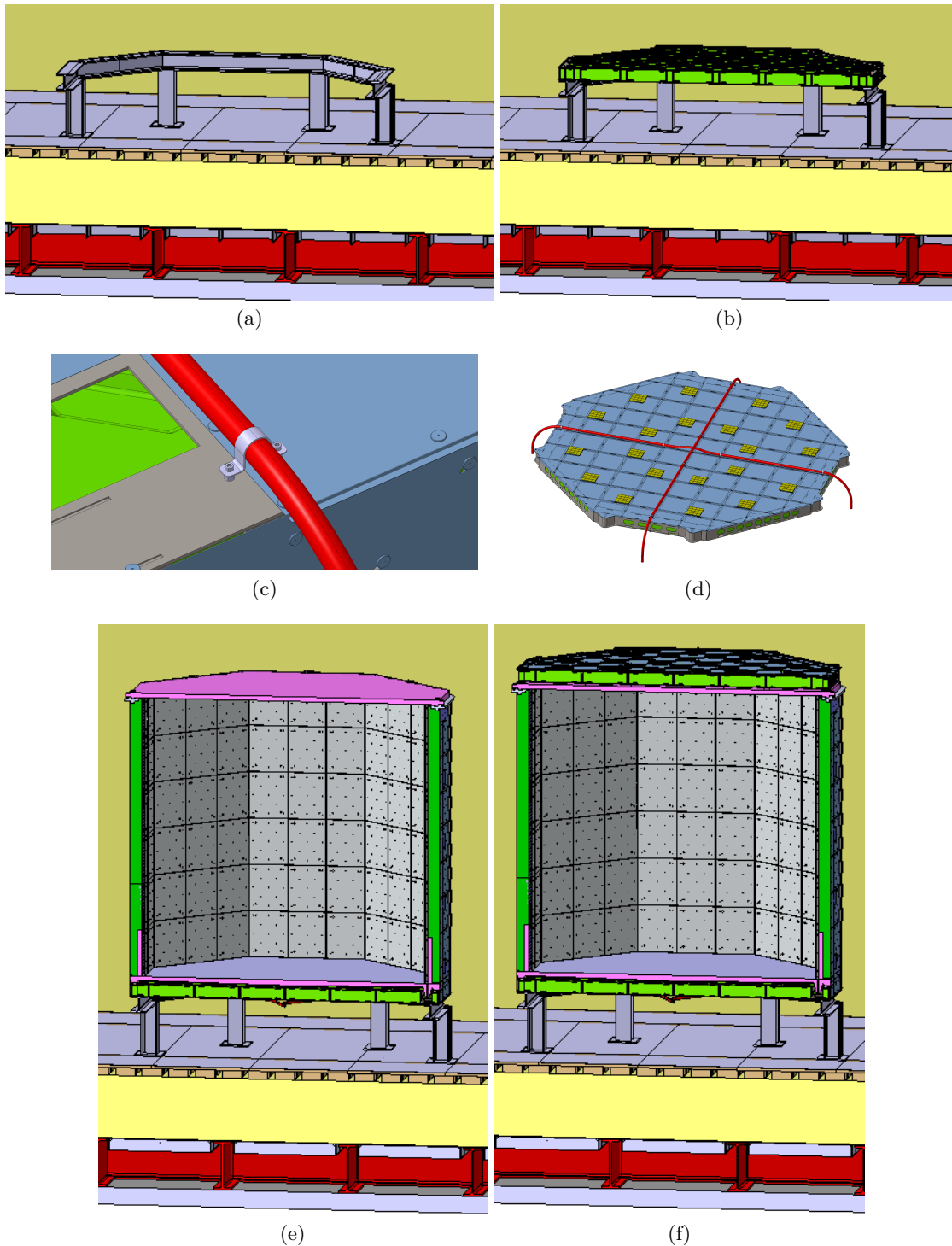


FIG. 155. (a) Temporary support structure placed inside the cryostat. (b) Bottom Optical Plane (BOP) on top of the temporary support structure. (c) and (d) Details of the calibration pipes lower sections integration. (e) TPC acrylic vessel on top of BOP. (f) Top Optical Plane (TOP) on top of the TPC acrylic vessel.

- 5991 • The cryostat tertiary membrane modules will be welded together in a procedure such that
 5992 contaminants entering the cryostat are avoided.
 5993 • The four DSS assemblies will be installed, as shown in Fig. 159(c). The load spreading beams
 5994 will be connected with the warm structure of the cryostat roof. The support rods will also

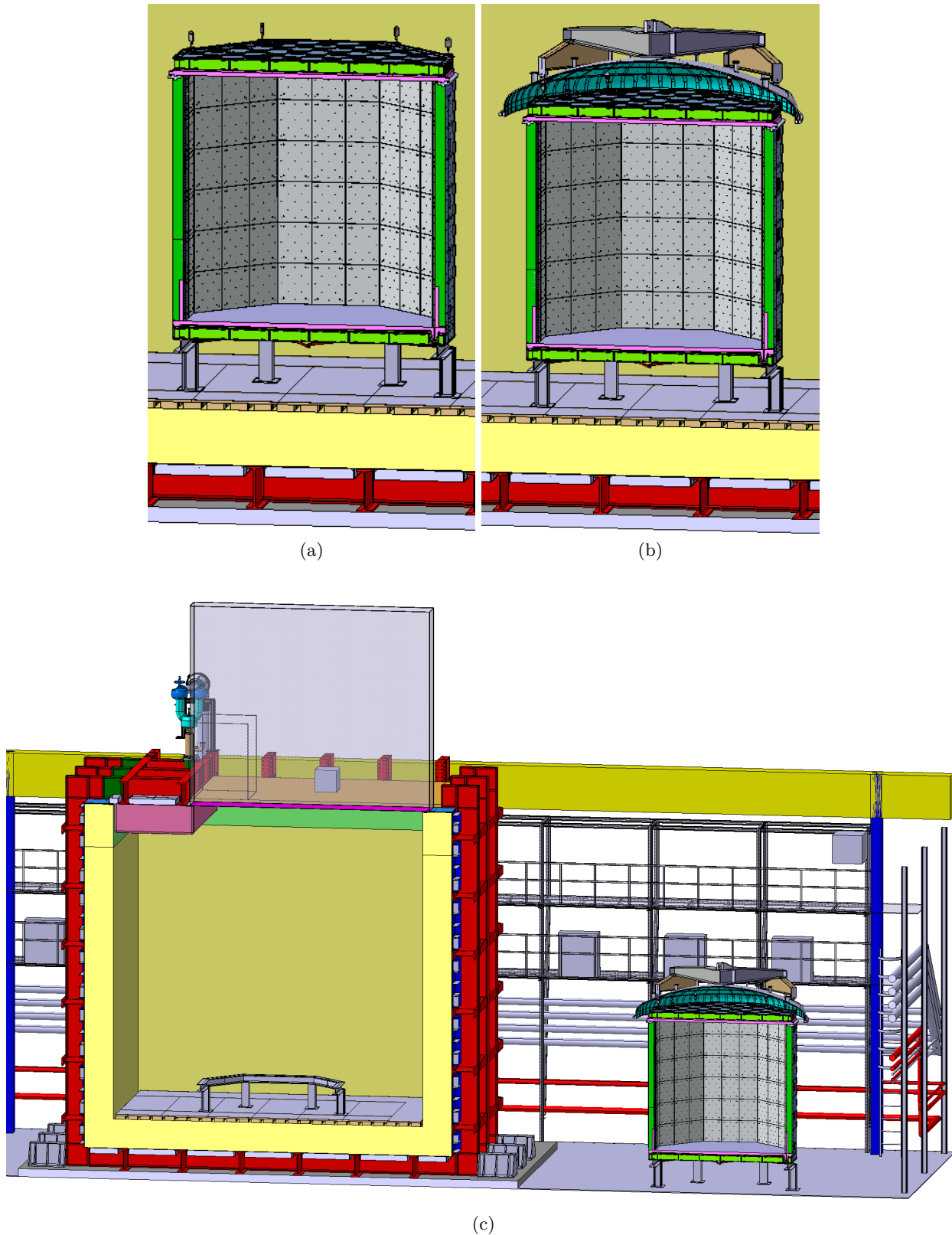


FIG. 156. (a) Integration of the 8 spring-loaded rods. (b) Integration of the Ti vessel top dome and of the lifting beam. (c) Lifting out of the detector integrated with Ti vessel top dome.

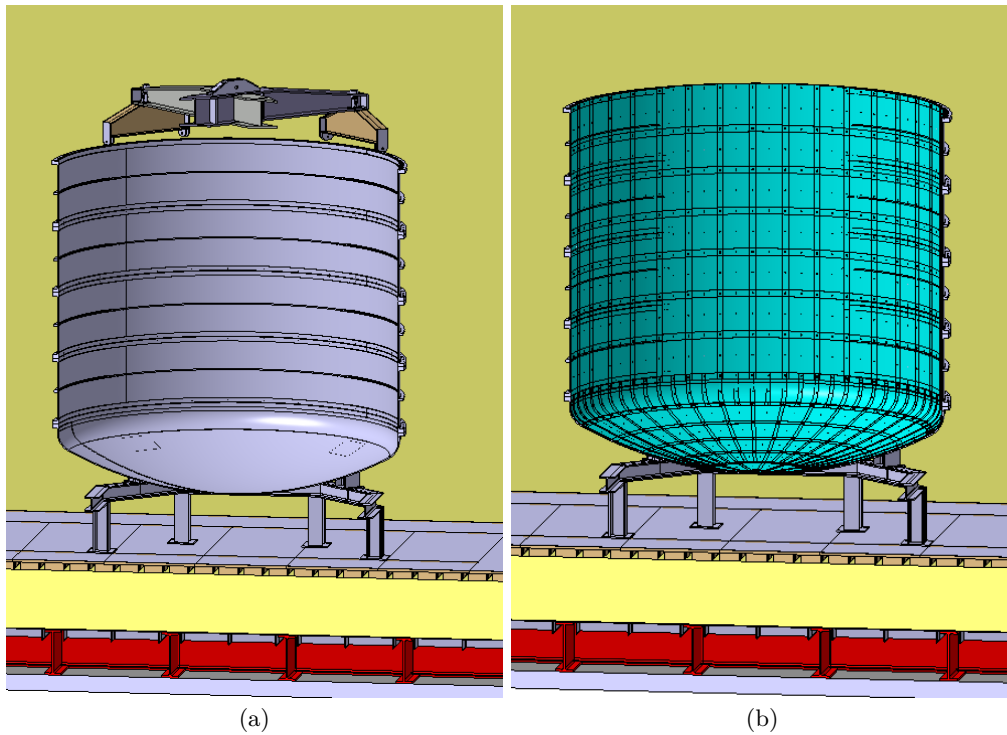


FIG. 157. (b) Titanium vessel insertion. (c) Reflector foils mounting.

be installed and connected with clevises to beams on the lifting structure. The lifting jacks and load cells will be mounted on the load spreading beams at this time. A bellows for each cryostat penetration will help with any mis-alignments. The DSS will also be connected to the DAQ.

- The titanium vessel will be lifted with the DSS allowing for removal of the temporary support structure, titanium vessel feet, scaffolding, and the false floor through the DN700 manhole flange. This is shown in Fig. 159(d).
- The final piping connections between the titanium vessel and the cryostat penetrations, including the calibration system and the UAr inlet and outlet will be made. This is shown in Fig. 159(e).
- The calibration system equipment, comprising of the glove box and motor box, will be installed on the cryostat roof, as shown in Fig. 159(f).

11.8. Cryogenics commissioning

During commissioning, the UAr volume will be prepared while the ProtoDUNE cryostat begins filling. Because a titanium vessel is being used to isolate the UAr and the AAr volumes, a pressure differential between can be tolerated until the titanium vessel becomes buoyant. Thus, simultaneous filling of the two volumes is not critical. There are three level sensing methods to monitor filling: 1) The AAr level monitor located on the outside of the titanium vessel. 2) The weight monitor on the DSS load cells which are supporting titanium vessel and contents. 3) The UAr ullage top fill indicator. The AAr level sensor and load cell readings will be used during the entire filling process until the UAr reaches the ullage level sensor.

The UAr lines starting from the gas storage bottles up to the cryogenic system will be flushed with ultra high purity gaseous nitrogen. This is in addition to the particulate filter nearest the TPC at the condenser, but will be done to avoid accumulation of dust within the filter. Following this, the system will be evacuated and fully leak checked. Operating at the design cooling power, 40 d

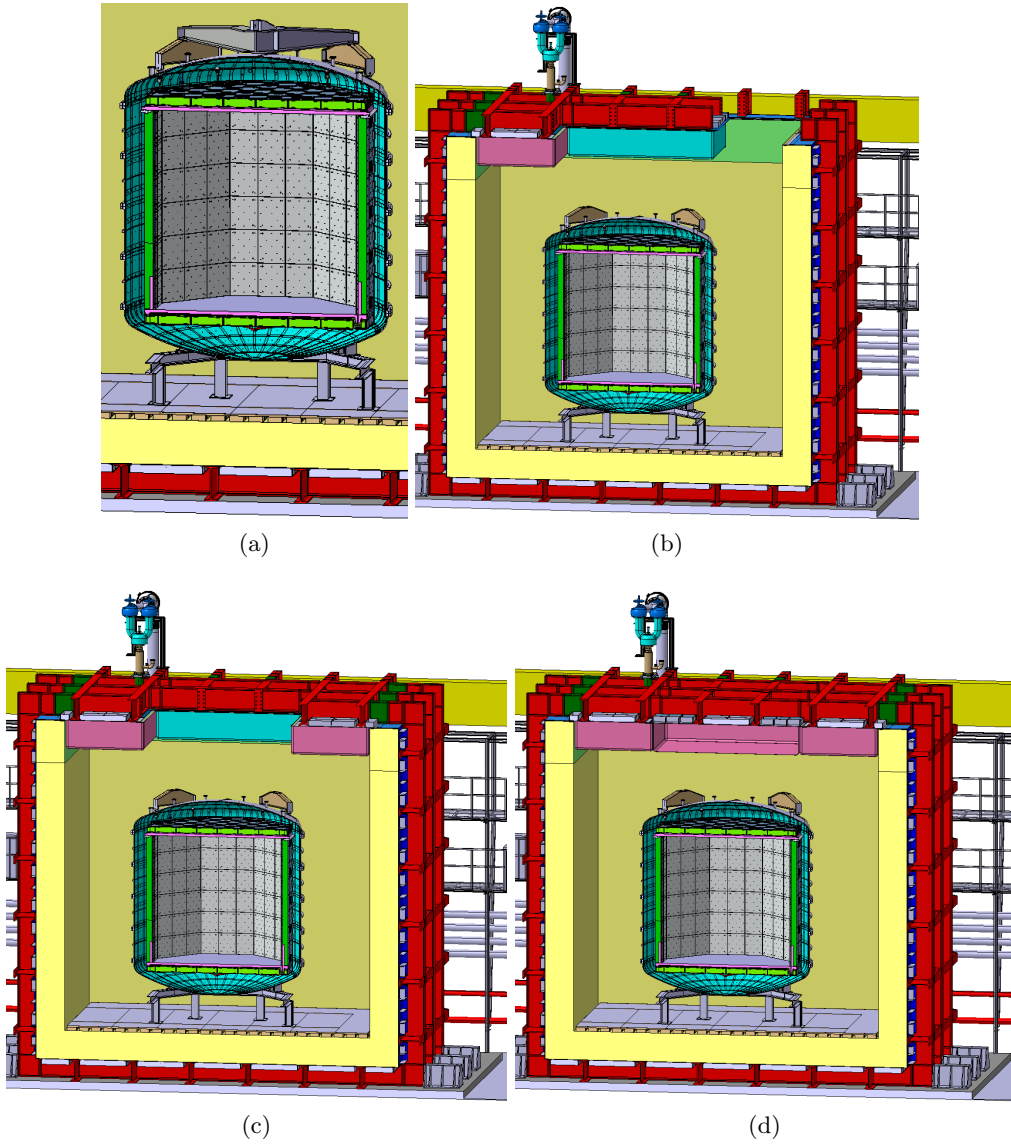


FIG. 158. (a) Detector insertion inside the titanium vessel. (b), (c), (d) Cryostat top caps installation: at first the top caps are only bolted to the rest of the structure waiting for the warm test of the full electronics and DAQ chain.

6020 are needed for filling, and this operation requires that the recovery compressor is already installed
 6021 and tested. The connection of TPC wire grid, first field cage ring, and the cathode will also be
 6022 continuously monitored during cooldown and filling.

6023

11.9. Detector commissioning

6024 We note here that the scope of this document ends with commissioning of the UAr cryogenics
 6025 system, described in section 11.8. This section gives a very brief outline of the order of operations
 6026 that follow for detector commissioning. The details of the AAr fill and detector commissioning plan
 6027 are the subject of a separate, future document.

6028 Once the AAr filling is complete, the UAr will complete a few days later. Then, when the
 6029 system is stable, the detector commissioning can begin. The UAr circulation loop will run at
 6030 full speed during filling, and will continue until S2 signals are observed. Following this, the lower

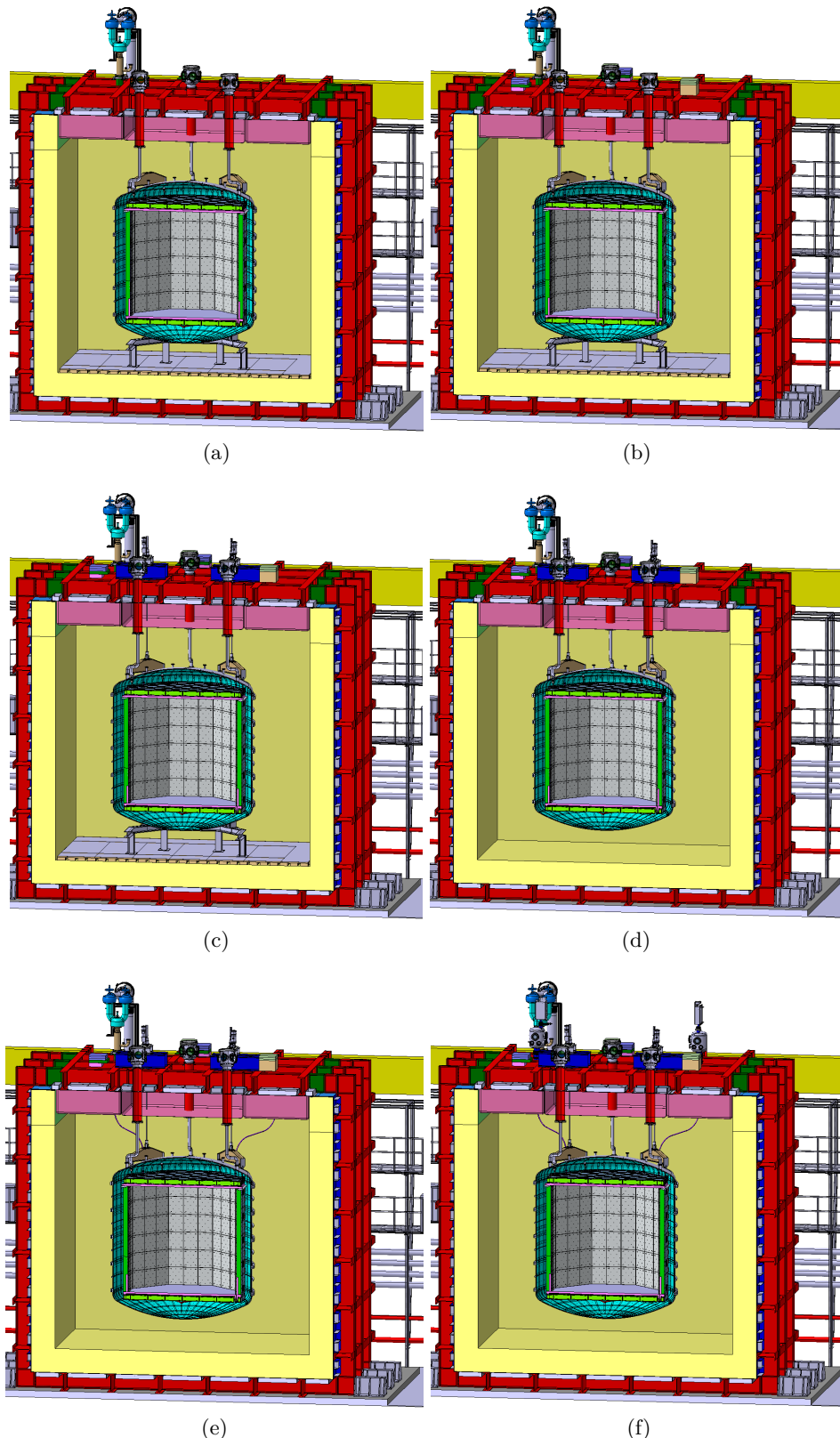


FIG. 159. (a) Chimney installation. (b) DAQ system installation. (c) Detector Support System (DSS) installation. (d) Detector lifting via DSS and removal of the temporary support structure and titanium vessel temporary feet. (e) Final piping connections. (f) Calibration equipment installation.

6031 circulation speed for operation can be determined. The gas pocket can then be created, and an
6032 electroluminescence field can be applied without a drift field. Final leveling adjustments can then
6033 be made by observing the S2 signal response across the horizontal detector plane. Once the detector
6034 leveling is complete, the HHV can be gradually increased while monitoring the argon purity. This
6035 process will continue until the design drift field is reached, and the readout and photoelectronic
6036 systems can begin commissioning.

6037 12. VALIDATION OF THE CHOICES AND EXPECTED PERFORMANCES

6038 12.1. Monte Carlo results for TPC key performance parameters

6039 This subsection describes how the proposed detector design and technical choices meet the physics
 6040 requirements, with respect to light output, pulse shape discrimination, xy reconstruction, and
 6041 dynamic range, which play a crucial role in detector sensitivity. The performance of the TPC was
 6042 evaluated using Monte Carlo simulation and reconstruction codes described in subsection 7.7.

6043 12.1.1. TPC Light Yield

6044 G4DS provides the accurate simulation of light production, propagation, and detection for back-
 6045 ground and signal events in the LAr TPC in order to fully reproduce the responses of the detector
 6046 in S1, S2, and time, the three primary variables on which the discrimination of β/γ background is
 6047 based. The light generation in LAr and GAr is handled using a custom Geant4 physical process,
 6048 since details of atomic excitation, ionization, nuclear quenching, and electron-ion recombination
 6049 effects are poorly known in argon, especially in the presence of strong electric fields. A theoretical
 6050 model based on an effective description of recombination was developed, which was tuned on cal-
 6051ibration data and is able to accurately describe the light response of DarkSide-50 in both S1 and
 6052 S2.

6053 Another critical ingredient of G4DS is the tuning of optical properties of the materials through
 6054 which light is propagated, and of the surfaces where light can be absorbed, reflected, or dif-
 6055 fused. These parameters were either tuned by comparisons with selected data samples from the
 6056 DarkSide-50 LAr TPC; or assumed from external measurements. Table L summarizes the materials
 6057 and the interfaces implemented in the simulations and the references to the underlying modeling.

6058 Under these assumptions, the probability for a 128 nm photon to generate a photo-electron in the
 6059 silicon of the TPC readout system is $19.39 \pm 0.05\%$, averaged across the whole active volume. Figure
 6060 160 shows the dependence of the detection probability on the vertical coordinate of the emission
 6061 location. The projected light yield, not including SiPM correlated noise sources, is 9.9 PE/keV at
 6062 null-field and 8.5 PE/keV at the energy of the ^{83m}Kr decay (41.5 keV) with the nominal drift field
 6063 of 200 V/cm.

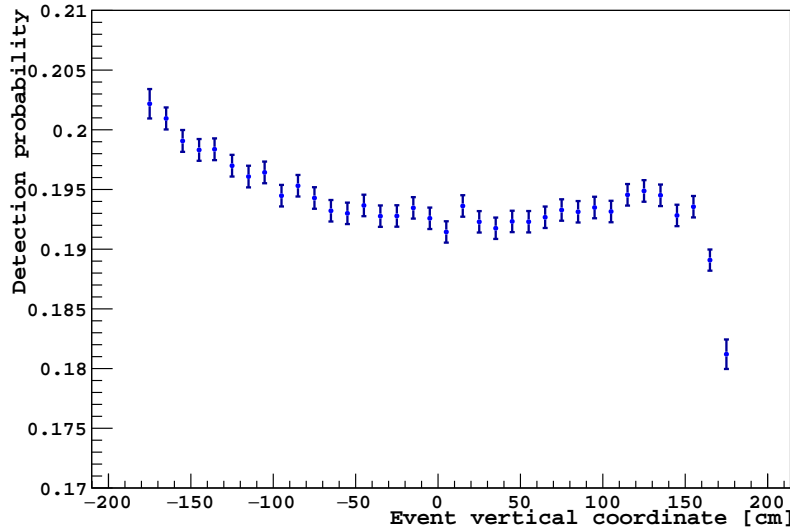
6064 The predicted light yield scales linearly with the PDE of the SiPM. While describing the PDE
 6065 wavelength dependence [1], we conservatively assumed a peak value of 40%. This is approximately
 6066 10% lower than the measured PDE reported in section 3.2.7. Reflectivity is also an important
 6067 contribution: as an example, assuming 95% reflectivity for the ESR reflector, rather than the
 6068 nominal 98%, would reduce the overall detection probability to 17.8% (8% relative reduction).

6069 12.1.2. PSD performance

6070 The pulse shape discrimination (PSD) power is attenuated by instrumental effects, such as pho-
 6071 ton propagation in the detector, light collection efficiency, SiPM time response, correlated and
 6072 dark noise, and reconstruction effects. The Monte Carlo sample statistics ($\sim 10^9$) needed to probe
 6073 the PSD power requires significant computing resources, preventing the use of the full DarkSide
 6074 Monte Carlo and reconstruction chain. The approach adopted here is therefore effective, based
 6075 on Geant4-simulated light maps, which accounts for the photon travel time. The SiPM photo-
 6076 detection efficiency (42%), as well as dark current rate (DCR) per Tile+ (5 Hz), Afterpulsing (AP)
 6077 per Tile+ (6%), direct cross talk (DiCT) per Tile+ (30%), and external cross talk (eCT) per Tile+
 6078 (25% emission probability), are accounted for in the effective model. The values given correspond
 6079 to operating SiPMs at 7 VoV, as reported in the measurements described in section 3.2.6. Each
 6080 hit time, where a hit corresponds to a SiPM avalanche induced either by photon or noise, is jit-
 6081 tered with a Gaussian term of 7 ns to account for the single photoelectron time resolution. The

Material/Interface	Value/Model	Reference
Center to TPC side		
UAr	VUV and visible absorption length: 100 m VUV scattering length: 45 cm Refractive index from experimental measurement.	[86], [87], [13]
UAr to TPB	Effective model for TPB WLS, with 100% absorption-emission efficiency, diffuse emission.	Model tuned on DarkSide-50 [13].
TPB to ESR reflector	Specular reflector, 98% efficiency for visible light.	Manufacturer specification.
Center to TPC Top		
UAr	Optical properties of UAr as described above.	
UAr to anode grid	Transmittance as function of angle implemented, with 95% transmittance at normal incidence	DarkSide-50 internal characterization
UAr to Gaseous Argon	Fresnel optics	
Gaseous Argon to TPB	Fresnel optics. TPB modeled as described above.	[87]
TPB to acrylic window	Acrylic absorption length and refractive index from DEAP-3600	[88], [89]
Acrylic window to UAr	Fresnel optics	
UAr to Silicon	Fresnel optics to determine reflected fraction. PDE vs wavelength for transmitted fraction (peak normalized at 40%).	[1]

TABLE L. in the G4DS simulation of the LAr TPC.

FIG. 160. Photon detection efficiency as a function of the vertical position of a scintillation event. $z = 0$ corresponds to the TPC center, the LAr-GAr interface is at $z = 175$ cm.

reconstruction efficiency of hit identification is estimated to be 97% (see subsection 7.7).

The PSD estimator, f_{200} , is defined as the fraction of light detected in the first 200 ns with respect to the $8 \mu\text{s}$ acquisition gate. Vertical slices of the S1 vs f_{200} 2D distributions, corresponding to a narrow S1 range, are used to determine the nuclear recoil (NR) acceptance as a function of f_{200} for each value of S1, and the corresponding expected electronic recoil (ER) background. The NR acceptance curve is calculated by requiring at most 0.1 ER background events in the full exposure (200 t·yr). We used an analytical fit to extrapolate tails at the levels of 10^{-9} for the ER distributions. The effective model used for the acceptance calculation, referred to as the “tail” model, was probed on both DEAP-3600 and DarkSide-50 data.

The NR acceptance is extracted as a function of S1 and then converted to a function of true NR energy, as shown in Figure 161. This distribution is shown considering no grouping of channels

6093 within a PDU (1x1 configuration), grouping channels 2x1 and grouping 2x2 (the selected baseline).
 6094 Grouping 2x2 has minimal impact on the NR acceptance; the slightly larger acceptance region
 6095 for the 1x1 configuration is explained by the lower hit occupancy per channel, which favors the
 6096 identification of hits.

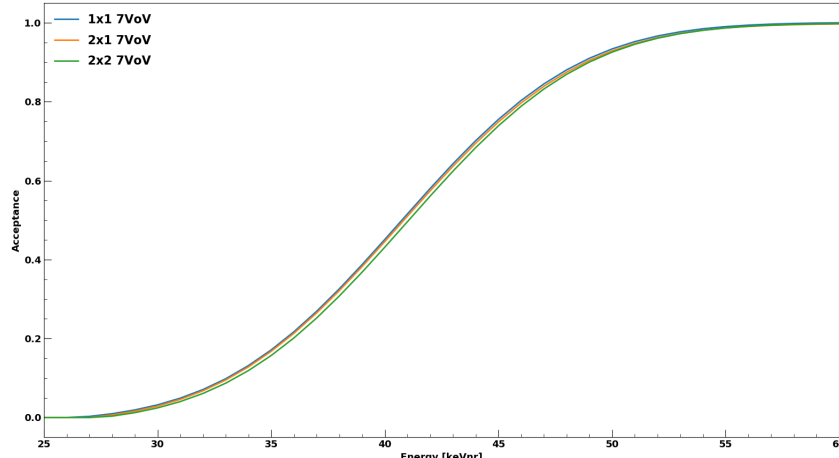


FIG. 161. NR acceptances for the 1x1, 2x1, and 2x2 configurations, assuming 7 Volt over voltage.

6097

12.1.3. Position reconstruction resolution

6098 The S2 electro-luminescence pulses, generated close to the top-array of photodetectors, are used to
 6099 localize the event in the horizontal plane. As the position reconstruction is used for fiducialization,
 6100 the fiducial volume (FV) background event rate will increase when events outside the FV are
 6101 incorrectly reconstructed as being inside the FV.

6102 The xy resolution of DS-20k was examined for three configurations: $5 \times 5 \text{ cm}^2$ Tile+ corresponding
 6103 to 1x1 grouping, $5 \times 10 \text{ cm}^2$ corresponding to 2x1 grouping of Tile+ in the PDU+ readout, and
 6104 $10 \times 10 \text{ cm}^2$ corresponding to 2x2 grouping (the baseline configuration). Simulations established
 6105 that an xy resolution better than 10 cm has a negligible effect on the FV event rates of uniform
 6106 background sources. For neutron-induced NRs and gamma-ray ERs which exponentially fall in
 6107 rate from TPC wall, an xy resolution of 10 cm leads to an acceptable FV rate increase of a few
 6108 percent relative to the 1x1 case.

6109 A sample of events in the WIMP search region distributed throughout the full TPC volume were
 6110 reconstructed using the charge barycenter for the $5 \times 5 \text{ cm}^2$ case, centered on the PDM with the most
 6111 S2 light. We demonstrated that when using $5 \times 5 \text{ cm}^2$ PDMs with a 1 cm offset, the projected xy
 6112 resolution for DS-20k is 1.77 cm, notably better than required. Similar results are obtained when
 6113 using $5 \times 10 \text{ cm}^2$ groups (1.83 cm resolution) or $10 \times 10 \text{ cm}^2$ groups (1.83 cm resolution) at the same
 6114 offset. No significant degradation of the resolution is observed near the periphery of the detector,
 6115 meaning the leakage of surface events in the FV will be minimal.

6116

12.1.4. Dynamic Range

6117 The dynamical range which can be achieved by a readout channel was assessed via Monte Carlo
 6118 simulations looking at two topical cases. Dynamic range limitation can occur at the level of the
 6119 single tile saturating, or at the summing stage of multiple tiles grouped together as in the baseline
 6120 2x2 grouping configuration.

In the first case, S1 signals from the highest energy ER background are considered. This background is due to the intrinsic radioactivity of SiPMs and comes from 2.6 MeV gamma rays originating from the bottom SiPM array where lower detection efficiency is expected. In the second case, S2 signals with energies corresponding to the upper bound for NR in the WIMP search region are considered. In both cases, different configurations are examined where both the SiPM arrays are offset by 1 or 5 cm together. Three Tile+ grouping options, 1x1, 2x1 and 2x2 (see Sec. 12.1.3 for details) are also studied. Moreover, the saturation is studied both in the full and in the fiducial volume of the detector, where the latter is defined by excluding roughly 40 cm from top and bottom of the TPC.

An event is considered saturated if the amplitude of the waveform in any readout channel exceeds the threshold determined by the electrical characteristics of the summing stage amplifier (described in section 3.3).

The analysis of the various configurations yielded the following conclusions. Saturation does not occur in the S2-NR sample regardless of the configuration. On the contrary, saturation affects the S1 of high-energy ER events ($\sim 9\%$ or $\sim 1\%$ in the full volume) when using $10 \times 10 \text{ cm}^2$ or $5 \times 10 \text{ cm}^2$ readout channels with 1 cm offset for the SiPM array. This effect is compensated ($< 0.1\%$) by moving the sensors away from the volume.

Saturation affects the linearity of the detector energy response when it is extrapolated to high energies. But, given the experience of DarkSide-50 this effect can be compensated, e.g. using a fraction of the S1 signal. Nevertheless, in the simulated cases although saturation is present for a fraction of high energy ER events, it does not alter the detector energy resolution at the absorption peak of the 2.6 MeV gamma ray guaranteeing a precise ER background model.

12.2. Monte Carlo simulation results on neutron Veto performance

12.2.1. Neutron veto inefficiency

The neutron veto efficiency was assessed in the full G4DS simulation by generating neutrons at their source positions, with rates based on radio-assay of detector materials, with the appropriate (α,n) energy spectra, propagating them through the full detector geometry, and applying the neutron rejection cuts listed in Sec. 5.8.4. The main groups of detector materials, their typical radioactivity content and their (α,n) neutron yield is listed in XXIX.

Simulations showed that there is a significant dependence of the neutron survival probability on the position of generation of neutrons, whilst this probability is only marginally affected by the initial energy spectrum. We identified the five most important topical positions in the detector for generating neutrons: the cryostat insulating foam, the gadolinium-doped acrylic panels making up the TPC walls, the veto PDUs, the TPC PDUs and the titanium vessel. Large statistics simulations of these neutrons were generated to assess the probability to induce a background event for each one of these locations.

A full optical simulation of the interaction of neutrons in the LAr TPC and surrounding Veto detector was performed to evaluate the neutron veto efficiency. A detailed optical model was implemented in the G4DS simulation code for the materials of the Veto based on the measurements described in Sec. 3.7. This optical model of PEN included refractive indices, absorption length, Rayleigh scattering length, wavelength shifter efficiency, emission time, the measured emission spectrum in cryogenic temperatures and optical surfaces between PEN and adjacent detector volumes. Furthermore, the simulation implements the parameters and models described in table L, the reflectivity of the walls of the Veto reflectivity of the SiPM surfaces (both active and passive parts) and the photon detection efficiency and fill factor of the SiPMs. The resulting mean light yield from simulating 1 MeV electrons releasing all their energy in the UAr is 2000 PE/MeV, with an RMS of 60.7 PE/MeV. Consequently, the resolution (RMS/mean), not including the effect of event reconstruction, is 3.0% averaged across the Veto detector. Fig. 162 shows the number of collected photoelectrons as a function of the z coordinate.

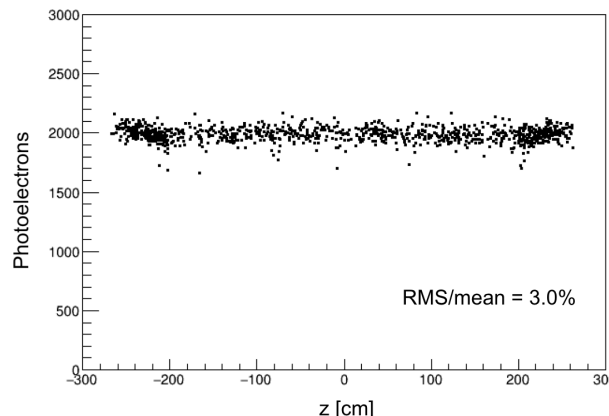


FIG. 162. Number of collected photoelectrons in the Veto as a function of the z coordinate. The results are from 1 MeV electrons releasing all their energy in the UAr.

Once generated, the neutron identification cuts are applied. These selection criteria, listed in Sec. 5.8.4, rely on using both the visible energy in the TPC and the Veto and requiring that these energy depositions coincide within a window of $800 \mu\text{s}$.

The first step of the analysis is to select WIMP-like NR events. A set of LAr TPC cuts requires that events have a single reconstructed (or multiple but unresolved) interaction in the TPC with a scintillation yield falling within the DM ROI, and be reconstructed as a NR-like event not rejected by PSD, with a vertex within the fiducial volume (FV). NRs depositing less than $0.4 \text{ keV}_{\text{nr}}$, corresponding to 2.5 e^- extracted in the gas phase, are not included in the NR-like single interaction count. The FV is defined as the volume contained by a surface of 30 cm removed from the lateral boundary and 70 cm from the top and bottom surfaces of the active UAr target.

The second step of the analysis is a search for energy deposits in coincidence with the WIMP-like NR event, in the TPC or in the Veto indicating a neutron capture following the NR event. The coincidence window, determined by the average capture times ($35 \mu\text{s}$ for captures on Gd, $200 \mu\text{s}$ for captures on Ar), extends up to $800 \mu\text{s}$ following the S1 of the NR event in the TPC. Events which deposit more than $50 \text{ keV}_{\text{ee}}$ in the TPC or $200 \text{ keV}_{\text{ee}}$ in the veto, within the time coincidence window, are tagged as neutron-induced.

The neutron detection inefficiency, using both the TPC and Veto to identify neutron captures in coincidence with NR TPC events, is defined as the ratio between the number of events that survive all the cuts and the total number of simulated events. Table LI reports the fraction of neutrons surviving after both TPC and Veto cuts.

The neutron detection inefficiency was also studied as a function of the Gadolinium doping concentration in the Gadolinium-doped acrylic, simulating neutrons from both Veto and TPC PDUs. The simulations have been done for a Gadolinium concentration of 0%, 0.05%, 0.2%, 0.5%, 1% and 2% in mass and the resulting inefficiency, after both TPC and Veto cuts, is shown in Fig. 163. On the basis of this study, 1% Gadolinium loading is selected, with a uniformity tolerance of 50% (discussed in section 3.8).

Neutron source	Fraction inducing at least 1 NR in the TPC	Fraction surviving TPC and WIMP ROI	Fraction surviving TPC and Veto cuts
TPC PDMs	1.80e-01	3.6E-5	2.2E-6
Veto Gd-Acrylic	8.55e-02	1.5E-4	5.8E-6
Veto PDMs	1.43E-02	5.4E-7	8.7E-7
Vessel	3.40e-03	6.8E-6	6.8E-6
Cryostat	4.0E-4	4.9E-9	2.2E-10

TABLE LI. Neutron Veto inefficiency from topical positions in the detector.

To calculate a more realistic value of the neutron detection inefficiency, a waveform simulation

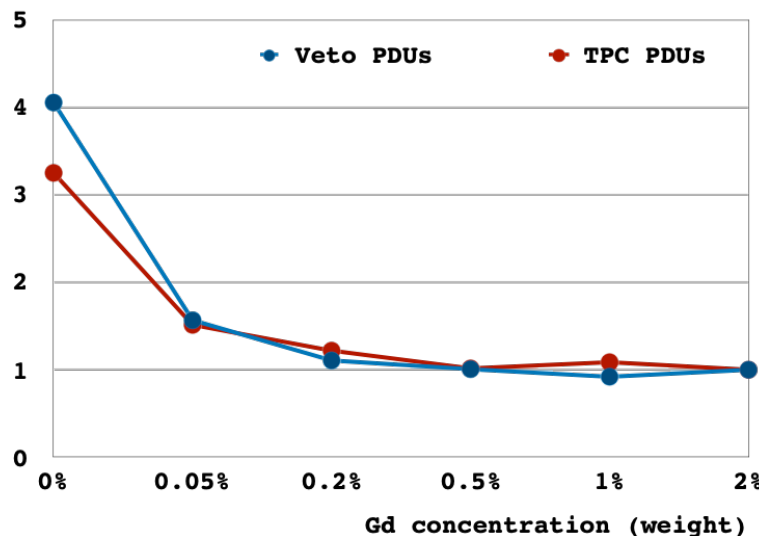


FIG. 163. Relative increase of the neutron tagging inefficiency for neutrons from the Veto PDUs and from the TPC PDUs as a function of the Gadolinium doping concentration.

6197 was developed taking into account SiPM noise sources (dark rate, afterpulsing, direct cross talk) at
 6198 their measured rates (section 3.2.6), electronics noise associated based on digitized veto PDM data
 6199 from the Genova test stand (shown in section 3.3.4), and pile-up with other source of background
 6200 (described in section 5.8.6). The waveform simulation starts from the Monte Carlo-generated opti-
 6201 cal photons that hit vPDMs, from the full neutron background simulation described above. The
 6202 electronics noise was simulated both as Gaussian (white noise), and using the measured noise power
 6203 spectrum vs. frequency from the Genova test stand. The simulation constructs a waveform con-
 6204 sisting of the neutron capture event SiPM signals superimposed with SiPM signals associated with
 6205 pile-up events coming from ^{39}Ar and γ s, simulated at their respective rates based on radioassays
 6206 in a coincidence time window of 800 μs .

6207 The neutron inefficiency is estimated in the waveform analysis with the same set of cuts, however
 6208 the energy cuts are applied to the reconstructed number of photoelectrons. A realistic voltage
 6209 vs. time waveform is generated as described above, and the hit reconstruction algorithm identifies
 6210 hits in the waveform; an example is shown in Fig. 164, left. The charge integral of each hit is
 6211 calculated. The charge integral is used to reconstruct the number of photoelectrons in a hit as it
 6212 most accurately reconstructs the true number of photoelectrons when after-pulsing and cross-talk
 6213 are included. Monte Carlo simulations were used to find the calibration factor between the charge
 6214 integral and the number of photoelectrons. The comparison of reconstructed and Monte Carlo truth
 6215 photoelectrons is shown in Fig. 164, right, and as expected the reconstructed value is higher as it
 6216 includes additional hits from direct cross talk, after-pulsing, and dark current. This distribution is
 6217 used to calculate the equivalent reconstructed photoelectron threshold corresponding to the Monte
 6218 Carlo truth threshold of 200 keVee deposited energy in the veto.

6220 The inefficiency is estimated in the waveform simulation as the fraction of events that pass the
 6221 TPC cuts but escape the Veto cuts, i.e. the fraction of events in which the number of detected
 6222 photoelectrons is lower than the threshold corresponding to a nominal energy deposit of 200 keV
 6223 in the VetoThis threshold is 570 photoelectrons, given the simulated light yield of 1.9 photoelec-
 6224 trons/keVee and the ratio of reconstructed to truth photoelectrons of ~ 1.5 , as shown in Fig. 164,
 6225 right. This analysis shows that the photo-detector response, noise effects and pile-up degrade the
 6226 expected veto performance for neutron identification by approximately 20% with respect to the
 6227 Monte Carlo truth analysis.

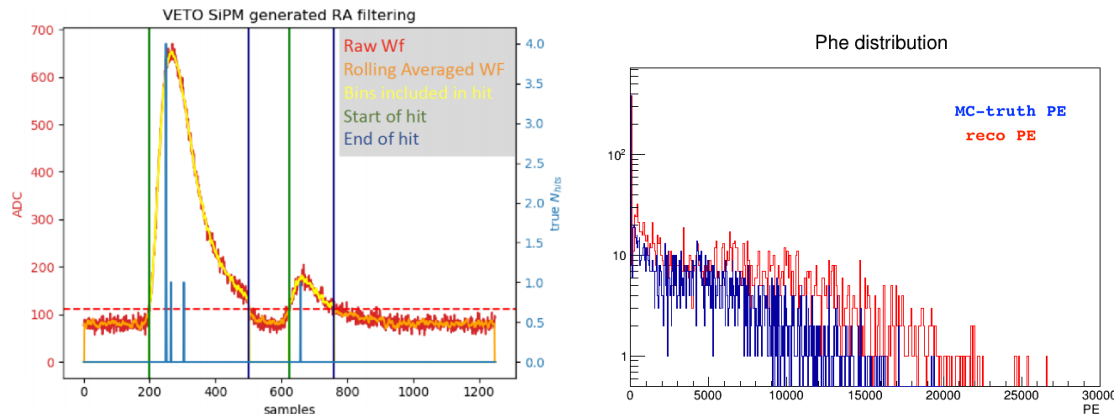


FIG. 164. Left: Example of the hit finding algorithm developed for the veto. This shows the raw waveform in red and the true phe generated in the montecarlo in light blue. It also shows the resulting waveform after the moving average ,orange, and shows the two sections of waveform that are detected as hits. Finally the start and stop times of the hits are shown by the dark green and dark blue lines respectively. The threshold used to determine a hit is shown by the red dotted line. Right: photoelectron distribution in the Veto in blue the MC truth photoelectrons, without noise effects, in red reconstructed photoelectrons, with noise effects.

6228

12.2.2. Dead-time induced by the neutron tagging strategy

6229 The dead-time is estimated as the probability to tag an event induced by ^{39}Ar decay or a γ -ray
 6230 interaction as neutron because it happens in coincidence with a true WIMP event within a time
 6231 window of 800 μs .

6232 The main sources of random coincidences with WIMP events within the time window ΔT are:
 6233 (i) the decays of ^{39}Ar in the inner Veto or TPC : (ii) events due to γ -rays depositing energy in the
 6234 inner Veto or TPC; and, (iii) pile-up events, which are two events of any of the previous categories
 6235 happening so close in time that we cannot recognize them as distinct events. Pile-up events can be
 6236 caused by two independent decays of ^{39}Ar in the same volume (veto or TPC), or by a decay of ^{39}Ar
 6237 and an independent γ interaction, or two γ interactions in the same volume. ΔT_p is defined as the
 6238 maximum time delay between two events originating a single pileup event. The value of ΔT_p may
 6239 depend on the details of the analysis algorithms and on their capability to separate events which
 6240 are physically distinct. Here we assume $\Delta T_p=200$ ns. The total dead time probability is obtained
 6241 as the sum of the contributions originated by all the different sources. We define

- 6242 • $R_{\text{Ar}}^{\text{TPC}}$ the rate of decay of ^{39}Ar in the TPC
- 6243 • R_{γ}^{TPC} the rate of energy deposit in the TPC of γ coming from any source in the detector.
- 6244 • $R_{\text{Ar},\text{Ar}}^{\text{TPC}}$ the rate of pileup of two ^{39}Ar decays in the TPC .
- 6245 • $R_{\gamma,\gamma}^{\text{TPC}}$ the rate of pileup of two γ events originating signals in the TPC .
- 6246 • $R_{\gamma,\text{Ar}}^{\text{TPC}}$ the rate of pileup of one γ event and one ^{39}Ar decay in the TPC.
- 6247 • $R_{\text{Ar}}^{\text{veto}}$ the rate of decay of ^{39}Ar in veto buffer
- 6248 • R_{γ}^{veto} the rate of energy deposit in veto buffer of γ coming from any source in the detector.
- 6249 • $R_{\text{Ar},\text{Ar}}^{\text{veto}}$ the rate of pileup of two ^{39}Ar decays in the veto buffer .
- 6250 • $R_{\gamma,\gamma}^{\text{veto}}$ the rate of pileup of two γ events originating signals in veto buffer .
- 6251 • $R_{\gamma,\text{Ar}}^{\text{veto}}$ the rate of pileup of one γ event and one ^{39}Ar decay in veto buffer.

6252 Given the energy threshold E , f_a^E is defined as the fraction of events of type a with energy above
 6253 threshold E . The rate of random events of any category with energy above the threshold is then
 6254 $f_{\text{Ar}}^E R_{\text{Ar}}^{\text{in}}$ and $f_{\gamma}^E R_{\gamma}^{\text{in}}$, $f_{\text{Ar},\text{Ar}}^E R_{\text{Ar},\text{Ar}}^{\text{in}}$, and so on.

6255 The rate of pileup of events of type a and b where a and b are Ar, Ar or γ, γ or Ar, γ in one
 6256 volume (TPC or veto) is

$$R_{a,b} = \frac{(2)}{\Delta T_p} \cdot (1 - e^{-R_a \Delta T_p}) \cdot (1 - e^{-R_b \Delta T_p}) \quad (4a)$$

$$\simeq (2) \cdot R_a \cdot R_b \cdot \Delta T_p \quad (4b)$$

with the approximate expressions holding when the argument of the exponential is $<< 1$ (i.e. the mean number of counts in ΔT_p is small). The factor 2 in parenthesis in relations 4 is present only if the two sources a and b are different. The dead time probability P_d^{in} (P_d^{out}) due to the events in one volume is then obtained by the following sum

$$P_d^{veto} = (P_d)^{veto}_{Ar} + (P_d)^{veto}_\gamma + (P_d)^{veto}_{Ar,Ar} + (P_d)^{veto}_{\gamma,\gamma} + (P_d)^{veto}_{Ar,\gamma} \quad (5)$$

with $(P_d)^{in}_{Ar}$, $(P_d)^{in}_\gamma$, $(P_d)^{in}_{\gamma,\gamma}$, $(P_d)^{in}_{Ar,\gamma}$ obtained by applying relation 4 including the energy threshold. Similar results are valid for the TPC. The total dead time is the sum of all contribution coming from veto and TPC

$$P_d = P_d^{veto} + P_d^{TPC}. \quad (6)$$

Considering the background rates reported in table XXXV, the estimated dead time due to accidental coincidence in the inner Veto region is 7.6%, while coincidences in the TPC contribute for an additional 6.1%. For this estimate a nominal coincidence window between the TPC and Veto signal of 800 μ s is used, and an energy threshold of 50 keVee in TPC and 200 keVee in the Veto is considered. A conservative estimate of the overall dead time from summing these two contributions gives a total dead time of 13.7%; this is conservative in the sense that it assumes the two contributions are independent, whilst in reality we expect a significant fraction of events to deposit energy in both TPC and Veto.

12.3. Pile up rate in TPC and overall acceptance loss

The WIMP signature is a single sited interaction in the FV, reconstructed as a one-S1 and one-S2 event. Events with one-S1 pulse and multiple S2 pulses are generally attributed to γ -rays, inducing multiple Compton interactions. In a traditional dark matter search, events with multiple S1 pulses within the same acquisition window are rejected, due to the uncertainty on the attribution of the S2 pulses to the corresponding S1. The probability of having multiple S1 events in a single acquisition window of 3.5 ms, corresponding to the maximum drift time, is calculated using the expected background rates from ^{39}Ar β -decays and γ -rays presented in table XXXV. Monte Carlo simulations accounting for the typical spatial distribution of these events are performed. Events with a non ambiguous topology, namely where there is no uncertainty on the S1 - S2 combination do not contribute to the acceptance loss estimation. It is found that 36% of the events exhibit a more complex topology, namely more than one S1 pulse in the acquisition window and not obvious attribution of the S2 pulses.

The same Monte Carlo simulation is used to evaluate the performance of a simple algorithm that uses position reconstruction along the vertical direction to reduce the rate of ambiguous events. Such an algorithm can exploit the S2 pulse width, which is proportional to the drift length, thanks to the longitudinal diffusion of drifting charges [16].

The effectiveness of this algorithm depends on the resolution of the vertical position reconstruction. With perfect resolution, the S2-based estimate of the vertical position will match the one obtained from the drift time, the S2-S1 time difference. Events where at least one S2 pulse can be attributed to more than one S1 pulse, due to finite resolution of the S2-based estimate, will contribute to the acceptance loss. The fraction of these unresolved events is 16.6% (8.5%) assuming a S2-based vertical position reconstruction resolution of 50 cm (25 cm). The acceptance loss induced

6295 by the pile up rate is correlated to the neutron tagging strategy. The combined acceptance loss,
 6296 obtained by running a dedicated Monte Carlo simulation, is 21.7% (17.3%) for a vertical position
 6297 reconstruction resolution of 50 cm (25 cm).

6298 The resolution upper limit (50 cm) is obtained from full simulation of S2 waveforms from NRs of
 6299 40keV originating in the fiducial volume. The waveform simulations include the effect of digitization
 6300 and reconstruction algorithms. The S2 pulse rise time is used as a proxy for the measurement of
 6301 the pulse width. The result is expected to improve when the photo-electron time distribution is fit
 6302 with an analytical function describing the expected signal shape.

6303 DarkSide-50 has demonstrated a vertical position reconstruction resolution better than 5 cm for
 6304 a drift length of 300 μ s, at an energy well above the WIMP ROI [16]. Work is ongoing to determine
 6305 the effectiveness of the combination of S2 and S1-based position reconstruction methods to further
 6306 reduce the acceptance loss induced by event pile-up.

6307 12.4. Random pile up and dust background sources

6308 We examined the possibility that pathological events producing S1-only and S2-only events may
 6309 combine to create random pile-up events that could be mistaken as nuclear recoils in the dark
 6310 matter ROI. The S2-only events of concern are due to ionizing events in the immediate proximity
 6311 of the internal TPC ullage - the gas pocket where the secondary scintillation signal S2 is excited. In
 6312 this region, owing to the very short drift length, a complete disentangling of the S1 and S2 signals
 6313 can be difficult, and their combination can be reconstructed as S2-only events. S1-only events
 6314 are instead expected at the TPC surfaces, and, specifically, S1-only events of possible concern are
 6315 those characterized by a timing profile possibly mimicking that of nuclear recoils, *i.e.*, α decays
 6316 (their random time coincidence allows them to appear to originate in the fiducial volume). U/Th
 6317 contaminants within the Gd-loaded PMMA, which is the construction material of the TPC barrel
 6318 and it is sited behind the ESR layer and separated from it by a LAr gap, produce very small S1 light
 6319 (more than a 8σ spread below the 50 PE lower edge of our ROI) due to the low light transmittance
 6320 of the ESR, and thus cannot be responsible for production of any background of relevance. The
 6321 role of all other sources of S1-only signals of potential interest was also duly evaluated: α 's from
 6322 the ESR surface and bulk, from the UAr layer filling the gap between the support PMMA frame
 6323 and the ESR, from the UAr region sitting in between the overlapping regions of the TPB-coated
 6324 ESR films, as well as α decays augmented by Cherenkov radiation in any PMMA layers. To
 6325 minimize the potential background associated with these sources, it is important that the TPC
 6326 construction strictly adhere to the following two recommendations: the overlapping gap of the ESR
 6327 films should be kept below 1 mm, and the specific composition chosen for the PMMA should contain
 6328 trace UV absorbers helpful in suppressing Cherenkov radiation. Under the working hypothesis of
 6329 careful enactment and deployment of the two recommendations, assuming for all other contributing
 6330 factor the most conservative scenarios, we determine that restricting the ESR surface α 's plate-out
 6331 activity below the required level of $30 \mu\text{Bq}/\text{m}^2$ is sufficient to keep the potential background from
 6332 these sources well below 0.05 events in the 200 t yr fiducial exposure of DS-20k. The maximum
 6333 allowable plate-out activity stated above as our requirement compares to the $20 \mu\text{Bq}/\text{m}^2$ record of
 6334 the ${}^3\text{He}$ proportional counters of SNO [90] and is significantly higher than the $500 \text{nBq}/\text{m}^2$ achieved
 6335 for the nylon containment vessels of Borexino [34, 91].

6336 We also explored the background impact of the potential presence of dust in the fiducial volume.
 6337 Signals mimicking nuclear recoils in the dark matter ROI could indeed be originated by α decays
 6338 from dust specks with linear dimensions of $O(10 \mu\text{m})$ or larger and embedded U/Th impurities.
 6339 Large dust specks floating inside the UAr fill are very dangerous, as they bring to the core of the
 6340 dark matter target extraneous materials that can absorb ionizing events without the production
 6341 of scintillation photons and electron-ion pairs: utmost care must be given to their mitigation and
 6342 control. α 's embedded in large dust specks inside the core dark matter target would lose all or
 6343 part of their energy in the non-scintillating speck material before reaching the UAr, where they
 6344 would deposit only a small part of their energy. The ensuing signal would be degraded in energy,

so that it could slip from the multi-MeV range below 100 keV, right in the nuclear recoil ROI for dark matter searches. These events would certainly provide a troubling source of background, as the timing characteristics of the S1 primary scintillation signal of stopping α 's directly mimics that of nuclear recoils.

The details of dust composition impact the fraction of α 's that appear in the region of interest, due to the different stopping powers. Figures 165, 166, and 167 show the distribution of energy deposits in the UAr target of α 's embedded in dust particles of different origin: the spectra shown in these figures demonstrate that the dust particles of concerns must have significant linear dimensions, $O(10 \mu\text{m})$ or larger, to result in the significant signal degradation required to shift the reconstructed energy of the event into the nuclear recoil ROI for dark matters. Dust specks with these linear dimensions, $O(10 \mu\text{m})$ or larger, are visible to the eye and can be safely eliminated from the dark matter fill via the insertion of sub- μm point-of-use filters in the rapid recirculation and purification loop.

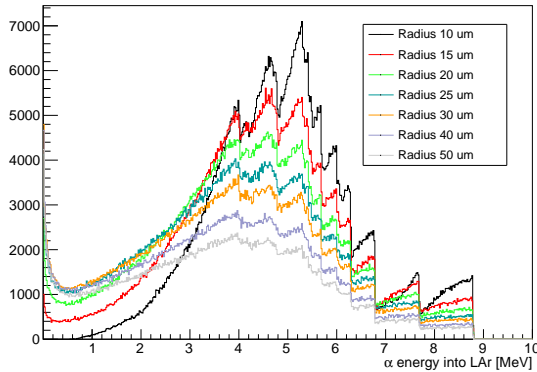


FIG. 165. The distribution of energy deposited in LAr due to alpha decays within Gd-loaded PMMA dust particles of various radii. For each radius 10^6 events are simulated. For larger dust radii the number of alphas reaching the LAr decreases resulting in less entries in the histogram.

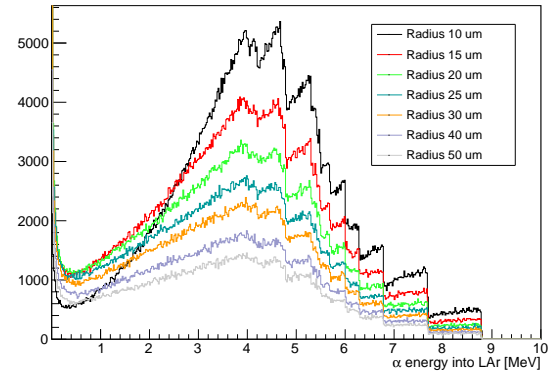


FIG. 166. The distribution of energy deposited in LAr due to alpha decays within Norite dust particles of various radii. This plot is produced with the same level of statistics as Fig. 165.

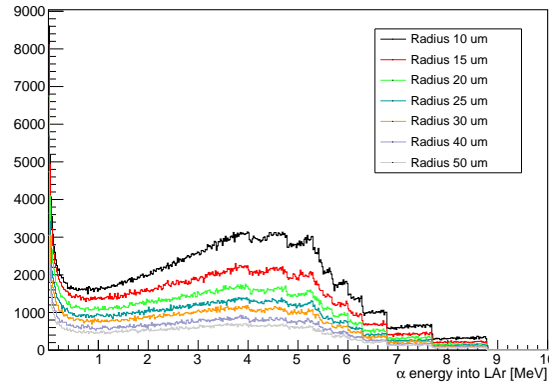


FIG. 167. The distribution of energy deposited in LAr due to alpha decays within copper dust particles of various radii. This plot is produced with the same level of statistics as Fig. 165.

Considering the above spectral distortions and fraction of spectra degraded in the ROI, making the worst case assumption of dust with ppm-level contaminants in U/Th, the tolerable amount of

dust in the UAr fiducial volume target is $5 \mu\text{g}$, which sets the DS-20k requirement. It is worth to note that similar considerations apply to all Xe-based TPC. We note that LZ plans to reach the same goal of reducing background from dust to a negligible level while relying on the requirement of 500 ng/cm^2 [27, 92] for dust contamination on a surface of the order of $O(10^6 \text{ cm}^2)$. A similar requirement is adopted in the construction phases of DS-20k inner detector. What makes this goal at all possible, in all two-phase noble liquid TPCs, is the combined presence of four strong mitigating factors: first, a very fast recirculation and purification loop (including the presence of a point-of-use sub- μm filter) needed to guarantee the noble liquid purity levels (ppt) of electronegative impurities allowing the very long drifts of free ionization electrons; second, the amount of dust which actually migrates from the surfaces and into the fiducial volume is expected to be very limited; third, only the inner TPC surfaces contribute, since the recirculation and purification loop introduces freshly purified and filtered noble liquid inside the active region of the detector, displacing liquid into the buffer (veto) region, where it is collected for recirculation; last, but not least, any dust speck in a TPC, if charged, will get trapped on detector surfaces due to the presence of very large electrostatics forces, or settle out if of different density.

A precise estimate or measurement of the numerical strength of the four mitigating factors described above, whose role is crucial in mitigating the migration of dust specks from surfaces to the UAr dark matter fill, is difficult. In addition, the complexity of the wetted surfaces of the DS-20k TPC is very significant, as they include:

- Clevios- and TPB-coated anode and cathode plates;
- Gd-loaded PMMA, with machined channels, each coated with Clevios, with coating edges accounting for a total length of 2 km;
- resistor voltage divider chains and mounting hardware;
- 576 cylindrical stand-offs;
- 144 PMMA backing plates;
- 144 TPB-coated ESR overlapping film sheets;
- 1872 push-pins;
- wire-frame and wire-grid;
- multiple HV feedthroughs;
- multiple ports for filling/draining.

In consideration of all of the above arguments and uncertainties, the Collaboration is intent in mounting the strictest program and protocols to ensure cleanliness and to prevent Rn plate-out through the procurement of all materials and construction of the detector. In particular, it will be crucial to apply to all materials composing the wetted surfaces of the TPC the well-known procedures for supervision of the production and, where needed, Rn deposition mitigation, in use for the procurement of materials and construction of the nylon film for the Borexino scintillator containment system and for the PMMA for the SNO heavy water containment system.

6397

12.5. Sensitivity Projections

The dark matter search sensitivity projections are carried out within the software framework discussed in 7.7, using a Profile Likelihood Ratio (PLR) approach, using predictions of the WIMP signal for masses in the $[50, 10000] \text{ GeV}/c^2$ range and the principal background sources described in section 5.8.4, including the irreducible neutrino background from coherent scattering off nuclei. The signal generation uses the canonical assumptions of the Standard Halo Model. The spatial distribution of the signal and neutrino components is assumed to be uniformly distributed in the volume. The neutrino component includes the solar, atmospheric and cosmic contributions and has an overall normalization error of 20%. The neutron component event rates and spatial distributions are extracted from full G4DS simulations of the detector geometry, including particle tracking and event selection as described in 5.8.4. The error on the normalization of the neutron components is set to 30%.

The PLR is based on three binned observables: S_1 , the reconstructed x - y position, the drift

time defining the z coordinate. A toy MC is used to simulate reconstruction effects, such as the S1 resolution due to the non-uniform collection efficiency, 1 cm resolution on the XY position and 1 mm resolution on the vertical coordinate. The toy MC generates, event by event, multi-dimensional spectra for signal and backgrounds. Each event is finally weighted by the NR acceptance determined by the PSD. The NR acceptance, given as function of the true recoil energy of Ar recoils, is shown in Fig. 161.

The NR acceptance is constructed by requiring that the surviving ER background will be < 0.1 events in the FV in the full exposure of 200 t yr. The surviving ER background, described by a uniform S1 distribution in both S1 and in the volume, is not included in the PLR analysis.

The nuclear recoil background is dominated by the neutrino component, with an expected rate of 3.2 events, weighted by the NR acceptance, in the FV in the full exposure of 200 t yr. The current expectation for the instrumental NR background is ~ 0.13 events, considering the contributions to the NR background in table XXVI which are estimated with confidence— coming from (α,n) neutrons from U and Th, Fission neutrons from U-238, neutrons from Rn-222 diffusion and surface plate-out, and neutrons from the lab rock. Including the contributions for which we have only upper limits— coming from cosmogenic neutrons and random surface α decay + S2 coincidence— approximately doubles this rate. Fig. 168 shows the relative change of the discovery reach as a function of the sum of NR backgrounds for various WIMP masses. The relative change of discovery reach is defined as the ratio between the minimal WIMP-nucleon cross-section at which it is possible to claim a 5σ discovery with increased background and the same quantity computed at the nominal background levels. Fig. 168 shows that doubling the background expectation to account for the uncertain background contributions modifies the discovery reach by $< 5\%$. The scaling as a function of the NR background scaling factor is the same for both the discovery reach and the exclusion potential.

The PLR approach is used to perform a search exploiting the whole active volume rather than the FV only. The signal and background probability distribution functions are extended to the whole active mass. The NR background components are, in this case, dominant compared to the neutrino background. The spatial and energy characteristics of the various fit components are used to discriminate between signal and backgrounds. Using the assumptions described above, and neglecting the NR acceptance change due to the increased ER statistics, the gain in sensitivity of this approach, with respect to the FV only search, is shown in Fig. 2 for both discovery and exclusion.

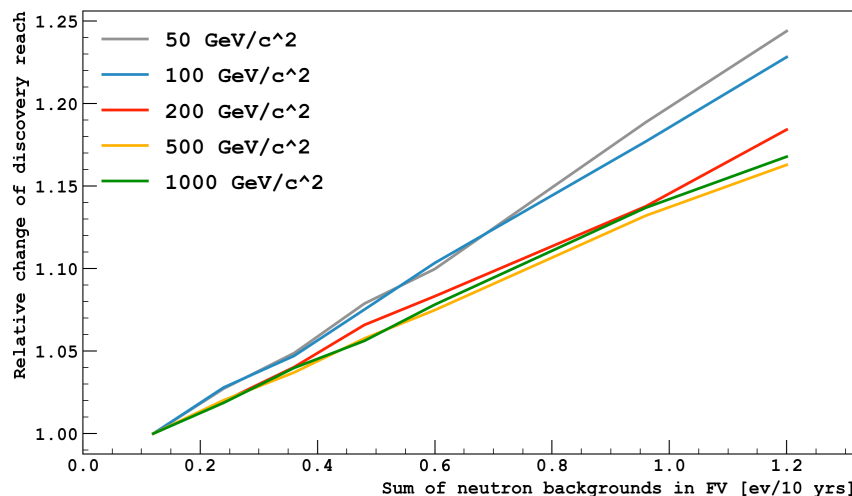


FIG. 168. Relative change of the discovery reach as a function of the sum of NR backgrounds for various WIMP masses.

6442

12.6. Validation Studies for the DAQ system

6443

12.6.1. TPC Readout Data Rates

6444 The expected data rate flowing from digitizers that read out the TPC detector (Sec. 7.6.1) to
 6445 the FEPs (Sec. 7.6.3) nodes is discussed within this section.

6446 This estimate depends on the background rates and the detector design. We study the dependence
 6447 on the number of SiPM tiles summed together to form a single readout channel. The current design
 6448 based on the PDU+ design implies summing 4 Tile+ together.

6449 For this study two assumptions are made about the DAQ. The first assumption is that the number
 6450 of FEPs is 16 regardless of channel summing. In the case where PDM channels are summed together
 6451 and fewer digitizers are used the number of digitizers per FEP will be reduced. In particular the
 6452 hypothesis of 8 digitizers per FEP node is studied when considering every single SiPM tile as a
 6453 readout channel (1x1 grouping), 4 digitizers for each FEP in the case of summing 2 tiles (2x1
 6454 grouping), and 2 digitizers for each FEP in the case of the sum of 4 channels (2x2 grouping).
 6455 Uniform assignment of readout channels from top and bottom optical planes to each of the digitizers
 6456 is assumed for load balancing purposes in all scenarios. The second assumption about the DAQ
 6457 regards the behaviour of the digitizers. They are assumed to identify pulses within the waveform
 6458 and forward waveform segments of a predefined length to the front end processors (FEPs). Further
 6459 compression, such as the extraction of charge and time of the pulses (QT), is assumed to occur
 6460 past the digitizer level of the DAQ, as discussed in Sec. 7.6.

6461 The mean data rate into all the FEPs can be calculated analytically using Eq. 7. B is the sum
 6462 is over individual backgrounds, where R_B is the activity of the background in Bq, f_B is the trigger
 6463 efficiency of the backgrounds (taken to be the probability that the decay produces at least one PE
 6464 in the TPC) and \bar{D}_B is the mean data produced during the events which trigger detector.

$$I = \sum_B R_B \times f_B \times \bar{D}_B \quad (7)$$

6465 The two final terms in Eq. 7, f_B and \bar{D}_B , are obtained using MC simulation of the background
 6466 within the detector. f_B is obtained by dividing the number of events which produce at least 1
 6467 photo-electron (PE) in the detector by the total number of events simulated. The second term \bar{D}_B
 6468 is more complicated to evaluate. It is calculated by combining the true PE times from the G4DS
 6469 simulations into waveform segments by emulating the digitizers. The data size is then calculated
 6470 from these waveform segments. It should be noted that this study does not consider the impact of
 6471 afterpulsing and optical crosstalk within the SiPMs on the data rate, therefore the actual rate will
 6472 be approximately 10% higher than the one calculated here.

6473 To calculate the waveform segments the following procedure is used. First, depending on the
 6474 channel summing the PE on various channels are grouped together. After the channel grouping
 6475 the PE for each channel are sorted in time. The PE are then iterated through; when a PE is
 6476 found, a waveform segment is created within a fixed predefined length. The code then looks at
 6477 subsequent PE and checks whether their waveform segments overlap. If they do overlap then the
 6478 waveform is extended to encompass the subsequent PE. The extension of the waveforms can be
 6479 done in multiple ways. For the variable extension, the waveform segment is assumed to be able
 6480 to have any length (in samples), the end of the waveform segment is defined such that there is a
 6481 certain gap between the last PE in the segment and the end of the waveform, to ensure the tail of
 6482 the SiPM pulse is contained within the waveform segment. For the fixed extension, the waveform
 6483 segments are assumed to only have a base length and are only allowed to have a length of multiples
 6484 of this, for example a waveform with a base length of 625 samples ($5\ \mu\text{s}$) would only be allowed
 6485 to have a length of 625, 1250, 1875 samples etc., for multi PE segments the waveform segment is
 6486 extended by the fixed amount until there is a certain gap between the last PE in the segment and
 6487 the end of the waveforms.

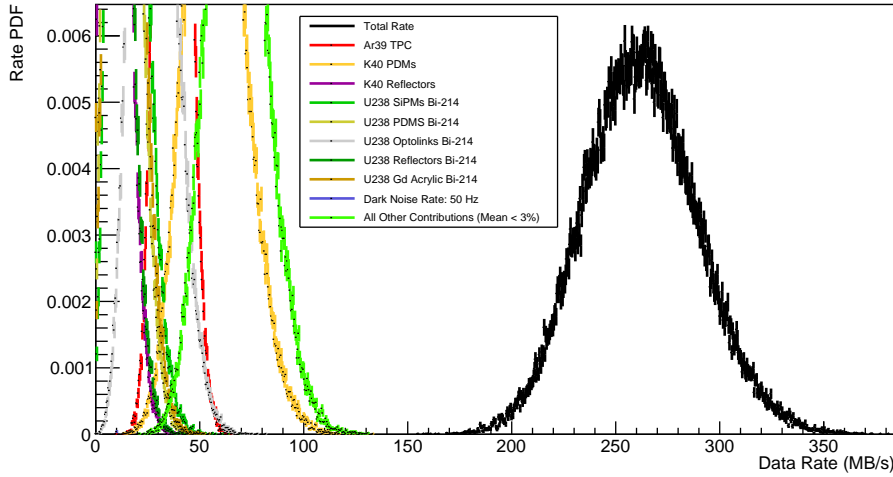


FIG. 169. The data rate contributions of the various backgrounds in the TPC. The distributions assume a $5 \mu\text{s}$ base window with a fixed extension size. The graph shows the scenario with two individual SiPM tiles summed in a single readout channel.

6488 After the waveform segments have been constructed, the size of the waveforms (in bytes) can be
 6489 calculated. The size of a waveform segment is given below in Eq. 8 where D_H is the size of the
 6490 waveform header (in the following studies this is assumed to be 8 bytes), L_W is the length of the
 6491 waveform segment in samples, and the factor 2 is due to the fact the digitizer uses 2 byte words
 6492 for each sample.

$$D_W = D_H + L_W \times 2 \quad (8)$$

6493 The data for each background is then given by summing up all the waveform segments for a
 6494 simulated event $D_B = \sum_W D_W$. The mean data per event \bar{D}_B is the mean amount of data per
 6495 event for all the simulated events for a given background event.

6496 A ToyMC performs a similar calculation but takes into account fluctuations in the rate and data
 6497 per event to get a mean and spread in the expected data rate due to the backgrounds.

6498 Figure 169 shows the data rate broken down into the various backgrounds. The dominant back-
 6499 grounds are due to gamma emitters in the photo-detector assembly and the ^{39}Ar in the TPC.
 6500 Figure 170 shows the total data rate into a single FEP node with a comparison of the fixed exten-
 6501 sion and variable extension algorithm in the digitizers. The variable extension results in a slightly
 6502 lower rate due to the increased flexibility in the length of the waveform segment. The theoretical
 6503 bandwidth limit imposed by the digitizer output channel is also shown. A standard 1 GbE link
 6504 saturated by each of the digitizers connected to a FEP will in fact correspond to a maximum input
 6505 of 8 Gbps = 1000 MBps for the single tile readout scenario with 8 digitizers per FEP. This number
 6506 reduces to 500 MBps and 250 MBps for the 2x1 and 2x2 grouping scenarios respectively.

6507 It can be seen that summing 4 channels results in little margin available to cope with corre-
 6508 lated pulses not accounted for in this study, network inefficiencies, possible unexpected higher rate
 6509 from detector materials, and, more importantly, from the need to leave some spare bandwidth for
 6510 increased interaction rates during calibration runs using external or internal radioactive sources.

6511 Possible mitigation measures include the use of a yet unavailable 10 GbE (effectively 2.4 Gbps)
 6512 speed link out of the digitizers, more aggressive data compression strategies (Sec. 12.6.3), and, lastly
 6513 the use of fewer channels instead of fully populating the 64 channels available in each digitizer board.
 6514 Thus the baseline configuration described as the conservative estimate in section 7.6 is to populate
 6515 half the available channels in each digitizer board, to maintain appropriate safety margin.

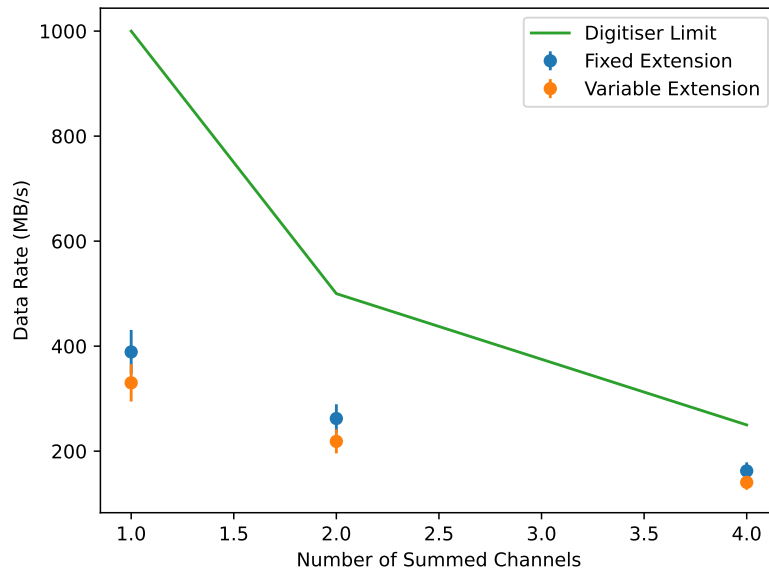


FIG. 170. The effect of summing channels and varying the waveform segment extension criteria on the data rate. Also shown is the limit imposed by the 1 Gb connection on the digitizers. The uncertainty on the rates are calculated using the ToyMC procedure described in the text.

6516

12.6.2. Studies and test with DS-Proto0 data and other test data

6517 In this section we report on studies that were completed using DarkSide-Proto0 data taken in Nov
 6518 2019 at CERN, together with data obtained from tests performed at liquid nitrogen temperature
 6519 with single tiles at LNGS, and with several complete PDU prototypes in the PDU test facility at
 6520 Napoli.

6521 The data taken with a laser provides us with a unique opportunity to prototype and test the
 6522 proposed DAQ front end software. The light arrives at a fixed time and we can do a simple baseline-
 6523 subtracted charge integration within a fixed window to the photon "truth" information which allows
 6524 us to test various analysis schemes for their efficiency and information loss. The two data taking
 6525 environments were very different - at LNGS the waveforms were sampled at 1 GHz in a very quiet
 6526 environment for single tiles whereas in DS-Proto0 is a real TPC with a built in radioactive source
 6527 and much noisier electronics due to imperfect grounding and a preliminary signal transmission
 6528 stage. Both of these are extreme compared to what is expected in DS-20k.

6529

Exponential Filter

6530 The average waveform over ~200K laser events for a tile at 6 VoV LNGS is shown in figure 171.
 6531 Due to the high laser occupancy (86%) this is not strictly speaking a single photoelectron trace
 6532 but corresponds roughly to 2.15 PE. One feature of the shape is the "gaussian spike" (RMS of
 6533 12.6 ± 0.7 ns from the fit in red). It is quite pronounced in the average of the LNGS test data
 6534 but much less so in the DS-Proto0 data, in part due to the slower sampling, cable termination and
 6535 much higher superimposed high frequency noise. The recharge tail on the other hand is unique to
 6536 real pulses and sampled over many points with high statistics, and is thus a robust feature. The
 6537 cyan curve shows an exponential fit with a time constant of 533 ± 14 ns. It is therefore natural to
 6538 consider using an exponential type filter. Exponential type filters are very good simple first pass
 6539 filter that can easily be implemented in the FPGA. Figure 171 (right) shows a trace in blue with the
 6540 exponentially filtered waveform in red. The smoothing of the noise is obvious and the separation

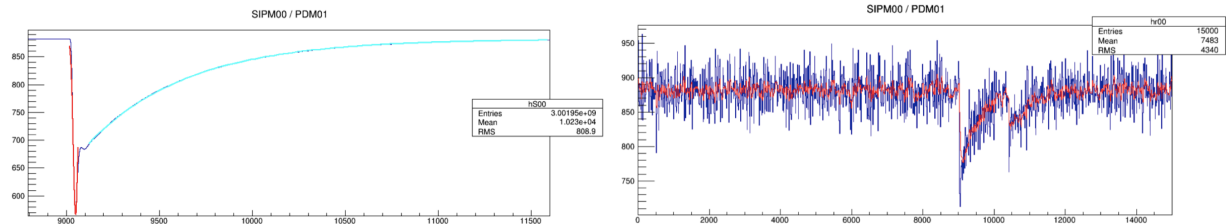


FIG. 171. **Left:** Single tile PDM from averaging laser events in the LNGS setup at 6 VOV. **Right** Exponential filter (in red) overlaid on a typical DS-Proto0 event with two nearby PE

and definition of the two pulses is quite clear. However it ignores the gaussian feature which means we cannot use it as a measure of charge or prominence but for pulse finding it is expected to be high performance for isolated photo-electrons.

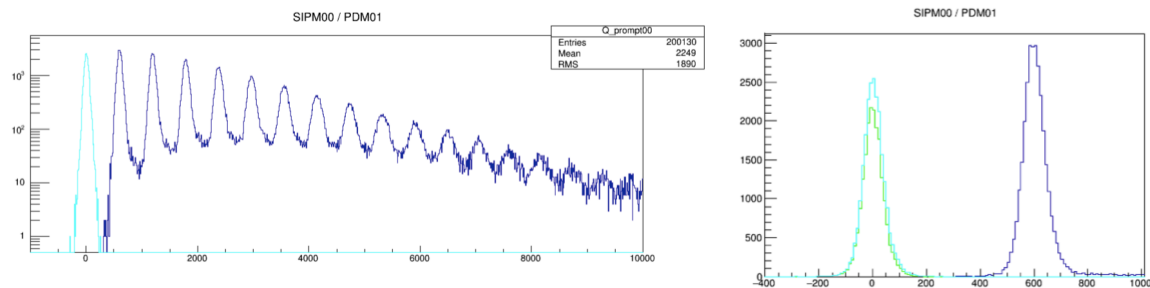


FIG. 172. **Left:** Charge spectrum from LNGS laser data with exponential filtered data (see text). **Right** Exponential filter finder compared to a simple threshold pulse finding algorithm

A charge spectrum from the LNGS tile data is reported in Fig. 172, left. Overlaid on the data are (in cyan) events where the exponential pulse finder did not fire. The cyan and the blue curves are identical below $1/3$ PE. This means that the exponential filter has a 100% efficiency for finding pulses above $1/3$ photoelectron and no 0 photoelectron events are misidentified as real ones or more than single photoelectron events. On the expanded right hand panel of Fig. 172 we show, overlaid in green, events where a conventional threshold type trigger did not fire. The green curve is well within the cyan which means that the conventional threshold type trigger is less effective than the exponential in rejecting 0 photoelectron events. The mislabeled fraction is a very steep function of the threshold. The exponential trigger on the other hand is much less sensitive due to the SNR being much higher in the exponentially-filtered data. For the DS-Proto0 data the results are essentially the same for the exponential pulse finder with 100% above $1/3$ of a photoelectron and no misidentified events below. This is encouraging since the noise level and the number of random pulses are considerably higher in DS-Proto0.

6557

Feature Extraction

Accurate timing information is somewhat harder to extract than just finding or separating pulses, without a lot of processing. The timing generally relies on many fewer points of the waveform (e.g. the leading edge) rather than the entire tail for pulse finding. Using a matched filter is CPU intensive and requires stability of the signal shape over time and intensity. Consequently it is desirable to investigate simpler methods like deriving the timing from, for example, the zero crossing of a running average trapezoidal filter, or a constant fraction type filter. Such filters are easy to implement and are, to a very high degree, pulse height independent. Figure. 173 shows a histogram of the trapezoidal zero-crossing time for the first event within the prompt laser window

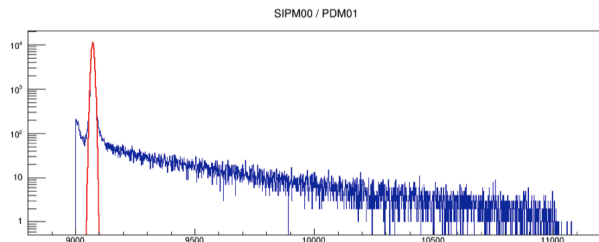


FIG. 173. Arrival time of signal as determined by a trapezoidal filter using zero crossing algorithm.

6566 used for the charge integration. The "upturn" at early times is due to tails from random pre-laser
 6567 photons. A fit to the peak (in red) shows an RMS of 6 ns which is within the specification for timing
 6568 resolution (section 3.4.1). The continuum is sloped as one would expect from random pulses. The
 6569 equivalent DS-Proto0 data has a somewhat worse RMS at 7.7 ns and the background is almost flat
 6570 due to the much higher random rate but the method still works.

6571 *12.6.3. Data compression in the frontend*

6572 Most data reduction in the readout boards is obtained by suppressing the baseline data outside
 6573 of the self-trigger window and automatically adjusting the acquisition window length to match the
 6574 actual duration of the pulse. Additional compression can be applied (either at the digitizer board
 6575 level or at the front-end server level) as a safety measure against inaccuracies in the data-flow
 6576 predictions or against potential network limitations.

6577 These compression algorithms may include a combination of lossless and lossy techniques:

- 6578 i) Removing part of the LSB of the message may result in a bandwidth saving of at least 25%
 (the ADC effective number of bits is 12, to be compared with the 16 bit word used for each
 sample). Further compression is possible when also considering the (dominant) electrical
 noise not originating in the ADC.
- 6582 ii) Downsampling of the raw waveform (from 125 MSPS to 62.5 MSPS) does not have an appre-
 ciable impact on the reconstruction performances, while saving a factor of 2 in bandwidth.
- 6584 iii) Prediction based on low-order polynomial extrapolation (i.e. delta or delta-of-delta) allows
 the encoding of prediction errors (differences between input samples and predictions) featur-
 ing distributions concentrated around zero. When followed by Fibonacci or Huffman encoding
 (with a dictionary updated once per run at most), can be applied to the MSB of the mes-
 sage. This compression is lossless and does not degrade reconstruction performances. When
 applied to single-photoelectron pulses, preliminary studies of these algorithms demonstrate
 a compression factor of 1.5 (1.35) for 5-us windows sampled at 125 (62.5) MSPS. For long-
 period waveforms sampled at 250 MBPS with 14-bits ADCs (DarkSide-Proto0), compression
 factor is greater and equal to about 2.3 (6 bps). Downsampling of the waveforms performed
 by averaging two and four samples deteriorates results by about 1 bps and 1.5 bps, respec-
 tively. This corresponds to a compression factor of 2 and 1.86, respectively. A slightly lower
 compression factor is expected on windows containing multiple overlapping photoelectron
 pulses.
- 6597 iv) Linear Predictive Coding (LPC) applied after prediction based on low-order polynomial ex-
 trapolation enables a further improvement of the compression efficiency. LPC uses FIR filters
 to utilize correlations between samples in close neighborhoods. For long-period waveforms
 sampled at 250 MBPS with 14-bits ADCs (DarkSide-Proto0), compression factor is in the
 range 2.57-2.67 (5.25-5.45 bps) and depends on the filter length and the extrapolation poly-
 nomial order at the preceding processing stage. In particular, the best results are achieved
 for delta prediction (zero order polynomial). When computing the prediction with LPC filter,
 the main improvement comes from the correlation from several directly preceding samples.
 For example, the improvement in bit rate between four-tap and 16-tap filters is 0.04 bps and

- 6606 0.12 bps when the preceding processing stage utilizes delta and delta-of-delta predictions,
 6607 respectively. All these results are summarized in Table LII for the entropy limits, i.e., pre-
 6608 sented results neglect small deterioration (a few hundredths of bps) introduced by Huffman
 6609 coding.
- 6610 v) The study on compression efficiency for pulse selection (windowing) was performed taking into
 6611 account the processing described in point iv. Pulse detection was implemented by thresholding
 6612 signal with reference to median waveform value. The threshold was calculated as a 10-fold
 6613 variance of the waveform. Results are slightly worse compared to long-period waveforms, as
 6614 summarized in Table LIII.
- 6615 vi) Downsampling of input data with the factor of two involves bit rates increased by 1 bps
 6616 when leveraging LPC. This increase is similar to scenario without LPC, however, LPC itself
 6617 improves the results by about 0.5 bps also for downsampled waveforms. Huffman coding
 6618 usually introduces some redundancy to output codestreams as codewords cannot assume
 6619 fractional bit numbers. The conducted study proves that the redundancy (bit rate increase
 6620 with respect to entropy) is smaller than 0.03 bps. Results for downsampled waveforms are
 6621 summarized in Table LIV separately for long-period waveforms and pulses.
 6622 Overall, a data-reduction of a factor of about 2 for lossless compression is expected to be reached
 6623 in the frontend after downsampling. The main factor limiting the compression efficiency is noise
 6624 present in acquired waveforms. When discarding LSB bits from input samples, the compression
 6625 factor can be significantly increased (3, 4 or more) since noise affects mainly these bits. However,
 6626 this comes at the cost of distortions/losses introduced to the signal. An alternative lossy method is
 6627 the quantization of prediction errors after LPC. With this method, the losses can be lower at the
 6628 same bit rates.

	Filter Order			
	4	8	12	16
Prediction at first stage	4	8	12	16
Waveform median	5.2916	5.2731	5.2711	5.2636
Polynomial 0	5.2632	5.2413	5.2352	5.2209
Polynomial 1	5.4260	5.3744	5.3529	5.3043
Polynomial 2	5.6797	5.5785	5.5359	5.4465

TABLE LII. Entropy limits of waveform compression for different prediction methods at the first processing stage and different filter orders at the second/LPC stage, for 10 μ s long waveform without selection.

	Filter Order			
	4	8	12	16
Prediction at first stage	4	8	12	16
Waveform median	5.4240	5.3888	5.3874	5.3828
Polynomial 0	5.3959	5.3956	5.3845	5.3910
Polynomial 1	5.4952	5.4768	5.4695	5.4538
Polynomial 2	5.7049	5.6383	5.6123	5.5632

TABLE LIII. Entropy limits of waveform compression for different prediction methods at the first processing stage and different filter orders at the second/LPC stage, for 10 μ s long waveform, passing a threshold of 10 times the variance

	Waveforms		Pulses	
	Polynomial 0	Polynomial 1	Polynomial 0	Polynomial 1
Entropy - no LPC	6.9281	7.0458	7.3312	7.2286
Entropy - LPC	6.4362	6.5219	6.8123	6.8913
Huffman bit rate for LPC	6.4642	6.5424	6.8350	6.9148
Huffman redundancy	0.0280	0.205	0.0227	0.0235

TABLE LIV. Bit rates for waveforms and pulses downsampled with a factor of two

6629

13. SAFETY AND ENVIRONMENTAL ASPECTS

6630 The GADM Collaboration aims at establishing outstanding performance in matters of Health,
6631 Safety and Environment (HSE). The whole experimental collaboration is involved in the effort to
6632 achieve these targets. During the DarkSide-50 installation at LNGS, the collaboration acquired a
6633 strong safety background. We can rely on skilled researchers, technicians and professionals with
6634 proven experience in the design, construction, commissioning and operation of complex plants.
6635 All aspects of the experiment, both technical and managerial, are handled in conformity to all
6636 applicable US, European and Italian HSE Regulations and Standards, as well as to the LNGS
6637 internal guidelines and procedures.

6638 The collaboration continues to develop and adopt its own policy statements and safety manage-
6639 ment planning documents, in accordance with the ISO and OHSAS codes. In cooperation with the
6640 LNGS HSE Staff, Environmental and Safety handbooks, procedures and operating instructions are
6641 developed and carefully applied for relevant activities and for the management and operation of
6642 the experimental process plants.

6643 As stated above, the intent of the GADM Collaboration is to continue, and if possible, enhance
6644 the performance in environmental, healthy and safety (EHS) matters, fulfilling the LNGS Policy.
6645 For this reason, all collaboration members will be mandated to follow the relevant EHS regulations
6646 during all the phases of life of the experimental apparatus.

6647 In detail, the filling of any detector volume and any other operations involving fluids, and/or
6648 potentially generating waste materials, will be performed in accordance with Italian regulations,
6649 UNI EN ISO regulations and the prescription of the LNGS Environmental Management System
6650 (EMS) and Safety Management System (SMS). Moreover, DS-20k will draft procedures and operat-
6651 ing instructions designed to minimize and manage EHS hazards and risks estimated with the guide
6652 of the LNGS Environmental and Safety Protection Services. A crucial point of the LNGS MS is
6653 the appointment of a Collaboration member as GLIMOS & RAE (health/safety and environmental
6654 contact of the experiment). The GLIMOS & RAE acts as the link-person between the experimental
6655 collaboration and the LNGS MS for all the subjects concerning the EHS impact. The GLIMOS &
6656 RAE is appointed by the LNGS Director upon recommendation by the Collaboration management.

6657

13.1. Italian and European and Regulations

6658 The GADM Collaboration will comply with all European Directives and corresponding Italian
6659 Regulations throughout the design, construction, commissioning, operation, and management of
6660 the DS-20k apparatus and plants.

6661 The relevant HSE Italian Regulations will be applied in DS-20k in order to fulfill all legal re-
6662 quirements ensuring the safety of personnel, of the experiment and of all the related infrastructures
6663 and facilities.

6664 In particular, the DS-20k design will strictly follow the Italian anti-seismic regulations. Specifi-
6665 cally, NTC18 code “Norme Tecniche per le Costruzioni” (D.M. Jan 17, 2008) and the specific and
6666 the severe regulations adopted by LNGS will be the reference documents for the requirements for
6667 the Experiment infrastructures.

6668 Concerning the HSE aspects, the standards will be those of the Italian “Testo Unico in Materia
6669 di Salute e Sicurezza nei Luoghi di Lavoro” (D.Lgs. 81/2008, and subsequent amendments and
6670 additions). As regards the environmental matters, the standard is the Italian “Norme in Materia
6671 Ambientale”(D.Lgs. 152/2006, and subsequent amendments and additions). Any change and/or
6672 minimal modification that could intervene during the construction and commissioning phases of the
6673 project will comply with the above regulations. The most delicate operations and activities will also
6674 be subject to additional, specific regulations and procedures as described in the following paragraph.
6675 Individual machines and equipment used in construction of the infrastructure are subject to the
6676 rules of construction and must adhere to the use of general and specific regulations of the European
6677 Community:

- 6678 i) Pressure Equipment Directive (PED) 2014/68/EU;
6679 ii) Machinery Directive 2006/42/EC;
6680 iii) CE conformity marking.

6681 *13.1.1. Procedural Process Authorization*

6682 The GADM Collaboration will comply with the Authorization Process required by LNGS before
6683 starting the operating phase of the experiment. As already implemented for DarkSide-50, prior to
6684 the start of operations, the DarkSide Collaboration will develop and provide to LNGS a complete
6685 risk assessment in 2 steps of the major hazards for DS-20k: the whole documentation will include
6686 both a Preliminary Risk Assessment (PRA) and a Quantitative Risk Assessment (QRA).

6687 **13.2. Work-site Organization and Preparation to Start**

6688 Once the authorization process is concluded and the approval is released by the LNGS Directorate
6689 to the Collaboration, the work-site preparations can begin, always focusing the needed attention
6690 upon all the possible consequences of the installation in the underground labs, both as regards
6691 safety and environment.

6692 The construction activity of DS-20k represents an important phase in term of HSE matters. The
6693 work required to build the facilities and structures of the Experiment will be performed by external
6694 contractors working under the direction of the collaboration. As foreseen by Title IV of the Italian
6695 law (D.Lgs. 81/2008), for large construction works, "registered professionals" must be appointed to
6696 prepare, elaborate, sign and apply mandatory safety-related document, e.g., the Piano di Sicurezza
6697 e Coordinamento (PSC): Safety and Coordination Plan. A safety coordinator in phase of design
6698 (CSP) must be appointed: the CSP must prepare a safety & coordination plan (PSC) specific for
6699 the foreseen activities; the PSC must be submitted to specific authorities. In a certain sense the
6700 PSC is a real design for the Safety over the whole installation process. Throughout the execution,
6701 the Safety Coordinator in phase of Execution (CSE) is appointed: the CSE is in charge of managing
6702 all interference risks related to the work-site, for all the phases and activities detailed in the PSC.

6703 For minor activities not subjected to the Title IV of the Italian D.Lgs. 81/2008, and not related
6704 to the main work-site for the installation process, the so called DUVRI (unique document for the
6705 evaluation of the risk of interference) is still required, accordingly to the Italian D.Lgs. 81/2008
6706 (and subsequent amendments and additions). As regards the work-site, the CSE will call for
6707 coordination meetings involving all the operators involved; participation is mandatory.

6708 In order to achieve a tight and effective coordination between LNGS Services, experimental
6709 Collaborations, and contracting companies (outsourcing personnel) operating in the Underground
6710 Lab, LNGS reserves the right to organize periodic meetings of all parties. The GADM Collaboration
6711 will actively promote the efficient coordination and management of all activities, in order to ensure
6712 compliance with the highest HSE levels required and targeted by LNGS.

6713 **13.3. Information, Education and Training**

6714 Information, education and training (IET) of the Collaboration members is a crucial aspect of
6715 the operation of the experiment. IET activities can be divided in two synergistic phases: general
6716 LNGS IET and experiment-specific IET. As required by the LNGS SMS and general access control
6717 rules, in order to be qualified to access and operate in the Underground Lab, all users are required
6718 to attend safety training conducted by LNGS.

6719 In addition, the GADM Collaboration, under the guidance of the GLIMOS and RAE, will hold
6720 specific HSE courses for all Collaboration members in order to inform and train them about the
6721 hazards and risks of the apparatus and the related facilities and plants. This will include an

6722 "in situ" safety tour and an on-line safety test, intended to verify the overall understanding and
6723 comprehension of HSE rules of the experiment. Members of the Collaboration's operating group
6724 will be trained for the specific operations to be carried out in the Underground Lab. Furthermore,
6725 all Collaboration members involved in operations codified by specific procedures will be trained
6726 accordingly.

6727

14. MANAGEMENT

6728 The Project Management Plan (PMP) is described in a separate document. Summary information
 6729 on cost and schedule from that document is integrated here; we refer the reader to the PMP
 6730 for details of the collaboration organization and management processes.

6731

14.1. Summary of the available funding

6732 The DS-20k experiment has been independently reviewed and approved by the funding agencies
 6733 listed below, considering the scientific and technical aspects as well the financial requests and their
 6734 basis of estimate. The primary funding for the experiment was approved by INFN at the end of
 6735 2016, with funds available from financial year 2017. At the time of writing this document, funds
 6736 have been granted by

- 6737 i) Istituto Nazionale di Fisica Nucleare (INFN-Italy), both through the standard funding sup-
 6738 port of the National Scientific Committee 2 (CSN2) and through additional funds as shown
 6739 in table [LV](#). Support is granted for Urania, Aria and DS-20k
- 6740 ii) United Kingdom Science and Technology Facilities Council (STFC-United Kingdom) (DS-20k).
- 6741 iii) Canadian Foundation of Innovation (CFI-Canada) with contributions to Urania and DS-20k.
- 6742 iv) National Science Foundation (NSF-USA), with a contribution to Urania and with funds
 6743 labeled as NSF Construction in table [LV](#). Additional funds, labeled as NSF Midscale, are
 6744 associated with a specific proposal for contributions to the DS-20k detector submitted in
 6745 April 2021. Its institutional scope and final budgets have been reviewed by the Large Facilities
 6746 Office of NSF, with a final decision due in Q1 of 2022.
- 6747 v) Department of Energy (DOE-USA), with contributions to Urania and project management.
- 6748 vi) The European Commission (Darkwave project) through a contribution to DS-20k included
 6749 in a Horizon 2020 Twinning grant led by Astrocent (Warsaw), with INFN and GSSI partici-
 6750 pation.
- 6751 vii) Institute for High Energy Physics of Beijing (IHEP) (DS-20k).
- 6752 viii) A joint grant of Russian and Italian groups from the “Programma di Cooperazione Scientifica
 6753 e Tecnologica bilaterale tra Italia e Federazione Russa” (DS-20k).

6754 Table [LV](#) specifies the amount of funding from each source in the categories of capital investment
 6755 (including both the R&D and the construction of the detector), labor, research support, travel,
 6756 management activities and, whenever explicitly available, the funds granted as contingency. The
 6757 contributions are all reported in € using exchange rates at the time of writing. The last column
 6758 reports the total amounts expressed in the original currency. The comparison of the contributions
 6759 in the second column requires care because of different rules for classification of funding of these
 6760 items in the various funding sources. For example, in case of INFN, there are additional funds for
 6761 contracts for postdoctoral researchers or PhD students locally administrated by each group, often
 6762 in co-funding mode with the local Universities, that are not listed in the table.

6763 The distribution of the construction scope of each funding source is reported in the Project Man-
 6764 agement Plan. We summarize here the same information, grouped following the description of the
 6765 items as presented in the PBS in figure [55](#): the Detector Elements scope is shown in tables [LVI](#) and
 6766 [LVII](#), the Photo-detectors scope is shown in table [LVIII](#), and the Argon extraction and distillation
 6767 scope is shown in table [LIX](#). Support Facilities items are distributed across these tables, in general
 6768 grouped together with the products the facilities deliver.

6769 The work break down structure (WBS), the cost prediction and funding allocations for the entire
 6770 detector are managed through the Primavera P6 software, under the responsibility of DOE. The
 6771 WBS structure is described in the PMP.

	Capital (k€)	Labor, travel, management	Contingency	Total	Total
	(k€)	(k€)	(k€)	(k€)	
DS-20k					
INFN CSN2	5383	970	-	5383	5383 €
INFN CIPE	15000	3000	-	18000	18000 €
INFN PON	17254	-	-	17254	17254 €
INFN Masterplan	-	2000	-	2000	2000 €
INFN Computing	2400	-	-	2400	2400 €
UK-STFC	387	1733	270	2120	1956 £
CFI	5633	2559	-	8192	11872 CAD
DOE	-	3059	-	3059	3702 \$
NSF Construction	770	119	-	889	994 \$
NSF Midscale	4382	3086	2210	9679	11712 \$
IHEP	230	-	-	230	1665 CNY
Astrocent	240	250	-	490	490 €
Italy-Russia	300	200	-	500	500 €
Aria and Urania					
Aria INFN	9731	2027	-	11759	11759 €
Aria not INFN	173	200	-	173	173 €
Urania INFN	8402	200	-	8402	8402 €
Urania NSF	2603	119	-	2721	3294 \$
Urania DOE	2644	1418	-	4062	4916 \$
Total	76788	20624	2480	99893	

TABLE LV. Summary of the major financial contributions to the DS-20k experiments. In kind contributions are not reported.

6772

14.2. INFN funds for DS-20k

6773 Table LX reports the present high level allocation of the INFN-CIPE and INFN-PON funds.
 6774 This table reflects that two choices adopted in the present design on the basis of their technical
 6775 and scientific impact– the use of electrical, instead of optical, signal transmission and the sum of
 6776 amplified tile signals– have saved approximately 4000 k€ previously allocated on INFN CIPE funds.

6777 While the destination of the INFN PON funds is quite rigid, that of INFN CIPE has more flex-
 6778 ibility. This feature, together with the technical choices mentioned above, enables grant resources
 6779 to fund some items that have extra cost with respect to the original prediction or were not included
 6780 in funded grants. We note the following about LX:

- 6781 • the item "Cryostat Project and Installation Support" includes the cost of professional services,
 6782 rent of space for temporary storage of the cryostat material during the construction phase,
 6783 material transportation, crane operators, surveyor services expected during the construction
 6784 of the cryostat and an estimation of tools needed during the installation
- 6785 • the item "NOA" includes the construction of the clean room and the procurement of all the
 6786 infrastructures necessary for the photo-detectors assembly
- 6787 • the cost of the titanium vessel is based on a preliminary quotation
- 6788 • items necessary in CR2 for the assembly of the inner detector are not included, as they are
 6789 part of the CFI and NSF contributions
- 6790 • the temporary structure on top of the cryostat in Hall C necessary during the installation is
 6791 not included as it is expected to be procured by CFI collaborators
- 6792 • 600 k€ are available for the procurement of a Rn abatement system for NOA-CR2, as dis-
 6793 cussed in 5.8.5
- 6794 • 1000 k€ are presently left unassigned to compensate for possible additional extra costs and
 6795 uncertainties in the cost evaluation
- 6796 • as of today (Dec. 2021) 7460 k€, approximately one half of the total amount, of INFN-CIPE
 6797 funds have been spent

6798 Table LXI reports the destination of the INFN-CSN2 capital funds. The allocation to the various

Overview of DS-20k Construction Scope	
Inner detector (TPC and inner Veto)	
INFN	<ul style="list-style-type: none"> Space within the NOA clean room potentially with radon mitigation for pre-installation assembly of the TPC and its integration with PDU, Veto and vPDU Recipe to produce Gd-loaded PMMA Procurement of Gd-loaded PMMA and other veto materials Procurement of Veto assembly mechanical tools Integration of ESR,PEN with LAr-TPC and supporting structures Integration of vPDU in the inner detector Procurement and installation of the titanium vessel
NSF	<ul style="list-style-type: none"> Final design engineering of the inner detector Procurement of PMMA and other materials Fabrication of HV system, gas pocket system, reflector panels and field cage resistor link, wire grid and titanium optical plane structure Procurement and fabrication of manipulator assembly fixtures for the NOA CR2 clean room space and adjacent staging area Technical personnel for assembly of the LAr-TPC components and PDM integration Design, procurement, fabrication of support hangers which suspend the LAr-TPC from the roof cap of the cryostat, and are integrated with the LAr-TPC mechanical structure Flanged feed-through chimneys passing detector power and signals between the interior and exterior of the cryostat Transport and delivery of the pre-assembled inner detector to underground area, ready for installation
CFI	<ul style="list-style-type: none"> Final design engineering of PMMA anode and cathode; Machining of PMMA anode and cathode Coating facilities TPB coatings Engineering, procurement & fabrication of the TPC assembly and transportation handling system
IHEP	<ul style="list-style-type: none"> Procurement of Gd-loaded PMMA
Astrocent	<ul style="list-style-type: none"> Procurement of ESR and PEN
Russia	<ul style="list-style-type: none"> Contribution to the procurement of titanium

TABLE LVI. Distribution of the construction scope by funder: Detector Elements PBS branch, TPC & inner Veto items.

6799 items, and the specific amounts approved in 2017 are reported in the column labeled as "planned".
 6800 Some minor refinements were applied during the subsequent years as the funds are made available
 6801 on a year-by-year basis. The column "spent" reports the sum of the funds assigned, including the
 6802 assignments already approved for the year 2022 (with the "sub-judice" funds of 2022 excluded).
 6803 The last column shows the difference of the first two and it represents the residual amount to be
 6804 granted.

6805 14.3. Collaboration funds for DS-20k

6806 The funding is summarized in table LV. Our current evaluation of the construction costs is very
 6807 close to the total of the available funds, under the hypothesis that the NSF Midscale funds will be

Overview of DS-20k Construction Scope	
Outer Veto	
STFC	<ul style="list-style-type: none"> Procurement of assembly materials for outer veto SiPM tiles and photo detector units (vPDU) Assembly line facility and personnel for production of outer vPDU in the U.K
NSF	UAr cryogenics Design, procurement, fabrication and installation of a cryogenics system serving the underground argon volume in the LAr-TPC
Calibration	
NSF	<ul style="list-style-type: none"> Design, procurement, fabrication, assembly of a guide tube system with sources, used for moving sources between the exterior of the cryostat and the inner detectors Controls software and monitoring devices for the guide tube system
Electronics and DAQ	
INFN	<ul style="list-style-type: none"> Procurement of digitizers for prototype systems Procurement of CPU and storage for prompt experiment data analysis Installation of equipment in Hall C
CFI	<ul style="list-style-type: none"> Procurement of digitizers, cabling, VME crates, timing and trigger system hardware, front-end DAQ computers, network switches and network cabling Installation of equipment in Hall C
Cryostat and AAr cryogenics	
INFN	<ul style="list-style-type: none"> Procurement, fabrication of a membrane cryostat in a CERN-designed steel structure, and its installation in Hall C of LNGS Design, fabrication and installation of a cryogenics system serving the atmospheric argon volume within the membrane cryostat
Installation	
INFN	<ul style="list-style-type: none"> Procurement and installation of infrastructures serving the experiment (metallic structure for cryogenic system support, support items for the cryostat installation, connections to cryogens supply, electrical power, control room) Provision of installation support such as: lifting fixtures, scaffolding, temporary supports for detector elements, ventilation for enclosed spaces, etc. Coordination and oversight of detector installation activities
Data	
XX	xx

TABLE LVII. Distribution of the construction scope by funder: Detector Elements PBS branch for items other than TPC & inner Veto.

- available. In this case, we have identified a small number of critical items:
- Shipping vessels of the UAr: a part of the cost is not granted (~ 2400 k€) and it will be inserted in a funding request that will be submitted to CFI in June 2022
 - the cost of the Gd compound (estimated to be $\sim 300\text{-}400$ k€) is presently not covered by available grants. The decision about the PMMA mixing recipe is expected at the beginning of 2022 and funds will be requested to INFN or to IHEP, depending on details of the technical choice. We note that, for what concerns INFN funds, in table LXI there are funds still available for Veto items which could cover a large fraction of the cost of the Gd compound. This is because the present design of the inner detector and of the vPDU+ implemented some

Overview of DS-20k Construction Scope	
	Photo-Detectors
INFN	<ul style="list-style-type: none"> Validation of the cryogenic SiPMs and their procurement Final design of the photo detector units for TPC (PDU) and Veto (vPDU) Procurement and fabrication of assembly materials for production of PDUs Procurement of printed circuit boards, electronics, radiopure connectors and mechanical components for the full production of PDU and vPDU NOA clean room facility, outfitted for processing of all SiPM wafers and personnel for the production line of all TPC SiPM tiles and PDU Infrastructure and operations of the PDU test facility All cabling inside the cryostat and all power supplies
STFC	<ul style="list-style-type: none"> Procurement of assembly materials for veto SiPM tiles and photo detector units (vPDU) Assembly line facility and personnel for production of vPDU in the U.K. Infrastructure and operations of the vPDU test facility

TABLE LVIII. Distribution of the construction scope by funder: Photo-detectors PBS branch.

Overview of DS-20k Construction Scope	
	Urania
INFN	Design and fabrication of the gas separation plant components, and delivery to CO
NSF	<ul style="list-style-type: none"> Design and civil construction of the plant site in CO, with electrical and mechanical systems adequate for supporting the plant, and with a shipping and receiving area for transport of the underground argon Installation of the plant components Commissioning of the plant components
CFI	<ul style="list-style-type: none"> Procurement of vessels for shipping UAr between North America and Europe Gas analysis system within the Urania facility
DOE	Operation of the gas separation facility for the period necessary to extract the volume for the DS-20k detector
Aria	
INFN	<ul style="list-style-type: none"> Construction of the Aria cryogenic distillation facility Operation of Aria for the processing the UAr for DS-20k Purified UAr ready to be delivered to LNGS Transportation costs of UAr from Urania to Aria and to LNGS

TABLE LIX. Distribution of the construction scope by funder: Argon extraction and distillation PBS branch.

- 6817 simplifications allowing reduction in costs with respect to the original prediction.
 6818 • Significant resources are allocated for the Rn abatement system in NOA-CR2 (see table LX),
 6819 however it is not yet established that they are sufficient. A joint working group, including
 6820 LNGS staff working on the NOA infrastructure and DS-20k collaborators, should be urgently
 6821 established to study and address the most reasonable technical choices considering the oper-
 6822 ations of the facility.
 6823 • Funding for the procurement of the AAr for filling the cryostat (~ 800 k€) are not included
 6824 in the present budget.

item	INFN	CIPE	INFN	PON	Total
	k€		k€		k€
NOA	6713		1900		8613
SiPM	685		5435		6120
Electronics prototypes	385		-		385
LNGS Lab. Infrastructures	286		-		286
Cables	333		-		333
Electronics Components full production (not ASIC)	683		-		683
PCB full production	1000		-		1000
ASIC	150		-		150
Cryostat Project and Installation Support	981		-		981
Cryostat Construction	-		5872		5872
AAr Cryogenics	-		2320		2320
Cryogenic support structure	-		205		205
Titanium vessel	673		737		1400
Installation in Hall C	635				635
Rn abatement in NOA CR2	600				600
CIPE budget available for extra costs	1000		-		1000
Power supplies	650		-		650
Outreach	67		-		67
Other	24		-		24
Electrical system LNGS	-		795		795
Total	15015		17234		22600

TABLE LX. High level allocation of INFN-CIPE and PON funds

item	planned	spent	expected
	k€	k€	k€
SiPM and electronics	3141	2163	977
Veto	861	126	735
DAQ	345	182	162
Red	390	262	127
Proto	396	317	79
TPC Installation	200	-	200
Safety	50	50	-
Total	5383	3101	2282

TABLE LXI. Summary of the INFN-CSN2 funds.

6825

14.4. Schedule

6826 A high-level summary of the technically-driven schedule for the construction of DS-20k is shown
 6827 in figure 174. The longest operation is the delivery of the UAr. The end of the construction
 6828 (December 2024) is expected before the full amount of UAr will be delivered in LNGS. As such,
 6829 the present organization of the construction and installation work has some modest contingency
 6830 for unexpected delays.

6831 We identify the major critical items as the construction of the cryostat and the AAr cryogenics.
 6832 The construction of these two items is granted through INFN PON funds with technical expertise
 6833 at CERN. Following initial contacts between the CERN and INFN administration during 2019, the
 6834 expected procedure to purchase the two items was through an order issued by INFN to CERN fol-
 6835 lowing the italian rules of "Codice degli appalti pubblici". However, administrative difficulties from
 6836 CERN lead the INFN management to investigate and set up an alternative approach, based on a
 6837 Memorandum of Understanding between CERN and INFN. Contacts are presently in progress with
 6838 the Italian Ministry to get the proper authorization to spend the money through this new procedure.
 6839 All these procedures are not managed directly by INFN and not by the GADM Collaboration.

6840 A draft of the INFN-CERN MoU is in advanced stage and it contains the schedule reported here,
 6841 that optimistically assumes the process starts in December 2021 with orders for materials placed

6842 by CERN. The schedule of figure 174 shows that a delay longer than 5 months in reaching the
 6843 milestone that the interior of the cryostat is ready, to transform into a clean room to initiate the
 6844 detector installation, will affect the schedule of the construction by the same amount of time.

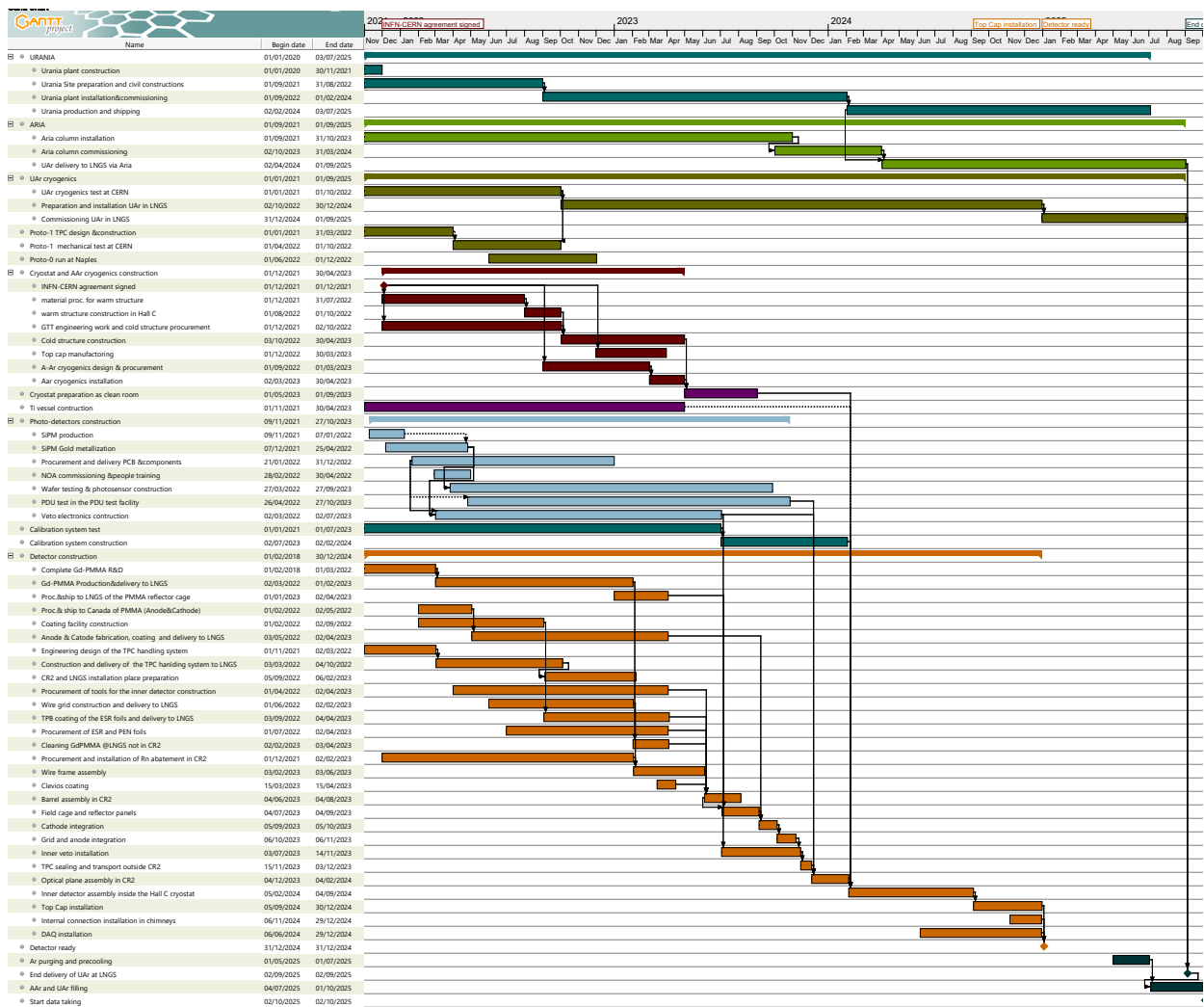


FIG. 174. Schedule of the construction of the DS-20k detector.

6845

14.5. Commissioning of the detector

6846 This document describes the design, construction and assembly of the DS-20k detector. The
 6847 operations necessary to fill it with AAr have not been described here, and the cost evaluation
 6848 presented here also does not include the purchasing of the AAr or any additional commissioning
 6849 costs. As reported in section 11.9, the details of the AAr fill and detector commissioning plan are
 6850 the subject of a separate, future document.

6851

14.6. Memorandum of Understanding

6852 The present Technical Design Report has been approved by the DS-20k Institutional Board on
 6853 November 30, 2021. Based on this document, a Memorandum of Understanding among all the

6854 Institutions contributing to the project is going to be prepared.

6855 **14.7. Summary of the requests to the LNGS laboratory**

6856 We summarize here the main interfaces and requests to the LNGS laboratory, integrating the
6857 discussion throughout this document.

- 6858 • preparation of the Hall C floor for the cryostat installation, as discussed in section 11.1
- 6859 • no additional chemicals with respect to the ones already listed in the VINCA document
6860 prepared in 2021 by the collaboration and the LNGS safety group
- 6861 • cryogenic cooling power of 10.5 kW in Hall C (during the standard data taking period) with
6862 the possibility of temporary reaching 12.5 kW in case of liquid AAr re-circulation, as presented
6863 in section 7.1.5
- 6864 • use of the DarkSide-50 control room in Hall C
- 6865 • estimation of the electrical power: 267 kW (90 kW for the DAQ computers in the control
6866 room, 90 kW for the air conditioning system, 10 kW for the electronics on top of the cryostat,
6867 27 kW for the AAr cryogenic plant as from extrapolation of the data of Proto-Dune, 50 kW
6868 for ancillary equipment including the Rn abatement and air circulation inside the cryostat
6869 during the installation).
- 6870 • proper air conditioning in the control room (see above)
- 6871 • use of the entire NOA clean room for the photo-detector and inner detector systems assembly,
6872 with its standard specifications (ISO Class 6 clean room, UPS 80 kVA)
- 6873 • Rn abatement system ($\sim 600 \text{ m}^3/\text{h}$), reaching $100 \text{ mBq}/\text{m}^3$ during the time of the inner
6874 detector assembly in NOA CR2 (see section 5.8.5. A joint working group including people
6875 of the LNGS NOA team and of the collaboration should elaborate details toward the most
6876 suitable solution.
- 6877 • availability of space near the west area of CR2, as described in section 11.7.2
- 6878 • grounding system of the cryostat to be discussed and agreed
- 6879 • office space above ground. The number of rooms should be discussed with LNGS directorate
6880 according to the rules for room occupancy.
- 6881 • Use of the noble gas compressor system (under procurement for LNGS-wide service with
6882 funds from BMBF);
- 6883 • space for UAr skids, as discussed in section 10.1.2
- 6884 • safety system in Hall C to handle the liquid argon

6885 For the DarkSide-50 program the Collaboration, supported by funds from the U.S. NSF, built the
6886 two radon-suppressed clean rooms CR1 and CRH and refurbished the CTF for operation of small
6887 cryogenic payloads with associated cryogenic systems sited in CRH. The Collaboration retains an
6888 interest in the facilities and will discuss their potential use for DS-20k with the LNGS Director.

- 6889 [1] A. Gola et al., *Sensors* **19** (2019).
- 6890 [2] C. E. Aalseth et al. (The DarkSide Collaboration), *Eur. Phys. J. Plus* **133**, 131 (2018).
- 6891 [3] P. Agnes et al. (The DarkSide Collaboration), *Phys. Rev. D* **98**, 102006 (2018).
- 6892 [4] P. A. Amaudruz et al. (The DEAP-3600 Collaboration), *Phys. Rev. Lett.* **121**, 071801 (2018).
- 6893 [5] R. Ajaj et al. (The DEAP Collaboration), *Phys. Rev. D* **100**, 022004 (2019).
- 6894 [6] P. Agnes et al. (The DarkSide Collaboration), *Phys. Lett. B* **743**, 456 (2015).
- 6895 [7] P. Agnes et al. (The DarkSide Collaboration), *JINST* **11**, P12007 (2016).
- 6896 [8] P. Agnes et al. (The DarkSide collaboration), *JINST* **11**, P03016 (2016).
- 6897 [9] P. Agnes et al. (The DarkSide Collaboration), *Phys. Rev. D* **93**, 081101 (2016).
- 6898 [10] P. Agnes (Université Paris Diderot), Ph.D. thesis, Université Paris Diderot (2016), URL <https://tel.archives-ouvertes.fr/tel-01497505v1>.
- 6900 [11] P. Agnes et al. (The DarkSide Collaboration), *JINST* **12**, P12011 (2017).
- 6901 [12] P. Agnes et al. (The DarkSide Collaboration), *JINST* **12**, P01021 (2017).
- 6902 [13] P. Agnes et al. (The DarkSide Collaboration), *JINST* **12**, P10015 (2017).
- 6903 [14] P. Agnes et al. (The DarkSide Collaboration), *JINST* **12**, T12004 (2017).
- 6904 [15] P. Agnes et al. (The ARIS Collaboration), *Phys. Rev. D* **97**, 10 (2018).
- 6905 [16] P. Agnes et al. (The DarkSide Collaboration), *Nucl. Inst. Meth. A* **904**, 23 (2018).
- 6906 [17] P. Agnes et al. (The DarkSide Collaboration), *Phys. Rev. Lett.* **121**, 081307 (2018).
- 6907 [18] P. Agnes et al. (The DarkSide Collaboration), *Phys. Rev. Lett.* **121**, 111303 (2018).
- 6908 [19] B. Abi et al. (The DUNE Collaboration), *JINST* **15**, T08008 (2020).
- 6909 [20] B. Abi et al. (The DUNE Collaboration), *JINST* **15**, T08009 (2020).
- 6910 [21] B. Abi et al. (The DUNE Collaboration), *JINST* **15**, T08010 (2020).
- 6911 [22] P. Agnes et al., *Eur. Phys. J. C* **81**, 359 (2021).
- 6912 [23] CERN, *Physics at the FCC-hh, a 100 TeV pp collider* (2017), URL <https://e-publishing.cern.ch/index.php/CYRM/issue/view/35>.
- 6913 [24] J. Billard, E. Figueroa-Feliciano, and L. Strigari, *Phys. Rev. D* **89**, 023524 (2014).
- 6914 [25] M. Pato et al., *Phys. Rev. D* **83**, 083505 (2011).
- 6915 [26] J. L. Newstead et al., *Phys. Rev. D* **88**, 076011 (2013).
- 6916 [27] D. S. Akerib et al. (The LUX-ZEPLIN Collaboration), *Phys. Rev. D* **101**, 351 (2020).
- 6917 [28] E. Aprile et al. (The XENON Collaboration), *JCAP* **2020**, 031 (2020).
- 6918 [29] E. Aprile et al. (The XENON Collaboration), *Phys. Rev. Lett.* **121**, 111302 (2018).
- 6919 [30] E. Bagnaschi et al., *Eur. Phys. J. C* **78**, 87 (2018).
- 6920 [31] P. Agnes et al., *Phys. Rev. D* **104**, 082005 (2021).
- 6921 [32] P. Agnes et al., *2021*, 043 (2021).
- 6922 [33] D. Franco et al., *JCAP* **2016**, 017 (2016).
- 6923 [34] M. Agostini et al. (The Borexino Collaboration), *Nature* **562**, 505 (2018).
- 6924 [35] T. Mróz, P. P. Czudak, M. Wójcik, and G. Zuzel, *Studies of bulk $^{210}\text{Po}/^{210}\text{Pb}$ contamination in high purity copper for low-background detectors* (2021), URL https://indico.ific.uv.es/event/6178/contributions/15941/attachments/9251/12395/TAUP_conference_2021_Tomasz_Mroz.pdf.
- 6925 [36] F. Alessandria et al., *Astroparticle Physics* **45**, 13 (2013).
- 6926 [37] F. Acerbi et al., *IEEE Trans. Elec. Dev.* **64**, 521 (2017).
- 6927 [38] G. Collazuol et al., *Nucl. Inst. Meth. A* **628**, 389 (2011).
- 6928 [39] G. Gallina and et al., *Nuclear Instruments and Methods in Physics Research, Section A: Accelerators, Spectrometers, Detectors and Associated Equipment* **940**, 371 (2019).
- 6929 [40] G. Gallina and F. Retière, *EPJ Web of Conferences* **227**, 02002 (2020).
- 6930 [41] A. N. Otte, D. Garcia, T. Nguyen, and D. Purushotham, *Nuclear Instruments and Methods in Physics Research Section A* **846**, 106 (2017).
- 6931 [42] G. Gallina and et al., *IEEE Transactions on Electron Devices* **66**, 4228 (2019).
- 6932 [43] M. D'Incecco et al., *IEEE Trans. Nucl. Sci.* **65**, 591 (2018).
- 6933 [44] M. D'Incecco et al., *IEEE Trans. Nucl. Sci.* **65**, 1005 (2018).
- 6934 [45] S. COMSOL AB, Stockholm, , *COMSOL Multiphysics® v. 5.6*, URL www.comsol.com.
- 6935 [46] M. F. Weber et al., *Science* **287**, 2451 (2000).
- 6936 [47] I. Ouchi, I. Nakai, M. Ono, and S. Kimura, *J. Appl. Polym. Sci.* **105**, 114 (2007).
- 6937 [48] H. Nakamura, Y. Shirakawa, S. Takahashi, and H. Shimizu, *EPL* **95**, 22001 (2011).
- 6938 [49] Kuźniak, M. Broerman, B. Pollmann, T. and Araujo, G. R, *Eur. Phys. J. C* **79**, 291 (2019).
- 6939 [50] J. Soto-Otón, *Measurements of the polyethylene naphthalate performance as a wavelength shifter in ProtoDUNE- DP* (2020), presented at Neutrino 2020, URL <https://doi.org/10.5281/zenodo.694450>.

- 6946 4252545.
- 6947 [51] Y. Abraham et al., arXiv:2103.03232v2 (2021).
- 6948 [52] R. Francini et al., *J. Instrum.* **8**, P09006 (2013).
- 6949 [53] M. G. Boulay et al., *Direct comparison of pen and tpb wavelength shifters in a liquid argon detector* (2021), 2106.15506.
- 6950 [54] E. Segreto, *JINST* **7**, P05008 (2012).
- 6951 [55] W. Daoud and K. Renken, *Science of The Total Environment* **272**, 127 (2001), radon in the Living Environment.
- 6952 [56] T. Yano, *Nuclear Instruments and Methods in Physics Research Section A: Accelerators, Spectrometers, Detectors and Associated Equipment* **845**, 425 (2017), proceedings of the Vienna Conference on Instrumentation 2016.
- 6953 [57] K. Hagiwara et al., *Progress of Theoretical and Experimental Physics* **2019** (2019), 023D01.
- 6954 [58] C. M. Nantais, B. T. Cleveland, and M. G. Boulay, *AIP Conf. Proc.* pp. 185–188 (2013).
- 6955 [59] C. Chuanya (For the Juno Collaboration), *A convenient approach to determine U/Th in acrylic to sub-ppt level* (2019), URL https://indico.cern.ch/event/716552/sessions/310940/attachments/1848752/3040841/A_Convenient_Approach_to_Sub-ppt_Level_Measuring_of_U_and_Th_in_Acrylic.pdf.
- 6956 [60] H. Cao et al. (The SCENE Collaboration), *Phys. Rev. D* **91**, 092007 (2015).
- 6957 [61] T. Alexander et al. (The SCENE Collaboration), *Phys. Rev. D* **88**, 092006 (2013).
- 6958 [62] M. G. Boulay (For The DEAP Collaboration), *J. Phys. Conf. Ser.* **375**, 012027 (2012).
- 6959 [63] P. Adhikari et al., *Eur. Phys. J. C* **80**, 303 (2020).
- 6960 [64] P. Adhikari, R. Ajaj, and M. e. a. Alpízar-Venegas, *Euro. Phys. J. C* **81** (2021).
- 6961 [65] X. Li (for the ReD Collaboration) (2021), 17th International Conference on Topics in Astroparticle and Underground Physics (TAUP 2021), URL <https://indico.ific.uv.es/event/6178/contributions/15829/>.
- 6962 [66] P. Agnes et al., *Eur. Phys. J. C* **81**, 1014 (2021).
- 6963 [67] S. Vinogradov et al., *IEEE Nuclear Science Symposium Conference Record* (2010).
- 6964 [68] S. S. Westerdale and P. D. Meyers, *Nucl. Inst. Meth. A* **875**, 57 (2017).
- 6965 [69] E. Mendoza et al., *Nucl. Inst. Meth. A* **960**, 163659 (2020).
- 6966 [70] A. J. Koning, *AIP Conf. Proc.* **769**, 1154 (2005).
- 6967 [71] H. Wulandari, J. Jochum, W. Rau, and F. von Feilitzsch, *Astropart. Phys.* **22**, 313 (2004).
- 6968 [72] D. Akimov et al., *Phys. Rev. Lett.* **126**, 012002 (2021).
- 6969 [73] M. Stein et al., *Nucl. Inst. Meth. A* **880**, 92 (2018).
- 6970 [74] R. N. Saldanha et al., *Phys. Rev. C* **100**, 024608 (2019).
- 6971 [75] J. F. Ziegler, *IBM J. Res. & Dev.* **42**, 117 (1998).
- 6972 [76] P. Adhikari et al., *Eur. Phys. J. C* **80**, 1 (2020).
- 6973 [77] Maximum Integrated Data Acquisition System, , *MIDAS home page*, URL https://midas.triumf.ca/MidasWiki/index.php/Main_Page.
- 6974 [78] G. Gallina et al. (The nEXO Collaboration), *Nucl. Inst. Meth. A* **940**, 371 (2019).
- 6975 [79] 4th Workshop on Electronics for LHC Experiments (LEB 98) (1998), Presentation at V. Radeka.
- 6976 [80] A. A. Abud et al., :2108.01902 (2021).
- 6977 [81] C. E. Aalseth et al. (The DarkSide Collaboration), *JINST* **15**, P02024 (2020).
- 6978 [82] CHIP QUIK, *Solder paste no-clean sn42/bi57.6/ag0.4 in jar 250g t4 mesh - datasheet revision 1.3* (2017 [Online]), URL <https://www.chipquik.com/datasheets/SMDLTLFP250T4.pdf>.
- 6979 [83] ASM AMICRA Microtechnologies GmbH, *Nova plus die bonder* (2021 [Online]), URL <https://amicra.com/products/die-flip-chip-bonder/nova-plus-die-bonder-and-flip-chip-bonder>.
- 6980 [84] Indium Corporation, *Nc-smq80 solder paste data sheet* (2021 [Online]), URL <https://documents.indium.com/qdynamo/download.php?docid=92>.
- 6981 [85] Hesse Mechatronics, *Fine wire bonder bondjet bj855* (2020 [Online]), URL <https://www.hesse-mechatronics.com/en/products/fine-wire-bonder/bj855/#toggle-id-2>.
- 6982 [86] G. Seidel, R. Lanou, and W. Yao, *Nuclear Instruments and Methods in Physics Research Section A: Accelerators, Spectrometers, Detectors and Associated Equipment* **489**, 189 (2002).
- 6983 [87] E. Grace, A. Butcher, J. Monroe, and J. A. Nikkel, *Nucl. Inst. Meth. A* **867**, 204 (2017).
- 6984 [88] P.-A. Amaudruz et al., *Astroparticle Physics* **108**, 1 (2019).
- 6985 [89] R. H. French, *Journal of the American Ceramic Society* **83**, 2117 (2000).
- 6986 [90] J. F. Amsbaugh et al., *Nucl. Inst. Meth. A* **579**, 1054 (2007).
- 6987 [91] G. Alimonti et al. (The Borexino Collaboration), *Nucl. Inst. Meth. A* **600**, 568 (2009).
- 6988 [92] D. S. Akerib et al., *The European Physical Journal C* **80**, 1044 (2020).